

Tensile Properties and Microstructures of Laser-Formed Ti-6Al-4V

J. Alcisto, A. Enriquez, H. Garcia, S. Hinkson, T. Steelman, E. Silverman, P. Valdovino, H. Gigerenzer, J. Foyos, J. Ogren, J. Dorey, K. Karg, T. McDonald, and O.S. Es-Said

(Submitted December 15, 2009)

The room temperature tensile properties of Ti-6Al-4V alloy prepared under two different processing routes were evaluated and compared. One group of samples was prepared by conventional casting-forging-rolling into flat plates. The other group was prepared by using Triton's Laser Free-Form Fabrication (LF3)TM processes, i.e., a laser was used to melt pre-alloyed powders of the required metallic composition as they were dropped onto a moveable substrate programmed to move in such a manner as to form a solid alloy plate. Five populations of Ti-6Al-4V were evaluated: a standard wrought form, an as-deposited form, a machined as-deposited form, a heat-treated as-deposited form, and a machined as-deposited and heat-treated form. The poorest mechanical properties occurred with the rough surfaces, likely due to existing microcracks and stress concentrations. The LF3TM as-deposited material had mechanical properties comparable to, if not higher than, the mechanical properties of the wrought material. Further evaluations of the laser-formed material for complex spacecraft piece parts were warranted, specifically in regards to improving the surface finish of the materials.

Keywords laser free-form fabrication (LF3), mechanical properties, microstructure, Ti-6Al-4V

1. Introduction

Ti-6Al-4V is the most widely used titanium alloy (Ref 1). It accounts for more than 50% of all titanium usage in the world, with the aerospace industry utilizing more than 80% of this usage. In its wrought form, this alloy accounts for more than 95% of the market (Ref 2, 3). Its applications are mostly in the aircraft industry for jet engine auxiliary parts, for aerospace frames and for chemical processing plants (Ref 1). Ti-6Al-4V alloys are widely used in industrial sectors due to their good stability at high temperature, high specific strength, especially at high operating temperatures, and good corrosion resistance in many corrosive media (Ref 3).

Ti-6Al-4V is an expensive material. Its nominal cost is approximately \$59.53 per kg (nominally \$27 per lb) (Ref 4). Through conventional means, Ti-6Al-4V components are typically made through casting, forging, and powder metallurgy processes, but Ti-6Al-4V castings are about two to three times the cost of superalloy castings due to the required process conditions. Forging processes cannot easily produce complex

shapes, and powder metallurgy processes result in components with lower mechanical properties (Ref 2). Additionally, Ti-6Al-4V is very difficult to weld, increasing the price to produce components by conventional means even further (Ref 2).

An approach based on laser deposition has been developed to overcome this waste of expensive metal. Laser deposition processes differ from traditional forming techniques in the sense that they require no mechanical contact and, therefore, offer the advantage of process flexibility (Ref 5). Laser forming can produce geometries and shapes that are pre-designed out of metallic components with minimal distortion. The inherent advantage of using laser melting techniques is to control both location of the beam and the resulting component microstructure, leading to better service performance of components (Ref 5, 6).

In laser forming, pre-alloyed metallic powder particles are dropped onto a mobile platform (a substrate surface) and are melted while in transit by a laser. Typical commercial laser deposition processes include the Laser Engineering Net Shape (LENSTM) process and AeroMet's Laser Additive Manufacturing (LAM) process. This article introduces a process known as the Laser Free-Form Fabrication (LF3TM) process. All three of these techniques are considered laser surface-melting (LSM) processes that allow the user to modify the surface properties of engineering components at selected areas with micron level precision and without distortion. A detailed description of these processes is given in Ref 7-16. Figure 1 demonstrates the LF3TM process.

Since rapid prototype manufacturing was first invented more than 25 years ago, there was demand within industry to make prototypes not just out of plastic/polymer resin materials, but out of more robust materials; even out of the end design material, if possible. At best, the early rapid prototyping parts could be used as patterns to investment cast parts out of the metal alloy of choice, but the ultimate goal remained to direct

J. Alcisto, A. Enriquez, H. Garcia, S. Hinkson, J. Foyos, J. Ogren, J. Dorey, and O.S. Es-Said, Mechanical Engineering Department, Loyola Marymount University, One LMU Drive, Los Angeles, CA 90045; **T. Steelman, E. Silverman, and P. Valdovino**, Northrop Grumman, Space Technology, One Space Park, Redondo Beach, CA 90278; and **H. Gigerenzer, K. Karg, and T. McDonald**, Triton Systems Incorporated, 200 Turnpike Road, Chelmsford, MA 01824. Contact e-mail: oessaid@lmu.edu.

manufacture near-net-shape components using only a CAD file and wire or powder forms of the metal alloy of choice. The evolution of LF3™, LENSTM, and other LAM processes from rapid prototyping basically involved the incorporation of higher power lasers and tighter control of the fabrication environment (ambient gases) as well as the development of equipment and techniques to accommodate the processing of metal alloys.

The purpose of this study was to develop an initial database in which the mechanical properties of Ti-6Al-4V prepared by two processing routes could be compared. The goal was to determine if the properties of the laser-formed material, using the LF3™ technique, were sufficiently close to wrought Ti-6Al-4V to allow this material to replace conventionally processed spacecraft hardware. The impetus for the activity was a desire to reduce the manufacturing cost of selected parts of spacecraft hardware.

2. Experimental

In this initial evaluation of the LF3™ process, simple rectangular plates were used as the test materials. The plates were furnished by Triton Systems, Inc. in the form of plates 10 by 20 by 0.2 cm (4 by 8 by 0.08 in.) in the *x*-, *z*-, and *y*-directions, respectively. One such plate is shown schematically in Fig. 2(a). The dotted lines in the figure depict the paths along which the alloy was deposited. The *x*-direction was arbitrarily chosen to be the “parallel” direction or the length, while the *z*-direction was chosen to be the “transverse” direction or the height, and the *y*-direction was the thickness. Figure 2(a) shows schematically the orientations of the tensile samples that were extracted from the plates. The tensile tests were conducted at least in triplicate, and the values quoted later in this article are the averages of the three measured values, Table 1.

The top surface shown in Fig. 2(b) and (c) is an as-deposited surface and, for all the plates, it was rough. These are the surfaces that will be denoted as not machined. The side surfaces of the tensile samples were always machined in the process of making tensile samples.

Triton Systems, Inc. deposited seven plates, which were designated as 1-7, Fig. 3. Some were not machined (1 and 7), others were machined (2-6), some were heat treated (5-7), and

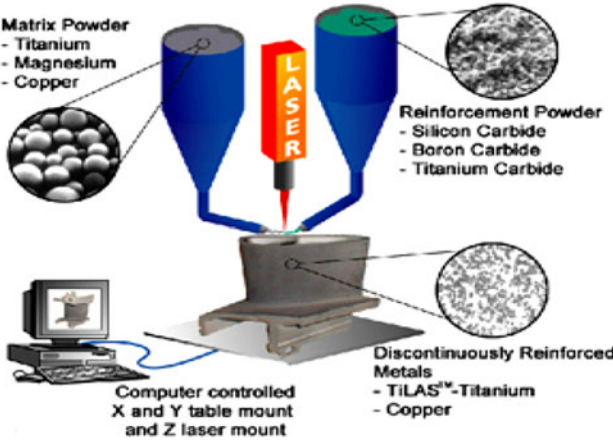


Fig. 1 Schematic view of laser forming

others were not (1-4). The deposition conditions and all compositional information regarding the plates are commercially sensitive and therefore are unavailable in detail. These deposition conditions and compositional information include some of the following process parameters and specifications. LF3™ process control involves parameters such as inert chamber gas type and quality (parts per million of oxygen), laser power, laser pulse rate, laser beam focal length and spot size at focus, powder feed rate, traverse speeds, bead overlap and others. The control of the metal alloy powder includes specifications such as alloy composition and oxygen content, porosity levels within particles, particle shape, and particle size. However, all plates were deposited using the same conditions.

Figure 3 depicts the orientations of the tensile samples extracted from the plates. The dotted lines indicate the path of the laser deposit. The *x*-direction indicates the length and the *z*-direction indicates the long transverse direction of the deposited material. Tensile bars designated (*x*) have the deposited layers along the length of the tensile bars, and those designated (*z*) have the layers perpendicular to the tensile bars, Fig. 2(b) and (c). The tensile samples in the *x* and *z* directions were machined from the seven plates and characterized by the number of the plate. For example, 1*x* characterized a tensile bar machined from plate 1 in the *x* direction.

Plates 2 and 3 differ in that the samples in plate 2 were extracted from a section of the plate that was deposited at the beginning of a particular run. In contrast, the samples in plate 3 were taken from the section of the plate that was deposited toward the end of a particular deposition run.

Plates 3 and 4 differ in that one is orthogonal to the other. In other words, plate 4 represents a run in which numerous short

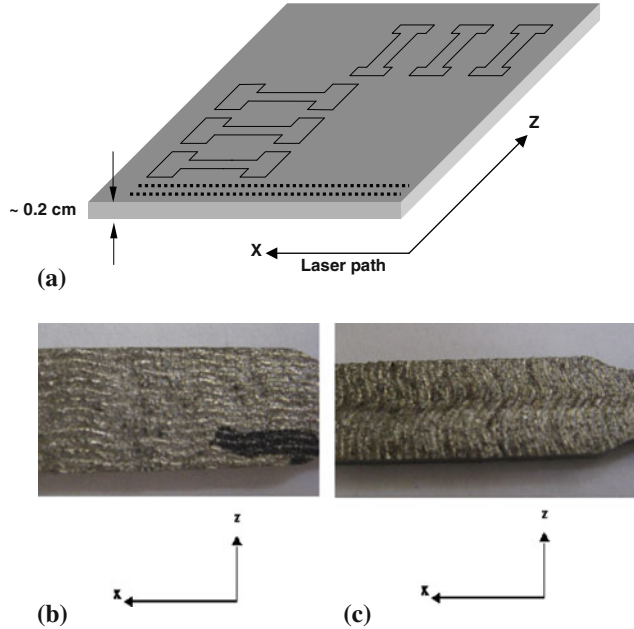


Fig. 2 (a) Schematic view of a laser-formed Ti-6Al-4V plate from which tensile samples were extracted. The dotted lines depict the path of metal deposition. The actual plates were approximately 0.2 cm (0.08 in.) thick. (b) As-deposited surface in the *x*-direction. The specimen is 0.9525 cm (0.375 in.) wide. (c) As-deposited surface in the *z*-direction. The specimen is 0.9525 cm (0.375 in.) wide

Table 1 Tensile properties of wrought and laser formed plates

Plate #	ID	Width cm, in.	Thickness, cm/in.		σ_u , ksi/MPa		σ_y , ksi/MPa		% Elong.	
			cm	in.						
Wrought	1a	1.27	0.50	0.24	0.093	153.1	1055.9	139.0	958.6	13.9
	1b	1.29	0.51	0.24	0.093	154.0	1062.1	140.5	969.0	16.7
	1c	1.26	0.49	0.24	0.093	154.0	1062.1	140.1	966.2	12.4
	1d	1.26	0.49	0.24	0.093	155.0	1069.0	140.9	971.7	13.9
	1e	1.26	0.49	0.24	0.093	154.5	1065.5	139.8	964.1	12.3
	Avg					154.1	1062.9	140.1	965.9	13.8
1 As-deposited not machined	1x1	0.67	0.26	0.25	0.1	132.4	913.1	129.7	894.5	6.0
	1x2(a)	0.65	0.25	0.25	0.1	133.9	923.4	131.3	905.5	6.0
	1x3	0.65	0.25	0.25	0.1	130.8	902.1	127.7	880.7	6.3
	1x4	0.64	0.25	0.25	0.1	131.2	904.8	128.8	888.3	7.2
	Avg					132.1	910.9	129.4	892.2	6.4
	1z1	0.66	0.26	0.25	0.1	119.0	820.7	75.7	522.1	1.5
	1z2	0.64	0.25	0.25	0.1	114.9	792.4	n/a	n/a	2.0
	1z3	0.65	0.25	0.25	0.1	110.4	761.4	n/a	n/a	1.4
	1z4(a)	0.65	0.25	0.25	0.1	118.0	813.8	75.8	522.8	2.0
	Avg					115.6	797.1	75.8	522.4	1.7
2 As-deposited machined	2x1	0.69	0.27	All thickness were within		156.0	1075.9	136.4	940.7	n/a
	2x2	0.64	0.25	0.15-0.2 cm		155.6	1073.1	139.1	959.3	7.7
	2x3(a)	0.68	0.27	(0.06-0.08 in.)		152.2	1049.7	137.0	944.8	5.9
	2x4(b)	0.69	0.27	(0.06-0.08 in.)		149.8	1033.1	n/a	n/a	n/a
	Avg					153.4	1057.9	137.5	948.0	6.8
	2z1	0.64	0.25	All thickness were within		145.5	1003.4	n/a	n/a	3.5
	2z2(a)	0.69	0.27	0.15-0.2 cm		149.4	1030.3	137.3	946.9	3.8
	2z3	0.68	0.27	(0.06-0.08 in.)		142.7	984.1	135.7	935.9	n/a
	2z4	0.68	0.27			148.7	1025.5	134.9	930.3	5.7
	Avg					146.6	1010.9	136.0	937.7	4.3
3 As-deposited machined	3x1	0.64	0.25	All thickness were within		160.8	1109.0	149.2	1029.0	4.6
	3x2	0.64	0.25	0.15-0.2 cm		156.2	1077.2	142.5	982.8	5.7
	3x3	0.64	0.25	(0.06-0.08 in.)		156.1	1076.6	142.3	981.4	4.4
	3x4	0.64	0.25			155.7	1073.8	144.4	995.9	n/a
	3x5(a)	0.64	0.25			156.3	1077.9	143.3	988.3	4.5
	Avg					157.0	1082.9	144.3	995.4	4.8
	3z2(a)	0.64	0.25	All thickness were within		148.5	1024.2	136.9	944.1	3.5
	3z3	0.65	0.25	0.15-0.2 cm		149.6	1031.8	141.0	972.4	4.0
	3z4	0.64	0.25	(0.06-0.08 in.)		149.7	1032.5	138.0	951.7	3.9
	3z5	0.64	0.25			150.9	1040.7	138.8	957.2	4.6
	Avg					149.7	1032.4	138.7	956.4	4.0
4 As-deposited machined	4x1	0.64	0.25	All thickness were within		157.2	1084.1	145.6	1004.1	5.0
	4x2	0.64	0.25	0.15-0.2 cm		153.2	1056.6	141.9	978.6	5.4
	4x3	0.64	0.25	(0.06-0.08 in.)		152.7	1053.10	142.7	984.1	n/a
	4x4	0.64	0.25			155.1	1069.7	144.1	993.8	5.8
	4x5	0.64	0.25			156.2	1077.2	146.5	1010.3	n/a
	Avg					154.9	1068.1	144.2	994.2	5.4
	4z1(b)	0.64	0.25	All thickness were within		150.5	1037.9	143.1	986.9	n/a
	4z2(a)	0.65	0.25	0.15-0.2 cm		152.2	1049.7	138.5	955.2	3.5
	4z3(b)	0.64	0.25	(0.06-0.08 in.)		147.7	1018.6	140.5	969.0	n/a
	4z4(b)	0.64	0.25			148.8	1026.2	137.6	949.0	3.3
	4z5	0.64	0.25			150.4	1037.2	141.0	972.4	2.4
	Avg					151.3	1043.5	139.8	963.8	3.0
5 Heat-treated machined(c)	5x1	0.60	0.23	All thickness were within		140.0	965.5	125.6	866.2	n/a
	5x2(b)	0.59	0.23	0.15-0.2 cm		137.5	948.3	n/a	n/a	n/a
	5x3(a)	0.64	0.25	(0.06-0.08 in.)		138.3	953.8	123.9	854.5	14.6
	5x4	0.63	0.25			136.9	944.1	123.0	848.3	10.6
	5x5	0.63	0.25			131.5	906.9	n/a	n/a	10.5
	Avg					136.8	943.7	124.2	856.3	11.9
	5z1	0.64	0.25	All thickness were within		135.5	934.5	n/a	n/a	7.0
	5z2(a)	0.63	0.25	0.15-0.2 cm		136.2	939.3	n/a	n/a	8.5
	5z3	0.62	0.24	(0.06-0.08 in.)		136.2	939.3	n/a	n/a	8.0
	5z4	0.64	0.25			139.6	962.8	122.8	846.9	8.1
	5z5	0.63	0.25			140.3	967.6	123.0	848.3	7.3
	Avg					137.6	948.7	122.9	847.6	7.8

Table 1 Continued

Plate #	ID	Width cm, in.	Thickness, cm/in.		σ_u , ksi/MPa	σ_y , ksi/MPa	% Elong.		
6 Heat-treated machined	6x1	0.64	0.25	All thickness were within 0.15-0.2 cm (0.06-0.08 in.)	139.4 139.5 139.8 138.8 140.2 139.5 136.2 134.9 136.8 135.0 135.5 135.7	961.4 962.1 964.1 957.2 966.9 962.3 939.3 930.3 943.4 931.0 934.5 935.7 935.7	128.9 124.6 124.4 123.9 122.2 124.8 121.9 119.2 117.7 119.5 118.4 119.3 119.3	889.0 859.3 857.9 854.5 842.8 860.7 840.7 822.1 811.7 824.1 816.6 823.0 823.0	11.0 11.7 11.7 11.4 12.6 11.7 12.6 12.6 11.7 10.8 10.8 11.7
	6x2	0.63	0.25						
	6x3	0.64	0.25						
	6x4	0.62	0.24						
	6x5	0.64	0.25						
	Avg								
	6z1	0.64	0.25	All thickness were within 0.15-0.2 cm (0.06-0.08 in.)					
	6z2	0.64	0.25						
	6z3	0.64	0.25						
	6z4	0.63	0.25						
	6z5	0.63	0.25						
	Avg								
	7	Heat-treated no machine							
7	7x1	0.64	0.25	0.25 0.1	103.8	715.9	89.9	620.0	5.2
	7x2	0.63	0.25	0.25 0.1	111.0	765.5	102.8	708.3	3.8
	7x3(a)	0.64	0.25	0.25 0.1	110.5	762.1	100.6	693.8	3.3
	7x4	0.64	0.25	0.25 0.1	109.0	751.7	100.2	691.0	6.8
	7x5	0.65	0.25	0.25 0.1	109.2	753.1	100.5	693.1	n/a
	Avg				108.7	749.7	98.8	681.2	4.8
	7z1	0.64	0.25	All thicknesses were within 0.15-0.2 cm (0.06-0.08 in.)	101.5	700.0	n/a	n/a	n/a
	7z2	0.63	0.25		105.2	725.5	94.7	653.1	4.6
	7z3	0.65	0.25		105.3	726.2	92.1	635.2	3.8
	7z4	0.64	0.25		103.8	715.9	90.0	620.7	2.9
	7z5	0.64	0.25	0.08 in.)	n/a	n/a	92.5	637.9	2.3
	Avg				104.0	716.9	92.3	636.7	3.4

(a) Samples used for metallography

(b) Sample broke *then* computer beeped; corresponding values not included in average

(c) Surface mill both sides

(10 cm) lines were deposited while, in contrast, plate 3 represents a case of fewer but longer deposition lines.

Heat treating of the as-deposited material was at 980 °C for one hour followed by furnace cool-down in vacuum. This thermal treatment is close to the solutionizing temperature, 900-970 °C for this alloy (Ref 17). Plates 5-7 were heat treated, Fig. 3. The transus temperature for Ti-6Al-4V is 1000 °C, so the heat treating at 980 °C did not result in a full beta anneal.

Tensile testing was performed on an Instron 4505 unit Model 4500 Control Module. Testing was at ambient temperature (23 °C) and in laboratory air. The sample gauge length was 2.54 cm (1 in.) and the widths of the samples are presented in Table 1. An extensometer was used during the tensile tests and the strain rate was 0.127 cm/min (0.05 in./min).

After tensile testing, the grip area of the coupons was used for metallographic examination. Both longitudinal and transverse samples were mounted in a cold setting plastic/polymer and were ground, polished, and etched (Keller's reagent) according to standard practice (Ref 18). No isostatic pressing was performed on any of the test materials.

3. Results

The tensile data are summarized in Fig. 4 and 5 and are compiled in Table 1 for all the samples. Yield and tensile strength bar charts are presented in Fig. 4 and 5; elongation values are in

Fig. 6. In every figure, data for the wrought material are included for comparison. The tensile values obtained for the wrought material, 966 MPa (140 ksi) in yield strength, are consistent with it being beta-annealed at 865 °C (Ref 1).

The strengths of the laser deposited not machined and heat-treated material (plates 1, 5-7) were generally less than that of the wrought material. An important exception is the as-deposited machined samples (plates 2-4). This material is stronger than the wrought material; however, its elongation is less (~5% compared to ~14%).

Optical micrographs of the wrought and the as-deposited laser formed samples (with and without heat treatment) are shown in Fig. 7-10. SEM micrographs of the fracture surface of the tensile bars are shown in Fig. 11. The microstructure of as-deposited laser formed material is shown in Fig. 8 and reflect the acicular α - β that is frequently found in such quenched structures.

The heat-treated-laser-formed microstructure is shown in Fig. 10 and shows all the features of Ti-6Al-4V that had been heat treated in the two-phase alpha-beta region of the Ti-Al phase diagram. The microstructure consists of platelets of the alpha phase (light color) in a matrix of an intimate mixture of alpha and transformed beta phase (Ref 19, 20).

Low magnification optical images shown in Fig. 2(b) and (c) show the rough top surface of the depositions. In Fig. 11(a), the fractured surface of a tensile sample from the wrought Ti-6Al-4V indicates ductile fracture with equiaxed dimples. Microvoid coalescence indicative of ductile fracture is shown and the percent elongation is 13.8%, as shown in Table 1.

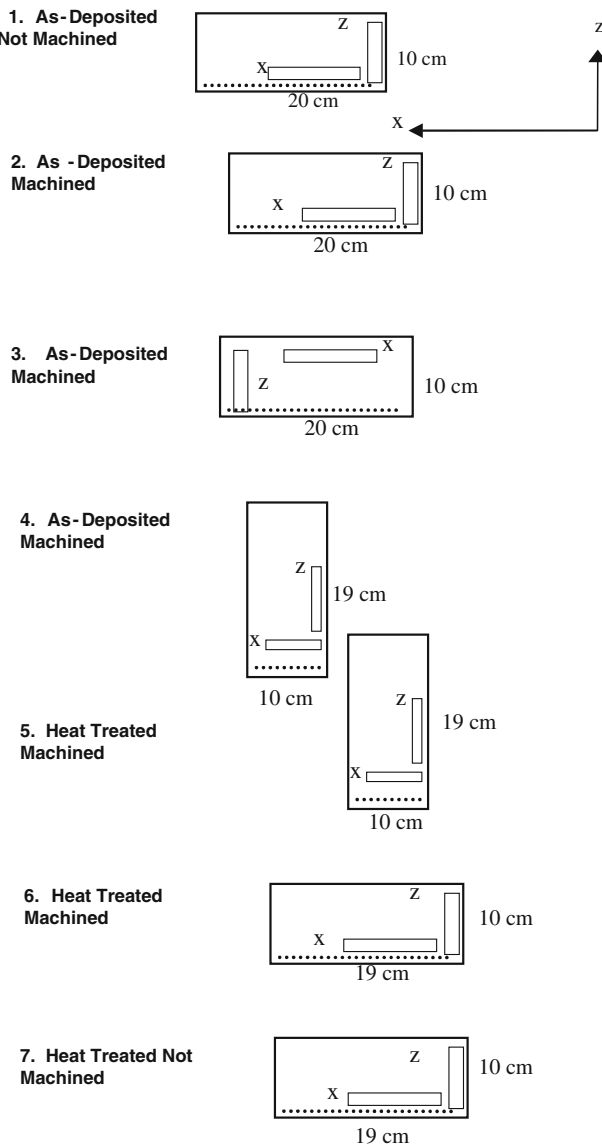


Fig. 3 Schematic views of the orientations of the tensile samples. This figure is intended to display the nomenclature used in this article

In Fig. 11(b) the top surface of an as-deposited laser formed sample is shown. The fractured surface is shown in Fig. 11(c) and (d). The fracture is ductile away from the pores, but these pores accelerate the fracture and lower the ductility. Figure 11(c) also appears to show delineation of prior powder particle boundaries on the fracture surface, to an extent that the responsible features likely participated in the fracture process and the development of properties. Figure 11(e) shows the fractured surface of a laser formed, machined, and heat-treated sample with equiaxed dimples and ductile fracture.

The as-deposited surface, shown in Fig. 11(b), is characterized by abundant splatter droplets, about 100 microns in diameter, and relatively large and deep crevices. The high points on the surface are the characteristic points measured when micrometer measurements were made of the dimensions of the samples when stress values were calculated from tensile loads. The micrometer-measured dimensions do not, in reality,

represent the dimensions of the bulk of the stressed material, and, as a consequence, the dimensions used for the cross-sectional areas were a little bit large, and the calculated stress values were slightly smaller than the true values.

4. Discussion

4.1 Effects of Laser Forming and Heat Treatment

The tensile and yield strengths of the wrought Ti-6Al-4V alloy were 1062.9 MPa (154.1 ksi) and 965.9 MPa (140.1 ksi), respectively. The percent elongation was 13.8, from Fig. 4, 7, and Table 1. These values are in accord with the SAE-AMS-T-9046 specifications (Ref 20). The microstructure, which is shown in Fig. 7(a) and (b), consist of a mixture of α and lean refined β phases, which inhibits dislocation slip. The mode of fracture however is ductile, Fig. 11(a). The tensile and yield strengths of the as-deposited non-machined plate 1 samples were 910.9 MPa (132.1 ksi) and 892 MPa (129.4 ksi), respectively. This is a 7-14% reduction in strength as compared to the wrought material. The percent elongation was 6.4, which is 53% lower than that of the wrought material.

The optical micrographs, Fig. 8(a) and (b), reveal numerous microcracks and voids throughout the microstructure, which are stress concentration factors. The microstructure consists of columnar prior-beta grains elongated in the solidification (build) direction; within it is a fine Widmanstatten (basket weave) platelet alpha, which indicates a relatively rapid cooling after solidification (Ref 16). The as-deposited “not machined” rough surfaces, Fig. 2(b) and (c) were responsible for the lack of fusion, interlayer porosity, and the weak strengths and ductility. Figure 11(b)-(d) reveals the mixed mode of brittle/ductile fracture of the as-deposited—“not machined” samples due to excessive voids.

The tensile and yield strengths of the as-deposited machined plates 2-4 were similar to the wrought material strength values. The inclusion of plates 3 and 4 will be discussed in the next section. The tensile and yield strengths of plate 2 are 1057.9 MPa (153.4 ksi) and 948.3 MPa (137.5 ksi), respectively, which is less than 2% differences as compared to the wrought values. The percent elongation is 6.8, which is 50% of the value of the wrought material. The microstructure shown in Fig. 9 reveals a similar microstructure of acicular alpha-beta like that of plate 1 but with less microcracks and pores which explains the improved ductility and strength as compared to those of plate 1, i.e., “not machined.”

The mechanical strengths and ductility values of the heat-treated plates 5-7 are summarized in Fig. 4-6. The inclusion of plate 6 will be discussed in the next section. Plates 5-7 were heat treated at 980 °C for one hour followed by furnace cool in vacuum. The tensile and yield strengths of plate 5 were 943.7 MPa (136.8 ksi) and 856.3 MPa (124.2 ksi), respectively, which is 10-11% reduction in strength as compared to the wrought material. The percent elongation was 11.9%, which is 14% lower than that of the wrought material. The microstructure of the heat-treated machined plate showed columnar beta grains with coarser Widmanstatten alpha and most of the porosity was healed, Fig. 10 and 11(e) (Ref 16).

In plate 7, no machining was performed. This was translated to the weak values of strength and ductility. The tensile and

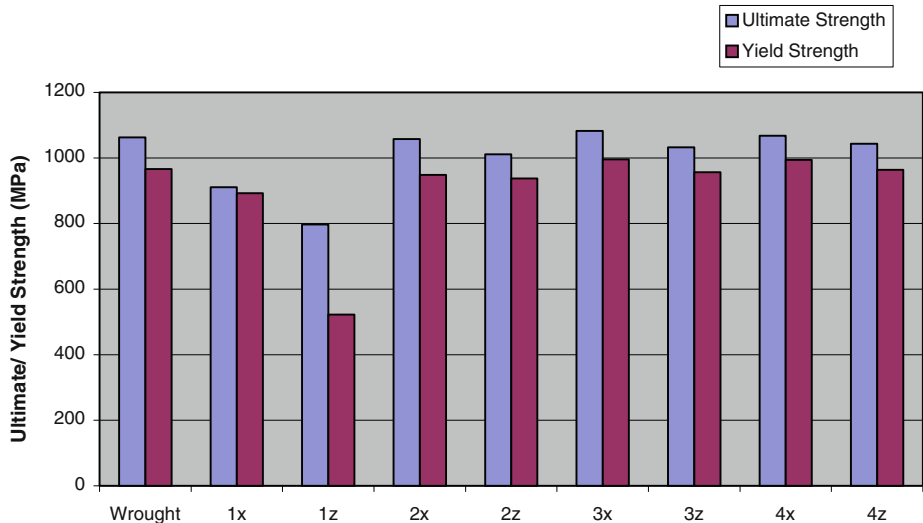


Fig. 4 Tensile values of laser-formed non-heat-treated Ti-6Al-4V. Values for wrought alloy are included for comparison

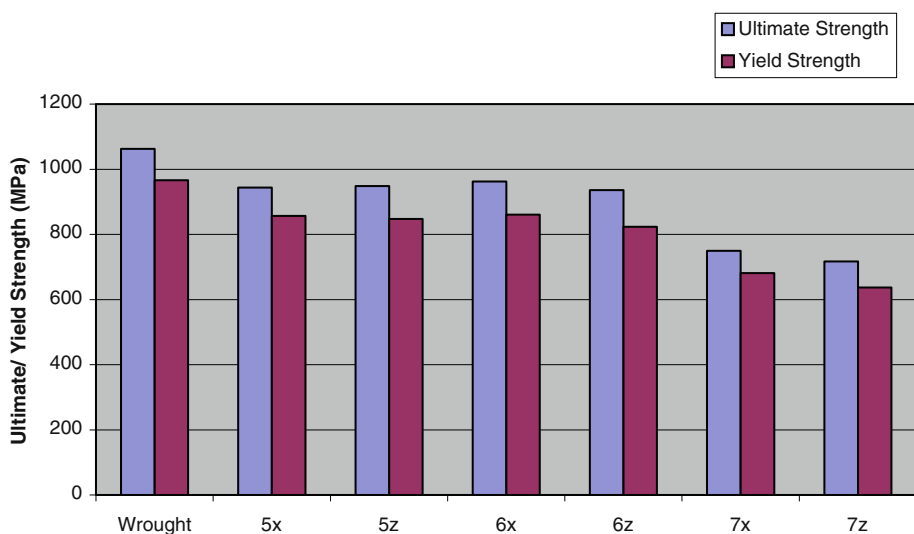


Fig. 5 Tensile values of laser formed heat-treated Ti-6Al-4V. Values for wrought alloy are included for comparison

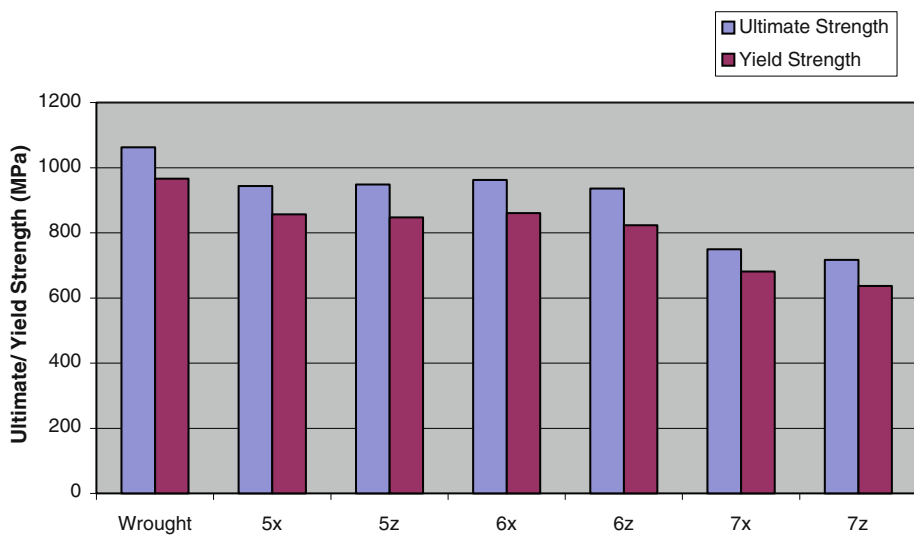


Fig. 6 Elongation values for laser-formed Ti-6Al-4V

yield strengths of plate 7 were 749.7 MPa (108.7 ksi) and 681.2 MPa (98.8 ksi), respectively. These values were around 30% lower than those of the wrought material and 20% lower than those of the heat-treated and machined plate 5. The percent elongation was 4.8, which is 65% of the value of the wrought material and 60% of the value of plate 5. The inclusion of plates 1 and 7 indicates the criticality of removing rough surfaces by machining of the final parts.

The effect of heat-treating the laser formed plates was the transformation of the acicular alpha-beta microstructure, Fig. 9 to a columnar beta grains and coarser Widmanstatten alpha grains and minimum porosity, Fig. 10. This transformation was responsible for around 10-12% decrease in strength and more than doubling of the percent elongation values, as compared to the non-heat-treated samples, Fig. 4-6. The mechanical strength values of plates 3 and 4 were slightly higher than those of the wrought material, however, the percent elongation was much lower, Fig. 4 and 6.

4.2 Effect of Location of Tensile Bars on the Mechanical Properties

In Fig. 3, plates 2 and 3 differ in that the tensile bars in plate 2 were extracted from a section of the plate that was

deposited at the beginning of a particular run while the tensile bars in plate 3 were taken from the section of the plate that was deposited toward the end of a particular run. Both plates 2 and 3 are machined and are not heat-treated, Fig. 4. The tensile strengths are similar, which indicates that laser forming process, produces uniform mechanical properties.

Plates 3 and 4 (non-heat treated and machined) and plates 5 and 6 (heat treated and machined) differ in that one is orthogonal to the other, plate 4 (and plate 5) represents a run in



Fig. 9 An isometric view of the microstructure of an as-deposited machined sample

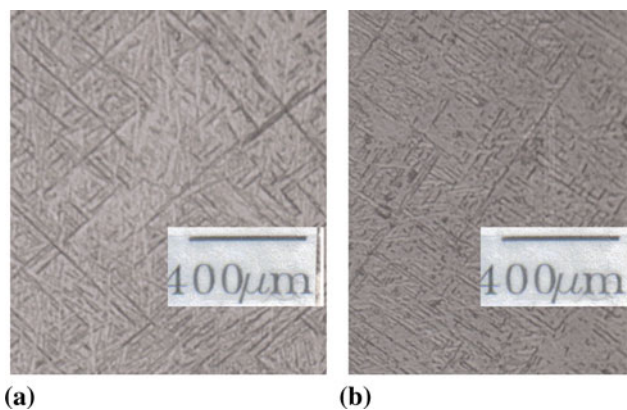


Fig. 7 Long (a) and rolling (b) direction views of the wrought Ti-6Al-4V microstructure after being annealed (beta-aged) at 865 °C

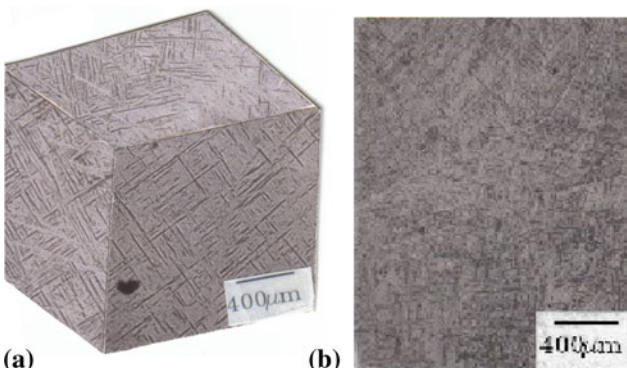


Fig. 8 (a) An isometric view of the microstructure of the as-deposited sample. (b) A longitudinal view of the microstructure of the as-deposited sample



Fig. 10 An isometric view of the microstructure of an as-deposited, machined, and heat-treated sample. The sample was heat treated at 980 °C for one hour

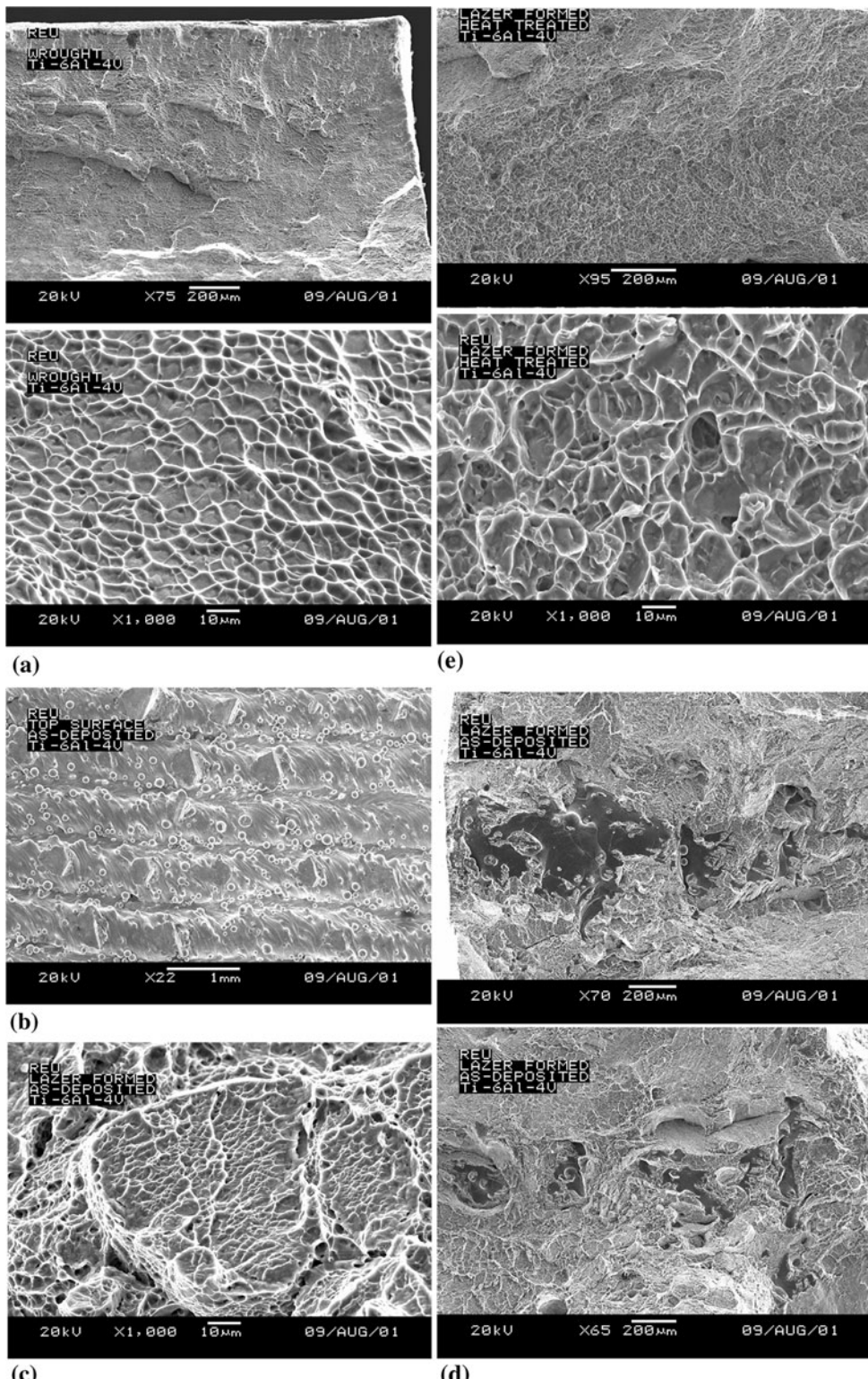


Fig. 11 (a) A scanning electron microscope view of the fractured surface of a tensile specimen of the wrought Ti-6Al-4V. (b) A scanning electron microscope view of the top as-deposited surface. Splatter is seen everywhere. (c) A scanning electron microscope view of the fractured surface of a tensile sample of an as-deposited laser formed sample, high magnification. (d) A scanning electron microscope view of the fractured surface of a tensile sample of an as-deposited laser formed sample, low magnification. (e) A scanning electron microscope view of the fractured surface of a tensile sample of an as-deposited/heat-treated laser formed sample

which numerous short (10 cm) lines were deposited while in contrast, plate 3 (and plate 6) represents a case of fewer but longer deposition lines. The tensile properties between plates 3

and 4 on one hand and plates 5 and 6 on the other hand confirm the homogeneity of properties in different locations of a laser formed product.

Table 2 Anisotropic values of tensile strengths

Plate	Anisotropy in tensile strength, %	Anisotropy in yield strength, %	Average percent elongation in x-direction	Average percent elongation in z-direction
1	12.5	41.4	6.4	1.7
2	4.4	1.1	6.8	4.3
3	4.7	3.9	4.8	4
4	2.3	3.1	5.4	3.0
5	-0.6	1.1	11.9	7.8
6	2.7	4.4	11.7	11.7
7	4.3	6.7	4.8	3.4

In all laser formed plates 1-7, Fig. 4-6 and Table 1, tensile bars tested in the *x*-direction had better tensile properties as compared to those tested in the *z*-direction. Anisotropy will be defined as:

$$\frac{\sigma_x - \sigma_z}{\sigma_x} * 100\% \quad (\text{Eq 1})$$

where σ is the tensile or yield strengths and σ_x and σ_z denote strengths at *x* or *z* directions. The anisotropy is shown in Table 2 for each plate. The anisotropic behavior was very significant in plate 1. The tensile strength in the *x* direction is 910.9 MPa (132.1 ksi) and in the *z* direction is 797.1 MPa (115.6 ksi) with a 12.5% anisotropy. The yield strength in the *x* direction is 892.2 MPa (129.4 ksi) and in the *z* direction is 522.4 MPa (75.8 ksi) with a 41.4% anisotropy. Plates 2-7 had less than 5% anisotropy except for the yield strengths in plate 7, 6.7% anisotropy, Table 2.

These results can be related to the work of Es-Said et al. (Ref 21). In this work, rapid prototype ABS (Acrylonitrile-Butadiene-Styrene) P400 samples were deposited in a 0° degree orientation, where the layers were deposited along the length of the tensile samples like the *x* direction tensile bars of this study, Fig. 2(b). They (Ref 21) also deposited the polymer samples in a 90° orientation, where the layers were at a 90° angle to the length of the tensile samples similar to the *z* direction tensile bars of this study, Fig. 2(c). The 0° degree orientation in the polymer rapid prototype study (Ref 21) not only was significantly higher in strength as compared to the 90° orientation, but was also significantly higher in toughness. The same is true in the *x* and *z* direction of plate 1 of this study, since the percent elongation is 6.4% for the *x* direction and 1.7% in the *z* direction. Es-Said et al. (Ref 21) related this behavior to weak interfaces in 2D layered materials (Ref 19). Weak interfacial layers at 0° orientation (*x* direction in this study) that are perpendicular to the crack front will absorb high amounts of energy due to interface delamination (Ref 19, 22). The delamination will blunt the crack tip, reduce the stresses ahead of the crack and cause higher amounts of energy to be absorbed for crack propagation. The weak interfaces are parallel to the crack front at the 90° orientation (*z* direction in this study) and will provide an easy path for crack propagation and cause small amounts of energy to be absorbed.

The low strength values of the *z* direction as compared to the *x*-direction in plate 1 confirm the hypothesis that the strength anisotropy is affected by the directional processing of the 2D laminates or the preferred orientation of weak interfaces and interlayer porosity (Ref 22).

The low strength values of both *x* and *z* direction in plate 1 compared to the strength values of all other plates 2-7 can be

explained by the presence of interlayer porosity (Fig. 8a, b, 11b-d). Interlayer porosity reduces the load-bearing area across the layers and hence provides an easy fracture path (Ref 19). It was clear that machining and/or heat-treating had the effect of significantly reducing the porosity and anisotropy in all other plates.

5. Conclusions

1. Laser-formed Ti-6Al-4V materials have been tested for mechanical properties, and have been found to exhibit mechanical strengths comparable, and in some tests, superior to the conventional wrought alloy. The percent elongation however was consistently lower than that of the wrought material.
2. The as-deposited laser formed surfaces were rough and showed crack initiation sites due to porosity. This was a cause also of anisotropy in the mechanical strength.
3. The tensile properties were uniform at all locations of a laser formed plate.
4. The tensile properties of the laser-formed material were isotropic within the plane of the deposited material when machined or heat treated or both.

Acknowledgments

The authors wish to acknowledge the financial support for this project from the National Science Foundation, Grant No. EEC 0097863. They also wish to thank Ms. Jaisey Simard and Mr. Roman Silva for preparing the manuscript.

References

1. M. Donachie, *Titanium, A Technical Guide*, 2nd ed., ASM International, Materials Park, OH 44073, 2000, p 5–8
2. H.R. Salimjazi, T.W. Coyle, and J. Mostaghimi, Vacuum Plasma Spraying: A New Concept for Manufacturing Ti-6Al-4V Structures, *JOM*, September 2006, p 50–56
3. R. Boyer, G. Welsch, and E.W. Collings, Ed., *Materials Properties Handbook: Titanium Alloys*, ASM International, Materials Park, OH, 1998, p 3–31
4. R. Witt, Inside Sales Manager, Service Steels Aerospace, (P) 800.624.8073, <http://www.ssa-corp.com/quotation.asp>, August 24, 2009
5. K.G. Watkins, S.P. Edwardson, J. Magee, G. Dearden, and P. French, Laser Forming of Aerospace Alloys, *Aerospace Manufacturing Technology Conference (AMTC)*, SAE, 2001, p 1–7
6. B.V. Krishna and A. Bandyopadhyay, Surface Modification of AISI 410 Stainless Steel Using Laser Engineered Net Shaping (LENS™), *Mater. Des.*, 2008, doi:10.1016/j.matdes.2008.08.003
7. R. Banerjee et al., Microstructural Evolution in Laser Deposited Composititionally Graded Alpha/Beta Titanium-Vanadium Alloys, *Acta Mater.*, 2003, **51**, p 3277–3292
8. D.M. Keicher and W.D. Miller, LENS Moves Beyond RP to Direct Fabrication, *Metal Powder Rep.*, 1998, **53**, p 26–28
9. B. Cleveland, Rapid Manufacturing Technologies, *Adv. Mater. Process.*, 2001, **159**(5), p 32
10. J. Brooks, C. Robino, T. Headley, S. Goods, and M. Griffith, *Microstructure and Property Optimization of LENS Deposited H13 Tool Steel. Solid Freeform Fabrication Proc*, University of Texas, Austin, 1999
11. P.L. Blackwell and A. Wisbey, Laser-aided Manufacturing Technologies; Their Application to the Near-Net Shape Forming of a

- High-Strength Titanium Alloy, *J. Mater. Process. Technol.*, 2005, **170**, p 268–276
12. K.P. Cooper, Building Components by Laser-Additive Processing, *JOM*, 2001, **53**(9), p 29
 13. P.A. Kobryn and S.L. Semiatin, *Mechanical Properties of Laser-Deposited Ti-6Al-4V*, AFRL/MLLMP, p 179–186
 14. S.M. Kelly, S.L. Kampe, and C.R. Crowe, Microstructural Study of Laser Formed Ti-6Al-4V, *Solid Freeform and Additive Fabrication Symposium*, Vol. 625, 2000, p 3–8
 15. P.A. Kobryn and S.L. Semiatin, The Laser Additive Manufacture of Ti-6Al-4V, *JOM*, 2001, **53**, p 40–42
 16. S.L. Semiatin et al., Plastic Flow and Microstructure Evolution during Thermomechanical Processing of Laser-Deposited Ti-6Al-4V Performs, *Met. Mater. Trans. A*, 2001, **32A**, p 1802
 17. MIL Standard H-812008, Jan 13, 1991
 18. G. Kehl, *Principles of Metallographic Laboratory Practice*, 3rd ed., McGraw-Hill Book Publishing Company, New York, 1949
 19. S.A. Salpekar, I.S. Raju, and T.K. O'Brien, Strain-Energy Release Rate Analysis of Delamination in a Tapered Laminate Subjected to Tension Load, *J. Compos. Mater.*, 1991, **25**, p 118
 20. SAE-AMS-T-9046, “Titanium and Titanium Alloy, Sheet, Strip, and Plate,” 17 September 1999
 21. O.S. Es-Said, J. Foyos, R. Noorani, M. Mendelson, and B. Pregger, Effect of Layer Orientation on Mechanical Properties of Rapid Prototyped Samples, *Mater. Manuf. Process.*, 2000, **15**(1), p 112
 22. A.S. Brown, *Rapid Prototyping: Parts Without Tools*, Aerospace America, 1991, p 18

Fabrication of Ti-6Al-4V Scaffolds by Direct Metal Deposition

G.P. DINDA, L. SONG, and J. MAZUMDER

Direct metal deposition (DMD) is a rapid laser-aided deposition method that can be used to manufacture near-net-shape components from their computer aided design (CAD) files. The method can be used to produce fully dense or porous metallic parts. The Ti-6Al-4V alloy is widely used as an implantable material mainly in the application of orthopedic prostheses because of its high strength, low elastic modulus, excellent corrosion resistance, and good biocompatibility. In the present study, Ti-6Al-4V scaffold has been fabricated by DMD technology for patient specific bone tissue engineering. Good geometry control and surface finish have been achieved. The structure and properties of the scaffolds were investigated by X-ray diffraction (XRD), scanning electron microscopy (SEM), transmission electron microscopy (TEM), and tension test. The microstructures of laser-deposited Ti-6Al-4V scaffolds are fine Widmanstätten in nature. The tensile and yield strengths of the as-deposited Ti-6Al-4V were 1163 ± 22 and 1105 ± 19 MPa, respectively, which are quite higher than the ASTM limits (896 and 827 MPa) for Ti-6Al-4V implants. However, the ductility of the as-deposited sample was very low (~4 pct), which is well below the ASTM limit (10 pct). After an additional heat treatment (sample annealed at 950°C followed by furnace cooling), both strength (UTS $\sim 1045 \pm 16$, and YS $\sim 959 \pm 12$ MPa) and ductility ($\sim 10.5 \pm 1$ pct) become higher than ASTM limits for medical implants.

DOI: 10.1007/s11661-008-9634-y

© The Minerals, Metals & Materials Society and ASM International 2008

I. INTRODUCTION

TISSUE engineering constitutes a promisingly alternative approach to the repair of damaged tissue or organs. Different biomaterials have been used as scaffolds, including bioactive metallic,^[1] ceramics,^[2] and polymers^[3] for bone tissue engineering. Ideally, the materials should exhibit adequate mechanical and biological properties. The primary roles of scaffold are (1) to serve as an adhesion substrate for the cell, facilitating the localization and delivery of cells when they are implanted; (2) to provide temporary mechanical support to the newly grown tissue; and (3) to guide the development of new tissues with the appropriate function. Moreover, the scaffold should be biocompatible. A titanium alloy, specifically Ti-6Al-4V, is widely used as an implant material for biomedical applications due to its relatively low modulus, good biocompatibility, and enhanced corrosion resistance when compared to more conventional stainless steels and cobalt-based alloys. The principal focus of this study is to produce ideal scaffolds of Ti-6Al-4V by the direct metal deposition (DMD) technique for patient specific bone tissue engineering with good mechanical and metallurgical properties.

Rapid prototyping, also known as solid freeform fabrication, is a manufacturing process that quickly produces physical prototypes directly from computer

aided design (CAD) solid models using a special class of fabrication technology. Direct laser deposition is a rapid prototyping method that can be used to manufacture near-net-shape components from their CAD files in one step. The DMD^[4,5] technology developed at the University of Michigan, direct light fabrication (DLF)^[6,7] developed at the Los Alamos National Laboratories, and laser engineering net shaping (LENS)^[8,9] developed at the Sandia National Laboratories in the early 1990s are all successful examples of direct laser deposition technology. The basic principles of DMD, DLF, and LENS processes are similar in that they use a focused laser beam as a heat source to melt metallic powder and create a three-dimensional (3-D) object. In addition, the DMD and LENS have a feedback control system that provides a closed-loop control of dimension during the deposition process. In the present investigation, the DMD system developed at the University of Michigan was used to fabricate complex shaped metallic scaffolds for medical implants, which are very difficult to process for conventional methods.

First, the CAD model of the component is sliced into a series of parallel layers with a certain build-height. During the DMD process, powder is fed at a controlled rate into the focal point of a high-power laser where the individual particles are melted. The CAD files control both movements of substrate in the *X-Y* plane and laser beam in the *Z* direction to add successive layers, thus directly generating a three-dimensional component without the necessity of any machining. There are many variables in this process that can affect the material properties and the microstructure of the resulting part, such as laser power, powder feed rate, and laser scanning speed.

G.P. DINDA, Research Fellow, L. SONG, Research Investigator, and J. MAZUMDER, Professor, are with the Department of Mechanical Engineering, University of Michigan, Ann Arbor, MI 48109. Contact e-mail: dinda@umich.edu

Manuscript submitted April 16, 2007.

Article published online September 17, 2008

The aim of the present work is to produce ideal Ti-6Al-4V scaffolds and to study the microstructural development and mechanical response for their applicability as hard tissue biomaterials.

II. EXPERIMENTAL PROCEDURE

A. Materials

Gas-atomized prealloyed Ti-6Al-4V powder ($-100 + 325$ mesh, Starmet Inc., Concord, MA) was used to fabricate 3-D scaffold. The powder had a composition (in wt pct) of 5.99 aluminum, 4.02 vanadium, 0.21 iron, 0.19 oxygen, 0.04 carbon, 0.02 nitrogen, 0.04 silicon, and balance titanium. Figure 1 shows that the as-received powder particles are rather spherical. Quantitative analysis of the SEM images of about 100 powder particles, measuring always the largest diameter and the diameter in the direction perpendicular to the long axis, showed that the mean particle size is about $84 \mu\text{m}$, whereas 82 pct of the powder particles are in the range between 60 and $120 \mu\text{m}$.

B. Scaffold Fabrication

There are five primary components of the DMD assembly: the laser system, the powder delivery system, sensors for feedback loop for dimension control, the controlled environment, and the CAD driven motion control system.^[10] A sketch of the DMD system is shown in Figure 2. A 6 KW CO₂ laser unit was used in the present experiment. The laser processing parameters used were as follows: laser scanning speed, 36.6 mm min^{-1} ; powder feed rate, 5 g min^{-1} ; and Z increment, 0.25 mm. The scaffold was fabricated on a substrate of Ti-6Al-4V rolled plate. During DMD processing, 300 W laser beam was focused on the substrate to create a melt pool into which the powder feedstock is delivered through an inert gas (He) flowing through a special nozzle, where the powder streams converge at the same point on the focused laser beam (beam diameter = 0.5 mm). An inert gas shroud

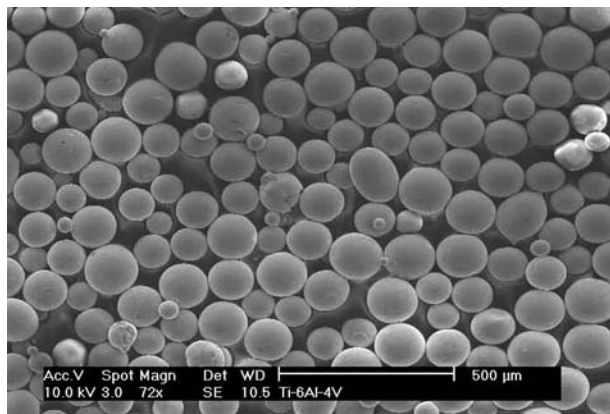


Fig. 1—Morphology of the as-received Ti-6Al-4V prealloyed powder.

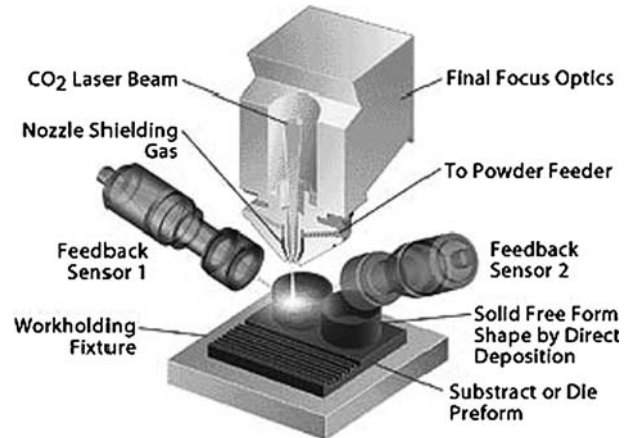


Fig. 2—Schematic description of the DMD system.

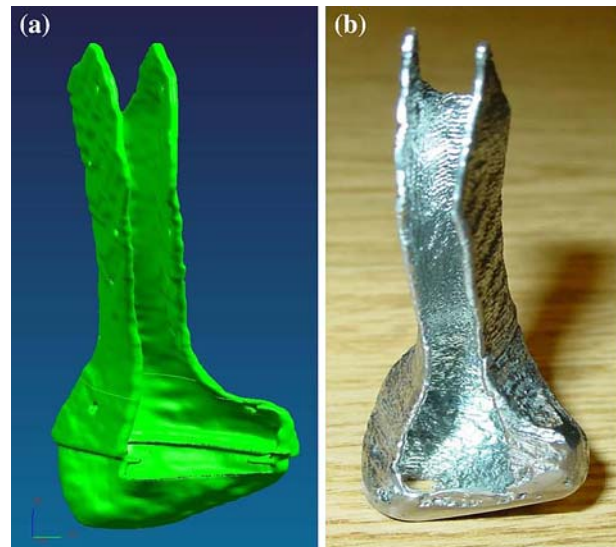


Fig. 3—(a) CAD image of the CRU of a Yucatan minipig. (b) An identical Ti-6Al-4V scaffold was produced by the DMD process.

containing a mixture of helium and argon was used as a protective atmosphere for preventing oxidation during deposition. No feedback control system was used in the present experiment. Without any feedback control, several identical scaffolds were successfully fabricated after subsequent layers deposition (Figure 3).

For mechanical tests, tensile specimens were fabricated according to the ASTM E 8 standard (gage length: 25 mm, width: 6.25 mm, and thickness: 0.7 mm) by the same laser deposition parameters that have used for scaffold fabrication. The specimens were then polished using different (240 to 1200) emery papers to improve the surface smoothness for the tension test. The tensile axis of all specimens was perpendicular to the deposit direction. The tensile specimens were tested in a universal testing machine (Instron 55005) at a crosshead speed of 0.5 mm min^{-1} . Three tests were conducted for each condition to ensure the reproducibility of the results. It should be mentioned that tensile fracture occurred near the middle of the gage section.

In order to improve the ductility of the laser-deposited samples, several tensile specimens were annealed at 950 °C and 1050 °C followed by either air cooling (AC) or furnace cooling (FC). The heat treatment was performed in a horizontal cylindrical furnace under an argon atmosphere for 1 hour.

C. Characterization

The microstructures of the laser-deposited scaffold were investigated by optical microscopy (OM) (Nikon eclipse ME600), scanning electron microscopy (SEM, PHILIPS* XL30 FEG scanning electron

*PHILIPS is a trademark of Philips Electronic Instruments Corp., Mahwah, NJ.

microscope), and transmission electron microscopy (TEM, JEOL**) 2010 transmission electron microscope

**JEOL is a trademark of Japan Electron Optics Ltd., Tokyo.

operating at 200 kV). The as-deposited samples were investigated using X-ray diffraction (Rigaku rotating anode XRD) with Cu K_{α} radiation. Specimens for OM and SEM were cut out from different parts of the scaffold. A Kroll's (10 mL HNO₃, 5 mL HF, and 85 mL H₂O) etchant was used for the OM and SEM. For transmission electron microscopy/selected area electron diffraction (TEM/SAD), 3 mm in diameter samples were mechanically punched out. Thereafter, the samples were thinned by ion milling with low accelerating voltage (3.5 kV) to minimize the beam effects on the microstructure.

The surface roughness of the DMD samples parallel to the build direction was measured over a length of 3 mm using a stylus profilometer (Form Talysurf 50, Taylor-Hobson). The roughness value was calculated by averaging the data from five measurements.

III. RESULTS

A. Surface Morphology

Figure 3(a) shows an image of the condylar ramus unit (CRU) of a Yucatan minipig. The image of the CRU was designed using a computed tomography (CT) scan on a 6-month-old Yucatan minipig. A detailed description of the CRU scaffold design technique may be found elsewhere.^[11] Several identical Ti-6Al-4V scaffolds for the porcine CRU bone tissue engineering were successfully manufactured by DMD (Figure 3(b)). However, the surface of the as-fabricated scaffold was relatively rough. Many granular particles were associated with the surface. However, with regard to the proposed use of scaffold, the surface particles *in vivo* would probably cause inflammation due to the macrophase activation. In order to remove the unwanted particles from the surface, a sandblasting operation was

Table I. Surface Roughness of the As-Deposited Ti-6Al-4V Scaffold after Sand Blasting and Chemical Etching

Roughness	As-Deposited	Sand Blasted	Sand Etched
R_a (average roughness)	25 μm	12 μm	8 μm
R_q (root-mean-square roughness)	31 μm	16 μm	12 μm
R_t (maximum peak-to-valley height)	146 μm	73 μm	49 μm

performed on the surface of the scaffold. The particle layer was removed from the surface after sandblasting. To further improve the surface quality, the sandblasted scaffold was chemically polished by a Kroll's reagent (10 mL HNO₃, 5 mL HF, and 85 mL water) for 5 minutes. The surface becomes very smooth (Table I) after optimal chemical polishing. The average surface roughness (R_a) reduces to 8 μm after chemical etching. The roughnesses of the as-deposited and sand-blasted scaffold were 25 and 12 μm , respectively.

Figure 4(a) shows an SEM image of the as-deposited scaffold surface. Many spherical particles, which had diameters from 50 to 120 μm , were associated with the surface. It was observed that the associated surface particles are spherical in shape and the particle size distribution is very close to that of the as-received powder particles. It should be noted that the surface particles are the excess unmelted powder particles. It can be seen from Figure 4(b) that the surface of the scaffold after sandblasting operation is free from particles. However, the surface becomes relatively rough due to the sandblasting operation. Finally, Figure 4(c) shows the rough sandblasted surface becoming smooth after an additional chemical etching by Kroll's reagent for 5 minutes.

B. XRD Analysis

Figure 5 shows the XRD scan of Ti-6Al-4V scaffold produced by DMD. The equilibrium microstructure at room temperature of Ti-6Al-4V alloy is a mixture of α (hcp) and β (bcc) phases. However, the nature of the α phase, whether it will be martensite or diffusion-controlled Widmästätten structure, varies based on the thermal history of the alloy. The XRD scan (Figure 5) shows that the Bragg peaks belong to either α or β phase. No other phase has been observed in the XRD scan.

C. Microstructure

1. Optical microscopy

Figure 6 shows typical optical micrographs of the as-deposited scaffold. It should be noted that the prior β grains were columnar in nature. The axes of the columnar grains are approximately parallel to the Z-axis, *i.e.*, the build direction of the deposit (Figure 6(a)). The width of columnar grains varies from 0.15 to 0.8 mm, whereas the average width of the columnar grains is around 0.3 mm. In addition to the columnar grain structure, a periodically bandlike struc-

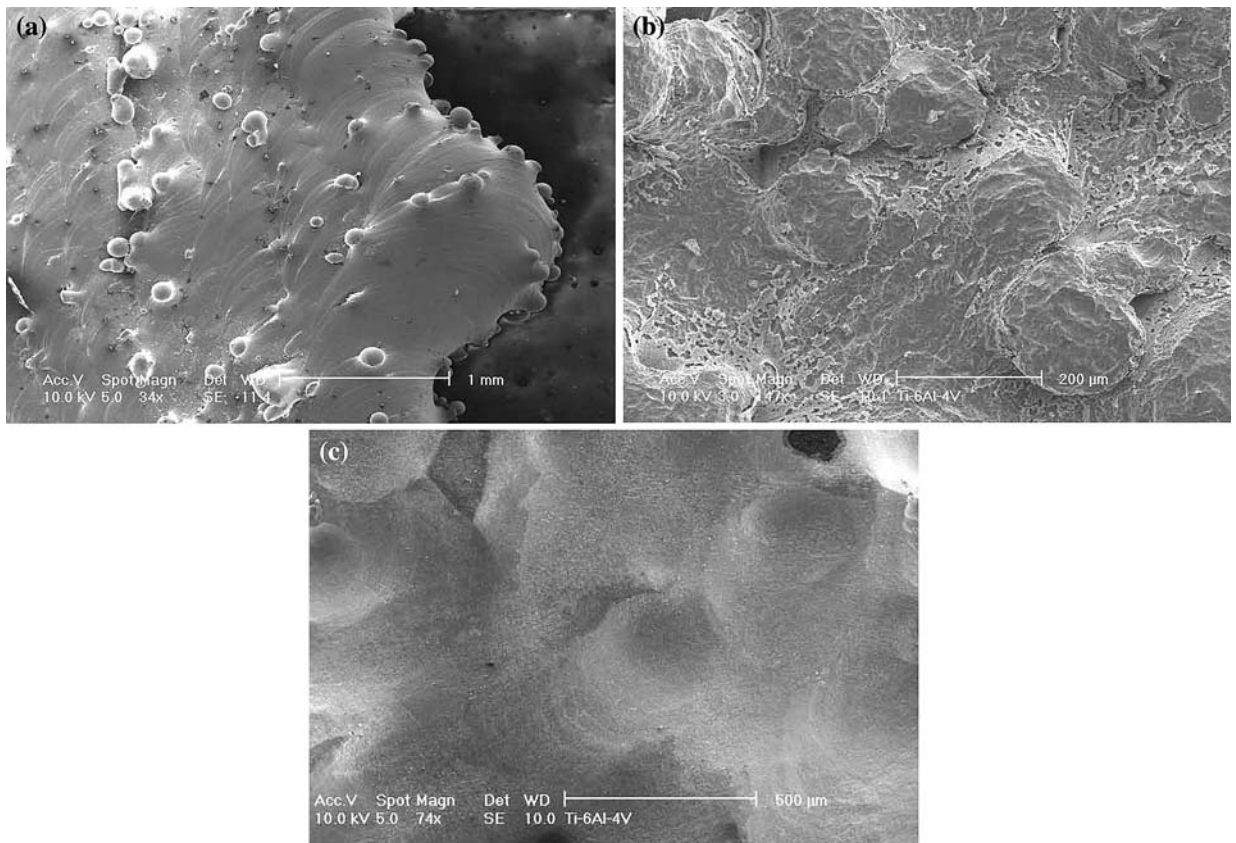


Fig. 4—SEM micrographs of (a) the as-fabricated scaffold surface (50 to 120 μm spherical particles were observed at the surface), (b) the sandblasted scaffold surface, and (c) the surface after chemical etching.

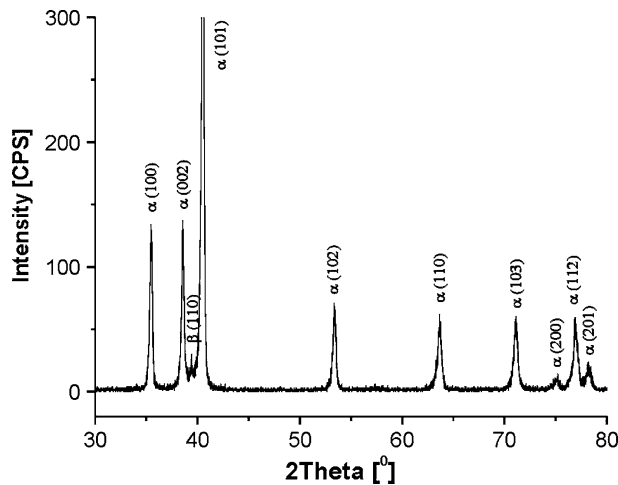


Fig. 5—XRD scan of as-deposited Ti-6Al-4V scaffold.

ture was observed in the optical micrograph (Figure 6(a)). The thickness of the band is ~ 0.25 mm, which is basically the thickness of each deposited layer. However, the microstructures within the prior β grains were fine Widmanstätten in nature (Figure 6(b)) with very fine α grains distributed both within the prior β grains and along the grain boundaries.

2. Scanning electron microscopy

The SEM micrographs (Figure 7) of the as-deposited scaffold clearly show that the observed microstructures are Widmanstätten in nature. In addition to the Widmanstätten α laths, Figures 7(b) and (d) also show that the prior β grain boundaries are decorated with α . Moreover, the size and distribution of α laths varies at different locations of the sample. For example, Figures 7(a) and (b) show the typical Widmanstätten lathlike morphology with a relatively large aspect ratio. Furthermore, the microstructure consists of intricately mixed multiple variants of α laths, often referred to as the basketweave microstructure, whereas Figure 7(d) shows more equiaxed-like morphology with a smaller aspect ratio of α laths. In addition, Figure 7(c) shows both fine (center part of the figure) and relatively coarse (top and bottom parts) Widmanstätten α laths.

3. Transmission electron microscopy

Figure 8 shows TEM micrographs of the as-deposited Ti-6Al-4V scaffold. The bright-field TEM image (Figure 8(a)) of the as-deposited scaffold confirms the observation of the scanning electron microscopy that the microstructure consists of fine Widmanstätten α . A selected area electron diffraction pattern (Figure 8(b)) of Figure 8(a) further confirmed the presence of α (hcp) phase in the microstructure. In addition to the Widmanstätten α formation in the as-deposited Ti-6Al-4V,

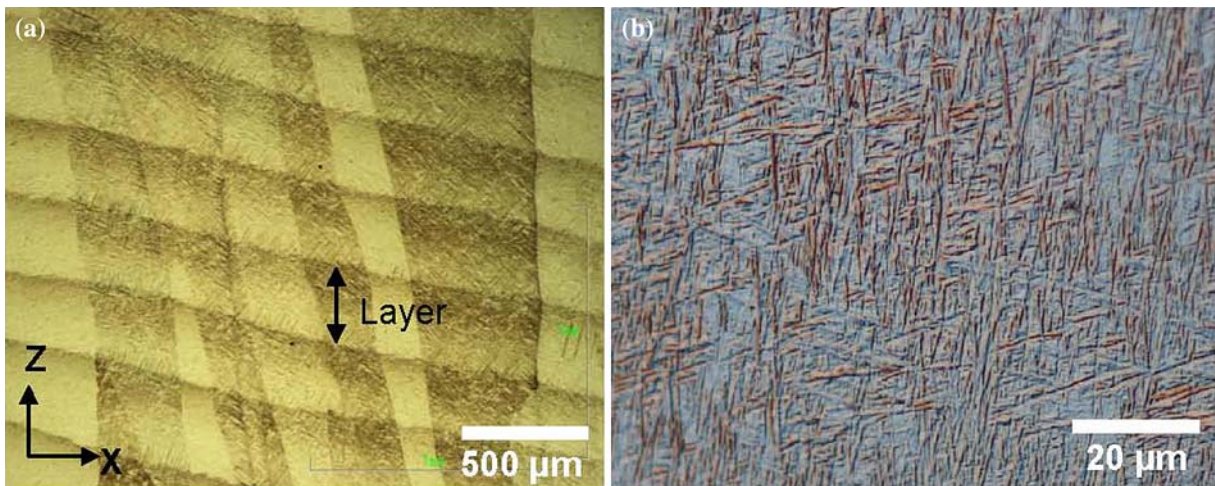


Fig. 6—Optical micrographs of as-deposited scaffold showing (a) columnar grains and (b) Widmanstätten structure.

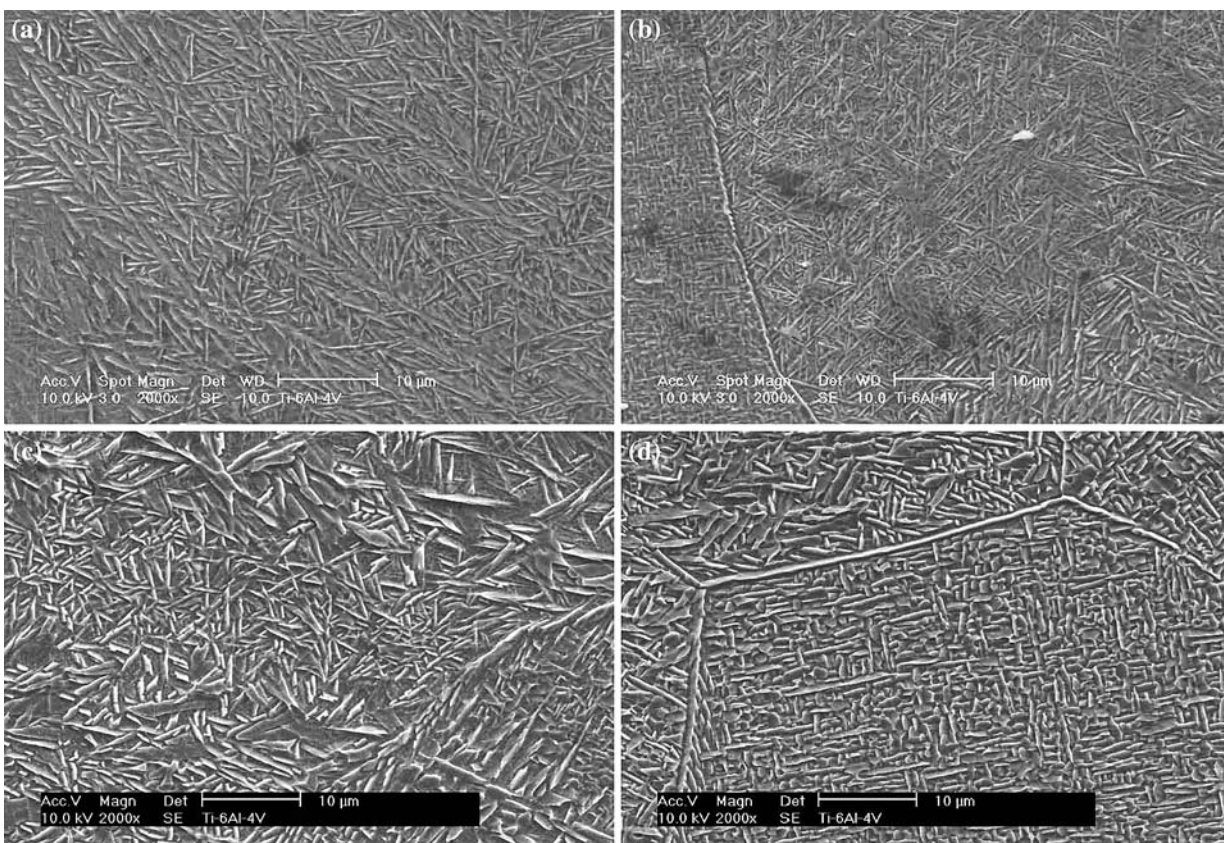


Fig. 7—SEM micrographs of as-deposited Ti-6Al-4V scaffold: (a) through (c) basketweave Widmanstätten α and (d) near equiaxed-like morphology with a smaller aspect ratio of α laths.

several dislocations were observed in the alpha laths. Moreover, careful TEM examination also showed that few (less than 1 pct) α laths contained parallel multiple twins (Figure 8(c)). However, twinning is not expected in Widmanstätten α unless extreme deformation conditions are imposed (cryogenic temperature and shock loading). On the other hand, twinning was frequently observed in martensitic α' .^[12,17] Hence, TEM investigation revealed that a small fraction of martensitic α'

might be present in the as-deposited sample. However, no clear martensitic structure was observed in the SEM investigation.

D. Mechanical Properties

A tensile test was performed in order to study the mechanical properties of the laser-deposited scaffold. For the medical implants, the scaffold should have

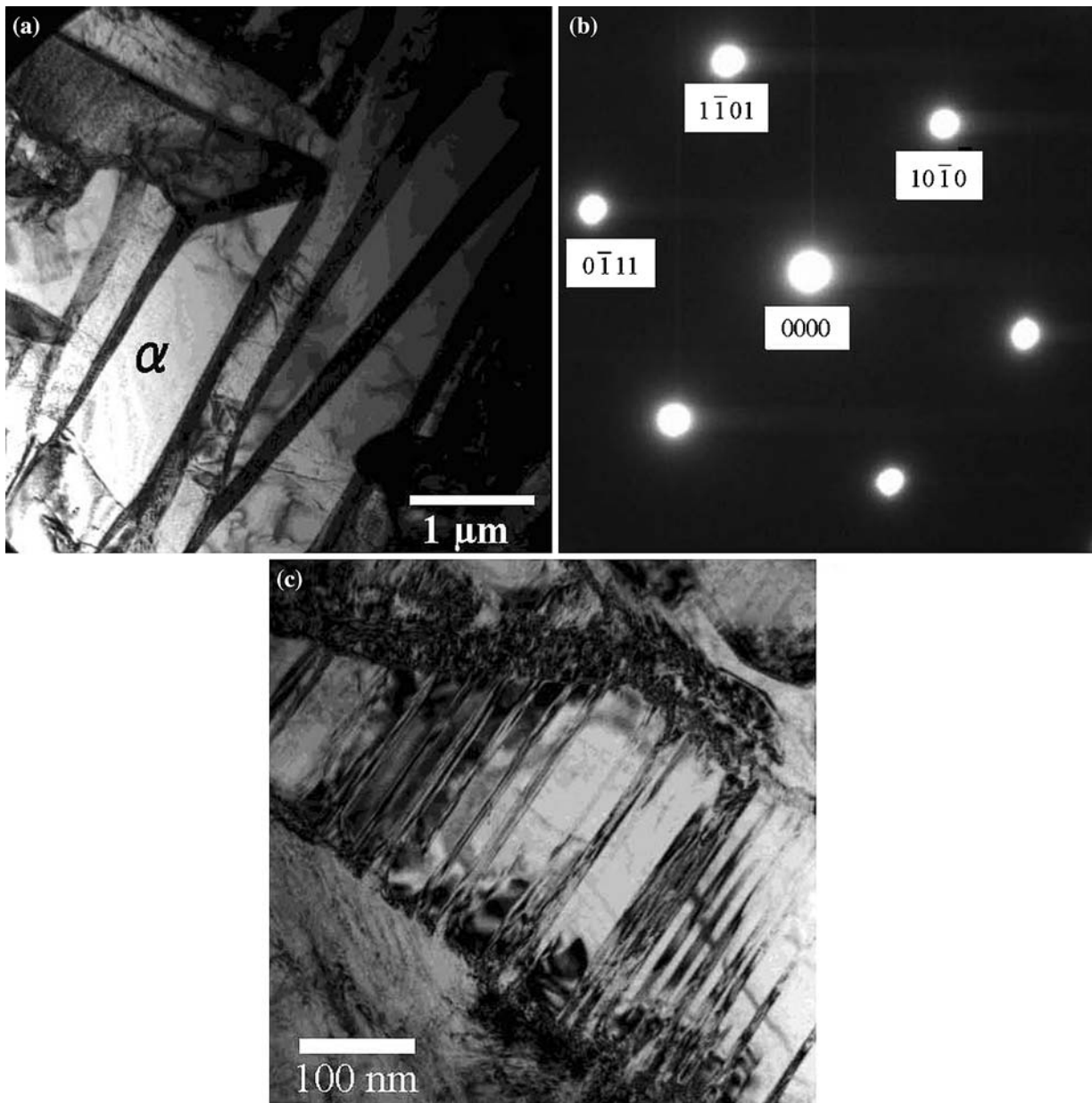


Fig. 8—TEM micrographs of the as-deposited Ti-6Al-4V: (a) bright-field image showing Widmanstätten α with high density of dislocations, (b) selected area diffraction pattern of image (a) {ZA = [12̄13]_x}, and (c) parallel twins.

sufficient mechanical strength, which should be more than that of living bone. Figure 9(a) shows the stress-strain curve of the laser-deposited Ti-6Al-4V after different heat treatments. The tensile test results are also shown in Table II. It can be seen from Figure 9(a) and Table II that the tensile and yield strengths of the as-deposited Ti-6Al-4V were 1163 ± 22 and 1105 ± 19 MPa, respectively, which are quite higher than the ASTM limits (896 and 827 MPa) for Ti-6Al-4V implants.^[12] However, the ductility (the breaking elongation) of the as-deposited sample was very low (~4 pct), which is well below the ASTM limit (10 pct). In order to improve the ductility, the laser-deposited samples were annealed at 950 °C and 1050 °C for 1 hour followed by either AC or FC. The best

combination of strength and ductility were found in the sample annealed at 950 °C followed by furnace cooling. Both strength (UTS $\sim 1045 \pm 16$ and YS $\sim 959 \pm 12$ MPa) and ductility ($\sim 10.5 \pm 1$ pct) of the furnace cooled samples were higher than the ASTM limits. It should be noted that the sample annealed at 1050 °C showed lower strength and ductility compared to the sample annealed at 950 °C. The observed difference of tensile properties of different heat-treated samples can be explained with the corresponding microstructure of the sample. Figures 9(b) through (f) show the SEM micrographs of as-deposited Ti-6Al-4V after different heat treatments. The most common observation of the as-deposited and additionally heat-treated samples is that all microstructure were Widmanstätten in nature.

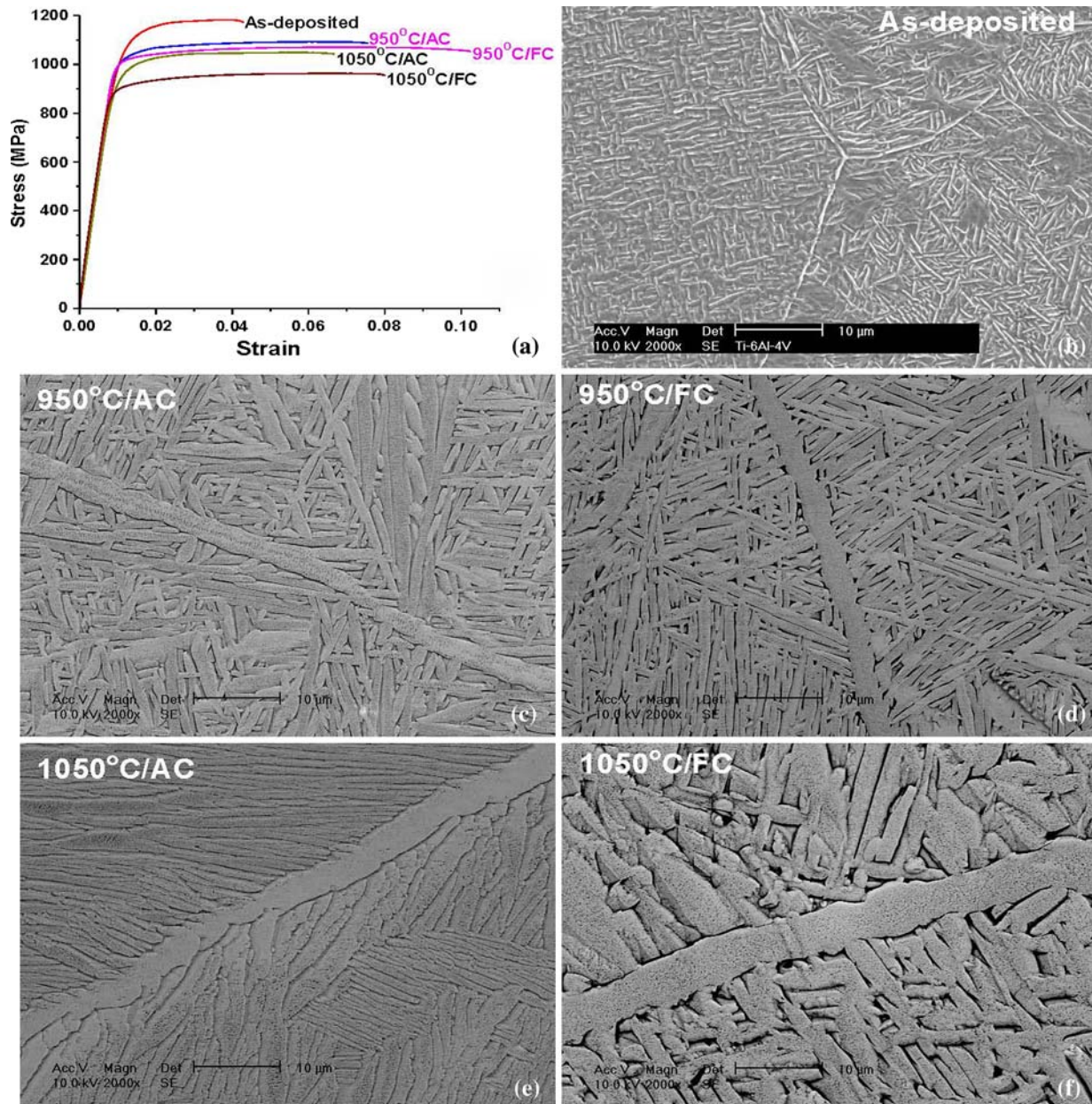


Fig. 9—(a) Stress-strain curves of the laser-deposited Ti-6Al-4V after different heat treatments. SEM micrographs of Ti-6Al-4V scaffold: (b) as-deposited, (c) annealed at 950 °C followed by AC, (d) annealed at 950 °C followed by FC, (e) annealed at 1050 °C followed by AC, and (f) annealed at 1050 °C followed by FC.

Table II. Tensile Properties of Direct Metal Deposited Ti-6Al-4V after Different Heat Treatments

Heat Treatment	Yield Strength (MPa)	Ultimate Strength (MPa)	Pct Elongation
As-deposited	1105 ± 19	1163 ± 22	4 ± 1
950 °C/air cool	975 ± 15	1053 ± 18	7.5 ± 1
950 °C/furnace cool	959 ± 12	1045 ± 16	10.5 ± 1
1050 °C/air cool	931 ± 16	1002 ± 19	6.5 ± 1
1050 °C/furnace cool	900 ± 14	951 ± 15	7.5 ± 1

In addition, the prior β grain boundaries are decorated with α . Moreover, the thickness of grain boundary α is higher as the annealing temperature is higher, being

$\sim 0.7 \mu\text{m}$ of as-deposited sample, $\sim 2.5 \mu\text{m}$ at 950 °C/AC, $\sim 2.7 \mu\text{m}$ at 950 °C/FC, $\sim 3.8 \mu\text{m}$ at 1050 °C/AC, and $\sim 4.7 \mu\text{m}$ at 1050 °C/FC samples. The higher strength and lower ductility of the as-deposited sample may be explained in terms of very fine microstructure (α , β) of the sample. However, the as-deposited sample shows a ductile fracture surface with classical dimple morphology (Figure 10). The annealed samples show better ductility due to the coarse and uniform microstructure. In contrast, the sample annealed at 1050 °C showed lower ductility because of the thicker grain boundary α compared to the sample annealed at 950 °C. It was found in the optical micrograph (Figure 6(a)) that the axes of the prior β grain, which is columnar in nature,

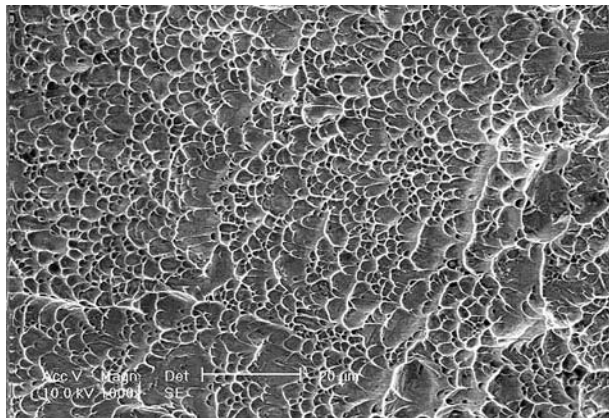


Fig. 10—Tensile fracture surfaces of the as-deposited Ti-6Al-4V shows a ductile fracture surface.

are parallel to the build direction. Hence, during tension testing, the grain boundary α was subjected to a tensile stress, because the tensile axis of the specimen was perpendicular to the deposit direction. Therefore, under tensile stress, cracks can easily propagate along the grain boundary and thicker grain boundary α enhanced the propagation of cracks along the grain boundary.

IV. DISCUSSION

According to the Ti-V phase diagram at 6 wt pct Al (Figure 11), the Ti-6Al-4V exhibits a microstructure consisting of a mixture of α (hcp) and β (bcc) phases at room temperature, whereas single-phase β is stable above 1000 °C. However, the room-temperature microstructure varies based on the thermal history of the alloy. For example, the cooling rate from the β -phase region to a temperature significantly below the β transus defines the nature of the α phase, whether it will be martensite or diffusion-controlled Widmästätten structure.^[13] Heat treatments can be used to alter the distribution, size, and morphology of the α phase, but generally do not have a large effect on the prior- β grains.

An optical micrograph (Figure 6(a)) shows that prior β grains are columnar in nature, whose axis is approximately parallel to the Z-axis, i.e., the build direction of the deposit. During laser deposition, cooling of a molten pool occurs mostly via the substrate and via the surrounding atmosphere. Heat loss through the substrate leads to more rapid cooling via the substrate than through convection and radiation. This leads to directional growth of the grains counter to the cooling direction and, subsequently, to the formation of columnar grains. The maximum height of the individual deposited layer is around 0.3 mm. However, we found that the length of columnar grains varies from 5 to 15 mm. Therefore, the columnar grains, nucleated at the first deposited layer, were continuously grown during deposition of the following layers. Recently, several researchers have also reported similar microstructural observation of laser-deposited Ti-6Al-4V.^[15-17]

It is very difficult to predict the microstructure of the DMD sample because of its very complex thermal

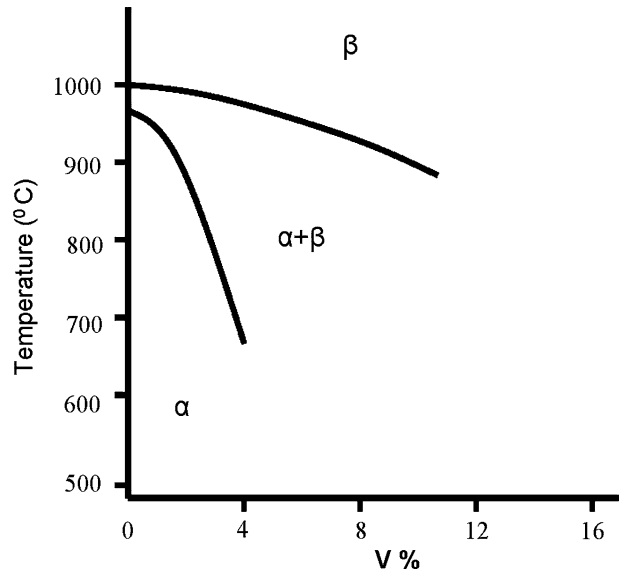


Fig. 11—Corner of Ti-V phase diagram at 6 wt pct Al.

history. Recently, Qian *et al.*^[14] have developed a finite element model for temperature history prediction in direct laser deposition samples. According to their model, during laser deposition, the very top layer cools from the liquid at a rate of $\sim 7 \times 10^4$ K s⁻¹ directly to a temperature significantly below the martensite start temperature. Ahmed *et al.*^[15] have shown that Ti-6Al-4V completely transformed to the martensitic structure at the cooling rate above 410 K s⁻¹. However, in the present study, no clear martensitic microstructure was observed even at the topmost layer of the as-deposited sample. Thus, it should be noted that the cooling rate of the present deposition process was less than 410 K s⁻¹. The SEM investigation revealed that the as-deposited microstructure is mainly various morphological forms of diffusion-controlled α . The observed microstructure is mostly a mixture of coarse and fine α laths. The observed microstructural difference at different locations of the sample can be explained in terms of the complex thermal history of the as-deposited sample. During DMD processing, the temperature of the pre-existing layers can exceed the β transus (~ 1000 °C) during the deposition of subsequent layers. As a result, a new heat-affected zone formed locally in the deposit every time the laser passed. This thermal excursion could result in coarsening of primary α laths, as found in Figure 9. Hence, the fine α laths are probably a result of the rapid cooling of the laser-deposited layer during the initial deposition process, whereas coarse α laths are a result of diffusion-controlled growth of the α laths during thermal excursion, with an additional layer added to the pre-existing layer.

V. CONCLUSIONS

The Ti-6Al-4V scaffold for the porcine CRU bone tissue engineering has been successfully fabricated by

DMD technology. It should be noted that the additional treatment including annealing and sandblasting was necessary in order to meet essential mechanical and surface criteria recommended for bone tissue engineering. The ductility of the as-deposited tensile sample was below the ASTM limit for Ti-6Al-4V implants. After a suitable heat treatment (sample annealed at 950 °C followed by furnace cooling), both strength (UTS \sim 1045 \pm 16, YS \sim 959 \pm 12 MPa) and ductility (\sim 10.5 \pm 1 pct) become higher than ASTM limits for medical implants.

ACKNOWLEDGMENTS

This work was supported by the Army Tank Command R&D group via Allion Corporation. Todd Richman was the program manager.

OPEN ACCESS

This article is distributed under the terms of the Creative Commons Attribution Noncommercial License which permits any noncommercial use, distribution, and reproduction in any medium, provided the original author(s) and source are credited.

REFERENCES

1. K. Wang: *Mater. Sci. Eng. A*, 1996, vol. 213, pp. 134–37.
2. Y. Zhang and M. Zhang: *J. Biomed. Mater. Res.*, 2001, vol. 55, pp. 304–12.

3. A.S. Goldstein, T.M. Juarez, C.D. Helmke, M.C. Gustin, and A.G. Mikos: *Biomaterials*, 2001, vol. 22, pp. 1279–88.
4. J.L. Koch and J. Mazumder: *Proc. ICALEO*, Laser Institute of America, Orlando, FL, 1993, pp. 556–65.
5. J. Mazumder, J.D. Dutta, N. Kikuchi, and A. Ghosh: *Opt. Las. Eng.*, 2000, vol. 34, pp. 397–414.
6. R. Mah: *Adv. Mater. Process.*, 1997, vol. 151, pp. 31–33.
7. G.K. Lewis, R. Nemec, J. Milewski, D.J. Thoma, D. Cremer, and M. Barbe: *Proc. Int. Congr. on Applications of Lasers and Electro-Optics*, Laser Institute of America, Orlando, FL, 1994, pp. 17–26.
8. D.M. Keicher, W.D. Miller, J.E. Smugeresky, and J.A. Romero: *Proc. TMS Annual Meeting*, San Antonio, TX, ASM INTERNATIONAL, Materials Park, OH, 1998, pp. 369–77.
9. D.M. Keicher and W.D. Miller: *Met. Powder Rep.*, 1998, vol. 53, pp. 26–28.
10. J.L. Koch and J. Mazumder: U.S. Patent Number 6,122,564, Sept. 2000.
11. C.L. Flanagan, S.J. Hollister, G.P. Dinda, and J. Mazumder: unpublished research.
12. *Annual Book of ASTM Standards, Medical Devices*, ASTM Standard No. F136-79, Section 13, ASTM International, West Conshohocken, PA, 1983, vol. 13.01, pp. 29–31.
13. T. Ahmed and H. Rack: *Mater. Sci. Eng. A*, 1998, vol. 243, pp. 206–11.
14. L. Qian, J. Mei, J. Liang, and X. Wu: *Mater. Sci. Technol.*, 2005, vol. 21, pp. 597–605.
15. P.A. Kobryns, E.H. Moore, and S.L. Semiatin: *Scripta Mater.*, 2000, vol. 43, pp. 299–305.
16. X. Wu, J. Liang, J. Mei, C. Mitchell, P.S. Goodwin, and W. Voice: *Mater. Des.*, 2004, vol. 25, pp. 137–44.
17. S.M. Kelly and S.L. Kampe: *Metall. Mater. Trans. A*, 2004, vol. 35A, pp. 1861–67.
18. F.J. Gil, J.M. Manero, M.P. Ginebra, and J.A. Planell: *Mater. Sci. Eng. A*, 2003, vol. 349, pp. 150–55.



ELSEVIER

Available online at www.sciencedirect.com**ScienceDirect**

Acta Materialia 87 (2015) 309–320

**Acta** MATERIALIAwww.elsevier.com/locate/actamat

Anisotropic tensile behavior of Ti–6Al–4V components fabricated with directed energy deposition additive manufacturing

Beth E. Carroll,^a Todd A. Palmer^{a,b} and Allison M. Beese^{a,*}^a*Department of Materials Science and Engineering, Pennsylvania State University, University Park, PA 16802, USA*^b*Applied Research Laboratory, Pennsylvania State University, University Park, PA 16802, USA*

Received 23 December 2014; accepted 29 December 2014

Available online 31 January 2015

Abstract—The present work investigates the anisotropic mechanical properties of a Ti–6Al–4V three-dimensional cruciform component fabricated using a directed energy deposition additive manufacturing (AM) process. The mechanical properties of the component in longitudinal and transverse orientations with respect to the build layers were measured under uniaxial tension. While the average ultimate tensile strength of ~1060 MPa in both directions agrees well with prior studies on AM Ti–6Al–4V, the achieved elongations of 11% and 14% along the longitudinal and transverse directions, respectively, are higher. The enhanced ductility is partially attributed to the lack of pores present in these components. The anisotropy in ductility is attributed to the columnar prior-β grain morphology and the presence of grain boundary α, which serves as a path along which damage can preferentially accumulate, leading to fracture. In addition, the effect of oxygen on the strength and ductility of the component was studied. The findings indicate that a combined effect of an increase of 0.0124 wt.% oxygen and a decrease in α-lath width due to differential cooling at different heights within the component resulted in an increase of ultimate and yield strengths without a significant loss of ductility. Furthermore, this study demonstrates that quasi-static uniaxial tensile mechanical properties similar to those of wrought Ti–6Al–4V can be produced in an AM component without the need for post-processing heat treatments.

© 2015 Acta Materialia Inc. Published by Elsevier Ltd. All rights reserved.

Keywords: Additive manufacturing; Titanium alloy; Mechanical properties; Anisotropy; Microstructure

1. Introduction

Titanium and its alloys, particularly Ti–6Al–4V, are widely used in the aerospace, sporting goods, medical device and petrochemical industries due to their relatively low density, high strength and good corrosion resistance [1,2]. However, there are formidable challenges in refining, casting, forming and machining titanium, which result in end products that are considerably more expensive than their steel or aluminum counterparts [3]. Given this initial material expense, the ability to produce net- and near-net-shape parts that require a minimum of follow-on machining and processing is of considerable interest.

Powder-based additive manufacturing (AM) is a near-net-shape production method in which a component is built by melting successive layers of metal feedstock onto a workpiece [4]. In these AM processes, a focused laser or electron beam is scanned in a preprogrammed pattern to melt the metallic feedstock material and produce a desired shape. Material can be delivered to the workpiece either by spreading and selectively melting individual powder layers in a powder bed fusion (PBF) process, or directed

continuously through coaxial nozzles to the melt pool in a directed energy deposition (DED) process [5,6]. AM can theoretically produce a fully dense three-dimensional part with highly complex geometric features [7,8]. It also offers the ability to fabricate parts with different geometries or compositions using the same machine, making the technique appealing for short production runs that would otherwise require prohibitively expensive tooling [2,9,10].

On the other hand, each location in the AM build experiences rapid melting and solidification with a complex thermal history, which can change significantly based on part geometry and path plan. In addition, the layer-by-layer method upon which the AM process is based leads to the introduction of lack-of-fusion defects at the interfaces between each laser pass and layer. As a result, it becomes difficult to fabricate fully dense or defect-free components and consistently produce components with repeatable mechanical properties across multiple lots in the as-deposited condition. Multiple researchers have used hot isostatic pressing as a method for closing pores while providing a post-fabrication heat treatment to homogenize microstructural features [8,10]. The present work demonstrates that a 99.999% dense component can be directly fabricated without the need for subsequent heat or pressure treatments, resulting in similar strength, and improved ductility, with respect to previous results in the literature.

^{*}Corresponding author; e-mail: amb961@psu.edu

PBF and DED AM processes are also characterized by significant differences in heat input, thermal histories and heat transfer methods. A simplified metric for comparing these laser-based processes is the approximate linear heat input, which is defined as the laser power divided by the scanning speed. While this metric does not account for differences in laser absorptivity or differences in heat transfer due to environmental and boundary conditions, it does provide a basic starting point for comparison between the two processes. PBF typically uses a linear heat input of $0.1\text{--}0.5 \text{ J mm}^{-1}$ and a layer thickness on the order of tens of microns, and heat transfer from the laser–powder interaction location is dominated by conduction through the unmelted powder surrounding the build. DED, on the other hand, typically uses a linear heat input of tens to hundreds of J mm^{-1} and a layer thickness of $\sim 0.3\text{--}1 \text{ mm}$, and heat transfer from the molten metal pool is controlled both by conduction through the component and attached baseplate as well as forced convection from the shielding gas and powder delivery nozzles.

Table 1 provides a summary of the deposition parameters and mechanical properties obtained from prior research on Ti–6Al–4V manufactured by DED, PBF and electron beam melting (EBM) [2,7,8,11–24]. These values are compared with accepted values for wrought Ti–6Al–4V tested in the annealed and solution treated and aged condition [2]. The yield and tensile strengths in laser-based AM components are generally higher than those in annealed material and in the same range as age-hardened Ti–6Al–4V, which is likely due to the presence of a fine-grained microstructure in laser-based AM components [24]. However, the tensile elongation values in laser-based AM components, which have previously been reported to be typically $\sim 6\%$ and a maximum of 11% , are substantially lower than the $12\text{--}17\%$ elongation range observed in wrought conditions. The strength values for EBM materials are typically lower, and elongation somewhat higher, than those for laser-produced parts. This is due in part to the fact that in the EBM process, the build is typically held at a temperature of over 600°C , allowing the part to anneal to an extent during fabrication [25]. It is noted that despite the fact that all of the studies in **Table 1** involve nominally the same material, the range of mechanical properties produced depends strongly on processing conditions.

Several possibilities exist for the low ductilities in the AM material: the presence and cracking of grain boundary hexagonal close-packed (hcp) α -phase [14], the fine-grained microstructure [15], and the presence of titanium martensite and low volume fractions of body-centered cubic (bcc) β -Ti phase [13]. Improvements in ductility are generally only obtained with post-fabrication heat treatments, such as sub- β transus annealing [20,26,23]. In addition, Vilaro et al. [23] observed that the prevalence of porosity in AM Ti–6Al–4V affects the mechanical behavior of the component, and that pore shape and orientation strongly influence macroscopic ductility. For example, lack of fusion defects can be formed when the inter-pass overlap is not properly maintained, resulting in the formation of internal porosity in the build. This type of internal process-induced defect has been difficult to prevent or even detect without destructive inspection.

While there is significant microstructural anisotropy in AM components [27], there has been little effort in the past to understand the connection between the anisotropic microstructure and macroscopic mechanical properties.

This microstructural anisotropy originates from the layer-by-layer nature of the AM process, which introduces a unique thermal history at each location within the part as each subsequent laser pass reheats the material [28,29]. The $\alpha\text{--}\beta$ titanium alloy Ti–6Al–4V is particularly sensitive to thermal history as it can develop a range of microstructures depending on temperature and cooling history [2,3]. The microstructure of as-fabricated Ti–6Al–4V components built by AM tends to be fine acicular or Widmanstätten $\alpha\text{--}\beta$. Columnar prior- β grains of several millimeters in length are also prominent features in the microstructure. These grains are oriented in the build direction, indicating that during solidification the high-temperature β phase nucleates onto itself and grows across the build layers [9].

In the present work, the role of microstructure in the location- and orientation-dependent properties in AM-fabricated Ti–6Al–4V is investigated. Because many of the previous studies have used directly fabricated mechanical test specimens (**Table 1**), the impact of changes in location and orientation on mechanical properties could not be obtained. In this work, by fabricating a discrete component and extracting mechanical test specimens directly from the component, location- and orientation-dependent properties in AM Ti–6Al–4V were investigated. The aim of this study is not AM process optimization, but rather characterization of the internal structure, microstructure and mechanical properties of an AM component. As such, the component was examined for porosity and internal defects using X-ray computed tomography. This showed that the component contained limited internal defects, and as a result, characterization of the mechanical properties of an AM component whose ductility was not limited by pores was performed. Based on the results of the mechanical and microstructural characterization of samples extracted from this build, a mechanism driving the anisotropic mechanical properties observed in Ti–6Al–4V structures is proposed. Additional analyses of the effect of changes in microstructure and oxygen content were performed and correlated with the location-dependent strength observed in the component.

2. Experimental

A Ti–6Al–4V cruciform structure was fabricated using a laser-based directed energy deposition process on a $152 \text{ mm} \times 152 \text{ mm} \times 12.7 \text{ mm}$ thick Ti–6Al–4V substrate. The deposition setup included an IPG Photonics® YLR-12000 laser system operating at a laser wavelength of $1070\text{--}1080 \text{ nm}$. The laser was delivered through a $200 \mu\text{m}$ diameter fiber into Precitec® YW-50 laser welding optics, which consist of a 200 mm focal length collimator and focusing optics. Powder was fed through a Precitec® YC-50 cladding head positioned 10 mm above the build. At this stand-off, a laser spot size diameter of 4 mm was obtained and used to fabricate the AM build. The cruciform structure used here was fabricated using a laser power of 2 kW and a travel speed of 10.6 mm s^{-1} , resulting in a linear heat input of 189 J mm^{-1} , which falls in the range of values previously reported for DED manufacturing [13,15] (see **Table 1**).

The fabrication of the cruciform was performed in an enclosed chamber purged with ultra-high-purity argon gas to minimize the oxygen contamination in the laser-deposited material. An argon gas flow of 9.4 l min^{-1} was used

Table 1. Summary of relevant Ti-6Al-4V mechanical properties reported in literature. Results for directed energy deposition (DED), powder bed fusion (PBF) and electron beam melting (EBM) are included. Where available, reported values are average \pm standard deviation.

Laser type	Linear heat input (J/mm)		Build path	Built part geometry	Tensile axis orientation	Yield strength (MPa)	Ultimate tensile strength (MPa)	Elongation (%)
	Laser power (W)	Scan speed (mm/s)						
<i>Directed energy deposition</i>								
Keicher & Miller, 1998	–	–	–	–	–	1069	1172	11
Zhang et al., 2001	CW Nd:YAG	15–22 130–190	8.5	–	Test coupon	– 950	–	~1
Dinda et al., 2008	CO ₂	492 300	2200	Raster	Test coupon	Longitudinal	1105 \pm 19	1163 \pm 22
Amsterdam & Kool, 2009	–	–	–	Tall wall	Longitudinal [§] Transverse [§]	1052 \pm 27 1045 \pm 24	1153 \pm 13 1141 \pm 15	5.3 \pm 2.1 9.2 \pm 1.1
Alcrista et al., 2011	–	–	–	Raster	Flat plate	Longitudinal Longitudinal [*]	984 \pm 25 870 \pm 37	1069 \pm 19 953 \pm 18
<i>Powder bed fusion</i>								
Hollander et al., 2006	Nd:G	–	–	Crosshatch	Test coupon	Longitudinal	1100 \pm 12	1211 \pm 31
Facchini et al., 2010	YAG	– 120–200	–	–	Test coupon	Longitudinal	1040 \pm 10	1140 \pm 10
Koike et al., 2011	–	0.55 5500	10,000	–	Test coupon	–	840	930
Vilaro et al., 2011	–	0.267 160	600	Crosshatch	Test coupon	Longitudinal Transverse	1137 \pm 20 962 \pm 47	1206 \pm 8 1166 \pm 25
Vrancken et al., 2012	SMYb:YAG	0.156 250	1600	Crosshatch	Test coupon	Longitudinal	1110 \pm 9	1267 \pm 5
Leuders et al., 2013	Yttrium fiber	–	–	–	Test coupon	Transverse	1008	1080
Rafi et al., 2013	–	–	–	–	Round tensile bar	Longitudinal Transverse	1195 \pm 19 1143 \pm 30	1269 \pm 9 1219 \pm 20
<i>Electron beam melting</i>								
Murr et al., 2009	–	–	–	Cylinder	Transverse	1100–1150	1150–1200	16–25
Koike et al., 2011	–	–	–	Round tensile bar	Transverse	750	780	2.2
Edwards et al., 2013	–	–	–	Finished flat dogbone	Longitudinal Transverse	783 \pm 15 812 \pm 12	833 \pm 22 851 \pm 19	2.7 \pm 0.4 3.6 \pm 0.9
Hrabe & Quinn, 2013	–	–	–	Wall	Longitudinal	982.9 \pm 5.7	1029.7 \pm 7.0	12.2 \pm 0.8
Rafi et al., 2013	–	–	–	Column	Transverse	984.1 \pm 8.5	1032.9 \pm 12.9	9.0 \pm 2.9
<i>Wrought</i>								
Donachie, 2000	* §	n/a n/a	n/a n/a	n/a n/a	n/a n/a	900 1100	970 1170	17 12

– Unspecified.

* Annealed.

§ Solution treated & aged.

to deliver the powder at a powder feed rate of 8 g min^{-1} . A second argon gas flow with the same 9.41 min^{-1} flow rate was also directed at the molten pool. This gas flow is normally used to shield the molten material from atmospheric contamination during cladding or deposition and is used here as well, even though the deposition is performed in an argon-purged chamber, to provide consistent forced convection conditions throughout processing. Each layer in the cruciform build consisted of three beads with a horizontal overlap distance of 2.29 mm. A vertical step size of 0.89 mm per layer was used to construct the 8.6 mm thick walls of the 100 mm tall cruciform. Fig. 1a shows the AM process schematically, and Fig. 1b shows the build path used for the cruciform. During the AM build process, the baseplate was water cooled. The prealloyed Ti-6Al-4V powder used (in wt.%: 6.17 Al, 3.98 V, 0.173 O, 0.018 C, 0.0022 H, 0.009 N, balance Ti) had a spherical morphology with an average diameter of 89 μm , and was manufactured through a plasma-rotating-electrode process (PREP[®]) by Timet Powder Metals.

During AM of titanium alloys, there is often potential for oxygen contamination. A failure during fabrication of the present cruciform resulted in the introduction of water vapor into the chamber during the deposition of a layer ~ 25 mm above the substrate. This portion of the build formed a straw-colored discolouration, as shown in Fig. 3a. Once the failed water-cooling line was repaired, the chamber was cleaned and purged with argon. When the original oxygen partial pressure was restored, the remainder of the build was completed without further

water contamination, allowing samples with different oxygen contents to be analyzed.

The interruption is not expected to have affected the thermal history of the part for the following reasons. Under normal operating conditions, it took 80–140 s for the laser to pass over the same point between subsequent layers, and prior thermal analysis on DED has shown that under similar operating conditions, Ti-6Al-4V layers cool to room temperature within 100–200 s of the laser moving away; thus, the material in the present study is expected to have cooled to close to room temperature between subsequent layers. Furthermore, the analysis suggests that the layers cool almost immediately (in under 100 s) to below 600 K, at which point microstructural changes will not occur [30].

The half of the cruciform that remained after extracting test coupons from the tested half is shown in Fig. 3a. Oxygen contents in the finished cruciform were measured by inert gas fusion from samples extracted 5 mm from the top of the wall and in a discolored region ~ 30 mm from the bottom of the wall, as shown in Fig. 3b. The oxygen content in the top of the cruciform was found to be 0.2046 wt.%, which is 0.0316 wt.% more oxygen than the initial powder, indicating oxygen pick-up during fabrication. The discolored region corresponding to a water release in the deposition chamber contains 0.2170 wt.% oxygen, which is 0.0124 wt.% more oxygen than measured at the top of the wall.

The cruciform was tested in the as-deposited condition, with no post-fabrication heat treatments. Tensile test specimens with gauge dimensions of $2 \text{ mm} \times 4 \text{ mm} \times 9 \text{ mm}$ were extracted from the walls of the cruciform component in two orientations with respect to the build direction. These dimensions were selected in order to allow for specimens to be extracted such that the location dependence and direction dependence of mechanical properties in the cruciform component could be quantified, while also aiming to incorporate of the order of 60 grains in the gauge region of the specimens. If ASTM E8 [31] were strictly followed, the specimen geometry would incorporate fewer than 30 grains, resulting in a stronger size-dependence on mechanical properties than the selected geometry. However, recognizing that a gauge length shorter than four times the effective diameter can act to inflate the vertical strain measurements with respect to values in accordance with E8, we extrapolate all strain values to a gauge length of four times the effective diameter of 3.19 mm by calculating the total effective strain as the sum of: (i) the uniform strain before necking; and (ii) the localized strain after necking, which is calculated as the change in length after localized necking divided by the ASTM E8 effective gauge length. We note that in previous studies the geometry of the specimens is frequently not fully defined, with several studies not mentioning accordance with standard measurement techniques [7,8,16,17,22,23,32]. Studies that have provided specimen dimensions as well as micrographs that show the prior β grain morphology are projected to have contained anywhere from 10 [18] to 60 [23] grains in the tested cross-section.

Fig. 3b shows the locations in the cruciform and baseplate from which the specimens were cut. Ten specimens were extracted from one wall of the cruciform such that their tensile axis was in the “transverse” direction, or parallel to the build axis, in two tiers of five specimens. Those cut from the bottom half of the cruciform were exposed to oxygen, while those extracted from the top half of the

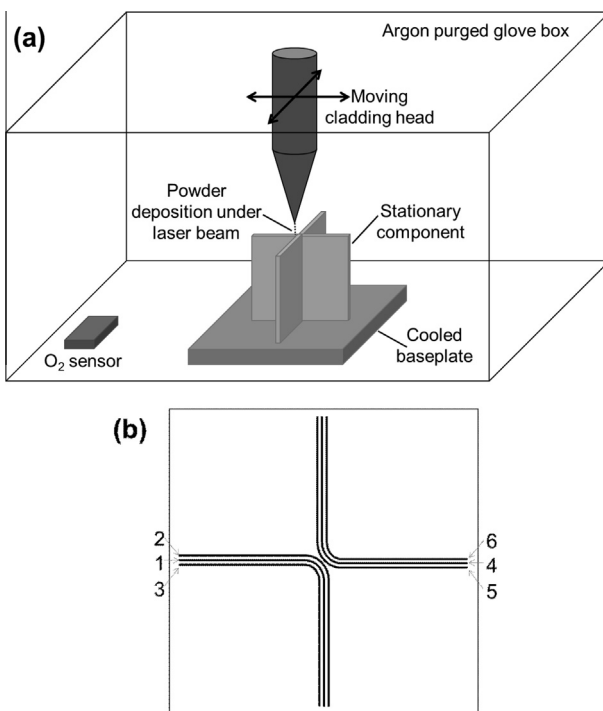


Fig. 1. (a) Schematic of the DED system. (b) Schematic of cruciform build path, showing the order in which the six passes per layer were laid down. Each subsequent layer followed the same order, but the starting point of the six lines alternated for each layer, meaning the odd layers were deposited as shown above, but in the even layers, the first three passes started from the bottom in the above schematic, and the second three passes started from the top.

cruciform represent specimens from a clean build. Eight specimens were machined “longitudinally” or with the tensile axis perpendicular to the build direction from another wall. For comparison, five specimens were cut from the wrought baseplate.

X-ray computed tomography (CT) is a radiographic-based non-destructive evaluation technique capable of $10\text{ }\mu\text{m}$ resolution and interrogation of internal features in bulk produced components. It was used here to examine the size and shape of internal pores or defects within the AM build, and to quantify the pore volume fraction. In this technique, the specimen is incrementally rotated and imaged using an X-ray beam, producing potentially thousands of individual radiographic projections, which are then combined into a three-dimensional rendering using CT algorithms. The three-dimensional representation of the part allows its entire volume to be analyzed and individual pores to be characterized in terms of both size and shape. This technique was used here to inspect both the bulk cruciform laser deposition and individual tensile testing specimens removed from the build.

A General Electric Phoenix v|tome|x m 300 cone beam CT cabinet system equipped with both a 300 kV xs|300d microfocus tube and a 180 kV xs|180nf nanofocus tube was used, and the resulting scans were analyzed using VGStudio Max 2.2 visualization and analysis software. The bulk cruciform was inspected using the microfocus tube with settings at 220 kV and 200 mA, a 500 ms scan time, and a voxel size of $147\text{ }\mu\text{m}$, while individual tensile specimens were inspected using the nanofocus tube with settings of 130 kV and 200 mA, a 333 ms scan time, and a voxel size of $15\text{ }\mu\text{m}$. A total of 1200 projections were obtained during the inspection of the cruciform, and 1500 projections were obtained for the individual tensile specimens. Conservatively, resolution of the system is limited by this voxel size, which in this case allows the tensile specimens to be interrogated at a much finer resolution. Analysis of the X-ray CT scans for the detection of internal defects within the tensile specimens was performed using the VGDefX (v. 2.2) algorithm in Volume Graphics

software (VGStudio Max, v. 2.2.6). The threshold to differentiate between material and void segments was set as the grayscale value of the surface of the tensile specimen. A noise reduction filter, which used a weighted average of the grayscale values for two neighboring voxels in all axes, was applied to each evaluated seed voxel. Additional filtering was performed on the data obtained from the inside surface of each defect to ensure that it was evaluated as a potential void or defect, rather than excluded as internal geometry. In the analysis of the defects, which appeared to be consistently spherical in morphology, a relative void probability threshold of 0.60 was applied, and a minimum void size was set at a volume of 8 voxels. After a visual examination of the results, additional false positives were removed, and the voids reported here had a relative probability ranging from 0.60 to 2.73 and volumes from 8 to 65 voxels, for a voxel edge length of $15\text{ }\mu\text{m}$.

Uniaxial tensile tests were carried out using a screw-actuated test frame (Instron model 4202) with a 10 kN tension load cell (Instron model 2512–147). Tests were run in displacement control at a strain rate of $3 \times 10^{-5}\text{ s}^{-1}$. Strains were calculated during testing through the optical monitoring of the surface deformation fields using digital image correlation with Vic2D software (Correlated Solutions). In this technique, a white background was painted onto the specimen gauge section, on top of which a black speckle pattern was applied, and digital cameras (Point Grey GRAS-50SSM-C) recorded images of the deforming gauge section at a rate of 1 Hz during testing. The displacement fields on the specimen surfaces were determined from the recorded images using the cubic B-spline interpolation algorithm of the Vic2D software. An 8.5 mm long virtual extensometer was used to calculate strains from the displacement fields. Representative vertical strain fields before fracture for an AM specimen and a specimen extracted from the base material are given in Fig. 2. The yield strength was measured by the 0.2% offset method.

Undeformed grip regions from tensile specimens were used for microstructure evaluation. These were etched using Kroll's reagent (2% hydrofluoric acid and 3% nitric

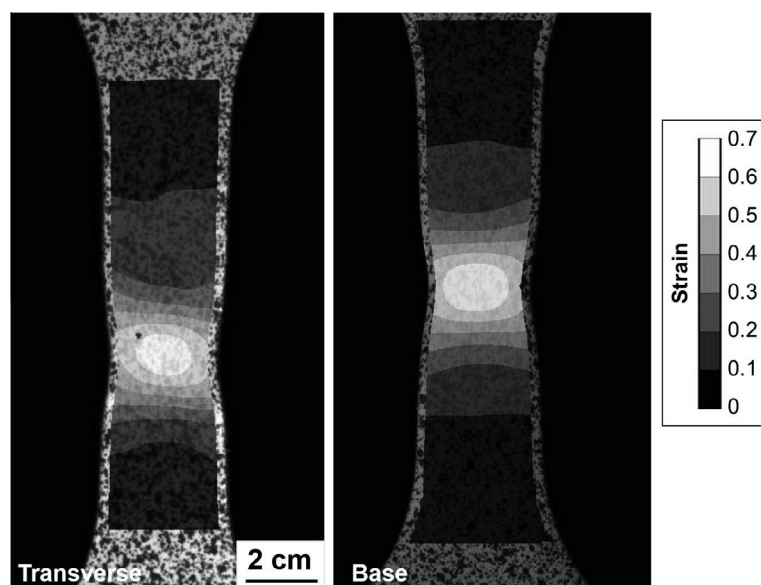


Fig. 2. Two-dimensional surface vertical strain contours immediately before fracture for representative base and transverse specimens.

acid in water). Microstructures were examined with an optical microscope (Keyence VHX-2000). Fracture surfaces from the tensile tests were examined by scanning electron microscopy (SEM; FEI Quanta 200).

3. Results and discussion

3.1. Overview

Representative engineering stress–strain curves for the longitudinal, transverse and baseplate specimens are given in Fig. 4, while the measured mechanical properties are given in Table 2. There is a significant difference in ductility between the longitudinal and transverse specimens, with an average engineering strain to failure of 11% in the longitudinal direction and 14% in the transverse direction. The yield and ultimate tensile strength values for all AM specimens of 959 ± 22 and 1064 ± 23 MPa, respectively, are commensurate with values obtained from the wrought baseplate of 973 ± 8 and 1050 ± 8 MPa. The yield and ultimate tensile strengths of the transverse specimens extracted

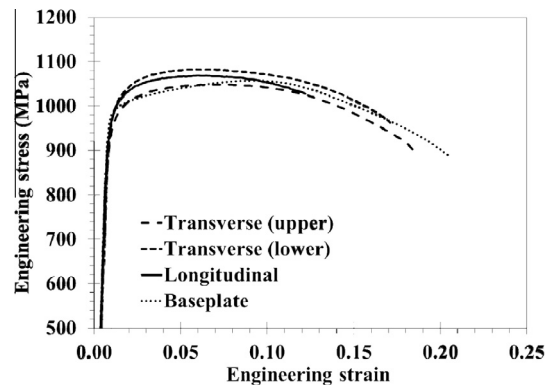


Fig. 4. Engineering stress–strain curves of representative specimens showing similar elastic responses, and highlighting the differences in strength and elongation values.

from the bottom of the wall (T6–T10 in Fig. 3b), where the component was exposed to oxygen, are 25 and 46 MPa higher, respectively, than those extracted from the upper

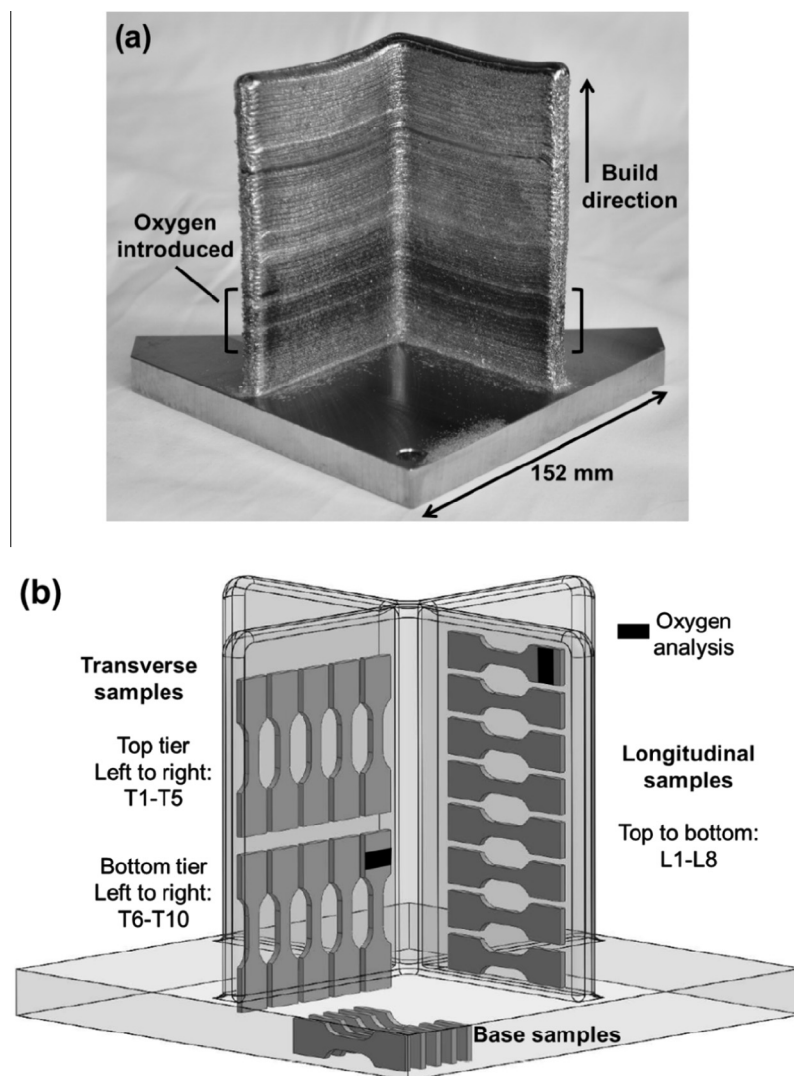


Fig. 3. (a) Half of the as-fabricated AM cruciform on a 152 mm baseplate; walls are ~100 mm tall. The vertical direction corresponds to the build, or transverse, direction. Brackets indicate the region of oxygen contamination. (b) Schematic showing how the tensile specimens were extracted from the component. The rectangular gauge sections of the tensile specimens were 4 mm × 2 mm × 9 mm.

Table 2. Summary of mechanical properties measured in this work. In specimens L1–L8, the tensile axis of each specimen was aligned with the longitudinal direction. In specimens T1–T10, the tensile axis of each specimen was aligned with the transverse, or build, direction. Specimens T1–T5 were extracted from the upper half of the cruciform, which was not exposed to oxygen, and T6–T10 were extracted from the lower half, which was exposed to oxygen. The base specimens were extracted from the wrought baseplate. Reported values are average \pm standard deviation.

	Transverse (upper tier)	Transverse (lower tier)	Longitudinal	Baseplate
Tensile strength (MPa)	1041 \pm 12	1087 \pm 8	1063 \pm 20	1053 \pm 7
Yield strength (MPa)	945 \pm 13	970 \pm 17	960 \pm 26	975 \pm 6
Measured elongation (%)	18.7 \pm 1.7	17.6 \pm 0.7	13.3 \pm 1.8	21.2 \pm 0.6
Elongation per ASTM E8 (%)	14.5 \pm 1.2	13.6 \pm 0.5	10.9 \pm 1.4	17.3 \pm 0.5

half of the wall (T1–T5 in Fig. 3b). While the measured strength values are similar to those in conventionally wrought Ti–6Al–4V, it is noted that the variability in the measurements from the AM component is higher than that in the wrought material, pointing to the importance of characterizing the mechanical properties of AM materials. The ductility of the specimens measured in the present study, with an average value of 13%, and a maximum of 16%, are notably higher than those found in previous studies on as-produced Ti–6Al–4V fabricated through laser-based AM, in which the reported average elongations were consistently below 11% (Table 1) for a range of different processing conditions.

3.2. Ductility

The increased ductility is attributed to the lack of porosity in the present study. Porosity appears in many of the previously published micrographs and fractographs of

AM Ti–6Al–4V [11,12,14], indicating that it is commonly present, often resulting in limited ductility. Previous studies were plagued by two types of pores: round gas entrapment pores and lack-of-fusion pores in which the melted metal in one layer did not completely fill the gaps between material passes in previous layers, resulting in thin flat cracks perpendicular to the build direction [9]. The sharp angles in lack-of-fusion pores result in local stress concentrations during loading; thus, these pores have been shown to play a significant role in early fracture, particularly in the transverse direction [23].

Given the prevalence and detrimental effects of porosity noted in previous studies, the present component was evaluated using X-ray CT. This analysis showed a very low pore volume fraction of 0.001%, with only spherical pores with an average diameter of 66 μm present. Fig. 5 shows a representative fracture surface from a specimen whose tensile axis was aligned with the transverse direction. All examined fracture surfaces exhibit ductile character, with

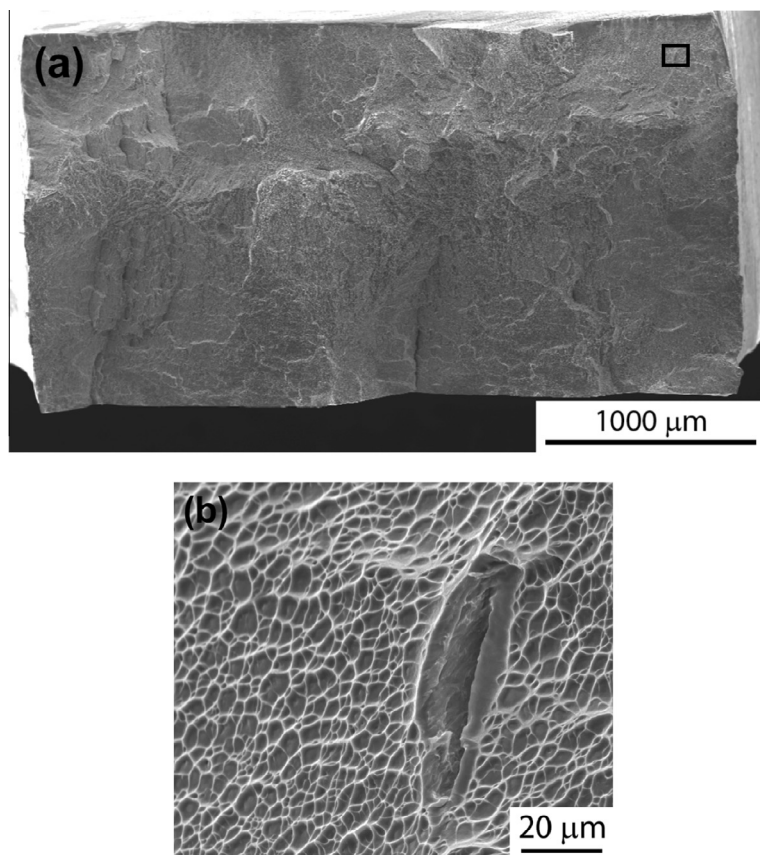


Fig. 5. Fracture surface of a specimen whose tensile axis was aligned with the longitudinal direction. (a) SEM image of entire fracture surface. (b) Enlarged image of inset in (a) showing a possible lack of fusion pore surrounded by ductile fracture features.

dimpled surfaces and evidence of tortuous crack growth. A pore $\sim 50 \mu\text{m}$ long was observed near one corner of a single longitudinal section (Fig. 5b), and no pores were found in any other fracture surfaces. Given the detrimental effect of pores on tensile ductility, the absence of porosity on the fracture surfaces is indicative of a fully dense material. The near-nonexistence of porosity suggests that the processing conditions used herein provide sufficient overlap between passes and suitable infiltration of melted material to prevent the formation of lack-of-fusion pores. Therefore, given the absence of both gas entrapment pores and lack-of-fusion porosity in fracture surfaces, it is concluded that porosity did not play a role in the elongation of the present specimens, resulting in higher ductility than observed in prior studies.

There is an impact of orientation on the ductility measured, as the ductility is higher in the transverse direction than in the longitudinal direction. This is the opposite of the trend observed in previous PBF studies (Table 1). It is hypothesized that the ductility in transverse specimens in prior studies was limited by the presence of lack-of-fusion porosity [8,12]. It may be concluded that the underlying mechanism for the anisotropy in ductility between longitudinal and transverse directions in the present study is directly related to the anisotropic microstructure of the AM part.

The microstructures of tested uniaxial tensile specimens extracted from the cruciform were analyzed. Fig. 6a shows a macroscopic image of a tensile specimen extracted in a longitudinal orientation with respect to the build direction. The horizontal build lines are visible, as is the morphology of the prior- β grains, whose long axes align with the build direction. In Fig. 6b, a higher-magnification view of the

build layers near the center of the wall shows a layer thickness of 0.5–1 mm and prior- β grains extending across multiple build layers, with light-colored layer bands appearing between each layer. This microstructure is similar to those observed by Kelly and Kampe [33] for laser-additive-manufactured builds of Ti-6Al-4V. This epitaxial growth of columnar β grains can be explained by the thermal gradient in the component, which is generated by conductive heat flow downward through the cooled substrate [34] and convective heat transfer outward into the process gas [35].

The prior- β grains in the component have long axes of 1.5 mm to >10 mm aligned with the build direction and short axes that are aligned perpendicular to the build direction and are on average 0.375 mm wide (Fig. 6). The boundaries of the prior- β grains are decorated with grain boundary α phase. It is well documented that the presence of grain boundary α phase tends to reduce elongation in conventionally processed Ti-6Al-4V by furnishing a preferential path for damage accumulation along the prior- β grain boundaries [2]. Tensile loads perpendicular to the grain boundary act to separate adjacent prior- β grains. Therefore, the morphology of the prior- β grains in the AM component results in different amounts of the grain boundary α phase being exposed to a tensile opening mode depending on whether tension is applied along the longitudinal or transverse direction. As shown schematically in Fig. 7, in specimens in which tension is applied along the transverse direction, only the short axes of the prior- β grain boundaries and grain boundary α are subjected to Mode I opening tension. Conversely, in specimens where tension is applied in the longitudinal direction, the long axes of the prior- β grains are loaded in tension, causing the entire length of the grain boundary α phase to be subjected to

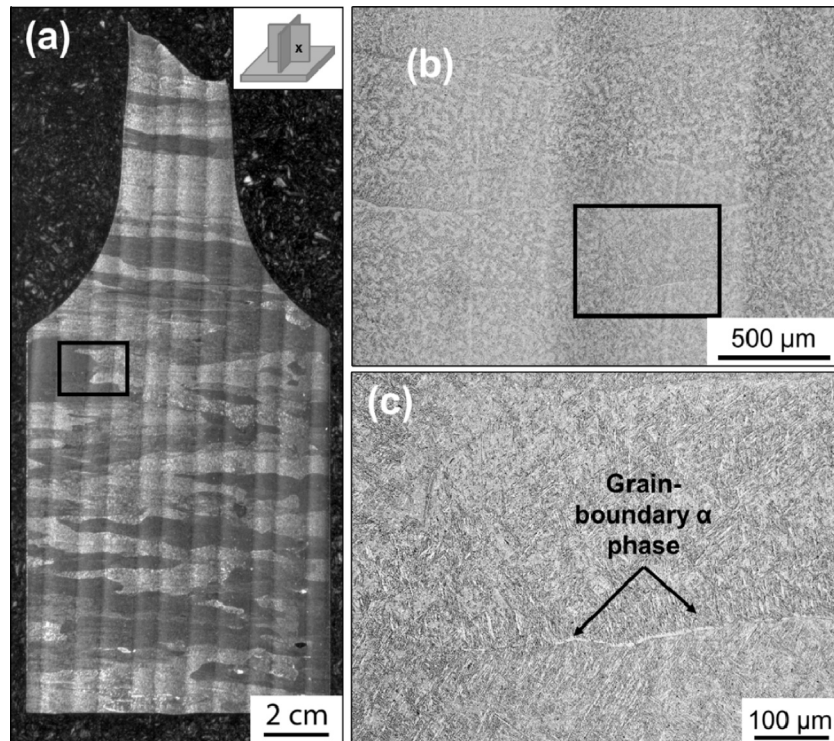


Fig. 6. Optical micrographs of etched microstructures, where build direction is horizontal. (a) Image of macrostructure, where build layers are vertical, and long and narrow prior- β grains are horizontal. (b) Micrograph of inset in (a) showing build lines (vertical) and prior- β grains (horizontal). (c) Micrograph of inset in (b) showing the acicular character of the microstructure as well as the presence of grain boundary α phase.

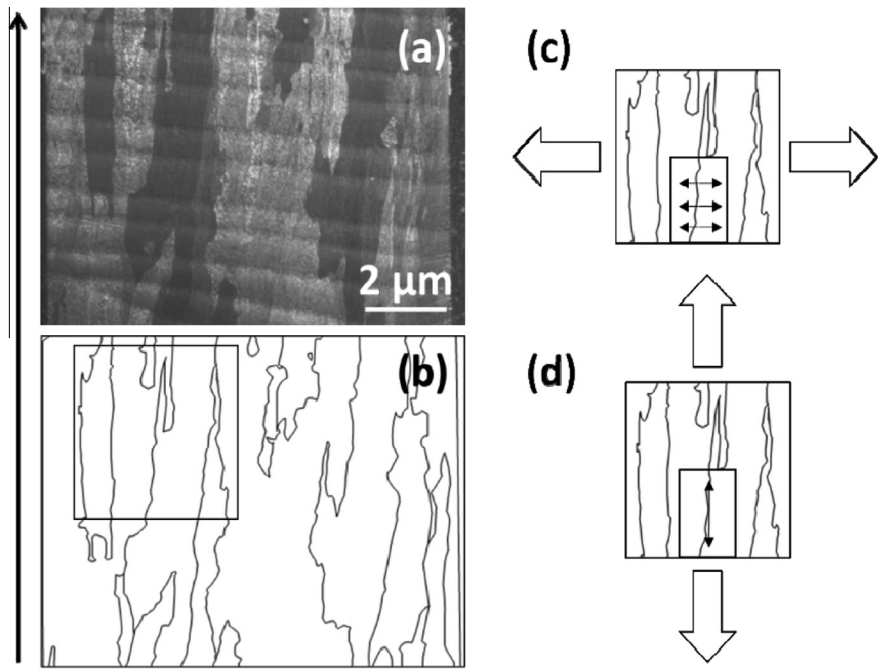


Fig. 7. (a) Micrograph showing build lines and longitudinal direction oriented horizontally, and prior- β grains and transverse direction oriented vertically; arrow indicates build direction. (b) Outline of prior- β grain boundaries from micrograph in (a), along which grain boundary α phase is present as shown in Fig. 6. (c) Enlargement of inset in (b) showing that when applying tension along the longitudinal direction, the grain boundary α will be subjected to Mode I opening failure, as tension is being applied perpendicular to the grain boundaries. (d) Enlargement of inset in (b) showing that when applying tension along the transverse or build direction, the tension acts parallel to the long prior- β grain boundaries, and therefore, the grain boundary α is not subjected to Mode I opening failure.

Mode I opening tension. Thus, the anisotropic microstructure predisposes the longitudinal specimens to Mode I opening failure along the prior- β grain boundaries, but not the transverse specimens. The reduced elongation of the longitudinal specimens compared with the transverse may be a result of discontinuous grain boundary α phase and the presence of the preferentially oriented prior- β grain boundaries. However, this morphological effect does not result in intergranular cracking, as the material remains ductile (Fig. 5).

As the microstructure of AM processed parts is morphologically anisotropic, crystallographic texture should be considered when accounting for variation in the mechanical behavior of these parts. Several authors report a strong fiber texture in the reconstructed prior- β grains corresponding to the columnar structure developed by the epitaxial growth of β phase from the melt on prior layers [25,36,37]. However, only a weak texture in the transformed microstructure is seen as all 12 possible variants in the Burgers orientation relationship between prior- β and transformed α phase appear seemingly at random in EBM material [25,36] and SLM material [37]. Similarly, no strong texturing of the transformed microstructure was observed in any direction in DED material [27]. Therefore, crystallographic texture is not expected to be a primary cause of the anisotropic ductility observed in this study.

As an aside, given the large size of the prior- β grains with respect to the 4 mm wide \times 2 mm thick gauge section, the coarse microstructure may result in size-dependent mechanical properties. Therefore, it should be noted that the properties reported herein are representative of this particular specimen size with the given microstructure, and

these properties could be affected if more or fewer grains were included in the gauge section. This coupling of mechanical properties and component geometry due to the size of the grains studied here presents a challenge for the design of AM structural components wherein the mechanical properties will not only depend on the processing conditions, but also the relative size of the component with respect to the microstructure, pointing to the importance for continued experimental and modeling work in this area.

3.3. Strength

Comparison of the strength values obtained in this study (Table 2) with those previously reported in the literature (Table 1) demonstrates that the material in the current study exhibits a reduction in yield and tensile strength with respect to previous values for AM Ti-6Al-4V. This difference is likely due, at least in part, to the direct fabrication of test coupons or very short walls from which to extract test specimens in prior studies, resulting in short structures as compared with the tall component built in the present study. Rapid cooling below the β transus of \sim 1000 °C produces a fine-scale α - β or martensitic structure within the prior- β grains [8]. Therefore, short structures would be able to disperse heat more efficiently into the baseplate, potentially cooling the part rapidly enough to form martensite, as compared to the tall cruciform component fabricated in this study in which heat must dissipate through conduction through the entire 100 mm tall wall as well as via convection.

Fig. 8 shows a pair of high-magnification optical micrographs from near the bottom (Fig. 8a) and near the top

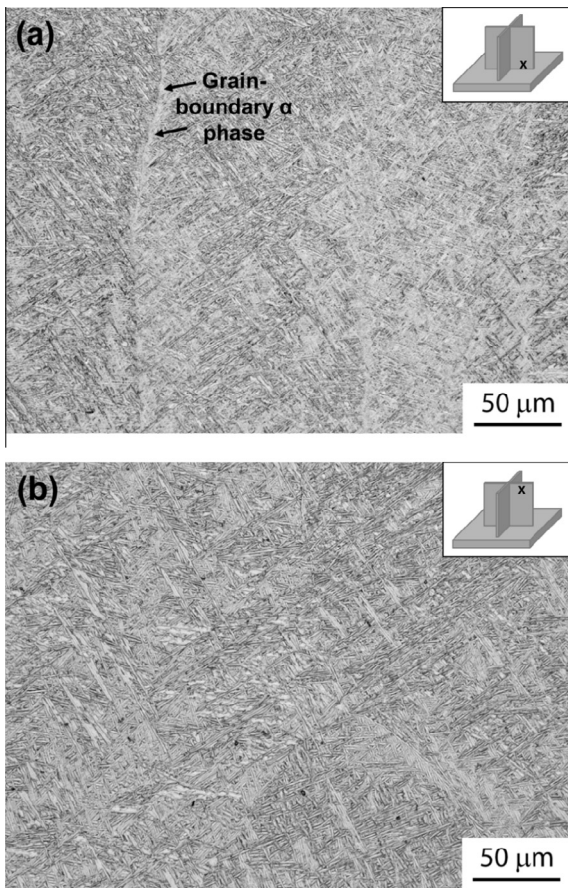


Fig. 8. Optical micrographs of samples showing (a) the microstructure near the bottom of wall with fine lamellar Widmanstätten structure and a small amount of grain boundary α phase indicated by arrows; and (b) the microstructure near the top of wall with variation in lath structures and slightly coarser Widmanstätten lamellae. The build direction is vertical in both images.

(Fig. 8b) of the cruciform wall. Both microstructures show a fine Widmanstätten structure, with lath widths on the order of one micron. There appears to be little α' (hcp martensite) in these structures, unlike the microstructures previously reported in as-fabricated AM parts [24]. This observation indicates that the cooling rate of the part from above the β transus, while rapid, was not sufficiently fast to allow the formation of martensite. Martensitic microstructures, owing to the presence of lattice strains, are generally stronger than α - β microstructures [1]. The absence of martensite may account for the reduction in yield and tensile strength observed in this study compared with previous results, but it should be noted that the strengths observed are well above the requirements for cast and wrought Ti-6Al-4V [38].

In addition to changes in the thermal history at different locations, differences in the oxygen contents may also affect the strength as a function of wall height in the component fabricated herein. The ultimate tensile and yield strengths in transverse specimens extracted from the oxygen-contaminated lower half of the wall were 46 and 25 MPa higher, respectively, than those extracted from the non-oxygen-contaminated upper half of the wall. Oxygen is an interstitial element in titanium alloys that strengthens and stabilizes the α phase. This effect is demonstrated in

Ti-6Al-4V by a small increase in both yield and tensile strength with increasing oxygen [39], usually accompanied by a reduction in ductility [10]. The variation in oxygen content between vertically spaced sites ~ 20 mm apart in AM Ti-6Al-4V has been measured to be 0.002 wt.% [33], which is considerably less than the 0.0124 wt.% variation observed here. Extrapolation of the ultimate and yield stress data as a function of oxygen content in Ref. [39] to the oxygen values in the present study suggests that an increase in yield strength of 16 MPa and an increase in ultimate tensile strength of 9 MPa is expected from the top tier to the bottom tier, due to the presence of the additional 0.0124 wt.% of oxygen alone. Furthermore, Vickers measurements (300 g load) in the discolored area show a hardness of 351 ± 18 HV, compared with a hardness of 333 ± 9 HV far from the discoloration.

In terms of differential thermal histories, the lower portion of the wall, which is closer to the baseplate, cools more rapidly than the upper portion [40], in which the heat must escape either by convection outward or conduction down the height of the wall [35]. In addition, Ti-6Al-4V has, for a metal, a low thermal conductivity of $\sim 7 \text{ W m}^{-1} \text{ K}^{-1}$ [39] at room temperature. The energy input from the laser is therefore dispersed more slowly with increasing wall height, and the wall temperature increases with height while the cooling rate decreases. Coarsened Widmanstätten microstructures resulting from reduced cooling rates in Ti-6Al-4V are known to correlate to reductions in yield and tensile strengths [41]. Quantification of the microstructures shown in Fig. 8 according to the method described by Tiley et al. [42] demonstrates an average α lath width of $0.88 \mu\text{m}$ at the bottom of the wall and $0.95 \mu\text{m}$ at the top of the wall where slower cooling is expected [43]. These observations follow the same trend as observed by Wu et al. [43]. In addition to the increase in strength due to higher oxygen content and finer microstructure in the lower half of the cruciform, there is also an apparent reduction in ductility. Therefore, it is probable that the 100 mm height of the wall resulted in a thermal history that varied as a function of wall height, creating gradients in both microstructure and tensile behavior.

4. Summary and conclusions

A Ti-6Al-4V cruciform-shaped component was fabricated using a laser-based directed energy deposition AM process, and the location-dependent, direction-dependent and oxygen-dependent mechanical properties were measured. The primary conclusions from this study are as follows:

- The mechanical properties in the AM component studied herein are commensurate with those of wrought material without the need for post-fabrication heat or pressure treatments. Of particular note is that the ductility values achieved in the present component exceed those previously found in AM Ti-6Al-4V, with significant ductility achieved in both the longitudinal and transverse directions. The ability to attain high ductility is dependent on the prevention of lack of fusion porosity in the finished component.
- The long and thin prior- β grains growing along the build direction result in anisotropic tensile elongation properties, rendering the ductility significantly higher along the transverse direction than the

longitudinal direction. It is hypothesized that the prior- β grain morphology, which results in grain boundary α -phase being subject to accelerated damage under a tensile opening mode when tension is applied in the longitudinal direction, leads to a lower ductility along the longitudinal direction with respect to the build or transverse direction.

- The presence of additional oxygen, of the order of 0.0125 wt.%, in the Ti-6Al-4V component increases both the ultimate tensile strength and yield strength, and only slightly reduces ductility; thus, the introduced oxygen contamination did not lead to embrittlement of the component.
- In addition to the dependence on oxygen, the location dependence of ultimate tensile and yield strengths within the tall build is partially attributed to the variance in thermal profile as a function of height. These differences in thermal history result in the presence of a finer microstructure at the bottom of the wall near the water-cooled baseplate, as compared to the larger α -lath width near the top of the wall. This differential thermal history results in higher strengths in specimens extracted from the bottom half of the cruciform as compared to the top.

Acknowledgements

The authors gratefully acknowledge the financial support of the National Science Foundation through award number CMMI-1402978. Any opinions, findings, and conclusions or recommendations expressed in this material are those of the authors and do not necessarily reflect the views of the National Science Foundation. We thank Professor Donald A. Koss for his valuable feedback on the manuscript. We also acknowledge Mr. Jay Tressler for fabrication of the cruciform, Mr. Griffin Jones for X-ray CT data, and Mr. Ed Good for use of his metallurgical laboratory.

References

- [1] M. Peters, J. Hempenmacher, J. Kumpfert, C. Leyens, Structure and properties of titanium and titanium alloys, in: C. Leyens, M. Peters (Eds.), Titanium and Titanium Alloys: Fundamentals and Applications, Wiley-VCH, Weinheim, 2003.
- [2] M.J. Donachie, Titanium: A Technical Guide, second ed., ASM International, Materials Park, OH, 2000.
- [3] G. Lutjering, J.C. Williams, Titanium, second ed., Springer-Verlag, Berlin, 2007.
- [4] D.D. Gu, W. Meiners, K. Wissenbach, R. Poprawe, Laser additive manufacturing of metallic components: materials, processes and mechanisms, *Int. Mater. Rev.* 57 (3) (2012) 133–164.
- [5] B. Dutta, F.H. Froes, Additive manufacturing of titanium alloys, *Adv. Mater. Process.* (2014) 18–23.
- [6] W.E. Frazier, Metal additive manufacturing: a review, *J. Mater. Eng. Perform.* 23 (6) (2014) 1917–1928.
- [7] D.A. Hollander, M. von Walter, T. Wirtz, R. Sellei, B. Schmidt-Rohlfing, O. Paar, H.-J. Erli, Structural, mechanical and in vitro characterization of individually structured Ti-6Al-4V produced by direct laser forming, *Biomaterials* 27 (7) (2006) 955–963.
- [8] S. Leuders, M. Thöne, A. Riemer, T. Niendorf, T. Tröster, H.A. Richard, H.J. Maier, On the mechanical behaviour of titanium alloy TiAl6V4 manufactured by selective laser melting: fatigue resistance and crack growth performance, *Int. J. Fatigue* 48 (2013) 300–307.
- [9] P.A. Kobryn, E.H. Moore, S.L. Semiatin, The effect of laser power and traverse speed on microstructure, porosity, and build height in laser-deposited Ti-6Al-4V, *Scr. Mater.* 43 (4) (2000) 299–305.
- [10] S. Das, M. Wohltert, J.J. Beaman, D.L. Bourell, Processing of titanium net shapes by SLS/HIP, *Mater. Des.* 20 (1999) 115–121.
- [11] L.E. Murr, E.V. Esquivel, S.a. Quinones, S.M. Gaytan, M.I. Lopez, E.Y. Martinez, F. Medina, D.H. Hernandez, E. Martinez, J.L. Martinez, S.W. Stafford, D.K. Brown, T. Hoppe, W. Meyers, U. Lindhe, R.B. Wicker, Microstructures and mechanical properties of electron beam-rapid manufactured Ti-6Al-4V biomedical prototypes compared to wrought Ti-6Al-4V, *Mater. Charact.* 60 (2) (2009) 96–105.
- [12] H.K. Rafi, N.V. Karthik, H. Gong, T.L. Starr, B.E. Stucker, Microstructures and mechanical properties of Ti6Al4V parts fabricated by selective laser melting and electron beam melting, *J. Mater. Eng. Perform.* 22 (12) (2013) 3872–3883.
- [13] N. Hrabe, T. Quinn, Effects of processing on microstructure and mechanical properties of a titanium alloy (Ti-6Al-4V) fabricated using electron beam melting (EBM), Part 1: distance from build plate and part size, *Mater. Sci. Eng., A* 573 (2013) 264–270.
- [14] N. Hrabe, T. Quinn, Effects of processing on microstructure and mechanical properties of a titanium alloy (Ti-6Al-4V) fabricated using electron beam melting (EBM), Part 2: energy input, orientation, and location, *Mater. Sci. Eng., A* 573 (2013) 271–277.
- [15] P. Edwards, A. O’Conner, M. Ramulu, Electron beam additive manufacturing of titanium components: properties and performance, *J. Manuf. Sci. Eng.* 135 (6) (2013) 061016.
- [16] D.M. Keicher, W.D. Miller, LENS moves beyond RP to direct fabrication, *MPR*, pp. 26–28, December 1998.
- [17] X.D. Zhang, H. Zhang, T.J. Lienert, C. Brice, H.L. Fraser, D.M. Keicher, M.E. Schlienger, Laser-deposited advanced materials, *J. Adv. Mater.* 33 (1) (2001) 17–23.
- [18] G.P. Dinda, L. Song, J. Mazumder, Fabrication of Ti-6Al-4V scaffolds by direct metal deposition, *Metall. Mater. Trans. A* 39 (12) (2008) 2914–2922.
- [19] E. Amsterdam, G.A. Kool, High cycle fatigue of laser beam deposited Ti-6Al-4V and Inconel 718, in: 25th ICAF Symposium, 2009, no. May, pp. 1261–1274.
- [20] J. Alcristo, A. Enriquez, H. Garcia, S. Hinkson, T. Steelman, E. Silverman, P. Valdovino, H. Gigerenzer, J. Foyos, J. Ogren, J. Dorey, K. Karg, T. McDonald, O.S. Es-Said, Tensile properties and microstructures of laser-formed Ti-6Al-4V, *J. Mater. Eng. Perform.* 20 (2) (2011) 203–212.
- [21] L. Facchini, E. Magalini, P. Robotti, A. Molinari, S. Höges, K. Wissenbach, Ductility of a Ti-6Al-4V alloy produced by selective laser melting of prealloyed powders, *Rapid Prototyp. J.* 16 (6) (2010) 450–459.
- [22] M. Koike, P. Greer, K. Owen, G. Lilly, L.E. Murr, S.M. Gaytan, E. Martinez, T. Okabe, Evaluation of titanium alloys fabricated using rapid prototyping technologies—electron beam melting and laser beam melting, *Materials (Basel)* 4 (12) (2011) 1776–1792.
- [23] T. Vilardo, C. Colin, J.D. Bartout, As-fabricated and heat-treated microstructures of the Ti-6Al-4V alloy processed by selective laser melting, *Metall. Mater. Trans. A* 42 (10) (2011) 3190–3199.
- [24] B. Vrancken, L. Thijs, J.-P. Kruth, J. Van Humbeeck, Heat treatment of Ti6Al4V produced by selective laser melting: microstructure and mechanical properties, *J. Alloys Compd.* 541 (2012) 177–185.
- [25] A.A. Antonysamy, J. Meyer, P.B. Prangnell, Effect of build geometry on the β -grain structure and texture in additive manufacture of Ti6Al4V by selective electron beam melting, *Mater. Charact.* 84 (2013) 153–168.
- [26] E. Amsterdam, G.A. Kool, High cycle fatigue of laser beam deposited Ti-6Al-4V and Inconel 718, in: 25th ICAF Symposium, 2009, no. May, pp. 1261–1274.
- [27] D. Clark, M.T. Whittaker, M.R. Bache, Microstructural characterization of a prototype titanium alloy structure

- processed via direct laser deposition (DLD), *Metall. Mater. Trans. B* 43B (2011) 388–396.
- [28] P.A. Kobryn, S.L. Semiatin, Microstructure and texture evolution during solidification processing of Ti–6Al–4V, *J. Mater. Process. Technol.* 135 (2–3) (2003) 330–339.
- [29] P.A. Kobryn, S.L. Semiatin, The laser additive manufacture of Ti–6Al–4V, *JOM* 53 (9) (2001) 40–42.
- [30] S.M. Kelly, S.L. Kampe, Microstructural evolution in laser-deposited multilayer Ti–6Al–4V builds: Part II. Thermal modeling, *Metall. Mater. Trans. A* 35 (2004) 1869–1879.
- [31] ASTM Standard E8: Standard Test Methods for Tension Testing of Metallic Materials, ASTM International, West Conshohocken, PA, 2014, pp. 1–28.
- [32] J. Alcristo, A. Enriquez, H. Garcia, S. Hinkson, T. Steelman, E. Silverman, P. Valdovino, H. Gigerenzer, J. Foyos, J. Ogren, J. Dorey, K. Karg, T. McDonald, O.S. Es-Said, Tensile properties and microstructures of laser-formed Ti–6Al–4V, *J. Mater. Eng. Perform.* 20 (2) (2010) 203–212.
- [33] S.M. Kelly, S.L. Kampe, Microstructural evolution in laser-deposited multilayer Ti–6Al–4V builds: Part I. Microstructural characterization, *Metall. Mater. Trans. A* 35 (2004) 1861–1867.
- [34] J. Chen, L. Xue, S.-H. Wang, Experimental studies on process-induced morphological characteristics of macro- and microstructures in laser consolidated alloys, *J. Mater. Sci.* 46 (2011) 5859–5875.
- [35] L. Costa, R. Vilar, Laser powder deposition, *Rapid Prototyp. J.* 15 (4) (2009) 264–279.
- [36] S.S. Al-Bermani, M.L. Blackmore, W. Zhang, I. Todd, The origin of microstructural diversity, texture, and mechanical properties in electron beam melted Ti–6Al–4V, *Metall. Mater. Trans. A* 41 (13) (2010) 3422–3434.
- [37] M. Simonelli, Y.Y. Tse, C. Tuck, On the texture formation of selective laser melted Ti–6Al–4V, *Metall. Mater. Trans. A* 45 (6) (2014) 2863–2872.
- [38] A.S.T.M. Standard, B348-13: Titanium and Titanium Alloy Billets and Bars, ASTM, International, West Conshohocken, PA, 2013.
- [39] G. Welsch, R. Boyer, E.W. Collings (Eds.), *Material Properties Handbook: Titanium Alloys*, ASM International, Materials Park, OH, 1994, p. 524.
- [40] L. Qian, J. Mei, J. Liang, X. Wu, Influence of position and laser power on thermal history and microstructure of direct laser fabricated Ti–6Al–4V samples, *Mater. Sci. Technol.* 21 (5) (2005) 597–605.
- [41] D. Lee, S. Lee, C.S. Lee, S. Hur, Effects of microstructural factors on quasi-static and dynamic deformation behaviors of Ti–6Al–4V alloys with Widmanstätten structures, *Metall. Mater. Trans. A* 34 (2003) 2541–2548.
- [42] J. Tiley, T. Searles, E. Lee, S. Kar, R. Banerjee, J. Russ, H. Fraser, Quantification of microstructural features in α/β titanium alloys, *Mater. Sci. Eng., A* 372 (1–2) (2004) 191–198.
- [43] X. Wu, J. Liang, J. Mei, C. Mitchell, P.S. Goodwin, W. Voice, Microstructures of laser-deposited Ti–6Al–4V, *Mater. Des.* 25 (2) (2004) 137–144.



Available online at www.sciencedirect.com

ScienceDirect

ELSEVIER

Procedia Engineering 114 (2015) 658 – 666

**Procedia
Engineering**

www.elsevier.com/locate/procedia

1st International Conference on Structural Integrity

Microstructure Evolution, Tensile Properties, and Fatigue Damage Mechanisms in Ti-6Al-4V Alloys Fabricated by Two Additive Manufacturing Techniques

Yuwei Zhai^{a,*}, Haize Galarraga^a, and Diana A. Lados^a

^a*Worcester Polytechnic Institute, Integrative Materials Design Center, 100 Institute Road, Worcester, MA 01609, USA*

Abstract

Additive Manufacturing (AM) technology is capable of building 3D near-net-shaped functional parts directly from computer models, using unit materials, such as powder or wire. AM offers superior geometrical flexibility with significantly reduced manufacturing lead time, energy, and material waste. These benefits make AM desirable for critical transportation applications, providing that structural integrity and performance requirements are met or exceeded. In this study, structural materials fabricated by two AM techniques were investigated: Laser Engineered Net Shaping (LENS) and Electron Beam Melting (EBM). Ti-6Al-4V alloys were produced using both methods and various processing conditions, which resulted in different microstructures and mechanical properties given their unique thermal histories. Characteristic microstructures were determined for all cases. Room temperature tensile and fatigue crack growth (FCG) properties were also evaluated and compared in different orientations with respect to the deposition direction. The effects of post-deposition heat treatment on tensile and FCG properties were determined. The results are systematically presented and discussed from both the material/process optimization, as well as structural design and fatigue life prediction perspectives.

© 2015 Published by Elsevier Ltd. This is an open access article under the CC BY-NC-ND license (<http://creativecommons.org/licenses/by-nc-nd/4.0/>).

Peer-review under responsibility of INEGI - Institute of Science and Innovation in Mechanical and Industrial Engineering

Keywords: Ti-6Al-4V, Microstructure evolution, Mechanical properties, Fatigue damage mechanisms, Laser engineered net shaping, Electron beam melting

* Corresponding author. Tel.: +1-508-831-5255.

E-mail address: yzhai@wpi.edu

1. Introduction and background

Additive Manufacturing (AM) technology represents a family of advanced near-net-shaping techniques that are able to build 3D geometries directly from computer models, using material units, most commonly powder and wire. Although various AM techniques were developed, their working principles can be generalized [1]. Standardized definition and terminologies were also developed specifically for AM (ASTM F2792-12a). Researches have been done to study the microstructures and tensile properties in AM-fabricated materials [2-10]. However, the materials' performances under cyclic loading, i.e., fatigue properties were rarely reported [11], neither was there a systematic comparison between microstructures and properties obtained using different AM techniques.

In this study, two AM techniques, Laser Engineered Net Shaping (LENS) and Electron Beam Melting (EBM) were studied and compared using Ti-6Al-4V alloys. Systematic investigation of the influence of processing parameters on microstructure evolution, tensile properties, and fatigue properties were performed. The effects of post-deposition heat treatments were also studied.

LENS technique was originally developed at Sandia National Laboratories and was commercialized by Optomec, Inc. in 1997 [12]. In the same year, the Swedish company ARCAM AB was founded, and published its first patent for EBM technique in 2001 [13]. Schematic representations illustrating the working principles of LENS and EBM are shown in Fig. 1 [1]. During LENS process, the laser beam creates a melting pool on a substrate placed onto the x-y table, material powder is then injected into the melting pool to fuse and solidify into a bead. At the same time, the substrate moves with the x-y table (in x-y directions), enabling the selective deposition of one layer. Then, the laser beam and material deposition head move together upward (in z direction) to start the deposition of the second layer. This procedure is repeated until a 3D geometry is completed. The finished geometry and the substrate can be separated by machining (apart from the cases where the process is applied for repairing). During EBM process, material powder is provided by powder hoppers instead, and is uniformly distributed in one layer on the build platform by a rake. Powder in this layer is then selectively melted by the electron beam. After the first layer is completed, the build platform lowers, allowing a new layer of powder to be uniformly distributed on top of the first layer. This new layer of powder is again selectively melted by the electron beam, and the process continues until the complete 3D geometry is built. The finished geometry is freed by blasting off the excess powder, which is usually partially recycled.

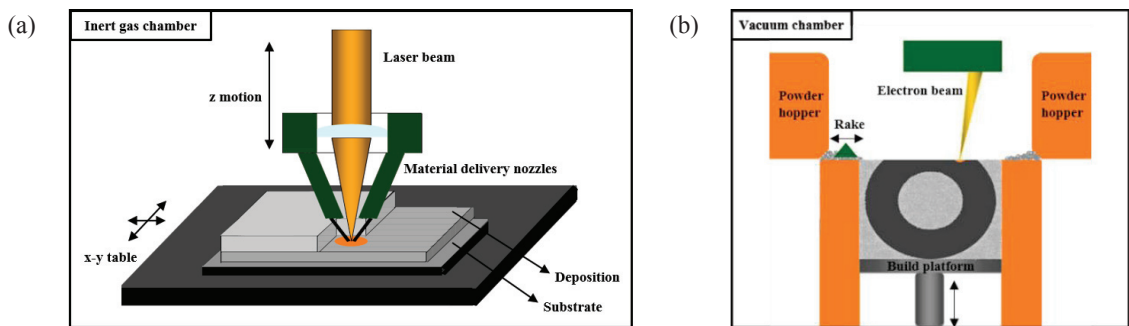


Fig. 1. Working principles of (a) LENS [1]; (b) EBM.

2. Experimental procedure

2.1. Powder precursors and sample fabrication

Spherical gas atomized (GA) Ti-6Al-4V powder is used in both LENS and EBM fabrications, Fig. 2. Particle sizes are similar for the two techniques. The powder used in EBM, Fig. 2(b), contains 50% recycled powder [14].

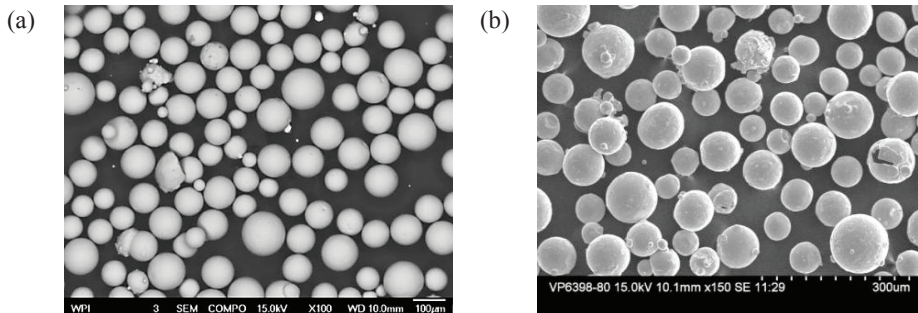


Fig. 2 Powder precursors used in (a) LENS and (b) EBM fabrication [14].

LENS samples were fabricated at Benét Laboratories, using an Optomec L850-R system. Two sets of processing parameters were applied, Table 1.

Table 1. LENS processing parameters.

	Low power (LP)	High power (HP)
Laser power (W)	330	780
Powder feed rate (g/min)	1.0	2.0
Layer thickness (mm)	0.3	0.4
Hatch spacing (mm)	0.5	1.0
Deposition speed (m/min)	0.6	0.8

Near-net-shaped rectangular depositions were built on top of mill-annealed Ti-6Al-4V plates (substrate). The geometries of the depositions were designed for the convenience of extracting tensile specimens, Fig. 3(a, b), and fatigue specimens, Fig. 3(c, d). Post-LENS annealing was also performed to generate comparison with the as-deposited cases. The annealing treatment used was: 760°C +/- 4°C for 1 hour in vacuum, followed by air cooling.

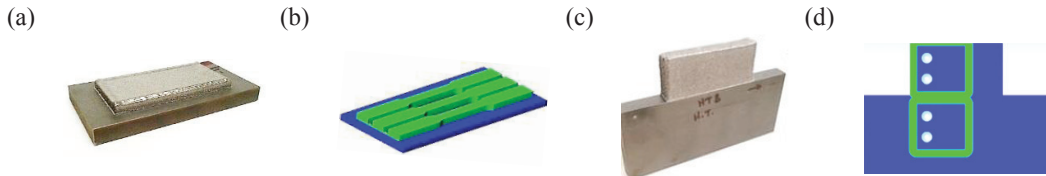


Fig. 3. LENS samples preparation: (a) near-net-shaped deposition for tensile tests; (b) extraction of tensile specimens; (c) near-net-shaped deposition for fatigue tests; (d) extraction of fatigue specimens (top: from bulk deposition; bottom: from substrate).

EBM samples were fabricated at Oak Ridge National Laboratory (ORNL) in two batches, B1 and B2, representing two different machine models A2 and Q10. The processing parameters were defined by the internal algorithm of the ARCAM machines. Similarly, near-net-shaped cylindrical and rectangular samples were designed for tensile and fatigue crack growth studies respectively, Fig. 4(a, b). The effects of solutionizing, annealing temperature and time, and aging temperature and time have been systematically evaluated for EBM fabricated Ti-6Al-4V [14], and the optimum heat treatment was used in this study: solutionizing at 950°C for 1 hour, water quenching to room temperature; aging at 500°C for 7 hours, and air cooling.

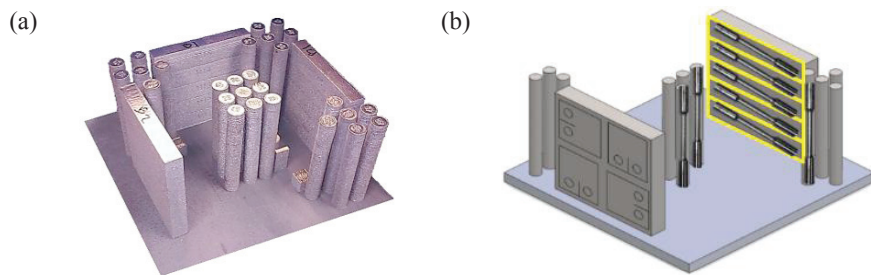


Fig. 4. EBM samples preparation: (a) near-net-shaped rectangular and round samples; (b) extraction of fatigue and tensile specimens.

2.2. Microstructure analysis and mechanical testing

Metallographic samples were mounted in Bakelite and polished using diamond suspension down to $0.05\mu\text{m}$. Samples were then etched by Kroll's reagent (2% HF, 6% HNO_3 and 92% DI H_2O). The microstructures were characterized using Nikon's MA 200 Eclipse optical microscope with Elements-D image analysis software.

Rectangular or round tensile bars were machined per ASTM E8, with a gage length of 25 mm. Room temperature tensile tests were conducted using an Instron universal testing machine, at a strain rate of 1.3 mm/min.

Fatigue crack growth (FCG) experiments were performed using compact tension specimens machined per ASTM E647. Overall specimen dimensions were 39 mm \times 38 mm \times 6 mm. The initial notch was introduced by electrical discharge machining (EDM), using a wire thickness of 0.25 mm. The initial notch length (measured from the pin holes) was 25 mm. Constant stress ratio tests at $R=0.1$ were performed at room temperature in lab air, with a relative humidity of 20-50%. The tests were run under K-control at a cyclic frequency of 20 Hz in order to generate data in Regions I and II. Specifically, a K-gradient of $-0.2/\text{mm}$ was used for the decreasing K part of the test to determine the crack growth threshold value, ΔK_{th} . Region II data were generated under increasing K tests with a K-gradient of $+0.2/\text{mm}$. The final part of the tests was run at constant load at a cyclic frequency of 5 Hz to generate data in Region III of fast crack growth. Generated FCG data were then analyzed using FTA Automated FCG Analysis software and plotted in Grapher. To establish the FCG damage mechanisms, one half of the fractured compact tension specimens was vertically sectioned through the middle of the thickness and then metallographically prepared for two dimensional examination of the crack path. The other half was used for examinations of the fracture surfaces, using a JEOL-7000F scanning electron microscope (SEM).

3. Results and discussion

3.1. Microstructure characterization

3.1.1. LENS fabricated Ti-6Al-4V

Panoramic images of the entire depositions were taken at low magnification for LP and HP cases, Figs. 5(a, b). Directional columnar β grains were found dominant as a result of heat extraction from the substrate; deposition-substrate interfaces (macro-HAZ) were observed as a result of partial melting of the substrate; layer bands could also be seen after etching, due to microstructure coarsening at the layer boundaries (micro-HAZ) from remelting of previous layers. Wider macro-HAZ ($\sim 800\mu\text{m}$) and thicker layers ($600\text{-}900\mu\text{m}$) were observed in HP fabrication, Fig. 6(a), than in LP fabrication ($\sim 500\mu\text{m}$ macro-HAZ, and $300\text{-}800\mu\text{m}$ layer thickness), Fig. 6(b) [1].

At high magnification, LP fabricated Ti-6Al-4V showed martensitic microstructure with acicular α' phases ($\sim 0.6\mu\text{m}$ thick), Fig. 5(c); while HP fabricated Ti-6Al-4V showed regions of parallel α lath ($\sim 1.7\mu\text{m}$ thick), and regions of acicular α' phases, leading to a mixed microstructure of $\alpha' + \alpha$ in prior β matrix, Fig. 5(d). At the prior β boundaries, $1\text{-}2\mu\text{m}$ thick α layers were observed in HP case but not in LP case, Figs. 5(c, d), indicating slower cooling during HP fabrication than LP fabrication. Substrate material was mill-annealed Ti-6Al-4V, with a typical microstructure of equiaxed α phases in β matrix, Fig. 5(e).

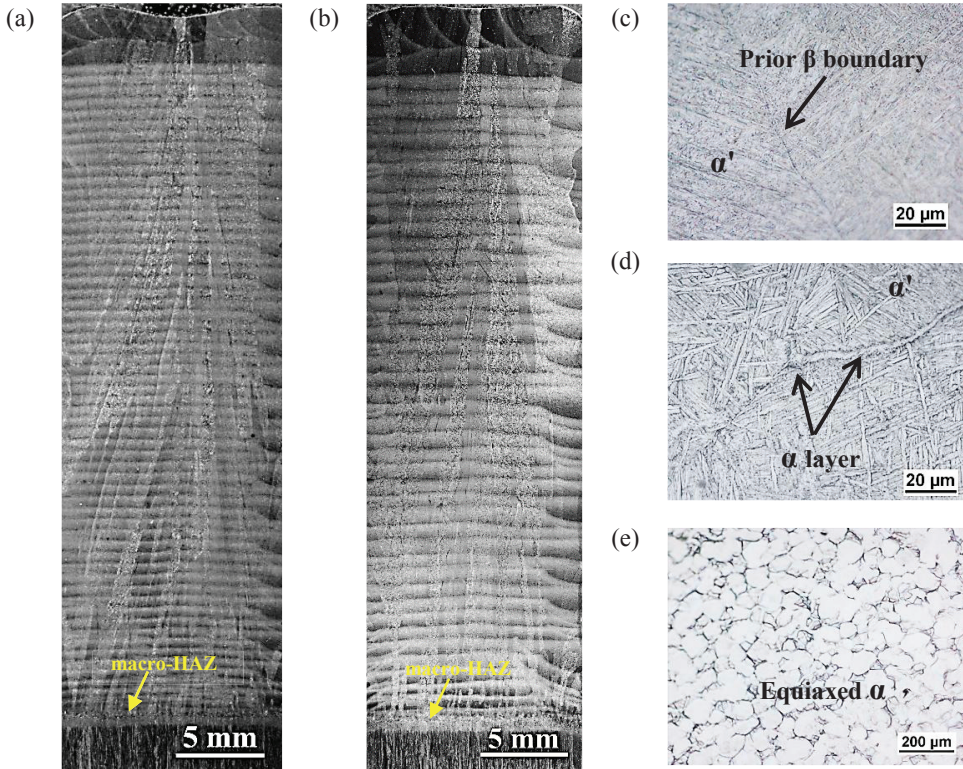


Fig. 5. Microstructures of LENS faricated Ti-6Al-4V: (a) LP fabrication; (b) HP fabrication; (c) acicular α' phases in LP fabricated Ti-6Al-4V; (d) mixture of α' and α in HP fabricated Ti-6Al-4V; (e) mill-annealed substrate.

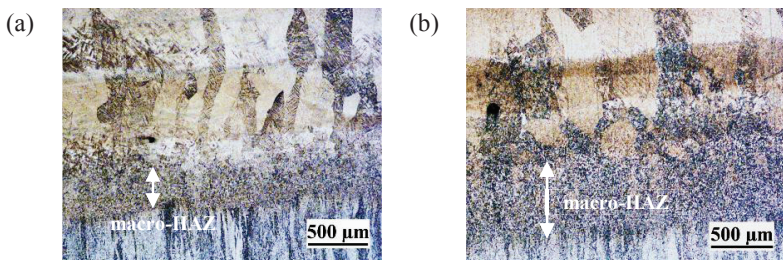


Fig. 6. Macro-HAZ and layer thickness in: (a) LENS LP and (b) LENS HP fabrication.

3.1.2. EBM fabricated Ti-6Al-4V

Columnar β grains were also found in EBM fabricated Ti-6Al-4V for both B1 and B2 batches, Figs. 7(a, b). Different from LENS fabrication which is typical of fast cooling, in EBM, the powder bed was held at 650–750°C through out the process, and was slowly cooled to room temperature when fabrication completed. Long period exposure under 650–750°C decomposed all the α' phases formed during solidification; and since the minimum cooling rate required to form martensitic microstructure in Ti-6Al-4V is 410°C/s [15], the slow cooling upon fabrication completion did not lead to any martensitic formation. The resulting microstrucure in EBM fabricated Ti-6Al-4V was found to be fine $\alpha + \beta$ lamellae, Figs. 7(c, d).

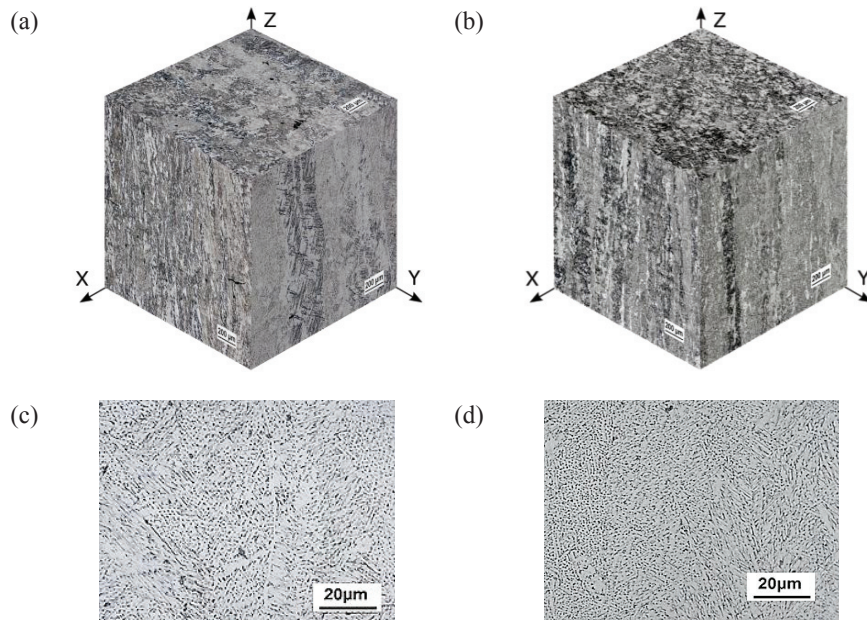


Fig. 7. Microstructures of EBM faricated Ti-6Al-4V: (a, c) B1; (b, d) B2.

3.2. Room temperature tensile properties and the influences of post-deposition heat treatments

3.2.1. LENS fabricated Ti-6Al-4V

For LENS fabrication, tensile tests were conducted only at horizontal orientation, Fig. 3(b). Tensile properties of LENS fabricated Ti-6Al-4V and a comparison with mill-annealed Ti-6Al-4V (substrate) are provided in Table 2. In general, the yield strength and ultimate tensile strength of LENS depositions are higher than those of the mill-annealed substrate. Comparing between LENS fabrications, LP as-deposited Ti-6Al-4V yielded higher strength, but significantly lower ductility due to the presence of α' martensite. After annealing, significant increase in ductility was observed as a result of α' decomposition into $\alpha + \beta$ lamellae. Similar heat treating effect was also found in HP fabricated Ti-6Al-4V alloys, as the elongation increased from 7% to 10% after annealing.

Table 2. Room temperature tensile properties of LENS fabricated Ti-6Al-4V.

	YS (MPa)	UTS (MPa)	%EL
LP as deposited	1005	1103	4
LP annealed	1000	1073	9
HP as deposited	990	1042	7
HP annealed	991	1044	10
Substrate (mill-annealed)	970	1030	16

3.2.2. EBM fabricated Ti-6Al-4V

For EBM fabrication, tensile tests were conducted at both horizontal and vertical orientations, Fig. 4(b). Tensile data for EBM fabricated Ti-6Al-4V are given in Table 3. Similar tensile properties were found in as-deposited B1 and B2 batches at two differnt orientations. Comparing these results with the as-deposited cases in LENS fabrication, EBM and LENS yielded comparable tensile strength, but EBM fabrication achieved much better

ductility than LENS fabrication due to the powder bed heating, which prevents the formation of martensitic α' phases. The optimum post-EBM heat treatment was found to be able to further increase the tensile strength while maintaining a moderate ductility.

Table 3. Room temperature tensile properties of EBM fabricated Ti-6Al-4V.

	YS (MPa)	UTS (MPa)	%EL
B1-horizontal as deposited	1006	1066	15
B1-vertical as deposited	1001	1073	11
B2-horizontal as deposited	973	1032	12
B2-vertical as deposited	1051	1116	15
Solutionized and aged	1039	1294	10

3.3. Fatigue crack growth (FCG) properties and mechanisms

For both LENS and EBM fabrications, FCG tests were conducted at two orientations: horizontal and vertical. An illustration of the compact tension specimens showing crack growth directions (arrows) with respect to the deposition direction (D) and columnar grains are shown in Fig. 8.

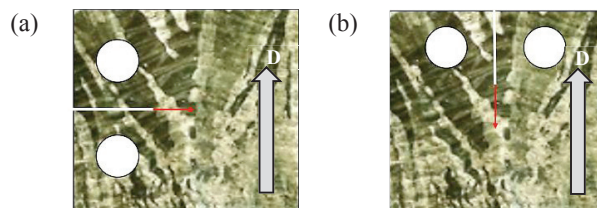


Fig. 8. Fatigue crack propagation directions (arrows) with respect to the deposition directions (D) and columnar grains: (a) horizontal propagation; (b) vertical propagation.

3.3.1. FCG properties

Experimentally measured FCG data of LENS and EBM fabricated Ti-6Al-4V are shown in Fig. 9. For LENS horizontal propagation cases, Fig. 9(a), LENS fabricated Ti-6Al-4V alloys in general showed lower threshold value ΔK_{th} but higher fracture toughness ΔK_{FT} than mill-annealed Ti-6Al-4V (substrate), indicating a better high cycle fatigue performance in mill-annealed Ti-6Al-4V, and a better low cycle fatigue performance in LENS Ti-6Al-4V. Comparisons between LENS fabricated alloys indicated that LP fabrication yielded slightly lower threshold value than HP fabrication due to the presence of martensitic α' phases. After annealing, slight increase in ΔK_{th} was found in LP fabricated Ti-6Al-4V as a result of α' decomposition. Similar observations were found in vertical propagation cases, Fig. 9(b).

In EBM fabricated Ti-6Al-4V alloys, B1 and B2 batches showed similar threshold and toughness values for both horizontal and vertical propagation directions, thus only data from B2 batch are plotted here in Fig. 9(c) against the heat treated conditions. Compared to LENS, EBM as-deposited alloys showed similar threshold to LENS HP fabricated alloys, i.e. higher threshold than LENS LP fabricated alloys, due to their similar microstructures. Fracture toughness values in as-deposited EBM Ti-6Al-4V alloys are comparable to those in LENS. After solutionizing and aging, significant increase in threshold was found in vertical propagation direction, achieving a threshold value comparable to the mill-annealed Ti-6Al-4V; while significant increase in fracture toughness was found in horizontal propagation direction.

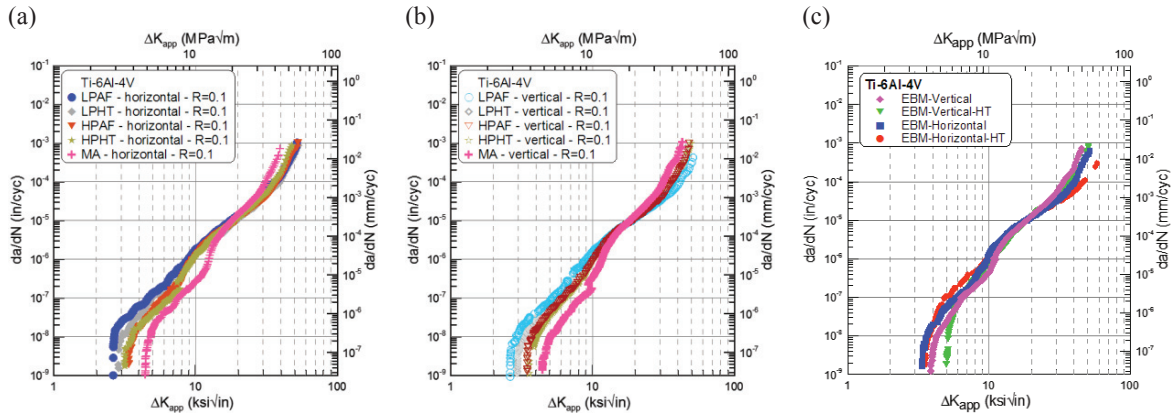


Fig. 9. FCG data of: (a) LENS fabricated Ti-6Al-4V at horizontal fatigue crack propagation direction; (b) LENS fabricated Ti-6Al-4V at vertical fatigue crack propagation direction; (c) EBM fabricated Ti-6Al-4V.

3.3.2. FCG mechanisms

The microstructures of LENS and EBM fabricated Ti-6Al-4V all contain columnar β grains, and very fine α morphologies (acicular α' in LENS LP; α' with $\alpha + \beta$ lamellae in LENS HP; $\alpha + \beta$ lamellae in EBM). This similarity yielded comparable FCG mechanisms in both materials. Crack growth side profiles at various ΔK levels and propagation regimes (i.e. threshold, Region II and Region III) for LENS, EBM and mill-annealed Ti-6Al-4V are shown in Fig. 10. Crack interaction with α'/α phases was found to be the primary propagation mechanism in LENS fabricated Ti-6Al-4V, and crack interaction with α lath and colonies controlled the crack growth in EBM fabricated Ti-6Al-4V. In mill-annealed Ti-6Al-4V, crack interaction with equiaxed α phases was found in Region I, and interaction with β phases instead was found in Region III.

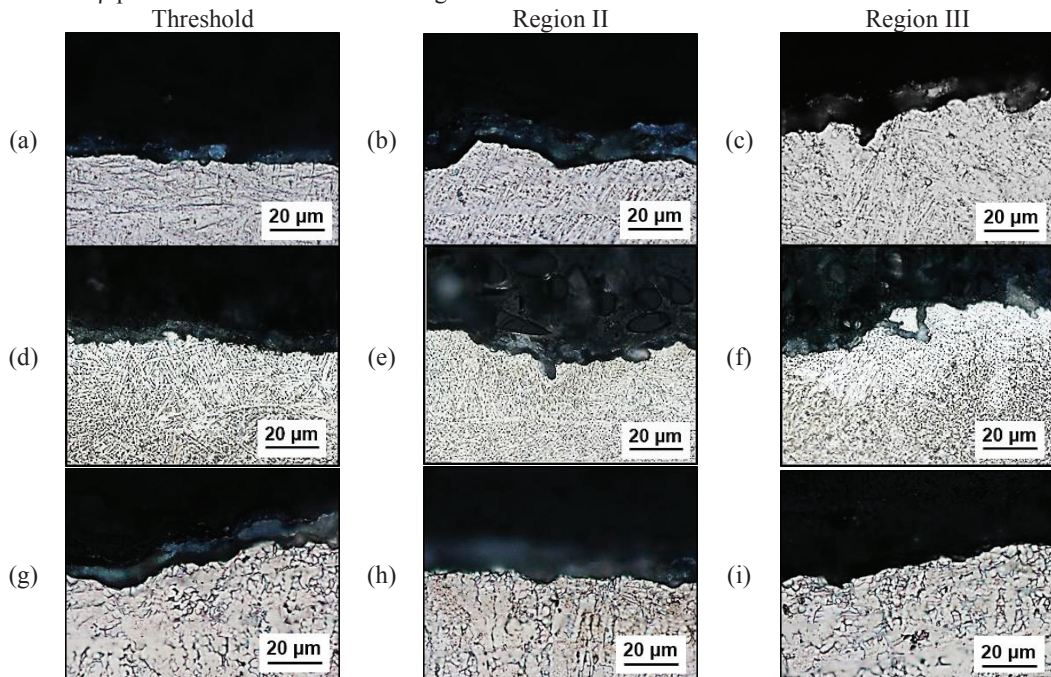


Fig. 10. FCG mechanisms in: (a, b, c) LENS; (d, e, f) EBM; (g, h, i) mill-annealed Ti-6Al-4V at different ΔK levels.

4. Conclusions

- i. The microstructures of LENS and EBM fabricated Ti-6Al-4V all showed directional columnar prior β grains parallel to the deposition directions.
- ii. The α morphology in LENS LP fabricated Ti-6Al-4V is acicular α' , indicating martensitic transformation; while in HP fabricated alloys, both areas of fine $\alpha + \beta$ lamellae and α' were observed, indicating a slower cooling rate in HP fabrication.
- iii. Post-LENS annealing at 760°C decomposes α' phases, and thus increases material's ductility.
- iv. The α morphology in EBM fabrication consists of fine $\alpha + \beta$ lamellae.
- v. EBM fabricated Ti-6Al-4V yielded comparable tensile strength but significantly higher ductility than LENS fabricated Ti-6Al-4V due to the absence of martensitic phases.
- vi. LENS fabrication yielded better low cycle fatigue performance, but poorer high cycle fatigue performance than mill-annealed Ti-6Al-4V.
- vii. LENS HP fabrication yielded higher FCG threshold values in Ti-6Al-4V than LP fabrication; EBM as-deposited Ti-6Al-4V have comparable threshold values to LENS HP cases.
- viii. Fracture toughness values are comparable between LENS and EBM fabrication.
- ix. For EBM fabricated Ti-6Al-4V, solutionizing and aging treatment significantly increased threshold value and fracture toughness in vertical and horizontal propagation directions respectively.
- x. FCG mechanisms were correlated primarily with α/α' phases and colonies in both LENS and EBM fabricated Ti-6Al-4V; in mill-annealed Ti-6Al-4V, the mechanism changes from interacting with α phases in Region I, to interacting with β phases in Region III.

References

- [1] Y. Zhai, D.A. Lados, J.L. LaGoy, Additive manufacturing: making imagination the major limitation, *JOM* 66 (5) (2014) 808-816.
- [2] L.E. Murr, E.V. Esquivel, S.A. Quinones, S.M. Gaytan, M.I. Lopez, E.Y. Martinez, F. Medina, D.H. Hernandez, E. Martinez, J.L. Martinez, S.W. Stafford, D.K. Brown, T. Hoppe, W. Meyers, U. Lindhe, R.B. Wicker, Microstructures and mechanical properties of electron beam-rapid manufactured Ti-6Al-4V biomedical prototypes compared to wrought Ti-6Al-4V, *Materials Characterization*, 60 (2) (2009) 96-105.
- [3] M.L. Griffith, M.T. Ensz, J.D. Puskar, C.V. Robino, J.A. Brooks, J.A. Philliber, J.E. Smugeresky and W.H. Hofmeister, Understanding the Microstructure and Properties of Components Fabricated by Laser Engineered Net Shaping (LENS), *MRS Proceedings*, 625 (2000) 9-20.
- [4] F. Wang, J. Mei, Xinhua Wu, Microstructure study of direct laser fabricated Ti alloys using powder and wire, *Applied Surface Science* 253 (3) (2006) 1424-1430.
- [5] X. Wu, J. Mei, Near net shape manufacturing of components using direct laser fabrication technology, *Journal of Material Processing Technology* 135 (2003) 266–270.
- [6] X. Wu, J. Liang, J. Mei, C. Mitchell, P.S. Goodwin, W. Voice, Microstructures of laser-deposited Ti-6Al-4V, *Material & Design*, 25 (2004) 137-144.
- [7] L. Qian, J. Mei, J. Liang, X. Wu, Influence of position and laser power on thermal history and microstructure of direct laser fabricated Ti-6Al-4V samples, *Material Science and Technology* 21 (2005) 597–605.
- [8] J. Gockel, J. Beuth, K. Taminger, Integrated control of solidification microstructure and melt pool dimensions in electron beam wire feed additive manufacturing of Ti-6Al-4V, *Additive Manufacturing*, 1–4 (2014) 119-126.
- [9] L. Facchini, E. Magalini, P. Robotti, A. Molinari, Microstructure and mechanical properties of Ti-6Al-4V produced by electron beam melting of pre-alloyed powders, *Rapid Prototyping Journal* 15 (3) (2009) 171-178.
- [10] L.E. Murr, E.V. Esquivel, S.A. Quinones, S.M. Gaytan, M.I. Lopez, E.Y. Martinez, F. Medina, D.H. Hernandez, E. Martinez, J.L. Martinez, S.W. Stafford, D.K. Brown, T. Hoppe, W. Meyers, U. Lindhe, R.B. Wicker, Microstructures and mechanical properties of electron beam-rapid manufactured Ti-6Al-4V biomedical prototypes compared to wrought Ti-6Al-4V, *Materials Characterization* 60 (2) (2009) 96-105.
- [11] S. Leuders, M. Thöne, A. Riemer, T. Niendorf, T. Tröster, H.A. Richard, H.J. Maier, On the mechanical behaviour of titanium alloy TiAl6V4 manufactured by selective laser melting: Fatigue resistance and crack growth performance, *International Journal of Fatigue* 48 (2013) 300-307.
- [12] R.R. Mudge, N.R. Wald, Laser engineered net shaping advances additive manufacturing and repair, *Welding Journal* 86 (1) (2007) 44-48.
- [13] L.E. Andersson, M. Larsson, Device and arrangement for producing a three-dimensional object, Patent WO 2001081031 A1.
- [14] H. Galarraga, D. Lados, Microstructure, static and dynamic properties, and damage mechanisms, and ICME in Ti-6Al-4V fabricated by electron beam melting, iMds internal report, 2015.
- [15] G. Lütjering, J.C. Williams, *Titanium*, Springer Berlin Heidelberg, 2003.

Producing Titanium Aerospace Components from Powder Using Laser Forming

F.G. Arcella and F.H. Froes

Titanium is an attractive choice for many components in the aerospace industry; however, its inherently high cost often negates its use. A cost-effective, near-net shape, laser forming approach to producing large and complex parts has been developed and is being commercialized.

INTRODUCTION

The excellent combination of specific mechanical properties (i.e., normalized to density) exhibited by titanium alloys such as Ti-6Al-4V are very attractive for aerospace applications.¹⁻³ However, the high cost of the final components, resulting from the high cost of producing raw titanium and processing and machining difficulties combined with buy-to-fly ratios that average 5:1 and can often be greater than 20:1, result in titanium being used only when it is the only material that can meet design requirements. There is generally a direct relationship between material cost and volume of use; consumption decreases with increasing cost. Thus, any process that can reduce the cost of titanium components is attractive to the aerospace industry.

One such process is the near-net shape LasformSM process⁴⁻⁸ being commercialized by the AeroMet Corporation of Eden Prairie, Minnesota. This process, shown schematically in Figure 1, is a laser additive manufacturing (LAM) process that combines high-power laser cladding technology with advanced rapid prototyping to directly manufacture complex, fully dense, three-dimensional components directly from computer-aided design images. The process fabricates shapes from titanium powder and target plates and is performed without the cost of molds or dies. The major advantages of Lasforming are near-net shape components, dramatically reduced delivery times, greatly reduced machining requirements, enhanced design flexibility, the ability to produce grade chemistries, repair capability of broken or worn components, feature addition ca-

pability, rapid prototyping, and rapid design modifications.

Development of the basic concept began more than 20 years ago, and technical feasibility and scale-up were demonstrated as part of an R&D program funded by the U.S. Defense Advanced Research Projects Agency, with the Office of Naval Research serving as the technical agent.⁴ This work, led by Johns Hopkins University, was conducted over a three-year period with Pennsylvania State University and MTS Systems Corporation, AeroMet's parent company, serving as subcontractors. The program demonstrated the viability of rapid prototyping of titanium-alloy parts and the production of cost-effective components very close to net shape (requiring only a final machining operation) with chemistry, microstructure, and mechanical properties meeting stringent aerospace requirements.

MTS Systems Corporation designed and fabricated the full-scale commercial Lasform system currently located at AeroMet's Eden Prairie facility (Figure 2). The system is being operated in collaboration with the U.S. Army Research Laboratory's Aberdeen Proving Ground,

Maryland, as part of a three-year cooperative research and development agreement program to further develop, evaluate, and validate the Lasform process for defense applications in a semi-commercial mode. Independent investor resources have supported the continued development of the process to the point of full commercialization.

THE LASFORMING PROCESS

A schematic of the process is shown in Figure 1, in which titanium powder is fed in a controlled fashion to the workpiece, where it is melted by the CO₂ laser, progressively building up a structure one layer at a time. Thus, for example, complex ribs and flanges can be built up on a starting plate, dramatically decreasing material loss (to machine chips). Typical laser-formed structures are designed to be 0.762–5.08 mm oversize. These built-up structures can be angled as much as 60° from the vertical. The deposition rate can be controlled based on heat-balance effects, so that metallurgically sound interfaces are formed between each fused powder layer. Normally, fully dense parts are produced at a deposition rate of 0.90–4.5 kg per hour. Typical lasformed parts after final machining are shown in Figure 3.

At least four types of precursor titanium powders^{9,10} have been successfully used to date, all in the –40 +325 mesh range: blended elemental (commercially pure titanium powder plus Al/V master alloy), gas-atomized, plasma-rotating electrode processed, and hydride-dehydride prealloyed powder. Good flow characteristics to the workpiece are required. Alloys produced include Ti-6Al-4V, Ti-5Al-2.5Sn, Ti-6Al-2Sn-4Zr-2Mo-0.1Si, and Ti-6Al-2Sn-2Zr-2Cr-2Mo-0.25Si.

The major advantage of the Lasform process is producing complex, laser-formed, near-net shapes (referred to as machining preforms) requiring only final machining and heat treatment.

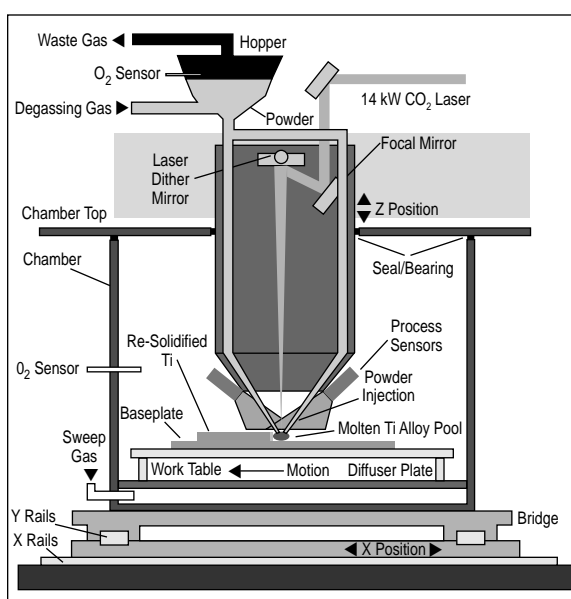


Figure 1. A schematic of the Lasform process.



Figure 2. The current AeroMet Corporation/ARL Lasform commercial-scale system.

Conventionally, these parts are produced by forging, which requires expensive tooling and extensive machining or a hog-out from a large slab or plate of hot-rolled material. The cost for relatively short production runs (up to 500 parts) is decreased, and design changes once a production run is underway can be achieved much easier. Delivery times are about 30–60 days as compared to as much as 15 months for the forge plus machine approach.

Post-laser-forming part inspection includes coordinate measuring machine verification of the dimensions, witness samples for mechanical property testing, and chemical analysis as well as ultrasonic inspection and x-ray radiography. After final machining, die-penetrant inspection can also be carried out.

The Lasform process can also be used as a feature addition technique in which lugs or extensions are added to forgings, castings, or extrusions. This allows simpler and economical dies and tools to be used and provides more efficient material utilization. There is also the possibility of repairing broken, mismatched, or worn sections of a component.

LASFORMED COMPONENT CHARACTERISTICS

The microstructure of lasformed Ti-6Al-4V consists of relatively fine prior beta grains that are about the same size as those in thin casting. These prior beta grains, which can be columnar or equiaxed, depending on the laser-system forming parameters used, transform during cooling to produce relatively thin and discontinuous grain-boundary alpha and transgranular alpha (Figure 4).

The mechanical properties of lasformed Ti-6Al-4V (post laser-form sub beta transus anneal and age) include 839 MPa yield strength, 900 MPa ultimate tensile strength, 12.3% elongation, a 23.5% reduction in area, and 104 MPa $\sqrt{\text{m}}$ KIC. As would be expected,^{1–3} these are equivalent to the mechanical properties typical of Ti-6Al-4V cast and wrought (ingot metallurgy) material.

The integrity of the lasformed parts produced has been found to be as good as or better than that of cast and wrought products, and these latter are not typically 100% defect free. For example,

powder-metallurgy approach to producing components from superalloys and titanium for demanding applications suffers from at least the perception that defects that will degrade mechanical properties can be present. Hence, even though superalloy Rene 95 parts have never exhibited a problem in T700 helicopter engine parts, near-net shapes are not allowed; instead, a quality-assurance forging step is included in final part fabrication.

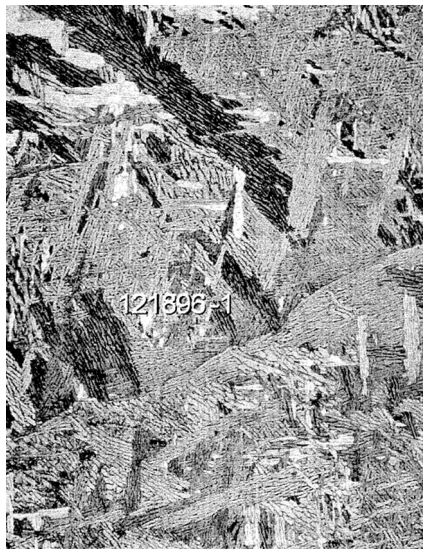
Fatigue initiation properties are very sensitive to the presence of inclusions. Thus, the data shown in Figure 5 are very encouraging. Here, the smooth S-N fatigue data for lasformed Ti-6Al-4V are at the high end of cast data, albeit the lower portion of the cast and wrought scatterband.^{1–3} This is probably at the lower end of the ingot data because of the nature of the microstructure of the lasformed material. A finer, more equiaxed microstructure would raise the data toward the upper part of the cast and wrought scatterband. More recent data show this improved S-N performance.

THE NEXT STEP

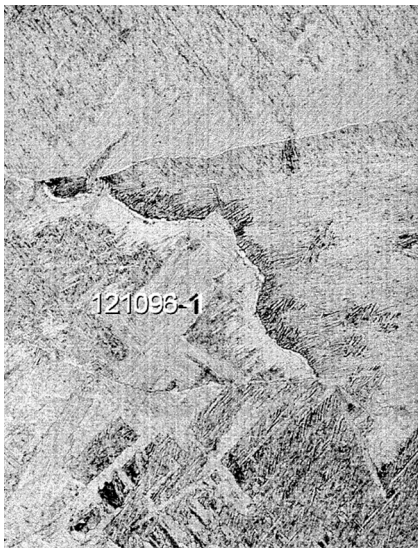
The current AeroMet/Army Research Laboratory production system is operating at 18–19 kW and allows parts 2.5 m long \times 1 m wide \times 1 m in height (up to nine tonnes in weight) to be produced with ± 0.076 cm reproducibility. A second planned unit (scheduled for commissioning in October) with a 30 kW CO₂ laser will allow parts up to 3.6 m \times 3.6 m \times 1.2 m to be produced at projected deposition rates of 5–7 kg per hour or greater. A third planned unit, which could be the same size or bigger than the second unit, will result in a total plant capacity of greater than 45–60 t/y depo-



Figure 3. Typical lasformed and machined components.



a



b

Figure 4. The microstructure of lasformed material, vacuum-mill annealed at 788°C for 2 h, argon cooled Ti-6Al-4V.

sition, offering total integrated part weights considerably beyond this when the weight of the starting plate is added in. Various full-scale subsections of integral reinforced rib on web and cylindrical parts (e.g., rings, cones, and flanges) formed by the Lasform process with Ti-6Al-4V are shown in Figure 3. AeroMet is currently preparing for an ISO9000 audit to receive quality-assurance certification.

Cost savings as compared to conventional approaches are projected to be generally 15–30%. Under an Office of Naval Research Dual Use Science and Technology program, four wing components for the F/A-18E/F will be fabricated using laser forming—the inner wing-splice fittings and the wing-fold fittings.¹² Based on a purchase of 400 aircraft, a cost savings of \$50 million is estimated. The prime contractors, Boeing and Northrop-Grumman, estimate that laser forming will result in a 75% reduction in delivery time and more than 20% cost savings.

The project's near-term thrust is to

produce titanium parts for full component testing, demonstrating cost savings and reduced delivery times at mechanical property levels equivalent to cast and wrought levels. Production orders are expected to follow. In the future, new concepts will be explored, such as built-up structures (unitized structures eliminating fasteners) and structures with functionally graded compositions (e.g., a disc with optimized low-cycle fatigue behavior in bore areas and maximized creep performance in the rim locations). The lasforming of components from other base materials, such as niobium, rhenium, inconel, and stainless steel, is also planned.

ACKNOWLEDGEMENTS

AeroMet/MTS Systems have made outstanding progress in the last few years in commercializing this new process. In addition, the authors acknowledge the early support of the technology described in this paper by the Defense Advanced Research Projects Agency (R. Crowe and L.N. Durvasula) under technical guidance from the Office of

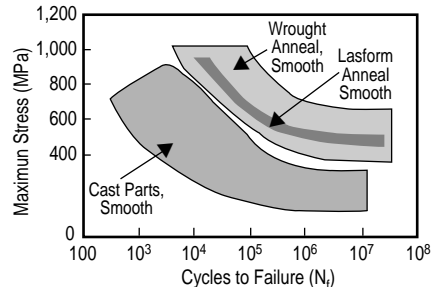


Figure 5. S-N fatigue data for lasformed Ti-6Al-4V, indicating a data scatter-band at the high end of cast material (coarse microstructure) and the low end of cast-and-wrought (ingot) material (fine microstructure).¹¹

Naval Research (G. Yoder), and the Army Research Laboratories (W. Roy). We also appreciate the assistance of Marlene Martonick and Beth Padgett in manuscript preparation.

References

1. F.H. Froes, D. Eylon, and H.B. Bomberger, "Titanium Technology: Present Status and Future Trends" (Paper presented at the ITA, Denver, CO, 1985).
2. F.H. Froes, T-L Yau, and G.G. Weidinger, *Titanium, Zirconium and Hafnium* (Weinheim, FRG: VCH Materials Science and Technology, 1996).
3. F.H. Froes, "Titanium Science and Technology," *Encyclopedia of Science*, ed. P. Bridenbaugh (in press).
4. F.G. Arcella, "Flexible Fabrication of Titanium," ONR contract no. N00014-95-C-0029 (February 1, 1995 through September 30, 1998).
5. D.H. Abbott and F.G. Arcella, "Laser Forming Titanium Components," *Advanced Materials and Processes*, 153 (5) (May 1998), pp. 29–30.
6. F.G. Arcella, "Laser Forming of Near Shapes," *Titanium '92 Science and Technology*, ed. F.H. Froes and I.L. Caplan (Warrendale, PA: TMS, 1992), pp. 1395–1402.
7. F.G. Arcella, "Rapid Prototyping in Titanium with Intelligent Systems," *41st Sagamore Conf. Proc.*, ed. W. Roy (Watertown, MA: ARL, 1994), pp. 145–156.
8. F.G. Arcella, D.H. Abbott, and M.A. House, "Rapid Laser Forming of Titanium Structures," *Proc. 1998 Powder Metallurgy World Conference and Exposition* (Princeton, NJ: MPIF, 1998).
9. F.H. Froes and D. Eylon, "Powder Metallurgy of Titanium Alloys," *Int. Mats. Reviews*, 35 (1990), pp. 162–182.
10. F.H. Froes and C. Suryanarayana, "Powder Processing of Titanium Alloys," *Rev. in Particulate Materials*, 1 (1993), pp. 223–275.
11. D. Eylon and R. Boyer, "Titanium Alloy Net Shape Technologies," *Proc. Int. Conf. On Titanium and Aluminum*.
12. <http://www.onr.navy.mil/onr/newsrel/nr990802.htm>.

Frank G. Arcella is with AeroMet Corporation. F.H. Froes is with the Institute for Materials and Advanced Processes, University of Idaho.

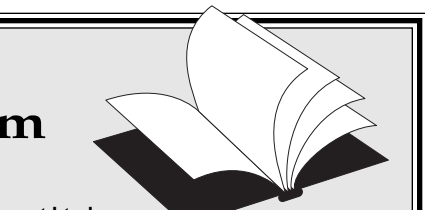
For more information, contact F.G. Arcella, AeroMet, 7623 Anagram Drive, Eden Prairie, Minnesota 55344; (612) 974-1800; fax (612) 974-1801; e-mail info@aerometcorp.com.

Reviewers Wanted for the JOM Book Review Program

JOM is looking for volunteer book reviewers for its Book Review Program, which publishes reviews of recent materials science and engineering publications every three to four months on the last page of the issue. Participants keep any book they review, provided a publication-quality review is submitted in a timely manner.

If you'd like to participate, here's how:

- Go to www.tms.org/pubs/journals/JOM/review-request.html
- Read the review program guidelines and submit your request using the form provided
- If your request is approved, JOM will mail you the book
- Go to www.tms.org/pubs/journals/JOM/review-form.html to submit your review within 90 days



Questions?

Telephone (724) 776-9000, ext. 224
Fax (724) 776-3770
E-mail jom@tms.org



ELSEVIER

Materials & Design

Materials and Design 21 (2000) 417–423

Practical considerations and capabilities for laser assisted direct metal deposition

Gary K. Lewis^{a,*}, Eric Schlienger^b

^a*Los Alamos National Laboratory, Los Alamos, NM, USA*

^b*Sandia National Laboratory, Albuquerque, NM, USA*

Abstract

Laser assisted direct metal deposition refers to the additive layered manufacturing technology for building components from a computer-aided design (CAD) model. A motion control program, developed from the CAD model of a desired metal component, is used to control the motion of a laser focal spot to trace all areas of the part, typically a planar layer at a time. Metal powders, injected into the laser focal zone, are melted and then re-solidify into fully dense metal in the wake of the moving molten pool created by the laser beam. Successive layers are then stacked to produce the entire component volume of fused metal representing the desired CAD model. Development of this technology has been pursued at both Los Alamos and Sandia National Laboratories and has resulted in the Directed Light Fabrication (DLF) and Laser Engineered Net Shaping (LENS™) processes. These processes have been proven feasible for fabricating components from nearly any metal system to near-net shape accuracy with mechanical properties approaching and in some cases exceeding the properties found in conventionally processed wrought structures. Single step processing by LENS and DLF produce cost savings realized by elimination of conventional multi-step thermo-mechanical processing. Design features such as internal cavities or over-hanging features can be made without joined assemblies. Hard to process materials such as intermetallics, refractory metals, and high temperature alloys can be processed in a single step. Functionally graded compositions can be created within three-dimensional components to vary the properties to match localized requirements due to the service environment. The technology offers the designer a rapid prototyping capability at the push of a button, without the need to fabricate dies or use forming equipment or extensive machining and joining processes to produce a part. Future development is still required for these processes to be commercially accepted and used in industry. Parts are deposited with a surface roughness of 10 µm, arithmetic average, making a secondary finishing operation necessary for some applications to achieve high accuracy and polished surface texture. Residual stress measurement and control is also required to avoid distortion of deposited components. Motion path and control code needs to be optimized to reduce overall process time from the CAD model to the finished part. © Published by Elsevier Science Ltd. All rights reserved.

Keywords: Laser; Deposition; Fabrication; Layered deposition; Rapid prototyping; Solid free-form fabrication

1. Introduction

The idea of fabricating useful plastic, metal and ceramic components by the build-up and addition of layers of material has led to the establishment of the current rapid prototyping industry. As early as 1934 [1], manual layered build-up of metal using oxy-fuel welding was invented, however, accuracy and resolution of

features was poor. Cladding technology followed using primarily arc and laser welding processes combined with wire and powder feed, however, limitations in accuracy and resolution still prevented building of useful metal components.

Development of laser and microprocessor technology for accurate control of laser beam position used to solidify liquid polymers or thermo-plastic powders, led to the invention and application of accurate layered deposition technology of polymeric materials in the early 1980s. Development of computer-aided-design

* Corresponding author.

(CAD) and computer-aided-manufacturing (CAM) technology provided the coupling between the representation of a desired component in three-dimensions and the deposition process to produce the part from the design. Tesselation of the part boundary surfaces (representing the part surface by small connected triangular facets) and planar slicing of the model to form deposition layers led to the development and use of stereo-lithography file formats (.stl) for layered deposition. Plastic components fabricated with this technology were primarily used for models to verify form and fit without meeting service requirements for high strengths and densities. But in the early 1990s the technology became linked to fabrication of metal components by making patterns for investment casting which has proven a fast and economical rapid prototyping method.

However, depositing metals directly by layered deposition technology, instead of making patterns, would eliminate the extra steps required for investment casting of metals and permit one-step fabrication of metal components from a CAD design. Various techniques have been tried [2] including: deposition of liquid metal, laser assisted chemical vapor deposition (CVD), selective laser melting and re-solidification of a bed of metal powder or plastic coated powder and laser melting and re-solidification of powders continuously fed into the laser focal zone. These processes combine the developed technologies of powder metallurgy, solidification metallurgy, CAD-CAM and rapid prototyping. Additionally, similar processing is being applied in the direct fabrication of ceramics by depositing the material in layers with a binder followed by drying and firing to form a densified ceramic component.

2. Process description

The processes addressed here are Directed Light Fabrication (DLF) [3–10], developed at Los Alamos National Laboratory, Los Alamos, New Mexico and Laser Engineered Net Shaping (LENSTM) [11–19] developed at Sandia National Laboratory, Albuquerque, New Mexico. Both processes supply a continuous powder feed to the laser focal zone where the powder is melted and re-solidifies in the ‘wake’ of the molten pool as the laser beam scans across the part. Fig. 1 schematically describes the process showing a computer system representing the development of the CAD model and the hardware system where deposition of the part takes place. Motion paths developed either in stereolithography format (LENSTM) or CNC tool-path format (DLF) command motion for one to five motion axes. Additional axes or robotic control could allow additional degrees of freedom if required. Processing is performed usually in inert gas (argon, helium, nitrogen) environments, typically to reduce oxidation. Multiple powder compositions can be fed simultaneously or sequentially to produce alloying at the focal zone or provide choice of material relative to location within a desired part. The motion path provides the control commands for the laser, powder feed and motion system to produce linear beads of material that are laid side by side with a designated amount of overlap. Each bead is typically started and terminated at the part boundary until an entire cross-sectional planar layer is formed by deposition of overlapping beads. The laser beam then indexes away from the part by the layer thickness controlled by the motion system. Laser power, powder feed rate, and traverse velocity are controlled

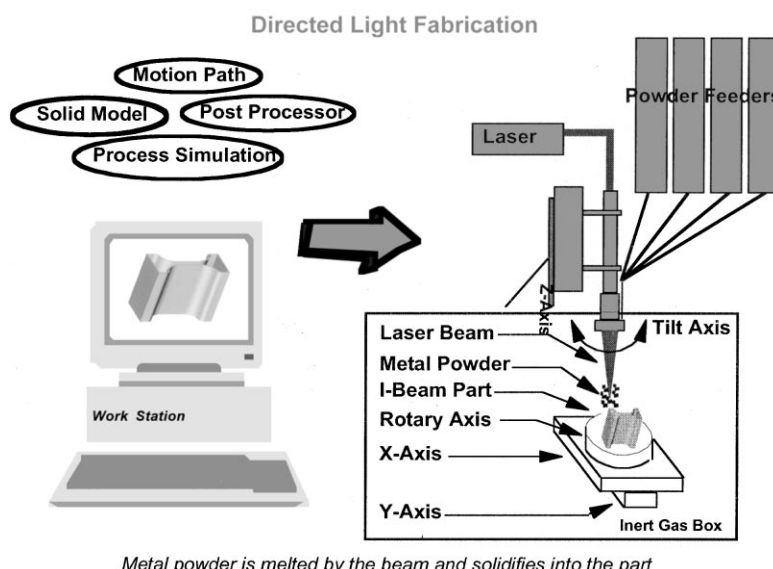


Fig. 1. Schematic representation of the DLF process. Five axes of motion are used and the system can deliver up to four different powder compositions. Processing is typically performed in argon or other inert gas with oxygen impurity below 5 ppm.

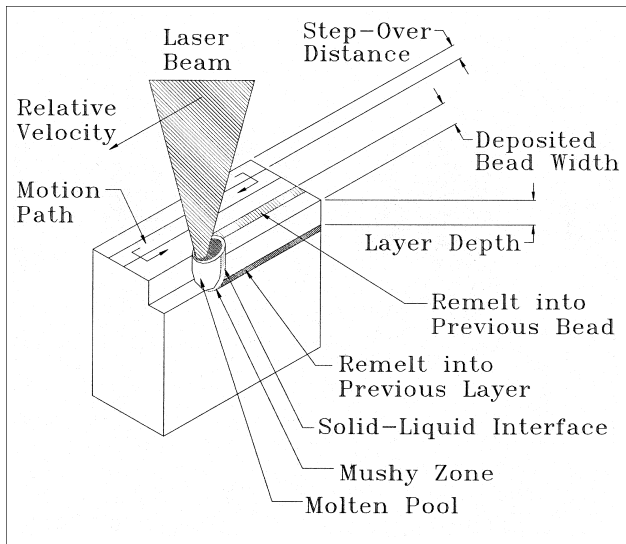


Fig. 2. Schematic representation of a plate being deposited by overlapping traverses of the molten pool across the width dimension of the plate. As-deposited properties of the solidified material depend on the molten pool characteristics produced by the process parameters chosen and the heat flow characteristics away from the pool.

to produce a full density layer for any given material. Successive layers are stacked and the entire part or specific feature of a part assembly is built additively. Features or assembly components that require deposition in planar layers at angled orientations to the parent or base feature can be deposited by tilting the laser beam-powder delivery head or tilting the work piece so that the beam axis is normal to the deposition plane. This capability provides a means of producing overhanging features without building underlying support structure typically required in plastic rapid-prototyping processes.

Fig. 2 schematically shows a plate type of structure being built. A small molten pool is created at the focal zone of the laser beam that can vary in size from one-half to five times the focal-spot diameter of the laser beam, depending on the power and velocity of the moving spot. For example, the Nd-YAG laser used in DLF processing is focused to 0.5 mm and has been used to produce solidified features 0.3–2.5 mm thick

with a single pass by varying the laser power and translation speed. Thicker components are made with multiple overlapping beads. The small molten pool is surrounded by solid material and is held in its place by surface tension, permitting 'overhead' deposition, much the same as welding in an overhead position. Molten pool size is also affected by underlying heat sinking of the substrate or previously deposited material. High heat flow away from the molten pool shrinks the pool width and low heat flow increases the pool width, making compensation desirable by controlling laser power and velocity process parameters.

Control of the molten pool determines the properties of the resulting solidified product. Bead-to-bead overlap and layer thickness must correlate to the molten pool width and depth to produce a fully dense product. Cooling rate and solidification velocity at the solid-liquid interface of the molten pool, affect the size, orientation and composition of microstructural features, which determine the strength and ductility of the deposit.

3. Part fabrication

Representative parts produced with this technology are shown in Fig. 3. Overhanging part features, assemblies and massive structures deposited represent the capability of the process. A typical development cycle to produce a part involves part design in three dimensions, motion path development, and optimization of process parameters to achieve full density at maximum deposition rate. Before the final or best part is produced, iterations of both the motion path and process parameter establishment are often performed, unless information from a process knowledge base on similar parts can be used. For parts with multiple features, this development cycle is often repeated for each feature. Once the motion path and process parameters are optimized the final part or multiple parts are produced. Changes to dimensions or geometry after the initial optimization require motion path regeneration followed by direct deposition without the need for more

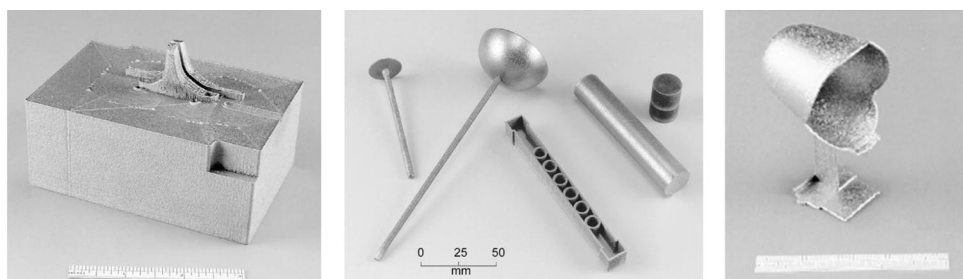


Fig. 3. Injection molding die insert (left), part assemblies and overhangs (center) and light reflector (right) are examples of parts made with the DLF process. Deposition times ranged from approximately 1 h for the shell type parts to 70 h for the die insert in an unattended process.

process optimization. Hence a designer can produce a prototype and modify it quickly after the initial optimization is performed on the first part. Each new material and each new part or feature geometry makes the optimization cycle a prerequisite to building the best part. However, establishment of a knowledge base of part processing expertise over time can eliminate much of the development required.

4. Accuracy and surface finish

A hexagonal cross-section, seven-hole-array structure shown in Fig. 4, was built to 356 mm in height from Inconel 690, a difficult to process high-temperature, nickel-base alloy. The nominal composition of Inconel 690 in wt.% is 58Ni, 29Cr, 9Fe. The part was deposited at a laser power of 160 W, speed of 12.7 mm/s, vertical layer increment of 0.25 mm, bead overlap of 0.27 mm, and the powder feed rate was approximately 9 g/min. Oxygen was controlled to less than 10 ppm in an argon atmosphere. Deposition time was 172 h at a rate of 0.04 lb/h in one continuous, unattended operation.

Dimensional inspection of the part features indicated hole diameters were produced within ± 0.05 mm of the specified diameter for six out of the seven holes and were centered within ± 0.13 mm of the specified location. Radial distance from the center of the cross-section to the center of the hexagonal faces was within ± 0.076 mm. Surface roughness was 12 μm , arithmetic average, which is similar to investment cast surfaces. However, one hole was smaller because of an extra deposition pass inserted into the inside radius of the hole motion path, making it a 12.62-mm diameter, and two extra passes were inserted for motion outside the desired hexagon boundary making it 24.33 mm instead of the specified 23.8 mm. These extra passes could

easily be removed from the motion path but a second part was not made.

5. Tensile properties

Material properties of deposits have been measured for several materials and are compared to conventionally processed material in Table 1. As-deposited tensile yield strength of DLF processed 316 stainless steel and Inconel 690 exceeded that of conventionally processed wrought material. Tensile elongation was 41% and 49% for the two materials. Tensile yield strength for Ti-6Al-4V, produced by DLF, fell in the equivalent range for wrought material, however, elongation was only 6% compared to 10% and higher for conventionally cast and wrought products.

Tensile data show that properties equivalent to wrought material can be achieved for some materials. This eliminates the need for multiple thermo-mechanical processing treatments in conventional processing. Chemical segregation in cast ingots, that make homogenization heat treatments and plastic deformation processing for grain refinement necessary in ingot metallurgy, are eliminated by using the direct deposition technology. Chemical homogenization is achieved through randomization of composition by using powders as input material and by limiting chemical diffusion in the liquid state to the boundaries of the small molten pool that is used to deposit the entire component.

6. Deposition microstructure

Fully dense material is desired for most part fabrication to achieve optimum mechanical strength to meet or exceed service requirements. Full density is achieved by optimization of both process parameters and motion

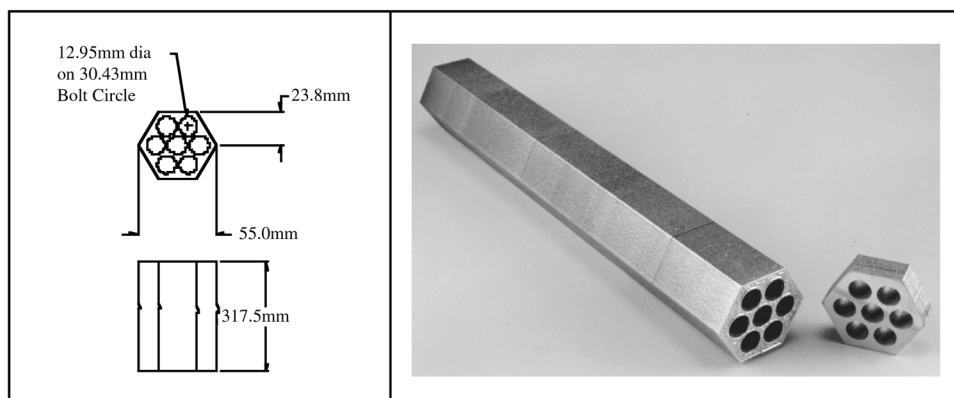


Fig. 4. Inconel 690 hexagon with seven-hole array made by DLF. Hole diameters are within ± 0.05 mm and centered on a bolt circle within ± 0.13 mm. Radial distance to hexagonal faces was within ± 0.076 mm. Surface roughness is 12 μm , arithmetic average.

Table 1
Tensile properties of DLF material compared to conventionally processed material

Material	0.2 years MPa (ksi)	UTS MPa (ksi)	Elong (%)
<i>Type 316 stainless steel</i>			
DLF (As deposited)	296 (43)	579 (84)	41
Wrought annealed	262 (38)	572 (83)	63
Investment cast 316	269 (39)	517 (75)	39
<i>Inconel 690 (58Ni–29Cr–9Fe)</i>			
DLF (As deposited)	450 (65.2)	666 (96.6)	48.8
Hot rolled rod	372 (54)	738 (107)	50
<i>Ti–6Al–4V</i>			
DLF with mill anneal	958 (139)	1027 (149)	6.2
Wrought bar (annealed)	827–1000 (120–145)	931–1069 (135–155)	15–20
Cast + anneal	889 (129)	1014 (147)	10

path to maintain a continuous molten pool that sweeps the entire volume of the desired part. Fig. 5 shows 316 stainless steel layers (left photo) and cellular microstructure (right photo, higher magnification) within the layers. Continuity from layer to layer is maintained by melt back into previous layers as a new layer is added. Depth of melt back varies from a fraction of the previous layer to re-melting through multiple layers, depending on process parameters chosen.

Porous microstructures result primarily from gas evolution during solidification and lack of fusion between layers or adjacent passes of the molten pool. Fig. 6 (left) shows porosity in a W-25Re alloy made by fusing blended tungsten and rhenium powders. Spherical cavities are formed during melting and remain in the solidified microstructure. Residual gas in the starting powder material or decomposition products produced by laser heating and melting typically result in this type of pore formation. Fig. 6 (right) shows porosity resulting from lack of fusion at layer boundaries. Increasing

laser power, lowering traverse speed, or using thinner layers can promote fusion and reduce or eliminate this type of void content.

7. Deposition of alloys, dissimilar metals, composites, functional grades

Unique alloy, dissimilar, and graded compositions, formed by pre-blending desired powder compositions or combining powders at the laser focal zone, provide the capability to control properties within a fabricated structure. Fig. 7 shows a transition from commercially pure titanium to Ti-20w/o Nb alloy. After building a pure titanium plate, Nb powder was proportionally added into the molten pool from a second powder feeder to form the 80Ti-20Nb composition. Laser power was increased from 200 to 320 W to produce complete melting of the Nb. Lower powers selectively melted the titanium and not the Nb to form a Ti matrix

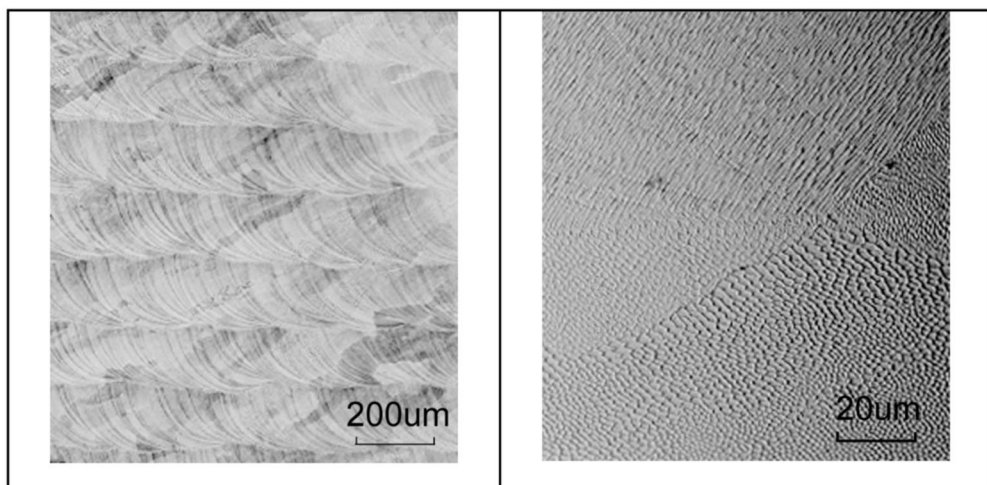


Fig. 5. Fully dense microstructure of a 316 stainless steel bar (left), showing the deposited layer structure (left) and cellular solidification microstructure within the layers (right).

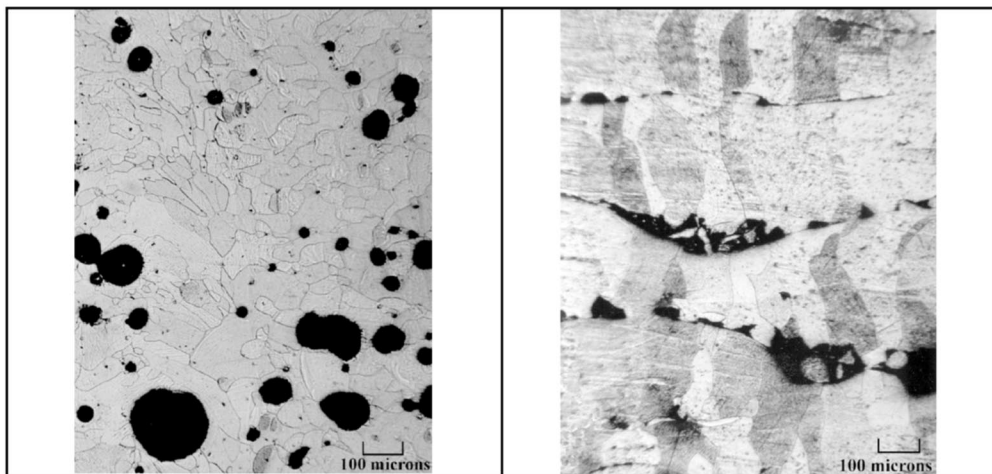


Fig. 6. Porosity observed in DLF deposits is caused by residual gas content in starting powders evolving upon solidification, shown in the blended W-25Re powder alloy (left), or lack of fusion between layer boundaries in the niobium deposit (right).

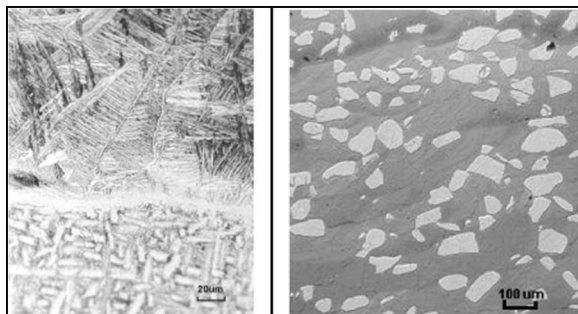


Fig. 7. A transition (left) from commercially pure titanium (top section—left photo) to Ti-20w/oNb was made by blending the two powders at the laser focal zone and raising the power from 200 to 320 W when the Nb was added. A microstructure (right) of non-melted Nb powder particles in a continuous Ti matrix (right) was formed at low power.

with Nb powder particles.

Powders can be either pre-alloyed or pre-blended and fed from one feeder into the molten pool to produce a desired composition. However, the capability to feed several different powders at the same time and control their feed rates individually provides added flexibility. Any desired alloy composition can easily be tried, eliminating the fabrication steps required for pre-alloyed powder. Segregation in blended powders, according to powder density, size, shape and surface characteristics, during agitation by feed systems is eliminated, by feeding powders separately. Functional grades of composition are made by ramping feed rates up or down proportionally with two or more feeders to obtain the desired compositional gradients.

8. Summary

The feasibility of depositing any metal and many

intermetallics into near-net shape parts in a single processing step has been demonstrated using the DLF and LENS™ process technology. Accuracy is within ± 0.12 mm with a 10- μm surface finish. Powder chemistry, particularly gas content, metallurgical stability, and distortion must be characterized for any particular component and material system. With this technology, materials that either can not be cast and thermo-mechanically processed, or that can not be consolidated successfully by powder metallurgy, can be formed. Features such as internal cavities, which can not be machined directly or require extensive welding and assembly, can be formed. Materials requiring multiple conventional processes can be formed in a single step, eliminating the need for dies and molds, capital equipment, and space associated with each additional process.

References

- [1] Patent 2,076,952. Production of Hard Metal Alloys by Layers. 8 June 1934.
- [2] Bourell DL, Beaman JJ, Crawford RH, Marcus HL, Barlow JW. Solid freeform fabrication symposium, 1997. Proceedings 11–13 Aug. University of Texas at Austin, Austin, Texas, 1997.
- [3] Lewis G, Cremers D, Cotton J, Milewski J, Preston D. Laboratory directed research and development program annual reports for FY92, FY93, FY94. The rapid formation of unique structural components by fusing airborne powders in a laser beam. Los Alamos National Laboratory, Los Alamos New Mexico, 97545.
- [4] Lewis GK, Nemec RB, Milewski JO, Thoma DL, Barbe MR, Cremers DA. Directed light fabrication. Proceedings of the ICALEO '94. Laser Institute of America, Orlando, Florida, 1994:17.
- [5] D.J. Thoma, G.K. Lewis, R.B. Nemec. Solidification behavior during directed light fabrication. In: J. Singh, editors. Beam processing of advanced materials. Cleveland, OH: ASM, 1995.

- [6] Thoma DJ, Charbon C, Lewis GK, Nemec RB. Directed light fabrication of iron-based materials. Advanced laser processing of materials — fundamentals and applications. Pittsburgh: MRS, 1996.
- [7] Lewis GK, Thoma DJ, Milewski JO, Nemec RB. Directed light fabrication of near-net shape metal components. World Congress on Powder Metallurgy and Particulate Materials, Washington, DC, 16–21 June 1996.
- [8] Thoma DJ, Lewis GK, Schwartz EM, Nemec RB. Near net shape processing of metal powders using directed light fabrication. Advanced Materials and Technology for the 21st Century, J Inst Metals, 1995 Fall Annual Meeting (117th) Hawaii, 13–15 Dec. 1995.
- [9] Lewis GK, Thoma DJ, Milewski JO, Nemec RB. Directed light fabrication of refractory metals. 1997 International Conference on Powder Metallurgy and Particulate Materials, Chicago, Illinois, 29 June–2 July 1997.
- [10] Lewis GK, Milewski JO, Thoma DB, Nemec RB. Properties of near-net shape metallic components made by the directed light fabrication process. The 8th Solid Free-Form Fabrication Symposium. University of Texas at Austin, Austin, Texas, 1997.
- [11] Griffith ML, Schlienger ME, Harwell LD, Oliver MS, Baldwin MD, Ensz MT, Smugeresky JE, Essien M, Brooks J, Robino CV, Hofmeister WH, Wert MJ, Nelson DV. Thermal behavior in the LENS process. Proceedings of the Solid Freeform Fabrication Symposium. Austin, TX, August 1998:89.
- [12] Schlienger ME, Griffith ML, Oliver M, Romero JA, Smugeresky J. Sacrificial materials for complex geometry fabrication. Proceedings of the Solid Freeform Fabrication Symposium. Austin, TX, August 1998:205.
- [13] Ensz MT, Harwell LD, Griffith ML. Software Development for LENS. Proceedings of the Solid Freeform Fabrication Symposium. Austin, TX, August 1998:359.
- [14] Schlienger E, Dimos D, Griffith M et al. Near net shape production of metal components using LENS. Proceedings of the Third Pacific Rim International Conference on Advanced Materials and Processing. Honolulu, HI, 12–16 July 1998:1581.
- [15] Griffith ML, Harwell LD, Romero JA, Schlienger E, Atwood CL, Smugeresky JE. Multi-material processing by LENSTM. Proceedings of the Solid Freeform Fabrication Symposium. Austin, TX, August 1997:387.
- [16] Smugeresky JE, Keicher DM, Romero JA, Griffith ML, Harwell LD. Laser engineered net shaping (LENSTM) process optimization of surface finish and microstructural properties. Proceedings of the World Congress on Powder Metallurgy and Particulate Materials. Chicago, IL, June 1997.
- [17] Griffith ML, Keicher DM, Atwood CL et al. Free form fabrication of metallic components using laser engineered net shaping (LENS). Proceedings of the Solid Freeform Fabrication Symposium. Austin, TX, 12–14 August 1996:125.
- [18] Keicher DM, Romero JA, Griffith ML, Atwood CL. Laser metal deposition of alloy 625 for free form fabrication. Proceedings of the World Congress on Powder Metallurgy and Particulate Materials. Washington D.C.D. M. Keicher, 16–21 June 1996.
- [19] Romero JA, Griffith ML, Atwood CL et al. Laser engineered net shaping (LENSTM) for additive component processing. Proceedings of the Rapid Prototyping and Manufacturing Conference. Dearborn, MI, 23–25 April 1996.

UNDERSTANDING THE MICROSTRUCTURE AND PROPERTIES OF COMPONENTS FABRICATED BY LASER ENGINEERED NET SHAPING (LENS)

M. L. Griffith*, M. T. Ensz*, J. D. Puskar*, C. V. Robino*, J. A. Brooks**, J. A. Philliber**, J. E. Smugeresky**, †W. H. Hofmeister

*Sandia National Laboratories, Albuquerque, NM 87185

**Sandia National Laboratories, Livermore, CA 94551

†Vanderbilt University, Department of Chemical Engineering, Nashville, TN 37235

ABSTRACT

Laser Engineered Net Shaping (LENS) is a novel manufacturing process for fabricating metal parts directly from Computer Aided Design (CAD) solid models. The process is similar to rapid prototyping technologies in its approach to fabricate a solid component by layer additive methods. However, the LENS technology is unique in that fully dense metal components with material properties similar to wrought materials can be fabricated. The LENS process has the potential to dramatically reduce the time and cost required realizing functional metal parts. In addition, the process can fabricate complex internal features not possible using existing manufacturing processes. The real promise of the technology is the potential to manipulate the material fabrication and properties through precision deposition of the material, which includes thermal behavior control, layered or graded deposition of multi-materials, and process parameter selection.

INTRODUCTION

Direct laser metal deposition processing is a promising manufacturing technology, which could significantly reduce the length of time between initial concept and finished part. To facilitate adoption of this technology in the manufacturing environment, further understanding is required to ensure routine fabrication of robust components with desired material properties. This requires understanding and control of the material behavior during part fabrication. This paper describes our research to understand solidification aspects, thermal behavior, and material properties for laser metal deposition technologies.

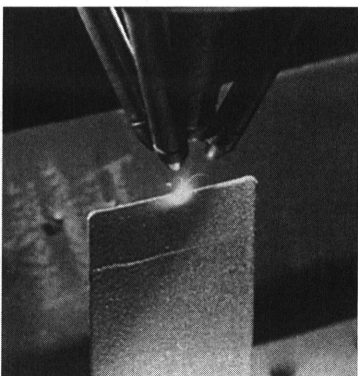
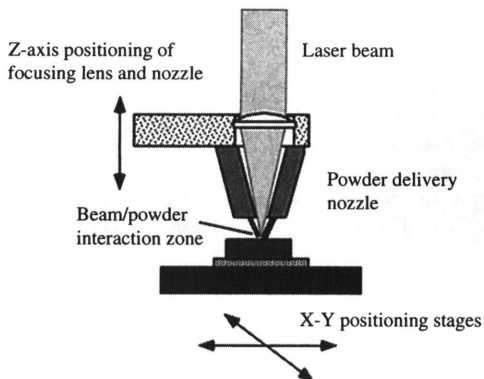


Figure 1: (a) Schematic of LENS process.

(b) In-situ wall fabrication.

The specific laser metal deposition technique used for this study is the Laser Engineered Net Shaping (LENS) process [1-5]. Figure 1a shows a schematic of the LENS process. A component is fabricated by focusing a laser beam onto a substrate while simultaneously injecting metal powder particles to create a molten pool. The substrate is moved beneath the laser beam in the X-Y plane to deposit a thin cross section, thereby creating the desired geometry for each layer. After deposition of each layer, the powder delivery nozzle and focusing lens assembly are incremented in the positive Z-direction, thereby building a three dimensional component layer additively. Figure 1b shows the deposition of a single pass wall in 316 stainless steel. LENS components have been fabricated from various alloys including stainless steel, tool steel, nickel-based super alloys, and titanium.

Any LENS fabricated component has a complex thermal history. It is important to understand the bulk and transient thermal behavior to reproducibly fabricate parts. The ultimate intent is to monitor the thermal signatures and to incorporate sensors and feedback algorithms to control part fabrication. With appropriate sensors and feedback, the geometric properties (accuracy, surface finish) as well as the materials' properties (e.g. strength, ductility) of a component can be designed into the part through the fabrication parameters.

To advance direct fabrication capabilities, the LENS process must be able to accommodate a wide range of materials and deposition styles. Over the past few years, we have built up an extensive material database to understand the range of materials processable by LENS. However, because LENS is a precision, point by point, fabrication process, we have expanded the deposition capability to include composites and graded structures [6]. Therefore, the designer can tailor physical properties critical to component performance. Examples include graded deposition for matching coefficient of thermal expansion between dissimilar materials, layered fabrication for novel mechanical properties, and new alloy design where elemental constituents and/or alloys are blended to create new materials.

In this paper, we will discuss our efforts to understand, model, and control microstructural evolution and material properties. We will also show advanced capabilities that are possible with a precision deposition process to tailor and enhance performance.

MATERIAL PROPERTIES

Material Database

As stated in the introduction, many alloys have been used to fabricate parts by LENS. Table I is a partial list of the room temperature mechanical properties for alloys ranging from stainless steel to titanium to nickel-based alloys. In most cases, the LENS properties are as good as if not better than the traditionally fabricated material. For stainless steel 316 (SS316), the yield strength is double that of wrought, while retaining a ductility of nearly 50%. This is most likely due to Hall-Petch grain size refinement, where finer grain sizes results in higher yield strengths. Typical LENS-processed grain sizes range from 1-10 microns, where traditional wrought material is around 40 microns. At 40 microns, this translates to a yield strength of 30 ksi, versus a 1 micron grain size should be equivalent to a yield strength 67 ksi [7]. As-process LENS SS316 has a yield strength of 63 ksi, indicating that grain size refinement is controlling strength properties.

Table I: Room temperature mechanical properties for various alloys fabricated by LENS. LENS properties are from as-process parts except where noted (*annealed, ** solution treated + annealed). LENS properties are compared to wrought material except when heat treated (HT), and properties are compared to same HT for traditional processing.

MATERIAL	UTS (KSI)		YTS (KSI)		EI (%)	
	Wrought	LENS™	Wrought	LENS™	Wrought	LENS™
SS 316	85	110	34	63	50	46
SS 304L	---	95	40	47	55	70
H-13	250	247	210	212	12	1-3
Ti-6Al-4V*	135	130-145	124	120-140	10	1-16
IN718**	200	203	168	162	20	16
IN 625	121	135	58	89	37	38
IN 600	---	106	---	62	---	40

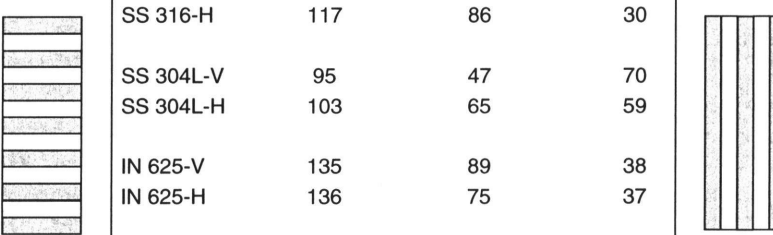
Effect of Layered Deposition

For LENS components that will be used in the as-processed state, it is important to understand the effect of layered deposition and the many layer interfaces on the resulting mechanical properties. In the worst case, the layers are not well fused during fabrication, forming large pores, resulting in poor mechanical properties. But for fully dense material, it is necessary to determine the effect of the layered deposition on resulting performance. This will be important as more complex schemes are used to deposit material (e.g. multi-axis).

Simple sample geometries were chosen where the tensile direction is either parallel (H) or perpendicular (V) to the layers. Table II shows the results for two stainless steel alloys and two nickel superalloys. The stainless steel alloys show the greatest effect of the layered deposition, where the strengths are lower for the vertical samples. This is most likely due to stress state condition where the layers are perpendicular to the pull direction and any imperfections will initiate fracture. Inspection of the fracture surfaces shows fracture initiation occurs at a layer interface [8]. However, microstructural inspection does not reveal any defects or other features at the interface that would result in this behavior. The yield strengths are much higher for the horizontal samples, with a tradeoff in ductility. The horizontal specimens do show secondary cracks forming at the interface, further indicating that there is some sort of weak microstructure at the interface. Further microstructural analysis is required to understand the effect of the interfaces on resulting properties.

The nickel superalloys show little effect of the layered deposition, and variations in properties are more likely a result due to the small sampling of parts. It should be noted that many LENS parts are post-heat treated, and after a solution heat treat, the layered deposition structure completely disappears.

Table II: A comparison of build direction on as-processed room temperature tensile properties for two stainless steel and two nickel alloys.



MATERIAL	UTS (KSI)	YTS (KSI)	EI (%)
V	SS 316-V	115	66
	SS 316-H	117	30
H	SS 304L-V	95	70
	SS 304L-H	103	59
V	IN 625-V	135	38
	IN 625-H	136	37
H	IN 690-V	88	45
	IN 690-H	108	48

Effect of Process Parameters

One of the main goals of this research is to determine the effect of various process parameters on resulting material properties. With an understanding of their effect, we hope to predict and tailor the final performance behavior. An initial set of experiments was performed using H13 tool steel. Simple hollow boxes (shell build), one line wide, were fabricated with the following dimensions and deposition parameters:

Size: 101.6 mm x 101.6 mm x 152.4 mm

Layer increment = 250 μm

Power: 200, 250 and 300 Watts

Velocity: 5.92, 7.62, and 9.31 mm/s

By changing the power and velocity values, the deposition energy or thermal input is varied which could have an effect on final strength and ductility properties. Figure 2 shows the room temperature tensile results for nine power and velocity combinations. By modifying the deposition energy, one can tailor the strength and ductility values. For low energy input, through low power or high traverse velocity, the molten bead will solidify quickly resulting in high yield and ultimate tensile strength values. If the performance requires significant ductility or strain capability, parts should be fabricated at high energy input using high power and/or slow traverse velocity. As with many fabrication technologies, and in the case of H13 tool steel, one cannot achieve the highest strength and ductility values simultaneously. The designer must consider what are the performance priorities and match the processing conditions to achieve those properties.

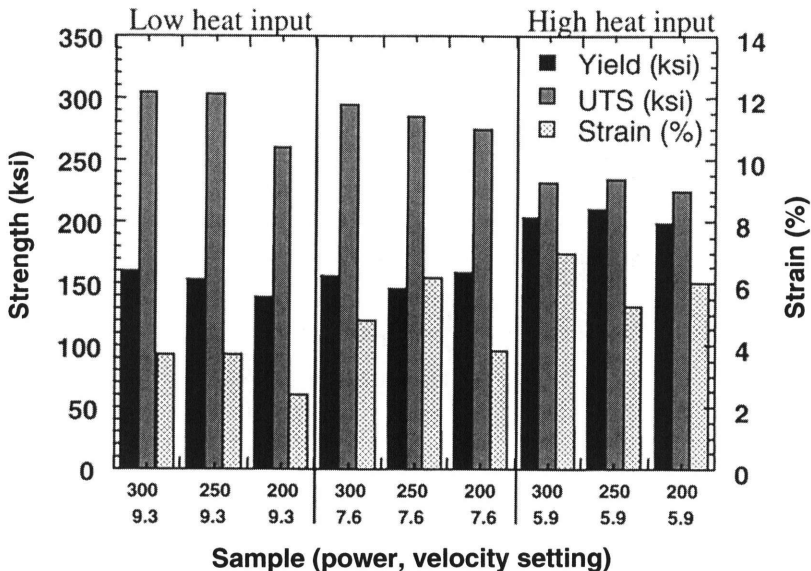


Figure 2: Comparison of room temperature tensile properties for H13 tool steel shell build samples fabricated at various power and velocity values.

MATERIAL UNDERSTANDING AND CONTROL

In order to understand the development of structure and properties in the solidified material, it is important to know the thermal gradients and cooling rates in and around the molten pool. These gradients control the morphology and size of the first solid to form, and are a primary factor in determining the properties of the sample. Thermal measurements, microstructural studies, and modeling can be combined to develop process parameters to control microstructural development and tailor the properties of samples for particular applications.

Thermal Imaging

It is known intuitively that a thermal gradient exists across the molten pool and into the bulk material created by the LENS process. The nature and extent of this gradient has not been fully characterized. Since mechanical properties are dependent upon the microstructure of the material, which in turn is a function of the thermal history of solidification, an understanding of the temperature gradient induced by LENS processing is of special interest. It would be particularly beneficial to use non-invasive thermal imaging to measure the temperature profile and gradients and to use these thermal profiles in feedback control.

Preliminary experiments were conducted using ultra high speed digital imaging techniques [9-11] during LENS processing to provide insight as to the size of the molten pool and the thermal gradients in 316 stainless steel (SS316) samples fabricated using the LENS process. Figure 3 shows a typical view of the molten pool seen from the top. The image has

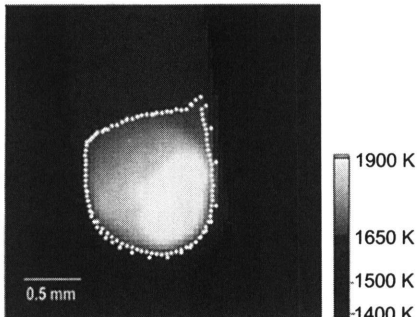


Figure 3: Image of molten pool during LENS processing. Dotted outline represents the solidification interface temperature, 1650 K, for stainless steel 316.

been converted to temperature and colorized according to the adjacent scale. In the figure, the bead motion is from top to bottom, as signified by the thermal tail. The solidification interface, or pool area, at 1650 K is outlined and this is monitored in real time. Note there is an abundance of extra energy or superheat within the molten pool (greater than 250 K), which will effect the thermal gradients and solidification microstructures.

The thermal profiles of the build reveal interesting non-linearities in the build process. Profiles were compiled for wall geometry builds as a function of laser power. These are presented in Figure 4 for SS316 alloy. The laser power for each profile is shown in the legend. The molten pool size increases with power up to 275W. Above 275W the energy of the laser drives the pool temperature up without significant change in the length of the molten zone. Note also that the slopes of the temperature profiles outside the molten zone generally increase as the power decreases. Higher power results in more bulk heating of the sample away from the molten zone. This results in a lower cooling rate in the sample after solidification. For example, the cooling rate of the 275W sample 0.5 mm from the solid-liquid interface is twice that of the 410W sample. The initial scale of the microstructure, however, should be determined by the cooling rate at the solid-liquid interface.

A complete series of line builds was analyzed to determine the cooling rate at the solid-liquid interface. These determinations are shown in Figure 5. At the interface the cooling rates are substantially higher at the low power levels and remain fairly constant at the higher powers. Thus, the highest quench rates are available at the lowest power, when the molten zone is small. As the laser power is increased, the quench rate at the interface settles at 1000-1500 K/s. All these results are for thin-walled features which show a great change in thermal gradients for changes in power. In contrast, for bulk solid fabrication, the cooling rates are not so varied. At the highest powers, the cooling rate is much lower, about 500 K/s, so that one may expect a more coarsened microstructure due to grain growth. With information about temperatures in and around the molten pool, pool size, and thermal gradients, we hope to utilize in-situ control to improve the capabilities of parts fabricated by LENS.

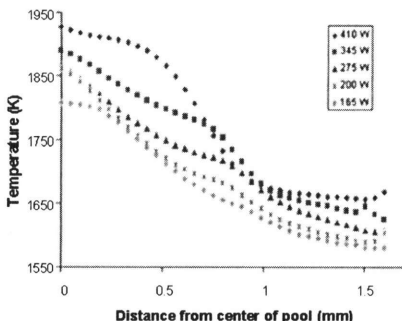


Figure 4: Thermal profiles from the center of the molten pool along the direction of translation for several different laser power settings.

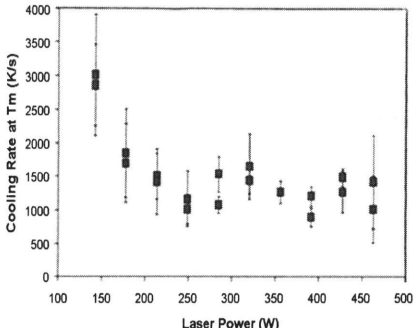


Figure 5: Cooling rates calculated from a large series of images as a function of laser power.

In-situ Control of Thermal Signature using Visible Imaging

With an understanding of the molten pool temperatures, thermal gradients, and steady state pool sizes, this information can be utilized to control the process. By matching the pool area to the specific thermal condition, one can extend the overhang capability in a 3-axis LENS system. Figure 6 shows a thin-walled hollow tube, two lines wide, with a 40° overhang. Without any control over the thermal behavior or molten pool area, only a 20° overhang is possible. Now, the pool area is matched to the geometric condition, in this case supported versus partially supported sections, to maintain a consistent, reliable build at 40°.

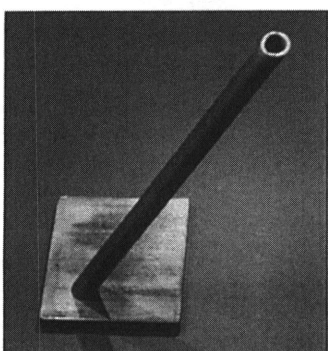


Figure 6: Photo showing advanced capability using closed loop control to fabricate double thick wall tube with 40° angle.

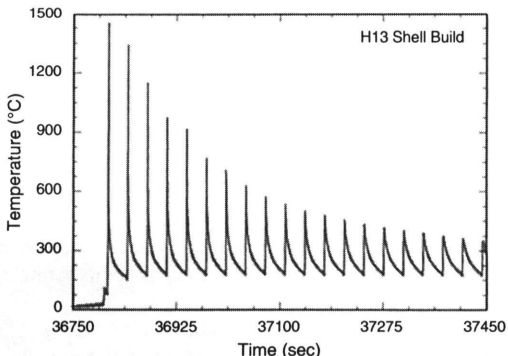


Figure 7: Temperature traces at one position as twenty layers are deposited on top of thermocouple inserted into H13 LENS shell build.

Thermocouple measurements to determine macro-thermal transients

A relatively easy way to obtain the thermal history during LENS processing is by inserting a thermocouple (TC) directly into the sample during fabrication [9]. Fine diameter (10 μm) Type C thermocouple wire is used for measurements to ensure no reaction during deposition, and care was taken to insert the TC bead into the deposition zone for accurate temperature measurements. Figure 7 shows the in-situ temperature readings for twenty deposition layers from a representative thermocouple inserted during fabrication of H13 tool steel. Each peak represents the thermocouple response as the laser passes over or near the thermocouple, from initial insertion to subsequent layer depositions. The thermal excursions dampen out when either the energy source moves away from the thermocouple during fabrication of a layer or subsequent layers are deposited. After the initial peak in temperature, approximately 1500 °C, the heat is quickly conducted away in about 15 seconds to a nominal value of 150 °C for the first layer. This initial thermal signature should result in a solidification process producing a high strength microstructure. Yet, for LENS processing, each subsequent pass reheats the previous layers, such that after the fifth layer is deposited, the initial layer still receives thermal excursions to 900 °C. Following thirteen deposition layers, the thermocouple nominally reads 500 °C. This complicated thermal cycling affects the material properties including residual stress and mechanical strength due to tempering or aging effects. This thermal behavior and effect on final properties is discussed in the next section.

Microstructure Evolution in LENS Fabrication

The characteristics of microstructural evolution in LENS fabrication can be complex due to the thermal transients and are dependent on the alloy system. However, some general considerations can be illustrated by discussion of a specific alloy system and the models which must be developed to describe the response of the alloy to processing. H13 tool steel provides a good example of an alloy system where there are several mechanisms for microstructural changes during processing. The LENS processing of this system has recently been described in more detail [12]. This is a commercially available secondary hardening alloy that is of significant industrial importance that, when conventionally heat treated, exhibits a martensitic structure strengthened by the formation of Mo and Cr containing alloy carbides.

Due to the layer additive nature of the LENS process, the thermal cycles associated with the LENS process can involve numerous reheating cycles. Thus, the goal of any assessment of microstructural evolution is to determine the response of the alloy to these cycles. For a shell build of H13, the peak temperature of the cycle provides a convenient means to classify the cycle and the response of the material. As shown in Figure 8, the build microstructure can be related to the H13 phase diagram, although it must be noted that, given the rapid heating and cooling rates, non-equilibrium conditions exist and the diagram can only be used as a general guide. The microstructure shown was taken from the final portion of the build, and can be separated into three different regions corresponding to peak temperature. Also shown is the height of the individual build passes.

Region I is composed of as-solidified H13 (last pass) and supercritically reheated (fully reaustenitized) material. Some segregation of alloying elements occurs as a result of partitioning during solidification, and little alloy element homogenization occurs due to the slow diffusion rates of substitutional alloying elements in austenite [13]. The exception is carbon for which the diffusivity is much more rapid and a uniform distribution is expected [13]. The supercritical region extends from the liquidus temperature to the ferrite + carbide two-phase region, which on

I - Solidification/Supercritical

II - Intercritical heating

III - Sub-critical heating

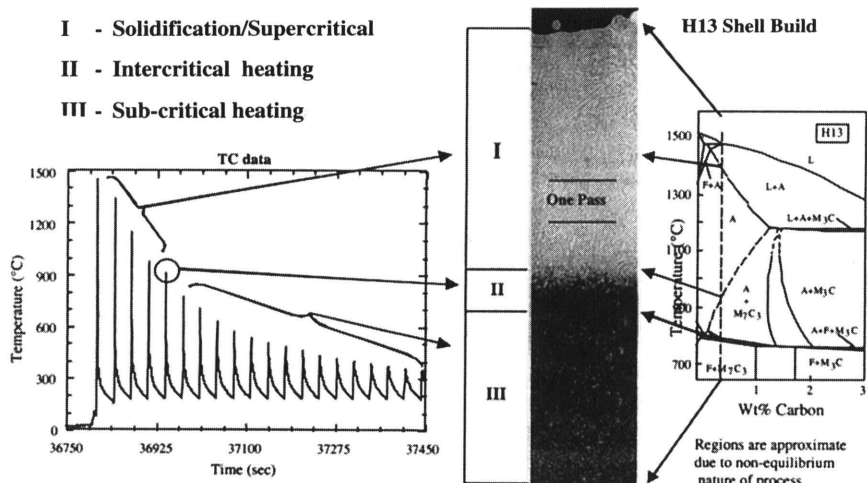


Figure 8: Correlation between measured thermal cycles, microstructure, and the phase diagram for H13 (0.04 wt% C) shell build. Three thermal regions are used to describe the behavior. The pass height for these conditions is approximately 0.25 mm.

the equilibrium diagram is approximately 925°C. The light etching material of the supercritical region is untempered martensite (hardness of 59 HRC) in which no carbides were detected using transmission electron microscopy (TEM).

Region II corresponds to material cycled into the intercritical two-phase and narrow three-phase regions shown on the diagram and corresponds to the fifth layer from the top of the build. This material had been previously cycled into the supercritical region, and is the uppermost dark etching region in Figure 8. It is interesting that the height of this region is close to that of a single pass height, and based on the phase diagram, would have contained a thermal gradient of roughly 150°/0.25 mm (~600°C/mm). For the thermal cycles shown, only the peak temperature of the fifth thermal cycle lies within this region. The region therefore consists of a mixture of carbides and martensite (formed from the austenite present at the peak temperature).

Region III contains the material that in addition to having experienced thermal cycles in the upper two regions, also experienced subcritical thermal cycles. For H13, the subcritical cycles can result in additional alloy carbide precipitation and/or carbide coarsening. The final microstructure (in the bulk of the build) therefore consists of martensite containing several types of alloy carbides. In this region, the hardness initially drops to a value of 54 HRC and can further reduce depending on the processing and thermal history [12].

Model Descriptions

Given the qualitative descriptions for the microstructural changes which occur in each build region, it remains to develop kinetic models for the various mechanisms. Here again, it is important to recognize that these models are necessarily alloy dependent, and must reflect the principal strengthening mechanisms operative in the alloy. For H13, the supercritically heated region (Region I) is relatively simple because the hardenability and cooling rates during the

cycles are both high. Thus the microstructure after the supercritical cycles is essentially single phase fresh (untempered) martensite, although there may be some residual inhomogeneity in the alloy element distributions through the martensite. The solidification segregation of alloy elements can be estimated with knowledge of the solidification partition coefficients and conventional solidification models. The extent to which alloy element concentrations are homogenized during the supercritical passes can be estimated by using conventional diffusion calculations, but it is important to note that the diffusion equations must be solved over the thermal cycle(s) and therefore generally require numerical methods.

The microstructural changes occurring in Region II are perhaps the most severe and difficult to describe from a model perspective. During the intercritical cycles, the martensite present after the supercritical cycles transforms into ferrite, austenite, and carbides. At the temperatures involved (above 800 °C), the rate of this transformation is very high and difficult to analyze experimentally. Efforts are underway to develop kinetics models for these types of transformations (see, for example 14), but for the present overview it is sufficient to note that these models must describe the nucleation and growth of the austenite and carbides as well as the fractions of each constituent (austenite, ferrite and carbide) as they evolve during the temperature transient. Here again, the athermal nature of the process generally necessitates a numerical approach. It is important to note here that steels (and titanium alloys) are the only common commercial alloys that undergo these types of solid state phase transformations. As a result, other alloys, such as Ni-based superalloys, are therefore significantly less complex in terms of microstructural evolution.

Although the influence of the subcritical cycles is less pronounced than that of the intercritical cycles, the effects of these cycles can still be significant in terms of the microstructural evolution and resultant properties. For H13, the principal effects are those related to the precipitation and coarsening of alloy carbides. There are a number of approaches to describing these changes, and an example of one such approach is given in Ref. 12. In that work, hardness was selected as the property of interest, and a simple kinetic model describing the evolution of hardness during the subcritical cycling was developed. Inasmuch as many alloys of commercial interest are precipitation hardenable, models of this type are generally applicable to a wide range of alloys.

EXPANDING MATERIAL DEPOSITION CAPABILITY

One of the unique aspects to LENS is the point by point deposition style. With this type of deposition, it is possible to optimize the build parameters in order to improve fabrication. Software has been developed to allow the designer to choose or correlate the build parameters- such as layer thickness, hatch spacing, power, velocity, material, etc.- to part position. This is useful in many aspects: 1) deposition rate is tailored to feature size, 2) surface finish is controlled through outside border parameters, 3) feature size is correlated to deposition parameters to improve accuracy, and 4) multiple materials can be selected to tailor properties in particular part sections. Figure 9 is a simple example of tailoring the parameters for fabrication of a gear. Finer parameters (layer thickness and hatch) and a hardfacing alloy are used in the tooth section for good surface finish, feature definition, and wear properties. The inside section is an example of bulk deposition with a different alloy where the deposition rate is doubled and the alloy has more ductile properties. Therefore, the choices in deposition parameters and materials open a whole new capability in part fabrication. Results for layered and graded fabrication have been shown elsewhere for LENS [6].

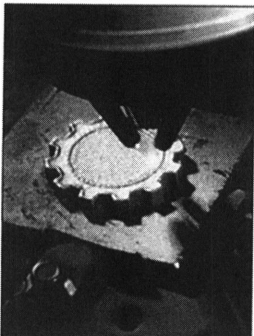


Figure 9: An example of tailored parameter and material fabrication for a gear section.

SUMMARY

In general, the evolution of microstructure and properties during LENS processing can be very complex. We are currently using visible and thermocouple techniques to determine the micro (molten pool) and macro (part) thermal history to gain an understanding of the LENS process. With in-situ monitoring, we have initiated process control through maintaining a setpoint for the molten pool area to extend the overhang capability. This control is coupled with new software to select deposition parameters that are tailored to the part geometry as well as the material performance through multi-material deposition. As we gain more knowledge of the process and resulting properties, we will further develop our models to predict and control the microstructural evolution.

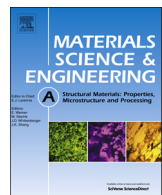
ACKNOWLEDGMENTS

This work supported by the U. S. Department of Energy under contract DE-AC04-94AL85000. Sandia is a multiprogram laboratory operated by Sandia Corporation, a Lockheed Martin Company, for the United States Department of Energy.

REFERENCES

1. M. L. Griffith, D. M. Keicher, C. L. Atwood, J. A. Romero, J. E. Smugeresky, L. D. Harwell, D. L. Greene, "Free Form Fabrication of Metallic Components using Laser Engineered Net Shaping (LENS)", *Proceedings of the Solid Freeform Fabrication Symposium*, August 12-14, 1996, Austin, TX, p. 125.
2. D. M. Keicher, J. A. Romero, M. L. Griffith, C. L. Atwood, "Laser Metal Deposition of Alloy 625 for Free Form Fabrication", *Proceedings of the World Congress on Powder Metallurgy and Particulate Materials*, June 16-21, 1996, Washington, D.C.
3. John E. Smugeresky, Dave M. Keicher, Joseph A. Romero, Michelle L. Griffith, Lane D. Harwell, "Using the Laser Engineered Net Shaping (LENS) Process to Produce Complex Components from a CAD Solid Model", *Photonics West SPIE Proceedings - Lasers as Tools for Manufacturing*, Volume 2993, 1997, p. 91.

4. E. Schlienger, D. Dimos, M. Griffith, J. Michael, M. Oliver, T. Romero, J. Smugeresky, "Near Net Shape Production of Metal Components using LENS", *Proceedings of the Third Pacific Rim International Conference on Advanced Materials and Processing*, July 12-16, 1998, Honolulu, HI, p. 1581.
5. C. L. Atwood, M. L. Griffith, M E. Schlienger, L. D. Harwell, M. T. Ensz, D. M. Keicher, M. E. Schlienger, J. A. Romero, J. E. Smugeresky, "Laser Engineered Net Shaping (LENS): A Tool for Direct Fabrication of Metal Parts", *Proceedings of ICALEO '98*, November 16-19, 1998, Orlando, FL, p. E-1.
6. M. L. Griffith, L. D. Harwell, J. A . Romero, E. Schlienger, C. L. Atwood, J. E. Smugeresky, "Multi-Material Processing by LENS", *Proceedings of the Solid Freeform Fabrication Symposium*, August, 1997, Austin, TX, p.387.
7. B.P. Kashyap, K. Tangri, *Acta metall. mater.*, Vol. 43, No. 11 pp. 3971-3981, (1995).
8. J. Philliber, J. Smugeresky, B. Somerday, M. Griffith, "Microstructure and Properties of LENS processed 304L Stainless Steel", Presented at the Annual meeting of TMS, Nashville, TN, March 13-15, 2000.
9. M. L. Griffith, M. E. Schlienger, L. D. Harwell, M. S. Oliver, M. D. Baldwin, M. T. Ensz, J. E. Smugeresky, M. Essien, J. Brooks, C. V. Robino, W. H. Hofmeister, M. J. Wert, D. V. Nelson, "Thermal Behavior in the LENS Process ", *Proceedings of the Solid Freeform Fabrication Symposium*, August, 1998, Austin, TX, p. 89.
10. M. L. Griffith, M. E. Schlienger, L. D. Harwell, M. S. Oliver, M. D. Baldwin, M. T. Ensz, J. E. Smugeresky, M. Essien, J. Brooks, C. V. Robino, W. H. Hofmeister, M. J. Wert, D. V. Nelson, *Journal of Materials Design*, volume 20 number 2/3, June 1999, p 107-114.
11. W. Hofmeister, M. Wert, J. Smugeresky, J.A. Philliber, M. Griffith, and M Ensz, *JOM*, Vol. 51, No. 7, available from *JOM-e* online at www.tms.org/pubs/journals/JOM/9907/Hofmeister/Hofmeister-9907.html.
12. J. Brooks, C. Robino, T. Headley, S. Goods, and M. Griffith, "Microstructure and Property Optimization of LENS Deposited H13 Tool Steel", *Proceedings of the Solid Freeform Fabrication Symposium*, August, 1999, Austin, TX, p.375-382.
13. J. A. Brooks, M. I. Baskes, and F. A. Greulick, *Metall. Trans. A*, 22A, (1991), pp. 915-925.
14. R. C. Dykhuizen, C. V. Robino, and G. A. Knorovsky, *Metall. and Mat. Trans. B*, 30B, (1999), pp. 107-117.



Fatigue behavior and failure mechanisms of direct laser deposited Ti–6Al–4V



Amanda J. Sterling^a, Brian Torries^a, Nima Shamsaei^{a,b,*}, Scott M. Thompson^{a,b}, Denver W. Seely^b

^a Department of Mechanical Engineering, Mississippi State University, Box 9552, Mississippi State, MS 39762, USA

^b Center for Advanced Vehicular Systems (CAVS), Mississippi State University, Box 5405, , Mississippi State, MS 39762, USA

ARTICLE INFO

Article history:

Received 24 October 2015

Received in revised form

7 December 2015

Accepted 11 December 2015

Available online 13 December 2015

Keywords:

Fatigue

Additive manufacturing

Laser Engineered Net Shaping (LENS)

Ti–6Al–4V

Titanium

Microstructure

ABSTRACT

In order for additive-manufactured parts to become more widely utilized and trusted in application, it is important to have their mechanical properties well-characterized and certified. The fatigue behavior and failure mechanisms of Ti–6Al–4V specimens fabricated using Laser Engineered Net Shaping (LENS), a Direct Laser Deposition (DLD) additive manufacturing (AM) process, are investigated in this study. A series of fully-reversed strain-controlled fatigue tests is conducted on Ti–6Al–4V specimens manufactured via LENS in their as-built and heat-treated conditions. Scanning Electron Microscopy (SEM) is used to examine the fracture surfaces of fatigue specimens to qualify the failure mechanism, crack initiation sites, and defects such as porosity. Due to the relatively high localized heating and cooling rates experienced during DLD, fabricated parts are observed to possess anisotropic microstructures, and thus, different mechanical properties than those of their traditionally-manufactured wrought counterparts. The fatigue lives of the investigated LENS specimens were found to be shorter than those of wrought specimens, and porosity was found to be the primary contributor to these shorter fatigue lives, with the exception of the heat-treated LENS samples. The presence of pores promotes more unpredictable fatigue behavior, as evidenced by data scatter. Pore shape, size, location, and number were found to impact the fatigue behavior of the as-built and annealed DLD parts. As porosity seems to be the main contributor to the fatigue behavior of DLD parts, it is important to optimize the manufacturing process and design parameters to minimize and control pore generation during the build.

© 2015 Elsevier B.V. All rights reserved.

1. Introduction

Additive manufacturing (AM) allows for the layer-by-layer fabrication of components via sequential material deposition, guided by a three-dimensional solid model and deposition path. Methods such as Powder Bed Fusion (PBF) and Direct Laser Deposition (DLD), each utilizing a laser to melt and join deposited materials, have demonstrated their viability for the AM of metals. Laser Engineered Net Shaping (LENS) [1], a common type of DLD process, utilizes injected powder, typically via multiple nozzles, and in-situ laser delivery for fabricating/repairing metal parts atop substrates (or build plates) [1–3]. A computer numerical controlled (CNC) stage, with attached substrate, travels relative to the deposition head in a pattern dictated by a user-generated path for fabricating individual tracks. The deposition head is then raised

and the process is repeated layer by layer, until a part is generated. Relative to PBF methods, such as Selective Laser Melting (SLM), DLD offers the ability to (1) repair precious components, (2) generate functionally-graded materials (FGMs) and (3) perform thermographic inspection of exposed parts during the build [4–9].

Since LENS is a powder-based AM method, its fabricated parts are susceptible to possessing porosity, such as cavities/voids and lack of fusion between layers, as well as inclusions, such as contamination, particle debris, and un-melted powder [10]. For LENS (and other DLD methods), baseline porosity can stem from utilizing porous particles and by secondary powder injection effects, such as particle-to-particle interactions, splashing, and in-flight phase change [2]. More pronounced porosity results from utilizing an ineffective combination of process parameters, including scanning strategy, hatch spacing, and layer height settings. This process-sourced porosity is primarily driven by gas entrapment and lack of fusion between layers due to adverse laser penetration and/or surface wetting effects [11]. The utilization of non-optimal deposition/energy-delivery parameters for a given material and part geometry can be detrimental to melt pool stability,

* Corresponding author at: Department of Mechanical Engineering, Mississippi State University, Box 9552, Mississippi State, MS 39762, USA.

E-mail address: shamsaei@me.msstate.edu (N. Shamsaei).

Nomenclature

$\frac{\Delta \varepsilon}{2}$	strain amplitude
$\frac{\Delta \varepsilon_e}{2}$	elastic strain amplitude
$\frac{\Delta \varepsilon_p}{2}$	plastic strain amplitude
$\frac{\varepsilon}{2}$	axial strain
ε_a	strain amplitude
ε_e	elastic strain
ε_f'	fatigue ductility coefficient
ε_p	plastic strain
σ	axial stress, MPa
σ_a	stress amplitude, MPa

σ'_f	fatigue strength coefficient, MPa
σ_m	mean stress, MPa
σ_u	ultimate tensile stress, MPa
σ_y	yield stress, MPa
b	fatigue strength exponent
c	fatigue ductility exponent
E	monotonic modulus of elasticity, GPa
E'	cyclic modulus of elasticity, GPa
K'	cyclic strength coefficient, MPa
$2N_f$	number of reversals to failure
N_f	number of cycles to failure
n'	cyclic hardening exponent

wettability, and its solidification. These material- and/or process-sourced defects can adversely impact final part mechanical properties, limiting their range of application [12].

In many applications, components are under cyclic loading; therefore, fatigue will likely be the dominant means for failure. Fatigue properties are directly affected by the microstructure and porosity of a component [13,14], with microstructure depending heavily on the local cooling rates experienced by a part during DLD. These cooling rates are sensitive to the utilized process parameters (e.g. laser power, travel speed, and powder flow rate) and employed design parameters (such as geometry and build direction) [2]. The utilization of uncontrolled, time-invariant process parameters produces a highly non-uniform and transient temperature field along the DLD part, resulting in anisotropic microstructure. These anisotropic and unique microstructural features, combined with the presence of pores/defects, can result in DLD parts having distinct fatigue behavior relative to their wrought counterparts [15].

Ti-6Al-4V is an attractive alloy for many applications given its corrosion resistance, strength retention at elevated temperatures, relatively high strength, and biocompatibility. For these reasons, the additive-manufacturability of Ti-6Al-4V is of immediate interest. In terms of biocompatibility, porous Ti-6Al-4V implants have been successfully fabricated using LENS for achieving new levels of customization, mechanically-matched bone integration, and susceptibility to tissue growth [16]. Via compression molding, functionally-graded titanium/ceramic hydroxyapatite dental implants have been manufactured and shown to be superior over pure titanium implants [17], suggesting the future applicability of AM of FGM for dental applications. In general, the utilization of LENS and other AM methods can reduce production lead times and enhance the customizability of biocompatible Ti-6Al-4V components, positively impacting the industry and consumer [18]. The unique properties of Ti-6Al-4V make it attractive for many aerospace, automotive and chemical applications, especially due to its high strength-to-weight ratio.

Fatigue properties of additively-manufactured Ti-6Al-4V have been reported in the literature [15,19–24]; however, due to unavoidable variation in specimen fabrication and post processing methods, and the current lack of sufficient AM part testing standards, the reported properties are inconsistent [19–22]. For example, Ti-6Al-4V samples built (vertically-upward) using wire-fed DLD, as well as SLM, have been reported to demonstrate high cycle fatigue (HCF) properties that match or exceed those of wrought Ti-6Al-4V [20]. However, Ti-6Al-4V samples manufactured via Electron Beam Melting (EBM), a PBF method, were found to have significantly lower fatigue strength than their wrought counterparts [21,22]. It appears that, in general, the mechanical properties of AM materials become more comparable

to their wrought forms as defects, such as pores and inclusions, are minimized [3].

Kobryn and Semiatin performed experiments to determine mechanical properties of DLD Ti-6Al-4V after either a stress-relieving heat treatment (performed in a vacuum for two hours at 700–730 °C) or hot isostatic pressing (HIP) [19]. The stress-relieved DLD Ti-6Al-4V samples were found to exhibit lower fatigue strength than their wrought and DLD/HIP'ed counterparts. Samples built vertically, with deposited layers oriented perpendicular to tensile loading direction, exhibited lower fatigue strength than those built in horizontal directions (with layers deposited parallel to tensile loading direction). These results demonstrate that stress-relieved DLD Ti-6Al-4V can still exhibit anisotropic mechanical behavior. The DLD samples subjected to HIP exhibited very little mechanical anisotropy and possessed fatigue strength comparable to that of wrought material [19]. The stress-relieved samples displayed a yield strength and modulus of elasticity comparable to that of wrought and DLD/HIP'ed Ti-6Al-4V; however, the ultimate tensile strength for vertically built samples and total elongation to failure was much lower due to non-treated porosity.

Amsterdam and Kool conducted mechanical testing on DLD Ti-6Al-4V samples (fabricated using LENS) that underwent the following heat treatment: solution treatment for 1 h at 970 °C, followed by water quenching, then aged for 4 h at 538 °C, and finally air cooled [23]. The heat treated DLD specimens were found to possess a yield stress (σ_y) and ultimate tensile strength (σ_u) similar to that of wrought Ti-6Al-4V that underwent solution heat treatment and aging. Limited high cycle fatigue (HCF) testing demonstrated that the heat treated DLD Ti-6Al-4V samples could exhibit superior fatigue properties when compared to annealed wrought Ti-6Al-4V. This held true only when there were no large or subsurface pores in the DLD samples. If such pores were present in the DLD samples, the fatigue properties were not as good; however, they were still comparable to those of annealed wrought Ti-6Al-4V [23].

The microstructure of DLD parts can greatly affect their fatigue properties. Coarse microstructures typically have greater crack propagation resistance due to them promoting rougher crack paths, leading to better low cycle fatigue (LCF) behavior. Parts with finer microstructures usually exhibit stronger crack initiation resistance than those with coarser microstructures, due to their increased slip band density, effectively leading to their enhanced HCF behavior [3]. However, the effects of grain size and morphology on fatigue behavior of the fabricated part may not be as pronounced with significant defects/porosity present [10].

There is a need to better understand and characterize the mechanical properties, fatigue behavior, and failure mechanisms of DLD Ti-6Al-4V, especially for accelerating its certification and use in various engineering applications [3,25]. Therefore, the goal

of this study is to aid in further assessing the mechanical traits, with emphasis on fatigue resistance, of as-built and heat treated DLD Ti-6Al-4V (fabricated via LENS) via mechanical testing and microstructural characterizations. Results are directly compared with those of wrought Ti-6Al-4V ELI to aid in these assessments. Since powder-based AM methods are prone to generating porous parts, the effect of porosity on the fatigue behavior of DLD Ti-6Al-4V is investigated by inspecting the fracture surfaces of fatigue specimens.

2. Experimental procedure and results

2.1. LENS parameter selection

An OPTOMECH LENS™ 750 machine (with a 1 kW Nd:YAG laser) was used to fabricate 36 cylindrical Ti-6Al-4V rods in batches of 6 samples per substrate (Ti-6Al-4V, 3.175 mm thick), all deposited in-series (i.e. one rod at a time) with enough distance to avoid thermal effects on previously-deposited rods. Spherical Ti-6Al-4V Grade 5 powder (Philly Materials Inc.), sourced from a Plasma Rotating Electrode Process (PREP), with a mesh size of –100/+325 (SAE AMS 4998C [26]), was utilized in the as-received condition. Process parameters (i.e. laser power, travel speed, and powder feed rate) were selected through a trial-and-error, build-and-inspect method with the goal of achieving fully-dense parts. All process parameters were held constant with respect to time during manufacturing. Prior to part building, single-track depositions were performed on the substrate to determine the quality of the parameter set. Individual ~25 mm lines/tracks were deposited onto the substrate for various process parameter combinations, and then examined for track-to-substrate adhesion and cross-sectional aspect ratio (width to height). A target aspect ratio of 2:1 was sought to better ensure track-to-track overlap for generating uniform layers with minimal pore generation.

Process parameters found to result in quality deposits were used to generate small cuboids that were 6.35 mm × 6.35 mm and five layers high. These builds were cut in half and polished via the Struers metallographic preparation method [27]. The polished faces were examined under an optical microscope for any obvious porosity or lack of fusion. After near-optimal process parameters were determined, cylindrical rods, as shown in Fig. 1(a), were additively manufactured using the LENS process. The final utilized process parameters (all approximate) consisted of a powder flow rate of 0.16 g/s, a traverse speed of 16.93 mm/s, and a set laser power of 350 W. Fabricated rods possessed a diameter of 10.92 mm and a height of 101.6 mm, with a layer thickness of 0.508 mm. The layer hatch spacing was 0.508 mm, with layer orientation alternating between 0° and 90° for each subsequent layer. Each layer was fabricated by first depositing a circumferential contour and then cross-hatching

in the remaining area. These rods were ultimately machined to tensile and fatigue specimens with the dimensions and configurations shown in Fig. 1(b).

The mechanical and microstructural properties of the LENS Ti-6Al-4V samples were ultimately compared with those of wrought Ti-6Al-4V Grade 23 (ELI). The chemical composition of the Ti-6Al-4V Grade 5 powder utilized herein fell within tolerances of Ti-6Al-4V Grade 23 (ELI), with the sole exception of a slightly higher oxygen content in its initial condition. However, trace oxygen content in powder used for laser-based AM enhances their absorptivity and thus their ability to be melted at lower laser powers. Although the oxygen content of the powder can decrease upon laser irradiation (e.g. ‘burn off’), the Ti-6Al-4V melt pool can quickly oxidize due to its elevated temperature. However, this chemical composition could possibly change during solidification. The final oxygen content in LENS samples is dependent on many factors, including: process parameters, purging gas flow rate and amount of air in the LENS chamber. Given the uncertainty and variation in oxygen content in laser-based AM parts, the baseline alloy for comparison was chosen to have minimized oxygen content.

2.2. Heat treatment process

Annealing Ti-6Al-4V parts has been shown to relieve any internal residual stresses [28] which for DLD, can form readily due to significantly high temperature gradients. Therefore, 15 of the LENS Ti-6Al-4V rods (hereafter referred to as the annealed samples) were annealed using a muffle furnace that was preheated to 704 °C (~1300 °F). The rods were placed into the preheated furnace and were allowed to soak for 1 hour, followed by free convection cooling to room temperature. From the annealed LENS Ti-6Al-4V sample group, one specimen underwent microstructural analysis, two underwent tensile testing, and the remaining samples underwent fatigue testing.

A different heat treatment schedule, proven to improve the HCF properties of SLM Ti-6Al-4V parts [28,29], was utilized for 11 of the LENS Ti-6Al-4V rods (hereafter referred to as the heat treated specimens). This particular heat treatment was utilized to achieve grain growth by bringing the samples above their β -transus temperature. An argon-purged tube furnace was preheated to 1050 °C (~1922 °F), and the samples were kept at this temperature for 2 h and then furnace-cooled to room temperature. One of the heat treated samples underwent microstructural analysis, two were used for tensile testing, and the remaining samples were fatigue tested.

2.3. LENS Ti-6Al-4V microstructure

In order to analyze microstructure, portions of the as-built, annealed, and heat treated LENS Ti-6Al-4V samples were removed from the center of their gage sections and were subsequently cut along their radial and longitudinal planes, as shown in Fig. 2. These samples were hot-mounted in PolyFast, and electro-polished (Struers LectroPol-5) using electrolyte A3. An optical microscope (Zeiss Axiovert 200) and a Scanning Electron Microscope (SEM) equipped with an Electron Backscatter Diffraction (EBSD) system were used to examine the microstructure. The EBSD scans were conducted at 20 kV, with a scanning area of $400 \times 400 \mu\text{m}^2$ and a step size of 0.5 μm .

The microstructure of the as-built LENS Ti-6Al-4V, shown in Fig. 2(a), was found to be predominantly columnar, agreeing with other reported results for AM Ti-6Al-4V [15,20,30]. This columnar grain structure is the result of more sustained cooling rates experienced by previously-deposited layers during manufacturing. As seen in Fig. 2(a), these columnar grains are near-parallel to the longitudinal axis (i.e. building direction) of the specimen,

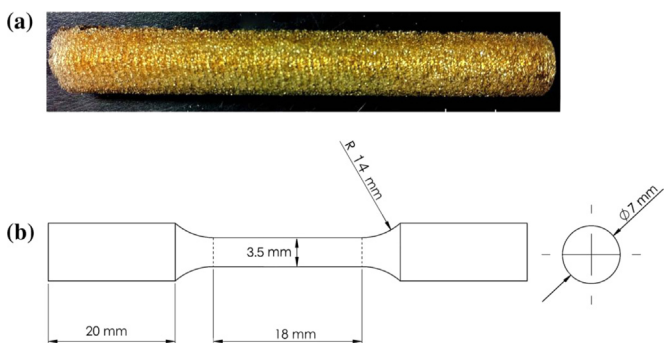


Fig. 1. LENS Ti-6Al-4V (a) as-built cylindrical rod and (b) dimensioned drawing of machined tensile and fatigue specimens.

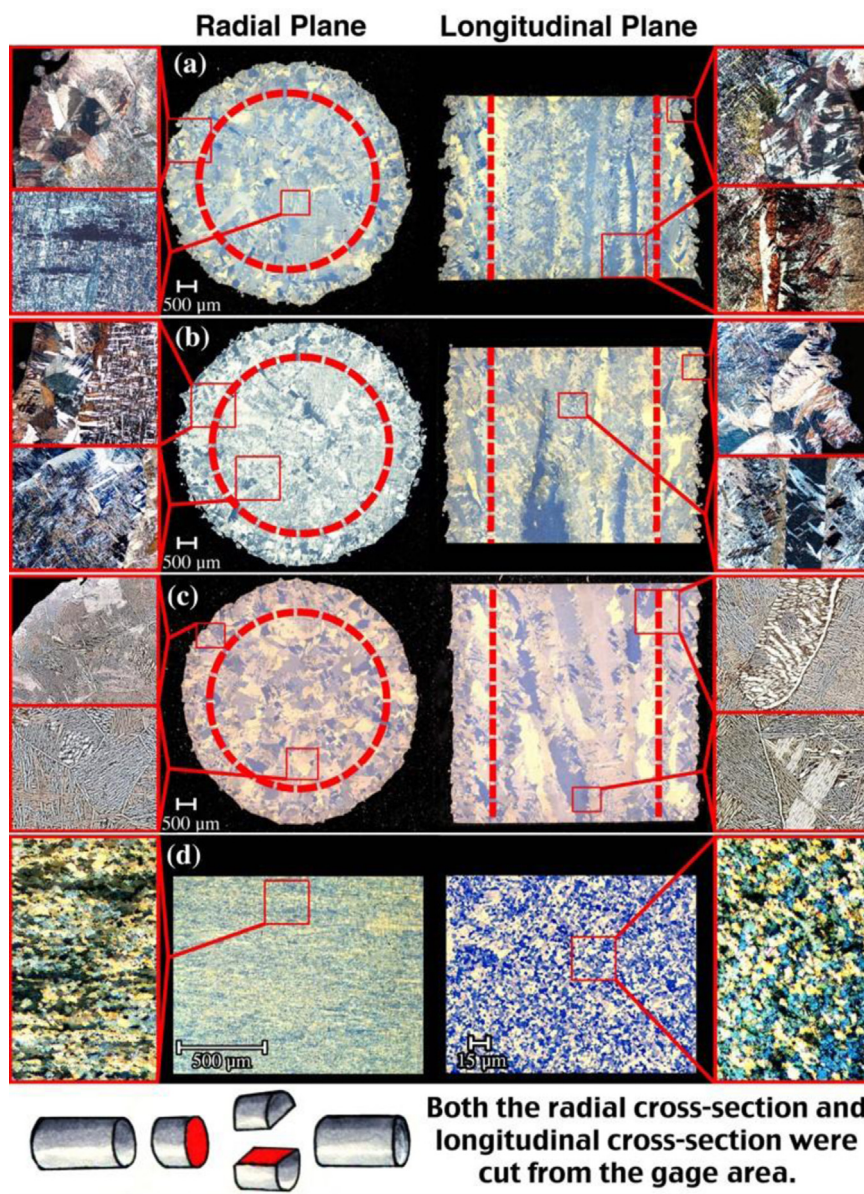


Fig. 2. Microstructure of (a) as-built LENS, (b) annealed LENS, (c) heat treated LENS, and (d) wrought Ti-6Al-4V. (For interpretation of the references to color in this figure, the reader is referred to the web version of this article.)

indicating a unidirectional solidification heat flux. It was observed that these columnar grains initiated and grew from the bottom of a deposited single line layer (the fusion zone between the deposited and previous layers) and grew upward [15,20,30]. The microstructure around the circumference of the specimen's cross-section, shown in Fig. 2(a), generally grew with less directional bias. This can be attributed to the more pronounced ambient heat transfer around the part during fabrication, making the grains appear more equiaxed. The cooling rates experienced during the deposition of the circumferential track for each new layer are, on average, higher, further promoting equiaxed grain formation. This can be attributed to (1) the initially higher temperature difference between the newly-deposited circumferential track and previously-deposited layer and (2) the circumferential track possessing a greater surface area exposed to the chamber atmosphere, leading to more convection and radiation heat transfer. Note that these larger, near-surface equiaxed grains were removed through machining before the tensile and fatigue tests were conducted. The red dotted lines in Fig. 2 show where the outer material was removed during the machining of the test specimens.

It was observed that columnar structures occurred near the center region of each deposited track, with the track periphery experiencing growth of what appeared to be equiaxed grains. Due to the utilized process parameters, the laser was found to sufficiently penetrate and remelt previously-deposited layers, leaving only columnar grains in the vicinity of a track cross-section. These grains served as initiation points in the newly deposited material, leading to their epitaxial growth through the layers [30,31]. Similar to titanium welding, the grains within the fusion and heat affected zones are found to influence size and growth of the solidifying grains in the melt pool [32]. While the specimens were built using a relatively high powder feed rate and laser power, which would normally result in coarser grains, the relatively faster travel speed utilized proved to foster the formation of finer grains.

Results from optical microscopy indicate that the selected annealing schedule had little effect on the microstructure of the LENS Ti-6Al-4V specimens. Comparison of the microstructure resulting from the annealing process, shown in Fig. 2(b), and the microstructure of an as-built sample, shown in Fig. 2(a), demonstrates that both specimens exhibit fine columnar grains within their

interior region and larger grains around their exterior. In addition, both sets of samples exhibited prior β grain growth through the layers during their LENS fabrication. One possible explanation for the seemingly unchanged microstructure is that the annealing process did not reach the β -transus temperature. The annealing treatment used here may have only relieved the residual stress within the samples; similar results have been reported for SLM Ti-6Al-4V [24].

The microstructure resulting from the selected heat treatment, shown in Fig. 2(c), differed greatly from the microstructure of the as-built and annealed samples. Rather than the long, needle-like grain geometry of the microstructure within the as-built and annealed Ti-6Al-4V, the grain shape of the heat treated LENS Ti-6Al-4V microstructure was generally shorter and wider. The microstructure appears to be α lamellar, with average grain dimensions of approximately 74 μm long and 11 μm wide. Colonies of α lamellae were as large as 500 μm . These larger grains are attributed to the samples being brought above the β -transus temperature and then being furnace cooled, promoting grain growth. The microstructure observed in the wrought Ti-6Al-4V differed greatly from that observed for the LENS Ti-6Al-4V. As shown in Fig. 2(d), the wrought microstructure lacked columnar grains and consisted predominantly of equiaxed grains. The equiaxed grains in the wrought samples were found to be much smaller than those present in the LENS samples. For example, the average grain diameter within the wrought material was $\sim 10 \mu\text{m}$ while the grains within the as-built LENS samples were approximately 138 μm long and 4 μm wide.

The results from the EBSD analysis of the as-built microstructure along the longitudinal face of the gage section are presented in Fig. 3. The grains were found to be almost exclusively columnar. Using candidate phases of HCP α and BCC β , results indicate that a predominantly α phase exists. This may be due to the deposited material reaching the β -transus temperature during building, allowing for β -grains to grow upward through the layers and then transition to α during the cooling process. An example of what appears to be a previous β grain boundary is indicated by an arrow in Fig. 3.

Note that α grains typically control the mechanical properties, including the fatigue behavior, of Ti-6Al-4V in ambient temperature applications, with larger grain sizes leading to reduced fatigue resistance. Additionally, large prior β -grains can promote creation of larger lamellar α colonies, obtained through heat treatment [32]. It has been found that cracks will propagate through α colonies of the lamellar structure if the axes of the lamellae are roughly parallel to the load axis, and will propagate along the α colony boundaries if the axes of the lamellae are

roughly perpendicular to the load axis. This results in tortuous, non-linear crack growth [33,34].

2.4. Tensile and fatigue test setup

The as-built, annealed, and heat treated cylindrical bars were machined to the final specimen dimensions shown in Fig. 1(b), complying with the ASTM E606-92 standard [35]. Post-machining specimen preparation involved polishing the gage section to a near mirror finish using sandpaper of progressively finer grits. Machining was performed after heat treatment to avoid any possible specimen distortion.

Tensile tests were conducted with a strain rate of 0.001 s^{-1} using an MTS 810 machine in conjunction with an MTS extensometer (model 634.31F-25), complying with the ASTM E8/E8M standard [36]. Fully-reversed strain-controlled uniaxial tension-compression fatigue tests were performed with an MTS Tabletop 858 machine in conjunction with an MTS extensometer (model 634.31F-25), complying with the ASTM E606-92 standard [35]. To keep the strain rates between tests similar and the frequency low enough to avoid any effects on the cyclic behavior in the ambient laboratory environment, a sinusoidal cyclic loading profile was used, with the frequency adjusted for each strain level. The number of cycles to failure, as well as load, displacement, and strain values, were collected for each test. To prevent the extensometer from slipping during the testing, epoxy was applied to the areas where the extensometer was attached. Parameters and results associated with the LENS Ti-6Al-4V fatigue testing

Table 1
Results of fully-reversed, uniaxial fatigue tests for as-built, annealed, and heat treated LENS Ti-6Al-4V.

ϵ_a (%)	$\Delta\epsilon_p/2$ (%)	σ_a (MPa)	σ_m (MPa)	2N_f (Reversals)
As-built LENS				
0.2	0.000	254	72	> 4,061,240
0.3	0.000	333	40	3,375,860
0.3	0.000	370	-12	619,936
0.3	0.000	367	32	491,592
0.35	0.000	400	40	119,954
0.35	0.000	519	127	100,646
0.4	0.000	542	128	91,080
0.4	0.000	453	30	90,218
0.5	0.000	519	-9	68,516
0.5	0.010	591	55	64,410
0.7	0.020	716	1	3422
0.7	0.030	797	5	2728
1.0	0.175	914	-7	998
1.0	0.131	877	2	746
Annealed LENS				
0.3	0.000	359	27	210,334
0.3	0.000	372	-65	119,506
0.35	0.000	365	8	166,322
0.35	0.000	424	13	102,712
0.4	0.000	466	-16	133,100
0.5	0.000	544	-30	25,616
0.5	0.000	613	69	15,026
0.5	0.000	629	-2	12,464
0.7	0.000	768	0	5266
Heat treated LENS				
0.3	0.000	372	29	1,250,890
0.3	0.000	342	39	627,774
0.35	0.000	412	19	922,610
0.35	0.000	443	2	864,070
0.5	0.001	580	9	74,054
0.5	0.002	578	27	51,990
1.0	0.237	865	-13	538
1.0	0.259	888	-13	244

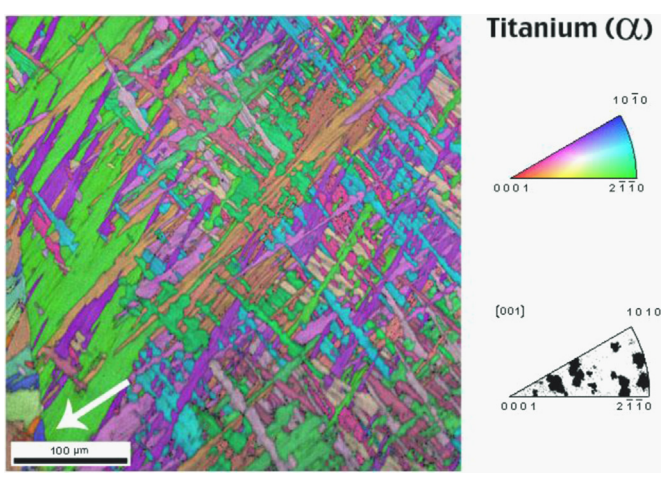


Fig. 3. EBSD diagram of as-built LENS Ti-6Al-4V showing predominantly α grains.

conducted herein are summarized in **Table 1**, which includes the applied strain amplitudes, ϵ_a , stress amplitudes, σ_a , mean stresses, σ_m , and fatigue reversals to failure, $2N_f$.

3. Monotonic and cyclic deformation behavior

Monotonic tensile stress-strain curves for the as-built, annealed and heat treated LENS samples, as well as the wrought Ti-6Al-4V specimens, are presented and compared in **Fig. 4**. Experimentally-measured average monotonic tensile properties, including modulus of elasticity, E , yield stress, σ_y , and ultimate tensile stress, σ_u , are listed in **Table 2**. Results indicate that all LENS specimens have less elongation to failure as compared to the wrought specimens [37]. This may be explained by the presence of defects within the LENS samples caused by process and/or powder imperfections. The heat treated specimens, which also exhibit lower elongation to failure, do not appear to have behavior driven by defects. Despite this, there was still minor scatter in the heat treated Ti-6Al-4V tensile results. Slight variation in elongation to failure was observed for samples with the same build condition.

Wrought specimens were found to have slightly higher σ_y and σ_u values than those of LENS specimens. As listed in **Table 2**, the annealing process slightly increased the σ_y of LENS specimens, while its effect was negligible on σ_u . The heat treated LENS specimens exhibited higher σ_y and σ_u values relative to the as-built LENS specimens. The percent increase in σ_y , for the heat treated and annealed samples, was found to be similar; however, there was some percent increase in σ_u for the heat treated samples as compared to the annealed ones. The average elongation to failure of the heat treated LENS samples was slightly lower than the as-built and annealed samples.

There is noticeable variation in the results of the tensile tests for the LENS specimens, which can most likely be attributed to internal defects [30]. There is a clear relationship between the elongation to failure of the specimen and the abundance of defects. Fewer defects within the material typically correlated to the part having a higher elongation to failure, similar to observations reported in [38]. The specimen with more internal defects had the lowest elongation to failure. Conversely, the as-built tensile specimen with the highest elongation to failure displayed the least amount of internal defects, based on post-test examination of fracture surfaces.

Fig. 5 presents the monotonic tensile data juxtaposed with Ramberg-Osgood curves fit to the cyclic stress-strain measured for the as-built, annealed, and heat treated LENS specimens. In order to generate the appropriate Ramberg-Osgood curves, stable

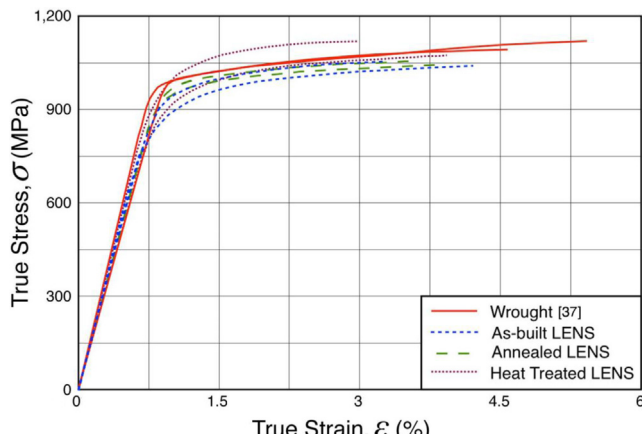


Fig. 4. Tensile stress-strain curves for wrought and LENS Ti-6Al-4V specimens.

Table 2

Monotonic and cyclic properties of the as-built, annealed, and heat treated LENS Ti-6Al-4V specimens.

	As-Built	Annealed	Heat treated
Tensile properties			
Monotonic Modulus of Elasticity, E (GPa)	119	112	118
Yield Stress (0.2% Offset), σ_y (MPa)	908	959	957
Ultimate Tensile Stress, σ_u (MPa)	1038	1049	1097
Elongation to Failure, %EL (%)	3.8	3.7	3.4
Cyclic properties			
Cyclic Modulus of Elasticity, E' (GPa)	106	117	121
Cyclic Strength Coefficient, K' (MPa)	3385	2065	1442
Cyclic Strain Hardening Exponent, n'	0.195	0.122	0.083
Fatigue Strength Coefficient, σ_f (MPa)	2310	4687	1807
Fatigue Strength Exponent, b	-0.135	-0.210	-0.111
Fatigue Ductility Coefficient, e_f	0.030	N/A	0.736
Fatigue Ductility Exponent, c	-0.530	N/A	-0.967

hysteresis loops were mapped from the midlife fatigue data reported in **Table 1**. Measured plastic strain amplitudes, $\Delta\epsilon_p/2$, were obtained from the hysteresis loops. The elastic strain amplitudes, $\Delta\epsilon_e/2$, were calculated by subtracting the measured plastic strain from the total strain amplitude, $\Delta\epsilon/2$, using Eq. (1) [39]:

$$\frac{\Delta\epsilon_e}{2} = \frac{\Delta\epsilon}{2} - \frac{\Delta\epsilon_p}{2} \quad (1)$$

The stress amplitudes were plotted against the plastic strain amplitudes on a logarithmic scale. The cyclic strength coefficient, K' , and the cyclic strain hardening exponent, n' , were obtained from the intercept and slope of the best fit line for the data, respectively. These values were then utilized in a Ramberg-Osgood relationship [39], as follows:

$$\epsilon_a = \frac{\Delta\epsilon_e}{2} + \frac{\Delta\epsilon_p}{2} = \frac{\sigma_a}{E} + \left(\frac{\sigma_a}{K'} \right)^{1/n'} \quad (2)$$

The cyclic modulus of elasticity, E' , cyclic strength coefficient, K' , and the cyclic strain hardening exponent, n' , for the as-built, annealed, and heat treated LENS specimens are listed in **Table 2**. Note that minor scatter exists in the measured cyclic modulus of elasticity due to scatter in the measured stress response obtained during fatigue testing.

Fig. 5(a)–(c) compare the monotonic and cyclic stress-strain curves for as-built, annealed, and heat treated LENS specimens, respectively. The Ramberg-Osgood curves in **Fig. 5(a)** and (c) are slightly lower than their corresponding monotonic tensile curves at higher strains, suggesting some level of cyclic softening in the presence of plastic strain. This was also validated through observing the recorded peak stresses taken from the fatigue tests of LENS specimens. All of the fatigue tests at 1% strain level showed a decrease in stress amplitude before stabilizing, again indicating a cyclic softening behavior.

As it may be seen in **Fig. 6**, the stress response of LENS (as-built, annealed, and heat treated) specimens is higher than those of wrought specimens. This demonstrates that the wrought material exhibits more cyclic softening behavior than the LENS Ti-6Al-4V material. In addition, the proximity of the annealed and heat treated LENS cyclic stress-strain curves reveals that both processes had similar effects on the hardening of the specimens, as evidenced by the similar increase in yield strengths listed in **Table 2**.

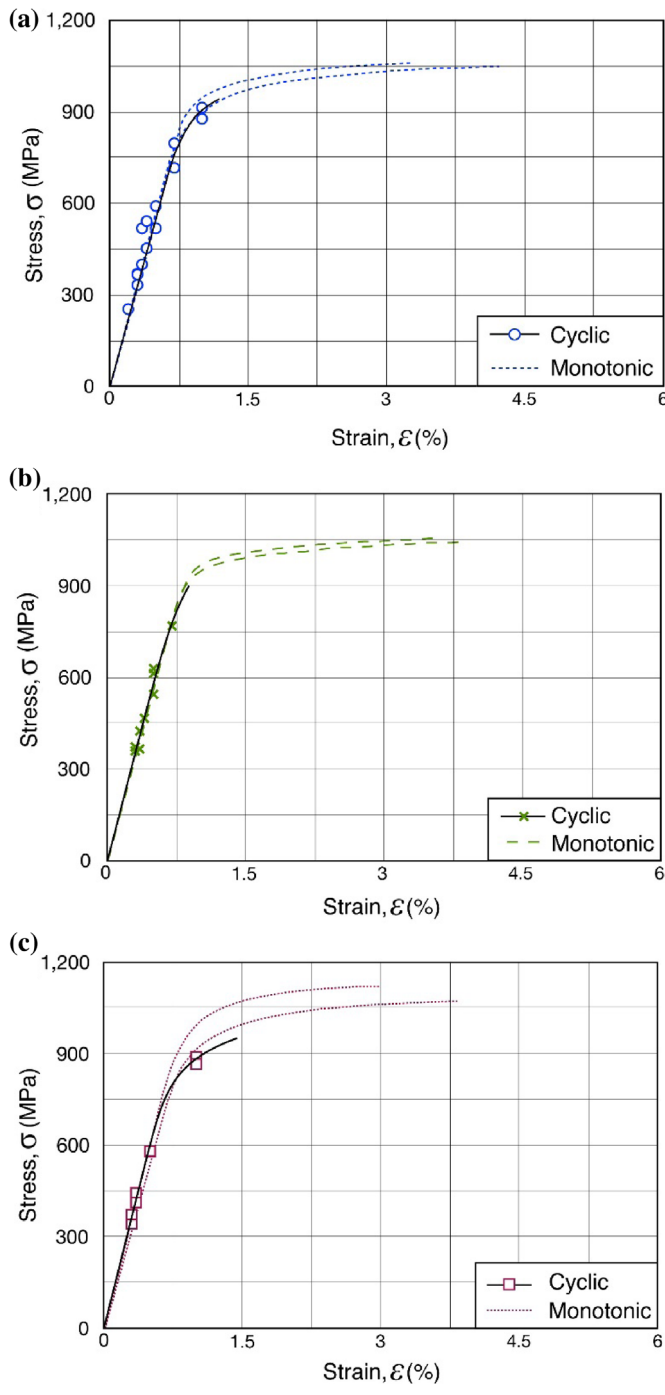


Fig. 5. Comparison of cyclic stress-strain curves (Ramberg–Osgood) with the monotonic tensile curves for (a) as-built, (b) annealed, and (c) heat treated LENS Ti–6Al–4V.

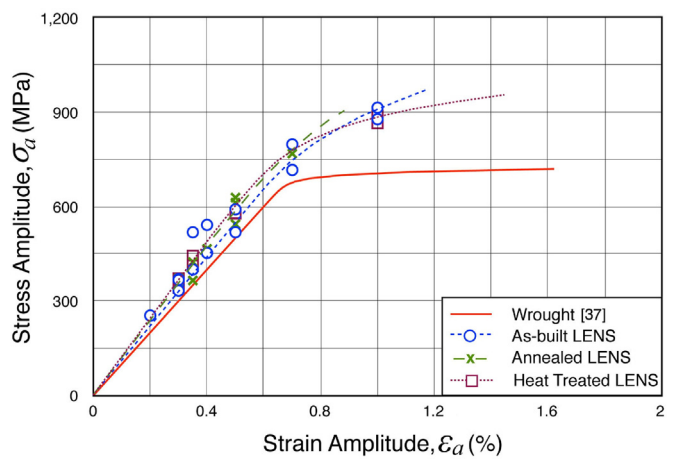


Fig. 6. Comparison of Ramberg–Osgood cyclic stress–strain curves for LENS Ti–6Al–4V in as-built, annealed, and heat treated conditions with wrought Ti–6Al–4V.

The fatigue ductility coefficient, ϵ_f' , and the fatigue ductility exponent, c , in Eq. (4) were also found as the intercept and slope of the best fit for the plastic strain-life data:

$$\frac{\Delta \epsilon_p}{2} = \epsilon_f'(2N_f)^c \quad (4)$$

The Coffin–Manson relationship, as presented in Eq. (5), was used to generate strain-life fatigue curves accounting for both elastic and plastic strain components for the as-built, annealed, and heat treated LENS specimens, shown in Fig. 7(a)–(c), respectively:

$$\frac{\Delta \epsilon}{2} = \epsilon_a = \frac{\Delta \epsilon_e}{2} + \frac{\Delta \epsilon_p}{2} = \frac{\sigma_f'}{E}(2N_f)^b + \epsilon_f'(2N_f)^c \quad (5)$$

It can be seen from Fig. 7 that the material responses are mostly elastic for the as-built and heat treated LENS specimens and entirely elastic for the annealed LENS specimens. Since the elastic and plastic strain-life curves do not intersect at any point for all LENS specimens, it appears that elastic deformation (or stress) is a dominant factor in fatigue failure of LENS Ti–6Al–4V in the investigated strain range.

A comparison of strain amplitude, ϵ_a , versus reversals to failure, $2N_f$, for wrought Ti–6Al–4V and as-built, annealed, and heat treated LENS Ti–6Al–4V is provided in Fig. 8(a). It may be seen that the fatigue lives of the LENS (as-built, annealed, and heat treated) specimens are shorter than those of the wrought specimens. The as-built specimens exhibited the best strain-life fatigue behavior of the LENS specimens, as well as the most scatter. Annealed LENS specimens exhibited strain-life behavior comparable to that of the as-built LENS specimens during LCF, but possessed the lowest fatigue resistance of all tested LENS samples during HCF. Heat treated LENS specimens had the lowest fatigue lives for all LENS samples investigated during LCF. However, the fatigue lives of the heat treated LENS specimens were found to be close to those of the as-built LENS specimens during HCF.

The shorter fatigue lives of the LENS specimens may be attributed to defects birthed from the powder-based LENS manufacturing process. In LCF, the lack of ductility in the LENS specimens may also contribute to their shorter fatigue resistance during strain-controlled testing. During HCF, it is most likely porosity that contributes toward the shorter fatigue lives of LENS Ti–6Al–4V specimens.

Fatigue lives of the annealed LENS specimens were shorter than those of the as-built LENS specimens during HCF. This is most likely due to the annealing process removing any beneficial effects

4. Fatigue behavior and failure mechanisms

4.1. Fatigue behavior

The elastic and measured plastic strain amplitudes, $\Delta \epsilon_e/2$ and $\Delta \epsilon_p/2$, respectively, were plotted against reversals to failure, $2N_f$, using a logarithmic scale. The fatigue strength coefficient, σ_f' , and the fatigue strength exponent, b , in Eq. (3) were found as the intercept and slope of the best fit line for the elastic strain-life data, i.e.:

$$\frac{\Delta \epsilon_e}{2} = \frac{\sigma_f'}{E}(2N_f)^b \quad (3)$$

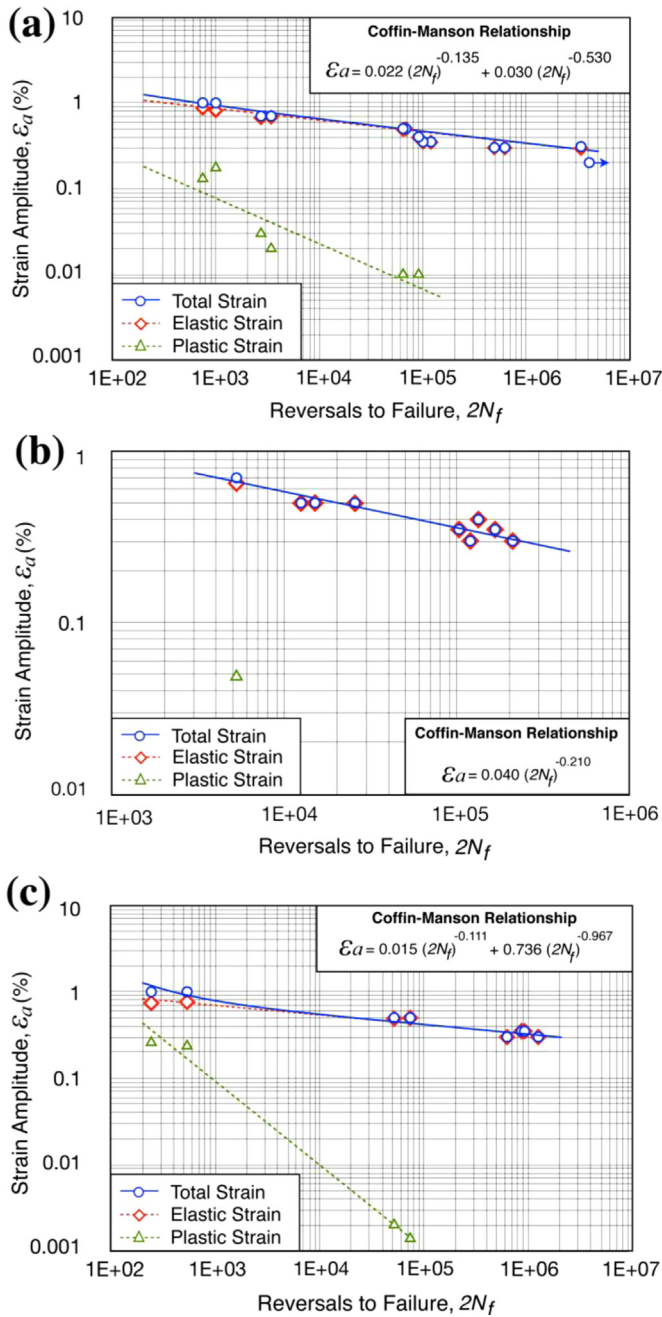


Fig. 7. Total, elastic, and plastic strain amplitudes versus reversals to failure for fully-reversed, strain-controlled fatigue tests of (a) as-built, (b) annealed, and (c) heat treated LENS Ti-6Al-4V.

provided by residual stresses produced during manufacturing. Any significant reduction in fatigue life was not observed for heat treated LENS specimens, as they possessed a more distinct microstructure that consisted of α lamellae rather than columnar grains. During LCF, fatigue lives of the heat treated LENS specimens were found to be shorter than those of the as-built LENS specimens. In the mid-life regime, the fatigue lives were comparable, and during HCF, the heat treated LENS specimens generally performed similarly to the as-built LENS specimens.

Fig. 8(b) shows a comparison of stress amplitudes, σ_a , and reversals to failure, $2N_f$, for wrought Ti-6Al-4V samples and as-built, annealed, and heat treated LENS Ti-6Al-4V samples. When compared with wrought Ti-6Al-4V, the LENS samples demonstrated superior load bearing capacity during LCF up to 5000 reversals

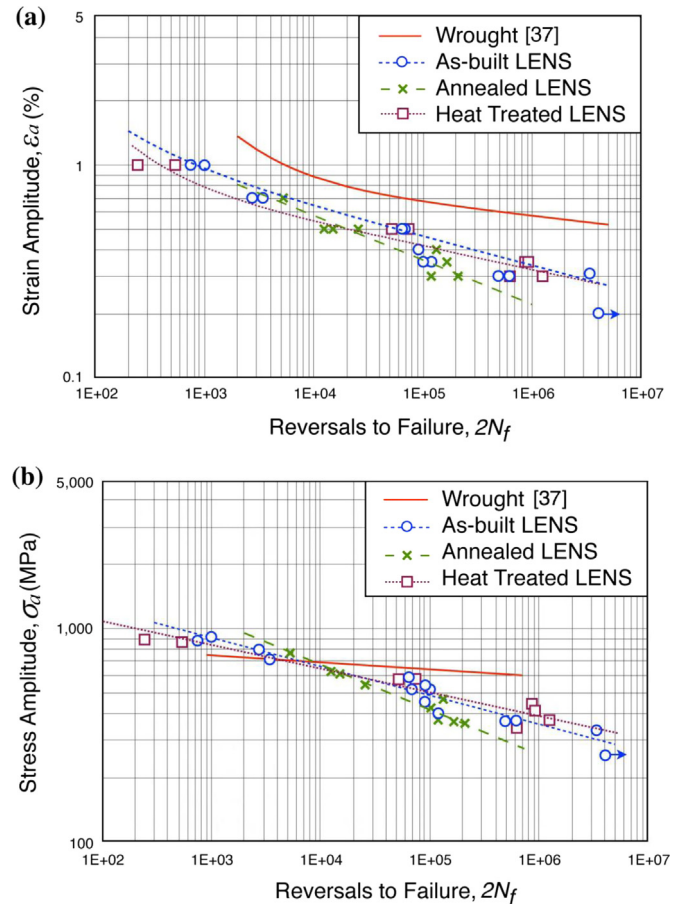


Fig. 8. (a) Strain amplitudes versus reversals to failure and (b) stress amplitudes versus reversal to failure for wrought Ti-6Al-4V and LENS as-built, annealed, and heat treated Ti-6Al-4V.

(2500 cycles). The trends observed for annealed LENS samples suggest they will outperform the other LENS materials investigated; however, all attempts at running higher strain fatigue tests (i.e. strains higher than 0.7%) on the annealed LENS samples resulted in buckling. While the wrought material demonstrated better performance against cyclic deformation, the load-bearing capacity of LENS Ti-6Al-4V during LCF is noteworthy. This may be explained by the significant cyclic softening behavior observed for wrought Ti-6Al-4V ELI [37]. Nevertheless, similar to strain-life fatigue behavior, wrought Ti-6Al-4V specimens possess significantly higher fatigue strength during HCF relative to the as-built, annealed, and heat treated LENS specimens when the comparisons were made based on the stress-life behavior in Fig. 8(b). Similar to the strain-life behavior shown in Fig. 8(a), annealed LENS Ti-6Al-4V specimens had the lowest stress-life fatigue strength in the high cycle regime as presented in Fig. 8(b).

4.2. Failure mechanisms

Parts fabricated via DLD, or any powder-based AM technique, are, to some degree, prone to porosity. Through the use of SEM, fractographic images of the LENS Ti-6Al-4V specimen fracture surfaces were collected and analyzed. The fracture surfaces were inspected for key features such as crack initiation sites, evidence of crack propagation, porosity, and inclusions.

A magnified view of a typical spherical pore found on the fracture surface of an as-built LENS Ti-6Al-4V specimen is shown in Fig. 9(a). Another, smaller pore (diameter of $\sim 23 \mu\text{m}$) is displayed in Fig. 9(b), where arrows show the propagation of

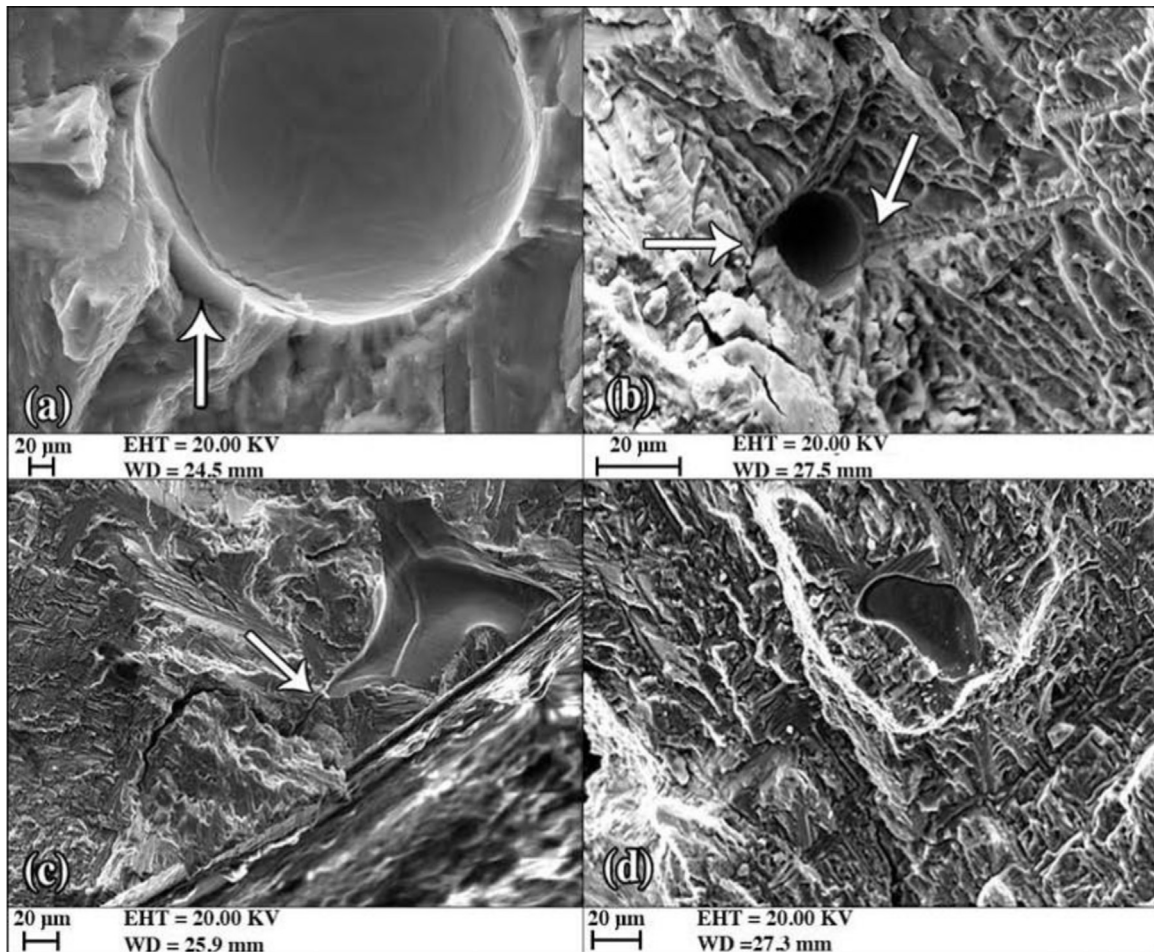


Fig. 9. (a) Porosity resulting from gas entrapment, as evidenced by the smooth lip protruding from the fracture surface of a fatigue specimen, (b) pore serving as a crack initiation site, (c) crack initiation and propagation off the tip of an irregularly shaped pore, and (d) two pores merged together to form a larger pore, observed on the fracture surfaces of as-built LENS Ti-6Al-4V fatigue specimens.

microstructurally-small cracks originating from the pore on different plane orientations. As pores form at different layers in the build, they can initiate cracks on different planes, which eventually merge and result in a tortuous fracture surface. While the majority of pores can form during the LENS process, it is possible for pores to form via residual pockets of gas within and around the utilized powders. Note that the current powder utilized for this study was manufactured using PREP, which, relative to more conventional gas atomization methods, is a process that provides for powders with high sphericity and essentially no porosity [40]. However, porosity may also exist in powder particles, contributing porosity to the final build. Fig. 9(a) demonstrates a pore on a fracture surface that could have been contained in a powder particle; this is indicated by the smooth lip protruding from the fracture surface. Another possible means for pore generation occurs when the shielding/carrier gas within the purged LENS chamber becomes trapped within the LENS part. This can occur due to vapor recoil within an unstable melt pool just prior to its solidification [41].

While most pores are spherical, non-spherical pores can also form. For example, Fig. 9(c) provides a pore with sharp angles, a pointed cavity and very smooth walls. Fig. 9(d) provides a pore that most likely formed due to the coalescence of two separate gas pockets originating during solidification, creating a “bean” shape with a dimension smaller than the laser-induced melt pool which was approximately 1.1 mm in diameter. This was the most commonly observed irregular pore shape in this study. Irregularly shaped pores can be detrimental to fatigue life, as they can possess

larger stress concentrations that subsequently affect mechanical behavior. Pores with sharp corners are more prone to initiating cracks due to this very phenomenon. A prime example of this is indicated by the arrow in Fig. 9(c).

As shown in Fig. 10(a), the wrought Ti-6Al-4V samples experienced crack initiation beginning at their outer surface during fatigue testing, with final failure occurring at an approximate 45° angle. The grayscale images to the right of Fig. 10 show the crack initiation location, crack propagation, and final fracture zones, as well as the areas where the specimen was monotonically pulled apart after fatigue failure criterion was reached (50% load drop). Both the as-built and annealed LENS specimens – shown in Figs. 10 (c) and (e), respectively – appear to have experienced failure due to defects only, with very little crack growth. Every crack appears to have initiated at a pore close to the outer surface, and, in most cases, crack initiation at multiple pores was observed. The samples exhibited a tortuous surface due to multiple crack initiation sites occurring at various depths within the volume. Since cracks coalesce to form the observed texture at failure, it is challenging to determine the exact fracture history. Despite the observed tortuous texture, the small crack propagation zones around pores were found to be generally flat.

Although the annealed LENS specimens experienced slightly longer crack propagation than the as-built LENS specimens, the majority of LENS specimens demonstrated very little crack growth. This can be seen from the fracture surface schematics on the right column of Fig. 10. The wrought samples possessed cracks that

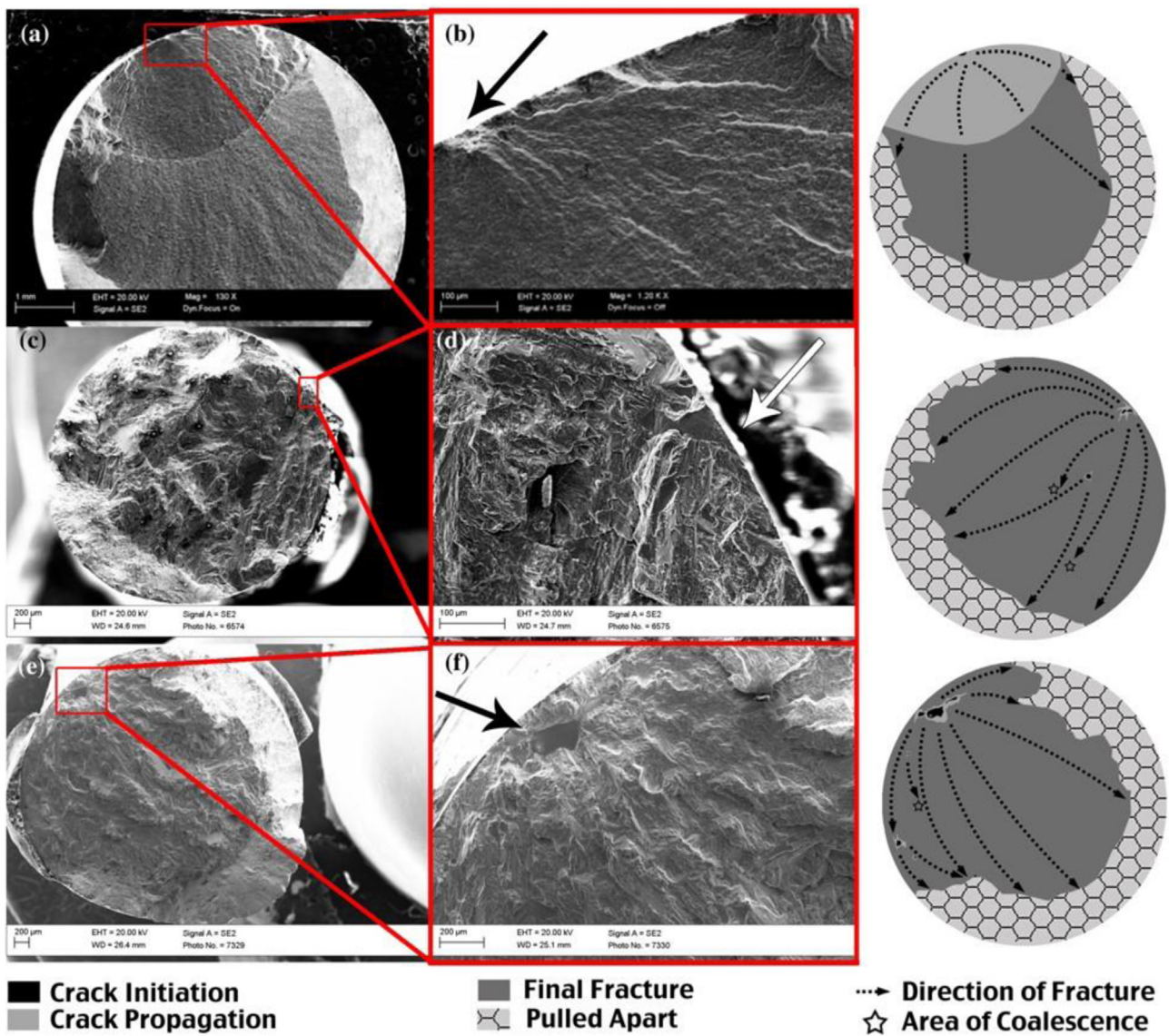


Fig. 10. Representative fracture surfaces for (a) wrought Ti-6Al-4V [37], (b) initiation site for wrought Ti-6Al-4V [37], (c) as-built LENS Ti-6Al-4V, (d) initiation site for as-built LENS Ti-6Al-4V, (e) annealed LENS Ti-6Al-4V, and (f) initiation site for annealed LENS Ti-6Al-4V. The grayscale images to the right show the crack initiation, crack propagation, final fracture, and monotonically pulled apart areas of the samples. The stars indicate an area where fractures traveling on separate layers coalesced.

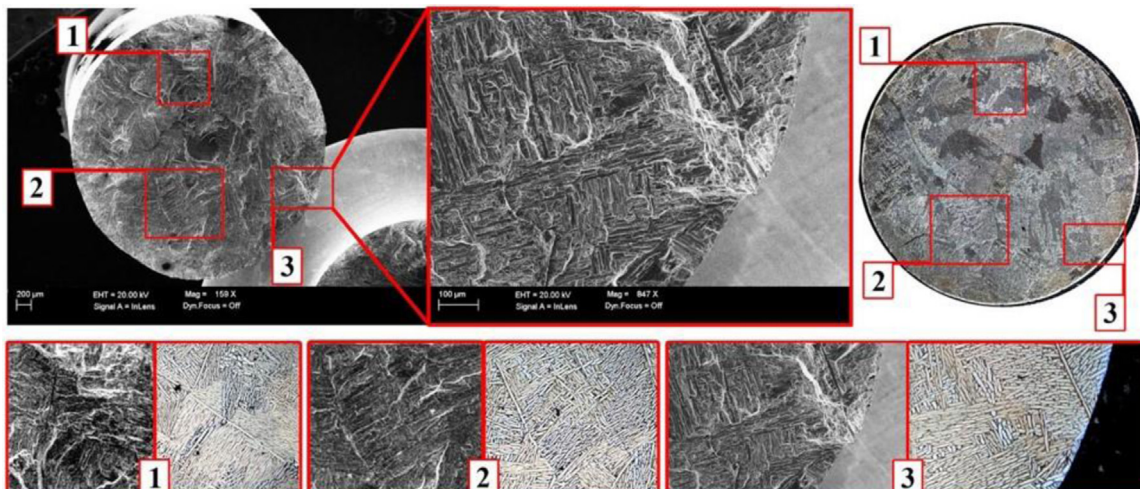


Fig. 11. The fracture surface of a heat treated LENS Ti-6Al-4V specimen and its magnification. Comparison of patterns visible on both the heat treated fracture surface and underlying microstructure are shown at the bottom.

initiated at their outer surfaces with crack propagation orders-of-magnitude larger than those experienced by the as-built and annealed LENS specimens. This agrees with the findings provided by the monotonic stress-strain curves in Fig. 4, which indicate LENS samples behaving in a more brittle fashion than their wrought Ti-6Al-4V counterparts.

Instead of relying on cracks initiated from pores, the fatigue failure mechanism for the heat treated LENS specimens was found to rely on cracks initiated from α colony boundaries at the outer surface. This is illustrated in Fig. 11, which contains comparisons of selected fracture surface features and the microstructure directly beneath them. To obtain these microstructure images, the fracture surface was mounted in PolyFast and polished until the inspected surface was midway between the high and low points of the fracture surface. During this process, the microstructure was examined at multiple levels, and it was verified that these features were reflected throughout the layers, due to epitaxial grain growth, with some shifts in location. This technique helped in determining the failure mechanism of the heat treated LENS Ti-6Al-4V material.

Similar to the as-built and annealed LENS specimens, the fracture surfaces of the heat treated LENS samples possessed tortuous texture, though not to the extent of the fracture surfaces belonging to the as-built LENS specimens. The heat treated LENS samples also possessed fracture surfaces with propagation areas orders-of-magnitude smaller than those of the wrought Ti-6Al-4V. Multiple crack initiation sites were observed on the fracture surface of heat treated LENS Ti-6Al-4V samples, all nucleated from α veins exposed to the perimeter.

It was found that fracture surface features of the heat treated samples were related to the orientation of the underlying α lamellae. Rather than initiating at pores, the cracks initiated, in general, where α lamellae were exposed to the outer surface due to machining. Similar to the fatigue crack growth, the final fracture path appeared to travel through α colonies of lamellar structures when the axes of the lamellae were parallel to the loading direction, and along the α colony boundaries when the axes of the lamellae were perpendicular to the loading direction. This resulted in tortuous final fracture paths observed for the heat treated LENS samples in this study; also reported as the reason for the typical tortuous crack growth path for lamellar wrought Ti-6Al-4V [33,34].

The general lack of ductility in LENS specimens may contribute to their shorter fatigue lives relative to wrought Ti-6Al-4V at higher strains (i.e. LCF). However, during HCF, it is mainly the defects, such as pores, which shorten the fatigue life and create more scatter in data. Hence, relationships between the data scatter and fatigue life to the pore characteristics within the tested samples were sought. The tested, as-built LENS Ti-6Al-4V specimens were separated into three categories: fatigue short life (1.0% and 0.7% strain amplitudes), midlife (0.5%, 0.4%, and 0.35% strain amplitudes), and long life (0.3% strain amplitude) regimes. Three important pore characteristics, which may have dominant effects on the fatigue life of samples for all fatigue regimes, were observed in this study and include the following: the size of the pore, distance from the outer surface, and irregularity of pore shape. At nearly every strain level investigated, specimens with shorter fatigue lives generally possessed larger, more irregular pores located closer to the outer surface.

Some general relationships between the porosity and fatigue life of the as-built and annealed LENS samples were observed and are now discussed in detail. First, the pore size was found to significantly impact fatigue resistance. In general, larger pores had a more detrimental impact on fatigue life. Only a weak correlation between the number of pores and the part fatigue resistance was found. However, when the fatigue life of a specimen was

compared with the number of pores located within 100 μm of its outer surface, a stronger correlation was revealed. This was especially true for samples that underwent LCF (higher strains). In these cases, specimens with pores closer to the outer surface generally had shorter fatigue lives than those with subsurface pores located closer to their center.

The shape of pores was found to impact the fatigue resistance of the LENS specimens. Irregularly-shaped pores with sharp corners, similar to the pore displayed in Fig. 9(c), typically led to shorter fatigue lives. The sharp-cornered, irregularly-shaped pores can lead to reduced fatigue life due to higher stress concentrations. Specimens with bean-shaped pores, similar to that shown in Fig. 9(d), had longer fatigue lives than specimens with sharp-cornered pores, implying a correlation between the fatigue life and the degree of shape irregularity.

The distance between neighboring pores was also found to impact the fatigue life of LENS samples. The fractography results suggest that densely-grouped pores are more detrimental to fatigue life. The results also indicate that the proximity of pores is more detrimental to fatigue life than the actual number of pores. These findings suggest that, given a pair of identically-manufactured LENS specimens, each consisting of a pore distribution with similar sizes, shapes and pore-to-pore distances, the specimen with the higher number of pores would not necessarily have the shorter fatigue life for a given test schedule. However, it is highly certain that, when the number of pores exceeds a critical value, its effect on fatigue life should become more dominant. For the current investigation, the number of pores along a fracture surface varied from 1 to 5.

Some of the pore-to-fatigue relationships observed herein have also been reported in other studies concerning the fatigue behavior of titanium alloys. For instance, Wang et al. found that as the size of pores increased, and their distance from the outer surface decreased, the fatigue behavior of TC18 was negatively affected [42]. Lin et al. reported that the number of pores more negatively affects the fatigue life of various titanium alloys (e.g. Ti-7.5 Mo with c.p. titanium, Ti-6Al-4V, and Ti-13Nb-13Zr alloys) when there are more pores closer to the outer surface [43].

5. Conclusions

The goal of this study was to characterize the fatigue behavior of LENS Ti-6Al-4V and its relationship to porosity, annealing, and heat treatment. The major conclusions are summarized as follows:

- 1) Due to the deposition path and build parameters used to create the LENS samples, the resulting as-built microstructure was found to be predominantly columnar, with deposited layers exhibiting epitaxial grain growth.
- 2) The as-built, annealed, and heat treated LENS samples consistently had lower fatigue lives than the Ti-6Al-4V ELI wrought material (comparing via a strain-life approach). However, when low-cycle, load-bearing capacity is the objective for a part's application, LENS Ti-6Al-4V materials may prove to be more beneficial over wrought.
- 3) Annealing the LENS specimens did not positively influence their fatigue lives. The heat treated LENS specimens, while inferior to as-built LENS specimens during LCF, exhibited similar fatigue behavior during HCF.
- 4) While the lack of ductility may have contributed to the shorter fatigue lives of the as-built and annealed LENS samples during LCF, defects such as pores were found to be the primary driver for their shorter fatigue lives during HCF and LCF.
- 5) Lack of ductility most likely contributed to the shorter fatigue lives observed during LCF of the heat treated LENS samples,

- while their increased strength helped extend their fatigue lives slightly during HCF. The failure mechanism of the heat treated LENS samples seemed to be independent of process-driven defects (i.e. porosity). Cracks initiated from α grain boundaries exposed to the outer surface, as opposed to any existing defects.
- 6) Pore shape, size, location, and number will impact the fatigue behavior of as-built and annealed DLD parts. Larger, non-spherical pores that are closer to the outer surface will more negatively affect the fatigue life. In addition, the presence of pores results in the fatigue life of LENS Ti-6Al-4V being less predictable (i.e. includes more scatter) during HCF. Less scatter in fatigue data was observed for the heat treated LENS specimens, as porosity-driven failure was reduced or non-existent.
 - 7) Different microstructures and porosity do affect the fatigue life and failure mechanisms of DLD parts, encouraging further efforts in creating and employing a microstructure-sensitive fatigue model for predicting fatigue life of AM fabricated parts.

While the annealing and heat treatment schedules utilized in this study did not allow for the LENS Ti-6Al-4V to match the fatigue life of the wrought material, it is possible that a more appropriate heat treatment may provide a solution for improving the fatigue life. Results indicate that porosity plays a major role in shortening the fatigue life and increases the unpredictability of the material behavior during mechanical loading. There are many practical difficulties in predicting the fatigue behavior of LENS parts due to the defects generated via LENS process anomalies and/or residual powder porosity. Hence, it is crucial to further optimize the LENS process to minimize the occurrence of pore generation and lack of fusion between deposited layers. Post-manufacturing processes, such as HIP, may improve the fatigue properties of as-built DLD parts by minimizing pore sizes. Controlled DLD/LENS systems, capable of changing process parameters with time, may also help in reducing pore formation.

To ensure the continual adoption of DLD parts by industry, the fatigue resistance of DLD parts must be predictable and quantifiable. This will allow for part certification for various applications that involve cyclic loading and public safety risks. In the near term, especially for Ti-6Al-4V, this will include applications within the biomedical (e.g. implants) and aerospace industries. In order to estimate the fatigue life of AM parts, correlations are needed between their porosity distribution and the parameters utilized for their production. This would allow for better quality control (i.e. minimizing porosity), porosity control (e.g. porous, biocompatible implants) and in predicting their mechanical performance. The development and calibration of microstructure-sensitive fatigue models to quantify the effects of porosity, defects, and microstructure on fatigue behavior would allow one to design against failure with more certainty. This would allow for the fatigue strength to be predicted based on microstructural features and defects statistics of the parts, enabling wider utilization of AM in many applications [44].

Due to variation in reported fatigue results for DLD Ti-6Al-4V (and other metals), it is clear that standards must be further developed to facilitate consistent fabrication and unbiased testing of AM materials. This can include standards for material fabrication, specimen preparation, and mechanical testing. Variation in powder quality, process parameters, build strategies (including build orientation and scanning pattern), and equipment conditions/setups can result in different microstructures and pore distributions within the part, which need to be addressed in material fabrication standards. Monitoring of the thermal history may isolate these variables, and provide an avenue for more consistent fatigue samples, and production-grade parts, with similar microstructure [2,3]. Standards should also focus on imposing limits on allowable porosity, as well as how porosity within an AM part is

measured. Specimen fabrication standards should discuss special requirements of AM specimens such as their surface quality, post-fabrication machining, geometry, and more. Finally, modifications to mechanical testing procedures and standards may need to be applied to better characterize mechanical behavior of AM parts. These standardizations should reduce variation in mechanical testing results and further facilitate the more widespread adoption of AM technology by industry as a whole.

Acknowledgments

All experiments, including specimen fabrication and preparation, were conducted at Mississippi State University's Center for Advanced Vehicular Systems (CAVS).

References

- [1] F.P. Jeantette, D.M. Keicher, J.A. Romero, L.P. Schanwald, Method Syst. Prod. Complex-Shape Objects, 2000, p. US006046426A.
- [2] S.M. Thompson, L. Bian, N. Shamsaei, A. Yadollahi, An overview of direct laser deposition for additive manufacturing; Part I: transport phenomena, modeling and diagnostics, *Addit. Manuf.* 8 (2015) 36–62.
- [3] N. Shamsaei, A. Yadollahi, L. Bian, S.M. Thompson, An overview of direct laser deposition for additive manufacturing; Part II: mechanical behavior, process parameter optimization and control, *Addit. Manuf.* 8 (2015) 12–35.
- [4] A.J. Pinkerton, W. Wang, L. Li, Component repair using laser direct metal deposition, *Proc. Inst. Mech. Eng. Part B: J. Eng. Manuf.* 222 (7) (2008) 827–836.
- [5] V. Fallah, S.F. Corbin, A. Khajepour, Process optimization of Ti-Nb alloy coatings on a Ti-6Al-4V plate using a fiber laser and blended elemental powders, *J. Mater. Process. Technol.* 210 (14) (2010) 2081–2087.
- [6] W. Liu, J.N. DuPont, Fabrication of functionally graded TiC/Ti composites by laser engineered net shaping, *Scr. Mater.* 48 (2003) 1337–1342.
- [7] A. Bandyopadhyay, B.V. Krishna, Xue, W., S. Bose, Application of laser engineered net shaping (LENS) to manufacture porous and functionally graded structures for load bearing implants, *J. Mater. Sci.: Mater. Med.* 20 (2009) 29–34.
- [8] J.E. Craig, T. Wakeman, R. Grylls, J. Bullen, On-Line imaging pyrometer for laser deposition processing, *TMS 2011 Annual Meeting and Exhibition*, San Diego, USA, 2011.
- [9] A.R. Nassar, J.S. Keist, E.W. Reutzel, T.J. Spurgeon, Intra-layer closed-loop control of build plan during directed energy additive manufacturing of Ti-6Al-4V, *Addit. Manuf.* 6 (2015) 39–52.
- [10] A.J. Sterling, B. Torries, D.W. Seely, M. Lugo, N. Shamsaei, S.M. Thompson, Fatigue behavior of Ti-6Al-4V alloy additively manufactured by laser engineered net shaping, in: *Proceedings of AIAA SciTech 2015 Kissimmee*, USA, 2015.
- [11] A. Yadollahi, N. Shamsaei, S.M. Thompson, D. Seely, Effects of process time interval on the mechanical and microstructural properties of direct laser deposited 316L stainless steel, *Mater. Sci. Eng. A* 644 (2015) 171–183.
- [12] L. Bian, S.M. Thompson, N. Shamsaei, Mechanical properties and microstructural features of direct laser-deposited Ti-6Al-4V, *J. Miner. Met. Mater. Soc.* 67 (3) (2015) 629–638.
- [13] A.L. Pilchak, A. Bhattacharjee, R.E.A. Williams, J.C. Williams, The effect of microstructure on fatigue crack initiation in Ti-6Al-4V, in: *Proceedings of International Conference on Fracture (ICF12)*, Ottawa, Canada, 2009.
- [14] A.L. Pilchak, K.I.I. Nakase, Y. Shirai, A.H. Rosenberger, J.C. Williams, The influence on microstructure and microtexture on fatigue crack initiation and growth in alpha + Beta titanium, Technical paper: ADA553373, Air Force Research Lab Wright-Patterson AFL, OH, 2011.
- [15] H.K. Rafi, N.V. Karthik, H. Gong, T.L. Starr, B.E. Stucker, Microstructures and mechanical properties of Ti6Al4V parts fabricated by selective laser melting and electron beam melting, *J. Mater. Eng. Perform.* 22 (2013) 3872–3883.
- [16] A. Bandyopadhyay, F. Espana, V.K. Balla, S. Bose, Y. Ohgami, N.M. Davies, Influence of porosity on mechanical properties and in vivo response of Ti6Al4V implants, *Acta Biomater.* 6 (2010) 1640–1648.
- [17] F. Watari, A. Yokoyama, F. Saso, U. Motohiro, T. Kawasaki, Fabrication and properties of functionally graded dental implant, *Compos. Part B* 28 (1–2) (1997) 5–11.
- [18] G. Chahine, M. Koike, T. Okabe, P. Smith, T. Kovacevic, The design and production of Ti-6Al-4V ELI customized dental implants, *J. Miner. Met. Mater. Soc.* 60 (11) (2008) 50–55.
- [19] P.A. Kobryni, S.L. Semiatin, Mechanical properties of laser-deposited Ti-6Al-4V, in: *Proceedings of Solid Freeform Fabrication Symposium, SFF*, Austin, USA, 2001.
- [20] E. Brandl, C. Leyens, F. Palm, Mechanical properties of additive manufactured Ti-6Al-4V using wire and powder based processes, in: *Proceedings of Trends in Aerospace Manufacturing 2009 International Conference, TRAM09*, IOP Conference Series: Materials Science and Engineering 26, 2011.
- [21] P. Edwards, A. O'Conner, M. Ramulu, Electron beam additive manufacturing of

- titanium components: properties and performance, *J. Manuf. Sci. Eng.* 35 (24) (2013) 1–7.
- [22] Khalid H. Rafi, N.V. Karthik, Thomas L. Starr, Brent E. Stucker, Mechanical property evaluation of Ti-6Al-4V parts made using electron beam melting, in: Proceedings of Solid Freeform Fabrication Symposium, SFF23, Austin, USA, 2012.
- [23] E. Amsterdam, G.A. Kool, High cycle fatigue of laser beam deposited Ti-6Al-4V and Inconel 718, in: Proceedings of International Committee on Aeronautical Fatigue and Structural Integrity Symposium, ICAF25, Rotterdam, Netherlands, 2009.
- [24] S. Leuders, M. Thöne, A. Riemer, T. Niendorf, T. Tröster, H.A. Richard, H.J. Maier, On the mechanical behavior of titanium alloy TiAl6V4 manufactured by selective laser melting: fatigue resistance and crack growth performance, *Int. J. Fatigue* 48 (2013) 300–307.
- [25] Y. Huang, M.C. Leu, J. Mazumder, A. Donmez, Additive manufacturing: current state, future potential, gaps and needs, and recommendations, *J. Manuf. Sci. Eng.* 137 (1) (2015) 014001.
- [26] SAE AMS 4998E, Titanium Alloy Powder 6Al-4V, SAE International, Warrendale, PA, 2013. (www.sae.org).
- [27] Metallographic Preparation of Titanium, Struers http://www.struers.com/re_sources/elements/12/104827/Application_Note_Titanium_English.pdf.
- [28] Gerd Lütjering, James C. Williams, Titanium (Chapter 5: Alpha + Beta Alloys), Springer-Verlag, Berlin (2007), pp. 203–258.
- [29] M. Thöne, S. Leuders, A. Riemer, T. Tröster, H.A. Richard, Influence of heat-treatment on Selective Laser Melting products – e.g. Ti6Al4V, in: Proceedings of Solid Freeform Fabrication Symposium, SFF23, Austin, USA, 2012.
- [30] C. Qui, G.A. Ravi, C. Dance, A. Ranson, S. Dilworth, M.M. Attallah, Fabrication of large Ti-6Al-4V structures by direct laser deposition, *J. Alloy. Compd.* 629 (2015) 351–361.
- [31] X. Wu, J. Liang, J. Mei, C. Mitchell, P.S. Goodwin, W. Voice, Microstructures of laser-deposited Ti-6Al-4V, *Mater. Des.* 25 (2) (2014) 137–144.
- [32] Matthew J. Donachie, Titanium: A Technical Guide, 2nd ed., ASM International, Materials Park, Ohio (2000), pp. 66–68.
- [33] R.K. Nalla, B.L. Boyce, J.P. Campbell, J.O. Peters, R.O. Ritchie, Influence of microstructure on high-cycle fatigue of Ti-6Al-4V: bimodal vs. lamellar structures, *Metall. Mater. Trans. A* 33A (2002) 899–918.
- [34] M. Benedetti, V. Fontanari, The role of bi-modal and lamellar microstructures of Ti-6Al-4V on the behavior of fatigue cracks emanating from edge-notches, in: Proceedings of European Conference on Fracture, ECF15, Stockholm, Sweden, 2004.
- [35] ASTM E606 / E606M-12, Standard Test Method for Strain-Controlled Fatigue Testing www.astm.org, ASTM International, West Conshohocken, PA, 2012.
- [36] ASTM E8 / E8M, Standard Test Method for Tension Testing of Metallic Materials www.astm.org, ASTM International, West Conshohocken, PA, 2015.
- [37] P. Carrión, N. Shamsaei, Cyclic Deformation and Fatigue Data for Ti-6Al-4V ELI Including Mean Strain/Stress Effects (submitted to Data in Brief), 2015.
- [38] A. Yadollahi, N. Shamsaei, S.M. Thompson, A. Elwany, L. Bian, Mechanical and microstructural properties of selective laser melted 17-4 PH stainless steel, in: Proceedings of International Mechanical Engineering Congress and Exposition (IMECE 2015), Houston, 2015.
- [39] R.I. Stephens, A. Fatemi, R.R. Stephens, H.O. Fuchs, *Metal Fatigue in Engineering*, 2nd ed., John Wiley and Sons, Inc., New York, 2001.
- [40] A.M. Miller, P.R. Roberts, *Rotating Electrode Process*, ASM International, Ohio, 1998.
- [41] L. Han, F.W. Liou, S. Musti, Thermal behavior and geometry model of melt pool in laser material process, *J. Heat Transf.* 127 (No. 9) (2005) 1005–1014.
- [42] Y. Wang, S. Zhang, X. Tian, H. Wang, High-cycle fatigue crack initiation and propagation in laser melting deposited TC18 titanium alloy, *Int. J. Miner. Metall. Mater.* 20 (2013) 665–670.
- [43] C. Lin, C. Ju, J.C. Lin, A comparison of the fatigue behavior of cast Ti-7.5 Mo with c.p. titanium, Ti-6Al-4V and Ti-13Nb-13Zr alloys, *Biomaterials* 26 (2005) 2899–2907.
- [44] B. Torries, A. Sterling, N. Shamsaei, S.M. Thompson, S.R. Daniewicz, Utilization of a Microstructure sensitive fatigue model for additively manufactured Ti-6Al-4V, *Rapid Prototyping J.* (2015) (in press).

Glossary

- AM: Additive Manufacturing;
 CNC: Computer Numerical Control;
 DLD: Direct Laser Deposition;
 EBM: Electron Beam Melting;
 EBSD: Electron Backscatter Diffraction;
 ELI: Extra Low Interstitials;
 FGM: Functionally Graded Material;
 HCF: High Cycle Fatigue;
 HIP: Hot Isostatic Pressing;
 LBAM: Laser Based Additive Manufacturing;
 LCF: Low Cycle Fatigue;
 LENS: Laser Engineered Net Shaping;
 PBF: Powder Bed Fusion;
 SEM: Scanning Electron Microscope;
 SLM: Selective Laser Melting.



Selective laser melting of a beta-solidifying TNM-B1 titanium aluminide alloy



Lukas Löber^{a,*}, Frank Peter Schimansky^b, Uta Kühn^a, Florian Pyczak^b, Jürgen Eckert^a

^a Leibniz Institute for Solid State and Materials Research Dresden, Germany

^b Helmholtz-Zentrum Geesthacht Centre for Materials and Coastal Research, Germany

ARTICLE INFO

Article history:

Received 18 November 2013

Received in revised form 28 February 2014

Accepted 2 April 2014

Available online 13 April 2014

Keywords:

Additive manufacturing

Selective laser melting

Titanium aluminide

Mechanical properties

Optimization of process parameters

ABSTRACT

The interest for a wider range of useable materials for the technology of selective laser melting is growing. In this work we describe a new way to optimize the process parameters for selective laser melting of a beta solidifying titanium aluminide. This kind of material has so far not been processed successfully by this method. The new approach is easy to conduct and well transferable to other materials. It is based on the fact that the parts generated from selective laser melting can be described by an addition of multiple single tracks. Multiple types of single track experiments are performed and in combination with knowledge from laser welding tests optimized parameter combinations are derived. Compact samples are built with the optimized process parameters and characterized in terms of microstructure, phase composition and mechanical properties. With this technique the generation of a TNMB1 titanium aluminide alloy sample with a density greater than 99% could be achieved. The mechanical properties are comparable with material produced by conventional techniques.

© 2014 Elsevier B.V. All rights reserved.

1. Introduction

Selective laser melting (SLM) is an additive manufacturing technology which works layer wise and was developed from selective laser sintering. With the availability of new higher powered lasers it is now possible to fully melt the material according to Bourell et al. (1992). In SLM a laser source selectively scans a powder bed according to the CAD-data (Computer Aided Design) of the part to be produced. This three-dimensional CAD model of the desired part is always the starting point for this processing technique. It has to be divided numerically in horizontal layers of a defined thickness. In addition to the geometry, each layer contains also specific information regarding the process parameters such as laser power, scanning speed or hatching. To fix the part on the substrate material, and to enhance heat conduction during SLM processing according to Hussein et al. (2013a), support structures have to be designed. Both the CAD model and the support structure have to be sliced as described by Löber et al. (2011). These filigree support structures are built up from the same material and in the same SLM process as the desired part and have to be removed mechanically afterwards as proposed by Hussein et al. (2013b). The complete

SLM process is a number of iterations of the same procedure which consists in applying powder, melting the selected areas of the powder bed with the laser and lowering the building platform to enable the next application of a new powder layer as described by Löber et al. (2013). A schematic of the process is shown in Fig. 1.

The high intensity laser beam makes it possible to completely melt and fuse the metal powder particles together to obtain an almost fully dense material. Successive layers of metal powder particles are melted and consolidated on top of each other resulting in near-net-shaped parts as found out by Kruth et al. (2004). Consequently, the laser melting and layered re-solidification of the powder particles is accompanied by the development of residual stresses, which arise from the high thermal gradients present in the material. This effect was discovered by Kruth et al. (2004). These stresses after Yadroitsev et al. (2013) can lead to part failure due to distortions, delamination or cracking. Besides the thermal stresses, the balling effect is also a severe impediment to interlayer connection. A last phenomenon encountered which was first described by Kruth et al. (2005) is the vaporization effect which occurs when the powder bed is irradiated with high energy intensities.

A lot of efforts are conducted to identify the crucial process parameters of SLM which influence the density of the parts as for example the work done by Mumtaz et al. (2008) on Waspaloy®. The process is so far validated for a small range of different materials such as different steels, pure titanium, some titanium base

* Corresponding author. Tel.: +49 3514659503; fax: +49 3514659452.

E-mail address: l.loeber@ifw-dresden.de (L. Löber).

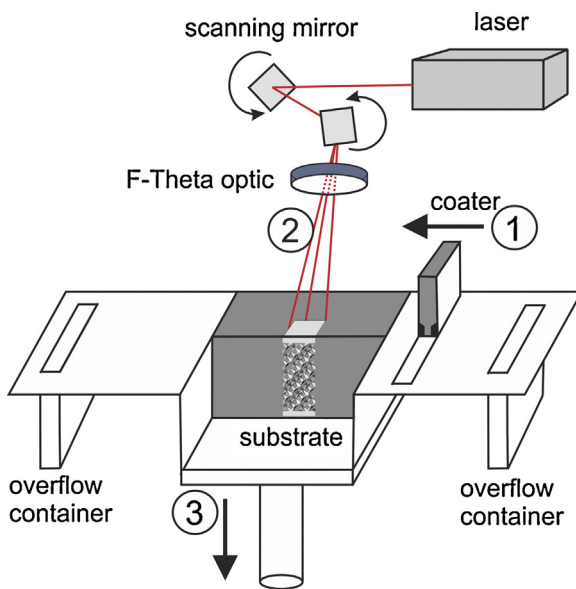


Fig. 1. Schematic of SLM machine; the arrows indicate the three main process steps: (1) application of a powder layer with the coater; (2) illumination of the powder bed with the laser; (3) lowering of the platform by the layer thickness.

alloys, Inconel, cobalt chromium and aluminum alloys. In this work we want to present the development of a suitable set of process parameters for a titanium aluminide (TiAl) alloy.

Intermetallic $\gamma\text{-TiAl}$ based alloys are believed to have great potential in high temperature applications. This is mainly due to their high specific mechanical properties such as tensile strength or creep resistance at elevated temperatures according to the work of Wu (2006). The low density of $3.8\text{--}4.2\text{ g/cm}^3$ of titanium aluminides is responsible for these high specific properties. TiAl has thus become the prime candidate for replacing nickel-based super alloys in gas turbine engines. The replacement of Ni-based super alloy parts with TiAl could reduce according to the work of Voice et al. (2005) the structural weight of high performance gas turbine engines by 20–30%. Therefore, a major increase in engine performance and fuel efficiency may be realized. One of the reasons why TiAl alloys are not already widely used in engines are difficulties associated with processing.

High strength Nb bearing $\gamma\text{-TiAl}$ alloys, which show only a small volume fraction of β -phase at hot-working temperature can only be forged under isothermal conditions and are extremely susceptible to cracking when tensile stresses occur which is nearly unavoidable in most forging routes. So while isothermal forging is in principle possible it is not economically feasible for most applications as demonstrated by Kremmer et al. (2008). In the past, the attractive properties of TiAl were outweighed by these difficulties in processing and machining. However, progress in manufacturing technologies as well as deeper understanding of TiAl 's microstructure, deformation mechanisms, and advances in micro-alloying, have led to first commercial uses of titanium aluminides. Examples can be found in high performance turbochargers for cars and recently an US aero-engine manufacturer announced the introduction of investment cast $\gamma\text{-TiAl}$ blades in the low-pressure turbine.

The so-called TNMTM alloys, as investigated in this work, are among the most promising candidates which reduce the difficulties in processing while retaining the good application properties of TiAl alloys. The name TNM is derived from niobium and molybdenum which are the main alloying elements. The overall composition of these alloys is in the range of Ti – (42–45) Al – (3–5) Nb – (0.1–2) Mo – (0.1–0.2) B (in at.%). This type of alloy is described in detail by Clemens et al. (2008a). Niobium and molybdenum alter the phase

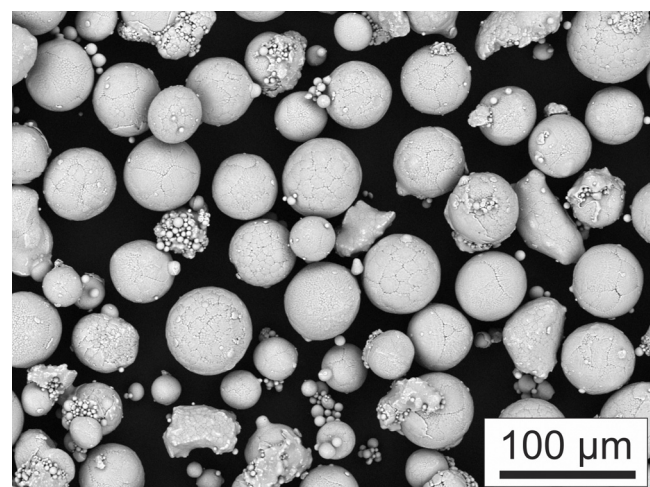


Fig. 2. Morphology of the TNMB1 powder (batch 45–63 μm).

diagram sufficiently to ensure solidification solely via the β -phase. Appel et al. (2006) found out that this leads to the formation of a relatively fine grained (with $d \leq 50 \mu\text{m}$) microstructure in a bulk ingot after casting and the presence of a larger forging window in contrast to other high strength $\gamma\text{-TiAl}$ alloys due to the presence of the disordered bcc β -phase at forging temperature. The β -phase provides a sufficient number of independent slip systems and therefore acts as a deformation accommodating phase during forging according to Schloffer et al. (2012). Nevertheless, the alloy composition is balanced in such a way that serious compromises in high temperature capability at application temperature are avoided.

2. Experimental

The starting material with a nominal composition of $\text{Ti-Al28.9-Nb9.68-Mo2.26-B0.024\text{ wt.\%}}$ was bought as an alloyed rod from the company GFE Gesellschaft für Elektrometallurgie mbH. The material was gas-atomized by the EIGA method (Electrode Induction-melting Gas Atomization). The process is well described by Gerling et al. (2004). The process works crucible-free under a protective argon atmosphere. In this technique the pre-alloyed rod dips into a conical induction coil. Upon operation of the coil the tip of the rod is heated and melts. This melt pours through the center of a gas nozzle and is atomized by argon gas (purity 99.999%). The powder was collected and sieved into four different batches: 0–45 μm , 45–63 μm , 63–95 μm and 95–125 μm . In this work, only the batch of 45–63 μm was used. The resulting powder can be seen in Fig. 2. The chemical composition of rod, powder and SLM material was measured via ICP-OES (inductively coupled plasma optical emission spectrometry).

Additionally, for comparison three rods with a diameter of 3 mm and a length of 40 mm were cast in a centrifugal casting machine high term titan 3.3 from the company Linn from the starting rod material. A conventional process route was seen apt for this comparison. 20 g of the starting rod material was placed in the casting machine. The machine was evacuated to a pressure of 10^{-5} mbar and then flooded with argon gas (purity 99.999%). The material was heated via an induction coil till melting occurred. The temperature of the melt during casting was around 1773 K.

The SLM experiments were performed on a commercially available SLM 250 hl machine (SLM Solutions GmbH). The machine is equipped with a 400 W Nd-YAG fiber laser which works in continuous mode, has a wavelength of 1075 nm and a spot size of approximately 80 μm in the focus. Before the illumination of the powder bed starts the building chamber is flooded with

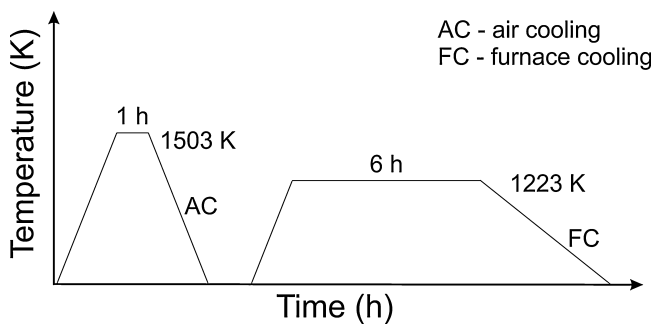


Fig. 3. Schematic of the applied heat treatment.

argon (purity 99.999%) until the residual oxygen content is below 200 ppm. The building chamber works under an overpressure of around 10 mbar. During the process the build chamber is monitored by two oxygen detectors. Residual oxygen levels of less than 200 ppm can thus be guaranteed.

For the single track experiments a layer of approximately 50 µm in thickness was applied on a titanium-base substrate. It has to be mentioned that the layer thickness might vary in a certain range ($\pm 10 \mu\text{m}$) depending on the substrate roughness, particularities of powder delivering, leveling and spreading, and granulometric characteristics of the powder.

Three different single track experiments with different parameter combinations were performed under the otherwise same experimental conditions. Only laser power and scanning speed were changed during the experiments. The used parameter combinations are given in Table 1.

For each parameter set two single tracks were produced in different substrate positions for comparison.

Based on the results from the single track experiments overlapping experiments with different hatchings were performed. The preparation and execution of the experiment was similar to the single track experiments.

The last set of SLM experiments included the production of cylinders for mechanical testing and microstructural analysis as well as some dodecahedron unit cells as representative of a more complex 3D structure. The process parameters used for these specimens were: laser power 100 W, scanning speed 50 mm/s for the volume contour, laser power 175 W and scanning speed 1000 mm/s for the outer contour, a hatching of 0.3 mm, and a layer thickness of 75 µm. The used scanning strategy was a stripe hatching. A detailed description of the different process parameters is given by (Louvis et al., 2011).

Heat treatment of selected cast and SLM samples was performed as a two-step heat treatment as shown in Fig. 3.

The heat treatment was conducted in air which leads to oxidation in the surface region. The heat treatment conditions were chosen from the work of Clemens et al. (2008b). In his work he describes the microstructural evolution caused by different heat treatments.

The surface of the single tracks was characterized with an optical microscope (Keyence VHX 2000) and a scanning electron microscope (LEO 1530 Gemini from the company Zeiss). The width of the melt tracks was measured with the VHX analyzing software. Selected specimens from the single track experiments were cut with a Struers Accutom 5. The samples were embedded into epoxy resin and metallographically prepared with a Rotopol. The specimens were grinded with decreasing grit size from 300 to 4000 and then polished with colloidal SiO particle with a size of 50 nm. The samples were then etched for 10 s with Kroll's agent (92 ml distilled water, 6 ml nitric acid and 2 ml hydrofluoric acid). The same preparation except the last etching step was performed for the compact

specimens which were characterized with a LEO 1530 Gemini scanning electron microscope from the company Zeiss in backscattered electron mode. One of the compression samples was cut into pieces for X-ray diffraction (XRD). X-ray analysis was also conducted on the powder material. Structural characterization was performed by X-ray diffraction using a D3290 PANalytical X'pert PRO with CoK α radiation ($\lambda = 0.17889 \text{ nm}$) in Bragg–Brentano configuration.

The density of the specimens was measured via the Archimedes method with a Sartorius density measuring set YDK-01 (OD).

Mechanical testing of the compression samples was performed on an Instron 5869 testing device. The compression samples were cut coplanar with a rotating cup wheel. The cast samples had a diameter of 3 mm and a height of 6 mm while the samples from SLM had a diameter of 4 mm and a height of 8 mm. The strain rate was set constant to 0.01 mm/s. The strain was measured via a laser extensometer (Fiedler Optoelektronik GmbH) and four attached reference measuring stripes on the samples. For each condition, at least three samples were tested. The mechanical testing was performed at room temperature.

3. Results and discussion

3.1. Powder

The morphology of the atomized powder is spherical. The chemical composition was only changed to a minor extent due to the atomization process (see Table 2). The aluminum content is slightly lower while the molybdenum content is slightly elevated. This is probably caused by the low boiling point of aluminum which caused evaporation during the atomization process. The flowability of the powder was tested with a modified hall flow meter. To better simulate the conditions of the SLM machine, the diameter of the hall flow meter was changed from 2.45 mm as demanded in DIN EN ISO 4490 to 3 mm. With this setup a full cylinder was emptied after 15.82 s.

3.2. Single track morphology

The variation of the scanning speed and the laser power has a great influence on the morphology of the melt tracks. Six different types of melt tracks could be identified (see Fig. 4). At low laser power (50 W) and slow scanning speeds (50–100 mm/s), but also at intermediate laser power (100 W) and very high scanning speeds (350–2100 mm/s), balling could be observed. The same effect was observed by Tolochko et al. (2004). According to his work is the effect of surface tension responsible for the molten pool to assume the general shape of a circular or segmental cylinder. Furthermore fragmentation of the tracks called balling effect is a well-known drawback of SLM. This is interesting because the balling effect described by Louvis et al. (2011) is observed for the combination of high powers and slow scanning speeds. The balling at higher scanning speeds can be explained by the Plateau–Rayleigh capillary instability of the melt pool which was described by Gusalov et al. (2007). Two factors normally stabilize the process with decreasing scanning speeds: reduction of the length-to-width ratio of the melt pool and increase of the width of its contact with the substrate. The instability of a liquid cylinder was initially described by Rayleigh (1878) and further by Nichols and Mullins (1965). Their analyses show that a cylinder of water is unstable in front of sinusoidal fluctuations when the wavelength λ is greater than the cylinder circumference $2\pi R$. The reduction of the surface energy with decreasing surface area is the driving force for the break-up of the liquid cylinder. However, there are various other parameters which influence the balling effect. An incomplete list according to Yadroitsev et al. (2007) include laser powder, layer thickness,

Table 1

Overview of the parameter combinations including the line energy input (J/mm^2).

Laser power (W)	Scanning speed					
	350 mm/s	700 mm/s	1050 mm/s	1400 mm/s	1750 mm/s	2100 mm/s
50	2.88	2.4	1.92	1.44	0.96	0.48
100	5.76	4.8	3.84	2.88	1.92	0.96
150	8.64	7.2	5.76	4.32	2.88	1.44
200	11.52	9.6	7.68	5.76	3.84	1.92
250	14.29	12.0	9.6	7.2	4.8	2.4

Laser power (W)	Scanning speed					
	50 mm/s	60 mm/s	70 mm/s	80 mm/s	90 mm/s*	100 mm/s
50	20.00	16.67	14.29	12.50	11.11	10.00
100	40.00	33.33	28.57	25.00	22.22	20.00
150	60.00	50.00	42.86	37.50	33.33	30.00
200	80.00	66.67	57.14	50.00	44.44	40.00
250	100.00	83.33	71.43	62.50	55.56	50.00

Laser power (W)	Scanning speed					
	100 mm/s	150 mm/s	200 mm/s	250 mm/s	300 mm/s	350 mm/s
50	10.00	6.67	5.00	4.00	3.33	2.86
100	20.00	13.33	10.00	8.00	6.67	5.71
150	30.00	20.00	15.00	12.00	10.00	8.57
200	40.00	26.67	20.00	16.00	13.33	11.43
250	50.00	33.33	25.00	20.00	16.67	14.29

substrate material, physical properties and granulomorphometry of the powder. A recording of such a balling can be seen in Fig. 5a.

Combining a low laser power of 50 W with high scanning speeds >350 mm/s does not lead to the formation of a visible melt track. It can be assumed that the line energy input of less than 2 J/mm^2 was either not sufficient to melt the powder and fuse it to the substrate or the powder was melted by the laser but the used energy input was too low to create a joint molten pool. In this case the powder would form rounded free surfaces as published in the work of Yadroitsev et al. (2010).

Staying at higher scanning speeds and increasing the power changes the morphology from balling to an instable melt track, as already mentioned above. The discussed morphology can be seen in Fig. 5b. Such instable melt tracks were already described by Niu and Chang (1999) with steel powder. They identified the oxygen content of the powder as main reason for the instabilities. In this case, the instabilities are probably caused by a bad connection between the melt track and the adjacent substrate. Also Childs

et al. (2004) showed instable melt tracks in their work on different steel powders. Unfortunately, no explanation was given for this phenomenon. A possible explanation might be found in the work of Kruth (2004). In this work the phenomenon of evaporation during the exposure of the powder particles is discussed. The vapor can interact with the laser radiation, becomes ionized and forms a plasma which decreases the laser power in the powder.

When going to lower scanning speeds (150–300 mm/s) at low power, melt tracks with pronounced cracks perpendicular to the scanning direction could be observed. A typical example is displayed in Fig. 5c. The shape of the track is similar to the ones where balling occurs but with the addition of multiple cracks. In literature, the problem of crack formation in the melt zone is often described for welding of titanium aluminides as for example discussed in the work of Guoqing et al. (2011). The crack formation is most probably associated with the high cooling rate during solidification, leading to residual stresses which are relieved by the formation of cracks.

Quite a broad range of parameter combinations in the intermediate region (scanning speed: 150–300 mm/s; laser power: 100–250 W) leads to stable melt tracks without balling or crack formation. The shape of these single tracks is quite sharp. In the field of welding such well-defined weld tracks are often associated with segregations and crack formation along the weld track. This effect is circumstantiated by Anik and Dorn (1995). The material at the solidification front has a lower solidification temperature due to micro segregations compared to the already solidified material. Therefore, the resistance against shrinkage is reduced and solidification cracks might form more easily. All the so far described parameter combinations were not further investigated due to their inherent problems.

The last morphology which could be found is a stable and smooth melt track for slow scanning speeds (50–100 mm/s) and intermediate to high laser powers (100–250 W) (for visualization, see Fig. 5d). In this case, the combination of a small super cooling of the liquid and a high thermal gradient leads to stalk-like solidification which is generally associated with low segregations. The surface of the melt track is even and the width of the track stays constant. These parameter sets seem appropriate for the process of selective laser melting and for the production of fully dense parts. In addition to the top surface observations, metallographic

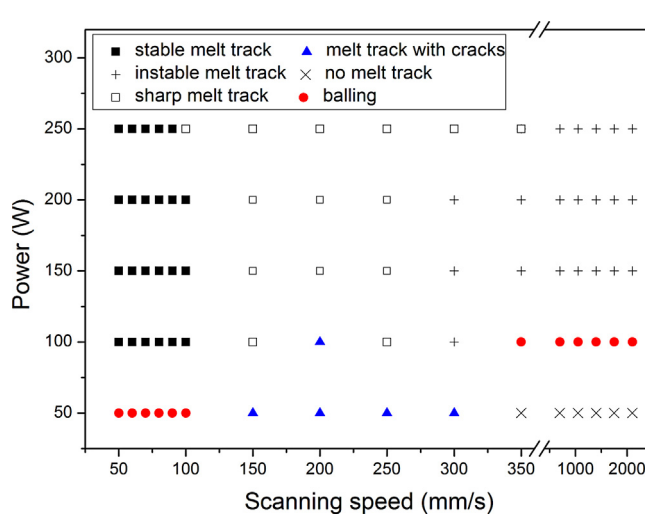


Fig. 4. Process map of the single track experiments with the indication of the different observed melt track morphologies.

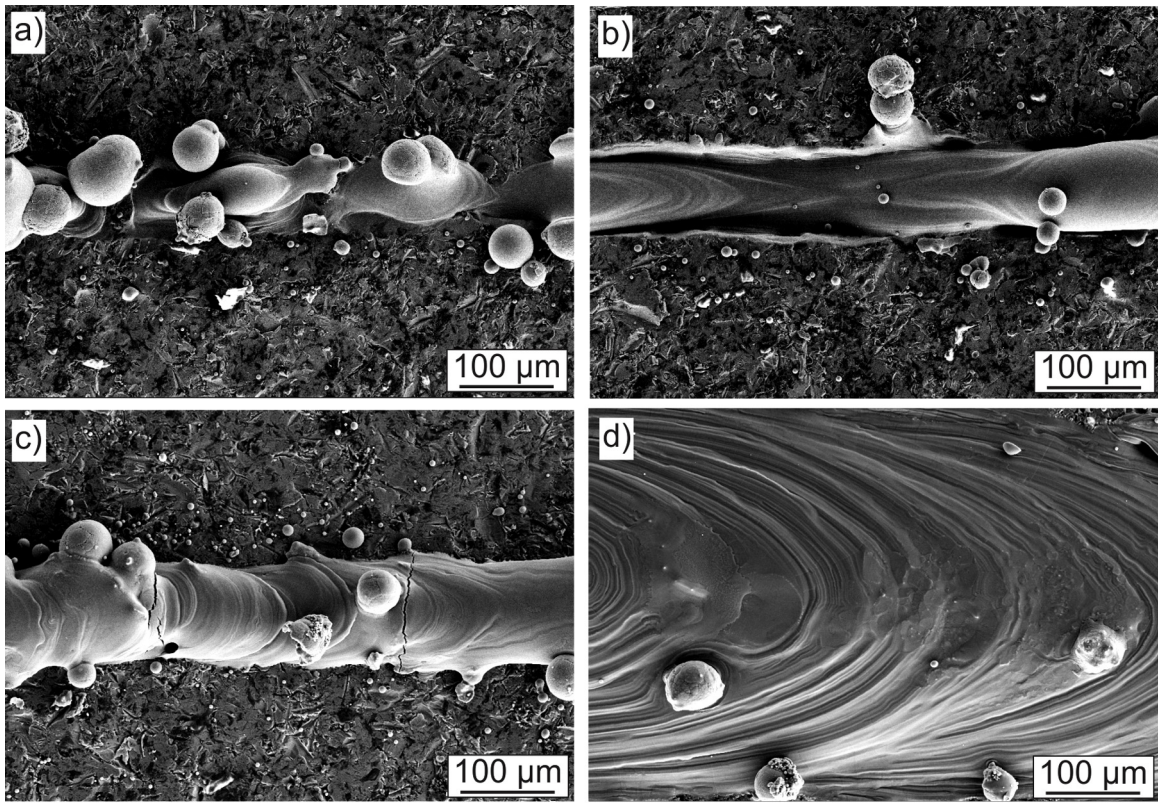


Fig. 5. Different melt track morphologies: (a) balling, (b) unstable melt track, (c) melt track with cracks and (d) stable melt track.

investigations of the cross-sections for the single tracks with a speed of 50 mm/s were conducted. The resulting micrographs can be seen in Fig. 6. The change in laser powers has a quite significant influence on the morphology of the melt tracks. When using a low

power of 50 W most of the energy is concentrated in the powder material (see Fig. 6a and c). The molten pool forms free circular cylinder with the ratio $\pi D/L \leq 1$; therefore, a capillary instability appears. Only a small amount of the substrate is molten for this

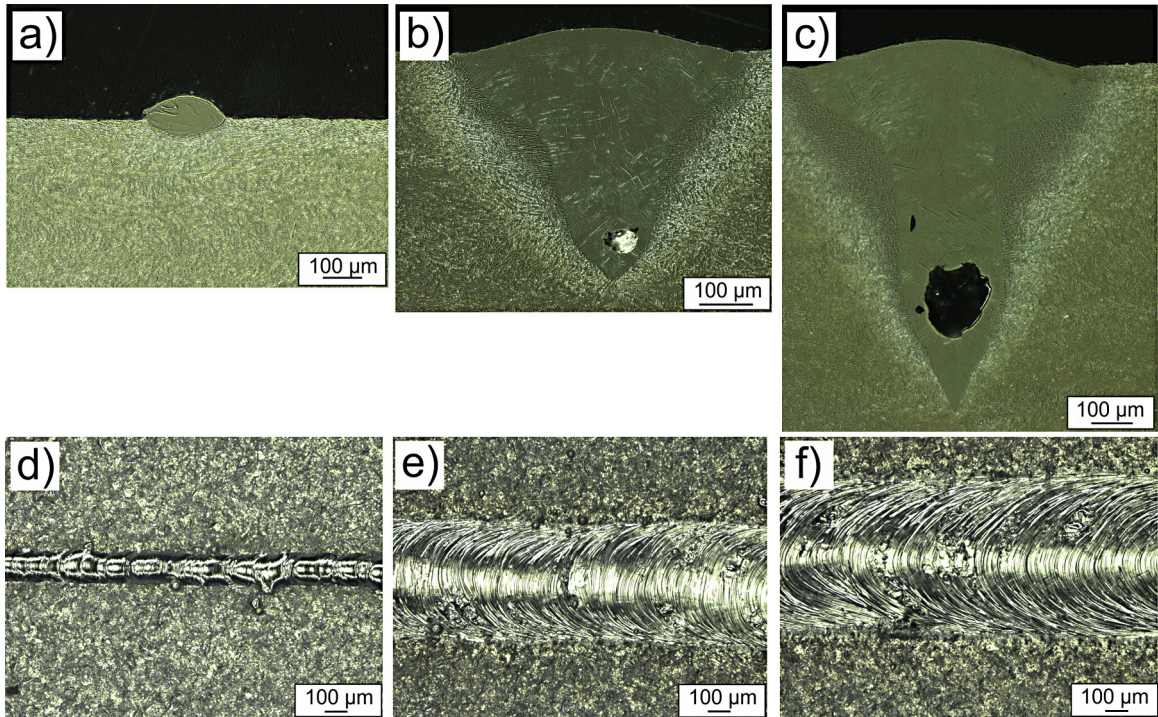


Fig. 6. Cross and top section views (after etching with Kroll' agent) of melt tracks with different process parameters (a) and (d) $P: 50 \text{ W}$, $v: 50 \text{ mm/s}$; (b) and (e) $P: 150 \text{ W}$, $v: 50 \text{ mm/s}$; (c) and (f) $P: 250 \text{ W}$, $v: 50 \text{ mm/s}$.

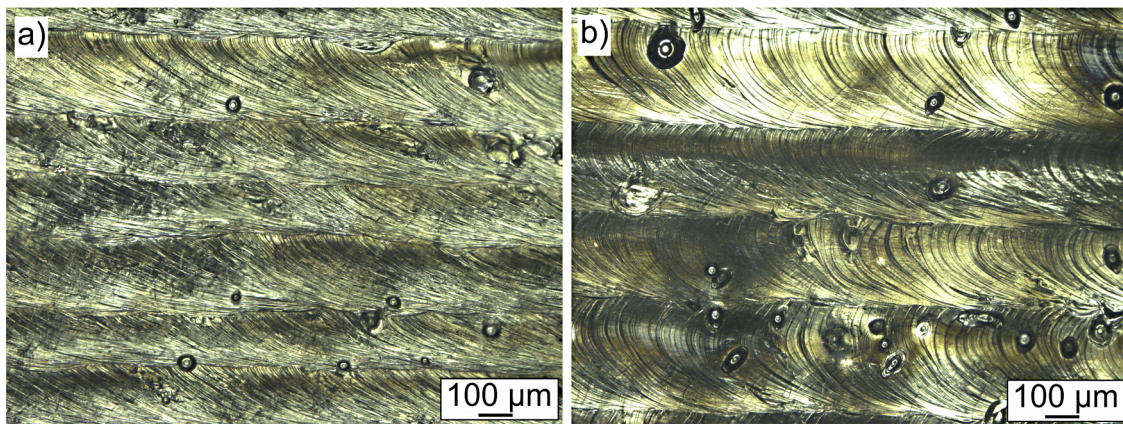


Fig. 7. Top view of the hatching experiments. $P: 150\text{ W}$, $v: 50\text{ mm/s}$ —(a) $dx: 0.2\text{ mm}$ and (b) $dx: 0.3\text{ mm}$.

set of parameters which might lead to a bad interface between the melt and the substrate. It has to be taken into consideration that this micrograph only reflects a snap-shot. Since this parameter combination is prone to the balling effect, the cross-section will look different a couple of μm away. With increasing power (150 W) the change is quite drastic (see Fig. 6b and c). The width of the track is more than tripled and the interaction with the substrate becomes more intense. The classic zones of a melt track can be properly observed: from the melting zone inside, over the zone of partial melting (darker area around the melting zone) and the heat-affected zone (bright area around the zone of partial melting) to the unaffected substrate. This indicates a good interaction between the melt pool and the substrate and guarantees a good

fusion between both. When further increasing the power to 250 W the width of the melt track becomes even broader (see Fig. 6b and c). Again all the classic zones of a melt track are well observable. The depth of the track is further increased to around 600 μm which would correspond to more than 10 layers of material. In addition a huge pore in the lower part of the finger-shaped melt track can be observed. This wormhole is generally caused when intermediate cooling rates are present. The solidification rate is higher than the buoyancy velocity of the entrapped gas in the melt. Another explanation might be due to an abnormal material flow during welding. [Bolsaikhan et al. \(2011\)](#) gave this explanation in their work for similar results. Since this is an undesired defect in the melt track, the parameter set with the lower power, where the defect is

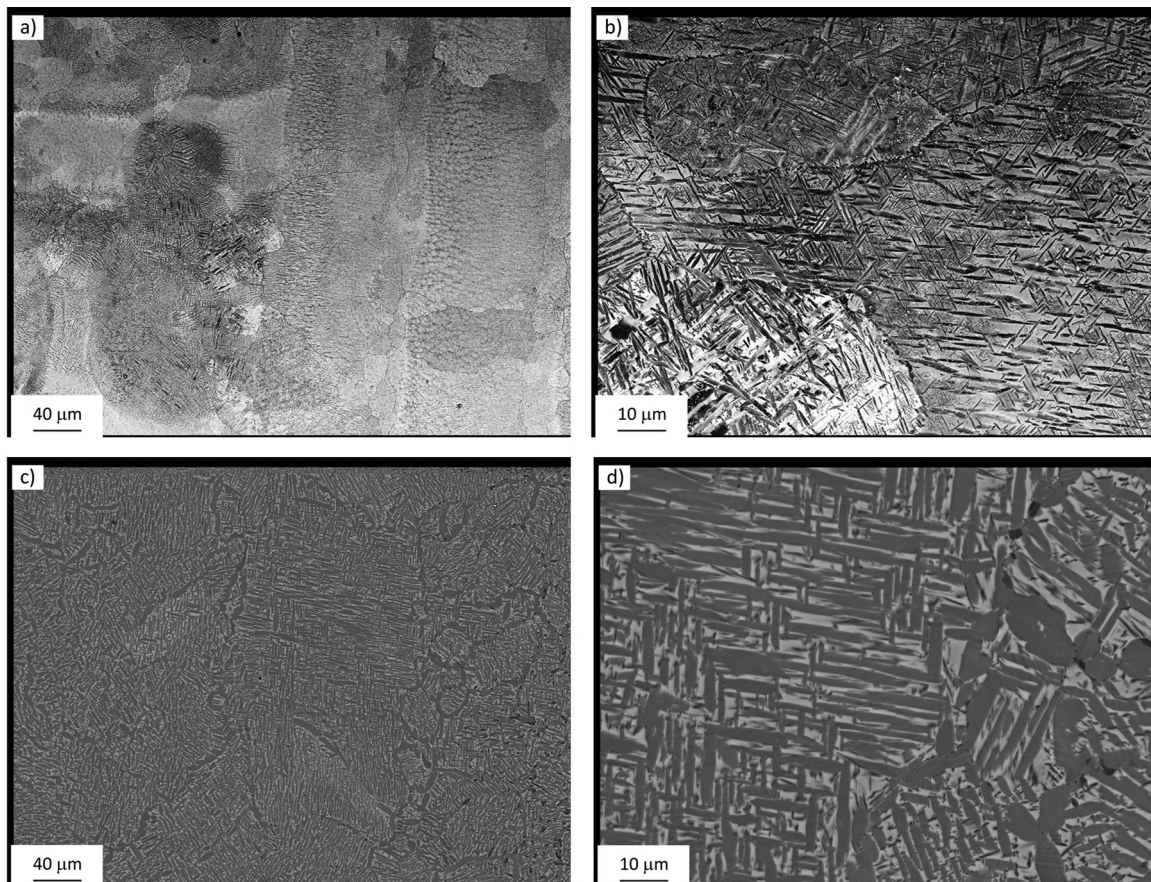


Fig. 8. SEM pictures of (a and b) SLM produced TNM sample and (c and d) the corresponding heat-treated sample (view is perpendicular to the building direction).

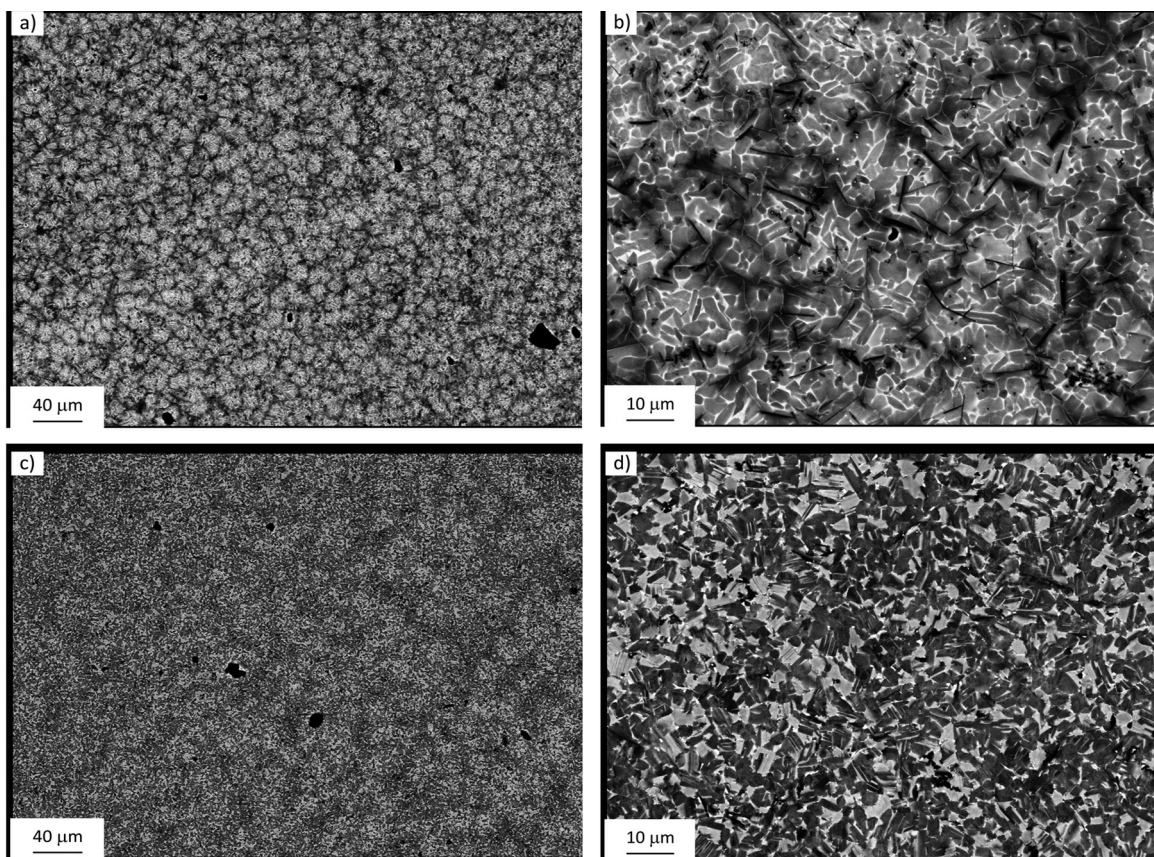


Fig. 9. SEM pictures of the (a and b) cast sample and (c and d) the corresponding heat-treated sample.

not that pronounced, was chosen for the further experiments. The width of each single track was recorded at 10 different points and an average was made from the measurements. The width varies from $110 \pm 5.8 \mu\text{m}$ for a power of 50 W and a speed of 100 mm/s to a width of $704 \pm 18.5 \mu\text{m}$ for a power of 250 W and a speed of 50 mm/s, respectively. The dependence between the width of the melt track and the used laser power is roughly linear.

To investigate the interaction between multiple scan tracks and to determine an optimal hatching, different experiments with overlapping scan tracks were conducted with a power of 150 W and a scanning speed of 50 mm/s. Similar to the single track experiments a thin layer of powder was applied and multiple scan tracks were placed with different distances next to each other. The measured width of the single track was taken, and accordingly overlaps of 25% and 50%, which correspond to a hatching of 0.2 mm and 0.3 mm, were conducted. The top views of these experiments can be seen in Fig. 7. Both experiments show a good and stable overlapping of the melt tracks. Since no apparent difference in the quality could be observed, a hatching of 0.3 mm corresponding to an overlap of 50% was chosen for the production of compact samples. By this, the amount of tracks which are needed, and thus the building time of the parts, is reduced.

3.3. Compact samples

Three of the produced compact cylindrical samples were removed from the substrate plate, freed of the support structure, cut co-parallel and their density was measured via the Archimedes method. First the density of the starting material was measured and taken as 100% relative density. A density of 4.144 g/cm^3 could be measured for the starting rod material. The SLM cylinders displayed a density of $4.102\text{--}4.122 \text{ g/cm}^3$ which corresponds to a relative

Table 2

Chemical composition of the TNM rod material, powder material and SLM sample.

Element (wt.%)	Titanium	Aluminum	Niobium	Molybdenum	Boron
Rod material	Balance	28.90	9.68	2.26	0.024
Powder	Balance	28.49	9.38	2.32	0.030
SLM	Balance	28.45	9.40	2.30	0.028

density of 98.89–99.46%. The residual porosity could be determined from a micrograph as small spherical pores (diameter 20–50 μm) evenly distributed throughout the material. This could either be caused by wormholes built during the solidification or by entrapped gas in the powder material as described by Biamino et al. (2010). The chemical composition of the samples was not affected by the SLM process (see Table 2).

Samples from the SLM process were prepared for compression testing, metallographic preparation and phase analysis. The corresponding microstructures can be seen in Fig. 8. The microstructure of the produced cast and heat-treated samples are shown in Fig. 9. Selected results from the compression tests of the SLM, cast, SLM heat-treated and cast heat-treated sample are shown in Fig. 10. The results from all the specimens are summarized in Table 3. The mechanical performance of the SLM samples is slightly lower

Table 3

Characteristic values from the compression test for the cast and SLM samples.

	Offset yield strength (MPa)	Ultimate strength (MPa)	Ultimate strain (%)
Cast	1611–1685	1918–2012	8.14–10.59
SLM	1620–1651	1816–1903	4.5–9.5
Cast + HT	1302–1324	1728–1768	12.3–15.4
SLM + HT	886–1071	1428–1671	12.3–16.5

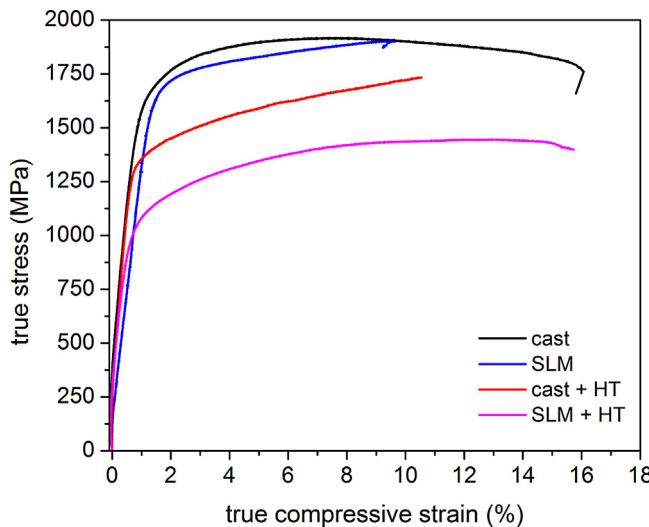


Fig. 10. True stress-true strain diagrams from the compression testing.

compared to the conventional cast sample. A possible explanation for this fact can either be found in the residual porosity of the SLM samples compared to the fully compact cast samples or in the microstructure of the specimens. It is noteworthy, that the cast samples also showed some porosity which can be seen in Fig. 9. The microstructure in z-direction of the build job of the SLM sample before and after heat-treatment is shown in Fig. 8. The microstructure of the SLM sample can be described as nearly lamellar β . The darker areas in the micrograph show the α_2 phase, while the brighter bone-like features correspond to the β -phase. The nearly lamellar β microstructure is associated with high strength, high creep strength and moderate room temperature ductility according to the work of Schweighofer et al. (2011). The two phases could also be identified by X-ray diffraction (see Fig. 11). The microstructural features clearly indicate that solidification occurred via the β -phase, i.e. $L \rightarrow L + \beta \rightarrow \beta \rightarrow \dots$, followed by a multitude of solid-state transformations and reactions. It is supposed that the reaction $\alpha_2 \rightarrow (\alpha_2 + \gamma)_L$ did not take place. The microstructure is not homogenous in the SLM sample and regions with coarser and finer microstructure are found next to each other as visible in Fig. 8a

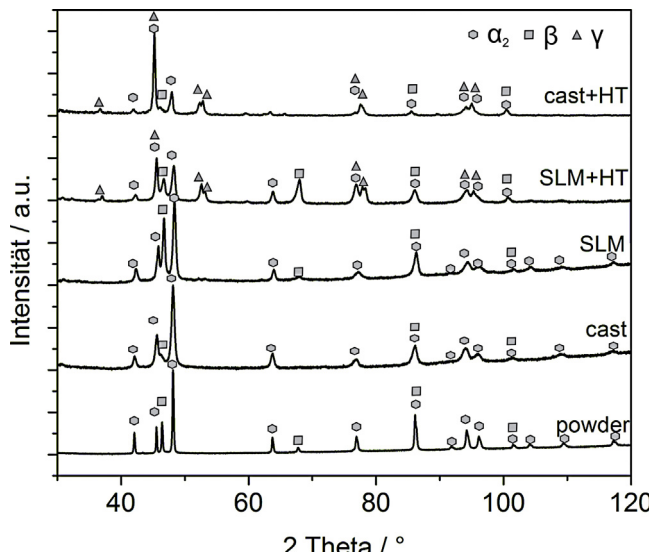


Fig. 11. X-ray diffraction patterns of the TNM powder, the cast sample, the SLM sample and the heat-treated SLM sample.

and b. This probably stems from local differences in the cooling rate during the SLM process. The heat-treated sample reveals a slightly different microstructure (compare Fig. 8c and d). Again the brighter areas correspond to the β -phase with darker α_2 phase regions in between. But in some positions of the broader β lamellae dark finer lamellae can be observed. Here the partial transformation from β to γ phase occurred. In general the microstructure coarsened during the heat treatment compared with the SLM sample. The three phases β , α_2 and γ can also be identified via X-ray diffraction. The applied two step heat treatment caused a microstructural homogenization in the first step at 1503 K in the α/β -region and allowed the precipitation of γ lamellae in the second step at 1223 K. While it is not clearly discernible from the SEM micrographs the cast heat-treated sample seems to display a lower content of β -phase compared to the SLM heat-treated sample, visible from the lower intensity of the corresponding XRD peaks around 48° and 68° (see Fig. 11). The microstructures of the cast and the cast and heat-treated samples are shown in Fig. 9. In the as cast microstructure (Fig. 9a and b) fine segregations of heavier elements probably niobium and molybdenum appear as bright regions in the backscattered electron image. In higher magnification it is discernible that the microstructure is composed from a bright phase with a branch like structure embedded in regions of a darker phase. In conjunction with the XRD data the brighter phase is identified as remnant β regions embedded in α_2 -phase. Black lines in Fig. 9b stem from borides which fell off during the specimen preparation. Subsequent to heat treatment a duplex structure consisting of β and α_2 grains with some γ lamellae in α_2/γ colonies is found. In general the cast microstructures tend to be finer and more isotropic than the corresponding SLM microstructures. This difference is especially pronounced when comparing the SLM and heat treated with the cast and heat-treated sample. This finer microstructure is probably the main reason why the cast samples exhibit in average a higher strength than the respective SLM specimen state.

4. Conclusions

In this work an easy and fast method of optimizing the process parameters for a new difficult to process alloy for selective laser melting was demonstrated. Starting from single tracks with various parameter combinations six different melt track morphologies could be identified: insufficient melting, balling, melt tracks with cracks, instable melt tracks, sharp melt tracks and round stable melt tracks. For high laser power settings, wormholes were found in the cross-section of otherwise stable melt tracks. From experiments with overlapping melt tracks, an optimal hatching for the



Fig. 12. Produced TNM-B1 3D-dodecahedron structures with optimized parameter set.

best combination of laser power and scanning speed was identified. The optimized parameter set consist of the following parameter values: laser power 100 W, scanning speed 50 mm/s for the volume contour, laser power 175 W and scanning speed 1000 mm/s for the outer contour, a hatching of 0.3 mm, and a layer thickness of 75 µm. The scanning strategy was a stripe hatching. These optimized parameters were applied for the production of bulk cylinders and dodecahedron unit cells as shown in Fig. 12. A relative density of around 99% and a fine grained nearly lamellar β microstructure was achieved. The mechanical performance of the samples is comparable to conventional cast samples. Heat treatment of the samples leads to the formation of γ phase.

Acknowledgements

This research was funded by the European Union and the Free State of Saxony (13795/2379) in the framework of the European Center for Emerging Materials and Processes (ECEMP). The authors are grateful to S. Donath for the execution of the casting experiments as well as S. Neumann for the conduction of the heat treatments.

References

- Anik, S., Dorn, L., 1995. *Schweißeignung metallischer Werkstoffe*. DVS Verlag.
- Appel, F., Oehring, M., Paul, J.D.H., 2006. Nano-scale design of TiAl alloys based on beta-phase decomposition. *Adv. Eng. Mater.* 8, 371–376.
- Biamino, S., Penna, A., Ackelid, U., Sabbadini, S., Tassa, O., Fino, P., Pavese, M., Gennero, P., Badini, C., 2010. Electron beam melting of Ti-48Al-2Cr-2Nb alloy: microstructure and mechanical properties investigation. *Intermetallics*.
- Boldsaikhan, E., Corwin, E.M., Logar, A.M., Arbegast, W.J., 2011. The use of neural network and discrete Fourier transform for real-time evaluation of friction stir welding. *Appl. Soft Comput.* 11, 4839–4846.
- Bourell, D.L., Marcus, H.L., Barlow, J.W., Beaman, J.J., 1992. Selective laser sintering of metals and ceramics. *Int. J. Powder Metall.* 28, 369.
- Childs, T.H.C., Hauser, C., Badrossamay, M., 2004. Mapping and modelling single scan track formation in direct metal selective laser melting. *CIRP Ann. Manuf. Technol.* 53, 191–194.
- Clemens, H., Chladil, H.F., Wallgram, W., Zickler, G.A., Gerling, R., Liss, K.D., Kremmer, S., Güther, V., Smarsly, W., 2008a. In and ex situ investigations of the beta-phase in a Nb and Mo containing beta-TiAl based alloy. *Intermetallics* 16, 827–833.
- Clemens, H., Wallgram, W., Kremmer, S., Güther, V., Otto, A., Bartels, A., 2008b. Design of novel β -solidifying TiAl Alloys with adjustable β /B2-phase fraction and excellent hot-workability. *Adv. Eng. Mater.* 10, 707–713.
- Gerling, R., Clemens, H., Schimansky, F.P., 2004. Powder metallurgical processing of intermetallic gamma titanium aluminides. *Adv. Eng. Mater.* 6, 23–38.
- Guoqing, C., Binggang, Z., Wei, L., Jicai, F., 2011. Crack formation and control upon the electron beam welding of TiAl-based alloys. *Intermetallics* 19, 1857–1863.
- Gusarov, A.V., Yadroitsev, I., Bertrand, P., Smurov, I., 2007. Heat transfer modelling and stability analysis of selective laser melting. *Appl. Surf. Sci.* 254, 975–979.
- Hussein, A., Hao, L., Yan, C., Everson, R., 2013a. Finite element simulation of the temperature and stress fields in single layers built without-support in selective laser melting. *Mater. Design* 52, 638–647.
- Hussein, A., Hao, L., Yan, C., Everson, R., Young, P., 2013b. Advanced lattice support structures for metal additive manufacturing. *J. Mater. Process. Technol.* 213, 1019–1026.
- Kremmer, S., Chladil, H., Clemens, H., Otto, A., Güther, V., 2008. Near conventional forging of titanium aluminides. *Jpn Inst. Metals* 6, 989–992.
- Kruth, J.P., Froyen, L., Vaerenbergh, J.V., Mercelis, P., Rombouts, M., Lauwers, B., 2004. Selective laser melting of iron-based powder. *J. Mater. Process. Technol.* 149, 616–622.
- Kruth, J.P., Mercelis, P., Van Vaerenbergh, J., Froyen, L., Rombouts, M., 2005. Binding mechanisms in selective laser sintering and selective laser melting. *Rapid Prototyp. J.* 11, 26–36.
- Löber, L., Flache, C., Petters, R., Kühn, U.J.E., 2013. Comparison of different post processing technologies for SLM generated 316l steel parts. *Rapid Prototyp. J.* 19, 173–179.
- Löber, L., Klemm, D., Kühn, U., Eckert, J., 2011. Rapid manufacturing of cellular structures of steel or titaniumalumide. *Mater. Sci. Forum* 690, 130.
- Louvis, E., Fox, P., Sutcliffe, C.J., 2011. Selective laser melting of aluminium components. *J. Mater. Process. Technol.* 211, 275–284.
- Mumtaz, K.A., Erasenthiran, P., Hopkinson, N., 2008. High density selective laser melting of Waspaloy®. *J. Mater. Process. Technol.* 195, 77–87.
- Nichols, F.A., Mullins, W.W., 1965. Surface-(Interface-) and volume-diffusion contributions to morphological changes driven by capillarity. *Trans. Metall. Soc. AIME* 233, 1840–1848.
- Niu, H.J., Chang, I.T.H., 1999. Instability of scan tracks of selective laser sintering of high speed steel powder. *Scr. Mater.* 41, 1229–1234.
- Rayleigh, L., 1878. On the instability of jets. *Proc. London Math. Soc* 10, 4.
- Schloffer, M., Iqbal, F., Gabrisch, H., Schwaighofer, E., Schimansky, F.-P., Mayer, S., Stark, A., Lippmann, T., Göken, M., Pyczak, F., Clemens, H., 2012. Microstructure development and hardness of a powder metallurgical multi phase γ -TiAl based alloy. *Intermetallics* 22, 231–240.
- Schweighofer, E., Schloffer, M., Schmoelzer, T., Mayer, S., Lindemann, J., Guether, V., Klose, J.H.C., 2011. Microstructural optimization of a cast and hot-isostatically pressed TNM alloy by heat treatments. In: 4th international TiAl Workshop, Nueremberg.
- Tolochko, N.K., Mozzharov, S.E., Yadroitsev, I.A., Laoui, T., Froyen, L., Titov, V.I., Ignatiev, M.B., 2004. Balling processes during selective laser treatment of powders. *Rapid Prototyp. J.* 10, 78–87.
- Voice, W.E., Henderson, M., Shelton, E.F.J., Wu, X., 2005. Gamma titanium aluminide TNB. *Intermetallics* 13, 959–964.
- Wu, X.H., 2006. Review of alloy and process development of TiAl alloys. *Intermetallics* 14, 1114–1122.
- Yadroitsev, I., Bertrand, P., Smurov, I., 2007. Parametric analysis of the selective laser melting process. *Appl. Surf. Sci.* 253, 8064–8069.
- Yadroitsev, I., Gusarov, A., Yadrotsava, I., Smurov, I., 2010. Single track formation in selective laser melting of metal powders. *J. Mater. Process. Technol.* 210, 1624–1631.
- Yadroitsev, I., Krakhmalev, P., Yadrotsava, I., Johansson, S., Smurov, I., 2013. Energy input effect on morphology and microstructure of selective laser melting single track from metallic powder. *J. Mater. Process. Technol.* 213, 606–613.

See discussions, stats, and author profiles for this publication at: <https://www.researchgate.net/publication/280573199>

Comparison of selective laser and electron beam melted titanium aluminides

Conference Paper · July 2011

CITATIONS
64

READS
3,124

7 authors, including:



Lukas Löber
Hochschule Esslingen
16 PUBLICATIONS 1,179 CITATIONS

[SEE PROFILE](#)



Sara Biamino
Politecnico di Torino
150 PUBLICATIONS 2,477 CITATIONS

[SEE PROFILE](#)



Ulf Ackelid
Freemelt AB
36 PUBLICATIONS 1,092 CITATIONS

[SEE PROFILE](#)



Paolo Fino
Politecnico di Torino
177 PUBLICATIONS 3,699 CITATIONS

[SEE PROFILE](#)

Some of the authors of this publication are also working on these related projects:



STAMP (Sviluppo Tecnologico dell'Additive Manufacturing in Piemonte) [View project](#)



Borealis - the 3A energy class Flexible Machine for the new Additive and Subtractive Manufacturing on next generation of complex 3D metal parts [View project](#)

COMPARISON OF SELECTIVE LASER AND ELECTRON BEAM MELTED TITANIUM ALUMINIDES

L. Loeber¹, S. Biamino², U. Ackelid³, S. Sabbadini⁴, P. Epicoco², P. Fino², J. Eckert¹

¹Leibniz Institute for Solid State and Materials Research Dresden

²Politecnico di Torino

³Arcam AB

⁴Avio SpA

Abstract

In the following paper we present the investigation of microstructure and mechanical properties produced by selective laser melting (SLM) and electron beam melting (EBM). The chosen alloy is a Ti-(46-48)Al-2Cr-2Nb alloy which has a great potential in replacing heavy weight Ni-base superalloys in turbine blades. Cylindrical specimens were produced and characterized by optical microscopy (OM), scanning electron microscopy (SEM) and chemical analysis to determine the microstructure and composition. In addition compression tests at room and elevated temperatures (700-800 °C) were carried out to identify the mechanical properties of the alloy.

Introduction

Titanium Aluminides (TiAl) alloys exhibit a wide range of interesting properties which makes them a good candidate for exchanging heavy weigh Nickel-based superalloys in jet turbine engines. They poses an excellent high temperature behavior in terms of strength, oxidation resistance, creep resistance and high melting point, while their density is only half as the one of Nickel [1-4]. Their poor room temperature ductility and their high reactivity with other materials makes them difficult to process [5,6]. Cost and time intensive methods like isothermal forging or special types of casting have to be used to produce useable parts.

The process technology of additive manufacturing is known for polymers like Polyethylene for almost 30 years now. Only recently with the possibilities of high power lasers the technology has been adapted to metallic and ceramic materials [13]. This development lead to the additive manufacturing technologies of selective laser melting (SLM) and electron beam melting (EBM). The high energy source allows it to melt and micro weld metallic or ceramic powder. The principle work process of all additive manufacturing techniques is quite similar. Starting with a thin powder layer an energy source is focused on specific local areas of the powder layer. The energy source can be a laser, electron beam or in case of polymers a simple light source. The energy input has to be high enough to micro weld the powder to a substrate plate and to micro weld the different powder layers together. This three step iterative process can be seen in Figure 1. The contact to the substrate plate is essential as this contact ensures the mechanical stability but mainly to guarantee good heat dissipation. In a second step the building platform is lowered by the layer thickness and finally a coating device applies a new layer of powder and the process starts over again. This three step work principle is iteratively repeated until the desired part is layer wise built.

The main benefit of additive manufacturing is the high amount of possible complex geometries. Almost every thinkable complex structure can be built. Examples are back tapers, cooling channels or special lattice structures. Even structures which other processing technologies can not build are possible to build with additive manufacturing. Another advantage is the complete use of the material. Powder which is not melted into the

parts can be sieved and used again. In contrast to subtractive manufacturing techniques where usually the process starts with a dense block and during the process material is taken away to create the desired part thus creating a lot of waste material like turnings. Additive manufacturing uses almost only the needed material for the parts and no waste material is created. As the selective laser melting is one of the younger process technologies the methods has only been applied to a clear number of materials like tool steels, stainless steels, aluminum alloys, Inconel, Cobaltchrome or some titanium alloys. In this work the adaption to the material class of titanium aluminides is presented. As there are already some publications about electron beam melting of titanium aluminides and the techniques are quite similar to another this work tries to compare both techniques on this special material.

As there are no existing process parameters for TiAl for SLM, an average between Titanium and Aluminum with the respect to the different heat conductivities, melting points and heat capacities for an orientation point was chosen for starting parameters. The following formula of the energy impact was used to produce different specimens with different energy impacts:

$$E_i = \frac{P}{v \cdot x \cdot h}$$

Where E_i is the energy impact in J/mm^3 , P is the laser power in W , v is the scanning speed of the laser in mm/s , x is the hatching of the laser tracks in mm and h is the layer thickness in μm . A high energy input mostly leads to a higher density of the parts. But with higher energy input the amount of residual thermal stresses also rises and as the room temperature ductility of TiAl is low a critical value should not be exceeded.

Some additional remarks have to be given to enlighten the main differences between SLM and EBM while processing TiAl. Both names already gives account to the main difference of both processes: while at SLM the energy source to melt and micro weld the powder is a laser the energy source of EBM is a focused electron beam. This main difference in the general set up of the machines lead to additional differences during the actual building. While an electron beam of high quality needs a good vacuum, usually in the range of 10^{-3} Pa, the whole building space has to be set under vacuum during the building. The laser is much less affected by the atmosphere so SLM only works with an inert gas, normally argon or nitrogen, in special cases also helium. Working with a vacuum has some major benefits like a clean environment, which is especially important while working with reactive elements like titanium. But it also helps to outgas impurities incorporated in the metal powder and gives a good thermal insulation. Another benefit is the possible high scanning rate of the electron beam to preheat the powder. The EBM machine has the capability of heating the powder up to 1100°C . This advantage is quite crucial as the room temperature ductility and the fracture toughness of TiAl is quite low. The material exhibits a brittle-ductile transition between 700 - 800°C [10,11].

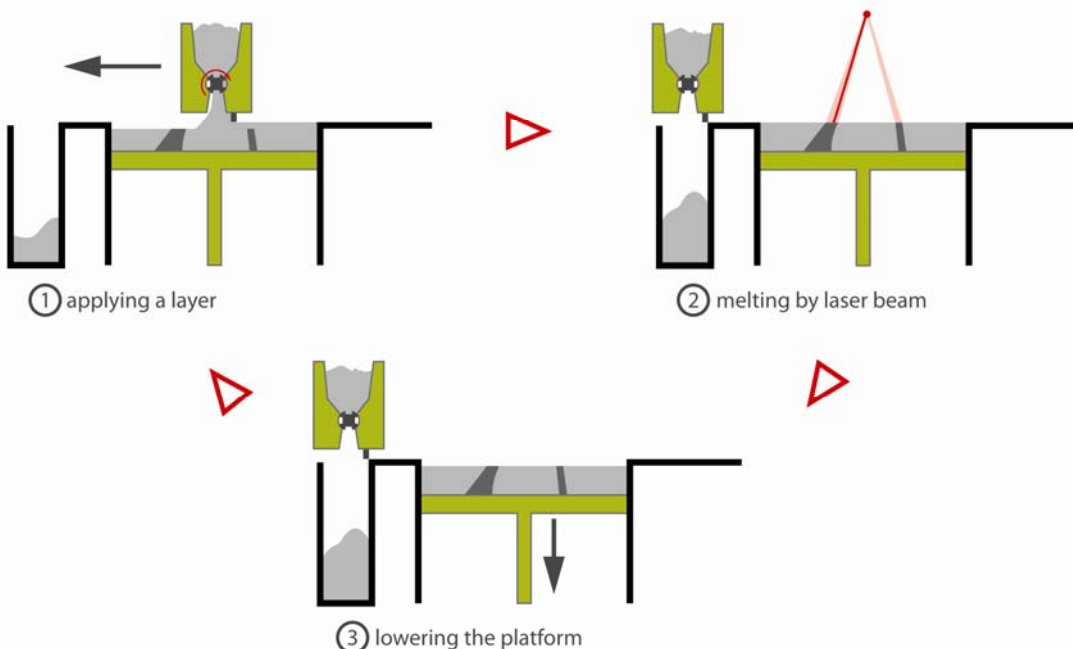


Figure 1 Three step iterative process of additive manufacturing

Materials and Methods

Simple cylinders with the dimensions of 5 mm diameter and 20 mm in height were created with a CAD program and then built in batches of 10 with a SLM 250 hl (SLM Solutions). The used gas atomized powder can be seen in Figure 2 a. The machine is equipped with a 400 W Yb-YAG fiber laser. The machine is also equipped with two oxygen sensors to ensure a low oxygen content during the building process as titanium is highly reactive with oxygen and titanium aluminides tend to lose their mechanical performance when they reach critical oxygen content [7,8]. Before starting the process itself the building chamber is flooded with 99,999% pure argon until a value below 0,02 % oxygen is reached. During the building of the specimens the building space was constantly flooded with argon ensuring a low oxygen content. With this process an oxygen content of around 100 ppm could be achieved. The specimens were directly built on a substrate plate without any further support structure which is normally used. The substrate plate had the same composition as the powder material: Ti-48Al-2Cr-2Nb and was micro pent before the process to ensure a good adhesion of the powder. The energy inputs of the specimens were chosen to be between 10-21 J/mm³. The laser power lied between 100-175 W, the layer thickness was set constant to 100 µm as the gas atomized powder has a powder size distribution of 45-100 µm and the layer thickness should not undercut the maximum powder size. The hatching was chosen to be between 110 µm and 150 µm.

The experimental conditions for building the EBM parts can be found elsewhere [9].

Both types of specimens of EBM and SLM have been characterized via optical microscopy and electron microscopy to determine the microstructure. Additional characterization of the chemical composition and the porosity has been made. Both types of specimens have been analyzed twice by the different institutes. The chemical composition was assessed by means of inductively coupled plasma (ICP), infrared adsorption and/or thermal conductivity (LECO instrument) in both institutes. Specimens for optical microscopy analysis were prepared by polishing and etching in Kroll's reagent, in order to investigate microstructure and porosity content. The porosity has been quantified according ASTM E 2109-01, while the amount of lamellar phase according ASTM E 562-01. The density of the SLM specimens were conducted via three types of density measurement: by simply measuring and scaling the specimens (geometric method), by the Archimedes method and by an area analysis of the polished samples. Mechanical testing in terms of compression test has been conducted with an Instron 8549. Additional compression tests at elevated temperatures have been carried out on the EBM specimens. For this measurement the cylinders have been electric eroded to smaller cylinders with a diameter of 3 mm and a height of 5-6 mm.

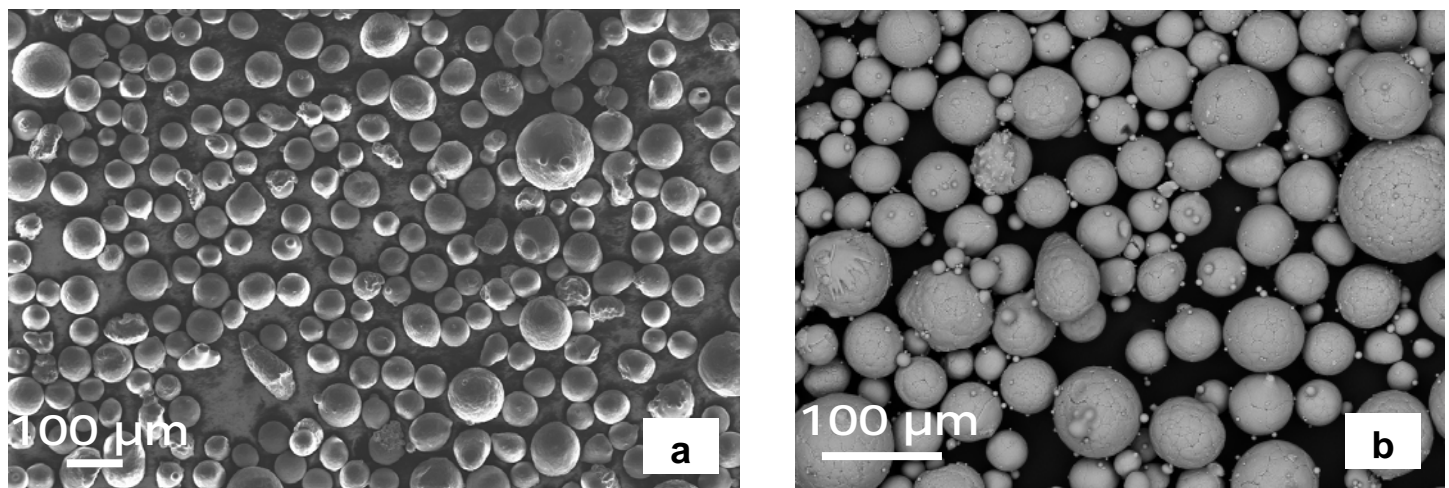


Figure 2. a SEM picture of the used powder for EBM and b SEM picture of the used powder for SLM

Results and discussion

The chemical composition of the base material of the SLM process, both powder types and both SLM and EBM specimens can be found in Table 1. It can be seen that the amount of impurities of the EBM powder is not changed during the building. It can be assumed that the vacuum helps to keep the amount of pick-up of these elements down. Both the amount of oxygen and the amount of nitrogen lie beneath the critical amount of around 1000 ppm for oxygen and 600 ppm for nitrogen. The composition of the SLM material could already be conducted with the base material. The amount of impurities in the SLM material and powder are in the same range as the EBM powder. The amount of nitrogen and oxygen are a little lower in the starting material. As the gas atomization is conducted in inert atmosphere and with a crucible free method the amount of impurities during this process is kept to minimum. Only the amount of oxygen was determined in the SLM powder, as the oxygen content has the biggest influence on the mechanical properties. It can also clearly be seen, that in contrary to the EBM process were no additional oxygen impurity arises during the process, the SLM process with its inert argon atmosphere leads to higher oxygen content in the SLM specimen. This is quite understandable, as even the purest argon still contains much more oxygen than a good vacuum. On the other hand can the vacuum of the EBM process lead to a higher evaporation of lighter elements such as aluminum. But the variation of the aluminum content of the EBM powder and specimen is around 0.3 wt.% and is thus not considered to have an influence. It is curious that the variation of Aluminum in the SLM specimens is further reduced by 0.1 wt% compared to the one of the EBM. The only explanation for this occurrence is that the energy input of the laser is not yet calibrated well enough thus leading to evaporation effects of the Aluminum. The chemical analyses were conducted on different places of the specimens to determine the homogenous distribution of the elements. The variation in the composition varied below 0.2 wt.% and is also considered to have no effect. The amount of the alloying elements such as Nb and Cr does not change.

Table 1. Chemical composition of the powder as received and the specimens

Elemental chemical composition in wt.%								
	Al	Cr	Nb	Fe	O	N	C	Ti
EBM powder (as received)	34.1	2.4	4.8	0.03	0.06	0.004	0.005	balance
EBM specimen	33.4	2.2	5.1	0.03	0.06	0.006	0.007	balance
SLM material (as received)	32.9	2.6	4.8	0.056	0.034	0.001	0.004	balance
SLM powder (as received)	32.7	2.6	4.8	-	0.05	-	-	balance
SLM specimen	32.3	2.6	4.8	-	0.08	-	-	balance

The amount and type of porosity has the biggest influence on the mechanical properties. The EBM process parameters have been adapted to produce a free macropore material. In the EBM material only one type of small pores still occur caused by entrapped argon gas during the gas atomization. The amount of residual porosity lies below 2.0 % and can further be reduced via hot isostatic pressing to below 1.0 %. The porosity of the SLM specimens looks a lot different. As these are the first specimens build with this technology the process parameters are not fully optimized leading to a much higher residual porosity. Still two types of defects can be determined. Regarding Figure 3.a it can be seen that there are simply some regions where the energy input was not high enough to melt all the powder leading to big porous areas with partially molten or unmolten powder around it reflected by the dark areas, especially in the outer region of Figure 3.b. On the other hand a great amount of cracks can be found in the whole specimen. It can be assumed that the contrary to the too low energy input leading to the bigger pores in some regions the energy input seems to be too high leading to thermal tensions which are not tolerated by the material and thus resulting in thermal induced cracks. Figure 4 shows the relative density in dependence of the used energy input of the different specimens. A clear tendency to higher

density with a higher energy input is visible for the SLM specimens. An asymptotic behavior can be observed. For the EBM specimens no value for energy input can be given. The difference in the three means of measurement for the density can be explained by the following reasons. The area analysis delivers at lower density even lower values of density. This effect is caused by the necessary metallographic preparation of the specimens which can cause nicks. At higher values this effect is minimized as fewer defects cause fewer nicks. The Archimedes method delivers higher values of density over the whole spectrum as the geometric method. This effect is probably caused by the closed porosity which causes wrong buoyancy during the scaling in water. Overall it can be stated that the density of SLM parts can achieve a maximum density of around 97% which is much less than their counterparts produced by EBM. A further optimization of the SLM process parameters have to be conducted in the future to improve the density.

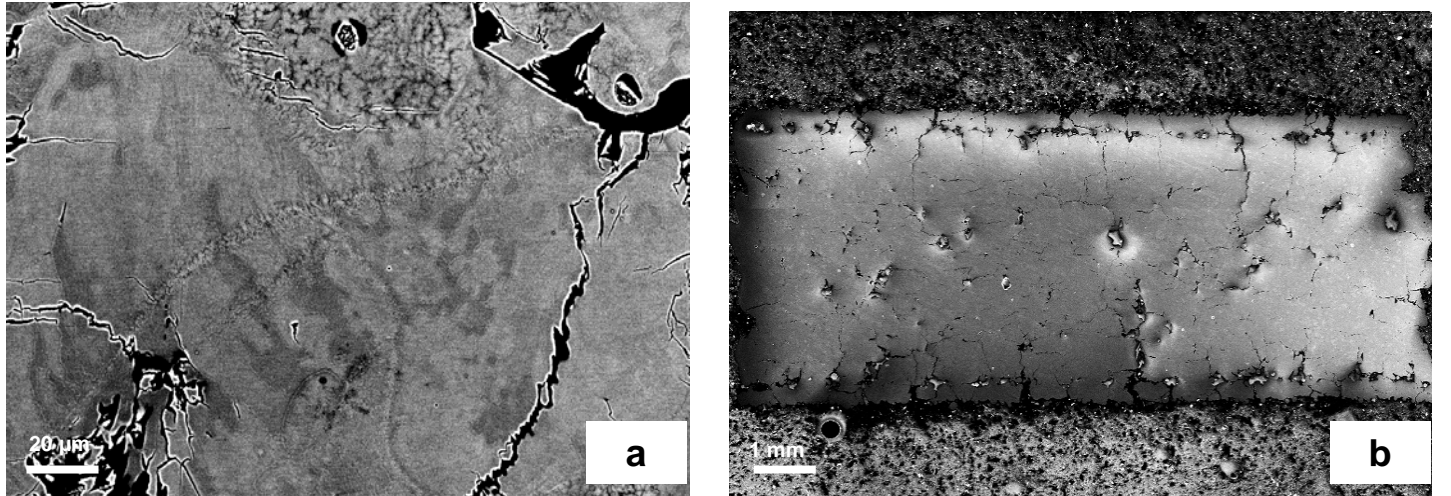


Figure 3: a Detailed SEM BSE picture of the SLM produced cylinder and b SEM overview of a whole cylinder cut in half

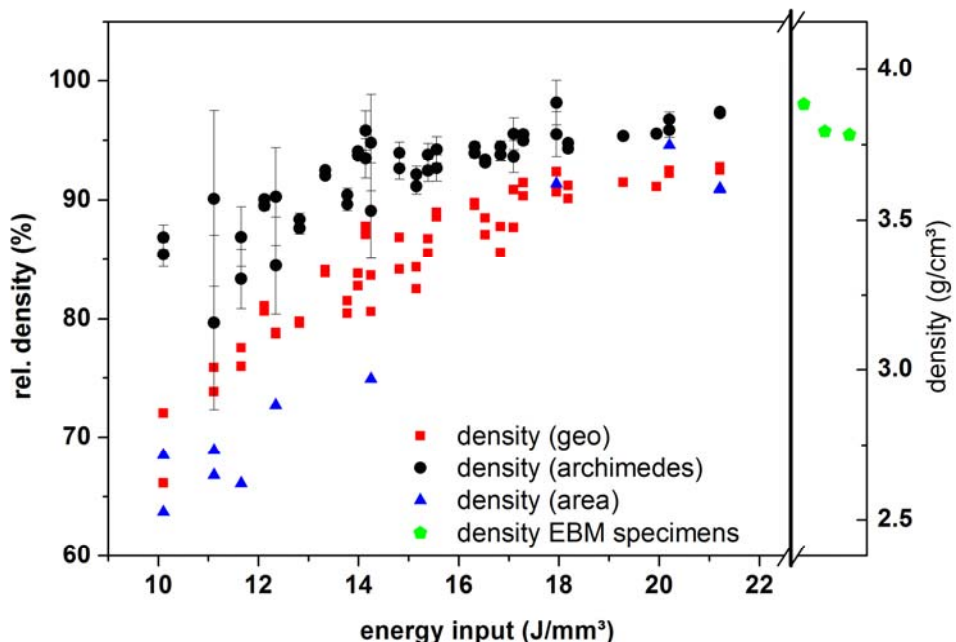


Figure 4. Relative and absolute density in dependence of the energy input of the produced SLM parts via geometric, Archimedes and area method and relative and absolute density of the EBM specimens before hipping

The surface of both EBM and SLM produced specimens can be seen in Figure 5. Both technologies are powder based and the energy input is localized on a small spot. This leads to partially molten powder which is fused with the surface. This effect is also responsible for the normally high surface roughness of EBM or SLM produced parts [14]. A post process like shot penning or simple grinding and polishing can be used to improve

the surface roughness. In the picture of the SLM produced specimens horizontal surface cracks can be observed. Compared with Figure 3.b it is notable that at the outer region of the specimens the cracks are horizontal while in the inner volume the cracks are vertical to the building direction. The horizontal outer cracks are probably caused by a wrong parameter choose for the contour. While the inner perpendicular cracks are caused by the effect the work principle of the technology that a hot layer is fused on a cold layer causing thermal and mechanical tensions. Both crack types are thus caused by too high thermal tensions which released in these cracks. The EBM produced surface on the other hand underlines the result from the density measurement that the parts are almost completely dense. No defects like open porosity or cracks can be found. A sort of repeating relief can be observed. This results from the bigger layer thickness in the EBM process.

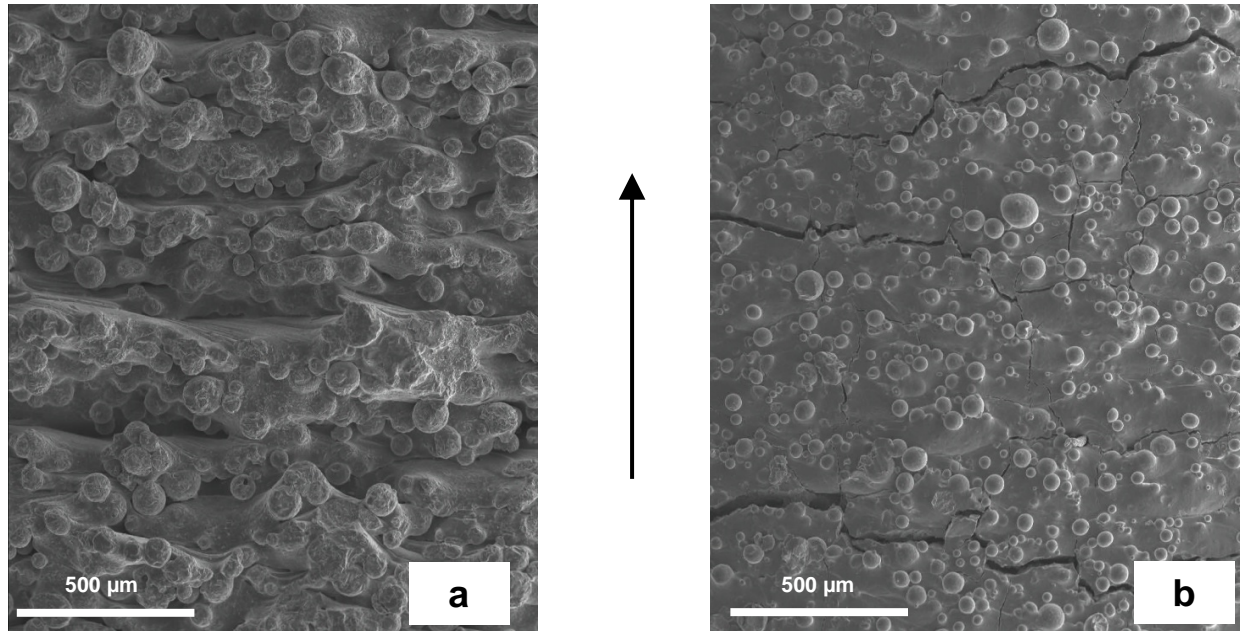


Figure 5: SEM picture of the surface of the specimens a) EBM, b) SLM (the arrow indicates the building direction)

Figure 6 shows the microstructure of both EBM and SLM produced specimens. The EBM specimen (Figure 6.a) clearly shows a fine bimodal microstructure alternated to some zone of bigger equiaxed grains generally under the secondary electron (SE) contrast. The zones of bigger (but still below 50 μm) typically follow the layerwise growing of the sample. In Figure 6.c this zones a mainly parallel to layers. The grain size is small which can be explained through the small size of the focused electron beam which leads to a rapid cooling. The SLM specimen on the other hand shows no clear microstructure under the SE contrast. No clear statement of the as-produced SLM microstructure can be made. However some features of the microstructure can be observed. Figure 3.a shows the microstructure under back scattered electron contrast (BSE). In the upper part of the figure an extreme fine dendritic structure can be seen. This is the original microstructure of the gas atomized powder which is also a rapid cooling process. This feature reflects the powder particles which are only molten on the surface while the volume keeps its original microstructure. Through the middle of the picture a line of fine small columnar grains can be seen. This structure reflects the connection of different layers which can be described as the melt track. In addition some darker areas can be seen in the picture. These are either caused by minor fluctuation of the element content on the micro level or caused by different orientations of the grains. In addition to this Figure 6.d) shows again the horizontal cracks at the outer region of the specimen and some pores with unmolten powder in it which underlines again the theory that the building parameters are yet to be optimized.

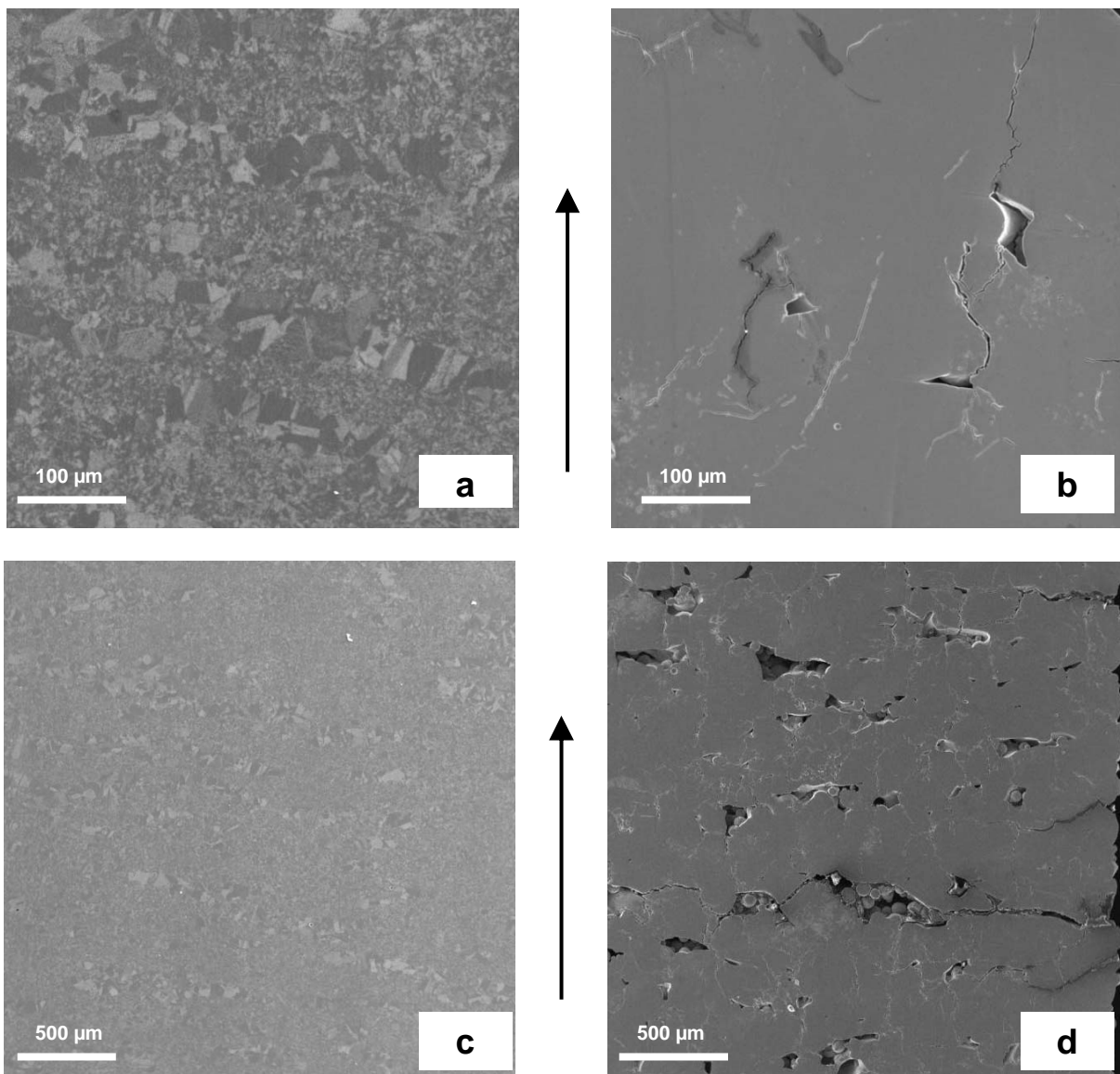


Figure 6: SEM picture of the microstructure of one of the a) EBM produced and b) SLM produced cylinders and more detailed picture of the same c) EBM specimen and d) SLM specimen (the arrow indicates the building direction)

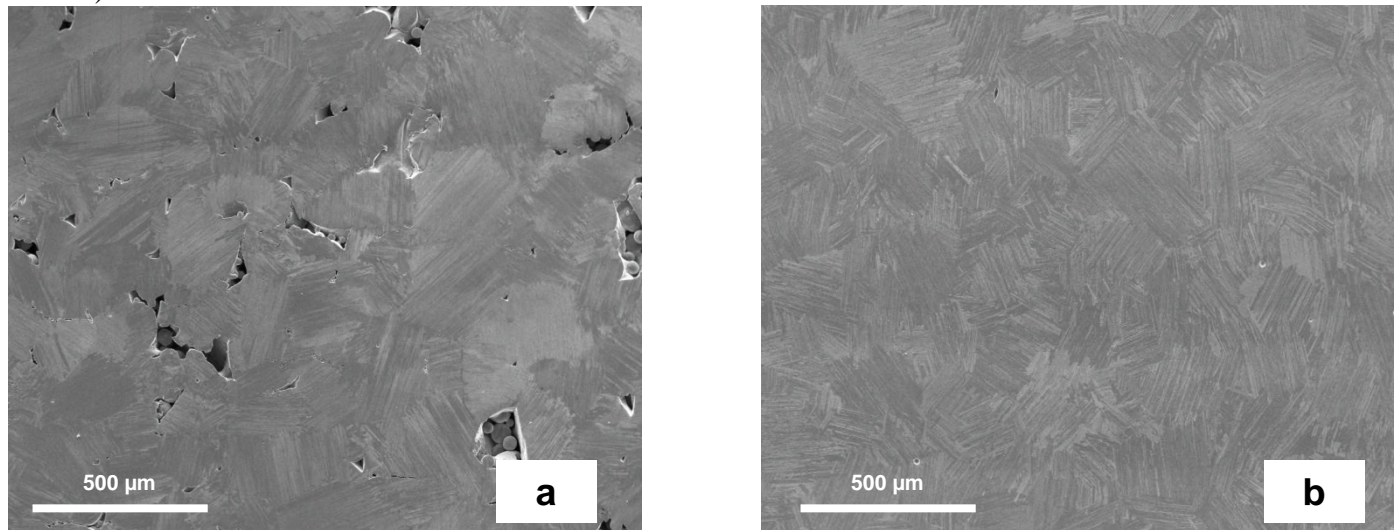


Figure 7: SEM picture of the micromicrostructure of one of the a) EBM produced and b) SLM produced cylinders after heat treatment

As no clear distinction in the microstructure of the SLM specimens could be made and thus no real comparison of SLM and EBM produced microstructure could be made, both types of specimens were treated with a heat treatment. In Figure 7 the microstructure of both EBM and SLM specimens after the heat treatment of 2h at 1400°C (above the alpha transition temperature) can be seen. It can be observed that both samples have changed into the same fine lamellar microstructure. The pores caused by unmolten powder can still be observed in the SLM microstructure.

Seven of the as-produced SLM specimens and eleven of the as-produced EBM specimens were mechanically tested under quasi static compression. Compression test were chosen instead of tensile testing because of the simpler testing geometry. For compression simple cylinders are sufficient while using tensile test complex tensile bars have to be produced or eroded out of a cylinder. The SLM specimens were only tested at room temperature as their high porosity already lead to poor results at room temperature. The EBM specimens were tested at room temperature (red curves; 2 specimens), at 700°C (blue curves; three specimens), at 800°C (rose and turquoise curve; three specimens) and at 850°C (green curves, three specimens). The poor results of the SLM specimens are not surprising when regarding the density values of the specimens of around 90%. The Young's Modulus could be estimated to an arithmetic value of 50 ± 13 GPa which is around a third of the normal value. It is not surprising that the Young's modulus is much smaller than expected as compression testing delivers normally a much smaller Young's modulus than tensile testing. Also the ultimate compressive stress lies with a value of 612 ± 56 MPa far beyond normal results of titanium aluminides [12]. The compressive strain of $1.98 \pm 0.55\%$ would be a good result for tensile testing but compression testing normally generates values of up to 20-30%. The overall performance of the SLM parts in the mechanical testing can very well be explained through the poor values of density. Further studies of the mechanical properties are not performed until the density can be enhanced to higher values.

The results from the EBM specimens then again show some really difference to the SLM specimens. At room temperature they achieve an ultimate compressive stress value of 1800 MPa which is in good agreement with other publications. The compressive strain of the samples however exceed the normal values of 20%. Also at higher temperatures the values of the compressive strain stay this high. The values for the ultimate compressive stress at higher temperatures (see Table 2) lie beneath the typical values from the literature. This effect results probably from the small grain size which makes the material at higher temperature more vulnerable to the effects of creep. The compressive strain values stay mostly at the same high level. It has to be taken in account, that the value of 15% for 850°C is the arithmetic mean of 33%, 8% and 6%. So even at high temperatures some specimens still perform at high levels while others fail much earlier. The Young's modulus at room temperature delivers the same value as the one of the SLM specimens. With higher temperature the value drops to 32 GPa.

Table 2: Results from the compression tests of the EBM specimens at room and at higher temperature

Temperature (°C)	Young's Modulus (GPa)	Ultimate compressive stress (MPa)	Stress at offset yield (MPa)	Compressive strain (%)
RT	54	1800	544	40
700	42	810	460	31
800	32	540	419	33
850	39	418	339	15

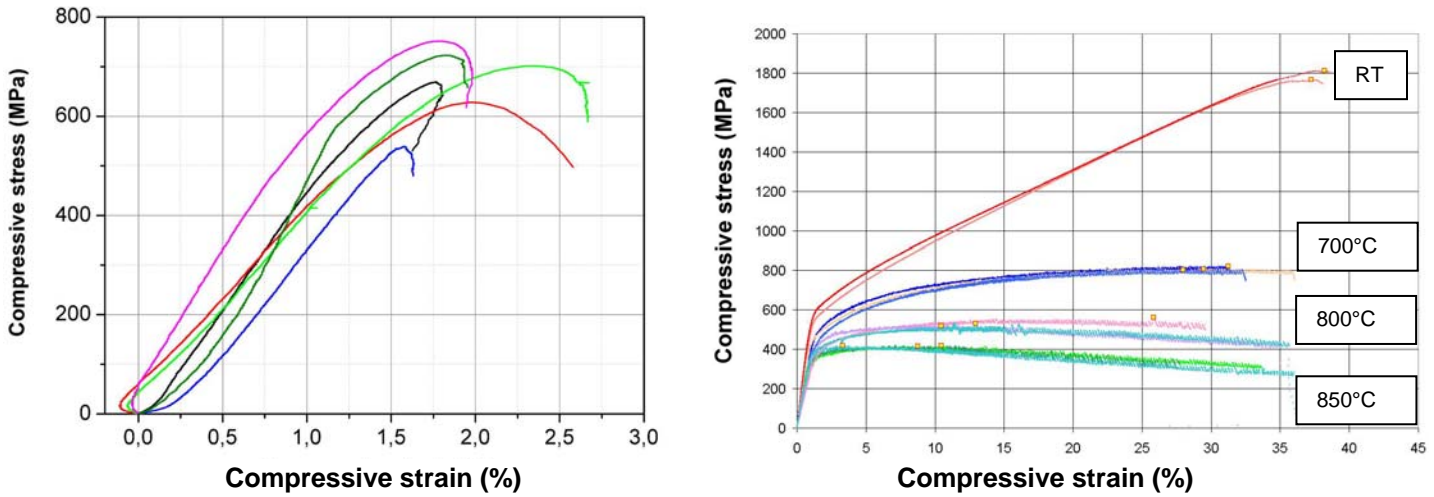


Figure 8 Results of the compression test a at room temperature of the as produced SLM specimens and b of the as produced EBM specimens at room temperature and at 700, 800 and 850°C

Summary and Conclusion

In this work we presented the differences between SLM and EBM produced cylindrical specimens of Ti-(46-48)Al-2Cr-2Nb. Although both processes are fairly similar to each other the results from the two techniques vary. With EBM working under a vacuum and with preheated powder the results in density exceeds the one of SLM. EBM produced specimens showed an as produced density of around 98 % density with only small spherical pores. With additional hipping of the specimens the density can be enhanced to a value of >99 %. The microstructure of the EBM specimens exhibits a bimodal microstructure. An altering pattern of bigger (still smaller than 50 µm) and smaller (below 10 µm) grains can be observed. The mechanical properties of the EBM specimens under compression are comparable to those produced by conventional techniques. The SLM produced microstructure is difficult to determine as pores and cracks do lead to a lost in contrast under SE contrast. Under BSE contrast different features such as unmolten areas or melt tracks can be observed. The maximum achievable density up till now lies around 97 %. But as the residual porosity is caused by cracks in the structure the mechanical performance under compression is poor.

So fare the EBM process with preheating of the powder and the vacuum surrounding during building seems to fit better for the additive production of TiAl. In the future a main focus has to be set on the optimization of the process parameters of the SLM process and the implementation of a heater to reduce thermal tension during cooling.

References

- [1] S. Herter: Spanbildung und Randzonenbeeinflussung beim Drehen intermetallischer Titaniumaluminide. thesis (2010) Technische Universität Berlin
- [2] Loria EA. Quo vadis gamma titanium aluminide. *Intermetallics* 2001;9:997-1001.
- [3] Appel F, Oehring M, Wagner R. Novel design concepts for gamma-base titanium aluminide alloys. *Intermetallics* 2000;8:1283-312
- [4] I. Shishkovsky, Y. Morozov, I. Smurov: *Applied Surface Science* 2009; 255, 5565
- [5] C. Leyens: *Titan und Titanlegierungen* Wiley-VCH, Weinheim, 2002, 380
- [6] Wu X. Review of alloy and process development of TiAl alloys. *Intermetallics* 2006;14:1114-22.

- [7] Lamirand M, Bonnantien JL, Ferrière G, Guérin S, Chevalier JP. Properties of Ti-48Al-2Cr-2Nb with fully lamellar and duplex microstructure. Metallurgical and Materials Transactions A 2006;37:2369-78.
- [8] Lasalmonie A. Intermetallics: why is it so difficult to introduce them in gas turbine engine. Intermetallics 2006;14:1123-9.
- [9] S. Biamino, A. Penna, U. Ackelid, S. Sabbadini, O. Tassa, P. Fino, M. Pavese, P. Gennaro,C. Badini Electron beam melting of Tie48Ale2Cre2Nb alloy: Microstructure and mechanical properties investigation
- [10] Hu D. Effect of composition on grain refinement in TiAl-based alloys. Intermetallics 2001;9:1037-43.
- [11] Wu X. Review of alloy and process development of TiAl alloys. Intermetallics 2006;14:1114-22.
- [12] M.Shazly, V. Prakash, S.Draper, Mechanical behavior of Gamma-Met PX under uniaxial loading at elevated temperatures and high strain rates, International Journal of Solids and Structures 2004, 41; 22-23 :6485-6503
- [13] Kruth, J.P., Froyen, L., Van Vaerenbergh, J., Mercelis, P., Rombouts, M., & Lauwers, B. 2004. Selective laser melting of iron-based powder. Journal of Materials Processing Technology, 149, (1-3) 616-622
- [14] I. Yadroitsev, I. Smurov, Surface Morphology in Selective Laser Melting of Metal Powders, Physics Procedia, Volume 12, Part 1, Lasers in Manufacturing 2011 - Proceedings of the Sixth International WLT Conference on Lasers in Manufacturing, 2011, Pages 264-270, ISSN 1875-3892

Fatigue performance of additive manufactured metallic parts

A.B. Spierings

Institute for Rapid Product Development (IRPD), INSPIRE – AG für mechatronische Produktionssysteme und Fertigungstechnik, St Gallen, Switzerland

T.L. Starr

Chemical Engineering Department, J.B. Speed School of Engineering, University of Louisville, Louisville, Kentucky, USA, and

K. Wegener

INSPIRE – AG für mechatronische Produktionssysteme und Fertigungstechnik, Zurich, Switzerland

Abstract

Purpose – Additive manufacturing technologies such as, for example, selective laser melting (SLM) offer new design possibilities for a wide range of applications and industrial sectors. Whereas many results have been published regarding material options and their static mechanical properties, the knowledge about their dynamic mechanical behaviour is still low. The purpose of this paper is to deal with the measurement of the dynamic mechanical properties of two types of stainless steels.

Design/methodology/approach – Specimens for dynamic testing were produced in a vertical orientation using SLM. The specimens were turned to the required end geometry and some of them were polished in order to minimise surface effects. Additionally, some samples were produced in the end geometry ("near net shape") to investigate the effect of the comparably rough surface quality on the lifetime. The samples were tension-tested and the results were compared to similar conventional materials.

Findings – The SLM-fabricated stainless steels show tensile and fatigue behaviour comparable to conventionally processed materials. For SS316L the fatigue life is 25 per cent lower than conventional material, but lifetimes at higher stress amplitudes are similar. For 15-5PH the endurance limit is 20 per cent lower than conventional material. Lifetimes at higher stress also are significantly lower for this material although the surface conditions were different for the two tests. The influence of surface quality was investigated for 316L. Polishing produced an improvement in fatigue life but lifetime behaviour at higher stress amplitudes was not significantly different compared to the behaviour of the as-fabricated material.

Originality/value – In order to widen the field of applications for additive manufacturing technologies, the knowledge about the materials properties is essential, especially about the dynamic mechanical behaviour. The current study is the only published report of fatigue properties of SLM-fabricated stainless steels.

Keywords Advanced manufacturing technologies, Fatigue, Stainless steel, Mechanical behaviour of materials, Additive manufacturing technologies, Selective laser melting, Direct metal laser sintering

Paper type Research paper

Introduction

Additive manufacturing (AM) technologies cover a wide range of layer-wise production processes, where the raw materials can be a fluid such as droplets (3D printing) or a resin bath (stereolithography), powders (selective laser sintering (SLS), selective laser melting (SLM), direct metal laser sintering (DMLS), electron beam melting (EBM)) or filaments (fused deposition modelling (FDM)). In all technologies, the development aims at widening the application areas by developing new materials and their processing windows, respectively, (Kruth *et al.*, 2004; Lopez *et al.*, 2008; Murr *et al.*, 2009; Niu and Chang, 1999; Ram *et al.*, 2008; Kumar, 2009;

Laoui *et al.*, 2000), and the optimisation of the material's integrity and part's quality. Thereby, the focus has mainly been put on the part density, the surface quality and their static mechanical properties (Sehrt and Witt, 2009; Spierings and Levy, 2009; Spierings *et al.*, 2011).

Today's evaluation of the state-of-the-art results in the conclusion that AM processes have already reached a certain level of maturity (Lan, 2009) and that some processes can be considered as entering a first stage of rapid manufacturing, where the parts produced are directly used for the end application. This is underlined by the observation that the layer-wise production of parts in diverse metallic materials (Badrossamay *et al.*, 2009; Levy *et al.*, 2003) becomes more

The current issue and full text archive of this journal is available at
www.emeraldinsight.com/1355-2546.htm



Rapid Prototyping Journal
19/2 (2013) 88–94
© Emerald Group Publishing Limited [ISSN 1355-2546]
[DOI 10.1108/13552541311302932]

The authors gratefully acknowledge Mr A. Frauchiger, who was responsible for the SLM production of the 316L specimens, and Messrs Christopher Scherzer and Alex Smith for the production of the 15-5PH specimens and for fatigue testing of the materials. The support of the US Office of Naval Research also is acknowledged.

Received: 18 April 2011

Revised: 15 December 2011, 13 March 2012

Accepted: 24 April 2012

and more interesting for diverse industrial sectors such as, e.g. medical (Murr *et al.*, 2009; Kruth *et al.*, 2005b, c; Rehme and Emmelmann, 2006; Vandenbroucke and Kruth, 2007; Hollander *et al.*, 2003) and aerospace, where a lot of effort is currently spent. For some materials, SLM parts are able to offer mechanical properties comparable to the properties of conventionally produced parts from bulk materials especially regarding their static mechanical properties (Abe *et al.*, 2001; Kruth *et al.*, 2005a; Rehme and Emmelmann, 2007).

However, for real AM, not only a high part density and good static mechanical properties are needed as typically the parts are dynamically loaded. Due to intensive costs of such measurements, currently there have been only few investigations into the dynamic mechanical behaviour of laser sintered parts. Sehrt and Witt (2010) published fatigue strength results of a SLM 17-4PH stainless steel under repeated bending. However, the samples have been produced in a horizontal orientation performing better results than in an upright orientation and the test setup was a rotating bending test, which is less severe than a tensile fatigue test. Furthermore, the results have not been compared to conventional standard materials, as a direct comparison of such experiments is difficult due to different possible experimental set-ups.

Therefore, for future investigations and a wider acceptance of the SLM-Technology in industry, more effort has to be spent for the dynamic mechanical behaviour of the processed materials in comparison to normal bulk materials. This paper investigates the S-N curves of two stainless steel types (316L, 15-5PH), processed using two different SLM machines from Concept Laser GmbH (Lichtenfels, Germany) and EOS GmbH (Munich, Germany). The focus of this work was on the comparison of the results of AM processed materials to the results of conventionally processed materials. The results point out that AM processed materials show some clear differences to conventional materials. However, knowing about the differences and the specific properties, the SLM process and the corresponding materials can be used for the production of parts for the real life in the sense of a rapid manufacturing. The fact of a lower dynamic strength of the investigated materials can be overcome by adapting the design of the parts in the sense of "Design for Additive Manufacturing" and using the wide degrees of freedom of design, resulting in lower stress concentration factors at the points of interest. Some first results of these investigations have already been discussed at the Solid Freeform Fabrication Symposium SFF 2010 in Austin, TX (Starr and Spierings, 2010).

Materials and methods

Two stainless steel materials were used for the production of specimens for dynamical tests: stainless steel 316L and 15-5PH. Cylindrical bars of these materials were built in a vertical orientation, i.e. the long axis perpendicular to the powder bed and the slice thicknesses were 30 µm for the 316L material and 20 µm for the 15-5PH material. The stainless steel 316L material was processed using a Concept Laser M1 machine, which is equipped with an Nd:YAG solid state laser with a maximal laser power of about 103 W. The scan strategy used to produce the samples in this study is a chessboard-like structure, where $5 \times 5 \text{ mm}^2$ are scanned. More details are described in Spierings and Levy (2009), Spierings *et al.* (2011), Lan (2009) and Badrossamay *et al.* (2009). The 15-5PH

material was processed with an EOS M270 equipped with a Yb-fiber laser with a maximum power of about 200 W. The scan parameters used were the EOS-recommended values for this material. The scan pattern was parallel stripes of 10 mm width. The orientation of the stripes was rotated for each layer. The 15-5PH bars were heat-treated at 482°C in air for 1 h and air cooled (condition H900). The particle size distributions of the powder materials and their processing parameters are characterized in Table I. The 15-5PH powder was obtained from EOS and is designated as their PH1 material. More details about the 316L material are given in Spierings and Levy (2009) and Spierings *et al.* (2011) – an overview about the material's static mechanical parameters is given in Table II, pointing out that their static properties are very much comparable or even better than the properties conventional materials.

Circular cross-section fatigue test specimens were turned from bars following ASTM E466 for specimens with a continuous radius between ends (Figure 1). Specimens for both materials had a minimum diameter of 3.0 mm. The continuous radius of the 316L bars was somewhat smaller than that of the 15-5PH bars, but both were greater than the ASTM-specified minimum.

One set of 316L specimens was fabricated to net shape and tested without any surface treatment except of a typical blasting operation used for SLM in order to clean the surfaces.

Fatigue testing within the high cycle fatigue (HCF) range ($N > \approx 10^4$) was performed at $R = 0.1$ using a 50 Hz sine cycle under load control to a maximum of 10^7 cycles (Instron Electropuls E10000 all-electric dynamic test machine). This test setup is more severe compared to a rotating bending test or a tension fatigue test at $R = -1$, which might be the typical load case in mechanical engineering – as the external loads always act crack-opened. Therefore, the test setup used here leads to lowest values defining a base line for the materials used in this study.

One set of 316L specimens was fabricated to net shape and tested without any surface treatment except of a typical blasting operation (Spierings *et al.*, 2011) used for SLM in order to clean the surfaces. Another set of 316L bars was hand polished after turning using a buffing wheel and rouge (CR1, Dico Products Corp., Utica, NY). Surface roughness

Table I Characterization of the powders used for the production of specimens for dynamical tests

	316L	15-5PH
Material parameters		
Manufacturer	A	EOS
D ₁₀ (µm)	7.1	30.1
D ₅₀ (µm)	15.1	39.7
D ₉₀ (µm)	24.2	53.6
Processing parameters		
Layer thickness (µm)	30	20
Laser power (W)	103	195
Scan speed (mm/s)	425	800
Hatch distance (mm)	0.13	0.10
Energy density (J/mm ³)	62	122

Note: The particle size distributions were not measured with the same measuring equipment

Table II Measured tensile strengths of laser sintered stainless steels are comparable to or higher than handbook values

Material	Source	Yield strength (MPa)	Ultimate tensile strength (MPa)	Elongation (%)
316L	Handbook	310	620	30
	SLM (Spierings <i>et al.</i> , 2011)	640	760	30
15-5 PH H900	Handbook	1,170	1,310	10
	SLM	1,100	1,470	15

Source: ASM Handbook (1993)

Figure 1 Machined dynamic test specimens, 316L

of 316L fatigue specimens was measured with a Dektak 8 Stylus Profiler (Bruker AXS, Inc., Madison, Wisconsin).

Results

After laser processing the 316L material showed an austenitic and the 15-5PH material a martensitic microstructure, as expected for these types of materials. A typical stress-strain curve for the two materials is shown in Figure 2.

S-N data ($R = 0.1$) for the austenitic 316L and the martensitic 15-5PH materials are shown in Figure 3 with 15 tests for the 316L and 12 tests for the 15-5PH. Both materials show log-linear behaviour, as expected. Even it is

known that face-centered cubic (FCC) materials like Austenite do not have a fatigue limit such a limit is taken for both materials as the highest stress at which the specimen did not fail after 10^7 cycles. For those specimens that failed, the normalized deviations from a log-linear fit are normally distributed (Figure 4(b)). The fatigue limit for the machined specimens of 255 and 849 MPa are 34 and 58 per cent, respectively, of the ultimate tensile strengths (UTS) of these two stainless steels, which were measured as 760 and 1,470 MPa (Table II).

The S-N data for the machined 316L specimens is plotted again in Figure 4 along with the results for the as-fabricated and the polished specimens. For fatigue life less than 10^6 there is no statistically significant difference among the three different surface finishes. However, the fatigue limit stress increases with decreasing roughness. The measured surface roughness (R_a) is 10.0, 0.4 and $0.1 \mu\text{m}$ for the as-fabricated, machined and polished specimens, respectively.

While the polished material shows the highest fatigue limit, the difference compared to the machined material is very small, but significant compared to the as-built specimens. While this may be due simply to the very low roughness of these machined specimens (Figure 4 right), the hand polishing method employed here may have been not homogeneous enough and therefore also limit the improvement observed. However, the standard error of the log-linear fit to the fatigue lifetime results is 0.16 (eight tests), 0.22 (12 tests) and 0.29 (12 tests) for the as-fabricated, machined and polished specimens, respectively.

Discussion

Both AM machines investigated here produce stainless steel alloys with properties at least partially comparable to those produced by conventional processing methods. Static properties are essentially identical. Fatigue performance is somewhat poorer (Figure 5); however, differences in alloy composition and surface finishing between the measured results for the AM manufactured specimens and the literature results for the metallurgically generated material make exact comparisons difficult.

Stainless steel 316L

Puchi-Cabrera investigated the HCF behaviour of annealed and polished 316L samples at $R = 0.1$ in a range of the maximal stresses between 400 and 476 MPa (Figure 5). The samples were notched (0.5 mm) with the purpose of exercising a better control on the nucleation of fatigue cracks.

Strizak *et al.* (2005) reports fatigue life of a 316LN alloy using test conditions similar to those reported here except for the frequency of 10 Hz instead of 50 Hz. The 316LN alloy is a nitrogen-strengthened austenitic alloy similar to 316L but

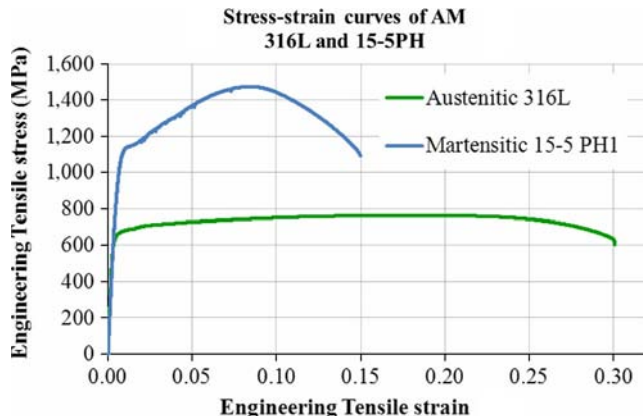
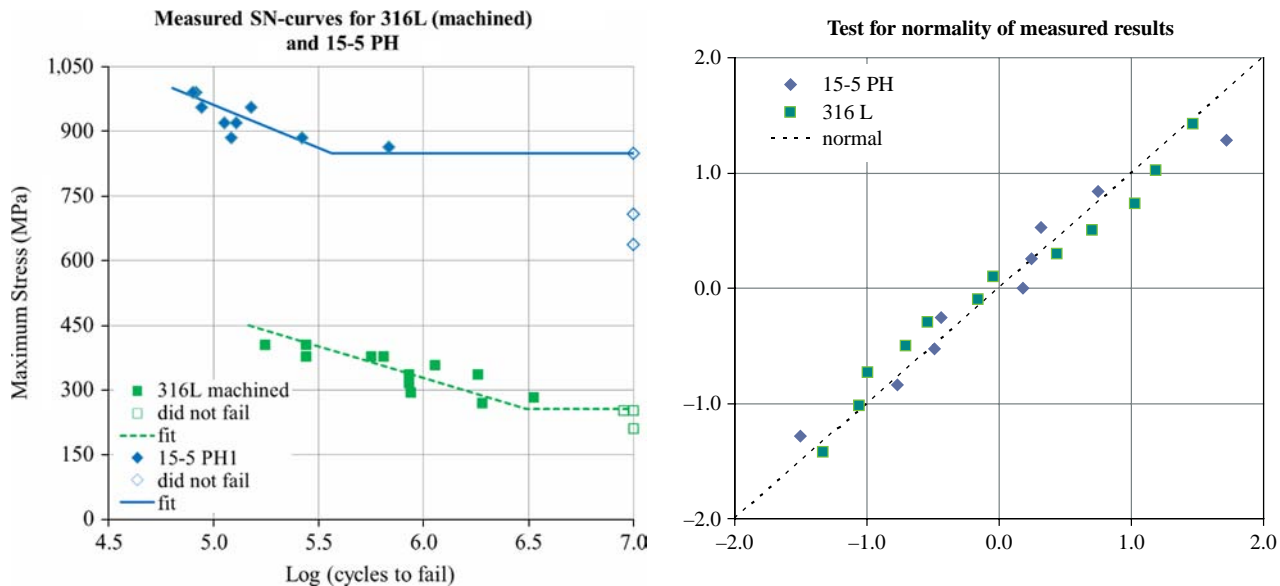
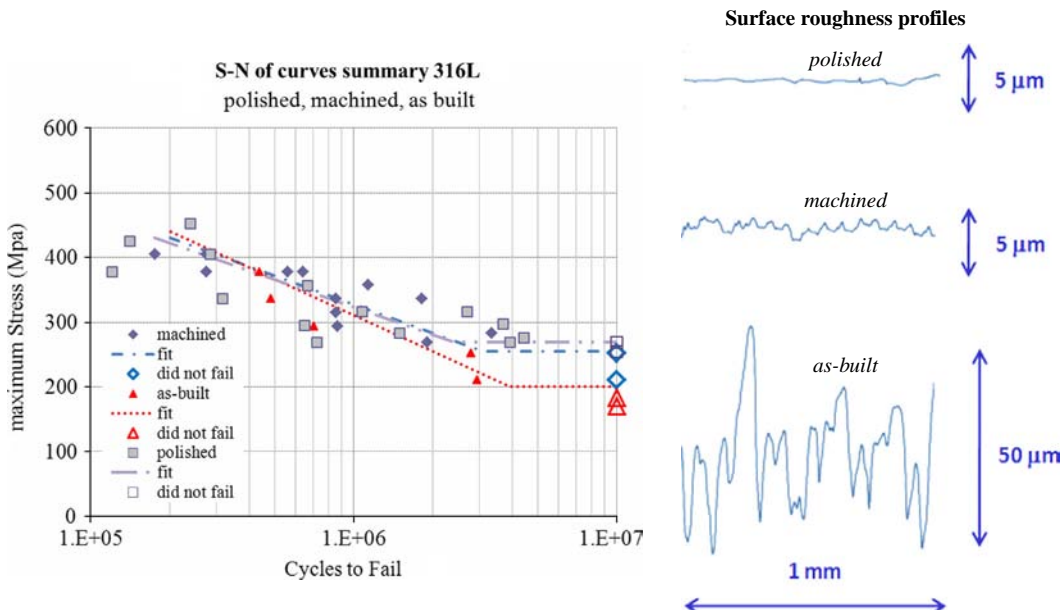


Figure 3 Fatigue performance of 316L stainless steel with three different surface finishes

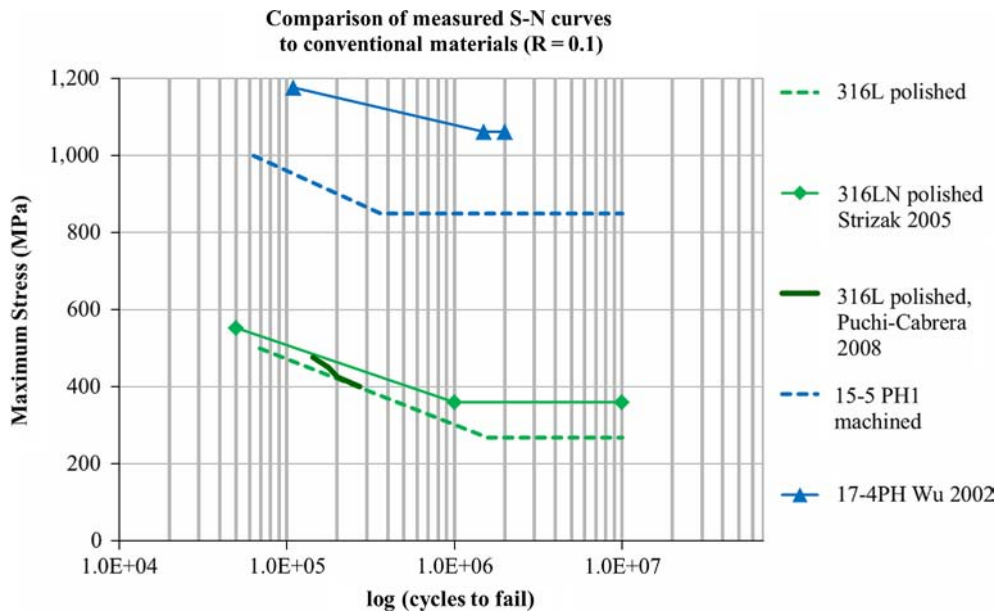
Notes: Maximum stress vs number of cycles and linear fit (left); deviations from the log-linear fit are normally distributed (right)

Figure 4 Fatigue performance of 316L stainless steel with three different surface finishes

Notes: Maximum stress vs number of cycles and linear fit (left); measured surface roughness (R_a) is 10.0, 0.4 and 0.1 μm for the as-fabricated, machined and polished specimen, respectively (right)

with lower carbon and higher nitrogen in the range 0.10–0.16 per cent. The reported yield strength and UTS of this alloy was 259 and 588 MPa, respectively. In the cold-worked condition the measured yield strength and UTS was 733 and 800 MPa, somewhat higher than the laser-fabricated material (Table II). The reported fatigue limit of 360 MPa is approximately 34 per cent higher than that of the laser-fabricated 316L and fatigue lifetimes at higher stress amplitudes are somewhat longer. The measured fatigue limit

of the polished specimens is 35 per cent of the UTS (Figure 5), which is significantly less compared to the fatigue limit of 61 per cent UTS reported by Strizak. However, the CES Edupack 2011 software package reports a fatigue limit (10^7 cycles) at $R = 0.1$ in the range of 141–207 MPa for wrought 316L and 157–242 MPa for 316LN, respectively. In this relation, the measured fatigue limit of 269 MPa is a high value indicating that AM processed 316L materials can compete with traditional materials. Using a typical

Figure 5 Fatigue performance of laser-fabricated 316L and 15-5 PH stainless steel is comparable to that of conventionally processed, similar materials

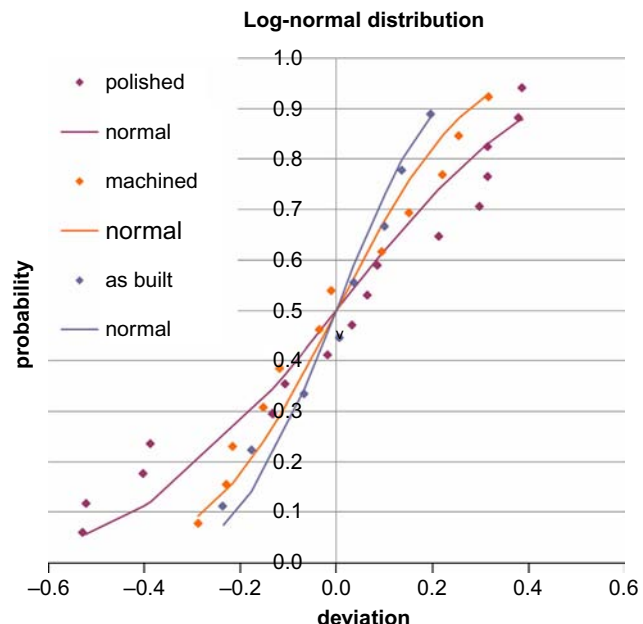
Smith Diagram ($> 10^7$ cycles) for steel, a calculation of the stress amplitude at $R = -1$ (mean stress = 0 MPa) is possible. This results in a fatigue strength of 172 MPa, which is in a good relation to the fatigue strength of 165 MPa reported by Kurgan and Varol.

Surface finish had a strong effect on the fatigue limit (Figure 4), although the very rough, as-fabricated surface provided surprisingly good dynamic performance at higher stress. While the overall roughness of the hand polished specimens is lower (see Figure 4 right), there may be areas of the surface that retained the original turned surface due to an improper treatment operation. This could be the reason for the somewhat wider scatter band of the observed results for the polished specimens in comparison to the other specimens with other surface treatments (Figure 6).

For the investigated 316L material, there seems to be no significant effect of surface treatment on fatigue lifetime. Therefore, the results of all specimens within the lifetime range and of all surface treatments are put into one S-N curve (Figure 7), indicating a 95 per cent confidence level range for additive processed 316L material.

Stainless steel 15-5PH

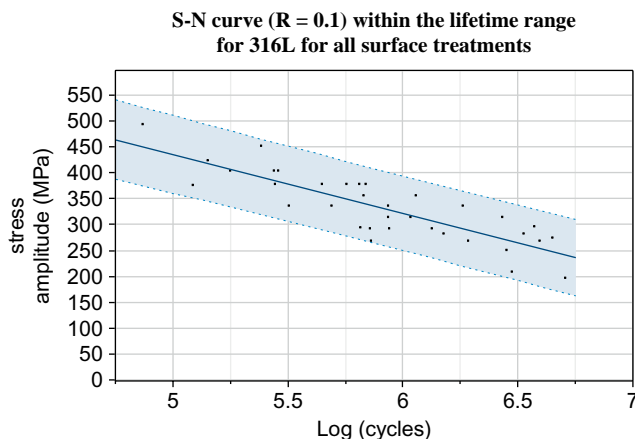
The CES Edupack 2011 software package reports for wrought stainless steel 15-5PH (condition H925) a fatigue limit ($R = 0.1$) in the range of 270–372 MPa. This is much less compared to the measured (Figure 5) or reported results by Wu and Lin (2002). They report fatigue performance of 17-4PH stainless steel with axial loading of cylindrical specimens at 20 Hz with $R = 0.1$ and with fatigue limit assumed after 2×10^6 cycles. 17-4PH is like the 15-5PH alloy a martensitic, precipitation hardenable alloy. The processing characteristics and properties are similar to the 15-5PH alloy used here. The H900 (482°C, 1 h) heat treatment yields the highest room temperature yield strength for both alloys and is used in both investigations. The tensile properties reported by Wu and Lin (1,387 MPa yield strength and 1,414 MPa UTS). This reported yield strength is significantly higher than that measured here or

Figure 6 Diagram of normal quantiles for the polished, machined and as-built specimens

listed in *ASM Handbook* (1993), although the UTS is somewhat lower than that of the laser-fabricated material. The reported fatigue limit for the 17-4PH is 75 per cent of the UTS, an exceptionally high value, and is 25 per cent higher than that measured for the laser-fabricated material.

Conclusion

The current results of additive manufactured stainless steels 316L and 15-5PH indicate that the dynamic behaviour can be compared to conventional materials although the results are not exactly the same. Within the lifetime range, the effect of

Figure 7 S-N curve ($R = 0.1$) for 316L for all surface treatments

Note: Confidence level 95 per cent

the rough, as-fabricated surface reduces the S-N curve compared to conventional materials (Figure 5). However, the differences between polished, machined and as-fabricated specimens on the maximal stresses within the lifetime range are small. A possible explanation is that the spherical powder particles fused at the surface do not create sharp surface cracks and do not act as a stress concentration features. Besides surface quality and structure, further effects can play an important role: for example, anisotropic effects are well known for the static performance of SLM materials (Sehrt and Witt, 2009; Spierings and Levy, 2009; Spierings *et al.*, 2011). Therefore, it is expected that comparable effects – beside possibly others – influence the dynamic behaviour of the materials as well, depending on the material type, processing parameters and heat treatments. Such influencing effects can be the powder type in combination with the layer thickness and processing parameters (laser power and speed) (Sehrt and Witt, 2009; Spierings and Levy, 2009). They typically affect the size and distribution of internal pores and the SLM specific very fine grain size. Especially the grain size may influence the dynamic behaviour in a specific way as in vertically built specimens, the long axis of the columnar grains are stretched whereas in horizontally built specimens, the smaller diameter of the columnar grains are in tension direction, combined with an accordingly higher number of grain boundaries. These effects play an important role regarding the fracture toughness and crack propagation. Therefore, it is expected that the dynamic mechanical properties of additively processed materials can be a useful means for further process parameter optimisation, taking into account several influencing affects.

However, further analysis is needed in order to increase the knowledge about these effects and to define specific measures to improve the SLM process. As a first step, S-N curves of horizontally built SLM specimens are needed in order to complete the results from this study. It is expected that the dynamic strength of horizontally built specimens would be higher compared to the vertically built samples, as already known for the static strength (Sehrt and Witt, 2009; Spierings and Levy, 2009). In this respect, the current results indicate a base line for the investigated materials.

Depending on the application and the sectors where the parts are produced for, the current results indicate that

surface finishing of structural parts may not be needed to achieve design lifetime for SLM-fabricated components, as long as the parts are designed in the sense of “Design for Additive Manufacturing”, taking into account the possibilities and current limitations of the process. However, especially for sectors where high requirements dominate, such as, e.g. the medical or aerospace sector, the current material integrity of metallic AM parts may not yet be sufficient. Thus, the development and optimisation of appropriate surface finishing techniques is needed to improve the fatigue limit of complex structural parts.

Outlook

Additional work is needed to fully understand the mechanical performance of these SLM-fabricated materials. Strain-controlled testing of notched specimens is needed to obtain a crack growth rate data and to separate crack initiation and crack propagation phenomena. Laser-fabricated materials are known to be anisotropic and the effect of build orientation needs to be investigated in detail.

References

- Abe, F., Osakada, K., Shiomi, M., Uematsu, K. and Matsumoto, M. (2001), “The manufacturing of hard tools from metallic powders by selective laser melting”, *Journal of Materials Processing Technology*, Vol. 111 Nos 1-3, pp. 210-13.
- ASM Handbook (1993), *Volume 1: Properties and Selection: Irons, Steels, and High-Performance Alloys* 1993, ASM International, Materials Park, OH.
- Badrossamay, M., Yasa, E., Van Vaerenbergh, J. and Kruth, J.-P. (2009), “Improving productivity rate in SLM of commercial steele powders”, paper presented at SME-RAPID, Schaumburg, IL, USA.
- Hollander, D.A., Wirtz, T., von Walter, M., Linker, R., Schultheis, A. and Paar, O. (2003), “Development of individual three-dimensional bone substitutes using ‘selective laser melting’”, *European Journal of Trauma*, No. 4.
- Kruth, J.-P., Vandenbroucke, B., Van Vaerenbergh, J. and Mercelis, P. (2005a), “Benchmarking of different SLS/SLM processes as rapid manufacturing techniques”, paper presented at Int. Conf. Polymers & Moulds Innovations (PMI), Gent, Belgium.
- Kruth, J.-P., Vandenbroucke, B., Van Vaerenbergh, J. and Naert, I. (2005b), “Rapid manufacturing of dental prostheses by means of selective laser sintering/melting”, paper presented at European Forum on Rapid Prototyping & Manufacturing AFPR, Paris, France.
- Kruth, J.-P., Vandenbroucke, B., Van Vaerenbergh, J. and Naert, I. (2005c), “Rapid manufacturing of dental prostheses by means of selective laser sintering/melting”, *Proceedings of the AFPR*, S4.
- Kruth, J.-P., Froyen, L., Van Vaerenbergh, J., Mercelis, P., Rombouts, M. and Lauwers, B. (2004), “Selective laser melting of iron-based powder”, *Journal of Materials Processing Technology*, Vol. 149 Nos 1-3, pp. 616-22.
- Kumar, S. (2009), “Manufacturing of WC-Co moulds using SLS machine”, *Journal of Materials Processing Technology*, Vol. 209 No. 8, pp. 3840-8.

- Lan, H. (2009), "Web-based rapid prototyping and manufacturing systems: a review", *Computers in Industry*, Vol. 60 No. 9, pp. 643–56.
- Laoui, T., Froyen, L. and Kruth, J.-P. (2000), "Effect of mechanical alloying on selective laser sintering of WC-9Co hard metal powder", *Powder Metallurgy*, Vol. 42 No. 3, pp. 203–5.
- Levy, G.N., Schindel, R. and Kruth, J.P. (2003), "Rapid manufacturing and rapid tooling with layer manufacturing (LM) technologies, state of the art and future perspectives", *CIRP Annals – Manufacturing Technology*, Vol. 52 No. 2, pp. 589–609.
- Lopez, G., Williams, S., Miranda, R.M., Quintino, L. and Rodrigues, J.P. (2008), "Additive manufacturing of Ti-6Al-4V based components with high power fiber laser", in Bartolo, P.J. (Ed.), *Virtual and Rapid Manufacturing*, pp. 369–74.
- Murr, L.E., Quinones, S.A., Gaytan, S.M., Lopez, M.I., Rodela, A., Martinez, E.Y., Hernandez, D.H., Martinez, E., Medina, F. and Wicker, R.B. (2009), "Microstructure and mechanical behavior of Ti-6Al-4V produced by rapid-layer manufacturing, for biomedical applications", *Journal of the Mechanical Behavior of Biomedical Materials*, Vol. 2 No. 1, pp. 20–32.
- Niu, H.J. and Chang, I.T.H. (1999), "Selective laser sintering of gas and water atomized high speed steel powders", *Scripta Materialia*, Vol. 41 No. 1, pp. 25–30.
- Ram, G.D.J., Esplin, C.K. and Stucker, B.E. (2008), "Microstructure and wear properties of LENS deposited medical grade CoCrMo", *Journal of Materials Science: Materials in Medicine*, Vol. 19 No. 5, pp. 2105–11.
- Rehme, O. and Emmelmann, C. (2006), "Rapid manufacturing of lattice structures with selective laser melting", *Laser-based Micropackaging, Proceedings of SPIE*.
- Rehme, O. and Emmelmann, C. (2007), "Generative Fertigung von Ti-Legierungen: Laserstrahl vs. Elektronenstrahl", *Werkstoffe in der Fertigung*, HW-Verlag, Hamburg.
- Sehrt, J.T. and Witt, G. (2009), "Auswirkungen des anisotropen Gefüges strahlgeschmolzener Bauteile auf mechanische Eigenschaftswerte", *RTejournal*, Vol. 6.
- Sehrt, J.T. and Witt, G. (2010), "Dynamic strength and fracture toughness analysis of beam melted parts", paper presented at International MATADOR Conference, Manchester, Lancashire, UK.
- Spierings, A.B. and Levy, G. (2009), "Comparison of density of stainless steel 316L parts produced with selective laser melting using different powder grades", *Proceedings of the Annual International Solid Freeform Fabrication Symposium, Austin, Texas*.
- Spierings, A.B., Herres, N. and Levy, G. (2011), "Influence of the particle size distribution on surface quality and mechanical properties in additive manufactured stainless steel parts", *Rapid Prototyping Journal*, Vol. 17 No. 3, pp. 195–202.
- Starr, T.L. and Spierings, A.B. (2010), "Tensile and fatigue performance of laser sintered stainless steels", *Proceedings of the Annual International Solid Freeform Fabrication Symposium, Austin, Texas*.
- Strizak, J.P., Tian, H., Liaw, P.K. and Mansur, L.K. (2005), "Fatigue properties of type 316LN stainless steel in air and mercury", *Journal of Nuclear Materials*, Vol. 343 Nos 1–3, pp. 134–44.
- Vandenbroucke, B. and Kruth, J.P. (2007), "Selective laser melting of biocompatible metals for rapid manufacturing of medical parts", *Rapid Prototyping Journal*, Vol. 13 No. 14, pp. 196–203.
- Wu, J.H. and Lin, C.K. (2002), "Tensile and fatigue properties of 17-4 PH stainless steel at high temperatures", *Metallurgical and Materials Transactions A: Physical Metallurgy and Materials Science*, Vol. 33 No. 6, pp. 1715–24.

Corresponding author

A.B. Spierings can be contacted at: spierings@inspire.ethz.ch

Metallurgical and Mechanical Evaluation of 4340 Steel Produced by Direct Metal Laser Sintering

ELIAS JELIS,^{1,2} MATTHEW CLEMENTE,¹ STACEY KERWIEN,¹
NUGGEHALLI M. RAVINDRA,^{2,3} and MICHAEL R. HESPOS¹

1.—U.S. Army ARDEC, Picatinny, NJ 07806, USA. 2.—Interdisciplinary Program in Materials Science & Engineering, New Jersey Institute of Technology, Newark, NJ 07102, USA.
3.—e-mail: nmrvindra@gmail.com

Direct metal laser sintering (DMLS) was used to produce high-strength low-alloy 4340 steel specimens. Mechanical and metallurgical analyses were performed on the specimens to determine the samples with the highest strengths and the least porosity. The optimal process parameters were thus defined based on the corresponding experimental conditions. Additionally, the effects of fabricating specimens with both virgin and recycled powders were studied. Scanning electron microscopy and electron-dispersive spectroscopy were performed on both types of powders to determine the starting morphology and composition. The initial tensile results are promising, suggesting that DMLS can produce specimens equal in strength to wrought materials. However, there is evidence of cracking on several of the heat-treated tensile specimens that is unexplained. Several theories point to disturbances in the build chamber environment that went undetected while the specimens were being fabricated.

INTRODUCTION

Direct metal laser sintering (DMLS) is a process in which layers of powder are deposited and melted in succession with laser energy to produce net shaped geometries that are defined by three-dimensional files including computer-aided design (CAD) models and scan data.^{1,2} DMLS is an emerging technology because it can produce reliable components without additional tooling.³ It can also manufacture geometries with high accuracy, which are difficult to produce with traditional manufacturing methods such as lattice structures (Fig. 1) and irregular shapes.^{4,5} The benefits of the DMLS process can lead to a reduction in lead time, decreased cost to produce parts at low quantities, and in some cases, large quantities of custom parts.⁶ The process is somewhat scalable in that larger components can be produced within larger build chambers. However, the components cannot be produced in short durations.

Support structures, surface roughness, high thermal stress, low volumetric build rate, and restricted build chamber size are some of the major drawbacks of this process.^{7–11} DMLS should be seen as a complement to current technologies but is often not a total solution.¹²

Steel alloy 4340 is known for its high strength and toughness.¹³ It is commonly used for making structural components in the defense, aerospace, energy, and automotive industries. Several parts that can be made using 4340 steel include landing gear components, rock drill components, connecting rods, and crankshafts.^{13–16} The current laser additive manufacturing techniques that use 4340 include laser cladding for repair and laser welding.^{17,18} These techniques are limited in their geometries and applications. In regions of rapid heating followed by rapid cooling, the microstructures produced by these techniques are primarily martensitic, which offer toughness. The fabrication of components using 4340 steel, with the DMLS process (EOSINT M270 machine (EOS, Krailling/Munich, Germany) with 200 Watt Ytterbium fiber laser), is investigated in this article.

The objective of this research is to determine the optimal process parameters for DMLS 4340 (Carpenter Technology Corporation, Wyomissing, PA), which will produce mechanical properties that are comparable with wrought steel. Optimal process parameters are the parameters that produce a uniform microstructure with minimal porosity and low residual stress.

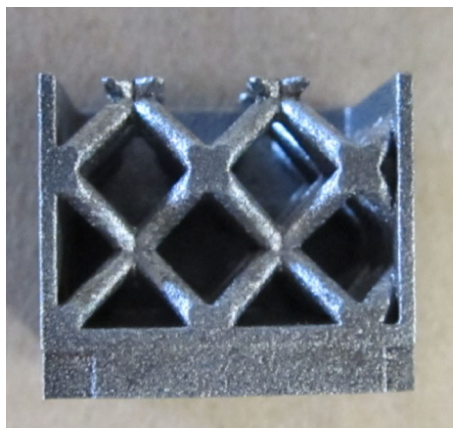


Fig. 1. Photograph of 4340 steel lattice structure component produced by DMLS after bead blasting.

EXPERIMENTAL PROCEDURE

Steel alloy 4340 powder, used in this experiment, was manufactured by Carpenter Technology Corporation. The particle size used was -325 mesh $+10\ \mu\text{m}$. The surface structure of the unused powder was investigated using a scanning electron microscope (JEOL-JSM-6510LV; JEOL Ltd., Tokyo, Japan, JEOL Ltd., JEOL USA, Inc., Peabody, MA) to determine the morphology of the powder and analyze the fracture surface of the cracked tensile bars. The particle size distribution of the virgin powder was analyzed by laser diffraction with a Horiba LA-950 V2 (HORIBA Instruments Inc., Irvine, CA) system. The chemistry of the powder was analyzed by Carpenter Technology Corporation and was confirmed by electron-dispersive spectroscopy (EDS) and carbon/sulfur combustion analyses. The oxygen analyses of the virgin and recycled powder were analyzed by EDS.

Ninety-six ($10\ \text{mm} \times 10\ \text{mm} \times 10\ \text{mm}$) cubes were fabricated with various exposure parameters including laser scan speed and power. The cubes were processed to obtain a layer thickness of $20\ \mu\text{m}$ with the re-circulating filter fan speed set at 1.5. Subsequently, 25 cubes were made using parameter sets that proved most favorable by microstructure evaluation. The microstructure was analyzed using optical microscopy (Nikon Eclipse MA200; Nikon Corporation Melville, NY). Nital (95% methanol and 5% nitric acid by volume) was used to etch the microstructure. Image analysis techniques were used to determine the microstructure with the optimal sintering parameter set. The mechanical properties of the cubes were analyzed with a Vickers indenter (Struers-Duramin A300; Struers Inc., Westlake, OH). The chemical composition of the specimens was determined by x-ray fluorescence with a Niton XL3t 900 (Thermo Fisher Scientific Tewksbury, MA).

Three x - y -oriented tensile specimens, using optimal parameters (as determined by having the

Table I. Chemical composition of virgin powder from Carpenter Technology Corporation certification

Element	Analysis of powder from manufacturer, wt.%	4340 steel requirement, wt%
Fe	Balance	Balance
C	0.39	0.38–0.43
Mn	0.71	0.60–0.80
Ni	1.74	1.65–2.00
Cr	0.80	0.70–0.90
Mo	0.25	0.20–0.30
Si	0.24	0.15–0.30
P	0.01	0.035 max.
S	0.01	0.04 max.

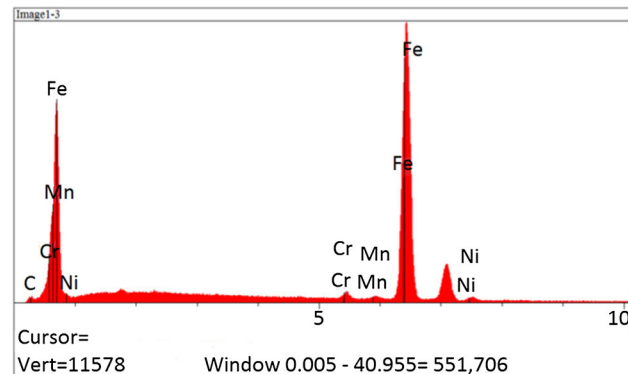


Fig. 2. EDS spectrum of virgin steel alloy 4340 powder.

least porosity), were each processed using virgin powder (run A) and once-recycled powder (run B). The tensile testing was performed after all the six specimens were stress relieved at $593.33\ ^\circ\text{C}$ for 1 h.

An additional set of five x - y -oriented tensile specimens were produced using twice-recycled powder using the same machine parameters (run C). The samples were normalized at $898.89\ ^\circ\text{C}$ for 1 h, passively cooled to room temperature, heated to $815.56\ ^\circ\text{C}$ for 1 h and quenched in water, and finally tempered at $190.56\ ^\circ\text{C}$ for 2 h. All eleven tensile bars were $3/8''$ diameter and $6''$ long and then machined into $1/4''$ round specimen in accordance with ASTM E8.

RESULTS AND DISCUSSION

Virgin Powder

The chemistry of the powder closely matches 4340 steel according to the results obtained from the powder manufacturer (Table I). There was no significant oxygen concentration in the virgin powder because there was no peak associated with oxygen in the EDS spectra (Fig. 2). The particle size was confirmed using laser diffraction and is presented in Table II. The powder was predominantly spherical

Table II. Steel alloy 4340 particle size distribution results using laser diffraction particle analyzer

Mean size	26.2 μm
Median size	24.1 μm
Mode size	24.5 μm
Standard deviation	12.5 μm
D10	12.5 μm
D90	42.5 μm

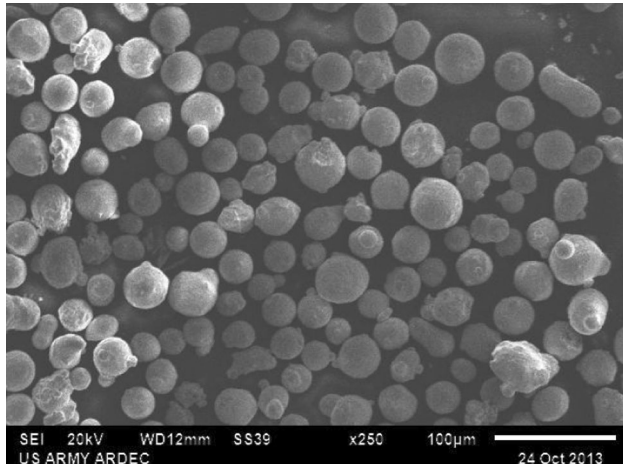


Fig. 3. SEM image of virgin powder at 250 times magnification; micron marker scale = 100 μm .

according to Fig. 3. The spherical surface morphology and chemistry of the powder confirms that it is gas atomized powder.

Recycled Powder

After the powder has been used, it is recycled and passed through an 80- μm sieve to remove any oversized particles, including overexposed condensate particles. The condensate has significant oxygen concentration, which is indicated by the oxygen peak in the EDS spectrum shown in Fig. 4a and b. Some particles with a significant oxygen concentration do pass through the sieve; this can be seen in Fig. 5a and b. Because of the significant oxygen concentration, the iron-based melt pool does not effectively wet on an oxide surface.¹⁹ As a result, it leads to balling of the melt pool. This balling phenomenon will result in an increase in porosity.²⁰ An increase in oxygen either from the chamber environment or powder will lead to degradation of the mechanical properties of the components due to an increase in porosity. One way to reduce these particles from the recycled powder is by increasing the recirculating fan speed to remove condensate particles from the chamber and store the powder in an inert environment. It will lead to an increase in the

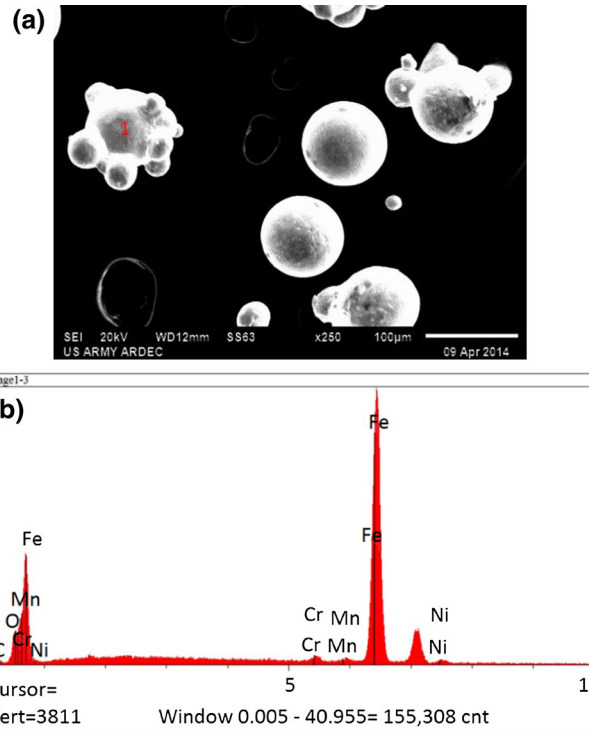


Fig. 4. (a) Image of the oversized condensate at 250 times magnification; micron marker scale = 100 μm . (b) EDS spectrum—oxy-gated particle 1 from Fig. 4a.

collection of the condensate particles by the recirculation filters. The recirculating filters recycle nitrogen gas back into the chamber after being filtered to remove the condensate particles.

Microstructure/Microhardness

The microstructure of the as-sintered and stress-relieved samples, using optimal machine parameters (Table III), in the longitudinal and transverse directions are analyzed. In Fig. 6, a schematic of the hatch distance and stripe width is presented. In the longitudinal direction, the etched microstructure reveals evidence of the melt pool boundaries and banding of grains oriented in the Z direction as indicated in Fig. 7a. The maximum melt pool height is approximately 50 μm , which means that the laser energy melts the underlying surface for strong adhesion. In transverse direction, there is a fine-grained structure and the defined melt pool boundaries are shown in Fig. 8a. The hardness in the as-sintered condition, in transverse and longitudinal directions, was between 45 and 49 HRC (Rockwell hardness on the C scale)—as summarized in Table IV. When the bars were stress relieved at 593.33 °C, the banding along with the melt pool boundaries was not visible (Figs. 7b and c, and 8b and c). The resulting stress-relieved microstructures were similar in all directions with hardness

between 42 and 44 HRC, as shown in Table IV. The microstructures of the as-sintered and stress-relieved conditions were predominantly martensitic with fine grains because of the rapid cooling of the melt pools. The results of the microstructure are in agreement with the literature wherein DMLS was used to sinter plain carbon steels with the EOSINT M250 Xtended machine to produce similar fine-grain microstructure using S50C and S75C plain carbon steel with a CO₂ laser.²¹ The approximate interpolated applied energy density, with the M250 (400 J/mm³) needed to produce fully dense structures with a carbon content of 0.4 wt.%, is much higher than 4340 steel with the M270 (141.7 J/mm³) mainly because the metal powder can absorb

significantly more laser energy from a fiber laser than a CO₂ laser.²²

The resulting microstructure of the heat-treated tensile samples from run C is tempered martensite with a hardness of 51 HRC (Fig. 9).

Tensile Results

All the tensile specimens from runs A and B were stress relieved. The hardness of the bars was between 41 and 43 Rockwell C. The chemical composition of both closely matches that of the steel alloy 4340. The carbon content is slightly lower than the starting powder, but it is close to the lower limit of wrought steel alloy 4340 specification (Table V). The results of the modulus of elasticity, yield strength,

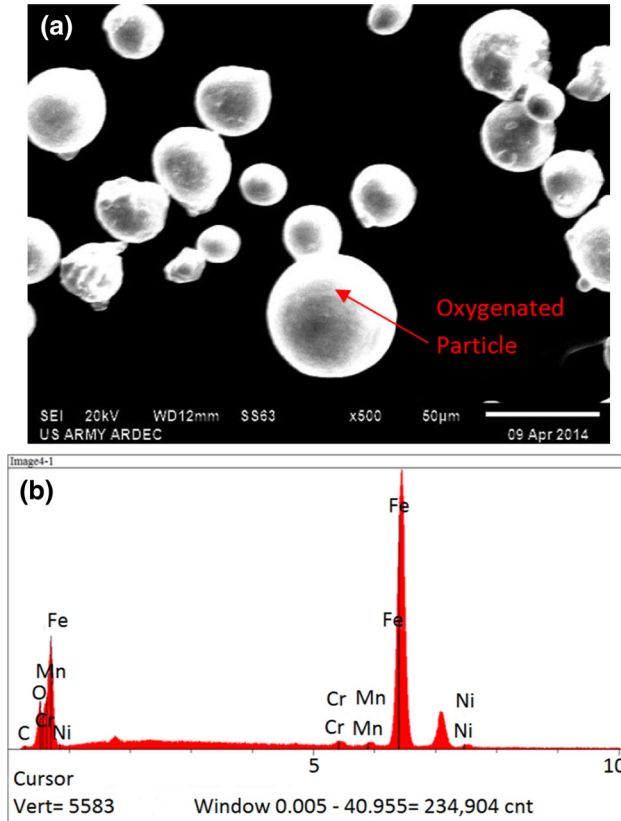


Fig. 5. (a) Image of the recycled powder at 250 times magnification; micron marker scale = 50 µm. (b) EDS spectrum—oxygenated particle from Fig. 5a.

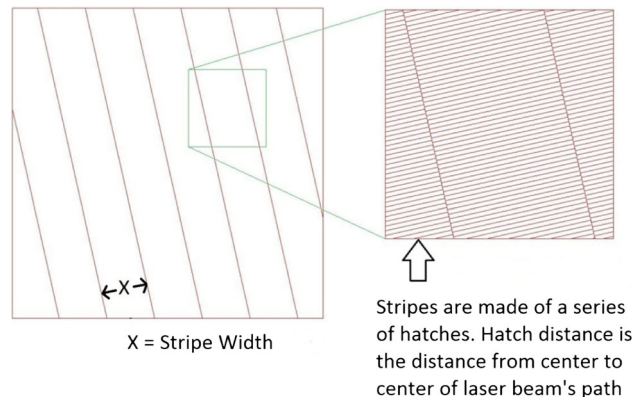


Fig. 6. Image illustrating the hatch distance and stripe width.

Table IV. Hardness of materials as sintered and after stress relief at 593.33 °C

Specimen	Microhardness	Hardness
Longitudinal as sintered	462–495 HV	46–49 HRC
Transverse as sintered	440–471 HV	45–47 HRC
Longitudinal stress relieved	411–431 HV	42–44 HRC
Transverse stress relieved	410–432 HV	42–44 HRC

The hardness values were converted using ASTM E140

Table III. Optimal exposure parameters for DMLS

Scan speed	Power	Hatch distance	Stripe width	Layer thickness	Applied energy density
600 mm/s	170 W	0.1 mm	10 mm	20 µm	141.7 J/mm ³

Hatch distance and stripe width are illustrated in Fig. 6

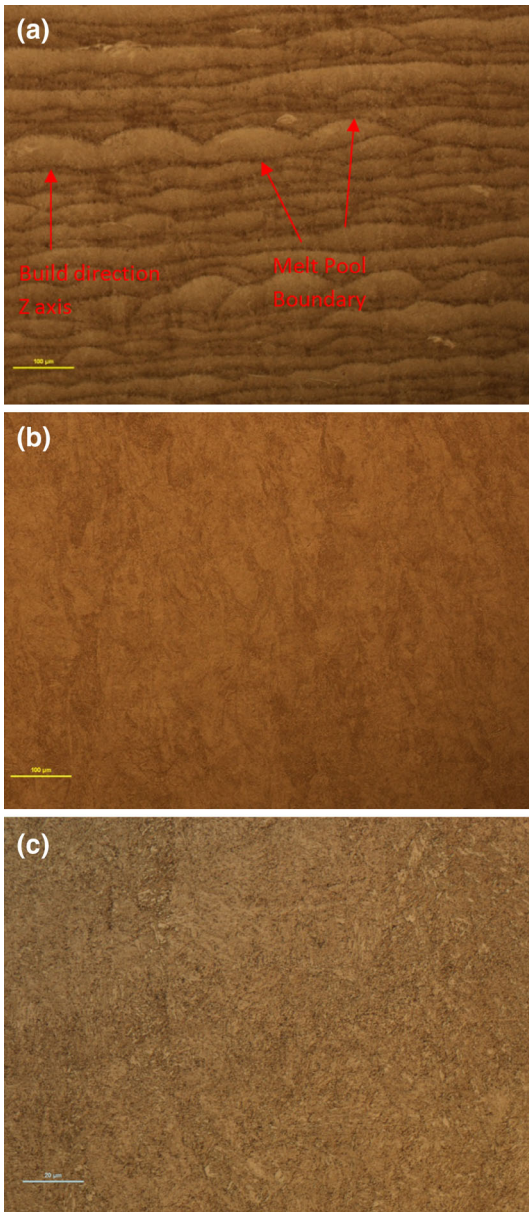


Fig. 7. (a) Optical micrograph longitudinal section of the cube using the parameters from Table IV at 100 times magnification; micron marker scale = 100 μm . (b) optical micrograph of the longitudinal section after stress relief at 100 times magnification; micron marker scale = 100 μm . (c) Optical micrograph of steel alloy 4340 stress relieved in the longitudinal direction after stress relief at 500 times magnification; micron marker scale = 20 μm .

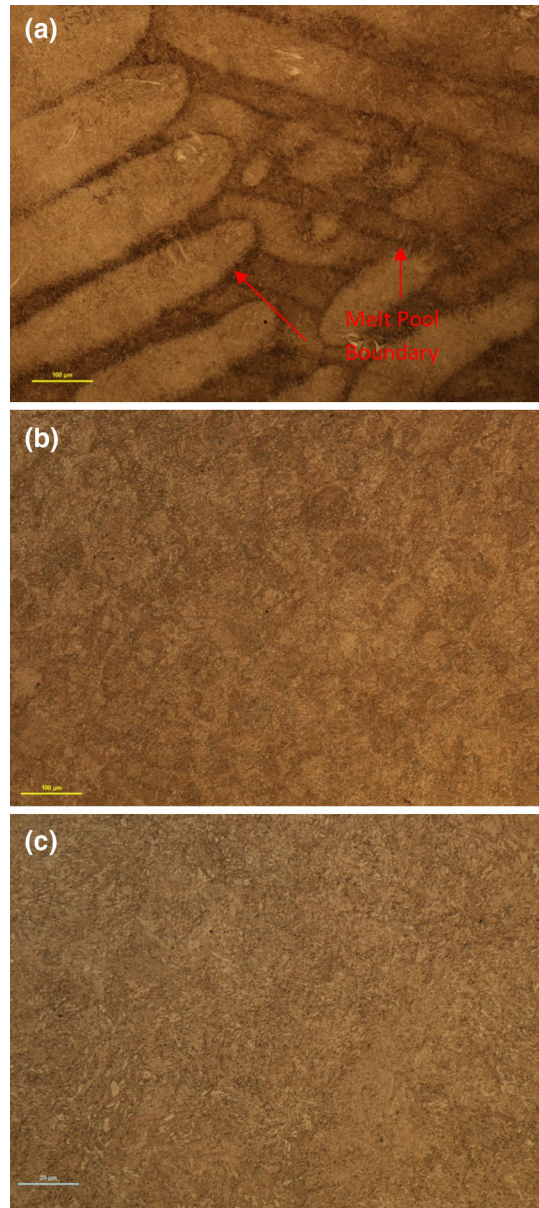


Fig. 8. (a) Micrograph of the transverse section in the as-sintered condition at 100 times magnification; micron marker scale = 100 μm . (b) Micrograph of the transverse section after stress relief at 100 times magnification; micron marker scale = 100 μm . (c) Micrograph of steel alloy 4340 stress relieved in the transverse direction after stress relief at 500 times magnification; micron marker scale = 20 μm .

tensile strength, and elongation are very similar to wrought 4340 which are shown in Table VI and Fig. 10a and b. The stress-strain curves for all specimens from runs A and B follow the typical behavior for structural steel. As a result, the mechanical properties of runs A and B are comparable with wrought.

Alloy steels (4xxx series) are used in structural components where high strength and toughness are required. The alloying elements provide higher

toughness, strength, and hardness than plain carbon steels with equivalent or lower carbon content.²⁶

Five tensile bars from run C were heat treated to 51 HRC. Four of the five bars showed mechanical properties near wrought steel alloy 4340 except for the lower elastic modulus according to Table VII and Fig. 11. The stress-strain curve behavior of the intact tensile specimens, after heat treatment, match closely to the engineering stress-strain curve

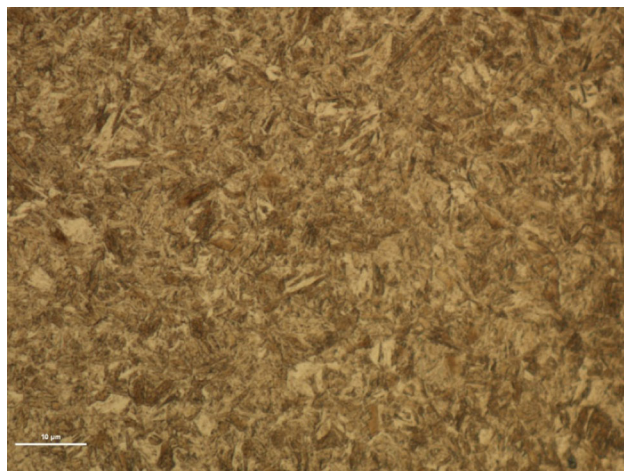


Fig. 9. Micrograph of steel alloy 4340 at 1,000 times magnification after heat treatment to 51 HRC; micron marker scale = 10 μm .

Table V. Chemical composition using XRF and carbon/sulfur combustion for Runs A–C

Element	4340 steel requirement, wt.%		
	Run A	Run B	Run C
Fe	Balance	Balance	Balance
C	0.37	0.37	0.33
Mn	0.61	0.60	0.60
Ni	1.83	1.85	1.90
Cr	0.89	0.89	0.89
Mo	0.28	0.29	0.28
S	0.01	0.01	0.01
			0.04 max.

for structural steels, which indicates that they failed in a ductile manner. During run C, the chamber door was not sealed properly and the condensate escaped out of the chamber door during the build. One tensile specimen failed prematurely because there was a crack at the grip, and there is evidence of cracking in the other run C bars as well (Fig. 12a and b). The cracks were most likely present prior to heat treatment because there was evidence of decarburization near the crack region (Fig. 13). The hardness is also significantly lower around the crack than the substrate (Table VIII). According to a scanning electron microscopy (SEM) analysis of the fracture surface of the failed specimen, there is evidence of ball formation and brittle failure (Fig. 14a and b). Thus, this is an indication of poor wetting and adhesion from higher oxygen content at the powder bed resulting from the open chamber door.^{19,20} The high oxygen content is likely from the external environment and/or condensate. The significantly higher absorption of laser energy caused by an increase in oxygen will lead to defects.²⁷ The presence of oxygen can explain cracking, balling effect, and lower overall carbon content from run C. The lower elastic modulus is possibly caused by the defects (cracking) from higher oxygen concentration at the powder bed surface during lasing.²⁸

CONCLUSION

DMLS of 4340 high-strength low-alloy (HSLA) steel specimens has been investigated in this study. The results show that the mechanical properties of

Table VI. Tensile data of 1100°F stress-relieved laser sintering 4340 steel

Material Condition	Modulus	Yield Strength	Tensile	Elongation
Typical wrought 4340 properties from ASM International ^{23,24}	29000 ksi	183 ksi	199 ksi	15%
Run A: DMLS of virgin powder	31000 ksi	189–190 ksi	199 ksi	16–17%
Run B: DMLS after once recycled powder	31000 ksi	187–190 ksi	198 ksi	16–17%

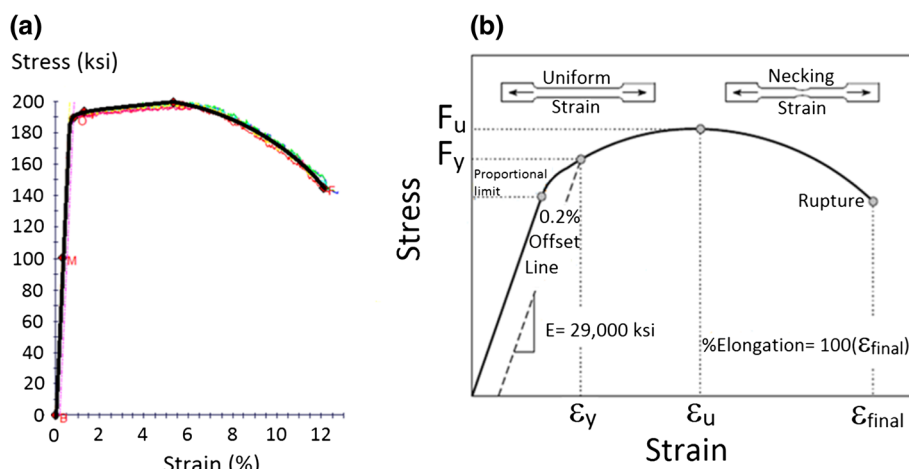


Fig. 10. (a) Engineering stress versus strain data for runs A and B. (b) Typical stress-strain curve for structural steel.²⁵

the stress relieved specimens are comparable to wrought steel alloy 4340. The carbon content and modulus of elasticity of heat-treated tensile bars were significantly lower than wrought. The

Table VII. Tensile data of four tensile bars heat treated to 51 rockwell C laser sintering 4340 steel

Material condition	Modulus of elasticity	Yield strength	Tensile strength	Elongation
Typical wrought properties ^{23,24}	29000 ksi	253 ksi	271 ksi	12%
Used twice (heat treated)	17000 ksi	228–234 ksi	295–299 ksi	9–14%

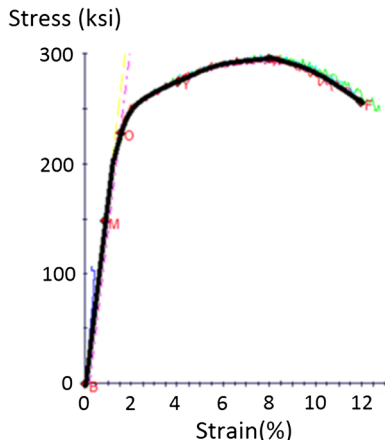


Fig. 11. Engineering stress-strain data for run C.

presence of oxygen in the chamber more than likely contributed to the reduced performance of the tensile bars.

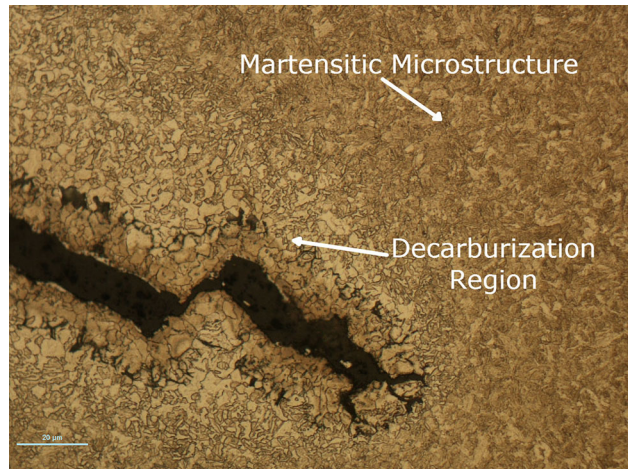


Fig. 13. Optical micrograph at 500 times magnification of heat-treated sample showing the microstructure; micron marker scale = 20 μm .

Table VIII. Hardness of materials as sintered and after stress relief

Specimen	Microhardness	Hardness conversion using ASTM E140
Near the crack	202–338 HV	95 HRB–34 HRC
Bulk material	549–597 HV	52–55 HRC

The hardness values were converted using ASTM E140

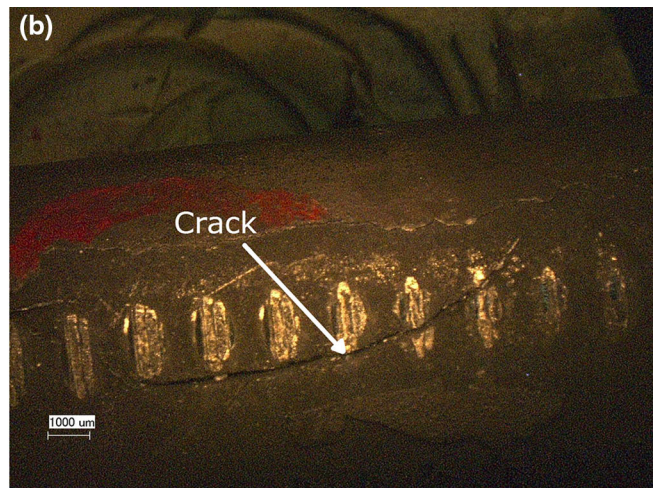
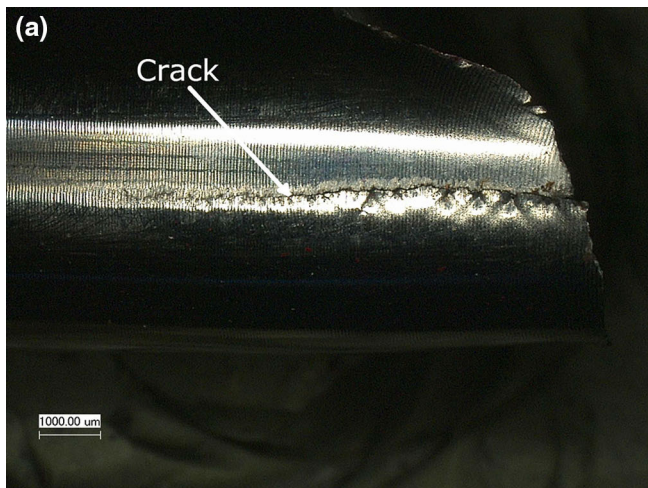


Fig. 12. Low-magnification photographs of two samples from run C tensile specimens that did not fail prematurely. There is strong evidence of significant cracking of these specimens, although they failed in a ductile manner in accordance with the stress-strain curve; micron marker scale = 1000 μm .

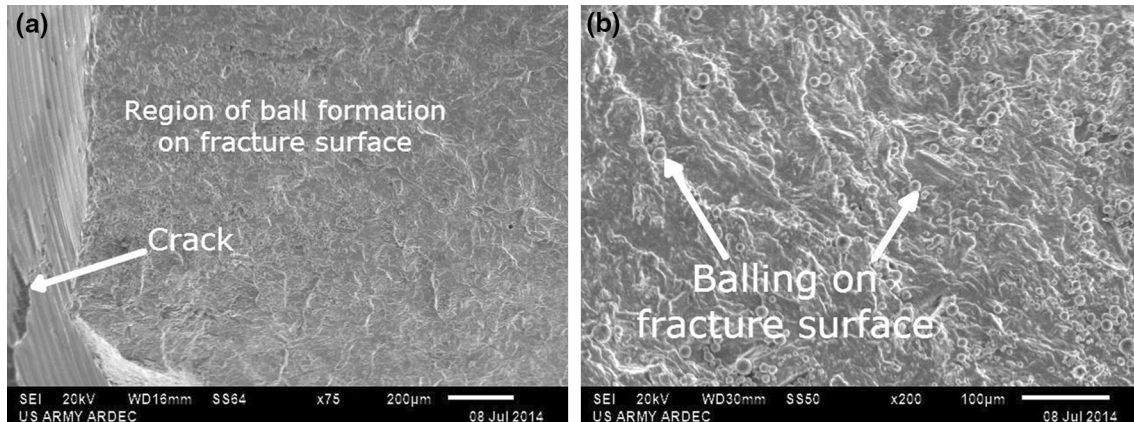


Fig. 14. SEM images of the fracture surface of the failed tensile specimen from run C at 75 times magnification and 200 magnification, respectively: (a) micron marker scale = 200 μm and (b) micron marker scale = 100 μm .

ACKNOWLEDGEMENT

Elias Jelis acknowledges with thanks the award of the SMART Fellowship by the US Department of Defense.

REFERENCES

1. P. Rochus, J.-Y. Plesseria, M. Van Elsen, J.-P. Kruth, R. Carrus, and T. Dormal, *Acta Astronaut.* 61, 352 (2007).
2. R.M. Sherekar, P. Anand, and P.B. Bernardes, *Am. J. Mater. Sci. Appl.* 5, 69 (2014).
3. K.A. Mumtaz, N. Hopkinson, and P. Erasenthiran, *J. Mater. Process. Technol.* 195, 77 (2008).
4. S.L. Campanelli, N. Contuzzi, A.D. Ludovico, F. Caiazzo, F. Cardaropoli, and V. Sergi, *Materials* 7, 4803 (2014).
5. T. Puskar, D. Jevremovic, R.J. Williams, D. Eggbeer, D. Vukelic, and I. Budak, *Materials* 7, 6486 (2014).
6. J.-P. Kruth, B. Vandebroucke, J. Van Vaerenbergh, and I. Naert, *Proceedings of the Virtual Modeling and Rapid Manufacturing Conference—VRAP* (New York: Taylor & Francis, 2005), pp. 139–146.
7. A.B. Spierings, G. Levy, L. Labhartand, and K. Wegener, *Innovative Developments in Virtual and Physical Prototyping* (Boca Raton, FL: CRC Press, 2011), Chap. 120, pp. 785–790.
8. D.M. Jacobson and G. Bennett, *Proceedings of the 16th Solid Freeform Fabrication Symposium*, ed. D.L. Bourell et al. (Austin, TX: University of Texas at Austin, 2006), pp. 728–739.
9. J. Navratil, M. Stanek, M. Manas, D. Manas, M. Benarik, and A. Mizera, *Proceedings of the 22nd International DA-AAM Symposium* 22(1), 1507 (2011).
10. H. Pohl, A. Simchi, M. Issa, and H.C. Dias, *Proceedings of the 12th Solid Freeform Fabrication Symposium* (Austin, TX: University of Texas at Austin, 2001), pp. 366–372.
11. B. Dutta and F.H. Froes, *Adv. Mater. Process.* 172, 18 (2014).
12. C. Cirić-Kostic and A. Vranic, *Mech. Transp. Commun.* 10, 7.10 (2012).
13. W.-S. Lee and T.-T. Su, *J. Mater. Process. Technol.* 87, 198 (1999).
14. H.W. Mishler, R.E. Monroe, and P.J. Rieppel, *Def. Tech. Inf. Center* 1 (1959).
15. S.Y. Sirina, K. Sirinb, and E. Kalucc, *Mater. Charact.* 59, 351 (2008).
16. R.G. Bonora, H.J.C. Voorwald, M.O.H. Cioffi, G.S. Junior, and L.F.V. Santos, *Procedia Eng.* 2, 1617 (2010).
17. A. Cardoso, A.J. Abdalla, and C.A.R.P. Baptista, *Adv. Mater. Res.* 1507 (2006).
18. S.D. Sun, Q. Liu, M. Brandt, V. Luzin, R. Cottam, M. Janardhana, and G. Clark, *Mater. Sci. Eng. A* 606, 46 (2014).
19. J.-P. Kruth, G. Levy, F. Klocke, and T.H.C. Childs, *Ann. CIRP* 56, 730 (2007).
20. C. Hauser, T.H.C. Childs, K.W. Dalgarno, and R.B. Eane, *Proceedings of the Solid Freeform Symposium* (Austin, TX: University of Texas at Austin, 1999), pp. 265–272.
21. T. Nakamoto, N. Shirakawa, Y. Miyata, and H. Inuib, *J. Mater. Proc. Technol.* 209, 5653 (2009).
22. L. Li, *Encyclopedia of Life Support Systems*, Vol. 4, ed. Y. Mikhailovitsch Tsipenyuk (Oxford, U.K.: EOLSS Publishers Co. Ltd, 2002), pp. 148–202.
23. T.V. Philip and T.J. McCaffrey, *Properties and Selection: Irons, Steels, and High-Performance Alloys*, *ASM Handbook*, Vol. 1 (Materials Park, OH: ASM International, 1990), pp. 430–448.
24. B. Boardman, *Properties and Selection: Irons, Steels, and High Performance Alloys-ASM Handbook*, Vol. 1 (Materials Park, OH: ASM International, 1990), pp. 673–688.
25. M. Lwin, *Steel Bridge Design Handbook* 1, 1 (2012).
26. H.A. Youseff, H.A. El-Hofy, and M.H. Ahmed, *Manufacturing Technology: Materials, Processes and Equipment*, Vol. 4 (Boca Raton, FL: CRC Press, Taylor & Francis Group, 2011), pp. 57–89.
27. A. Simchi, *Mater. Sci. Eng. A* 428, 148 (2006).
28. H.-K. Zhu and J.A. Joyce, *Eng. Fract. Mechan.* 85, 1 (2012).

Study of mechanical properties of AISI 316 stainless steel processed by “selective laser melting”, following different manufacturing strategies

Itziar Tolosa · Fermín Garciandía · Fidel Zubiri ·
Fidel Zapirain · Aritz Esnaola

Received: 19 October 2009 / Accepted: 16 March 2010 / Published online: 29 April 2010
© Springer-Verlag London Limited 2010

Abstract Considering additive manufacturing (AM) as a field of major interest, this paper is focused on the study of the mechanical properties and their variability with manufacturing orientation (anisotropy) for a metallic alloy manufactured by AM, using the technology of selective laser melting (SLM). This study has been performed on an austenitic stainless steel—AISI 316 L—used for many industrial fields as chemical, cellulose, and medical, among them. Finally, the obtained properties have been analyzed and compared, for this steel, to those properties standardized and tested for “wrought” products. In this paper, previously published results are complemented, as the mechanical tests have been performed in all the possible directions of manufacturing by SLM and not only in two main directions. High mechanical values have been obtained, especially yield strength (significantly improved, compared with wrought or cast products) while keeping high values of ductility and notch impact resistance. For widespread industrial acceptance, AM parts need to be produced to high tolerances and with well-understood mechanical properties, and the aim of this paper is to contribute to this objective.

Keywords Additive manufacturing · Selective laser melting · Metallic materials · Stainless steel · Mechanical properties

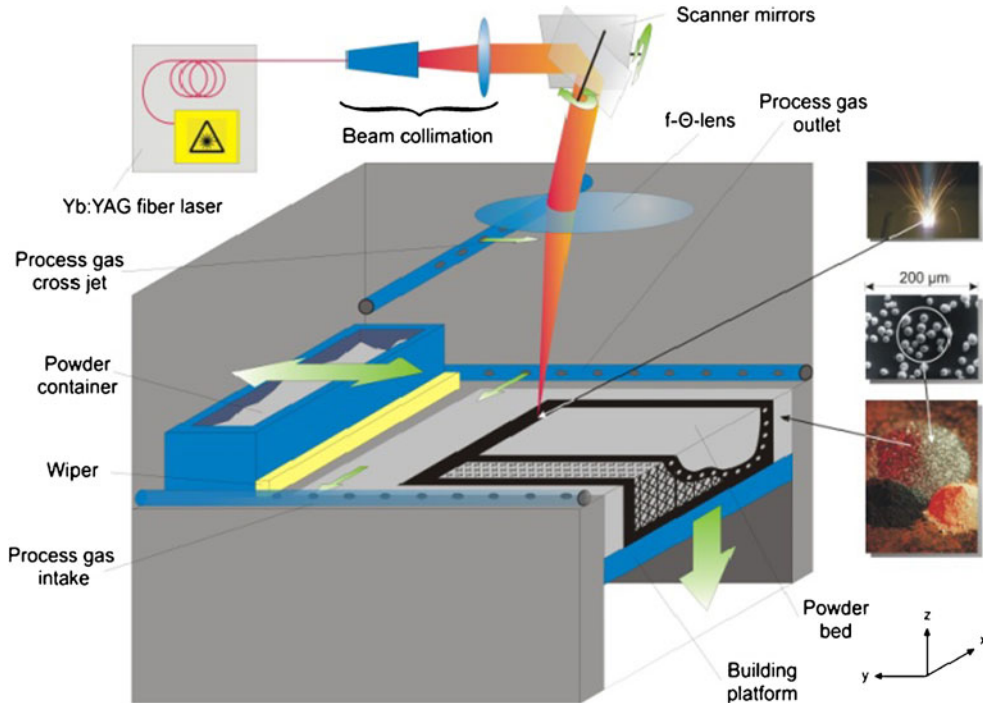
1 Introduction

Additive manufacturing (AM) techniques open a wide range of possibilities of manufacturing for different material families. AM is an umbrella term to cover many types of manufacturing where material is used in an additive way to build up three-dimensional parts. One of the processes is the selective laser melting (SLM) which fabricates metallic components—layer-by-layer—directly from 3D-CAD data. The starting material used in the SLM process is a metal powder which is deposited as a thin layer on a substrate. The powder is selectively melted by a laser beam according to the CAD model. After each layer is completed, the substrate plate is lowered by one layer thickness and a new powder layer is deposited above. Again, this layer is selectively melted and metallurgical-bonded to the layer below. Hence, the final component is built of many single layers. In the case of metallic materials, the possibility of efficient and complex designs—parts with absence of fixtures or assemblies, customized patient implants, and inner channels in molds and dies, for instance—open interesting new generations of applications in different industry fields (as is already happening in medicine, aeronautic, plastic injection, sports, electronic, customized products, and so on) [1–3]. Current applications of the studied steel (316 L) processed by SLM: dental caps; ultra-light structures with over 450 holes and channels per cubic meter for aircraft, automotive, and medical industries; thin-walled (0.5 mm) 40×40-mm assembly parts; and surgical devices. But, before a general implantation of this type of manufacturing technology occurs for many of these kinds of applications, different technical issues still remain to be solved [4]. Among these points, a very important one is to know the properties of the alloys after being processed by the corresponding AM process.

I. Tolosa · F. Garciandía · F. Zubiri · F. Zapirain (✉) · A. Esnaola
LORTEK,
Bº La Granja, s/n.,
20240 Ordizia, Guipúzcoa, Spain
e-mail: fzapirain@lortek.es
URL: www.lortek.es

Table 1 Composition of studied alloy: austenitic stainless steel AISI 316 L (percentage in weight)

C	Si	Mn	P	S	Cr	Mo	N	Ni
≤0.03	≤1.00	≤2.00	≤0.045	≤0.015	16.50–18.50	2.00–2.50	≤0.110	10.00–13.00

Fig. 1 SLM process

As it has been already stated—and building upon previous work—this paper is focused on the study of mechanical properties and their anisotropy with manufacturing orientation for a metallic alloy manufactured by AM, using the technology of SLM. The material analyzed is an austenitic stainless steel—AISI 316 L—which has a wide field of industrial applications. In this case, the good mechanical properties obtained open the use of the technology, if the corrosion properties are kept to those inherent to wrought products (by a solution heat treatment–hyper quench). At this moment, this material and manufacturing process are been validated for different commercial products.

The aim of this paper is to show the influence of a new manufacturing process (AM) on the “in service” properties, which are obtained in a metallic alloy (in this case, an austenitic stainless steel), and the effects of different manufacturing strategies, and not only its chemical composition, in the same specified alloy. The process studied is the SLM in metallic alloys. In this case, part performance is affected by building conditions. It is well-known that the properties of many metallic materials are given not only by their chemical composition but, besides, by their microstructure. The micro-

**Fig. 2** SLM equipment from MTT

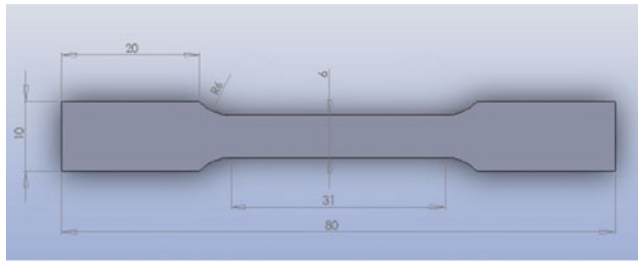


Fig. 3 Tensile test sample

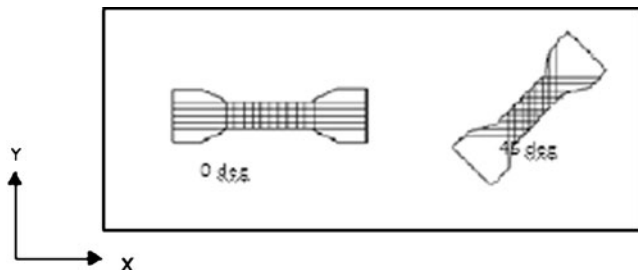


Fig. 4 Orientation of samples with base geometry in $X-Y$ plane, case A

structure in a metallic material is obtained by the processes involved in its manufacturing path (melting, hot or cold rolling, heat treatment, hot forming, cold forming, welding, etc.). That means that the very same alloy may show very different properties (and not only mechanical, but dynamic, corrosion resistant, wear-resistant, and physical properties) depending on its manufacturing processes. This study has shown that the properties obtained in a metallic alloy processed by SLM may differ significantly from the properties obtained in the same alloy by other more common processes.

2 Alloy

This study has been done using an austenitic stainless steel in the form of metallic powder (diameter of particles between 10 and 45 μm). The alloy studied is the AISI 316 L, whose composition is shown in Table 1 (1.4404 or X2CrNiMo17-12-2 after European standard “EN 10083”). These steels achieve their anti-corrosion properties through the formation of an

invisible and adherent chromium-rich oxide surface film. This oxide forms and heals itself in the presence of oxygen. This oxide layer gives to these steels their corrosion resistance properties. Other elements added to improve particular characteristics include nickel (main gamma-gamma element in austenitic stainless steels), molybdenum, copper, titanium, aluminum, silicon, niobium, nitrogen, sulfur, and selenium.

Specified properties of this alloy for wrought products will be detailed later for comparison purposes with obtained properties in samples made with different SLM strategies.

3 Additive manufacturing by selective laser melting

The SLM process is an additive manufacturing process that fabricates metallic components—layer-by-layer—directly from 3D-CAD data. This process enables the production of nearly unlimited complex geometries [5]. The starting material used in the SLM process is a metal powder—in this case: AISI 316 L stainless steel—which is deposited as a thin layer (50 to 100 μm) on a substrate plate inside a closed process chamber. The powder is selectively melted by a laser beam according to the CAD model. After each layer is completed, the substrate plate is lowered by one layer thickness and a new powder layer is deposited above. Again, this layer is selectively melted and metallurgically-bonded to the layer below. Hence, the final component is built of many single layers (Fig. 1, courtesy of MTT).

4 Experimental equipment (SLM)

Fabrication of all samples by SLM was done using MTT equipment, model SLM 250 Realizer MCP. In Fig. 2, a picture of this machine may be observed.

Main characteristics of the equipment are the following:

Layer thickness: 30–100 μm
Scanning speed: up to 1,000 mm/s
Laser spot size: 80–300 μm
Powder size: 10–45 μm



Fig. 5 Samples manufactured with base geometry in $X-Y$ plane (case A)



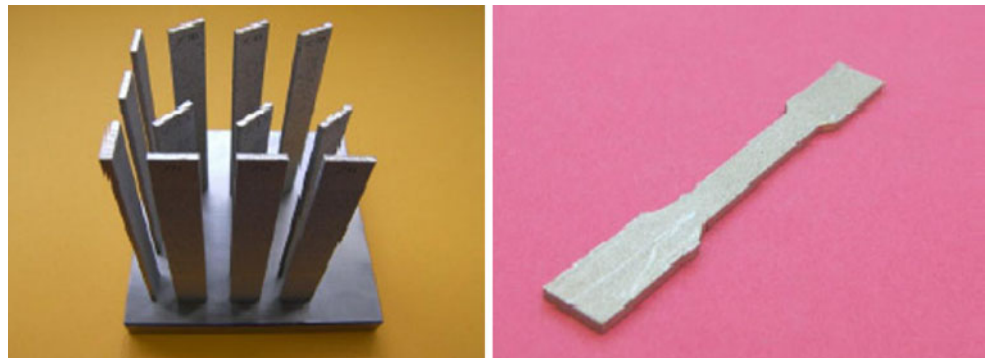
Fig. 6 Tensile test samples manufactured in case B

5 Experimental study

For this study, the technology of additive manufacturing by selective laser melting has been used. This study has been performed after achieving, in all samples/pieces, integrity higher than 99.9% in all the manufacturing orientations followed to build up the experimental samples. This means that a previous experimental study was carried on in order

mean anisotropy in properties [6]. A fixed component may be manufactured by different building strategies (which may suppose notable differences in manufacturing times, too). The selection of the orientation in space of the building layers for a designed component, means that the properties and their anisotropy could be different according to the manufacturing strategy (orientation building of layers inside the component) followed [7–9].

Fig. 7 Testing samples obtained by SLM in case C



to obtain the optimum process parameters for each of these manufacturing orientations. In the following tests, process parameters have been the same: 200 W of power laser, 50 μm of layer thickness and $50 \text{ cm}^3\text{h}^{-1}$ of building rate. In all the experimental tests included in this study, only the manufacturing orientation of samples growth has changed.

AM by selective laser melting means that components manufactured by this kind of technology are obtained by a succession of molten layers in a direction, so this could

Different mechanical tests have been performed and their corresponding testing samples have been manufactured by means of AM by SLM. Here follows a short description:

5.1 Ultimate tensile strength

Tensile tests have been done following ASTM standards. In Fig. 3, dimension and geometry of the testing samples are shown. All samples are grown in the z axis of the SLM

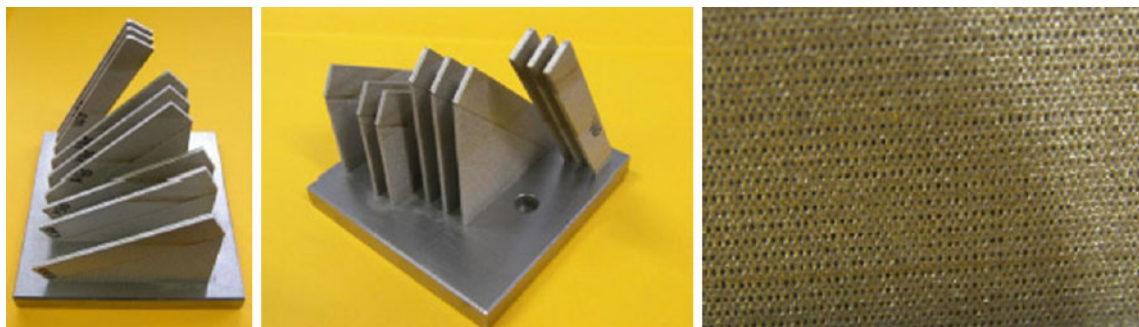


Fig. 8 Some samples and detail of a support structure, case D

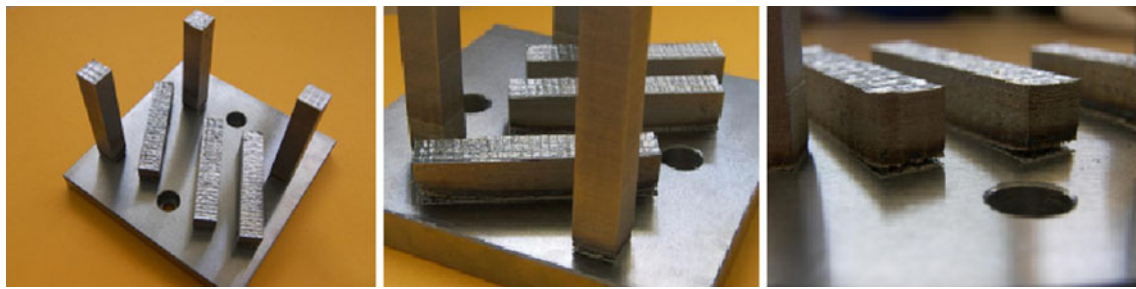


Fig. 9 Samples for Charpy tests

equipment working area; the difference, in each case, is in which plane and direction is contained the base geometry of the sample as may be seen in Fig. 3.

Case A: Samples manufactured with base geometry in $X-Y$ machine plane (with different rotation angles).

In this case, it has to be considered that melting angle is different in the calibrated zone, depending on the scanning angle (Fig. 4). Samples have been manufactured at 0° , 30° , 45° , and 90° with respect to X axis.

Manufactured samples by SLM may be observed in Fig. 5.

Case B: Samples manufactured with base geometry in $Z-X$ to $Z-Y$ plane (with different rotation

Table 2 Tensile tests results for samples with base geometry in $X-Y$ plane, case A

Angle with regard to the horizontal		0°		
		Rm (MPa)	Re (MPa)	E (%)
1		678	656	26
2		689	663	20
3		688	671	28
Average value		685	663	25
Standard deviation		5.3	6.3	3.6
Angle with regard to the horizontal		30°		
		Rm (MPa)	Re (MPa)	E (%)
1		666	661	26
2		668	656	36
3		738	718	36
Average value		691	678	33
Standard deviation		33.6	28	4.7
Angle with regard to the horizontal		45°		
		Rm (MPa)	Re (MPa)	E (%)
1		681	673	30
2		688	669	33
3		687	677	30
Average value		685	673	31
Standard deviation		3.2	3.1	1.6
Angle with regard to the horizontal		90°		
		Rm (MPa)	Re (MPa)	E (%)
1		685	653	30
2		683	658	33
3		690	673	30
Average value		686	662	31
Standard deviation		2.9	8.5	1.6

Rm tensile strength, *Re* yield strength, *E* elongation

Table 3 Results of tensile tests in samples manufactured in case B

Angle with regard to the horizontal		0°		
		Rm (MPa)	Re (MPa)	E (%)
1		661	634	30
2		657	632	30
3		674	541	30
Average		664	602	30
Standard deviation		7.4	47.2	0
Angle with regard to the horizontal		30°		
		Rm (MPa)	Re (MPa)	E (%)
1		664	630	33
2		670	620	33
3		674	650	30
Average		669	634	32
Standard deviation		3.9	12.5	1.6
Angle with regard to the horizontal		45°		
		Rm (MPa)	Re (MPa)	E (%)
1		659	639	33
2		679	659	33
3		653	620	33
Average		664	639	33
Standard deviation		11	15.9	0
Angle with regard to the horizontal		90°		
		Rm (MPa)	Re (MPa)	E (%)
1		662	614	33
2		680	668	27
3		680	633	30
Average		674	638	30
Standard deviation		8.5	22.2	2.7

Rm tensile strength, *Re* yield strength, *E* elongation

Table 4 Results of tensile tests in samples manufactured in case C

Angle with regard to the horizontal	0°	Rm (MPa)	Re (MPa)	E (%)
1	586	544	43	
2	608	577	43	
3	581	551	40	
Average	591	557	42	
Standard deviation	11.7	14.1	1.6	
Angle with regard to the horizontal	30°	Rm (MPa)	Re (MPa)	E (%)
1	590	544	43	
2	580	534	43	
3	568	508	43	
Average	579	529	43	
Standard deviation	8.9	15.2	0	
Angle with regard to the horizontal	45°	Rm (MPa)	Re (MPa)	E (%)
1	578	536	47	
2	573	517	47	
3	555	529	40	
Average	568.6	527.5	44.4	
Standard deviation	9.8	7.8	2.8	
Angle with regard to the horizontal	90°	Rm (MPa)	Re (MPa)	E (%)
1	608	548	47	
2	583	549	43	
3	579	537	43	
Average	590	545	44	
Standard deviation	13.1	5.8	1.6	

Rm tensile strength, Re yield strength, E elongation

angles) and main axis of the sample in $X-Y$ plane.

To avoid the use of supports from samples to the platform, samples have been manufactured with prismatic geometry and then slightly machined to the final geometry (Fig. 6).

Case C: Samples made with base geometry in the $Z-X/Y$ plane (with different rotation angle) and main axis of the sample in Z direction.

Samples have been also obtained with a prismatic geometry and then slightly machined to final geometry (Fig. 7). This is the worst case (from the tensile properties point of view) as the layers have been produced one after another in the tensile test direction.

Case D: Samples made with base geometry in the $Z-X$ to $Z-Y$ plane (with different rotation angle) and

main axis of the sample bowed with respect to Z direction.

In order to obtain better properties on components made in vertical position (case C), a strategy of growing the components/samples with some inclination with respect to Z axis has been proposed. The need of supports depends on the angle of fabrication (with respect to the horizontal plane): as much as this angle is larger (sample closer to vertical axis), the less is the need for these supports. In the pictures corresponding to Fig. 8, some of these manufactured samples are shown; the supports may be observed as well as a detail of the surface of these supports. In the case of 30° and 45°, the supports are needed in all the length of the samples, while for the case of 60°, these supports is only needed at the beginning of the angles.

5.2 Notch impact (Charpy) tests

The same criteria have been followed for the notch impact tests (Charpy). In this case, samples have been manufactured by SLM, too. Batches of three standardized samples of $10 \times 10 \times 55$ mm have been produced in two orientations corresponding to the ones with best and worst tensile results (case A, 30° in the $X-Y$ plane and case C, 0° with z axis). Samples are shown in Fig. 9. Supports of 1.5 mm high have been used to ease the extraction of samples from the base platform. It should be noted that residual stresses have been produced in the first layer and have distorted the corners of it, modifying locally the geometry of the sample (Fig. 9).

The sides of the samples with higher roughness have been shot-peened with corindon and polished.

6 Obtained results and discussion

As it has been already explained, different mechanical tests have been performed, and their corresponding testing samples have been manufactured by means of AM by SLM. These samples have been manufactured with different orientation strategies (cases A to D). Most important part of mechanical testing has been ultimate tensile strength tests, but resilience and microhardness tests have been performed, too.

6.1 Ultimate tensile strength tests

It should be noticed the high relation Re/Rm in all cases, with minimum values of Re higher than 525 MPa (it must be underlined that in wrought products these values are lower than 300 MPa), but keeping high elongation values (in most cases above 30%, which means—indirectly—high cold ductility).

Table 5 Tensile tests for samples obtained at different angles in case D

The samples are placed in the Y axis with an angle to Z axis		30°	Rm (MPa)	Re (MPa)	E (%)
1		644		627	37
2		654		641	33
3		651		616	40
Average		649.8		628	36.7
Standard deviation		4.29		10.24	2.72
The samples are placed in the Y axis with an angle to Z axis		45°	Rm (MPa)	Re (MPa)	E (%)
1		660		625	40
2		676		664	33
3		671		659	33
Average		669.3		649.3	35.6
Standard deviation		6.6		17.4	3.1
The samples are placed in the Y axis with an angle to Z axis		60°	Rm (MPa)	Re (MPa)	E (%)
1		667		654	37
2		658		628	37
3		676		628	33
Average		667		636.4	35.6
Standard deviation		7.5		12.4	1.6

Rm tensile strength, Re yield strength, E elongation

Here are detailed the obtained results:

Case A: Samples manufactured with base geometry in X-Y plane (with different rotation angles).

Results obtained in these samples are detailed in Table 2 (Rm and Re in Mega Pascal (MPa); elongation in percentage).

As it may be observed in Table 2, best results have been obtained for 30°, but the homogeneity for all angles of manufacturing is high.

Case B: Samples manufactured with base geometry in Z-X to Z-Y plane (with different rotation angles) and main axis of the sample in X-Y plane.

Results obtained in tensile tests in these samples are collected in Table 3 (Rm and Re in Mega Pascal (MPa); elongation in percentage). In this case, similar values have been obtained for all angles.

Case C: Samples made with base geometry in the Z-X plane (with different rotation angle) and main axis of the sample in Z direction.

Results obtained in tensile tests in these samples are collected in Table 4 (Rm and Rp in Mega Pascal (MPa); elongation in percentage).

Best results of strength have been obtained with 0°. Best results for elongation both with 45° and 90°. As it was expected, this is the worst case for resistance properties, but, on the other hand, it shows the best elongations values.

Case D: Samples made with base geometry in the Z-X to Z-Y plane (with different rotation angle) and main axis of the sample bowed with respect to Z direction.

In this case, tensile tests have been done, too. In Table 5 are detailed the results (Rm and Rp in Mega Pascal (MPa); elongation in percentage). In this case, an important increase in tensile properties with respect to case C is observed:

In this case, the best strength properties are observed at 45°, while the best ductility is obtained at 30°. Taking into account

Table 6 Mechanical properties for wrought AISI 316 L steel

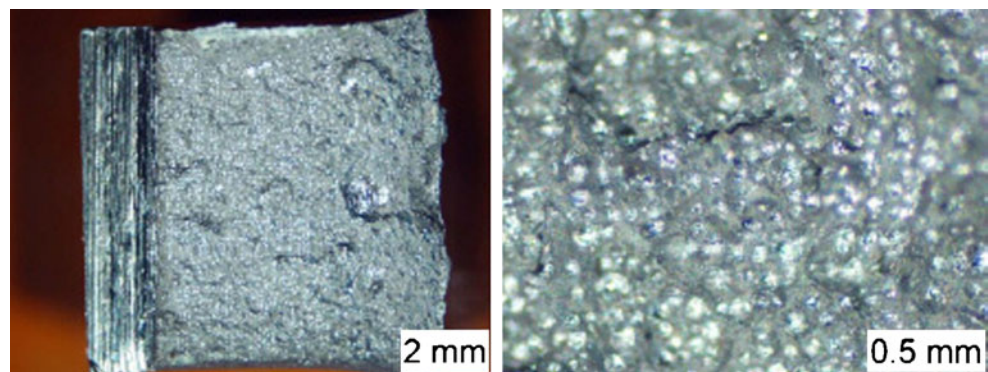
Material	Rm (MPa)	Re (MPa)	Elongation (%)
AISI 316 L	520–680	220–270	40–45

Rm tensile strength, Re yield strength

Table 7 Results of Charpy tests at room temperature

Case A/30° (J)	Case B/0° (J)
58	65
70	42
62	44
Average: 63.3	Average: 50.3

Fig. 10 Detail of fracture surface in tested Charpy samples



average values, the strength is increased by 80 MPa with respect to case C; so, if the piece is going to suffer strength in the Z axis in service, it would be necessary to find a solution of compromise, assessing both, the necessary strength and the supports needed to manufacture the component (this in case that case A is not possible).

With respect to all cases studied in this paper, it is clear that, from the point of view of strength, the best option is the building strategy of case A (with maximum values of medium Rm and Re of 691 and 678 MPa, respectively). On the other hand, best ductility values (elongation) are measured for case C (with medium values higher than 44%).

6.1.1 Tensile tests in wrought material

In order to be able to compare the obtained properties with those obtained by “conventional” ways of manufacturing (in this case, rolling), tensile test properties for rolled sheet of the 1.4404 (AISI 316 L) steel are collected in Table 6 (standard EN 10083).

As it may be appreciated, properties for strength obtained with SLM technology are comparable to those of wrought products; in all cases, the results for strength properties are higher in components obtained by SLM. Tensile strength is, in all cases, in the range, and, in case A, above this range. Yield strength in selective laser melting is always clearly above the values of this property for wrought products. Elongation values are lower but with high enough values for most of applications. Special mention is for the obtained yield strengths, which are significantly higher of those for wrought products but, as it has been mentioned, maintaining high elongation values. Usually, for metallic alloys an increase in the ratio Re/Rm means severe decrease of elongation (Re/Rm for this wrought alloy is usually around 0.4, while for this SLM-processed alloy, it has been usually higher than 0.9). This means that besides the design freedom given by the RM process, additional material savings and weight reductions may be achieved with this manufacturing technology.

The study with this material has included a metallographic analysis which, due to space limitations, is not included in this paper. As it has been stated before, mechanical properties

depend not only in the composition of the alloy, but in its manufacturing route, i.e., its final microstructure. The microstructure obtained when processing this alloy by SLM is a succession of fine layers ($<50 \mu\text{m}$) composed of very fine grains of austenite.

6.2 Notch impact (Charpy) tests

Obtained results in Charpy tests at room temperature (20–25°C), are the following (Table 7):

The average value is 56.8 J, which is a value lower than expected. Reference value was ≥ 75 J. Anyway, this value is also high enough for a large variety of applications. The study of mechanical properties for SLM-manufactured components has to be done for each application taking into account (besides alloy) design and building strategy and costs. Analyzing the fracture surface, a ductile fracture morphology has been observed; porosity previous to rupture has not been observed, and joining between layers has not been visible (pictures of Fig. 10 show the fracture surface and a detail of the final contact area).

6.3 Vickers microhardness tests

Vickers hardness tests have been done across the section of each sample, every 0.4 mm. In Fig. 11, a representative hardness distribution is showed. The mean value obtained—235 HV—is in consonance with the values expected for this

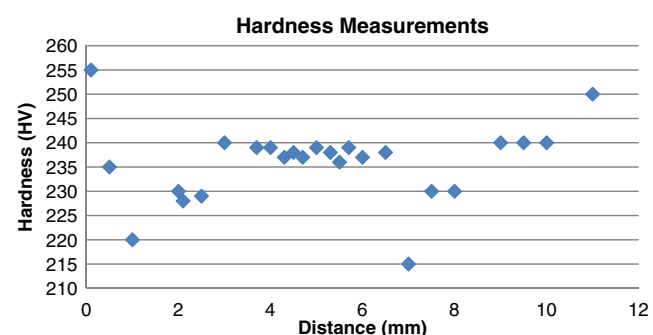


Fig. 11 Obtained Vickers hardness distribution in AISI 316 L alloy

material. Obtained hardness values have been very similar in all of the four cases.

7 Conclusions

Results collected in this paper are focused in the AISI 316 L austenitic stainless steel after being processed by selective laser melting as an additive manufacturing technology. In this paper, previous published results are complemented, as the mechanical tests have been performed in all the possible directions of manufacturing by SLM and not only in two main directions. The goal of this study has been to know the mechanical properties of the mentioned steel after being processed by SLM, and its properties variations with different manufacturing strategies, i.e., different layer-by-layer building orientations. Finally, properties have been compared with those specified for this steel for “wrought” products.

Samples for mechanical tests have been manufactured directly by SLM, with different manufacturing strategies (orientations in the space). These samples have been manufactured with SLM parameters which guaranteed a density higher than 99.9%.

Tensile properties: for this steel, strength properties after SLM process are higher to corresponding properties to this alloy in the rolled condition. Special mention is for the obtained yield strengths, which are significantly higher than those for wrought products but maintaining high elongation values. Usually, for metallic alloys, an increase in the ratio Re/Rm means severe decrease of elongation (Re/Rm for this wrought alloy is usually around 0.4, while for this SLM-processed alloy, it has been usually higher than 0.9). This means that besides the design freedom given by the AM process, additional material savings and weight reductions may be achieved with this manufacturing technology. Results for elongation (ductility) are lower to those for wrought products, but higher enough for many applications (higher than 30% in most cases). In both cases, properties show anisotropy and depend on the direction in which the sample has been manufactured.

Resilience tests (Charpy) In this case, results also show anisotropy, and values are slightly lower to those specified to wrought products (average values among 63 and 50 J at room temperature, 25°C).

Hardness tests (Vickers) Results are homogeneous and similar to those found in wrought products of this alloy.

As a concluding remark, it may be said that, in the case of the AISI 316 L steel, the technology of RM by SLM has proven to be—from the point of view of mechanical properties—a very challenging technology for manufacturing demanding products.

References

- Some successful examples of AM implementations and business models in biomedical applications. P. Reeves. 2nd Rapid Manufacturing Forum: Manufacturing reinvented for medical and biomedical applications". 29th of June, 2009. Barcelona, Spain
- Emmelman C, Petersen M, Goecke A (2009) Laser freeform fabrication for aircraft applications. Proceedings of the International Conference, Lasers in Manufacturing (LIM), Munich, Germany
- Dormal T. Rapid manufacturing of mould inserts for tooling improvements. International Conference on Additive Technologies 2008 September 17th–18th, Ptuj, Slovenia
- Metals powder bed Additive Layer Manufacturing: The good, the bad... and the ugly. Carl Brancher. Industrial Laser Application Symposium (ILAS) July 2009. Great Britain
- Sutcliffe C. Selective laser melting: developments in SLM equipment and processes. MTT Technologies Group. Industrial Laser Application Symposium (ILAS) July 2009. Great Britain.
- Bassoli E, Gatto A, Sewell NT, JohnsOn D (2009) The effects of build orientation in powder-fed additive layer manufacture of steel 316 L. In: Bártołko et al (eds) Innovative developments in design and manufacturing. Taylor and Francis Group. pp 263–268
- Thivillon L, Novichenko D, Bertrand PH, Smurov I (2009) Mechanical properties of parts manufactured by direct metal deposition technology. Lasers in Manufacturing (LIM), Munich
- Yadroitsev I, Bertrnd PH, Smurov I (2009) Selective laser melting technology: study of parameters influencing single track formation and properties of manufactured samples. Lasers in Manufacturing (LIM), Munich
- Kahlen F-J, Kar A (2001) Tensile strength for laser-fabricated parts and similarity parameters for rapid manufacturing. ASME J Manuf Sci Eng 123:38–44

Microstructural Architecture, Microstructures, and Mechanical Properties for a Nickel-Base Superalloy Fabricated by Electron Beam Melting

L.E. MURR, E. MARTINEZ, S.M. GAYTAN, D.A. RAMIREZ, B.I. MACHADO, P.W. SHINDO, J.L. MARTINEZ, F. MEDINA, J. WOOTEN, D. CISCEL, U. ACKELID, and R.B. WICKER

Microstructures and a microstructural, columnar architecture as well as mechanical behavior of as-fabricated and processed INCONEL alloy 625 components produced by additive manufacturing using electron beam melting (EBM) of prealloyed precursor powder are examined in this study. As-fabricated and hot-isostatically pressed (“hipped”) [at 1393 K (1120 °C)] cylinders examined by optical metallography (OM), scanning electron microscopy (SEM), transmission electron microscopy (TEM), energy-dispersive (X-ray) spectrometry (EDS), and X-ray diffraction (XRD) exhibited an initial EBM-developed γ'' (bcc) Ni₃Nb precipitate platelet columnar architecture within columnar [200] textured γ (fcc) Ni-Cr grains aligned in the cylinder axis, parallel to the EBM build direction. Upon annealing at 1393 K (1120 °C) (hot-isostatic press (HIP)), these precipitate columns dissolve and the columnar, γ , grains recrystallized forming generally equiaxed grains (with coherent {111} annealing twins), containing NbCr₂ laves precipitates. Microindentation hardnesses decreased from ~2.7 to ~2.2 GPa following hot-isostatic pressing (“hipping”), and the corresponding engineering (0.2 pct) offset yield stress decreased from 0.41 to 0.33 GPa, while the UTS increased from 0.75 to 0.77 GPa. However, the corresponding elongation increased from 44 to 69 pct for the hipped components.

DOI: 10.1007/s11661-011-0748-2

© The Minerals, Metals & Materials Society and ASM International 2011

I. INTRODUCTION

NICKEL-BASE superalloys, essentially γ (fcc), NiCr solid solution strengthened by additions of Al, Ti, Mo, Ta, and Nb to precipitate a coherent, ordered fcc metastable phase γ' (Ni₃(Al, Ti, Nb)) or γ'' (bcc) phase (Ni₃Nb),^[1] comprise a broad range of compositions, which have found widespread applications over the past half century. Examples of the more prominent and contemporary applications include jet engine components such as turbine blades, high speed airframe parts, and fossil fuel and nuclear power plant components. These alloys also find a wide variety of corrosion and elevated temperature oxidation envi-

ronment applications, especially CUSTOM-AGE 625*

*CUSTOM-AGE 625 is a registered trademark of Carpenter Technology Corp., Reading, PA.

plus and ALLOY 625**, which are superior to

**ALLOY 625 is a registered trademark of Carpenter Technology Corp., Reading, PA.

INCONEL 718[†],^[2] and used in refinery and chemical

[†]INCONEL 718 is a trademark of Special Metals Corporation, New Hartford, NY.

process industries.^[3–9]

Directional (or unidirectional) solidification processing^[10] was extensively applied in the production of aligned eutectic structures, directional columnar structures, and single-crystal Ni-base superalloy turbine blades. These single-crystal turbine blades solidify with a dendritic structure containing microsegregation and second-phase (γ') particles formed by eutectic reactions. In eutectic alloys with reinforced composite properties, a planar

L.E. MURR, Professor and Chairman, E. MARTINEZ, P.W. SHINDO, and J.L. MARTINEZ, Undergraduate Research Assistants, S.M. GAYTAN, D.A. RAMIREZ, and B.I. MACHADO, Graduate Research Assistants, are with the Department of Metallurgical and Materials Engineering, The University of Texas at El Paso, El Paso, TX 79968. Contact e-mail: lemurr@utep.edu F. MEDINA, Manager, and R.B. WICKER, Professor and Director, are with the W.M. Keck Center for 3D Innovation, The University of Texas at El Paso. J. WOOTEN, President, and D. CISCEL, Vice President, are with CalRAM, Inc., Simi Valley, CA 93065. U. ACKELID, Senior Scientist, is with Arcam AB, Mölndal SE-431-37, Sweden.

Manuscript submitted December 20, 2010.

Article published online June 15, 2011

solid-liquid (phase equilibrium) interface can be established for ingot solidification of eutectic composition carried out under a steep axial thermal gradient achieved by slow withdrawal of the ingot from a furnace such that uniaxial heat flow conditions are established.^[11] When this occurs, the two solid eutectic reaction phases (matrix/eutectic) deposit at the liquid/solid interface and grow parallel to the direction of movement of this reaction front. Consequently, two phases are formed oriented in (or parallel to) the direction of solidification. This often forms eutectic fibers, embedded in the continuous matrix, or parallel lamellae of each phase. Variations in solidification rates of the two phases into the melt create variances in the microstructural features, often forming complex dendrite or related branching patterns.

Jackson and Hunt,^[12] in very early investigations, showed that the morphology or architecture observed for unidirectionally solidified eutectic structures will depend upon the relative volume fraction of each phase. Fiber or rod morphology prevails when one phase is present in amounts less than $1/\pi$ of the total volume. Alternately, when the minor phase constitutes more than $1/\pi$ of the total volume, a lamellar structure consisting of alternate platelets of the two phases is preferred. Often associated with these parallel microstructures are preferred crystallographic relationships between the interpenetrating crystals of the two phases. This is particularly true for Ni-base eutectic systems such as implicit in γ - γ' structures.^[13]

The second-phase particles formed in directionally solidified Ni-base superalloys provide composite, coherency/ordered/strengthening of the fcc γ matrix. In INCONEL 718 alloys (53Ni-19Cr-3Mo-5Nb-19Fe-0.07C) aging reactions produce fine γ'' Ni₃Nb (bct, DO₂₂) coherent disc-shaped precipitates on the γ {100} planes and ordered fcc (Li₂) γ' precipitates with a cube-cube {100} orientation relationship with the γ (Al) matrix. Alloy 625 (INCONEL 625) is similarly strengthened by γ' and γ'' (Ni₃(Nb, Ti, Al)) during aging, forming fcc cubes and bct discs, respectively, both coincident with the matrix (NiCr) fcc (γ) {100} planes. In HASTELLOY[‡] B (a Ni-Mo alloy), ordered bct

directional solidification processing,^[3,10,11] a relatively new process, electron beam melting (EBM), builds components by the additive layer-by-layer melting of metal or alloy powder layers.^[15-17] In this process, illustrated schematically in Figure 1, precursor powder in cassettes is gravity fed onto a build table, where it is sequentially raked into a layer ~50- to 100- μm thick (depending on the powder size and size distribution), which is preheated by multiple-pass electron beam scanning, and then selectively melted with a melt scan directed by a CAD program. Recent fabrication of Co-base alloy components by EBM from atomized powder produced a novel, discontinuous columnar architecture composed of Cr₂₃C₆ (cubic, fcc) precipitates forming columnar arrays spaced ~2 μm .^[17] Similar arrays of Cu₂O precipitates with similar microstructural architecture features were observed in EBM-fabricated Cu components.^[18]

This article describes a novel microstructural architecture observed in Ni-base superalloy (alloy 625) components fabricated from atomized powder using EBM. It also represents a comprehensive microstructural and mechanical property characterization study. Optical metallography (OM), scanning electron microscopy (SEM), and transmission electron microscopy (TEM) were used for microstructural characterization, along with energy-dispersive (X-ray) spectrometry (EDS) with the SEM and TEM, and X-ray diffraction (XRD) analysis. Mechanical properties (hardness and tensile, including fracture surface analysis in SEM) were also measured and compared.

II. EXPERIMENTAL METHODS

A. EBM Processing

As illustrated in Figure 1(a) and described briefly previously, EBM processing involves the building of three-dimensional (3-D) components layer by layer from powder. Unlike directional solidification, where melt front propagation creates microstructural architecture, EBM allows for layer-by-layer melt/solidification thermal cycling, which provides complex thermal arrays whose dimensions are determined by electron beam focus and scan spacing. Each melted portion of a raked powder layer is directed by CAD software or model construction, which can also include CT scans of 3-D products.^[3] In this program, cylindrical components measuring 20 mm in diameter and 80 mm in length were fabricated from alloy 625, rotary atomized, rapidly solidified, prealloyed precursor powder illustrated in Figure 1(b) using an Arcam S-12 EBM system (Arcam AB, Molndal, Sweden). Figure 1(c) shows the powder particle sizes and size distribution, having an average size (particle diameter) of 22 μm . Cylindrical components were convenient for examining transverse (horizontal) and longitudinal (vertical) plane structures and microstructures as well as residual hardness. Cylindrical geometries were also convenient for machining tensile specimens for test and analysis. Comparative rectangular specimens measuring 20 mm \times 20 mm \times 80 mm were also cut from rectangular plates measuring 20 mm \times 80 mm \times 80 mm.

[‡]HASTELLOY is a registered trademark of Haynes International, Inc., Kokomo, IN.

Ni₄Mo and fcc Ni₃Mo precipitates form, while in HAYNES[§] 242 alloy (Ni-Cr-Mo), fine Ni₂ (MoCr)

[§]HAYNES is a registered trademark of Haynes International, Inc., Kokomo, IN.

precipitates can form.^[3,4,7,14]

Recent development of powder metallurgy, especially for aeronautical applications, demonstrated more homogeneous microstructures suitable for high-temperature components.^[9] These processed Ni-base alloys are represented by Udimet products (Seco Tools AB, Fagerston, Sweden). In contrast to conventional

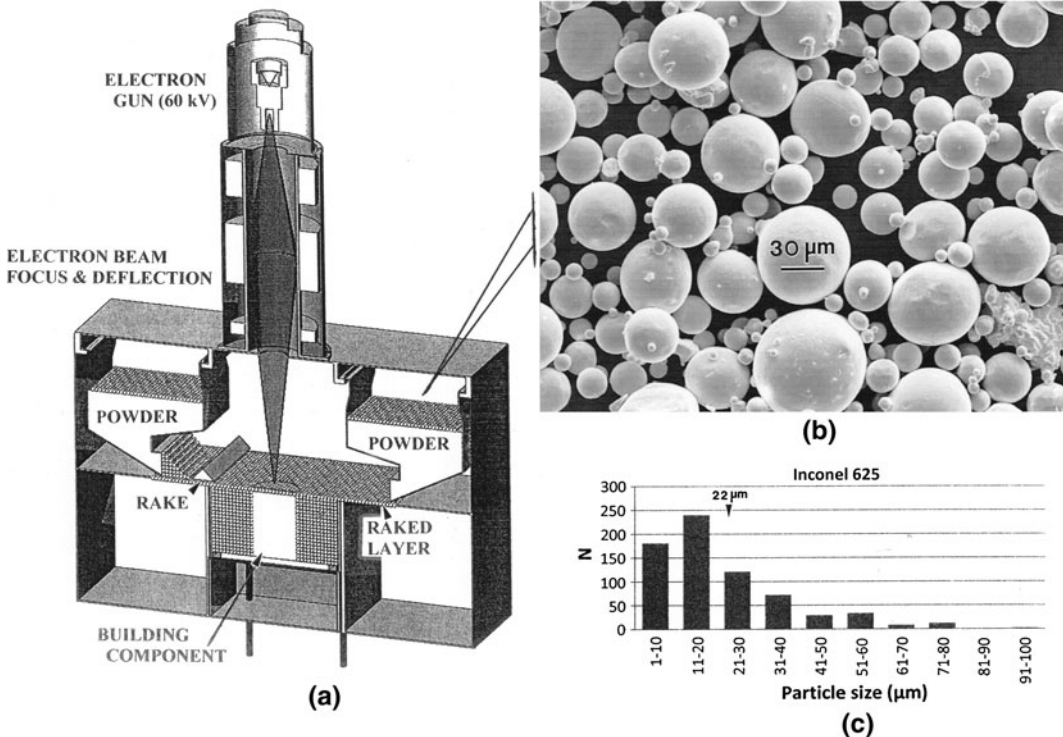


Fig. 1—(a) EBM system schematic. The precursor powder loaded into cassettes shown is gravity fed and raked onto the build platform in successive layers ~50- μm thick. Selected areas of each layer are melted by the scanned beam. (b) SEM view of precursor powder showing spherical particles with varying sizes, as shown in the histogram in (c).

Table I. Chemical Composition for Alloy 625 Precursor Powder and EBM-Fabricated Components

Material component	Element (wt pct)									
	Ni	Cr	Fe	Mo	Nb	C	Mn	Si	Al	Ti
Nominal standard	61	22	3.2	9.0	3.5	0.02	0.1	0.1	0.2	0.3
Precursor powder mass analysis	65.7	21.3	0.4	9.3	3.7	0.004	—	—	—	0.002
Precursor powder EDS analysis	59.1	18.8	—	7.6	3.0	*	—	—	—	—
As-fabricated cylinder EDS analysis	61.1	19.2	—	8.8	4.7	*	—	—	—	—

*Variances of C and O are recorded in the EDS analyses. Oxygen varies from 3.3 pct in the powder to 2.6 pct in the as-fabricated products. C varies from 8 to 5 pct, respectively, and is not considered to be a real compositional feature for the alloy since mass analysis showed essentially no C or O.

Table I compares the alloy 625 standard (or nominal) chemical analysis compared with the mass analysis for the precursor powder in Figure 1(b) and corresponding EDS analysis of both the precursor powder (Figure 1(b)) and the fabricated cylinders.

B. Structural and Microstructural Analyses: OM, SEM, TEM, and XRD

Microstructures for the initial alloy 625 powder and the EBM-fabricated cylindrical samples were initially observed by OM and XRD, followed by SEM and TEM analyses, both employing ancillary EDS attachments for elemental analysis and elemental mapping. TEM analysis also employed selected-area electron diffraction (SAED) analysis and associated dark-field imaging.

OM used a Reichert MEF4 A/M metallograph using digital imaging (Reichert, Inc., Depew, NY). Initial alloy

625 powder (Figure 1(b)) was embedded in an epoxy-base mounting material and ground and polished to expose particle sections, which were electroetched with a solution consisting of 70 mL phosphoric acid and 30 mL water, at room temperature, using 5 V for etching times varying from 5 seconds to 2 minutes. Samples were also etched with 5 pct hydrochloric acid for etching times ranging from 1 to 10 seconds to bring out annealing twin structures or double etches (phosphoric – water + hydrochloric acid). Coupons cut and similarly mounted from the transverse (horizontal) and longitudinal (vertical) planes of fabricated cylinders were also electroetched, as described for the precursor powder. As-fabricated cylinders were also hipped at 1393 K (1120 °C) at 0.1 GPa pressure for 4 hours in argon, and these processed cylinders were similarly examined by OM.

XRD spectra were analyzed for the precursor powder (Figure 1(b)) and coupons extracted from the horizontal

and vertical planes for the as-fabricated cylindrical specimens and the hipped specimens. The XRD system was a Brucker AXS-D8 Discover system using a Cu target (Brucker AXS, Madison, WI).

SEM analysis employed a Hitachi S-4800 field emission SEM (Hitachi America, Pleasanton, CA) fitted with an EDAX EDS system and operated at 20 kV in both the secondary electron and backscatter electron (BSE) imaging modes. The TEM analysis of coupons extracted from the experimental alloy 625 samples, as outlined previously for OM, used sections ground and polished to thicknesses of ~200 μm . Three-millimeter standard TEM discs were punched, mechanically dimpled, and electropolished in a Tenupol-5 dual jet system (Product of Struers, Inc., Cleveland, OH) at temperatures ranging from 247 K to 245 K (~26 °C to ~28 °C), using an electropolishing solution consisting of 200 mL perchloric acid, 800 mL methanol at 13 V. TEM analysis was performed in a Hitachi H-9500 high-resolution transmission electron microscope operated at 300 kV and fitted with a goniometer-tilt stage, a digital imaging camera, and an EDAX-EDS elemental (X-ray) mapping analysis attachment (EDAX r-TEM^{§§} detector). This

^{§§}EDAX r-TEM is a trademark of EDAX, Inc., Mahwah, NJ.

system can map areas as small as 20 nm on a side.

C. Mechanical Testing

Micro- and macroindentation hardness measurements were made on specimen sections extracted from as-fabricated and hipped cylinders in the transverse (horizontal) and longitudinal (vertical) planes. Microindentation hardness was also measured for the mounted, polished, and etched precursor powder. The microindentation (Vickers) hardness (HV) was measured using a Vickers diamond indenter in a Shimadzu HMV = 2000 tester (Shimadzu Scientific Instruments Inc., Columbus, MD) (using 25 and 100 gf or 0.25 and 1 N load, respectively, for ~10-second load time). Macrohardness measurements were made using a Rockwell tester with a 1.5 N load and a C-scale indenter (HRC).

Tensile specimens were machined from the as-fabricated and hipped EBM cylinders and tested in an upgraded TINIUS-OLSEN[¶] Universal Testing machine

[¶]TINIUS-OLSEN is a trademark of Tinius-Olsen, Inc., Hansham, PA.

(SIN 175118) at a strain rate of ~10⁻³ s⁻¹ at room temperature [295 K (22 °C)]. Specimens as-fabricated and hipped were also tested at 811 K (538 °C). Fracture surface examinations were also performed for failed tensile specimens in the SEM. Tensile specimens were machined from the as-fabricated cylinders hipped at 0.1 GPa for 4 hours at 1393 K (1120 °C) in argon. This represented ~0.84 T_M , where T_M , the melting temperature, was 1608 K (1335 °C).

III. RESULTS AND DISCUSSION

A. Structural and Microstructural Characterization of As-Fabricated Cylinders

Figure 2 shows the characteristic microdendritic structure for the powder particles produced by atomization or rapid solidification rate (RSR) processing.^[19,20] The 2- μm interdendritic spacing shown in Figure 2 is essentially the same as that exhibited by other RSR-processed Ni-base superalloy powders (e.g., MAR M-200 (60Ni-Zr, Co, Cr, Al, Ti) over the past several decades).^[21] Correspondingly, the etched particle section view inserted in Figure 2 confirms that the microdendritic structure exists throughout the particle volume. Vickers microindentation hardness measurements made on sections similar to the optical metallographic image insert in Figure 2 indicated an average value of HV 260 or 2.6 GPa. Figure 3 shows an etched, OM composite view typical of an EBM-fabricated cylinder showing the horizontal plane (normal to the cylinder axis and in the build direction), for comparison with the corresponding powder structure, and the corresponding vertical section views. This structure is characterized by somewhat regular arrays of precipitates spaced ~2 μm . The microindentation hardness average for these horizontal sections was measured to be HV 280 (2.8 GPa). For the corresponding vertical plane OM views of a fabricated cylinder (parallel to the cylinder

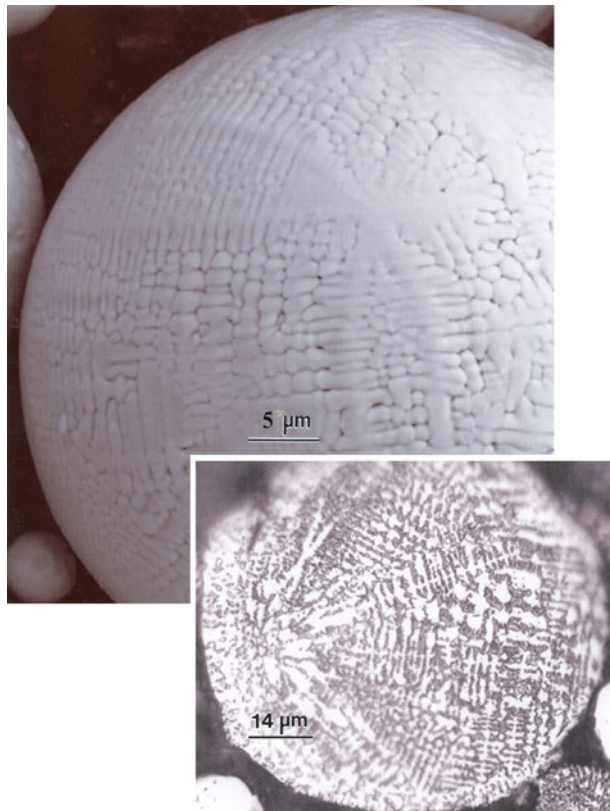


Fig. 2—Magnified SEM view of the INCONEL 625 powder particle showing classical RSR microdendrite structure, with OM view for the corresponding etched cross section inserted, showing the interior microdendritic structure.

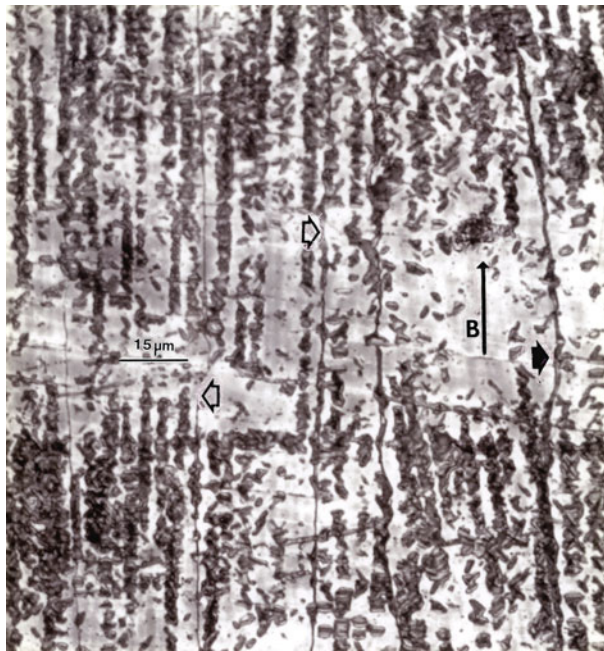


Fig. 3—OM view for a corresponding vertical reference plane parallel to the build direction (B) and the cylinder axis with reference to Fig. 1(a) showing columnar precipitate architecture in the build direction along with columnar grains with GBs indicated by large arrows.

axis and the build direction) shown in Figure 3, the microindentation hardness average was measured to be HV 250 (2.5 GPa). In contrast to, and in addition to, the horizontal plane arrays in Figure 4, Figure 3 shows irregular or discontinuous columnar-like grain structures composed of precipitate platelets coincident with specific and repetitive fcc Ni-Cr matrix planes. In addition, columnar grains ~20- μm wide and in some cases as long as 500 μm are observed (arrows in Figure 3). Most precipitate platelets are viewed edge-on in Figure 3, but numerous perspective views for different crystallographic coincidence plane sections, as indicated by arrows in Figure 3, are apparent. For example, the two opposing, unfilled arrows in Figure 3 indicate columnar grain boundaries (GBs), which differ from the one filled arrow at the right. The average spacings of the columnar precipitate structures are dimensionally consistent with the transverse (horizontal plane) views in Figure 4.

The columnar microstructural architectures in Figures 3 and 4 are essentially the same as those characterized by columnar precipitate arrays of M_{23}C_6 carbides in a Co-base superalloy fabricated by EBM,^[17] as well as columnar precipitate arrays of Cu_2O in EBM-fabricated Cu.^[22] Similar columns of small (~10 nm) γ'' (Ni_3Nb) precipitates coincident with {100} γ have also been observed in the EBM fabrication of an INCONEL 718 alloy by Strondl *et al.*^[23] In the microstructural architectures of precipitate arrays observed in EBM-fabricated materials, including Figures 3 and 4, the arrays were characterized by columnar precipitate geometries spaced ~2 to 3 μm ^[17,22] or larger.^[23] These features are created by the EBM-beam scans, which include rapid multipass, orthogonal (x-y), fixed spatial

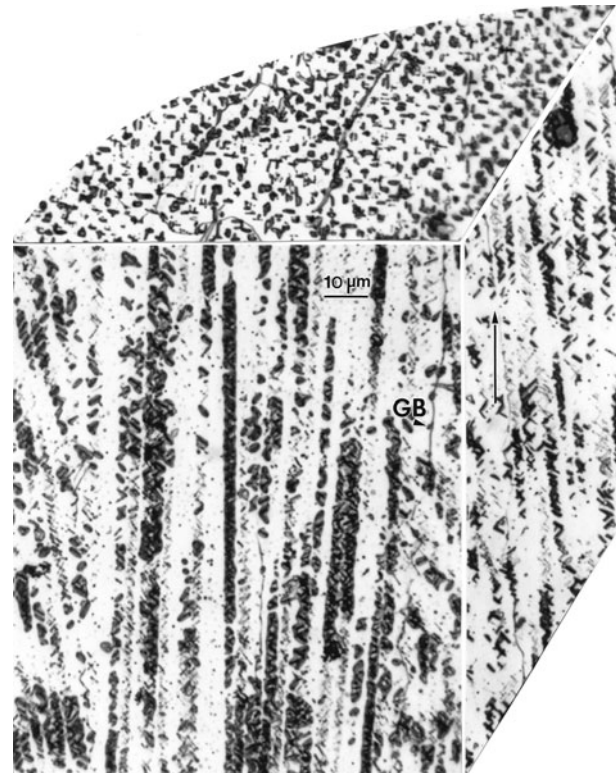


Fig. 4—Magnified OM 3-D reconstruction showing columnar precipitate (microstructural) architecture and columnar GBs containing precipitates. The arrow indicates the EBM process build direction.

rastering of the beam to preheat the layers, as well as the final x-y melt scan.^[17,22] The orthogonally rastered zones create thermal partitioning in each layer, conducive to precipitation, which is additively extended forming the columnar architectures. The partial remelting of successive layers also promote a layer-by-layer epitaxy responsible for the partially unidirectional columnar grain growth (Figure 3).

As noted earlier, aged alloys 718 and 625 can produce fcc and bct Ni_3Nb disc and cubic precipitates coincident with the fcc (Ni-Cr) matrix {100} planes including the recent EBM work by Strondl *et al.*^[23] In addition, other Ni-base superalloy compositions commonly also produce fcc $\text{Ni}_3\text{Cr}_{2-}$ and bct Ni_4Mo precipitates.^[3,4,7,14,23] XRD analysis for the precursor powder is reproduced in Figure 5(a). Since the dendritic (microdendritic) structure for the alloy 625 precursor powder does not exhibit any precipitation features (Figure 2), the spectral indices indicated are coincident with solid-solution fcc NiCr ($a = 0.359 \text{ nm}$; space group: $Fm-3m$). The prominent (111) peak in Figure 5(a), along with the corresponding fcc Ni-Cr peaks, characterizes the dendritic structure and matrix shown in Figure 2. In comparison, the XRD spectrum for the solid, cylindrical component horizontal plane (or section) in Figure 4 is shown for comparison in Figure 5(b). Here (Figure 5(b)), the (111) peak intensity is very low, along with all other peaks (in Figure 5(a)), except for the prominent fcc (200) peak and the (400) fcc peak, absent in Figure 5(a) (XRD for the powder). However, the (400) peak also matches the (226) reflection for $\gamma''\text{-Ni}_3\text{Nb}$ (bct: $a = 0.362 \text{ nm}$,

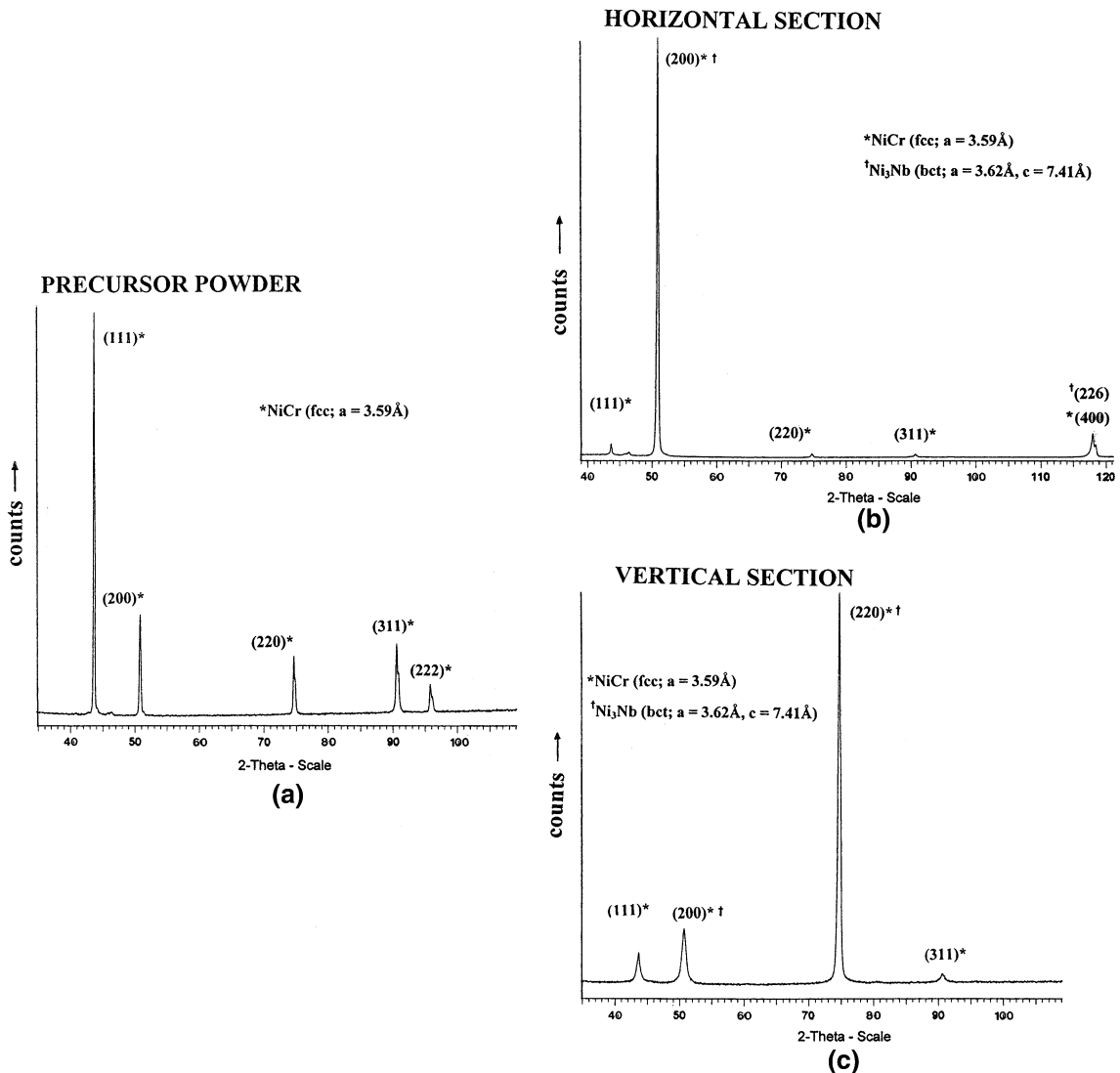


Fig. 5—XRD spectra for (a) precursor alloy 625 powder, (b) EBM-fabricated cylinder horizontal plane, and (c) vertical plane section.

$c = 0.741\text{ nm}$; space group: $I4/mmm$). Of course, this peak may simply arise due to the prominent (200)[200] horizontal plane texture, although the $\gamma''(\text{Ni}_3\text{Nb})$ bct (200) peak also matches the $\gamma(\text{NiCr})$ 200 peak. The [200] texture in Figure 5(b) represents the growth of the columnar grains shown in Figures 3 and 4 parallel to the build direction and the cylinder axis. The γ'' precipitates in the columns shown in Figures 3 and 4, as noted earlier, are arrayed in apparent coincident fcc crystal planes for the γ Ni-Cr matrix. The vertical plane (or section) XRD spectrum in Figure 5(c) shows the (220) fcc γ peak to be most prominent, with no significant (400) fcc or (226) bct peak. These peak shifts and XRD peak prominences on comparing Figures 5(a) through (c) illustrate corresponding texture variations from the precursor powder particle microdendritic microstructure to the horizontal and vertical build planes, respectively. The vertical plane texture should vary with the geometry or crystallographic coincidence of the vertical sectioning. The weak (226) peak and overlapping (200) peak in Figure 5(b) for the γ'' Ni₃Nb may arise from the very

small platelet volume fraction when viewed down the precipitate columns in the horizontal reference plane. However, in the vertical plane, the platelet volume fraction is reduced to a less detectable level, and the (226) peak disappears. However, since there is a nearly exact γ (200)/ γ'' (200) peak match as well as γ (220)/ γ'' (220) and γ (311)/ γ'' (311), it is not possible to determine the γ'' contribution unambiguously from the XRD data (Figure 5).

While the actual GB features are not particularly prominent in the horizontal reference plane in Figure 4, the corresponding vertical reference planes in Figure 3 show columnar grains and GBs $\sim 15\text{-}\mu\text{m}$ wide. Corresponding equiaxed grains in the horizontal plane also average $15\text{ }\mu\text{m}$ in size, as shown in Figure 6(a). These boundaries (Figure 6(a)) are observed to have some precipitates in the boundaries, and it is not clear that they are the same as the Ni-Nb columnar, crystallographic precipitate platelets in Figures 3 and 4. In contrast to the horizontal plane structure in Figure 4, Figure 6(a) and areas similar to it occur irregularly

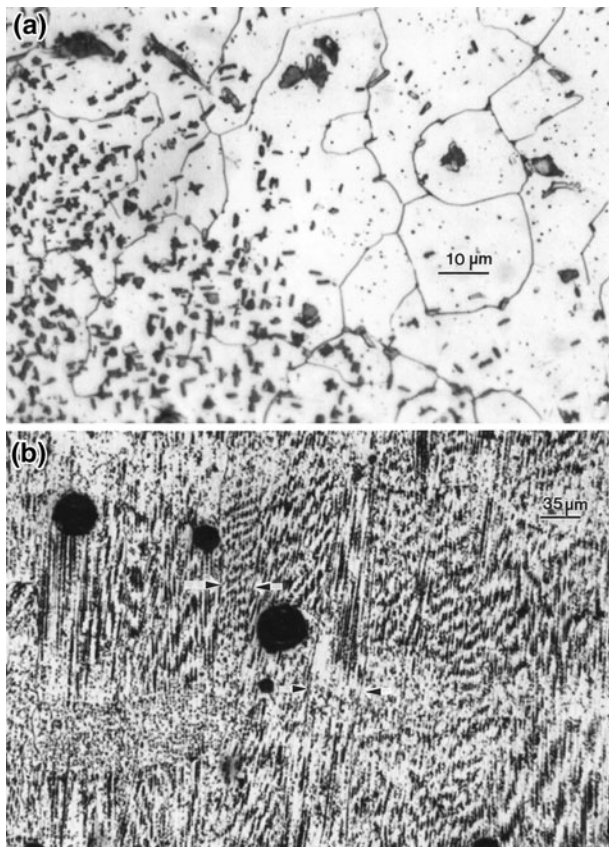


Fig. 6—OM images for horizontal plane section from an EBM-fabricated cylinder showing (a) equiaxed grain structure, and vertical plane section showing columnar precipitates and grains (arrows), and spherical voids (b).

because of EBM scan or localized thermal variations. Very similar observations were shown by Strondl *et al.*,^[23] where the precipitates in the boundaries were γ' in contrast to γ'' precipitates in discontinuous columns similar to Figure 3. The elongated grains in Figure 3 illustrate columnar [200] grains (Figure 5(b)) extending hundreds of microns parallel to the build direction as in the work of Strondl *et al.*,^[23] where they also noted a [100] columnar grain texture. Figure 6(b) shows a lower magnification vertical reference plane section, where directional/grain columns are apparent (arrows). Figure 6(b) also shows some evidence of porosity, where the hemispherical voids correspond to the precursor powder diameters (Figure 1(b)). The measured density for the as-fabricated samples was $\sim 8.4 \text{ g/cm}^3$ in contrast to a theoretical density of 8.45 g/cm^3 , representing a very low porosity. The density measured after hipping was $\sim 8.5 \text{ g/cm}^3$, indicating some porosity reduction. The columnar grains shown in Figures 3 and 4 are also shown by the arrows in Figure 6(b). It can be concluded that the propensity of horizontal plane grain structures are associated with (200)[200] texture, while the vertical, elongated grains are characteristically a strong (220)[220] texture (comparing the prominent XRD peaks in Figure 5(b) and (c)). This applies at least for the position or geometry of the longitudinal cut

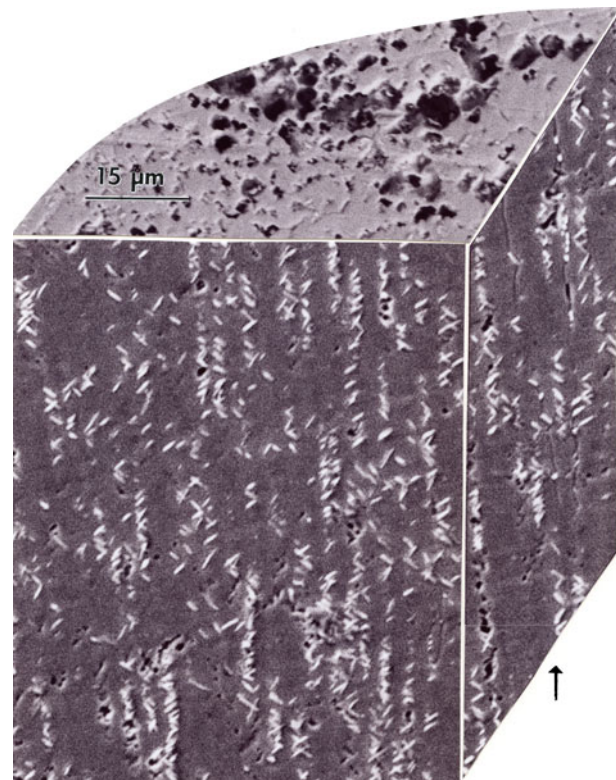


Fig. 7—SEM 3-D composite for precipitate columns in an EBM-fabricated cylindrical component. The horizontal section is a SE image, while the vertical sections are BSE images.

exposing the vertical specimen plane parallel to the build direction, as noted previously.

SEM observations of the precipitate columns provided a clearer view of their nature and geometry (or implicit crystallography), while EDS elemental mapping confirmed their general Ni_xNb composition. These features are illustrated in the sequence of observations shown in Figures 7 through 9. Figure 7 shows a mixed secondary electron (SE)-BSE 3-D image composition for precipitate column architectures consistent with Figure 3, while Figure 8 shows higher magnification and more detailed views. Figures 8(a) and (b) confirm the platelet features of the precipitates and their apparent crystallographic geometries. The magnified view in Figure 8(b) shows the precipitate platelet thicknesses to be <50 to 100 nm . The etchant to reveal them has created pits and surrounding etched regions, which, as can be observed in Figures 3, 4, and 7, exaggerate them. This etching, especially at the precipitate platelet edges, would indicate higher energy regions, and these may occur by coherency strains arising by mismatch between the precipitate platelets and the fcc matrix coincident planes.

EDS mapping for a section of a precipitate column in Figure 8 confirmed the Nb component. There was no evidence for Mo or Cr precipitation or precipitate contribution. Taken together with the XRD spectrum in Figure 5(b) for the horizontal plane for the cylindrical specimen builds, the γ'' Ni_3Nb platelet characterization becomes more convincing. However, because the

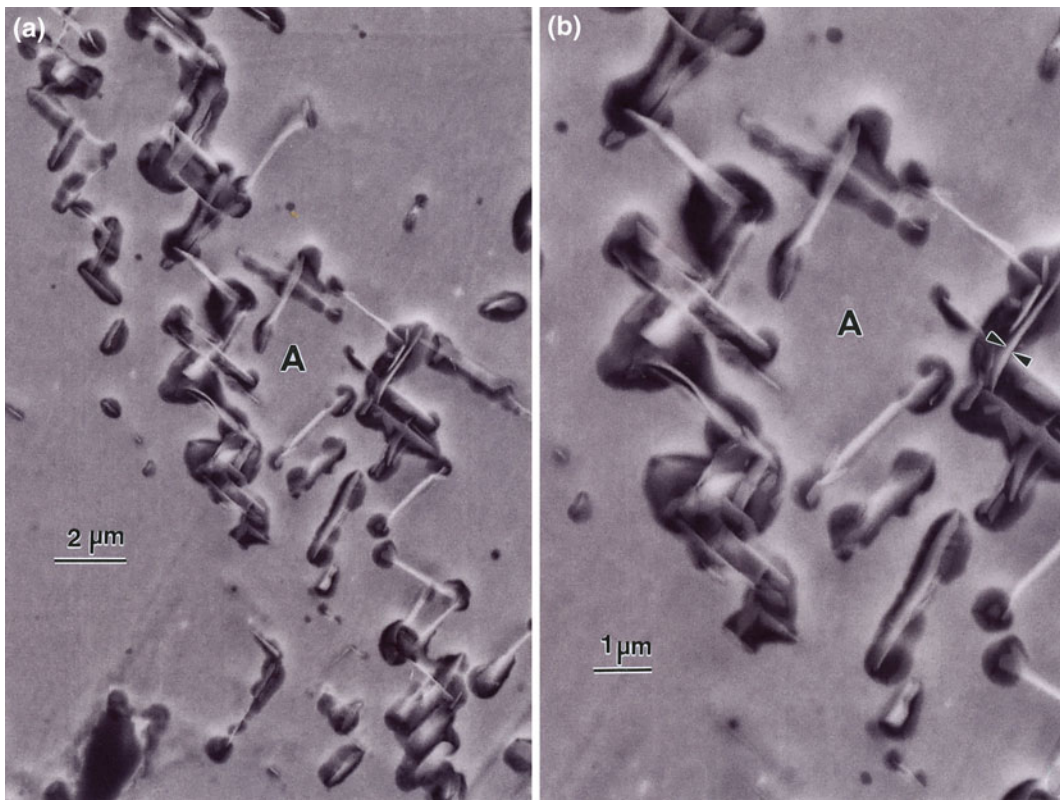


Fig. 8—(a) and (b) Magnified BSE (SEM) images, showing precipitate platelets composing the columnar architecture in Fig. 7. The reference area is denoted A.

precipitates are so thin in contrast to the etched material around them, as shown in Figure 8, the EDS signal (or X-ray count) for Nb was low.

TEM observations of γ'' precipitate platelets do not exhibit recognizably large strain fields and coincide with crystallographic trace directions consistent with the geometries or implicit crystallography observed in both the horizontal and vertical reference planes by OM and SEM (including SE and BSE imaging), as illustrated in Figures 4, 7, and 8. These features are unambiguously shown in Figures 9 and 10. Figure 9(a) shows a horizontal plane-view section exhibiting thin γ'' platelets coincident with the NiCr fcc matrix, while Figures 9(b) and (c) show corresponding vertical plane views (parallel with the build direction noted by the arrow). A TEM column portion (Figure 9(b)) with a corresponding BSE image (Figure 9(c)) shows these thin precipitates perfectly matching the crystallographic trace directions and their intersection geometry, respectively. Both the TEM horizontal and vertical plane section views in Figures 9(a) and (b) were (110) orientations determined by SAED. The trace directions (arrows) noted in Figure 9(a) correspond to **a** – [1 $\bar{1}$ 0], **b** – [112], and **c** – [112], characterizing the fcc matrix (111), ($\bar{1}$ 11), and (111) planes, respectively. Figure 9(b) shows the same (110) orientation in the vertical (longitudinal) plane showing the traces for the same ($\bar{1}$ 11) and (111) matrix planes, which coincide exactly with the edge views of the precipitate platelets in Figure 9(c) and Figures 4, 7, and 8. Indeed, these {111} planes are normal to the (110)

surface plane. The normal, edge-on views of the precipitate platelets in Figure 9(b) indicate them to be lenticular (with the thickness greatest in the plate centers). Measurement of the average edge-on platelet thickness produced values ranging from <50 nm in the thinnest plate sections to ~100 nm in the plate centers, consistent with estimates from the OM images, as noted previously. The irregular shapes of the precipitate platelets observed on inclined (111) planes in Figure 9(a) correspond to the **a** – [110] trace direction (**a** in Figure 9(a)). Figure 10 shows a magnified vertical plane TEM view of thin γ'' precipitate platelets in a (311) orientation. The precipitate platelets are coincident with {111} fcc (matrix) planes inclined with the (311) thin section surface, and intersecting along the [011] and [121] trace directions, respectively, in Figures 10(a) and (b). Figure 10(a) shows the bright-field TEM precipitate platelet image, while Figure 10(b) shows the corresponding aperture dark-field TEM image using the γ'' (bct) Ni₃Nb diffraction spot in the SAED pattern insert shown at the arrow. The geometry and crystallography of the Ni₃Nb platelets in Figures 8 through 10 are consistent with the XRD-[110] ([220]) texture shown in Figure 5(c) for the vertical plane parallel to the build direction. Figures 9(b) and 10 also illustrate considerable densities of dislocations. Figure 10(a) and (b) show dislocation structures within or associated with the γ'' precipitate platelets, which may also result in relieving coherency strains.

The nature of Ni-Nb precipitates in nickel-base superalloys was extensively studied more than 4 decades

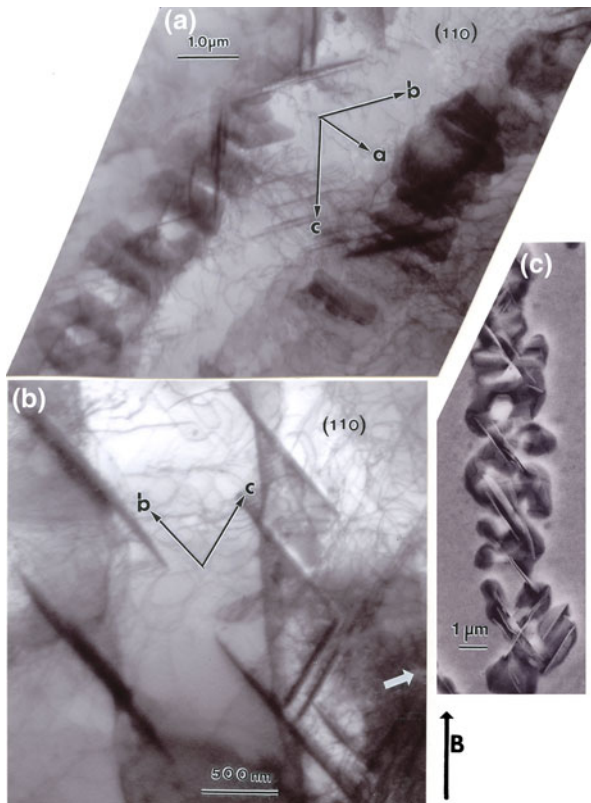


Fig. 9—(a) and (b) TEM bright-field images showing precipitate platelets in (110) plane sections representing the horizontal and vertical sections corresponding to Fig. 7. (c) A comparison with (b) of a BSE image, as in Fig. 8, for the precipitate column (white arrow). The build direction is shown at B. Crystallographic trace directions corresponding to a [110] zone axis are shown by **a**, **b**, and **c** in (a) and (b) and are described in the text.

ago. As noted earlier in this article, γ'' Ni_3Nb discs coherent with the γ (100) planes as well as ordered γ' Ni_3Nb cube precipitates coherent with γ (100) planes were described.^[3,4,7,14,23] However, much earlier work by Quinn *et al.*^[24] on Ni-Nb alloy subjected to directional solidification showed δ - Ni_3Nb Widmanstätten platelets (orthorhombic, $a = 0.511$ nm, $b = 0.424$ nm, $c = 0.454$ nm; space group: $Pmmn$) to be defined crystallographically by $(111)_\gamma/\!(010)_\delta$ by XRD. A similar relationship was found by Senicourt and Annaruma^[25] using electron diffraction. Forbes *et al.*^[2] also described acicular δ (Ni_3Nb)-orthorhombic acicular plates coincident with $\{111\}$ planes in overaged INCONEL 718 and γ'' (bct) Ni_3Nb laths on $\{111\}$ planes during aging of custom age alloy 625. Annaruma and Turpin^[26] also reported a semicoherent interface between γ and δ phases and the presence of mismatch dislocations at the interface, where the mismatch along the γ growth direction was ~ 0.5 pct. In addition, the thermal stability of this alloy after extended heat treatment also provided evidence that the γ/δ interface was low energy.

Since the XRD spectra for the horizontal and vertical reference planes for the EBM-fabricated cylinders (Figure 5(b) and (c)) can be indexed with some well-matched $\{hkl\}$ or d -space values for γ' - Ni_3Nb (fcc), γ'' - Ni_3Nb (bct), δ - Ni_3Nb (orthorhombic), as well as

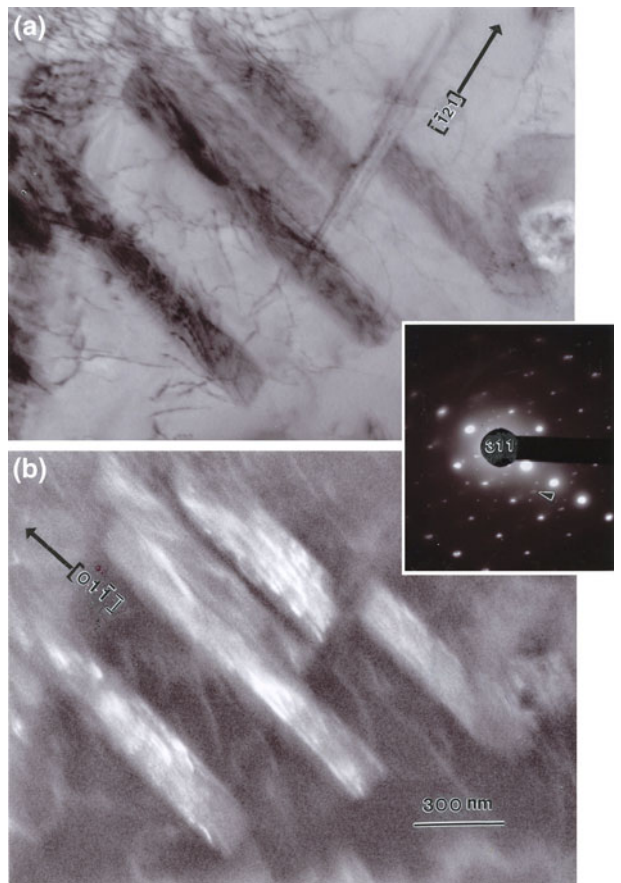


Fig. 10—TEM (a) bright-field and (b) dark-field image sequence showing Ni_3Nb precipitate platelets coincident with $\{111\}$ planes in the $[011]$ trace direction in a $[311]$ zone. The aperture dark-field image used the Ni_3Nb -bct reflection shown at the arrow in the SAED pattern insert.

$\text{Ni}_{0.85}\text{Nb}_{0.15}$ (fcc), the identification of the precipitate platelets rests upon the collective observations (OM, SEM, and TEM) and the SAED evidence, represented typically by Figure 10. Here, the platelets are unambiguously identified as γ'' - Ni_3Nb (bct) with the Ni-Cr (fcc) matrix/ γ'' - Ni_3Nb interface crystallography defined by $\| (111)_\gamma \| (010)_\gamma$. This precipitation phenomenon is a consequence of the unusual thermal conditions in EBM additive-layer fabrication, which can be regarded as a special case of directional solidification. It is interesting to note that the $\{111\}_\gamma$ plane coincidence of γ'' is different from the $\{100\}_\gamma$ plane coincidence in INCONEL 718 EBM components.^[23]

Figure 11 amplifies (and confirms) the precipitate identification by providing a high-magnification, bright-field TEM image showing precipitate-plate geometry (Figure 11(a)) in the vertical reference plane. The corresponding SAED pattern, illustrating the plate geometry in the context of the $\{111\}$ plane coincidence, as noted above (and including bct precipitate diffraction spots) (Figure 11(b)), the EDS spectrum showing Ni-Nb-Cr-Mo peaks (Figure 11(c)), and the corresponding elemental X-ray maps collectively support the precipitate identification. It can be noted in Figure 11(a)

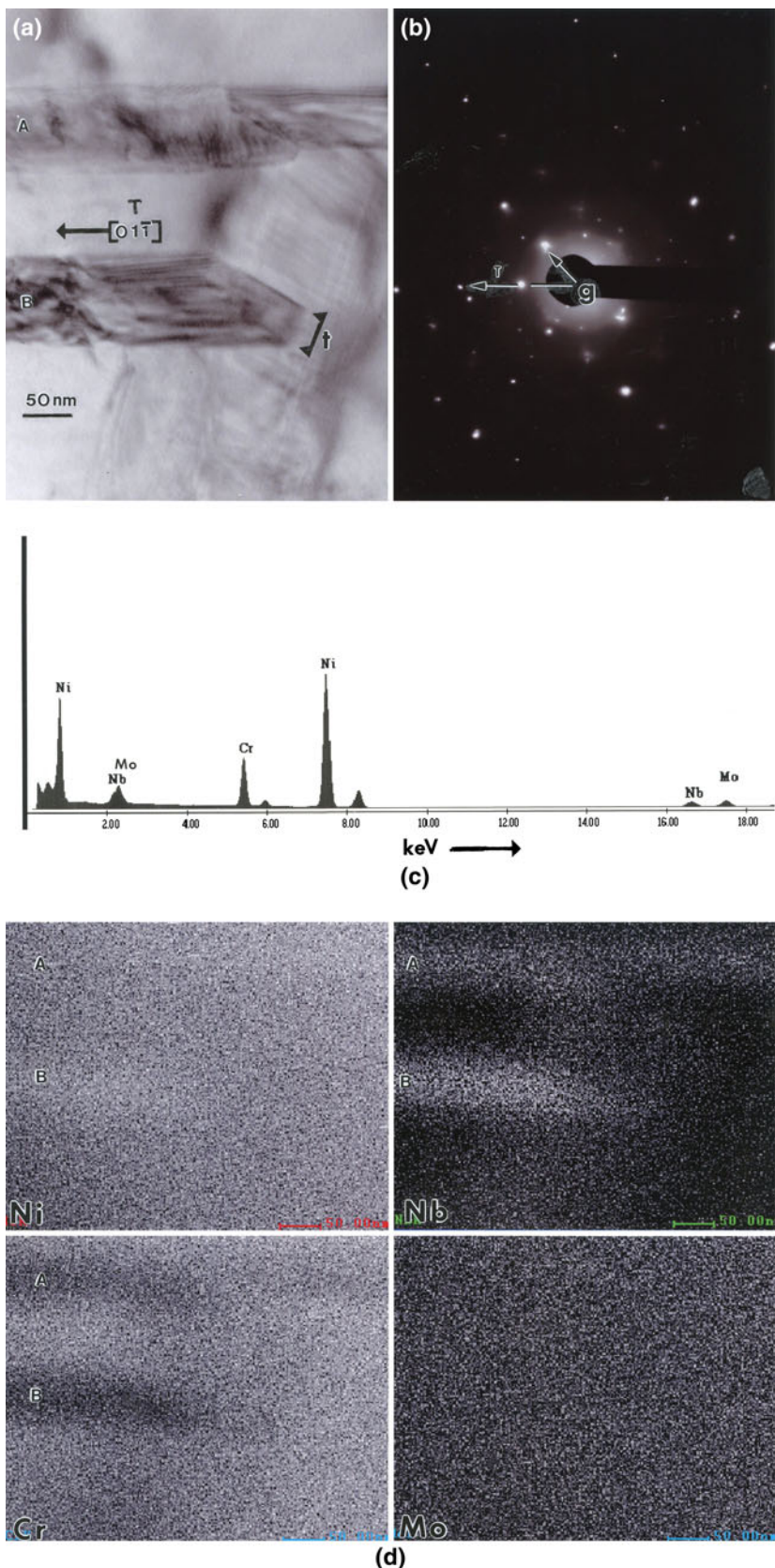


Fig. 11—TEM analysis sequence for Ni_3Nb precipitate platelet identification/verification. (a) Bright-field image for (111) coincident precipitate platelets at A and B, with thickness denoted t . (b) SAED pattern corresponding to (a) showing $[01\bar{1}]$ trace direction (T) and operating reflection ($\mathbf{g} = [020]$) in a [100] zone axis pattern. Note in (a) the precipitate at t intersects another out-of-contrast platelet. (c) The corresponding EDS spectrum for (a). (d) Elemental mapping sequence for (c) showing Nb at A and B precipitate platelets in (a). Weak Ni just above the background is also noticed.

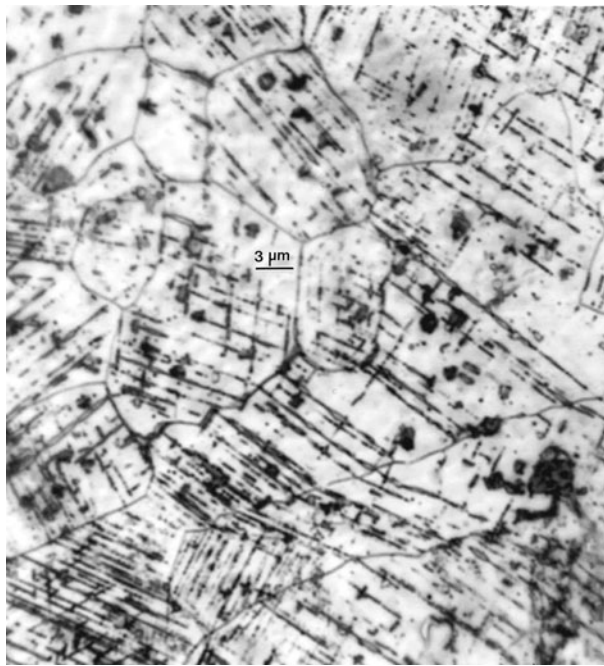


Fig. 12—Special OM image showing Ni_3Nb {111} plane coincident precipitates in the equiaxed grain structure in a horizontal plane section along a cylindrical specimen built by EBM. Some GB precipitates are also noticed.

that the rectangular precipitate (A) intersecting another, thinner precipitate plate, has a thickness (t) of ~ 50 nm. The precipitate is coincident with the (111) planes in the (100) thin section (inclined ~ 54 deg to the (100) crystal surface plane) characterized by the $[01\bar{1}]$ trace (T) direction, also shown in the coincident SAED pattern in Figure 11(b). The operating vector, \mathbf{g} , in Figure 11(b) is [020] and provides the diffraction contrast for the precipitates along $[01\bar{1}]$, denoted A and B in Figure 11(a). The precipitates, A and B in Figure 11(a), have slightly different diffraction contrasts, and they also exhibit complex, internal structure. Consequently, the X-ray signal is correspondingly similar in terms of X-ray photon counts, and this is illustrated along with the elemental X-ray maps in Figure 11(d). The precipitate positions indicated by A and B in the bright-field image of Figure 11(a) are similarly indicated in the maps in Figure 11(d). There is only weakly notable Ni above the Ni background for the B precipitate, while both A and B exhibit Nb only in the precipitates (A and B), and predominantly in B. There is Cr depletion in the precipitate platelets (A and B) as expected, while the Mo map illustrates a weakly uniform distribution.

Figure 12 illustrates an area in the horizontal plane normal to the build direction in a location within an EBM-fabricated cylinder, where the beam scanning or thermal environment caused the regular, columnar Ni_3Nb arrays shown in Figures 3 through 5 to become regularly precipitated along the {111} planes in continuous (linear) crystallographic arrays. This microstructure is a variance of the irregular features shown in Figure 6(a), but reinforces the propensity of the Ni_3Nb precipitate platelets to be organized within the grain

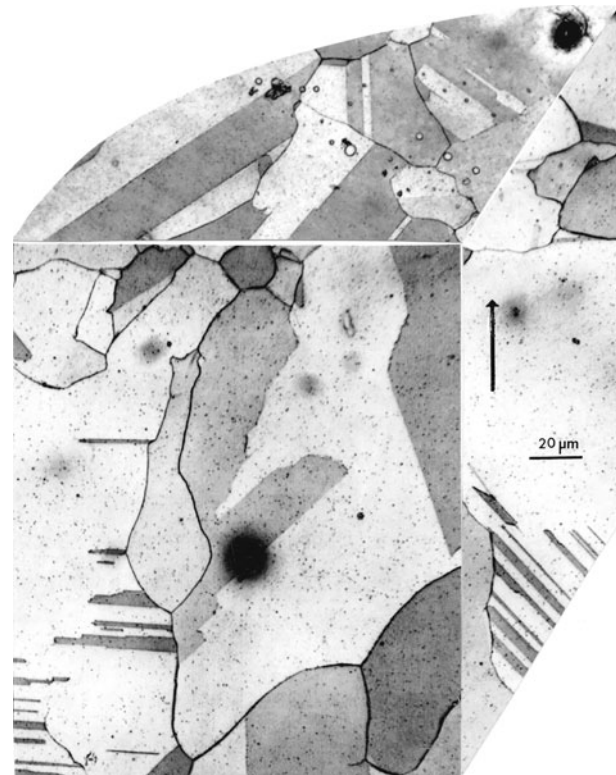


Fig. 13—OM 3-D-image reconstruction showing equilibrium, equiaxed grain structure in the hipped cylinder of EBM-fabricated alloy 625. Arrow indicates the build direction.

structures rather than the GBs, although some precipitation is observed along the columnar GBs in Figures 3 and 4 and in the corresponding horizontal plane GBs shown in Figure 6(a). These regular {111} precipitate arrays shown in Figure 12 also convincingly and more macroscopically support the observations of {111} coincidence illustrated collectively in Figures 8 through 10. Furthermore, Figures 6(a) and 12 attest to the generally equiaxed grain structure in the horizontal plane perpendicular to the build direction having an average grain size of ~ 20 μm , commensurate with the grain column widths shown in Figures 3, 4, and 6(b).

B. Structural and Microstructural Characterization of Hipped Cylinders

The HIPed cylinders, as described earlier, were effectively annealed at roughly 80 pct of the melting temperature for 4 hours. This temperature and treatment were sufficient to affect recrystallization and grain growth and other prominent microstructural changes, and these are implicit in the corresponding cylindrical-section, 3-D reconstruction shown in Figure 13, which represents a single electroetch with phosphoric acid described in Section II-B. In contrast to the columnar architecture arrays of Ni_3Nb precipitate platelets shown in Figures 3, 4, and 7 for the as-fabricated cylindrical components, Figure 13 illustrates an equiaxed grain structure in both the horizontal and vertical planes,

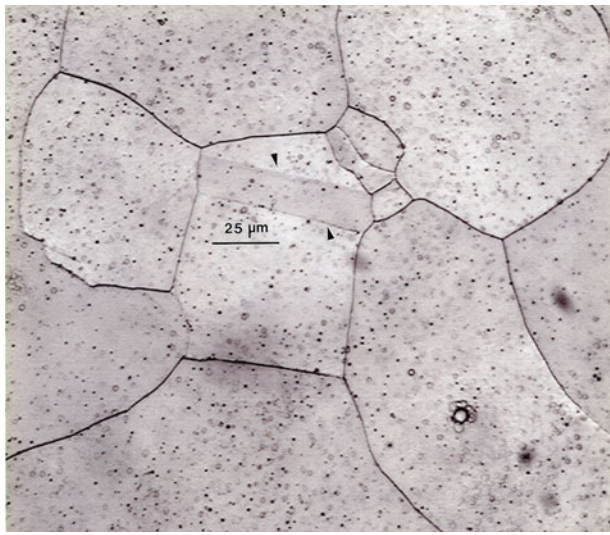


Fig. 14—OM of specially etched (phosphoric + hydrochloric acid) horizontal section, as in Fig. 13, showing globular precipitates and exaggerated GB etching.

although there were a few elongated grains along the build direction for vertical planes as well. These grain structures contain a significant fraction of annealing twins as an indication of more equilibrium structures in contrast to the nonequilibrium precipitate architectures in the as-fabricated EBM components. It is also notable that the Ni₃Nb precipitate platelet columns have apparently dissolved, and while the vertical plane grain structures exhibit some elongation (Figure 13), the columnar grains were reorganized by recrystallization, grain growth, and microstructural reorganization, including dissolution of the Ni₃Nb precipitate platelet columns. The grain sizes, including the annealing twins, vary over a wide range (Figure 13) and average ~50 μm in contrast to the as-fabricated component grain diameters of ~20 μm in the horizontal reference plane and ≤500-μm long grain columns with no annealing twins. Figure 13 also illustrates recognizable porosity similar to the as-fabricated specimens, as shown in Figure 6(b). This is an indication that the HIP anneal did not significantly alter the original porosity.

The contrast between the 3-D composition views in Figures 4 and 7 for the EBM-fabricated cylindrical builds, and the hipped/annealed cylinders in Figure 13, is essentially and conceptually identical to the microstructural variations between EBM-fabricated builds and the same builds after high-temperature annealing for a Co-base superalloy.^[17] In the Co-base alloy, columnar architectures composed of Cr₂₃C₆ precipitates with ~2-μm array spacings similar to those in the present work were annihilated after an annealing treatment, and the microstructure became an equiaxed, equilibrium grain structure containing a propensity of annealing twins similar to Figure 13. The Cr₂₃C₆ re-precipitated primarily on the equiaxed GBs, but not on the annealing twin boundaries (in the annealed Co-base superalloy^[17]), because at the elevated equilibrium temperature, the coherent twin boundary free energy for the Co-Cr fcc structure was less than a factor of 20 of the GB free energy

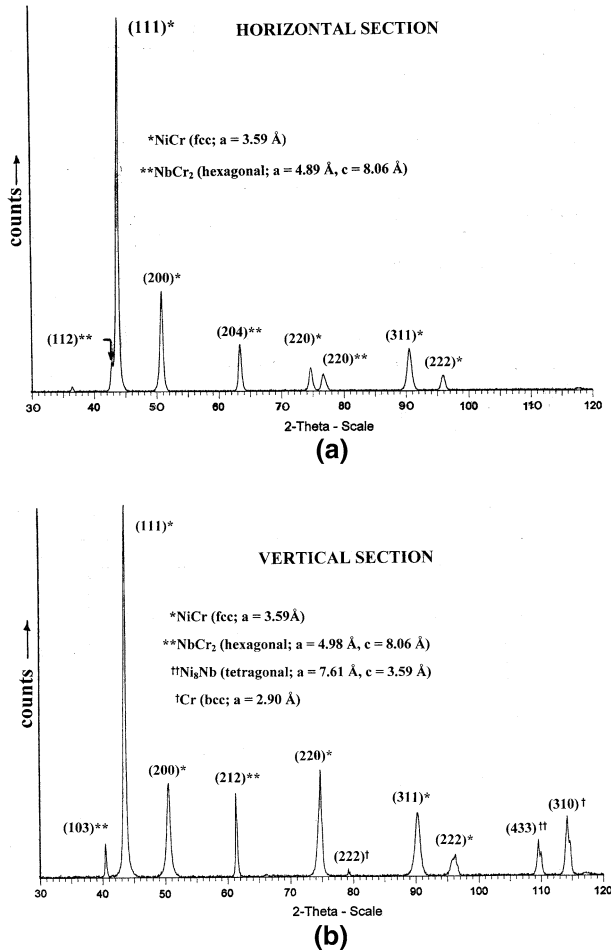


Fig. 15—XRD spectra representing (a) the horizontal reference plane section and (b) the vertical reference plane section in the 3-D composite in Fig. 13 for the hipped (annealed) alloy 625-fabricated (EBM) cylinders.

and, therefore, energetically unfavorable for precipitate nucleation.^[27] In addition, the low stacking-fault free energy for the fcc Co-Cr promoted a profusion of intrinsic stacking faults within the grains, as observed by TEM.^[17]

Figure 14 shows a horizontal section view similar to the 3-D–horizontal section view in Figure 13, but with a modified etch to reveal the homogeneous distribution of globular precipitates in contrast to the crystallographic precipitate arrays for the as-fabricated components shown in Figures 3, 4, and 12. The etching specific to Figure 14 also shows enhanced etching of the GBs relative to the coherent twin boundaries (arrows), but not revealing a propensity of GB precipitates relative to the grain interiors. This enhanced GB etching is a consequence of the much lower twin boundary free energy *vs* the GB free energy. The ratio of twin boundary free energy/GB free energy (γ_{tb}/γ_{gb}) for INCONEL 600 (Ni-Cr-Fe) or Ni-20Cr is ~0.023 at 1333 K (1060 °C), and the corresponding GB free energy is ~750 mJ/m².^[27] This is ~333 K (60 °C) below the hipping temperature [1393 K (1120 °C)].

Figure 15 shows the XRD analysis corresponding to the horizontal and vertical reference planes, respectively,

in the annealed (hipped) cylindrical components, as represented typically in Figure 13. In contrast to the precursor powder (Figure 5(a)) and the as-fabricated horizontal and vertical section reference planes (Figures 5(c) and (d)), the [200] horizontal and [220] vertical textures, respectively, are replaced by a uniform [111] horizontal and vertical plane texture for the annealed, equiaxed microstructure with annealing twins (Figures 13 and 14). There is some detectable Ni₈Nb (tetragonal: $a = 0.76$ nm, $c = 0.36$ nm; space group: P(0)) in the vertical section, indicating a nearly complete solutionizing of Ni-Nb precipitates. However, each reference plane section shows the presence of an NbCr₂ laves phase (hexagonal: $a = 0.49$ nm, $c = 0.81$ nm; space group: P631 mmc), which characterizes the globular precipitates shown in Figure 14. In addition, there is a prominent Cr (310) peak in the vertical section XRD in Figure 15(a) (bcc: $a = 0.29$ nm; space group: Im-3m). A globular laves phase was observed in INCONEL 718 weld metals (including electron beam welded components) by Radakrishna *et al.*^[29] Laves phase brittle, intermetallic, topologically close-packed (TCP) phase with hexagonal structure is normally detrimental to mechanical properties at room temperature.

Scanning electron microscopy (SEM) combined with EDS showed some segments of Nb prominence within the GBs, while the X-ray signal from the globular precipitates within the grains (Figure 14) exhibited erratic elemental prominence because of the large etched regions surrounding the precipitates similar to those regions surrounding the γ'' precipitate platelets, as illustrated in Figures 8 and 9(c).

Similar to the more dependable elemental mapping of γ'' precipitate platelets, as illustrated in Figure 11(d), the globular (laves) precipitates exhibited prominent Cr in EDS maps, as illustrated in the TEM image and EDS maps in Figure 16. As shown in Figure 16, many precipitates illustrated facets and regular crystalline forms, and some precipitates exhibited singular Cr maps apparently corresponding to the Cr (310) peak in Figure 15(a) (vertical section XRD spectrum). Figure 16(a) shows a small annealing twin with associated precipitates, while Figure 16(b) shows a magnified view of a precipitate in Figure 16(a) (arrow). Figure 16(c) illustrates the corresponding Cr map for Figure 16(b). Figures 16(d) and (e) show a precipitate aggregate and corresponding Cr EDS map, respectively. Several regular crystallographic precipitates are shown in Figure 16(f) near a GB, which exhibits complex ledge structure. This complex, high-energy structure could cause the selective GB etching illustrated in Figure 14.

The lack of a recognizable Nb signal for the precipitates in Figure 16 may be due, in part, to the weak elemental spectra in contrast to the elemental Cr particle spectra. The Ni stoichiometry is also not above the background Ni and therefore does not create recognizable contrast maps. In addition, the presence of Ni₈Nb in the XRD pattern in Figure 15 (vertical section) could be an indication of Nb depletion as a consequence of the HIP-anneal treatment for the EBM-fabricated components. However, we have no specific thermo.-kinetic or fundamental energy minimization data to support this

suggestion, except to note that this composition is at the edge of the Ni-rich region in the Ni-Nb phase diagram at the HIP-anneal temperature [1393 K (1120 °C)].^[7]

Unlike many Ni-base alloys subjected to various thermomechanical treatments, there were very few examples of stacking fault microstructures^[30] in the EBM-fabricated components (Figures 9 through 11) as well as the hipped and hipped and aged [811 K (538 °C)] components, even though the room temperature stacking-fault free energy for alloy 625 is estimated to be ~35 mJ/m².^[27] Figure 16 shows numerous examples of laves precipitates, which exhibit very prominent strain contrast fringe arrays when the foils were tilted in the TEM. In addition, all of the precipitates (Figure 16) exhibited associated dislocations or dislocation arrays, some extending long distances from the precipitate/ γ interface and some exhibiting dislocation generation at the precipitate/ γ interface. Figures 17(a) and (b) illustrate typical examples of these dislocation/precipitate phenomena. In addition, because of the nature of dislocation generation and propagation on the γ -{111} planes, the precipitates appear to be coincident with the {111} planes: (001) precipitate (laves) || (111). In Figure 17(a), complex dislocation loops generated at the precipitate/ γ interface are associated with two dipole network arrays on (111). Note the dislocations ending on the (110) surface plane along the [110] trace coincident with the (110) SAED pattern insert. Figure 17(b) shows precipitates in {111} planes characterized by intersecting (perpendicular) trace directions [022] and [0̄22] corresponding to intersecting (111) and (111) planes, each making an angle of ~54 deg with the (100) grain surface shown by the SAED pattern insert. Dislocation emission and propagation on these planes is prominently demonstrated in Figure 17(b).

While, as noted, stacking fault fringe contrast was only occasionally observed for specific tilt angles in the TEM, there were related, low-stacking-fault-energy-related microstructural features. Figures 17(c) and (d) illustrate typical examples. Figure 17(c) shows a precipitate, an 11-fold dissociated dislocation array (arrow), and a complex GB structure composed of ledges and dislocations similar to Figure 16(f). These GB structures were dominant representations of the GBs in the hipped and hipped plus tensile test aging at 811 K (538 °C). Figure 17(d) shows pairs of partial dislocation dipoles or a pileup of dissociated dipoles, which, like the dissociated dislocation array in Figure 17(c), is associated with low-stacking-fault free energy.^[30]

C. Analysis and Comparison of As-Fabricated and Hipped Mechanical Properties: Hardness and Tensile Tests

The average microindentation hardness (HV) for the precursor powder was 2.6 GPa, as noted earlier in reference to Figure 3, while the horizontal and vertical reference plane microindentation hardnesses (HV) were measured to be 2.8 and 2.5 GPa, respectively, for the as-fabricated cylindrical components (Figure 3). In contrast to these microindentation hardness measurements, the hipped (annealed) cylindrical components exhibited

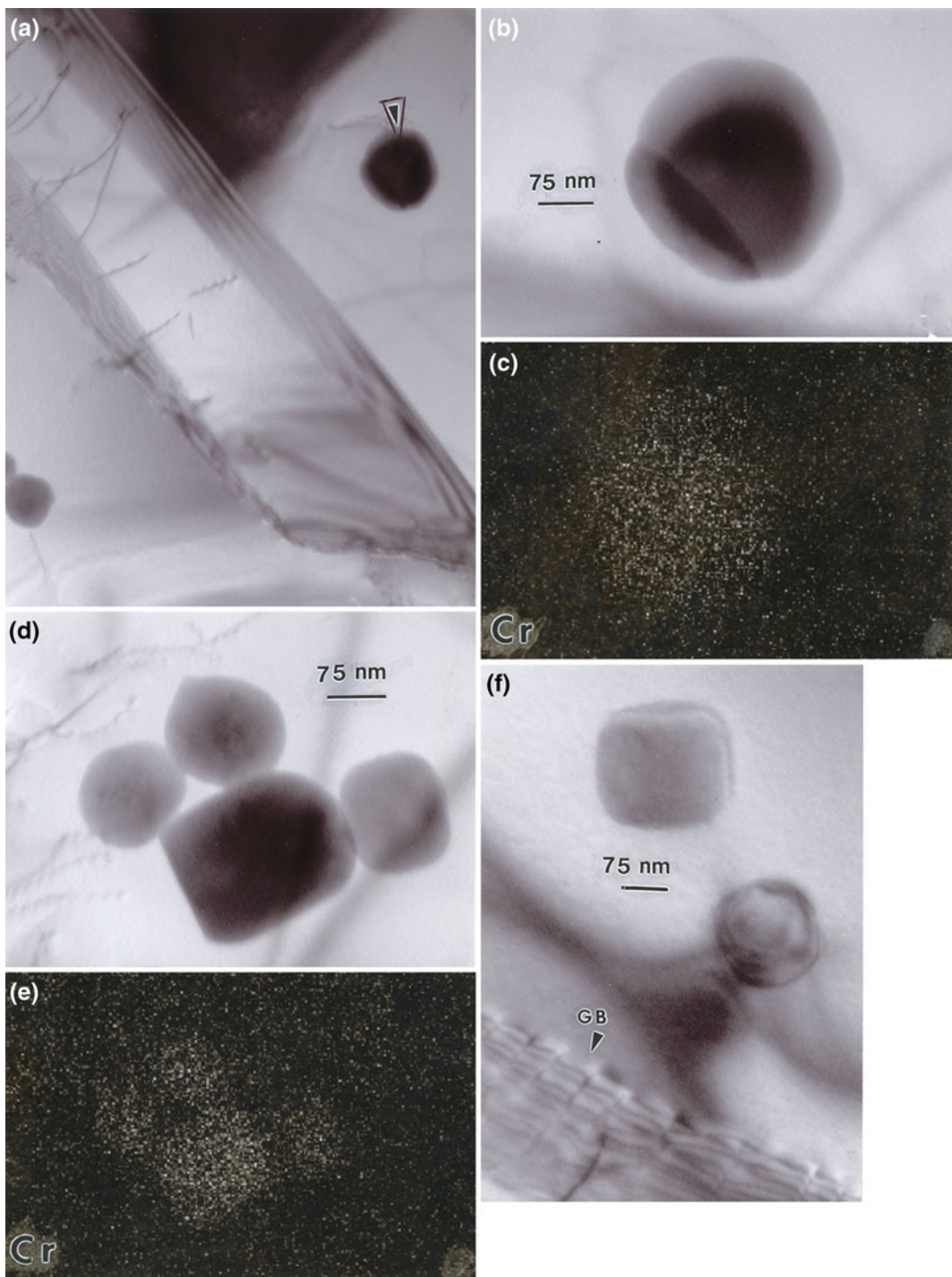


Fig. 16—Examples of laves (NbCr_2) precipitates in Fig. 14 observed in the TEM. (a) and (b) show precipitate and enlargement (arrow), while (c) illustrates the corresponding Cr map for (b). (d) and (e) Precipitate cluster and associated Cr map, respectively. (f) Precipitates near a complex structural GB. The larger precipitate appears to be ~ 50 -nm thick. Note that the precipitate particle in (b) is a bicrystal.

average values (HV) of 2.2 and 2.1 GPa for the horizontal and vertical reference planes, respectively, as illustrated in the 3-D composition of Figure 13, or a roughly 17 pct decrease from the EBM-fabricated component hardness. This is generally consistent with the overall microstructure variations (compare Figures 3 and 13).

Rockwell C-scale hardness (HRC) averages for the EBM-fabricated components, and these components following hot isostatic pressing, as well as samples tested in tension at 811 K (538 °C), are listed in Table II along with nominal wrought products and the corresponding Vickers microindentation hardness values (HV in units of GPa). The Rockwell C-scale (HRC) hardness variation

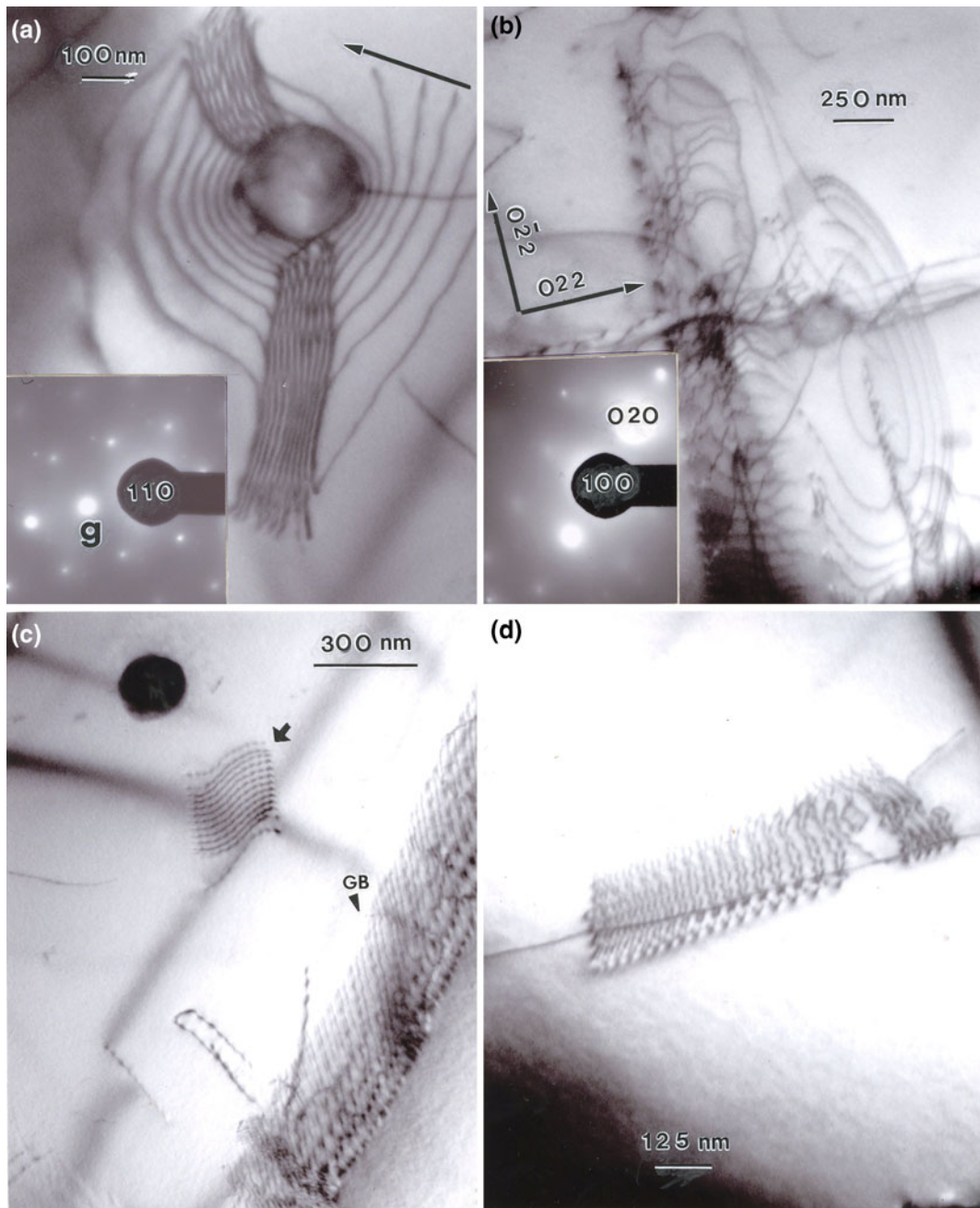


Fig. 17—TEM images of precipitate/dislocation microstructures in the vertical reference plane for a hipped + 811 K (538 °C) exposure (in the grip region of a tensile specimen). (a) and (b) Dislocation arrays associated with precipitates on {111} γ planes. The operating reflection, g , in (a) was [111]. (c) and (d) Arrays of dissociated partial dislocations on {111} planes (arrow in (c)). Note the complex GB structure in (c).

between cold-rolled wrought and annealed wrought alloy 625 is 50 pct, in contrast to nearly the same reduction percentage for the EBM-fabricated cylinders and the as-fabricated and hipped and as-fabricated-hipped and additional tensile heating at 811 K (538 °C). Note that the tensile-heated [811 K (538 °C)] samples were measured (hardness) and microstructurally examined in the grip region and not in the plastically deformed, necked region; therefore, they represent a small temperature (annealing) increment over the HIP anneal at 1393 K (1120 °C). Additionally, it can be

noted that the cold-rolled (as-fabricated) wrought alloy 625 HRC value is also roughly 65 pct greater than the corresponding EBM-fabricated value in contrast to roughly 60 pct for the annealed-wrought product and the EBM as-fabricated and hipped product.

In contrast to the hardness variations between the wrought-processed and EBM-processed alloy 625 illustrated in Table II, there is a corresponding 60 pct drop in yield stress for cold-rolled and annealed wrought material, but only a 20 pct drop in yield stress (0.2 pct offset) for the EBM-fabricated *vs* hipped product,

Table II. Mechanical Properties of EBM and Wrought Alloy 625

Material	HV* (GPa)	HRC**	YS ksi (GPa)	UTS ksi (GPa)	Elongation (Pct)
Precursor powder	2.6	—	—	—	—
Cold-worked wrought [†]	—	40	160 (1.10)	—	18
Annealed wrought [‡]	—	20	65 (0.45)	130 (0.89)	44
As-fabricated (EBM)	2.8/2.5 [§]	14	60 (0.41)	109 (0.75)	44
EBM fabricated + HIP [¶]	2.2/2.1 [§]	8	48 (0.33)	112 (0.77)	69
Wrought at 811 K (538 °C)	—	18	41 (0.28)	120 (0.83)	50
As-fabricated (EBM) at 811 K (538 °C)	2.6/2.8 [§]	14	44 (0.30)	86 (0.59)	53
EBM fabricated HIP at 811 K (538 °C)	2.3/2.2 [§]	6	34 (0.23)	89 (0.61)	70

Note: YS—0.2 pct offset yield stress, and UTS—ultimate tensile strength.

*Vickers (diamond) microindentation hardness (100 g load).

**Rockwell C-scale hardness (150 kg load) (average).

[†]Cold-worked (extruded) bar stock tensile tested at room temperature [~293 K (20 °C)].

[‡]Annealed 1 h at 1573 K (1250 °C) and tensile tested at room temperature.

[§]Horizontal plane/vertical plane hardness.

[¶]EBM-fabricated cylinders machined into tensile specimens and hipped, as described in the text.

although the EBM alloy 625 variance in the UTS increases by ~3 pct. As shown in Table II, the wrought alloy 625 elongation increases by 59 pct from the cold-rolled to annealed condition, in contrast to a 57 pct increase from EBM-fabricated to annealed (hipped) material. However, there is a 57 pct elongation increase between the annealed, wrought alloy 625 in contrast to the EBM-fabricated and annealed (hipped) alloy 625. Corresponding variances, especially elongation, are similarly observed for the additional tensile temperature exposure at 811 K (538 °C), as shown in Table II.

The significant increase in elongation for the annealed, EBM-fabricated alloy 625 vs the annealed, wrought alloy 625 (69 pct vs 44 pct in Table II), along with the corresponding 0.45 GPa vs 0.33 GPa yield strength reduction (Table II), is an indication of the microstructural variations implicit on comparing the EBM-fabricated alloy 625 product microstructures and microstructural architecture in Figure 4 with the correspondingly hipped (annealed) product in Figure 13.

Figure 18(a) shows the associated fracture surface features observed in the SEM at different magnifications, corresponding to ~44 pct elongation to fracture for an EBM-fabricated tensile test specimen. The fracture surface structure shows a characteristic ductile-dimple behavior with a mean, equiaxed dimple diameter of 1.4 μm , roughly half the size of the Ni_3Nb precipitate array spacing (Figures 3) in the horizontal reference plane normal to the tensile axis (and the EBM build direction).

These relatively small dimple diameters (Figure 18(a)) are considerably smaller than those observed for EBM-fabricated Ti-6Al-4V (4.4 μm), which, in contrast to larger ductile dimple diameters for wrought Ti-6Al-4V, were associated with a 58 pct increase in ductility over the wrought product.^[28] This feature may apply in the present case for EBM alloy 625 vs wrought, although comparative ductile dimple diameter data are not available for wrought alloy 625. However, as noted in Figure 18(b), representing the roughly 69 pct elongation to failure for the EBM-fabricated and hipped (annealed) component, the ductile dimple diameters shown in

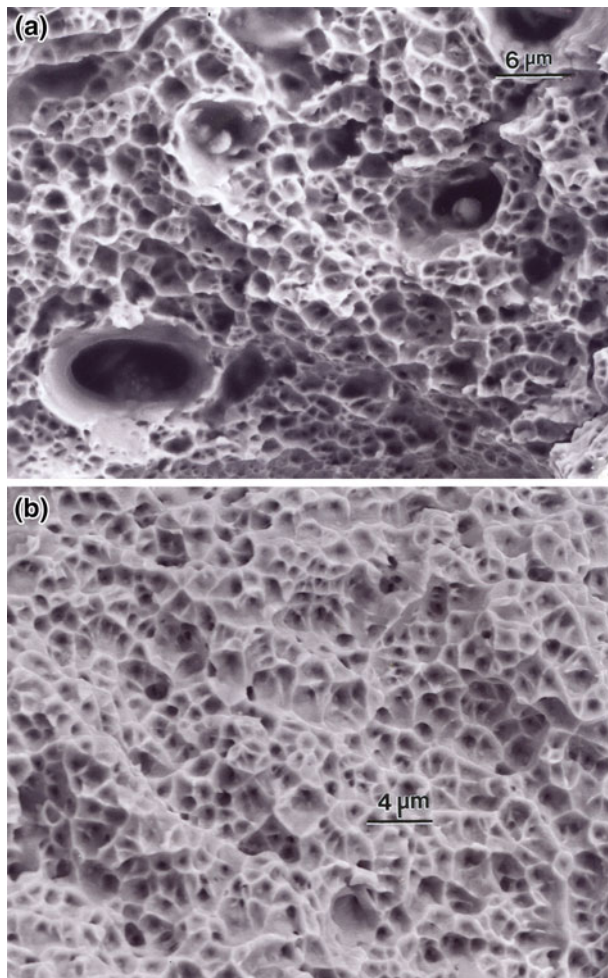


Fig. 18—SEM fracture surface structures for (a) EBM as-fabricated tensile sample and (b) EBM-fabricated and hipped (annealed) cylindrical component.

Figure 18(b) (~1.5 μm) are the same as those shown in Figure 18(a). In contrast to recent work on an EBM-fabricated Co-base superalloy, where the fracture-surface

ductile dimples exhibited a regular, cubelike (orthogonal) array exactly matching the 2- μm Cr₂₃C₆ columnar arrays, the ductile dimples in Figures 18(a) and (b) are more random arrays, slightly smaller than the Ni₃Nb precipitate arrays (spaced ~2 μm in Figure 3). This feature is possibly influenced by the precipitation in both the EBM-fabricated samples (Figure 3) and these same samples following hipping at 1120 °C (Figure 14).

It might be noted, as evidenced by small porosities in the as-fabricated EBM alloy 625 shown in Figure 6(b) and similar porosity features shown in Figure 13, that the exceptional elongation improvement in the hipped alloy 625 samples *vs* the as-fabricated samples is due more to the notable change in the microstructure. This change includes annihilation of the Ni₃Nb precipitate columnar architecture and columnar grain structure, and the development of a more equilibrium and equiaxed grain structure, with homogenous NbCr₂ laves precipitation in the grain interiors. As illustrated in Figure 17, these precipitates, even after HIP treatment, produced copious arrays of dislocations, and tensile straining would be expected to produce extensive slip, accommodating the extreme elongations noted in Table II. This phenomenon is contrary to the usual degradation of mechanical properties attributed to laves phase, as noted earlier.

IV. SUMMARY AND CONCLUSIONS

The EBM fabrication of primarily cylindrical components along with some rectangular components from prealloyed INCONEL 625 (66Ni, 21Cr, 9Mo, 4Nb; nominal weight percent) powder creates nearly fully dense (8.4 g/cm³) monoliths having a Ni-Cr (γ) fcc matrix. More importantly, the unique, orthogonal (x - y) electron beam melt scan produced columnar arrays (or architecture) of thin, crystallographically coincident γ'' (bct) Ni₃Nb precipitates. These columnar precipitate arrays were parallel to the build direction and the cylinder axis, and also parallel to columnar grains having a [200] texture along this axis. The bct γ'' precipitate platelets were coincident with the fcc γ {111} planes: (010) γ'' || (111) γ . The columnar γ'' precipitate platelet arrays assumed an irregular orthogonal (x - y) geometry spaced ~2 μm in the horizontal reference plane, consistent with the spacing of carbide precipitate columnar arrays in a Co-base alloy (ASTM-F75)^[17] fabricated by EBM using the same electron beam melt scan parameters as employed in the present work.

HIPing of the EBM as-fabricated cylinders at 1393 K (1120 °C) for 4 hours dissolved the γ'' (bct) Ni₃Nb precipitate columnar architecture and recrystallized the [200] oriented columnar grains (which measured ~20 μm in diameter and ≤500 μm in length along [200]) to form an equiaxed grain structure, containing coherent {111} annealing twins, with an average diameter of ~50 μm . These equiaxed grains contained mostly a homogeneous distribution of NbCr₂ laves phase (hexagonal) globular precipitates. While there were almost no stacking faults, the microstructure exhibited complex dislocation arrays,

including dipole arrays, emitted from the laves precipitates on {111} planes, as well as dissociated partial dislocation arrays on {111}, indicative of low stacking-fault free energy. Essentially all of the precipitates exhibited TEM tilt-sensitive strain contours, and all illustrated dislocation emission or attachment of some kind. In addition, the GB structure exhibited a noticeably high energy, as evidenced by selective etching at the GBs, and their structures were characterized by a complex arrangement of ledges and dislocations.

These two contrasting microstructure/microstructural architecture regimes (as-fabricated (EBM) components *vs* the as-fabricated and hipped components) exhibited correspondingly contrasting mechanical properties. For example, the γ'' (bct) columnar precipitate architecture in the as-fabricated components exhibited a Vickers microindentation hardness varying from 2.8 to 2.5 GPa in the corresponding cylinder horizontal and vertical reference planes. This microindentation hardness was reduced to 2.2 and 2.1 GPa in the horizontal and vertical reference planes for the hipped cylinder components with an equiaxed grain structure containing NbCr₂ (laves) precipitates. Correspondingly, the as-fabricated, tensile-tested cylinders had a yield stress of 0.41 GPa and a UTS of 0.75 GPa in contrast to 0.45 and 0.89 GPa for annealed, wrought alloy 625. The corresponding elongation for the EBM-fabricated alloy 625 matched that for annealed, wrought alloy 625 at 44 pct. However, the corresponding tensile data for the as-fabricated (EBM) and hipped cylinders exhibited a yield stress of 0.33 GPa, a UTS of 0.77 GPa, and an elongation of 69 pct. The extraordinary elongation in the EBM-fabricated and hipped cylinders (57 pct increase over un-hipped material) was observed to be more related to the annealed microstructure (equiaxed 50- μm grains containing NbCr₂ laves precipitates) than the closing of bubbles and small pores, although there was a roughly 1 pct decrease in porosity between the as-fabricated and hipped samples (a measured density increase from ~8.4 to ~8.5 g/cm³).

The tensile testing of EBM-fabricated cylinders at 811 K (538 °C) did not significantly alter the microindentation hardness from the EBM-fabricated cylinders tested at room temperature (~293 K (20 °C)) (measured in the grip region), but the yield stress dropped from 0.33 to 0.30 GPa and the UTS decreased by 23 pct. The corresponding elongation increased from 44 to 53 pct. Similarly, the EBM-fabricated and hipped cylinders when tensile tested at 811 K (538 °C) also illustrated no significant microindentation hardness in the grip area, but the yield stress decreased from 0.33 to 0.30 GPa, while the UTS decreased from 0.77 to 0.61 GPa. However, the elongation only increased from 69 to 70 pct on comparing the as-fabricated + HIP cylinders tested at room temperature, in contrast to the same cylindrical specimens tested at 811 K (538 °C). By comparison, wrought alloy 625 tensile tested at 811 K (538 °C) exhibited a yield stress of 0.28 GPa, a UTS of 0.83 GPa, and an elongation of 50 pct (Table II).

The ductile dimple diameters measured on the fracture surfaces for both the EBM-fabricated and EBM-fabricated + HIP components were essentially identical

at $\sim 2 \mu\text{m}$. This dimension matches dimple diameters for EBM-fabricated cylinders of a Co-base alloy tensile tested at room temperature.^[17] However, the dimples were not regular, orthogonal (x - y) arrays matching the γ'' precipitate architecture in contrast to dimple arrays, matching the orthogonal carbide precipitate columnar architecture in Co-base, ASTM-F75 alloy.^[17]

In contrast to more conventional Ni-base superalloys in cast and wrought forms, and with a variety of thermomechanical processing schedules, the EBM-fabricated and processed INCONEL 625 examined in this study demonstrated unusual microstructures and microstructural (columnar precipitate) architecture. These microstructural features were correlated with unique mechanical properties, especially elongations at room temperature, which exceeded worked wrought alloy 625 products by more than 283 pct and annealed, wrought alloy 625 products by 57 pct for EBM-fabricated and hipped (annealed) components (Table II). These unusual microstructure/microstructural architecture features in the EBM-fabricated and processed Ni-base (INCONEL 625) alloy illustrate the potential for EBM-fabricated products with controlled microstructural architectures and their engineering applications.

ACKNOWLEDGMENTS

This research was supported, in part, by Mr. and Mrs. MacIntosh Murchison Endowed Chairs (LEM and RBW) as well as graduate research assistantships at the University of Texas at El Paso. We thank ARCAM AB-Sweden and Metals Technology, Inc. for technical support and services.

REFERENCES

1. J.M. Oblak and B.H. Kear: *Trans. ASM*, 1961, vol. 61, pp. 519–26.
2. R.M. Forbes Jones and L.A. Jackman: *JOM*, 1999, Jan., p. 27.
3. *Superalloys*, E.F. Bradley, ed., ASM INTERNATIONAL, Materials Park, OH, 1988.
4. *Int. Symp. on Superalloys*, ASM, Metals Park, OH, 1980.
5. B.H. Kear: *Scientif. Am.*, 1986, No. 4, pp. 159–65 (see related articles in the same issue).
6. N.D. Souza, M.G. Ardkani, M. McLeah, and B.A. Shollock: *Metall. Mater. Trans. A*, 2000, vol. 31A, pp. 2877–85.
7. *Nickel, Cobalt and Their Alloys*, ASM INTERNATIONAL, Materials Park, OH, 2000.
8. R.C. Reed: *The Superalloys: Fundamentals and Applications*, Cambridge University Press, Cambridge, United Kingdom, 2006.
9. J.M. Silva, R.A. Claudio, A. Sousa, R. Brito, C.M. Branco, and J. Byrne: in *Materials Science Forum*, P.M. Vilarinho, ed., Trans. Tech Publications, Aedermannsdorf, Switzerland, 2006, vols. 514–516.
10. *Solidification Technology*, J.F. Burks, M.C. Flemings, and A.E. Gorum, eds., Brook Hill Publishing Co., New York, NY, 1974.
11. K.E. Eckelmeyer and R.W. Hertzberg: *Metall. Trans.*, 1972, vol. 2, pp. 609–15.
12. J.A. Jackson and J.D. Hunt: *Trans. AIME*, 1966, vol. 236, pp. 1129–35.
13. E.R. Thompson and F.D. Lemkey: *Trans. ASM*, 1969, vol. 62, pp. 140–47.
14. H.F. Merrick: *Int. Symp. on Superalloys*, ASM, Metals Park, OH, 1980, p. 161.
15. D. Cormier, D. Harryson, and H. West: *Rapid Prototyping J.*, 2004, vol. 10 (1), pp. 35–41.
16. S.M. Gaytan, L.E. Murr, F. Medina, E. Martinez, M.I. Lopez, and R.B. Wicker: *Mater. Technol.: Adv. Perform. Mater.*, 2009, vol. 24 (9), pp. 180–88.
17. S.M. Gaytan, L.E. Murr, E. Martinez, J.L. Martinez, B.I. Machado, D.A. Ramirez, F. Medina, S. Collins, and R.B. Wicker: *Metall. Mater. Trans. A*, 2010, vol. 41A, pp. 3216–27.
18. D.A. Ramirez, L.E. Murr, S.J. Li, Y.X. Tian, E. Martinez, J.L. Martinez, B.I. Machado, S.M. Gaytan, F. Medina, and R.B. Wicker: *Mater. Sci. Eng. A*, 2011, vol. 528A, pp. 5379–86.
19. R. Mehrabian, B.H. Kear, and M. Cohen: *Rapid Solidification Processing*, Claitor's Publishing Division, Baton Rouge, LA, 1978.
20. R.J. Patterson, II, A.R. Cox, and E.C. Vanreuth: *J. Met.*, 1980, vol. 32 (9), pp. 34–41.
21. M.A. Meyers, R.B. Gupta, and L.E. Murr: *J. Met.*, 1981, vol. 33 (10), pp. 21–27.
22. D.A. Ramirez, L.E. Murr, E. Martinez, D.H. Hernandez, J.L. Martinez, B.I. Machado, F. Medina, R.B. Wicker, and P. Frigola: *Acta Mater.*, 2011, vol. 59, pp. 4088–99.
23. A. Strondl, R. Fischer, G. Franmeyer, and A. Schneider: *Mater. Sci. Eng. A*, 2008, vol. 480, pp. 138–47.
24. R.T. Quinn, R.W. Kraft, and R.W. Hertzberg: *Trans. ASM*, 1969, vol. 62, pp. 38–44.
25. D. Senicourt and P. Annarumma: *C.R. Acad. Sci.*, 1969, Ser. C, vol. 269, pp. 591–99.
26. P. Annarumma and M. Turpin: *Metall. Trans.*, 1972, vol. 3, pp. 137–43.
27. L.E. Murr: *Interfacial Phenomena in Metals and Alloys*, Addison-Wesley Publishing Co., Reading, MA, 1975, reprinted 1990 and available from CBLS.CBLS.com.
28. L.E. Murr, E.V. Esquivel, S.A. Quinones, S.M. Gaytan, M.I. Lopez, E.Y. Martinez, F. Medina, D.H. Hernandez, E. Martinez, J.L. Martinez, S.W. Stafford, D.K. Brown, T. Hoppe, W. Meyers, U. Lindhe, and R.B. Wicker: *Mater. Charact.*, 2009, vol. 60, pp. 96–105.
29. C. Radhakrishna, K.P. Rao, and S. Srinivas: *J. Mater. Sci. Lett.*, 1995, vol. 14, pp. 1810–12.
30. B.H. Kear, J.M. Oblak, and A.F. Giamei: *Metall. Trans.*, 1970, vol. 1, pp. 2477–86.

Bending fatigue life characterisation of direct metal laser sintering nickel alloy 718

O. SCOTT-EMUAKPOR¹, J. SCHWARTZ¹, T. GEORGE¹, C. HOLYCROSS¹, C. CROSS¹ and J. SLATER²

¹Air Force Research Laboratory, Aerospace Systems Directorate, 1950 Fifth Street, Bldg 18D, Wright-Patterson AFB, Dayton, OH 45433, USA,

²Wright State University, Department of Mechanical and Materials Engineering, 3640 Colonel Glenn Highway, Dayton, OH 45435, USA

Received Date: 4 September 2014; Accepted Date: 6 January 2015; Published Online: 18 February 2015

ABSTRACT Bending fatigue behaviour of direct metal laser sintering (DMLS), Nickel (Ni) Alloy 718 has been assessed as preliminary qualification to additively manufacture advanced gas turbine engine components. Motivation for this work comes from the possibility of using DMLS to improve functionality of hot-section components. By using DMLS, turbine blades and heat exchangers cooling passages can be enhanced, leading to improved engine performance. This study focuses on vibratory high cycle fatigue (HCF) assessment of DMLS Ni Alloy 718 from two suppliers. Specimens were fatigued via vibration-based bending and compared with published rotating bending cold-rolled Ni Alloy 718. Tensile analysis and microscopy were also conducted to understand fatigue and fracture trends. HCF, tensile properties and microscopy comparisons show that fatigue and strength of DMLS Ni may be sensitive to post-fusion treatments. Nonetheless, fatigue performance of DMLS Ni compares well with rotating bending fatigue of cold-rolled Ni.

Keywords bending fatigue; statistical model strength; nickel base superalloy; vibration.

NOMENCLATURE

Alloy#	= Nickel composition identification number
<i>E</i>	= Elastic modulus
<i>G</i>	= Gravitational constant (9.81 m s^{-2})
<i>H</i>	= Rolling marks or DMLS build plane normal to load
Roll_dog bone	= Rolling direction of tensile specimen
Roll_plate	= Rolling direction associated with the plate stock
Specimen#	= Fatigued specimen number
Stock#	= Bulk stock number
<i>V</i>	= Rolling marks or DMLS build plane parallel to load
<i>N_{fail}</i>	= Number of cycles to failure
<i>N_{step}</i>	= Number of cycles per step
Ra	= Roughness Average
$\mu\varepsilon_a$	= Microstrain amplitude
σ_a	= Stress amplitude
σ_{fail}	= Stress amplitude during failed step
σ_{pr}	= Stress amplitude during previous step

INTRODUCTION

Since the inception of powered flight, improving component capabilities has been a key goal for advancing the technology. One approach to achieve component

enhancement is through the implementation of advanced design concepts. Novelties of designs, however, are typically limited by the capabilities of conventional manufacturing processes such as casting, forging and machining. Achieving advanced designs via conventional processes can be either cost-prohibitive or simply not possible. Difficulties in new component fabrications have

Correspondence: O. Scott-Emuakpor. E-mail: onome.scott-emuakpor@wpafb.af.mil

led to the exploration of additive manufacturing (AM) techniques such as direct metal laser sintering (DMLS).

In the DMLS process, thin layers of metallic powder are locally melted and fused together on a build plate by the controlled scanning of a laser energy beam.^{1,2} The benefits of DMLS could be witnessed in sixth generation fighter engine heat exchangers and small-scaled, internally cooled turbine rotors. Heat exchangers are thin-walled, layered structures limited by assembly processes (brazing/welding), which could induce tensile residual stresses that reduce material integrity. Similarly, integrally bladed, small-scaled turbine rotors are size limited, based on cooling wall thickness limitations during casting processes. The DMLS benefits to the respective components are the capability to build a normally multi-part component as a single structure and manufacturing components with small, complex geometric features.

Whilst DMLS is attractive for producing advanced geometric features, the process has not been fully qualified for the aforementioned hot section components. Monotonic tensile material properties of DMLS manufactured specimens have been favourably compared with the wrought material properties of a few aerospace alloys,^{3–6} which is acceptable for non-rotating and non-flowpath components. However, qualification for heat exchangers and turbine blades will be reliant on full characterisation of aeromechanics induced issues such as fatigue crack growth, low cycle fatigue (LCF) and high cycle fatigue (HCF) failure.⁷ Necessity of fatigue characterisation is based on the catastrophic nature of flowpath component damage during operation. For turbine rotors, up-stream and down-stream wakes created from stator vanes during operation can induce unwanted vibrations at high frequencies, which could lead to liberation of blades and unsteady rotation. Although less catastrophic than turbine rotors, failure to heat exchangers would result in a severe debit to engine performance capability. To ensure safety and performance in gas turbine engines, extensive fatigue failure knowledge is a necessary step for DMLS use on rotating and/or flowpath components.

The work in this paper provides a better fatigue failure understanding of DMLS parts by characterising the vibration fatigue behaviour of DMLS manufactured Ni Alloy 718. The characterisation was conducted by determining vibration-based bending fatigue behaviours of DMLS built specimens and comparing the results to rotating bending fatigue of cold-rolled Inconel Alloy 718. Vibration-based bending test was chosen for this study to represent the type of surface stress, resonance load conditions possible with a turbine blade or heat exchanger wall. The DMLS specimens used in the vibration-based bending tests were manufactured by two vendors with different manufacturing control parameters and post-fusion treatments in order to observe the process effects on material performance. Process

effects were assessed through comparisons of bending fatigue performances and supplemented with tensile material property and microscopy comparisons. The fatigue results show DMLS compares well with cold-rolled Inconel Alloy 718. Tensile results showed variation between each vendor and published cold-rolled data. The results for both the fatigue and tensile analyses were supported by the microscopy findings, which alludes to high sensitivity in process controls and post-fusion treatments. The following results are promising for the possibility of qualifying DMLS use for gas turbine engine applications.

DIRECT METAL LASER SINTERING SYNOPSIS

Direct metal laser sintering (DMLS) is a powder bed, laser deposition process that fuses layers of 20 µm thick metal powder with a 200–400 W Ytterbium-fibre laser until a part is completed.^{1,2} Powder fusion is conducted on a steel build plate inside a sealed chamber with argon gas between 40 °–100 °C. The DMLS process is automated, thus machines can be unattended whilst part builds are underway.² Despite the precision of the DMLS manufacturing capability, surface finish modifications are still necessary to reduce the roughness of manufactured components.¹

There are a number of benefits to manufacturing with DMLS as opposed to conventional methods. One benefit is the reduction in material waste and subtractive tooling wear during manufacturing.² This, along with part fabrication occurring in a controlled, automated environment means that DMLS requires less production time and labour than conventional methods.² Another benefit of using DMLS is the capability to manufacture components that have small and/or complex geometric features or that require assembling multiple parts.

Background studies were conducted on DMLS Ni Alloys to validate and improve the microstructure characteristics and mechanical properties.^{3–6} Two key disadvantages found in early studies were the presence of inhomogeneous residual stresses and porosity. Both of these issues favour crack nucleation during vibratory and quasi-static (monotonic) loading.^{3,4} Homogeneity of residual stresses and the reduction of porosity have been addressed for some materials by controlling the temperature of the build plate and incorporating post-fusion treatments such as shot peening, polishing, annealing, ageing, stress relief and hot isostatic press (HIP).^{3–5}

VIBRATION-BASED METHODOLOGY AND TEST SETUP

Experimental HCF failure results for this study were acquired using a vibration-based testing approach.^{8,9} The

purpose of this method is to experimentally acquire either uniaxial or biaxial fatigue life results at loading conditions similar to those that could cause HCF failure in turbine engine blades and vanes. Testing for this method is carried out by supplying a dynamic base excitation from an electrodynamic shaker to a cantilever specimen at a resonant frequency. The resonant frequencies required to generate either a biaxial or uniaxial bending load are based on the material composition and the geometry of the specimen. These geometries were determined using a geometric design procedure, which optimised the location of the maximum von Mises stress amplitude (the fatigue zone), so that it was not along the clamped-edge of the specimen.⁸

The work in this document focuses only on the uniaxial bending fatigue specimen pictured in Fig. 1. The dimensions of the specimen are $114.3 \times 165.1 \times 3.2$ mm with a square test-section area of 114.3×114.3 mm. In order to attain a maximum stress region away from the clamped edge of this particular geometry, a chord-wise bending (or two-stripe) mode is excited at a frequency of roughly 1600 Hz. Figure 2 illustrates the vibratory analysis of this mode with contour images of von Mises stress and displacements (mode shapes) with respect to a normalised maximum displacement.

The instrumentation used to measure data during vibration-based uniaxial fatigue tests are an Endevco 2271A accelerometer, a Micro-Measurements CEA-06-062UW-350 uniaxial strain gauge, and a non-contact Polytec OFV 505 single-point laser vibrometer. The location for the test instrumentations can be seen in Figs. 1 and 3. The accelerometer is used to control the acceleration force of a 90 kN Unholtz-Dickie electrodynamic shaker (Fig. 3), the strain gauge is placed at the fatigue zone of the test specimen to acquire strain amplitude, and the laser vibrometer is positioned near the two-stripe nodal line

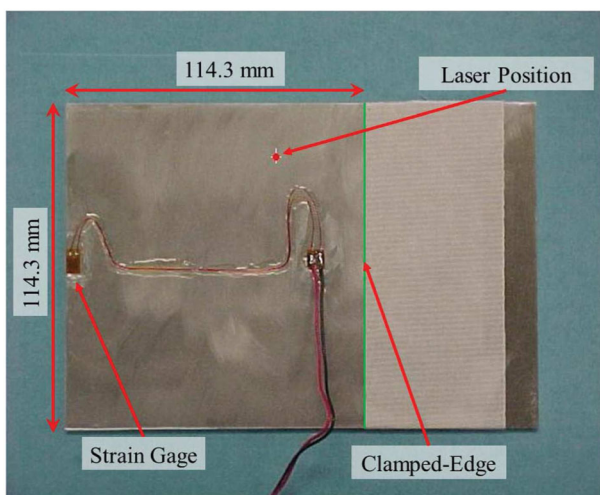


Fig. 1 Vibration-based uniaxial bending fatigue specimen.

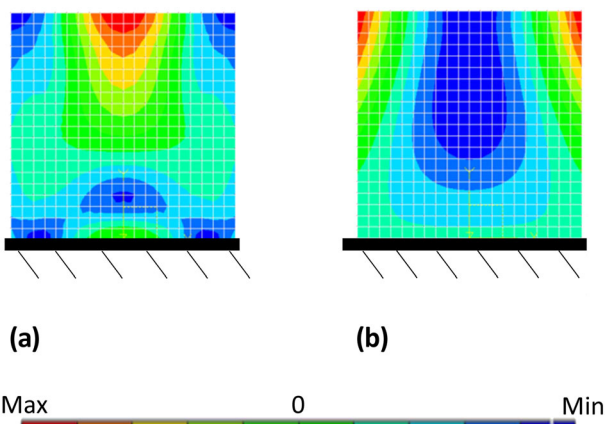


Fig. 2 Vibratory analysis of the chord-wise mode on a square plate: (a) von Mises stress and (b) mode shape.

of the vibrating specimen to measure velocity during testing.⁸ The strain gauge used in this experiment is not fatigue rated for the strain amplitudes and cycles accumulated during vibration-based bending. The fatigue rating for this strain gauge is $1500 \mu\varepsilon_a$ for 10^5 cycles, whereas most tests were conducted between 1700 and $2700 \mu\varepsilon_a$ for 2×10^5 – 10^7 cycles. Therefore, in order to determine strain amplitude values throughout the duration of a test, the velocity results from the laser vibrometer are linearly correlated with strain results from the gauge at sufficiently low strain amplitudes (below $1500 \mu\varepsilon_a$) and low loading cycles (50 Hz sinusoidal sweeps around resonance for 60 s durations). The velocity is then used to identify strain/stress amplitudes during fatigue testing.

Failure during a vibration-based test, which is defined as crack initiation, is determined by monitoring the frequency change with respect to time. Furthermore, observation of the shaker acceleration force versus time is also monitored to support the occurrence of failure. Figure 4 illustrates a plot of operating frequency and acceleration force over time during a fatigue test on an Inconel Alloy 625 specimen.¹⁰ Failure can be determined from this data as the instance the natural frequency, which is tracked by the driving frequency, shifts more than 0.1%. This frequency shift is due to a change in the stiffness of the plate as a crack appears and can be associated with crack lengths as small as 2–3 mm.¹⁰ Damping in the plate also increases with the presence of a crack, thus more force (i.e. higher shaker head acceleration) is required to maintain the desired velocity response. Note that in Fig. 4, the shaker acceleration limit is notched at 120 G despite having a rating of approximately 133 G for the armature payload of the vibration-based setup; the data spike above and below 120 G is because of the noise from the velocity controlled test.

Fatigue testing to failure is conducted two ways: sinusoidal amplitude dwell or the step test procedure. Sinusoidal amplitude dwell, referred to as dwell for the

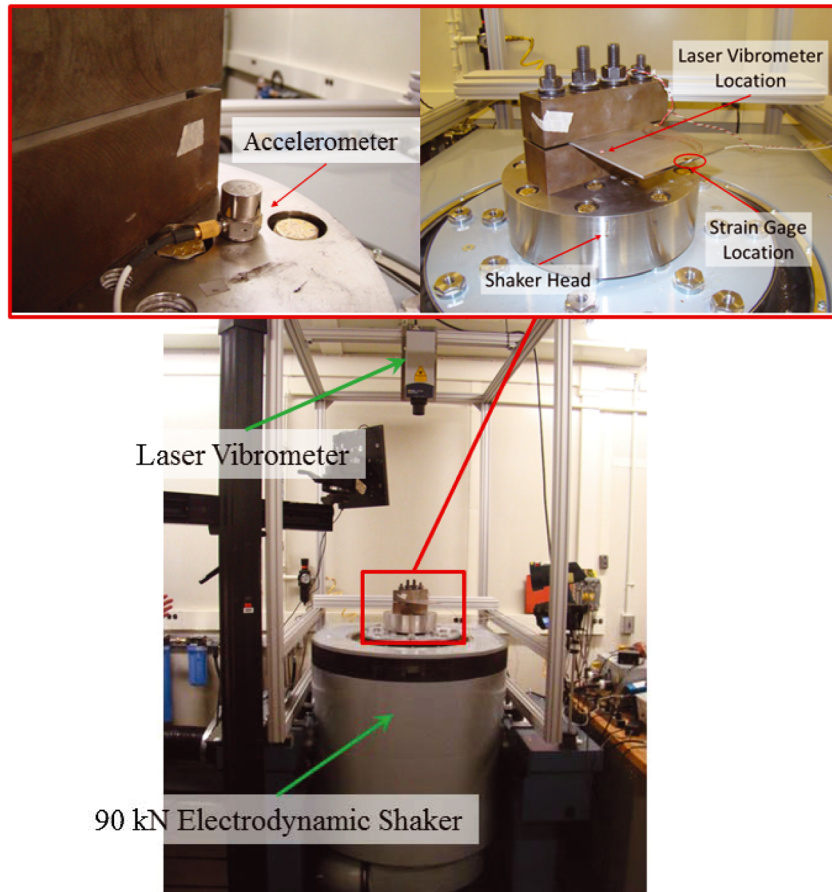


Fig. 3 Vibration-based test set-up and instrumentation.

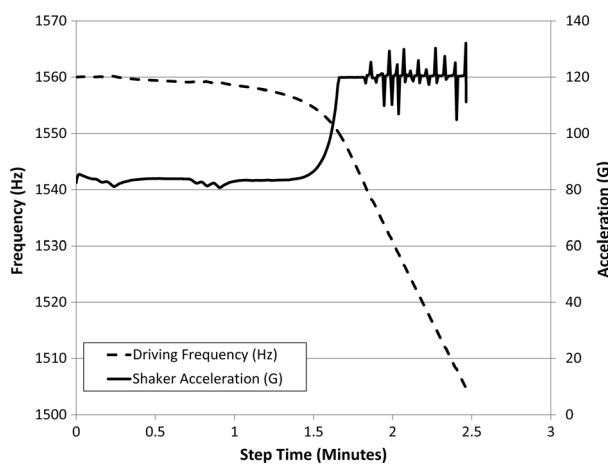


Fig. 4 Sinusoidal dwell time versus frequency and acceleration during vibration-based test: Inconel alloy 625.¹⁰

remainder of this manuscript, is conducted by controlling the strain amplitude, via the velocity amplitude, at a constant value throughout the duration of the test until failure occurs. The step test procedure, which was

utilised more than dwell in this study, is a series of dwell steps for a specified number of cycles (N_{step}), each step having consecutively increasing sinusoidal dwell amplitudes, where the failure stress is calculated by interpolating between the failure and previous steps.^{11,12} The initial step in the series of N_{step} cycles is subjected to a constant stress amplitude level well below the anticipated failure stress amplitude. For the vibration-based testing approach, the stress for the initial step is chosen at roughly 50% of the anticipated failure stress; however, there is no specific guideline for the choice of this value. When, or if, failure does not occur after N_{step} cycles, the stress amplitude is increased by 5% of the anticipated failure stress and the specimen is subjected to the new stress amplitude for another N_{step} cycles. These steps are conducted until failure occurs. When failure does occur, the failure stress amplitude (σ_a) is calculated in Eq. (1), where σ_{pr} is the stress amplitude during the previous un-failed step, σ_{fail} is the stress amplitude during the failed step and N_{fail} is the accumulated cycles to failure during the last step. Therefore, σ_a correlates to the failure stress amplitude for the controlled N_{step} cycles to failure.

$$\sigma_a = \sigma_{pr} + \frac{N_{fail}}{N_{step}} (\sigma_{fail} - \sigma_{pr}) \quad (1)$$

DIRECT METAL LASER SINTERING PROCESS FOR 718 PLATES

The Ni Alloy 718 DMLS specimens used in this study were fabricated by two different vendors in the build direction illustrated in Fig. 5. Each vendor, designated as Vendor I and Vendor II, used the same machines (EOSINT M 280; EOS of North America, Inc., Novi, MI, USA) but different DMLS process parameters and post-fusion treatments. The details of Vendor I DMLS parameters, for example cooling rates, laser power and atmosphere gas and temperature, were considered proprietary and not specified. Vendor II process was conducted in Argon atmosphere (temperature not furnished) with a laser beam diameter of 100 µm, a powder distribution layer of 30 µm, laser speeds varying between 800 and 3500 mm s⁻¹, depending on contour, core or support area fusion and a build plate thickness greater than 25.4 mm; the build plate thickness was determined by the specimen vendor to minimise thermal stresses and warping. Like Vendor I, further details regarding Vendor II parameters are deemed proprietary. Each vendor, however, did specify whether post-fusion treatments had been applied to the plates. Vendor I plates were solution heat treated (968 °C for 1.5 h), aged (718 °C for 8 h to 612 °C for 8 h and then cooled below 150 °C), HIP (1177 °C at 103 MPa) and stress relieved (1065 °C for 1.5 h and then argon cooled). Vendor II plates were originally believed to have been stress relieved,^{13,14} but further inquiry on the manufacturing process shows no record of any post-fusion treatment. The surface

roughness for the finished products varied between Ra values of 5.08 and 12.7 µm; however, each plate was polished with a Merit fine-grit buffering disc to Ra values between 1.27 and 5.08 µm. Porosity was not investigated in plates from either Vendor. A porosity density study will be carried out for both Titanium 6Al-4V and Ni Alloy 718 in future efforts.

Each Vendor experienced difficulties in building the fixture holes of the plate specimen. As shown in Fig. 6, the as-built fixture holes (25.4 mm diameter) resulted in pilling. This is because of the inability to support low angle slanting of the upper half of the holes. The issue of pilling was addressed by building specimens with smaller than nominal holes, then each hole was machined to size using a wire electrical discharge machining (EDM) process. The recast layer from the added EDM procedure would not affect experimental results because the holes are within the specimen clamping fixture (Fig. 3).

The precision of the as-built plates were observed using an optical three-dimensional metrology scanner. The scanner acquired millions of measurements along the surface of the specimen (point cloud data) with a measurement tolerance of 5 µm.¹⁵ The point cloud is then converted to a solid shell with a triangular mesh that is compared with the nominal Computer Aided Design (CAD) geometry of the plate. An example of this comparison can be seen in Fig. 7. Results from several comparisons show a thickness tolerance of 127 µm. This is similar to as-purchased tolerance of a sheet of cold-rolled Inconel Alloy 718. However, in areas where EDM machining is required, for example fixture holes and the edge surface attached to the DMLS bedplate, deviations as large as 1 mm were seen, specifically at the fixture holes that experienced severe pilling. This supports the notion that even though DMLS is advertised to manufacture part geometries as requested, lack of process control during and after DMLS fusion can still affect final manufactured geometry.

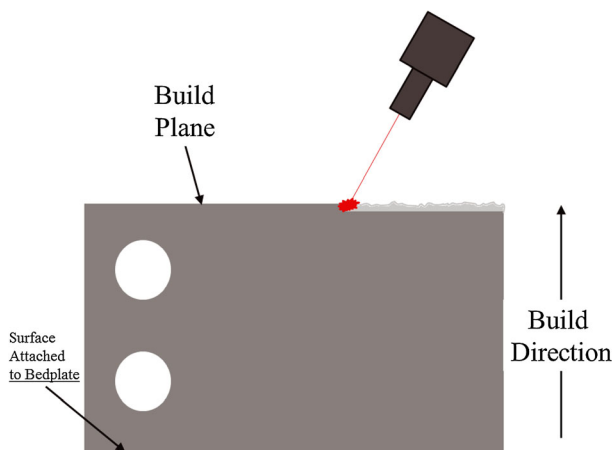


Fig. 5 Direct metal laser sintering build direction schematic.

EXPERIMENTAL RESULTS

Bending fatigue life comparison

The vibration-based testing approach was used to characterise bending fatigue behaviour for DMLS Ni Alloy 718. Using the 90 kN electrodynamic shaker shown in Fig. 3, fatigue life data was acquired from 24 DMLS plates (12 per vendor) with build directions normal to the axis of the anticipated crack path. Based on Vendor I pristine data and supporting strength properties from tensile testing mentioned later in this section, the chosen build direction corresponds to a worse case failure scenario. Four of the 12 fatigue experiments conducted

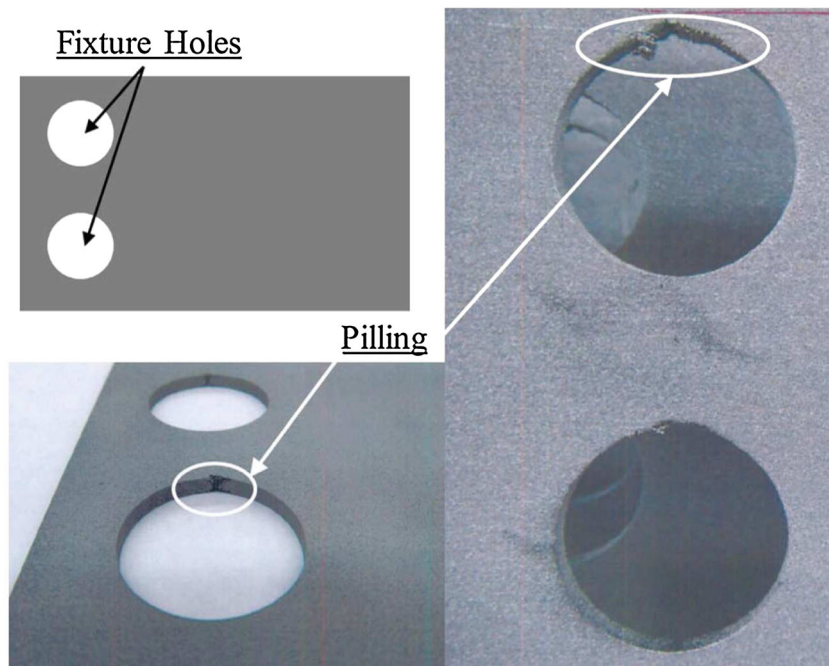


Fig. 6 Direct metal laser sintering plate with holes pilling.

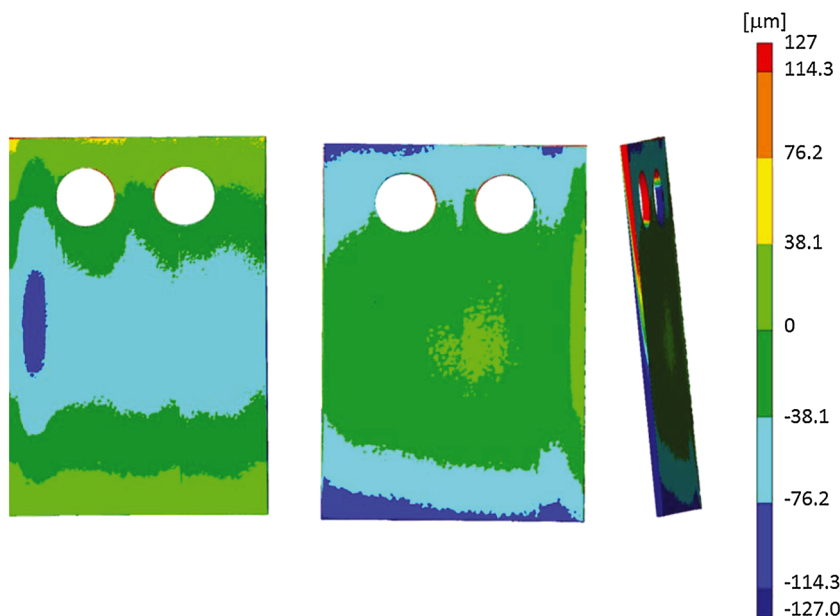


Fig. 7 Vendor II point cloud mesh to nominal geometry comparison: the colour contour denotes tolerance.

for each Vendor batch used the dwell testing application and the rest were fatigue using the step test method. Previous research on titanium and aluminium shows that although the step test has a lower life performance than dwell, the results are comparable with respect to normal fatigue data scatter.^{11,16,17} The prediction bounded comparisons between dwell and step test methods are provided in Figs 8 and 9 for Vendor I and II,

respectively.¹³ Observing the regression correlation of the experimental data, the comparison in Fig. 8 shows more deviation between the step test and the dwell results than the comparison in Fig. 9. However, based on 80% prediction intervals from the dwell regression correlations of each Vendor, the scatter of the step test data is acceptable to combine with dwell test data for comparison against cold-rolled Inconel Alloy 718 fatigue

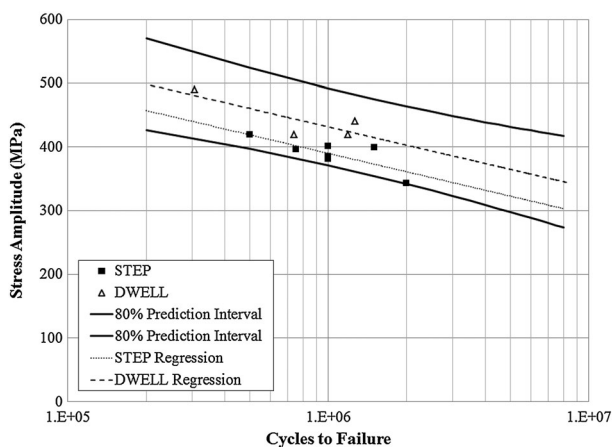


Fig. 8 Step test comparison against sinusoidal amplitude dwell: Ni Alloy 718, Vendor I.

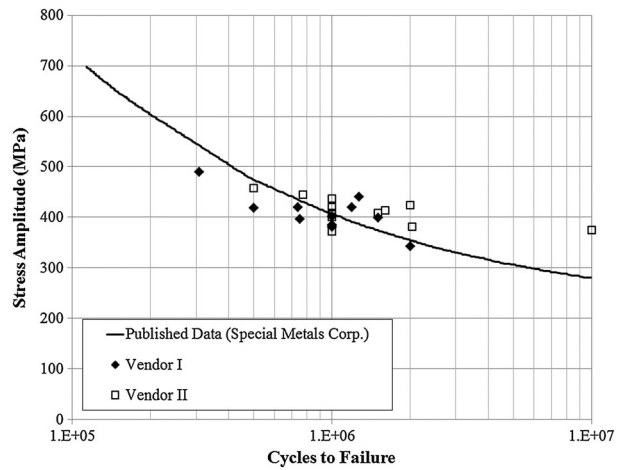


Fig. 10 Fatigue life comparison: direct metal laser sintering Ni Alloy 718 versus Inconel 718.¹⁷

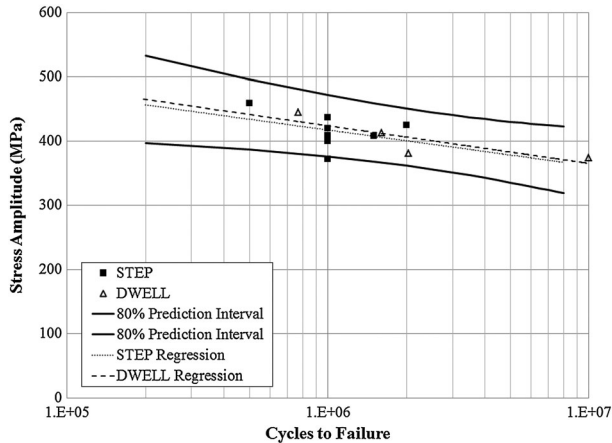


Fig. 9 Step test comparison against sinusoidal amplitude dwell: Ni Alloy 718, Vendor II.

performance.¹⁸ The step test and the dwell results were combined for both Vendors I and II and the data was compared against published rotating bending, cold-rolled data from Special Metals Corporation in Fig. 10.^{13,19} The comparisons show that the fatigue performances of both Vendors agree within a reasonable scatter with the published rotating bending results. Detailed justification for fatigue performance of each Vendor is addressed later in this section.

Monotonic tensile results

Tensile material properties were determined by pulling dog bone/coupon specimens monotonically until separation. Monotonic tensile tests were conducted with a Mechanical Test Systems (MTS) 312.21 load frame. The load frame is equipped with a 100 kN load cell, a linear variable differential transformer (LVDT) for

displacement control and an extensometer for strain measurement. The displacement loading rate and the specimen geometry used for monotonic tests were determined based on the American Society for Testing and Materials (ASTM) standard E 8-09 recommendations.²⁰ The displacement rate for each tensile test was 102 µm per second and the geometry of the tensile dog bone specimen is shown in Fig. 11.

In order to efficiently utilise available DMLS material and to correlate the strengths of specimens to respective fatigue lives, monotonic tensile data was acquired from dog bones cut out from fatigued plates.¹⁴ Four fatigued plates from each DMLS Vendor were analysed and six dog bone specimens with the geometry in Fig. 11 were cut from each plate. For half of the eight DMLS plates, dog bone specimens were cut longitudinal with the build direction of the plate and the other four were cut transverse to the build direction. The build direction shown in Fig. 12 (also shown in Fig. 5) was chosen under the assumption that it provided the worst case fatigue life results for the vibration-based specimen. As shown in Fig. 12, specimens that were cut longitudinal and transverse are respectively denoted by H and V to identify the fusion plane orientation with respect to the loading axis.

Tensile Dogbone

SI Units: Millimeters

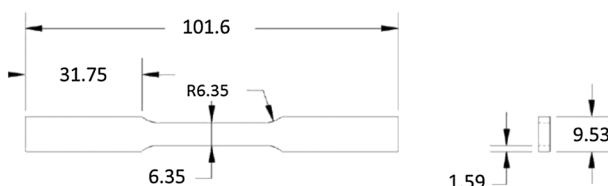


Fig. 11 Monotonic tensile specimen with American Society for Testing and Materials E 8-09 recommendations.

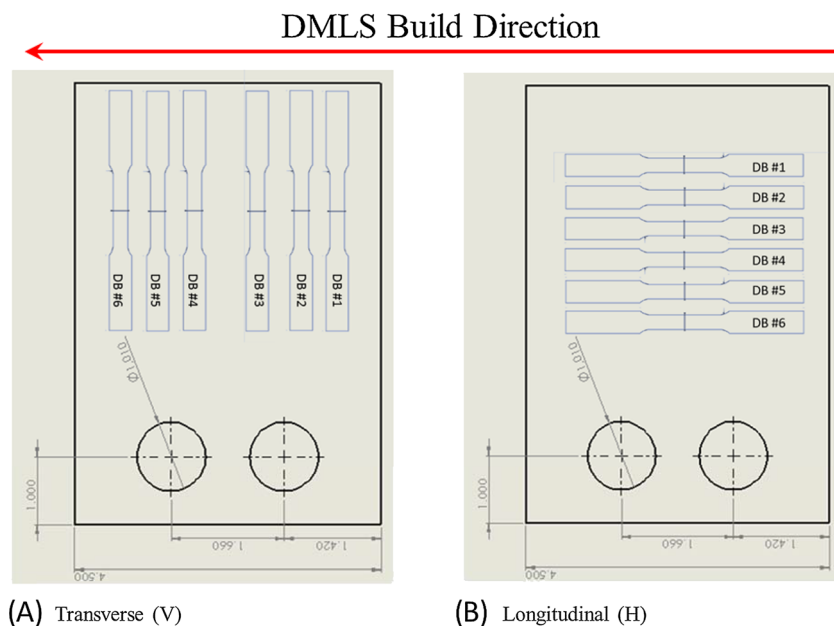


Fig. 12 Diagram for dog bone cutting configuration of direct metal laser sintering plate specimens.

This data was compared against two pristine (non-vibration affected) data points provided by Vendor I and MIL-HDBK-5J minus three sigma (referred to as min) material property values for long-transverse sheet/plate specimens with thicknesses between 0.254 and 25.4 mm.²¹

To understand the effects of minimal cyclic damage on tensile properties of Ni super alloys, a study comparing tensile results of non-vibrated (pristine) and vibrated specimens was first conducted on cold-rolled Inconel 625 and unhardened 718 alloys. Both alloys were chosen based on the closeness (625) and similitude (718) in chemical composition to the DMLS plates. The chemical compositions of the cold-rolled alloys investigated are listed in Table 1. Unhardened 718 specimens came from one $610 \times 610 \times 3.2$ mm plate stock, and the 625 specimens came from two $610 \times 305 \times 3.2$ mm plate stocks referred to as Stock I and Stock II. Each cold-rolled specimen was cut either along or transverse to the rolling marks of the bulk stocks and are respectively denoted as *V* and *H* to identify the rolling mark orientation with respect to the loading axis.

The results of the cold-rolled investigation are listed in Table 2. The Table shows the average Inconel 625 and 718 tensile results for ultimate and yield strength, elastic modulus (*E*) and total percent elongation before

separation. Specimen labels are defined as follows: for 625, *Alloy# Roll_plate Specimen# – Roll_dog bone*; and for 718, *Alloy# Roll_plate+Stock# Specimen# – Roll_dog bone*. Parameters *V* and *H* in both tables indicate all dog bones cut longitudinal and transverse to the roll direction, respectively. These labels are defined in the Nomenclature section. For 718, the rows of the vibration affected results are categorised by the fatigued plate labels; *718 H #3 – V* is a plate with chord-wise rolling direction and dog bones cut longitudinal to the roll and *718 V #1 – H* is a plate with span-wise rolling direction and dog bones cut transverse to the roll. Inconel 625 also categorises the vibration affected properties by the fatigue plate labels; *625 V1 #3 – H* is a plate from Stock I with span-wise rolling direction and dog bones cut transverse to the roll and *625 H2 #1 – V* is a plate from Stock II with chord-wise rolling direction and dog bones cut longitudinal to the roll. Because rolling direction will affect tensile properties, the variation for the combined pristine specimen properties (i.e. all pristine *H* and *V* specimens combined) were used for overall comparisons to simulate unforeseen manufacturer uncertainties not present in the studied material stocks. Results show a 0.3–1% increase in strength properties due to vibration on 625 specimens in the *V* direction and a 0.4–0.7% decrease in strength

Table 1 Chemical composition of cold-rolled Inconel Alloy 625 and 718

Ni Alloy	Ni	Cr	Nb	Mo	Al	Ti	Fe	Co	Si	Mn	C	S	Cu	B	Ta	P
625	bal	21.5	3.7	9	0.03	0.01	3.4	0	0.36	0.01	0.01	0.002	0	0	0	0
718	bal	18.36	5.06	2.9	0.56	1.04	19.58	0.07	0.07	0.08	0.05	0	0.02	0.003	0.01	0.007

Table 2 Cold-rolled Inconel Alloy 625 and 718 tensile property results

	Category	Yield (Mpa)	Ultimate (Mpa)	E (Gpa)	Elongation %	Samples #
Ni Alloy 718	Total	495	930	187	48	10
	V	507	943	181	48	5
	H	484	916	192	49	5
	718 H #3 – V	489	929	175	48	3
	718 V #1 – H	490	920	190	49	6
	MIL_HDBK-5J	481	942	205	30	n/a
	Total	491	914	194	50	12
Ni Alloy 625	Stock I – H	499	932	201	50	4
	Stock I – V	506	919	191	51	2
	Stock II – H	477	902	191	52	4
	Stock II – V	489	898	189	47	2
	Stock I – Total	502	928	197	50	6
	Stock II – Total	481	901	190	50	6
	625 V1 #3 – H	496	928	197	51	6
	625 H2 #1 – V	494	904	194	54	6

properties for specimens in the *H* direction. The 718 comparison shows the opposite results, where *V* specimens show roughly 1.5% decrease and *H* specimens show a 0.4–1.3% increase in strength properties because of the effects of vibration. These results do not indicate any trends based on cold-rolling direction or accumulated cyclic damage.¹⁴ Results also show that the vibration affected strength properties of each individual specimen are within one standard deviation of the total pristine results in Table 2 and display no particular trends with respect to tensile specimen location along the span of vibrated plates.

Results for the DMLS Ni Alloy 718 comparisons are shown in Table 3, where the final eight rows represent the vibration affected tensile properties. The average results for ultimate tensile and yield strength, the elastic modulus, and the total percent elongation before separation for vibration affected DMLS specimens are compared with two pristine data points provided by Vendor I. Also, the Table shows minus three sigma (referred to as min) material property values for long-transverse sheet/plate specimens with thicknesses between 0.254 and 25.4 mm.²¹ Both vendors show that the *V* specimens have

stronger tensile properties than the *H* specimens; however, this discrepancy is more noticeable in Vendor II than in Vendor I. Overall, Vendor I shows higher strength properties than both Vendor II and the published minimum data, but the ultimate tensile strength data for Vendor I are 1–3% less than the reference pristine data points from Vendor I. Other comparisons for the yield and ultimate tensile strength properties are shown in Fig. 13, respectively. These Figures conclude that Vendor II strength properties do not meet the minus three sigma material strength limits of the MIL-HDBK-5J published data.

Microscopy

Microscopy was conducted on cold-rolled Inconel 718 as well as Vendors I and II DMLS Nickel Alloy 718 to further investigate the fatigue and tensile strength performances from the previous sections. Micrographs from a scanning electron microscope (SEM) are shown for each observed composition in Fig. 14, where the loading/build and the crack axes refer to the vibration-based bending load and the fatigue crack path axes. The Figure illustrates finer

Table 3 Direct metal sintering nickel alloy 718 tensile property comparison

Category	Yield (MPa)	Ultimate (MPa)	E (GPa)	Elongation %	Samples #
MIL_HDBK-5J – min	1034	1240	203	12	n/a
Vendor I baseline – <i>V</i>	1068	1344	n/a	27	n/a
Vendor I baseline – <i>H</i>	1034	1309	n/a	27	n/a
Vendor I #1 – <i>H</i>	1070	1316	195	18	6
Vendor I #2 – <i>V</i>	1082	1331	199	20	6
Vendor I #5 – <i>V</i>	1071	1322	198	20	6
Vendor I #6 – <i>H</i>	1059	1293	191	17	6
Vendor II #2 – <i>H</i>	789	1059	174	31	6
Vendor II #3 – <i>V</i>	868	1162	182	26	6
Vendor II #4 – <i>H</i>	787	1034	185	31	6
Vendor II #5 – <i>V</i>	854	1148	172	26	6

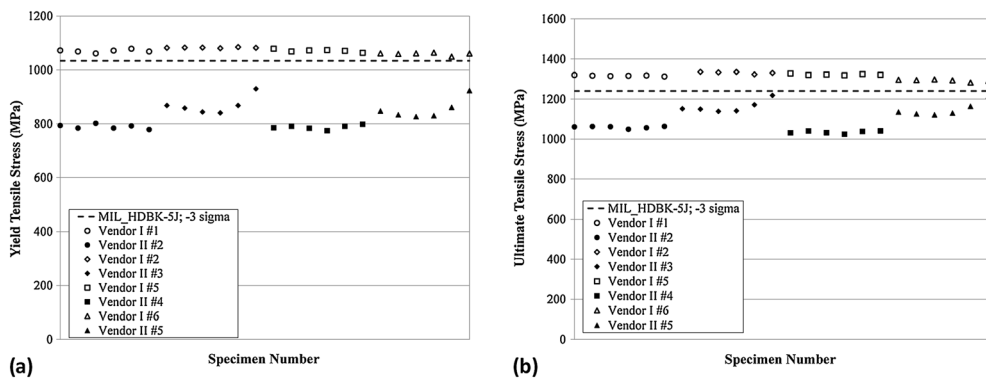


Fig. 13 (a) Yield and (b) ultimate tensile strength comparisons for direct metal laser sintering Nickel Alloy 718.

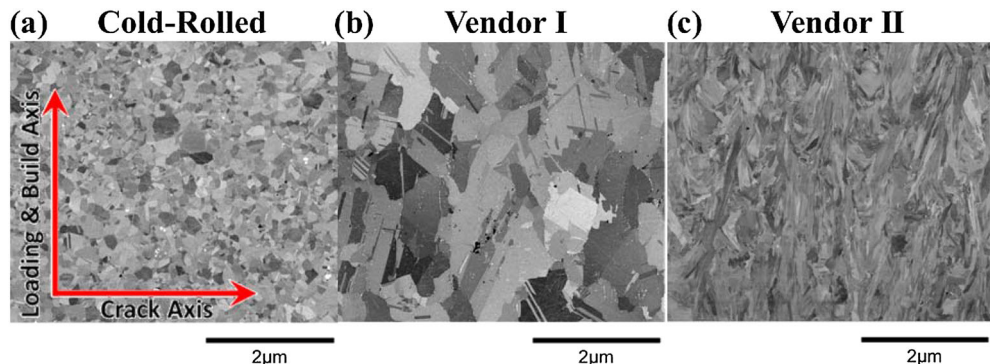


Fig. 14 Ni Alloy 718 scanning electron microscope micrograph.

grains in the cold-rolled alloy, coarser grains in the Vendor I DMLS alloy and elongated, columnar-like grains with indistinguishable grain boundaries in the Vendor II DMLS alloy. Previous studies show that as-built DMLS Ni Alloy 718 produce parts with melt pool overlapping artefacts and non-uniform columnar grains.^{22,23} The melt pool artefacts and grain structure non-uniformity can be eliminated with HIP and stress relief and the grain structure uniformity can be further increased with a 4-hour annealing process at 1160 °C.²³ HIP and stress relief also produce uniform distribution of γ precipitates. Further SEM investigation was conducted via an Orientation Image Microscopy (OIM). Because of the unique granular structure of Vendor II, OIM was only conducted on Vendor I plates. From the OIM illustrated in Fig. 15, the grain size calculated for Vendor I is ASTM 12.2 with a variation of ASTM 3-16. The grain size distribution for this OIM is illustrated in Fig. 16.

Previous work shows that grain size has a significant effect on both fatigue and tensile strength performances of materials.^{19,24,25} Comparing the Vendor I fatigue and microscopy results to AMS 5596 annealed and aged plate results¹⁹ (grain size values higher than ASTM

10) predicts a 10% reduction in stress amplitude in the DMLS plate versus rotating bending fatigue. Other high temperature Ni Alloy research also shows that a grain size difference of ASTM 11 to ASTM 7 between 350 and 550 °C results in a stress amplitude reduction of 27–28%.²⁶ These results support the belief that the difference in grain sizes is the reason behind Vendor I having lower fatigue strength than cold-rolled plates in Fig. 10. As for the Vendor II plates, despite the unique granular boundaries illustrated in Fig. 14, the grain size still appears to be small compared with both the Vendor I and cold-rolled Ni Alloy 718. Furthermore, the grains are elongated normal to the axis of the crack path, which creates a convoluted path for crack propagation, thus leading to longer fatigue life for Vendor II compared with cold-rolled and Vendor I alloys. Because of the indiscernible microstructural features of Vendor II, no significant effects of shape and distribution of γ precipitates were correlated to failure differences.

For a tensile loaded specimen, macro cracks form because of stress concentrations, most plausibly from dislocation pile-up, initiating slip in boundary grains.²⁵

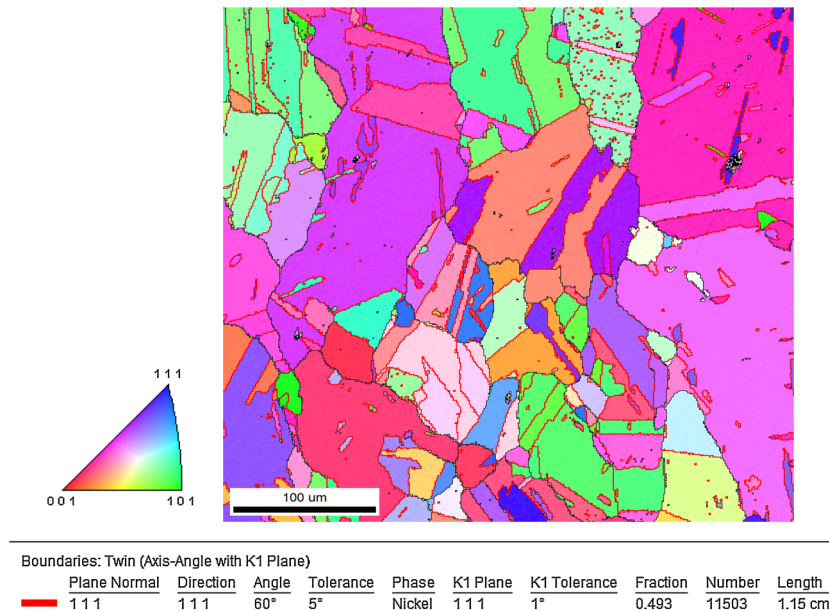


Fig. 15 Orientation image microscope of Vendor I plate with twin boundaries in red and untwined in blue.

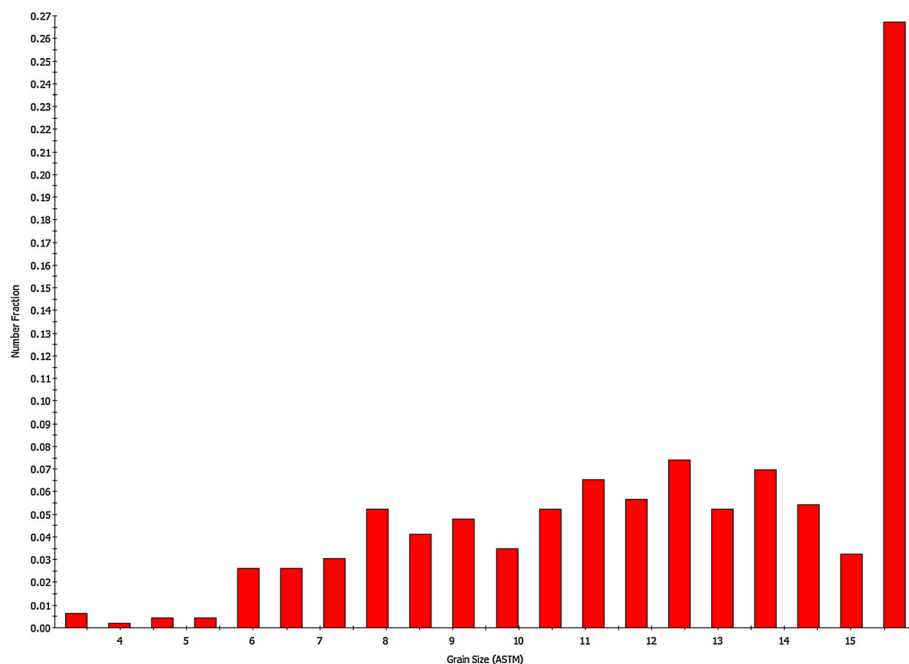


Fig. 16 Grain size distribution of Vendor I plate: correlates to Fig. 15 orientation image microscope.

Because it is argued that the applied stress will only increase as the number of dislocations increase, it is assumed that the finer grains will take longer to reach critical stress.²⁵ Considering no other factors, Vendor II should display higher strength values than cold-rolled and Vendor I results. However, both melt rate and the application of HIP have been known to improve tensile properties.^{27,28} Melt rates could not be

compared because of the proprietary nature of each vendor process, but the effect of HIP was investigated against results from previous studies. The addition of HIP treatment provides uniform grain sizes which, compared to as manufactured properties, improve ultimate tensile and yield strengths by 31 and 40%, respectively.²⁷ Because Vendor II plates did not receive post-fusion treatments and Vendor I plates underwent

ageing, HIP and stress relief, the respective 20 and 30% increase in ultimate tensile and yield strengths appear reasonable. Therefore, it can be stated that the post-fusion treatments make the Vendor I properties more consistent with wrought.

CONCLUSION

Fatigue and strength assessment of DMLS Ni Alloy 718 has been presented in this manuscript. DMLS assessment was made through comparison against cold-rolled data from both experimentation and refutable material data sources.²¹ DMLS specimens with and without post-fusion treatments were studied.

Observing the DMLS finished product, fixture holes of as-built specimens experienced pilling because of low angle slanting of the top half of the holes. It is suggested to fuse smaller than nominal holes and then EDM cut to size. Also, the as-built DMLS specimens showed similar thickness tolerances (<127 µm) as purchased cold-rolled plates.

Direct metal laser sintering tensile strength was compared with published cold-rolled data. DMLS results show mechanical properties may be sensitive to post-fusion treatments. In other words, the absence of HIP, solution heat treatment, ageing and stress relief may cause the increased uncertainty and debit in tensile strength properties.

Bending fatigue performance comparison between DMLS and cold-rolled shows good visual agreement between 2×10^5 and 2×10^6 cycles to failure. One DMLS vendor shows better performance than the other. Microscopy of DMLS and cold-rolled Ni shows granular structures corroborate with the fatigue conclusions. Like the tensile strength comparison, the discrepancy in fatigue comparisons can be better understood with fully disclosed process parameters.

Acknowledgements

The authors would like to thank the following organisations for funding, support and collaboration: the Turbine Engine Fatigue Facility (TEFF) of the United States Air Force Research Laboratory (AFRL), Universal Technology Corporation (UTC), the Department of Mechanical Engineering at Wright State University and the Departments of Mechanical and Aerospace Engineering at The Ohio State University. Also, the authors would like to acknowledge UTC contractor Tyler Kennedy for contributing to laboratory testing.

REFERENCES

- Lind, J.-E., Hanninen, J., Kotila, J., Nyrlila, O. and Syvanen, T. (2002) Rapid manufacturing with direct metal laser sintering. Materials Research Society Symposium proceedings, **758**, 17–22.
- Additive manufacturing – direct laser sintering of titanium and other metals, April 5, 2010, Next Big Future, <<http://www.nextbigfuture.com/2010/04/additive-manufacturing-direct-laser.html>>.
- Sanz, C., Garcia Navas, V., Gonzalo, O. and Vansteenkiste, G. (2011) Study of surface integrity of rapid manufacturing parts after different thermal and finishing treatments. 1st CIRP Conference on Surface Integrity proceedings, Vol **19**, 294–299.
- Zaeh, M. and Ott, M. (2011) Investigation on heat regulation of additive manufacturing processes for metal structures. CIRP Annals – Manufacturing Technology, Vol. **60**, 259–262.
- Santos, E., Masanari, S., Osakada, K. and Laoui, T. (2006) Rapid manufacturing of metal components by laser forming. *Int. J. Mach. Tools Manuf.*, **46**, 1459–1468.
- Murr, L., Quinones, S., Gaytan, S., Lopez, M., Rodela, A., Martinez, E.-Y., Hernandez, D., Martinez, E., Medina, F. and Wicker, R. (2009) Microstructure and mechanical behavior of Ti-6Al-4V produced by rapid-layer manufacturing for biomedical applications. *J. Mech. Behav. Biomed. Mater.*, **2**, 20–32.
- Engine Structural Integrity Program (ENSIP) MIL HDBK-1783B (USAF), 15 Feb 2002.
- George, T., Seidt, J., Shen, M.-H. H., Cross, C. and Nicholas, T. (2004) Development of a novel vibration-based fatigue testing methodology. *Int. J. Fatigue*, **26**, 477–486.
- George, T., Shen, M.-H. H., Cross, C. and Nicholas, T. (2006) A New multiaxial fatigue testing method for variable amplitude loading and stress ratio. *J. Eng. Gas Turbines Power, ASME*, **128**, 857–864.
- Scott-Emuakpor, O., Schwartz, J., Holycross, C., George, T., Cross, C. and Shen, M.-H. H. (2013) In-situ Study on Coaxing during Vibration-Based Bending Fatigue of Inconel 625 and 718. ASME/IGTI Turbo Expo, San Antonio, TX, Paper number: GT2013-94233.
- Nicholas, T. and Maxwell, D. (2003) Mean stress effects on the high cycle fatigue limit stress in Ti-6Al-4V. Fatigue and fracture mechanics: 33rd volume, ASTM STP 1417. In American Society for Testing and Materials. (Edited by W. G. Reuter and R. S. Piascik), Elsevier Science, West Conshohocken, PA, pp. 476–492.
- Nicholas, T. (2006) High Cycle Fatigue – A Mechanics of Materials Perspective. Elsevier, Oxford, UK.
- Scott-Emuakpor, O., Schwartz, J., George, T., Holycross, C. and Slater, J. (2014) Bending fatigue life comparison between DMLS and cold-rolled nickel alloy 718. Machinery Failure Prevention Technology (MFPT) Society Annual Conference, Virginia Beach, VA, 20–22.
- Scott-Emuakpor, O., George, T., Beck, J., Holycross, C., Schwartz, J., Shen, M.-H. H. and Slater, J. Material property determination of vibration fatigued DMLS and cold-rolled nickel alloys, ASME/Turbo Expo, Dusseldorf, Germany, 16–20 June 2014, paper No. GT2014-26247.
- Kaszynski, A., Beck, J. and Brown, J. (2013) Uncertainties of an automated optical 3D geometry measurement modeling and analysis process for mistuned IBR reverse engineering, ASME/IGTI Turbo Expo, San Antonio, Texas, paper No. GT2013-95320.
- Bellows, R., Muju, S. and Nicholas, T. (1999) Validation of the step test method for generating Haigh diagrams for Ti-6Al-4V. *Int. J. Fatigue*, **21**, 687–697.

- 17 Scott-Emuakpor, O., George, T., Cross, C., Wertz, J., and Shen, M.-H. H. 2012 A new distortion energy-based equivalent stress for multiaxial fatigue life prediction. *Int. J. Non Linear Mech.*, **47**, 29–37.
- 18 American Society for Testing and Materials, E739 - 10: Standard Practice for Statistical Analysis of Linear or Linearized Stress-Life (S-N) and Strain-Life (ϵ -N) Fatigue Data, ASTM Book of Standards, 2010; Vol. **03.01**, ASTM International, West Conshohocken, PA.
- 19 Special Metals Corporation, Inconel Alloy 718, New Hartford, NY, September 7, 2007, Publication No. SMC-045.
- 20 American Society for Testing and Materials. E 8M - 09: Standard Test Methods for Tension Testing of Metallic Materials, ASTM Book of Standards, 2009; Vol. **03.01**: ASTM International, West Conshohocken, PA.
- 21 Metallic materials and elements for aerospace vehicle structures, MIL-HDBK-5J (USAF), 31 Jan 2003.
- 22 Carter, L., Martin, C., Withers, P., and Attallah, M. (2014) The Influence of the laser scan strategy on grain structure and cracking behaviour in SLM powder-bed fabricated nickel superalloy. *J. Alloys Compd.*, **615**, 338–347.
- 23 Amato, K., Gaytan, S., Murr, L., Martinez, E., Shindo, P., Hernandez, J., Collins, S. and Medina, F. (2012) Microstructures and mechanical behavior of Inconel 718 fabricated by selective laser melting. *Acta Mater.*, **60**, 2229–2239.
- 24 Thompson, A., and Backofen, W. 1971 The effect of grain size on fatigue. *Acta Metallurgica*, **19**, 597–606.
- 25 Hall, E., and Petch, N. 1950 The cleavage strength of crystals. *J. Iron Steel Inst.*, **174**, 25–28.
- 26 Pieraggi, B. and Uginet, J. (1994) Fatigue and creep properties in relation with alloy 718 microstructure, TMS proceedings: Superalloys 718, 625, 706, and various derivatives, pp. 535–544.
- 27 Lee, S., Chang, S., Tang, T., Ho, H. and Chen, J. (2006) Improvement in the microstructure and tensile properties of Inconel 718 superalloy by HIP treatment. *The Japan Inst. Met.: Mater. Trans.*, **47**, 2877–2881.
- 28 Valencia, J., McCabe, T., Hens, K., Hansen, J. and Bose, A. (1994) Microstructure and mechanical properties of Inconel 625 and 718 alloys processed by powder injection molding, TMS proceedings: Superalloys 718, 625, 706, and various derivatives, pp. 935–945.

Mechanical and Microstructural Investigation of Nickel-Based Superalloy IN718 Manufactured by Selective Laser Melting (SLM)^{**}

By Johannes Strößner, Michael Terock and Uwe Glatzel*

Selective laser melting, a quite new layer-wise manufacturing process for metals, is used for processing the nickel-based superalloy IN718. The objective of this work is to compare the microstructure and the mechanical properties of the produced specimens, directly after the manufacturing process and additionally after two diverse heat treatments subsequent to the manufacturing process. As the resulting microstructure and properties for specimens manufactured by selective laser melting are directional, all investigations are made for specimens oriented vertically and horizontally. Optical, scanning, and transmission electron microscopy are carried out in order to characterize the microstructure explicitly. For investigating the texture of the material, additional EBSD measurements are undertaken. Mechanical tests include tensile testing at room temperature and at elevated temperatures and hardness measurements. The investigations reveal a very good quality of the SLM-produced specimens. Nonetheless, differences in the grain sizes, the orientation, and especially in the precipitation behavior could be found.

1. Introduction

New additive manufacturing techniques offer a broad range of advantages compared to conventional manufacturing techniques like casting, forging, or machining. Some of these advantages are the lower time to market, near net shape production, a high material utilization rate, high flexibility in production, and geometrical freedom.^[1] One primary representative of these additive techniques is selective laser melting (SLM). Parts are built up by layer-wise melting of metallic powder by laser irradiation, carried out under inert gas to prevent oxidation. After rapid solidification of the melt pools, a new powder layer is deposited and exposed to the laser again. The unmelted powder from the former layers serves as support for the adjacent layers. This process is repeated till the part is completely built up.^[2]

One important field of potential application for additive manufacturing processes is the area of aerospace technology. Especially the possibility to manufacture geometrically complex, hollow parts, to reduce cut off, thus saving of material, and the possible substitution of several individual processes, are the most promising advantages. Therefore, although selective laser melting is still a novel process, a lot of research groups all over the world are investigating the application of this technology to nickel-based superalloys, one important material for aerospace technology.

As the selective laser melting process is to some degree comparable to a continuous welding process, most publications cover superalloys like IN718, Waspaloy, and Nimonic 263 which show a good weldability.^[3–7]

Only less work has been done on superalloys which are more difficult to weld. Hagedorn *et al.* investigated MAR M 247 and showed that it is possible to generate dense parts.^[8] Rickenbacher *et al.* investigated IN738LC and could produce crack-free specimens by an SLM process with optimized processing parameters and a following HIP treatment.^[9]

Due to its good weldability and its good mechanical and structural stability up to temperatures of 650 °C, IN718 is (one of) the most widely used nickel-based superalloys for high temperature applications like gas turbines, aero-engines, and the most investigated alloy regarding additive manufacturing techniques.^[10] IN718 is a Ni–Fe–Cr superalloy whose primary

* Prof. Dr. U. Glatzel, J. Strößner, M. Terock
University Bayreuth, Metals and Alloys, Ludwig-Thoma-Straße 36b, D-95447 Bayreuth, Germany
E-mail: uwe.glatzel@uni-bayreuth.de

** The EBSD measurements were carried out at the Bavarian Research Institute of Experimental Geochemistry and Geophysics (BGI) of the University of Bayreuth with kind help of Ulrike Trenz and Florian Heidelbach.

strengthening precipitate is the metastable γ'' (Ni_3Nb) phase having a body-centered tetragonal (DO_{22}) crystal structure.^[11] Two other precipitates which can be found in the alloy are the γ' (Ni_3Al) phase with a $\text{L}1_2$ crystal structure and the stable orthorhombic (DO_3) δ phase with the composition Ni_3Nb .^[12]

In the present investigation, IN718 rods were manufactured by SLM. The investigation includes a detailed characterization of the microstructure and the resulting mechanical properties, directly after manufacturing and after two different heat treatments. The aim of the investigation is to extend the knowledge about microstructural evolution during the laser melting process and the subsequent heat treatments.

2. Experimental Section

2.1. Material

Gas-atomized powder of IN718 was used for the selective laser melting process. IN718 has the compositional range (all in wt%) [50.0–55.0] Ni—[17.0–21.0] Cr—[4.75–5.5] Nb—[2.8–3.3] Mo—[0.65–1.15] Ti—[0.20–0.80] Al—[≤ 1.0] Co—[≤ 0.35] Mn, Si—[≤ 0.08] C—[bal.] Fe. Cylinders with a diameter of 13 mm and a length of 70 mm were built with a powder layer thickness of 20 μm , parallel (horizontal) and normal (vertical) to the building platform. Figure 1 shows the orientation and building direction of the specimens.

For the scanning process, the area of the specimen is divided in stripes which are scanned in a meandering movement. The successive layer is rotated by an optimized, defined angle to achieve isotropic lateral properties. After cutting the bars from the building platform, two different heat treatments were performed. They are named "HT 1" and "HT 2" in the following. Both heat treatments include a stress relieving, a solution annealing, and an ageing step. "HT 1" is leaned on AMS 5662 standard (solution annealing: 980 °C/1 h, air cooling, two-step ageing: 760 °C/10 h, furnace cooling: 2 h to 650 °C, holding: 8 h). The stress relieving is in the same temperature range as the solution treatment. In case of "HT 2," one additional homogenization step was carried out before the solution annealing. The homogenization step is leaned on the solution treatment step described in AMS 5664 (1 065 °C/1 h) and is followed by the same solution annealing and ageing as described for "HT 1."

For a better understanding of the micrographs shown in this manuscript, the building direction of the specimens is

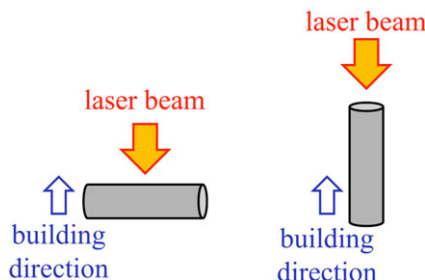


Fig. 1. Orientation of the built specimens.

given in the lower left corner of the micrographs. Microsections normal to the building direction are labeled with a cross, microsections parallel to the building direction are labeled with an arrow, directing toward the building direction.

2.2. Tensile Testing

Tensile testing was performed at room temperature and at elevated temperature (450 and 650 °C) in air in a Zwick Z100 standard tensile testing device. The tests were carried out following engineering standard EN 100 02-1 at room temperature, respectively, engineering standard EN 100 02-2 at elevated temperature. Strain was recorded with a contact extensometer appropriate for high temperatures. Temperature was measured with three type S thermocouples near the surface of the specimen to ensure a homogenous temperature distribution over the gauge length. Standard cylindrical specimens following DIN 50125 were used. For reasons of measurement uncertainties, three tensile tests were performed for each heat treatment and each orientation.

2.3. Hardness Measurements

Hardness measurements were performed for specimen sections in and normal to the building direction, directly after the manufacturing, and after the two different heat treatments. Rockwell hardness was measured with cone and a load of 150 kP (1 471 N). For reasons of comparison with other literature data, Vickers hardness was performed with a load of 10 kP (98 N).

2.4. Microstructural Investigations

Metallurgical investigations of the specimens were done directly after the manufacturing process and after two different heat treatments, in and normal to the building direction, respectively. Porosity measurements were done, using digital image processing. For analyzing the grain size and the morphology, specimens were electrolytically etched either in a solution of 50 ml hydroxypropionic acid, 150 ml hydrochloric acid, and 3 g oxalic acid with a constant current of 2 V for a few seconds, or in caustic soda with a constant current of 15 V for approximately 1 min. Scanning electron microscopy (SEM) investigations were performed on a 1540 EsB Cross Beam (Zeiss) with an energy dispersive spectrometer (EDS) for chemical analysis. Transmission electron microscopy (TEM) combined with EDS investigations was performed on a Libra 200 FE (Zeiss). Preparation of the foils for the TEM investigations was done by grinding coupons to a thickness of $\approx 100 \mu\text{m}$, punching discs with a diameter of 3 mm, and electropolishing them in a Tenupol-3 at a temperature of -30°C , using an etchant consisting of 200 ml perchloric acid and 800 ml methanol, at 20 V. For analyzing the orientation relationships, electron backscatter diffraction investigations (EBSD) were performed on a LEO Gemini 1530 (Zeiss). The size of the performed mappings was $600 \times 400 \mu\text{m}^2$ with a scanning step size of 1 μm . For processing the raw data obtained from the EBSD

Table 1. Mechanical properties at room temperature.

Heat treatment	"As built"		"HT 1"		"HT 2"		Wrought material ^[a]
Specimen orientation	h	v	h	v	h	v	
Tensile strength [MPa]	1 085 ± 11	1 010 ± 10	1 447 ± 10	1 357 ± 5	1 417 ± 4	1 387 ± 12	1 407
Rp.0.2 yield strength [MPa]:	816 ± 24	737 ± 4	1 227 ± 1	1 136 ± 16	1 222 ± 26	1 186 ± 23	1 172
Strain to failure[%]:	19.1 ± 0.7	20.6 ± 2.1	10.1 ± 0.6	13.6 ± 0.2	15.9 ± 1.0	17.4 ± 0.4	21
Heat treatment:	"As built"		"HT 1"		"HT 2"		
Cross-section orientation:	h	v	h	v	h	v	
Hardness HV 10:	341	307	452	453	439	448	
Hardness HRC:	35	30	45	45	44	44	

h, horizontal-oriented specimens; v, vertical-oriented specimens.

^[a] Inconel 718 technical data: www.hightempmetals.com.

measurements, the MatLab Toolbox MTEX^[13] was used. XRD measurements were performed on a D8 Advance (Bruker).

3. Results

3.1. Mechanical Testing

The results for the tensile tests at room temperature are shown in Table 1. All heat treatment states show a strong anisotropic behavior with respect to the building direction, which is more pronounced for the "as built" and "HT 1" samples. Horizontally built specimens show higher tensile strength but lower strain to failure properties than vertically built samples. In the "as built" state, the tensile strength is remarkably lower compared to both heat-treated states, which have akin mechanical properties with slightly better strain to failure values for "HT 2" specimens. Compared to values for wrought material taken from the literature, the tensile strength of SLM-fabricated material is in the same range, with lower strain to failure values.

The results for the hot tensile tests are shown in Figure 2. The black curves show the tensile strength, the orange curves the strain to failure. The symbols indicate the performed heat treatment, solid lines indicate a horizontal orientation of the specimens, and dashed lines indicate a vertical orientation of the samples. Both heat treatments show similar tensile properties with tensile strength at 650 °C still in a range of 1 100 MPa. As for the tests at room temperature, vertical-oriented specimens show lower tensile strength but higher

strain to failure values compared to horizontally oriented specimens. For the "as built" state, only RT tests have been performed.

In the second part of Table 1, the results for the hardness measurements are shown. For both heat treatments "HT 1" and "HT 2," no anisotropy in RT hardness could be observed. For both heat treatments, the hardness is about 45 HRC. For the "as built" state, vertical cross-sections show higher hardness (35 HRC) than the horizontal cross-sections (30 HRC).

3.2. Porosity and Grain Size

Porosity measurements performed by optical light microscopy confirmed a very good quality of the built samples with an extremely low porosity within the range of 0.02%, indicating a perfectly optimized SLM process. Grain size measurements revealed a very fine-grained microstructure with elongated grains in building direction. Figure 3 shows the grain size distribution for the "as built," "HT 1," and "HT 2" state analysis made for vertical cross-sections. The black bars show the intercept length parallel to the building direction, the red bars show the intercept length normal to the building direction. Clearly apparent is the alignment of the grains in building direction. For the "as built," and the "HT 1" samples, the intercept length parallel to the building direction is greater compared to the length normal to the building direction. The largest grains are elongated up to 140 µm parallel to the building directions and 80 µm normal to the building direction. The "HT 2" samples show a broader distribution shifted to larger grain sizes and with a clearly reduced alignment of the grains in building direction. The largest grains are elongated up to 140 µm in both directions.

3.3. Microstructural Investigations

3.3.1. "As Built" State

Figure 4a shows a typical microstructure of the "as built" state. The arrow on the left side

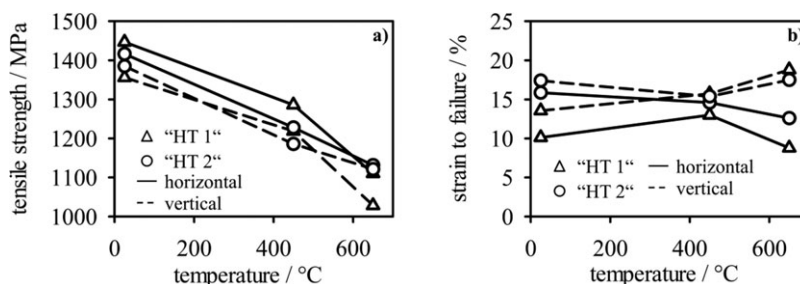


Fig. 2. (a) Hot tensile strength for "HT 1"- and "HT 2"-specimens, (b) strain to failure for "HT 1"- and "HT 2"-specimens. Solid lines describing horizontal-oriented samples, dashed lines for vertical-oriented samples.

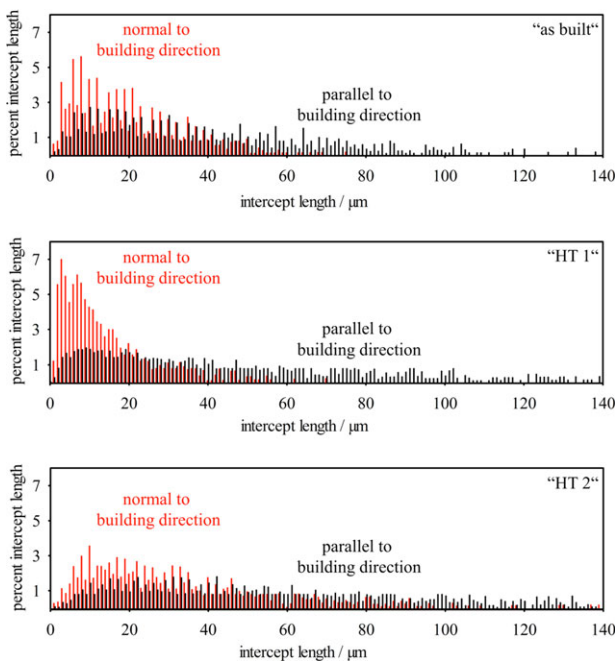


Fig. 3. Grain size distribution for vertical cross-sections for the “as built”-, “HT 1”-, and “HT 2” states. Black bars describing the intercept length of the grains parallel to the building direction, red bars the intercept length normal to the building direction.

of the micrograph indicates the building direction. Clearly visible are the melt pools consigned from the laser. Furthermore, columnar grains are observable which grow over several building layers, parallel to the building direction. The SEM images (Figure 4b) reveal a columnar-dendritic structure

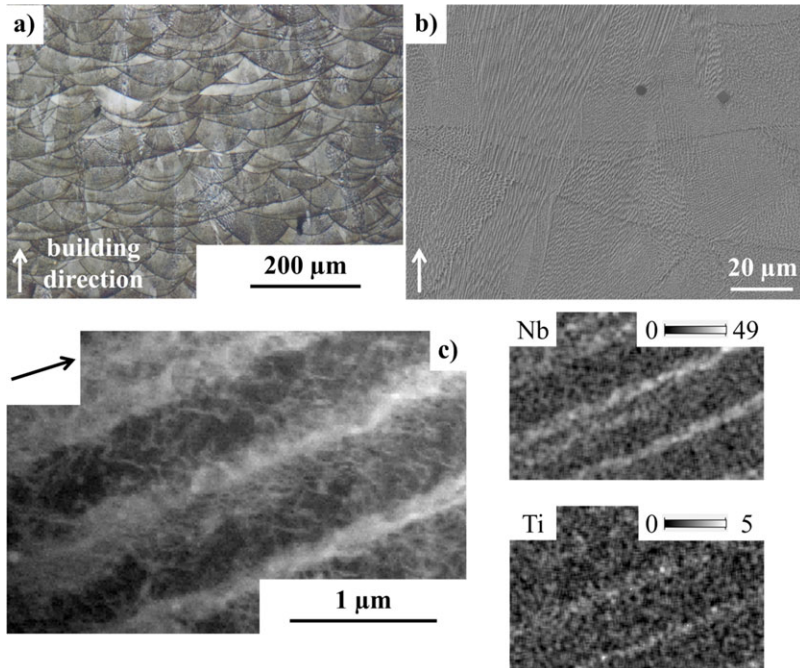


Fig. 4. (a) Reflected light micrograph of the “as built”-state showing the melt pools consigned from the laser, (b) SEM-SE micrograph of grains with a dendritic microstructure aligned in building direction growing other several building layers, (c) STEM-HAADF image of the “as built”-state showing the dendritic structure, elemental mapping (wt%) of the “as built”-state dendritic microstructure showing niobium and titanium content increase in the bright areas.

parallel to the building direction. As the dendritic structure was observed to be in the range of several 100 nm, EDS measurements within SEM cannot resolve chemical differences. Disregarding few blocky titanium carbonitrides, statistically distributed in the microstructure, no precipitates could be found in the micrographs of the “as built” state by scanning electron microscopy.

For a more detailed investigation of the fine dendritic structure, TEM foils have been prepared and investigated in scanning transmission electron microscopy mode (STEM) with a high-angle annular darkfield detector (HAADF). In the STEM image shown in Figure 4c, the dendritic structure of the specimen is clearly visible, with a gap in between the columns of \approx 500 nm. HAADF imaging leads to a bright Z-contrast where heavier elements are enriched. An EDS-elemental mapping of the dendritic structure reveals niobium and titanium segregations in these areas.

3.3.2. “HT 1” State

Figure 5a shows a SEM micrograph for “HT 1” state. Plate-like precipitates at the grain boundaries and inside the grains are observed. XRD measurements prove that there are δ precipitates. Figure 5b shows a STEM image with δ -phase plates with γ'' -depleted zones surrounding the precipitates. As for the “as built” state, the grains are still parallel to the building direction and there are no hints of recrystallization.

3.3.3. “HT 2” State

For the investigated “HT 2” state specimen, with the additional homogenization step, a recrystallized microstructure is observed. The SEM images (Figure 6a) show grains with a lot of twin boundaries and with δ -phase precipitations only at grain boundaries. The plate-like morphology of the δ particles is clearly apparent in Figure 6b. The alignment of the grains in building direction is still present in the recrystallized state, but evidently reduced.

3.3.4. XRD and EBSD Investigations

XRD measurements were performed for horizontal cross-sections for the “as built,” the “HT 1,” and the “HT 2” states. The XRD patterns are shown in Figure 7. They show small δ peaks only in case of “HT 1” samples, which is in good agreement with the SEM observations. For the “as built” state and the “HT 1” state, a prominent (200) peak becomes apparent, caused by the textured grains, which has a lower intensity for the “HT 2” state. The performed EBSD mappings cover $600 \times 400 \mu\text{m}^2$. Due to the varying grain sizes for the different heat treatment states, various numbers of grains are covered. For the “as built” and “HT 1” states about 1500 grains are covered, while for the “HT 2” state only about 700 grains are included in the mapping area.

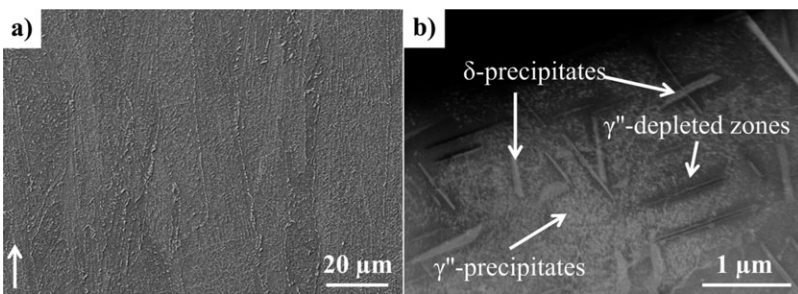


Fig. 5. (a) SEM-SE micrograph of the “HT 1”-state showing the aligned grains in building direction and precipitation at the grain boundaries and in the grains, (b) STEM-HAADF image showing plate-like δ precipitates with γ'' -depleted zones around the precipitates.

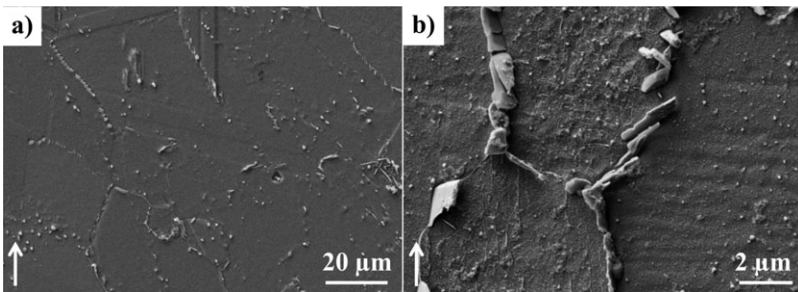


Fig. 6. (a) SEM-SE micrograph of the “HT 2” state showing a recrystallized microstructure, (b) SEM-SE micrograph showing plate-like δ -phase precipitation at grain boundaries.

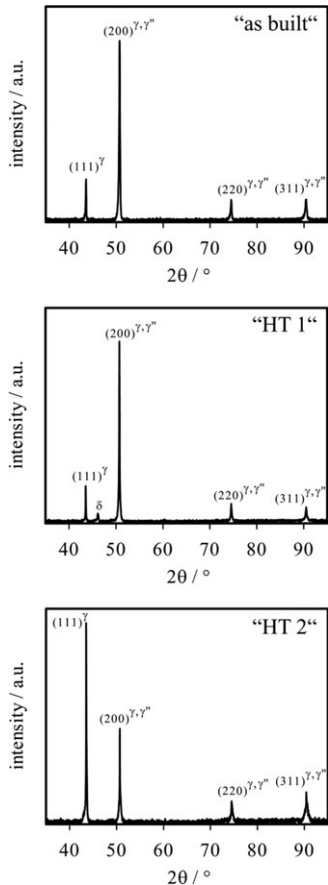


Fig. 7. XRD pattern of the “as built”-, “HT 1,” and “HT 2”-states for horizontal cross-sections.

In Figure 8, pole figures for the “as built,” “HT 1,” and the “HT 2” states, horizontal cross-sections obtained from the EBSD measurements are shown. The results are in good agreement with the XRD measurements. The “as built” and the “HT 1” state specimens show textures with grains oriented preferentially with one of their $<001>$ directions parallel to the building direction. For “HT 2”-state specimens, this orientation dependence is strongly reduced.

4. Discussion

4.1. Microstructural Investigations

4.1.1. “As Built” State

In the “as built” state, no precipitates could be resolved in the microstructure by light and scanning electron microscopy. As a reason of the high solidification rates, the microstructure shows a very fine dendritic structure with a spacing of about 500 nm between the columns. This is in agreement with the theoretical relationship, known from the literature describing the distance of the columns in dependence of the solidification rate and the temperature gradient ($[\lambda] = \mu\text{m}$, $[G] = \text{K mm}^{-1}$, and $[v] = \text{mm min}^{-1}$).^[14]

$$\lambda_D = \frac{750}{\sqrt[4]{G^2 \cdot v}} \quad (1)$$

For estimated cooling rate v of about 2 m s^{-1} ($120\ 000 \text{ mm min}^{-1}$) and temperature gradient G of about $3\ 500 \text{ K mm}^{-1}$,^[15,16] the estimated distance between the columns is in the range of 700 nm, which is in good agreement with the distances obtained from the micrographs. EDS measurements reveal niobium segregations in the bright areas. Niobium is known to be a strongly segregating element.^[17] Similar observations for the “as built” state were made in the

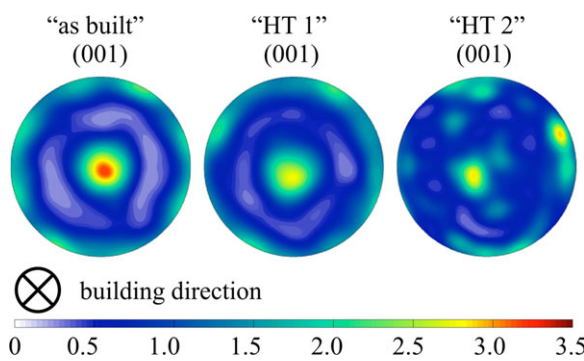


Fig. 8. Pole figures obtained from the EBSD measurements for the “as built,” “HT 1,” and “HT 2” states for horizontal cross-sections.

literature. Amato *et al.* also found elongated grains aligned with the building direction and a dendritic microstructure with dimensions in between 0.5 and 1 µm.^[3] Niobium segregations in the “as built” state were also found by Wang *et al.*^[5] In case of the related process electron beam melting, Strondl *et al.* investigated IN718 and observed similar microstructural features, but a more intense texture and a higher aspect ratio of the grains in building direction.^[18] The strong texture for IN718 manufactured by electron beam melting was also observed by Helmer *et al.*^[19]

4.1.2. “HT 1” State

For the specimens in the “HT 1” state, with no homogenization step, δ precipitations could be found at the grain boundaries as well as in the grains. “HT 1” is a standard heat treatment for wrought material. According to Figure 9, showing a TTT diagram for wrought, sufficiently homogenized IN718, no distinct δ-phase precipitation should take place.^[20] If at all, there is the possibility of δ-phase formation in small amounts at grain boundaries. The likely reason for the observed δ phase inside the grains is the higher Nb content in the brighter regions, enhancing the formation of the δ phase. Similar observations were made by Radhakrishna *et al.* for IN718 welds.^[21] For not homogenized but heat-treated material manufactured by selective laser melting, Wang *et al.* also found intragranular δ phase.^[5] As the investigations of the grain size distribution and the orientation of the grains show, no recrystallization took place during heat treatment and the preferred orientation of the grains aligned with one of their <001> directions parallel to the building direction is preserved.

4.1.3. “HT 2” State

For the specimens in the “HT 2” state, with an additional homogenization step, a recrystallized microstructure was observed, with a broader grain size distribution compared to the “as built” and the “HT 1” states. In contrast to the “HT 1” state, no δ precipitation inside the grains was observed. In conjunction with the recrystallization, the orientation dependence of the grains aligned with one of their <001> directions parallel to the building direction is reduced, see EBSD and

XRD measurements. For the “HT 1” and the “as built” states, elongated grains in building direction were observed. For the “HT 2” state, the elongation of the grains reduces significantly. Amato *et al.* also observed recrystallization for “as built” samples annealed in argon for 4 h at a temperature of 1 160 °C.^[3]

4.2. Mechanical Properties

The mechanical tests reveal very similar mechanical properties for both heat-treatment routes (“HT 1” and “HT 2”) with some remarkable differences. For all three heat-treatment states, different tensile properties were observed depending on the orientation of the specimen. But while there is a stronger difference for the “as built”-state and “HT 1”-state samples, the difference is smaller for the “HT 2”-state samples. The dependence of the mechanical properties on the orientation of the specimens can be explained by the number of layers, thus amount of joints perpendicular to the stress axis, and by the homogeneity of the alloy and therefore the distribution of the γ” phase. Vertically oriented specimens contain far more layers compared to horizontally oriented specimens. As the microstructural investigations revealed stronger niobium segregations at these joints, and therefore formation of δ phase during “HT 1,” it is evident that the joints are weak points resulting in worse tensile strength for the vertically oriented specimens. It is coherent that a longer heat treatment (“HT 2”) with a recrystallization of the grains results in more uniform distribution of the γ” phase and, therefore, more even mechanical properties regarding the orientation of the specimens.

The precipitation of the γ” phase during the ageing of the alloy is also the reason for the remarkable jump in the mechanical properties from the “as built” state compared to both heat-treated states, as the γ” phase is the crucial phase regarding the strength of the alloy. Compared to wrought material, the tensile properties are similar with slightly higher strain to failure values for the wrought material. As for the tensile properties, the hardness for the “as built” state shows direction-dependent values.

5. Conclusions

IN718 manufactured by selective laser melting was investigated in the “as built” state and after two different heat treatments. The main difference between the two heat treatments was an additional homogenization step after the stress relieving in heat-treatment “HT 2”. The investigation included a mechanical characterization of the samples by tensile testing at room temperature and at elevated temperatures, hardness measurements, and microstructural investigations using light, scanning electron, and transmission electron microscopy.

- The mechanical properties after heat treatment are similar for both different heat treatments (with and without additional homogenization step) and are comparable to wrought material.

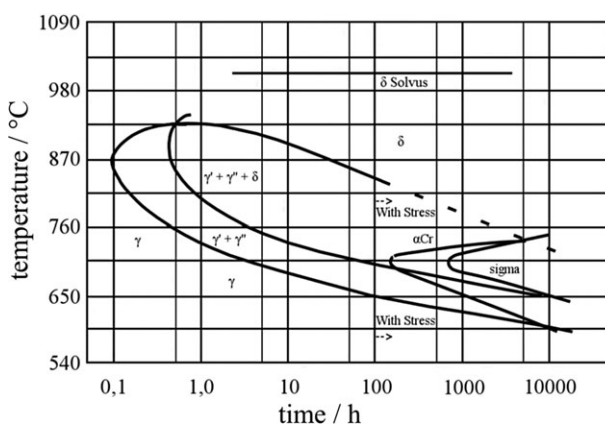


Fig. 9. TTT diagram for homogenized IN718.^[20]

- (ii) The manufactured specimens show anisotropic behavior; horizontally built specimens had better tensile strength and lower strain to failure values compared to vertically built specimens for all three states: "as built," "HT 1," and "HT 2".
- (iii) Microstructure investigations reveal a very fine grain size distribution, with grains aligned parallel to the building direction for the "as built" and "HT 1" states.
- (iv) A dendritic microstructure could be observed for the "as built" state with niobium microsegregations caused by the high cooling rates in the SLM process.
- (v) Intragranular δ -phase formation in case of "HT 1" is observed, resulting from niobium microsegregations.
- (vi) Recrystallization of the grains is observed for "HT 2" with grains free of δ phase.

Received: March 26, 2015

Final Version: May 6, 2015

Published online: June 5, 2015

-
- [1] L. Thjis, F. Verhaeghe, T. Craeghs, J. Van Humbeeck, J. P. Kruth, *Acta Mater.* **2010**, *58*, 3303.
 - [2] J. P. Kruth, P. Mercelis, J. Van Vaerenbergh, *Rapid Prototyping J.* **2005**, *11*, 26.
 - [3] K. N. Amato, S. M. Gaytan, L. E. Murr, E. Martinez, P. W. Shindo, J. Hernandez, S. Collins, F. Medina, *Acta Mater.* **2012**, *60*, 2229.
 - [4] Q. Jia, D. Gu, *J. Alloys Compd.* **2014**, *585*, 713.
 - [5] Z. Wang, K. Guan, M. Gao, X. Li, X. Chen, X. Zeng, *J. Alloys Compd.* **2012**, *513*, 518.
 - [6] K. A. Mumtaz, P. Erasenthiran, N. Hopkinson, *J. Mater. Process. Technol.* **2008**, *195*, 77.
 - [7] T. Vilaro, C. Colin, J. D. Bartout, L. Naze, M. Sennour, *Mater. Sci. Eng. A* **2012**, *534*, 446.
 - [8] Y. C. Hagedorn, J. Risse, W. Meiners, N. Pirch, K. Wissenbach, R. Poprawe, *High Value Manufact.: Adv. Res. Virtual and Rapid Prototyping: Proc. 6th Int. Conf. Adv. Res. Virtual Rapid Prototyping*, Leiria, Portugal **2013**, 291.
 - [9] L. Rickenbacher, T. Etter, S. Hövel, K. Wegener, *Rapid Prototyping J.* **2013**, *19*, 282.
 - [10] P. L. Blackwell, *J. Mater. Process. Technol.* **2005**, *170*, 240.
 - [11] J. M. Oblak, D. F. Paulonis, D. S. Duvall, *Metall. Trans.* **1974**, *5*, 143.
 - [12] M. Sundararaman, P. Mukhopadhyay, S. Banerjee, *Metall. Trans.* **1988**, *19*, 453.
 - [13] F. Bachmann, R. Hielscher, H. Schaeben, *Solid State Phenom.* **2010**, *160*, 63.
 - [14] D. Goldschmidt, *Materialwiss. Werkstofftech.* **1994**, *25*, 311.
 - [15] D. Buchbinder, *Generative Fertigung von Aluminiumbauteilen für die Serienproduktion, AluGenerativ Abschlussbericht*, BMBF 01RIO639A-D.
 - [16] H. Brodin, O. Andersson, *13th Int. Conf. Fract.* Beijing, China **2013**.
 - [17] R. Bürgel, *Handbuch Hochtemperatur-Werkstofftechnik*, Vieweg Technik, Braunschweig/Wiesbaden Germany **1998**, p. 375.
 - [18] A. Strondl, R. Fischer, G. Frommeyer, A. Schneider, *Mater. Sci. Eng. A* **2008**, *480*, 138.
 - [19] H. E. Helmer, C. Körner, R. F. Singer, *J. Mater. Res.* **2014**, *29*, 1987.
 - [20] A. Oradei-Basile, J. F. Radavich, *Superalloys* **1991**, *718*, 325.
 - [21] C. H. Radhakrishna, K. Prasad Rao, S. Srinivas, *J. Mater. Sci. Lett.* **1995**, *14*, 1810.

Processing AlSi10Mg by selective laser melting: parameter optimisation and material characterisation

K. Kempen^{*1}, L. Thijs², J. Van Humbeeck³ and J.-P. Kruth¹

Owing to their attractive combination of mechanical properties, high heat conductivity and low weight, the Al–Si alloys found a large number of applications in the Additive Manufacturing field for automotive, aerospace and domestic industries. However, due to their high reflectivity and heat conductivity, they are harder to process by Selective Laser Melting. This work elaborates on both the optimisation of process parameters, in order to get nearly fully dense parts, and the material properties resulting from this specific material process combination. A process parameter window is defined, in which the formed melt pool is stable and meets the set requirements. In this process window, the parameter set for optimal density is defined. It is shown that AlSi10Mg parts produced by SLM have mechanical properties higher or at least comparable to the cast material because of the very fine microstructure.

Keywords: Selective laser melting, AlSi10Mg, Mechanical properties, Keyholes, heat treatment

This paper is part of a special issue on Additive manufacturing

Introduction

Selective Laser Melting (SLM) is a laser additive manufacturing technique in which a three-dimensional product is built up in a layer-by-layer manner. Thin layers of powder are selectively scanned by a high-intensity laser. Owing to this high laser energy input, the metal powder melts and consecutively consolidates upon cooling. By subsequently repeating these steps for all layers, a three-dimensional metal part is built up. Owing to the layer-wise nature of the process, the production of complex near-net shape parts with internal cavities is enabled.¹ A schematic view of the SLM process and main components of an SLM machine are illustrated in Fig. 1.

Aluminium–silicon alloys are characterised by sound castability, good weldability and outstanding corrosion resistance. Owing to their excellent combination of low weight, high heat conductivity and good mechanical properties, these alloys find a large number of applications in aerospace and automotive industries, as well as conventional manufacturing industries.^{2,3}

The chemical composition of AlSi10Mg is shown in Table 1. Alloying magnesium to the Al–Si alloy enables the precipitation of Mg₂Si which significantly strengthens the matrix without compromising other mechanical properties. AlSi10Mg can be hardened through

precipitation by a specified T6 heat treatment.⁴ In this work, it will be shown that this T6 heat treatment is defined for cast material, and is not optimal for SLM produced parts.

Above all, the near-eutectic composition of this material, which is known to lead to a small solidification range compared to the high strength aluminum alloys like the 7000 series, makes it relatively easy to process AlSi10Mg by laser applications like SLM.^{5,6}

The combination of the material's properties, like high heat conductivity and low weight, and the advantages of the SLM process, such as the high geometrical freedom, can lead to new opportunities in applications that require complex structures and internal cavities like complex heat exchangers or lightweight structures.

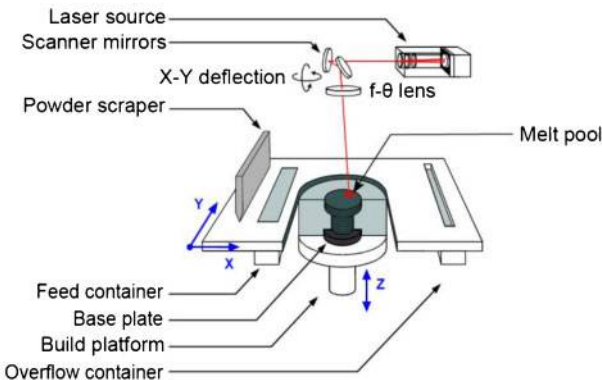
While it has been acknowledged that SLM is able to impart full density into parts, Brandl *et al.*⁷ affirmed the influential role of process parameters on the microstructure and fatigue and fracture behaviour for AlSi10Mg. The use of peak hardening and platform heating increases fatigue resistance and homogenizes the microstructure. Moreover, Louvis *et al.*⁵ concluded that the formation of an oxide layer occurs during processing of aluminum alloys, thus leading to the use of high laser power in order to break through this oxide film in order to densify the material. Olakanmi *et al.*⁸ found that the effect of alloying elements like silicon and magnesium do not affect the process window boundaries significantly, however they have a great influence on the formation of the melt pool and the evolved surface morphology. Later, Okalanmi *et al.*⁹ further explored the role of processing parameters on the densification is selective

¹University of Leuven (KU Leuven), Department of Mechanical Engineering, Celestijnenlaan 300, 3001 Leuven, Belgium

²LayerWise nv, Grauwmeier 14, 3001 Leuven, Belgium

³University of Leuven (KU Leuven), Department of Materials Engineering, Kasteelpark arenberg 44, 3001 Leuven, Belgium

*Corresponding author, email Karolien.Kempen@kuleuven.be



1 Schematic overview of SLM machine and its main components

laser sintering of Al–12Si, indicating that process parameters greatly influence the marangoni convection and spheroidisation of the melt pool. A similar investigation on the effect of process parameters on the process window and mechanical properties for the AlSi10Mg alloy however has not been investigated in depth.

Experimental methods

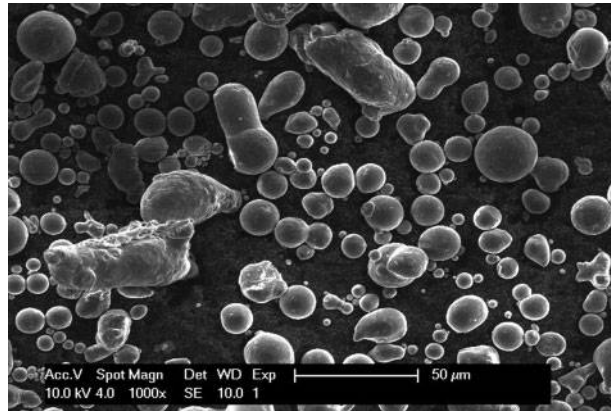
All SLM parts were produced on a modified Concept Laser M1 machine¹⁰ in a protective Argon atmosphere. The oxygen level is controlled to <1%. The machine is equipped with a 200W fibre laser that has a wavelength of 1·064 μm and a laser beam diameter of 150 μm (99%).

A wide range of scan speeds (mm s⁻¹) and laser powers (W) was examined. The layer thickness was kept constant at 30 μm and the hatch spacing was always 105 μm. Density was measured by the Archimedes method. The parts were weighed in air and in ethanol to determine the density. In this work, we depict the relative density as a percentage of the material's bulk density of 2·68 g cm⁻³.⁴

Gas atomised powder produced by LPW¹¹ was used. The size of the powder particles after sieving ranges from 15 to 45 μm in diameter (based on the sieving method). SEM image in Fig. 2 shows the nearly spherical powder particles before sieving, with some small satellite particles on the larger fraction.

Macrostructures were investigated under a Zeiss Axioscop 40 Pol polarising microscope and by a Philips XL40 scanning electron microscope.

To determine the mechanical properties, tensile, charpy and hardness tests were conducted. Flat tensile test parts with a gauge length (area where deformation and failure can occur) of 32 mm and a thickness of 5 mm, were produced with the parameters for optimal density. An Instron 4505 testing machine was used for tensile testing. All tests were performed according to ASTM E8/E8M-13. The tensile tests were performed at



2 SEM image of nearly spherical powder

a speed of 1 mm min⁻¹ and elongation was measured with an Instron 25 mm dynamic extensometer.

Micro-hardnesses were measured according to the Vickers hardness scale. The parts were measured according to the ASTM E 92-65 standard. A 0·5 kg load was used and five indentations were made in each sample. The average hardness and a confidence interval of 95% were calculated.

Results and discussion

First, single track scans were made, in order to determine a process window in which a stable melt pool is formed. By closely evaluating the single track scan, a lot of information on melt pool formation and stability can be gained, like melt pool size, shape and wetting.^{12,13} A range of laser powers and scan speeds will be determined for which the formed scan track meets the requirements. Next, the optimal parameter set for the production of almost fully dense parts will be determined within the previously defined process window. Then, the microstructure and related mechanical properties of the high density parts are taken under investigation.

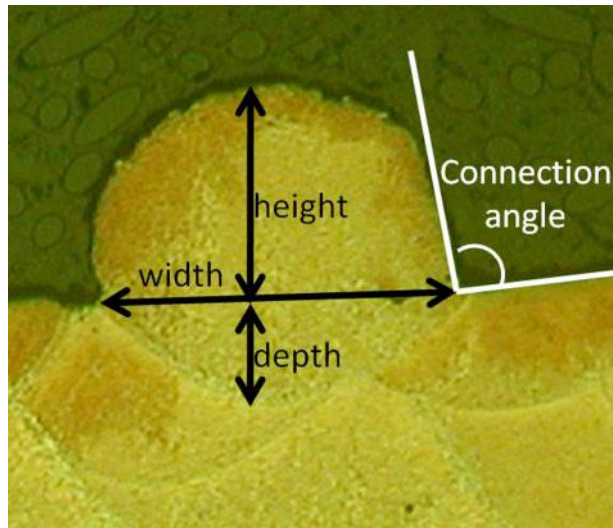
Single track scans

Single track scans clearly indicate the nature and the shape of the melt pool, depending on the scan speed and laser power. They are a fast and simple way to determine the process window in which the melt pool meets the set requirements. In this study, a laser power ranging from 170 to 200 W is used in combination with a scan speed varying between 200 and 1400 mm s⁻¹. The requirements for the melt pool that were set for a parameter combination to be submitted to the process window are:

- (i) the scan track must be uninterrupted, to avoid pores and irregularities in the part
- (ii) the scan track must slightly penetrate the previous layer, in order to get a good connection between the subsequent layers (good wetting of the layer underneath)
- (iii) the scan track must have a sufficient height (about half of the track width), in order to be able to build up three-dimensional parts
- (iv) the connection angle between scan track and previous layer should be close to 90°, to ensure good dimensional accuracy and high density. Larger connection angles will require a larger overlap between adjacent scan tracks.

Table 1 Chemical composition of AlSi10Mg, according to ISO3522

Al	Si	Cu	Mn	Mg	Zn	Fe
wt-%	Bal.	9–11	≤0·1	0·05	0·45–0·6	0·05



3 Requirements for single scan tracks: measurement protocol

The measuring protocol for these requirements is clarified in Fig. 3. As can be seen from Fig. 3, single track scans are made atop a multi-track deposit, to get a good representation of the in-process conditions. The formation of a single track scan on a cast surface is likely to be different.

Single scan tracks were evaluated both by top view (to check the continuity of the scan track) and by cross section (to measure the depth, height and connection angle). The top view images indicate that low scan speeds result in distortion and irregularities, due to the balling phenomenon, as also indicated by Kruth *et al.*¹ and Tolochko *et al.*¹⁴

As these tests only consider one scan track instead of a surface or volume, the results are analysed in function of the laser energy per unit length E' . The definition of E' is given in equation (1) with E' is laser energy per unit

length (J mm^{-1}), E is the laser energy (J), l is the length of the scan track (mm), P is the laser power (W), v is the scan speed (mm s^{-1})

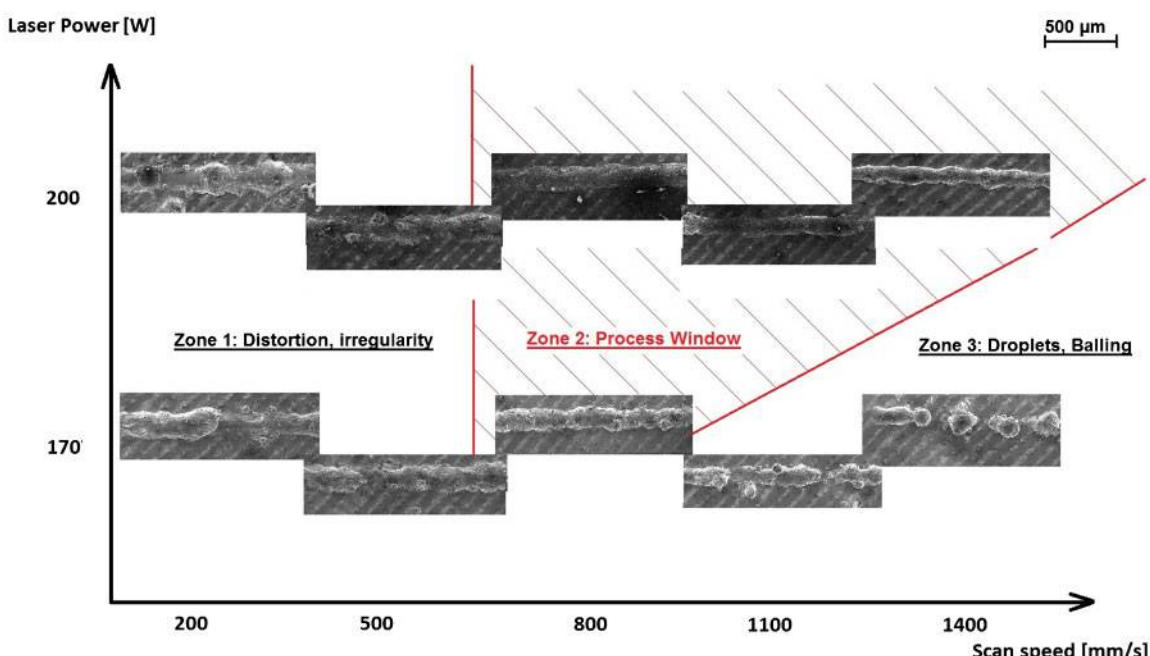
$$E' = \frac{E}{l} = \frac{P}{v}$$

When this laser energy per unit length is too high, for instance by increasing the laser power or decreasing the scan speed, the melt pool volume increases, and its viscosity decreases. The melt hydrodynamics become more important (Marangoni effect¹³) leading to irregularities and a very deep penetration into the substrate or the previously formed layers. This situation occurs in the top left scenarios in Fig. 4.

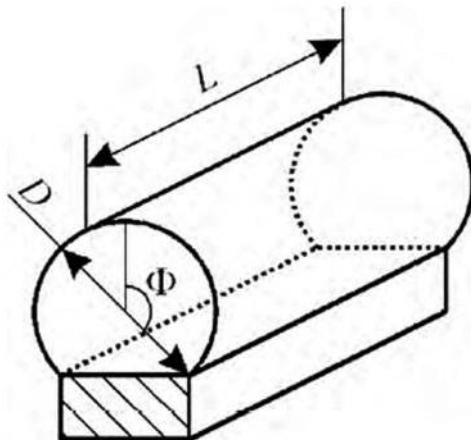
When the energy input per unit length is too low (bottom right situation in Fig. 4), the influence of the recoil pressure becomes more significant and causes the melt pool to distort. By severely increasing the scan speed, the width of the melt pool increases while its length decreases. Melt pools with a smaller circumference-to-length ratio show an unstable behaviour according to the Plateau-Rayleigh analysis of instability of a circular cylindrical liquid.¹³ Equation (2) gives the stability condition for a circular cylindrical liquid according to Plateau-Rayleigh. For a melt pool that partially penetrates the underlying layers or substrate, the liquid is only a segmental cylindrical (which has a cross section as a circular segment), and the stability condition was deducted by Yadroitsev *et al.*,¹³ and given in equation (3), with symbols as indicated in Fig. 5: D is the diameter of the track, L is the wavelength and Φ is the free contact angle

$$\frac{\pi D}{L} \geq 1$$

$$\frac{\pi D}{L} \geq 2^{1/2} \left[\frac{\Phi(1 + \cos 2\Phi) - \sin 2\Phi}{2\Phi(2 + \cos 2\Phi) - 3 \sin \Phi} \right]^{1/2}$$



4 Segmental cylinder of liquid on substrate¹³



5 Top view images of single scan tracks, produced with different process parameters

By observation of the cross sections, the other requirements for every single scan track can be checked. Figure 6 depicts these cross sections for different processing parameter sets. The bottom right zone depicts the scan tracks produced with a very low energy input per unit length. As observed, there is a very bad wetting and droplets are formed. There is insufficient connection to the previous layers.

When the energy input per unit length is too high (top left corner of Fig. 6), there is a very deep penetration into the previous layers and partial evaporation takes place. The laser melting phenomenon transitions from so called ‘conduction mode’ into ‘keyhole mode’ as similarly known and used in laser welding.¹⁵ When the laser intensity is sufficiently high, a deep penetrating vapor cavity is formed inside the melt pool. The stability of this keyhole is based on the equilibrium between the forces which open the cavity (plasma formation, material ablation) and the forces which tend to close it (gravity, surface tension). A small change in scan speed

or temperature in the melt pool can cause instability, resulting in a melt pool collapse, leaving entrapped gas, and thus small pores on the bottom of the melt pool. One of these so called ‘keyhole pores’ is seen in Fig. 6 in the cross-section for a scan track produced at 200 W and 200 mm s^{-1} .

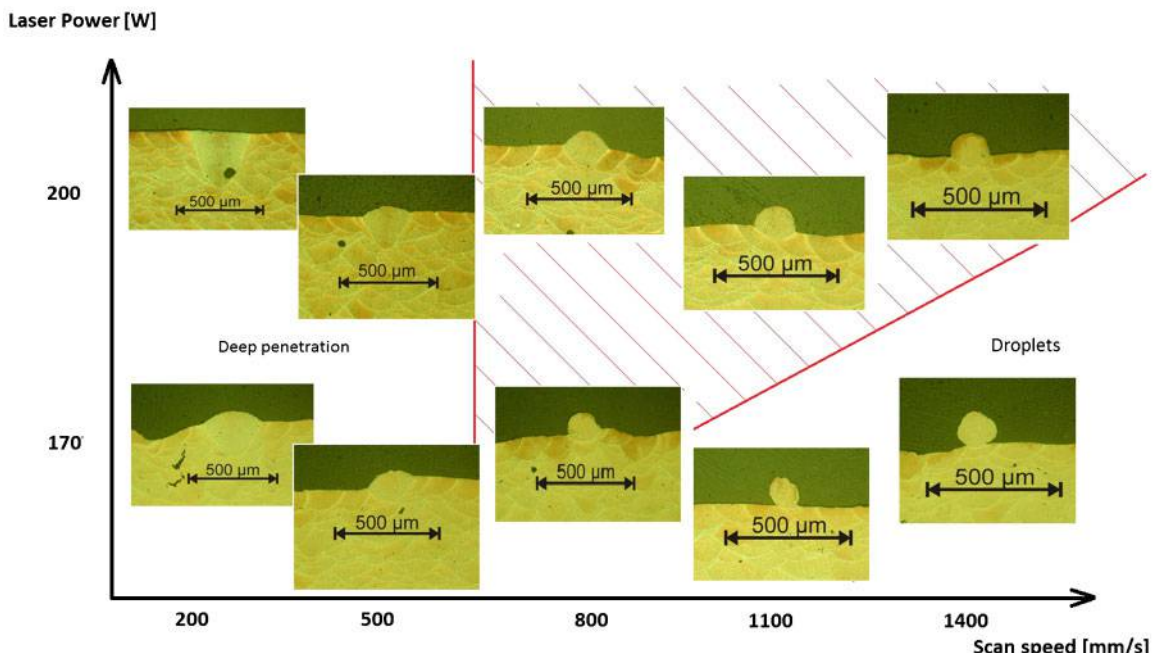
Taking all the set requirements into account, a process window is defined within this range of process parameters, marked with red lines. This zone indicates the stable processing conditions, corresponding to energy per unit length of $150\text{--}250 \text{ J m}^{-1}$.

Density optimisation

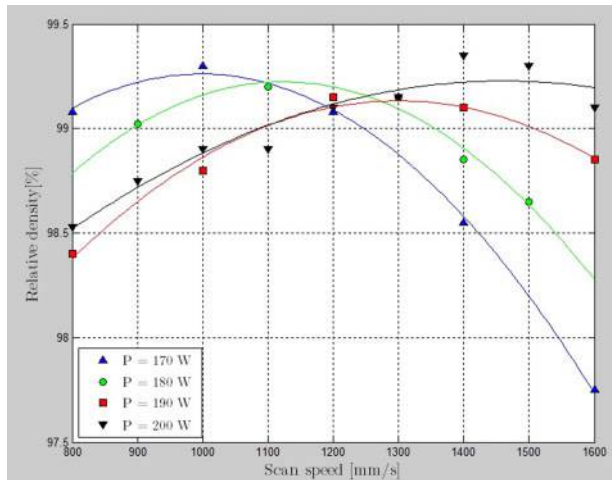
Part density is one of the most important parameters to optimise, because it has a direct influence on the part’s mechanical and physical properties. The part density depends on many process parameters, while this research focuses only on the effect of laser power P and scan speed v . Cubic parts of $10 \times 10 \times 10 \text{ mm}$ were produced with the laser power varying from 170 to 200 W in steps of 10 W, and scan speed ranging from 800 to 1600 mm s^{-1} in steps of 100 mm s^{-1} . The hatch spacing is chosen at $105 \mu\text{m}$, being 70% of the melt pool width, thus resulting in a 30% overlap between adjacent scan tracks.

The density of all parts is measured and depicted in Fig. 7.

As was expected from the observations in the single track scans, the density is low for parts produced with a very high energy density ($E' = 1000 \text{ J m}^{-1}$ when $P = 200 \text{ W}$ and $v = 200 \text{ mm s}^{-1}$) and for parts produced with a very low energy density ($E' = 106 \text{ J m}^{-1}$ when $P = 170 \text{ W}$ and $v = 1600 \text{ mm s}^{-1}$). The highest densities are reached when the energy input per unit length is optimal to produce a stable melt pool, which seems to be $140\text{--}160 \text{ J m}^{-1}$ for this aluminium alloy. As a result, and also noticeable in Fig. 7, the point of maximal density lies at low scan speed for low laser power, and at high scan speed for high laser power. Consequently, if production speed is an important factor, the optimal



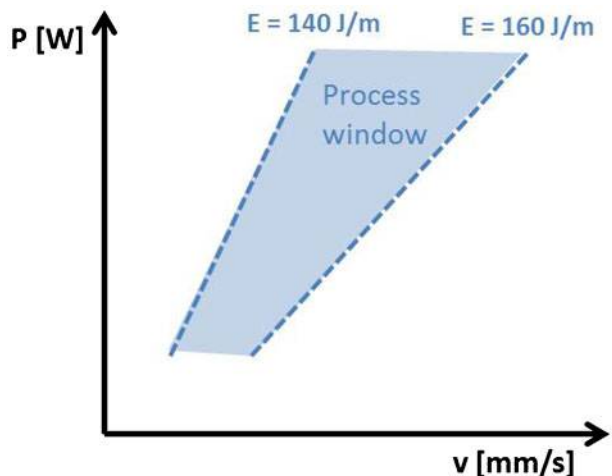
6 Cross-section images of single scan tracks, produced with different process parameters



7 Relative density of AlSi10Mg parts produced with different scan parameters

parameter set in these conditions is a laser power P of 200 W, a scan speed v of 1400 mm s $^{-1}$ and a hatch spacing h of 105 μm .

A second observation that can be made from both Figs. 6 and 7 is the broadening of the process window for higher laser power. When defining the optimal laser energy per unit length as $E_{\text{opt}}^* = P/v$, then E^* represents the slope of the $P - v$ graph. For E_{opt}^* between 140 and 160 J m $^{-1}$, the slopes of the curves indicating the border of the process window correspond to that 140 and 160 J m $^{-1}$ (Fig. 8). This results in a broader process window for a higher laser power. This observation can also be made in Fig. 7. When employing a higher laser power (for example 200 W), the zone of high density parts is wider (ranging from 1000 to ≥ 1600 mm s $^{-1}$). For lower laser power (for example 170 W), the zone of high density parts is more narrow (ranging only from 800 to 1200 mm s $^{-1}$). Note that the optimal energy per



8 Broadening of process window for high laser power

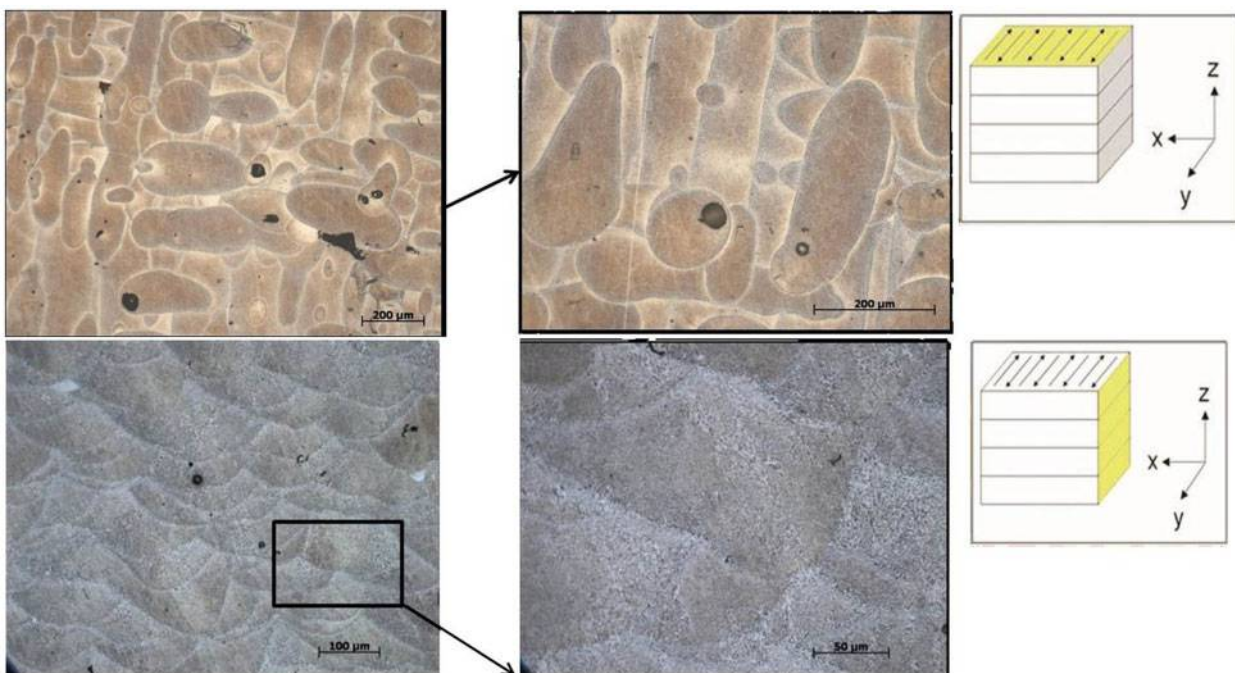
unit length is only optimised within the range of parameters that was tested: $P=170\text{--}200$ W, $v=200\text{--}1400$ mm s $^{-1}$.

Macrostructure

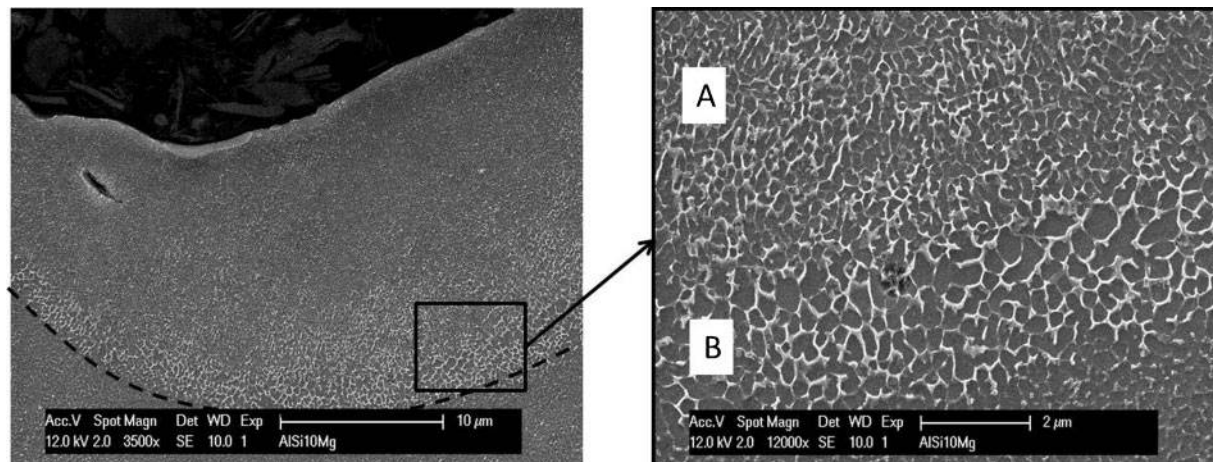
The high density parts were analysed by optical microscopy (OM). These parts were produced with a laser power of 200 W and a scan speed of 1400 mm s $^{-1}$. Optical microscopy images were taken of the top view (XY plane) and the cross-section (YZ plane). The Z direction indicates the building direction.

These microscopy images and the XYZ convention are shown in Fig. 9.

First, these OM images confirm the high density that was measured by Archimedes. The cause of the remaining porosity (0·6%) is threefold. The small spherical pores result from gas that was entrapped during melting and solidification. Entrapped gas may originate from:



9 Optical microscopy images of highest density parts, in both cross-section and top view



10 Cross-section of one melt pool: finer microstructure in centre of melt pool (**A**) coarser microstructure on melt pool boundary (**B**)

- (i) gas in the powder bed or gas inside the powder particles, resulting in very small spherical pores
- (ii) evaporation of the material/selected elements (e.g. Mg in this case of AlSi10Mg) leads to small spherical pores
- (iii) collapse of a keyhole in an unstable melt pool leaves a larger spherical pore behind.

These pores are located within the melt pool, as observed in the top view of Fig. 9. The second classification of pores is irregular in shape and is located at melt pool boundaries. These pores are formed due to unmelted powder or insufficient overlap between scan tracks. In addition to the pores, also oxides may be formed. They usually have a very irregular, flat-like shape, but were not observed in this work.

Etching with Keller's reagent reveals the melt pool boundaries. The images at higher magnification in Fig. 9 give a first indication of the coarser macrostructure at the melt pool boundaries. A more detailed SEM image is depicted in Fig. 10. Owing to the movement of the heat source, the solidification variables may vary across the melt pool. As illustrated in Fig. 10, the solidification time at the fusion line is longer than at the centerline of the melt pool. As a result, a finer microstructure is expected near the centerline of the melt pool than close to the fusion line. This translates in a finer cellular structure in the center of the melt pool ([A] in Fig. 10) and a coarser microstructure at the border of the melt pool ([B] in Fig. 10). A more in-depth research on the formed microstructure and resulting texture is reported by Thijs *et al.*¹⁶

Mechanical properties

Tensile tests were performed on both as built SLM parts (built in the XY-direction, flat onto the baseplate), and SLM parts that underwent a post-processing aging heat

Table 2 Mechanical properties of SLM as built and aged parts, compared to high pressure die cast (HPDC) parts, with and without T6 heat treatment

x±s	E/GPa	UTS/MPa	Elongation/%	HV
SLM	68±3	396±8	3.5±0.6	136±9
SLM+aging	66±5	399±7	3.3±0.4	152±5
HPDC ¹⁷	71	300–350	3–5	95–105
HPDC+T6 ¹⁷	71	330–365	3–5	130–133

treatment. The results of these tensile tests and additional micro-hardness measurements are summarised in Table 2 and compared to values for high pressure die cast parts, with and without standard T6 heat treatment. High pressure die casting is considered the casting process resulting in the best mechanical properties. All results represent the mean value for three specimens with a 95% confidence interval.

A standard heat treatment for AlSi10Mg is the T6 heat treatment, including annealing and aging, leading to the formation of Mg₂Si precipitates.¹⁸ For SLM parts however, superior mechanical properties (high hardness and strength) are reached in the as built condition, due to the very fine cellular microstructure which is inherent to the SLM process. The strength of the material directly correlates with the cell size according to the Hall-Petch equation

$$\sigma_0 = \sigma_i + \frac{k}{d^{1/2}}$$

This equation indicates that the strength of a metal is equal to the frictional stress plus a factor (*k*) times the inverse of the square root of the grain size (*d*). Reducing the grain size will cause the material to become stronger. Grain size reduction is also a means to increase the toughness of a metal. As reported by Thijs *et al.*,¹⁶ the cell size of SLM produced AlSi10Mg is below 1 μm, compared to about 10–50 μm in HPDC parts, depending on the casting parameters.¹⁹

As an annealing step would undo this fine microstructure, only an aging step of 6 h at 175°C was applied to the SLM parts, leading to an increased hardness up to 152±5 HV.

Overall, the mechanical properties like ultimate tensile strength, elongation at fracture and micro hardness in the as built condition are comparable or even exceed those of high pressure die cast parts which underwent a heat treatment.

Conclusions

1. Single track scans offer a great amount of information on the formation of a melt pool and its characteristics. A low energy input per unit length results in droplet formation and a bad wetting to the

previous layers or to the baseplate for the first layer. An energy input per unit length that is too high, causes distortions and irregularities due to big melt pool volumes and the balling effect.

2. Optimal density parameters lie within the defined process window. This process window is defined by a zone between two linear boundaries in the $P-v$ graph: $P=E^{\min} \cdot v$ and $P=E^{\max} \cdot v$. As E' represents the slope in the $P-v$ graph, the process window becomes broader for high laser powers.

3. Macrostructural analysis showed that both irregular and smaller spherical pores remain in the nearly full dense parts. The cellular microstructure was shown to be finer in the center of the melt pool and coarser at the melt pool boundary, since the thermal gradients are smaller there.

4. The mechanical properties like ultimate tensile strength, elongation at fracture and micro-hardness in the as built condition are comparable or even exceed those of high pressure die cast parts which underwent a heat treatment. Performing an aging step of 6 h at 175°C can even further increase the hardness of the SLM parts to 152 ± 5 HV.

References

- J.-P. Kruth, L. Froyen, J. V. Vaerenbergh, P. Mercelis, M. Rombouts and B. Lauwers: 'Selective laser melting of iron-based powder', *Mater. Process. Technol.*, 2004, **149**, (1), 616–622.
- T. Vilaro, S. Abed and W. Knapp: 'Direct manufacturing of technical parts using selective laser melting: example of automotive application', Proc. 12th European Forum on 'Rapid prototyping', Paris, France, March 2008, Protolabs.
- M. Wong, S. Tsopanos, C. Sutcliffe and I. Owen: 'Selective laser melting of heat transfer devices', *Rapid Prototyp. J.*, 2007, **13**, (5), 291–297.
- 'ASM handbook', Vol. 2, 'Properties and selection: nonferrous alloys and special-purpose materials', ch. 1, 3–14; 1990, Materials Park, OH, ASM International.
- E. Louvis, P. Fox and J. Sutcliffe: 'Selective laser melting of aluminium components', *J. Mater. Process. Technol.*, 2011, **211**, (1), 275–284.
- M. Voncina, P. Mrvar and J. Medved: 'Thermodynamic analysis of alsi10mg alloy', *RMZ Mater. Geoenviron.*, 2006, **52**, (3), 621–633.
- E. Brandl, U. Heckenberger, V. Holzinger and D. Buchbinder: 'Additive manufactured alsi10mg samples using selective laser melting (slm): microstructure, high cycle fatigue and fracture behaviour', *J. Mater. Des.*, 2012, **34**, 159–169.
- E. Olakanmi: 'Selective laser sintering/melting of pure al, al-mg and al-si powders: effect of processing conditions and powder properties', *J. Mater. Process. Technol.*, 2013, **213**, 1387–1405.
- E. Olakanmi, R. Cochrane and K. Dalgarno: 'Densification mechanism and microstructural evolution in selective laser sintering of al-12si powders', *J. Mater. Process. Technol.*, 2011, **211**, 113–121.
- C. L. GmbH: 'Concept laser'. On the WWW, May. <http://www.concept-laser.de>. 2014.
- L. Technology: Lpw technology ltd. On the WWW, May. <http://www.lpwtechnology.com>. 2014.
- T. Childs, C. Hauser and M. Badrossamay: 'Mapping and modelling single scan track formation in direct metal selective laser melting', *CIRP Annals – Manufactur. Technol.*, 2004, **53**, (1), 191–194.
- I. Yadroitsev, A. Gusarov, I. Yadroitseva and I. Smurov: 'Single track formation in selective laser melting of metal powders', *J. Mater. Process. Technol.*, 2010, **210**, (12), 1624–1631.
- N. Tolochko, S. Mozzharov, I. Yadroitsev, T. Laoui, L. Froyen, V. Titov and M. Ignatiev: 'Balling processes during selective laser treatment of powders', *Rapid Prototyp. J.*, 2004, **10**, (2), 78–87.
- J. Ion: 'Laser processing of engineering materials: principles, procedure and industrial application'; 2005, Oxford, Elsevier Butterworth-Heinemann.
- L. Thijs, K. Kempen, J.-P. Kruth and J. V. Humbeeck: 'Fine-structured aluminium products with controllable texture by selective laser melting of pre-alloyed alsi10mg powder', *Acta Mater.*, 2012, **61**, (5), 1809–1819.
- Flagship: 'Heat treated aluminium high pressure die castings', Technical data sheets, May 2014.
- 'ASM handbook', Vol. 1 to 4; 1991, Materials Park, OH, ASM International.
- J. G. Kaufman and E. L. Rooy: 'Aluminum alloy castings: properties, processes, and applications'; 2004, Materials Park, OH, ASM International.



Influence of process-induced microstructure and imperfections on mechanical properties of AlSi12 processed by selective laser melting

Shafaqat Siddique ^{a,b,*}, Muhammad Imran ^a, Eric Wycisk ^c, Claus Emmelmann ^{c,d}, Frank Walther ^a

^a Department of Materials Test Engineering (WPT), TU Dortmund University, Baroper Str. 303, D-44227 Dortmund, Germany

^b Higher Education Commission (HEC), H-9 Islamabad, Pakistan

^c Laser Zentrum Nord (LZN), Am Schleusengraben 14, D-21029 Hamburg, Germany

^d Institute of Laser and System Technologies (iLAS), Hamburg University of Technology (TUHH), Denickestr. 17, D-21073 Hamburg, Germany



ARTICLE INFO

Article history:

Received 19 August 2014

Received in revised form 30 January 2015

Accepted 12 February 2015

Available online 21 February 2015

Keywords:

Selective laser melting

AlSi12

Porosity

Microstructure

Tensile properties

Fatigue performance

ABSTRACT

Selective laser melting (SLM) offers high potential for manufacturing complex geometries and custom-made parts due to its unique layer-wise production process. A series of samples of AlSi12 have been manufactured by SLM process to study the effect of process parameters and post-build heat treatment on the microstructure and the corresponding mechanical properties. Optical microscope, scanning electron microscope, quasistatic tests, continuous load increase fatigue tests and constant amplitude fatigue tests have been employed for characterization. A remarkable eutectic microstructure, with dendritic width changing with SLM process parameters, has been observed. Relationship between SLM process parameters, resulting microstructure and the consequent changes in mechanical properties has been discussed. Base plate heating has been found critical in controlling the in-process microstructure. Mechanical properties of SLM parts outperform those of conventionally manufactured alloy, and can be varied as per requirement, by altering the build rate, keeping the process costs in control. Fatigue scatter can also be controlled by heating the base plate during the process.

© 2015 Elsevier B.V. All rights reserved.

1. Introduction

Additive manufacturing processes allow free-form manufacturing which enables time and cost savings for complex and customized parts and yields shortened product development cycles. The functional integrity of the product can thus be assured and improved at an early design stage. SLM offers a high potential for manufacturing complex geometries which, otherwise, are time- and cost-extensive or even impossible to produce. Owing to improvements in powder quality and laser technology as well as machine systems, SLM goes a step ahead- from rapid prototyping to rapid manufacturing. Employment of the SLM parts as functional units must, however, be carefully and critically investigated to ensure the performance reliability. For that purpose, mechanical properties should be correlated to the processing route

in such a way that an optimized set of parameters is achieved for manufacturing functional components. SLM process is based on a powder-bed approach where a layer of powder, 30–80 µm thick, is applied onto a building platform and fused selectively with energy input of the laser beam. Component geometry is provided to the SLM system in the form of a computer aided design (CAD) model which has to be ‘sliced’ horizontally into 2D part contours. The slicing is realized such that the slice thickness corresponds to the layer thickness of the powder material. A scanner scans a specific cross-section of the sliced model, and the powder material corresponding to the scanned cross-section is melted by thermal energy of the laser beam. After scanning and melting one layer, the building platform is moved equivalent to one layer thickness down and the process is repeated for the next layer until the entire component is manufactured (Emmelmann et al., 2012). AlSi12 is an important alloy to be processed by SLM process due to small difference in its melting and solidification temperatures (Bartkowiak et al., 2011).

The processing of several alloys like steel, titanium, aluminum and nickel-based super alloys have been studied with regards to developing process window as well as determination of mechanical properties. Grade 5 titanium alloy, due to its widespread applications, is the most investigated alloy among SLM-manufactured

* Corresponding author at: TU Dortmund University, Materials Test Engineering, Baroper Str. 303, 44227 Dortmund, NRW, Germany. Tel.: +49 231 755 8165; fax: +49 231 755 8029.

E-mail addresses: shafaqat.siddique@tu-dortmund.de, shafaqat400@yahoo.com (S. Siddique).

materials. Thijs et al. (2010) have studied the evolution of microstructure during selective laser melting of Ti-6Al-4V using different scan speeds. They have found that grains are formed in the orientation of the build direction; however, their alignment with the build direction experiences a diversion at higher scan speeds. High scan speeds also resulted in fine martensite due to high cooling rates. Yadroitsev et al. (2014) have investigated the influence of heat treatment on microstructure of Ti-6Al-4V for medical applications. They have reported that anisotropic behavior of microstructure was not changed after post-heat treatment until β -transus temperature. Heat treatment above this temperature would make re-nucleation of the phases. The process is capable of producing required microstructure within a narrow range of few hundreds of microns, as well as controlling the process parts resulting in multi-microstructural parts consisting of α , β , $\alpha+\beta$ and α' as referred by Murr et al. (2009). Wycisk et al. (2013) have studied the high cycle fatigue (HCF) behavior and (Leuders et al., 2013) have studied the fatigue and crack growth behavior of Ti-6Al-4V. They have reported that HCF and fatigue crack growth values of SLM manufactured parts are comparable to those of conventional alloys; however, micro-level porosity causes a high scatter in the fatigue performance. Song et al. (2014) have studied the fabrication of NiCr alloy parts with different scan speeds. They report an increase in yield strength and ultimate tensile strength with increase of scan speed which is due to growth of columnar grains axially, favoring fine grains. Vilaro et al. (2012) have investigated the microstructural modifications for Nimonic 263 super alloy. They report an out-of-equilibrium microstructure with the presence of γ -dendrites and residual stresses. Post-process heat treatment had relieved these stresses, and the dendritic structure is demolished with solution heat treatment due to diffusion. However, for applications, where such post-process treatments which change the microstructure are required, the SLM process still has the competitive advantage of achieving geometrical intricacy. The processing of Al-Si alloys by SLM and the corresponding quasistatic mechanical properties have also been studied by some scientists. Dinda et al. (2012) have carried out a detailed investigation of the development of microstructure in direct metal deposition (DMD) of Al4047 alloy and reported that microstructural morphology can be differentiated at different locations of the substrate. They have extended their study (Dinda et al., 2013) and have correlated the microstructural changes to the local cooling rate in the process. However, the processing parameters need to be correlated to the resulting mechanical properties. Buchbinder et al. (Hirsch, (2008)) have investigated the effect of post-process heat treatment and SLM build direction on the quasistatic and cyclic deformation behavior of AlSi10Mg samples. They found that the post-process heat treatment has the most significant and the build direction has the least effect on the mechanical properties. Effect of build direction on the fatigue performance of Ti-6Al-4V was also investigated by Wycisk et al., and no significant difference was found in the fatigue performance at a build direction of 45° and 90° to the base plate. Manfredi et al. (2013) have characterized AlSiMg alloy processed by direct metal laser sintering (DMLS) process. They have studied the effect of size and morphology of starting powder material on the microstructure and mechanical properties of parts built at different orientations parallel and perpendicular to the plane of powder deposition. They have found a difference in mechanical properties at the two orientations with the parts built in xy-direction having higher mechanical performance than those built along z-direction. Kempen et al. (2011) have investigated the effect of laser power, scan speed and different powder size and distribution on roughness of the manufactured part. They have studied the microstructure under optical microscope with a focus on process-induced defects. Buchbinder et al. (2011) have investigated the processing of aluminum parts using high laser power until 1 kW. They have reported

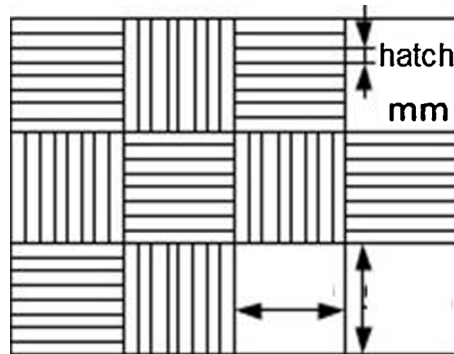


Fig. 1. Chessboard scanning strategy used for manufacturing the samples.

more fine grains due to higher cooling rate at 1 kW as compared to 400 W. A recent study by Buchbinder et al. (2014) has investigated the effect of base plate heating for AlSi10Mg processed by high power laser. They have reported grain coarsening with a pre-heating of the substrate plate at 220 °C. These studies give an overview of the work already carried out in the framework of microstructural modifications and process-induced defects for the investigated alloys. This study aims at determining the process-structure-property relationships for AlSi12 alloy and extends the investigations for fatigue problems, as many of the applications of SLM processed alloys in aerospace and automotive industry require cyclic loading. Specific issues investigated include the effect of base plate heating on the remnant defects and the changes in dendritic structure, and their corresponding effect on tensile and fatigue performance. The influence of processing parameters on fatigue scatter is also investigated. For that purpose, investigations are carried out for a single build direction based on the study of (Wycisk et al.) regarding its effect on cyclic properties. The marginal change in mechanical properties due to process-caused residual stresses is also addressed. At the same time, one of the issues is to decrease the process costs such that the process could find applications where effect of porosity is of secondary importance. For this purpose, the marginal change in mechanical properties as a function of imparted energy density is investigated.

Aluminum and aluminum alloys have a large number of applications especially in automotive and aerospace industry. Aluminum-silicon alloy has extensive applications as heat exchangers and is the most important filler alloy (Wong et al., 2007). AlSi12 consists of 11–13 wt.% Si which makes it a eutectic system. This study investigates the effect of SLM process parameters on the mechanical properties of AlSi12 alloy. Specimens were manufactured at different levels of energy density. Stress-relieving heat treatment was carried out to half of the samples to investigate its level of influence as compared to the effects of base plate heating. Base plate heating was carried out to investigate its effect on microstructure and subsequently on mechanical performance. Quasistatic mechanical properties have been correlated to process parameters. Cyclic tests have been carried out and the influence of defects, caused by the processing route, has been investigated.

2. Experimental methodology

The SLM system *SLM 250 HL* (*SLM Solutions*) was used to manufacture all specimens analyzed in this study. The machine system is equipped with a 400 W fiber laser and has a build chamber of 250 × 250 × 280 mm. Argon is used as inert gas in the build chamber. For manufacturing, a chessboard scanning strategy (Fig. 1) with an edge length of 7.47 mm for each quadratic chess field was chosen. The single fields are filled with hatches alternating by 90° in orientation between white to black fields. From layer

Table 1
Full-factorial test plan for quasistatic tests.

Batch	Factors			
		Energy density [J/mm ³]	Base plate heating	Post-build stress relief
A	Low (20)	Low (0 °C)	Low (as-built)	
B	Low (20)	Low (0 °C)	High (240 °C)	
C	Low (20)	High (200 °C)	Low (as-built)	
D	Low (20)	High (200 °C)	High (240 °C)	
E	High (39.6)	Low (0 °C)	Low (as-built)	
F	High (39.6)	Low (0 °C)	High (240 °C)	
G	High (39.6)	High (200 °C)	Low (as-built)	
H	High (39.6)	High (200 °C)	High (240 °C)	

to layer, the orientation of fields is incrementally rotated by 79°. The whole volume of the part was scanned with the same strategy and parameter set. The melting state of the powder depends upon the energy density which is a function of the scanning parameters. The build rate R (mm³/s) and the energy density E (J/mm³) are given as: $R = v \times d \times t$; $E = \frac{P}{v \times d \times t}$ where P =laser power (W), v =scan speed (mm/s), d =hatch distance (mm), t =layer thickness (mm).

Further details of the process set up can be found in (Siddique et al., 2015) A full factorial test plan (Table 1) was set-up to investigate the marginal effects of energy density, base plate heating and post-process stress-relieving heat treatment. The tests were conducted with a replication of 300%. The parameters were varied to result in two build rates and energy densities such that the resulting mechanical properties can be compared to the process economy. Parts were intentionally built at low energy density to explore the possibility of reducing process costs for non-critical components. The chosen parameter set for high process speeds with low energy input results in a build rate increase by factor 1.7. To show the potential of increased process speeds on manufacturing costs, an SLM demonstrator is used for calculation with the build rates chosen in this study. The demonstrator represents a light-weight rod designed in lattice structures with outer dimensions of 34 × 25 × 200 mm³ and a total part volume of 47 cm³. Twenty-five single parts are calculated in one manufacturing batch with Fig. 2a showing the manufacturing time taken and Fig. 2b the breakdown of the manufacturing costs for a single part. The calculations performed at Laser Zentrum Nord (LZN) show that an increase in build rate by factor 1.7 results in a decrease in manufacturing time of 33% leading to an overall manufacturing cost reduction of 27%. The calculations are based on SLM production equipment available at LZN and industrially competitive machine-hour rates. Parts were built with low (0 °C) and high (200 °C) heating of the base plate. A post-process stress-relieving heat treatment was performed, before the specimens were machined to final geometry, at 240 °C followed by oven cooling. All the specimens were manufactured at a build direction perpendicular to the base plate.

Powder material of the AISI12 material was supplied by SLM Solutions. The range of particle size of the powder material was 20–63 µm with an average diameter of 33 µm. Cuboidal specimens of size 10 × 10 × 15 mm were manufactured for microstructural and surface observations. The specimens for microstructural and surface observations were ground and then polished until grit of 0.5 µm using oxide polishing suspension. Porosity was measured in terms of pore area. The pore area was measured by image correlation software DHS. Twelve images at different sections were captured by an Olympus microscope and analysed with DHS software to give an average value of porosity. Specimen preparation for microscopic analysis was carried out using cold embedding. Specimens for microstructural analysis were prepared using Barker's reagent and latter with HNO₃ and NaOH for analysis in the scanning electron microscope (SEM).

Table 2
Residual stresses for the batches E–H.

Batch designation	E	F	G	H
Residual stress (MPa)	36 ± 4	13 ± 2	8 ± 2	4 ± 2

Cylindrical specimens were manufactured by the SLM process for tensile and fatigue testing and was machined afterwards to the final geometry (Inset of Fig. 6). Turning was carried out to achieve the average roughness R_a of 2.5 µm. Surface roughness was measured on two sets of specimens. First, for the as-built specimens without any machining; and second, on the machined specimens to be used for quasistatic and cyclic mechanical tests. For the specimens of the mechanical tests, it was measured at the gage length of the test samples. The measurements were carried out by a tactile measuring device MarSurf M 300 C (Mahr). Measurement of residual stresses was carried out at the surface in the gage length of the machined specimens, such that it can be related to the mechanical properties determined by using similar specimens. Residual stresses were measured applying $\sin^2\psi$ diffraction method using Cu K_{α} -beam with $2\Theta = 137.47^\circ$. Intermediate Lorentz function was used as the fitting technique. These measurements were carried out for batches E–H as shown in Table 2. There are tensile residual stresses in the specimen built without base plate heating and without post-process stress relief (batch E) which were relieved sufficiently after stress relieving heat treatment (batch F). However, the effect of base plate heating (batch G) in terms of residual stresses is more significant as compared to post-process stress relief. Quasistatic tensile tests were carried out on an Instron 3369 system with a load cell of 50 kN at a strain rate of 1.67×10^{-3} s⁻¹. Tests were carried out according to ISO 6892-1:2009. An extensometer with a gage length of 15 mm was used for calculation of strain values during tensile tests. Microstructures as well as fractured specimens were observed under scanning electron microscope Tescan Mira XMU (EOS).

Fatigue behavior was characterized making use of load increase tests combined with constant amplitude tests explained in Walther and Eifler (2007) and the technique has been successfully applied to many classes of materials in Walther (2014). Inset of Fig. 9 shows the testing methodology developed for such short-time investigations for exploratory research. A continuous load increase test (LIT) is carried out with starting amplitude at which the material is expected to be damage-free, 30 MPa in this case. Stress amplitude is increased slowly, at a rate of 10 MPa/ 10^4 cycles for instance, until failure. The response parameter is measured to record the current state of fatigue damage. The stress amplitude at which the material response starts to change considerably is termed as the first material reaction. This point refers to a permanent change in the material condition. After that, crack propagation occurs according to material-specific damage model until failure. Continuous load increase tests were performed on an Instron 8872 servohydraulic test system with a load cell of 10 kN. An extensometer with a gage length of 10 mm was used for measuring the plastic strain amplitude $\epsilon_{a,p}$ during the fatigue tests. This methodology makes possible to determine the fatigue-critical load range for further testing at constant amplitude loading.

3. Results and discussions

3.1. Surface morphology and density

Surface roughness measurements of the as-built samples resulted in average roughness (R_a) of 7.98 ± 1.50 µm and maximum roughness (R_z) of 53.98 ± 10.07 µm. For the machined test samples, the corresponding values of 2.73 ± 0.30 and 19.73 ± 5.56 were

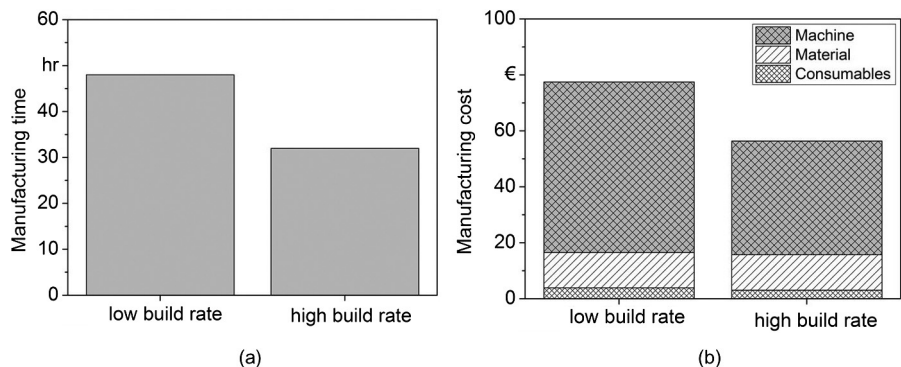


Fig. 2. Comparison of low build rate and high build rate samples for a demonstrator in terms of manufacturing time (a); and manufacturing cost (b).

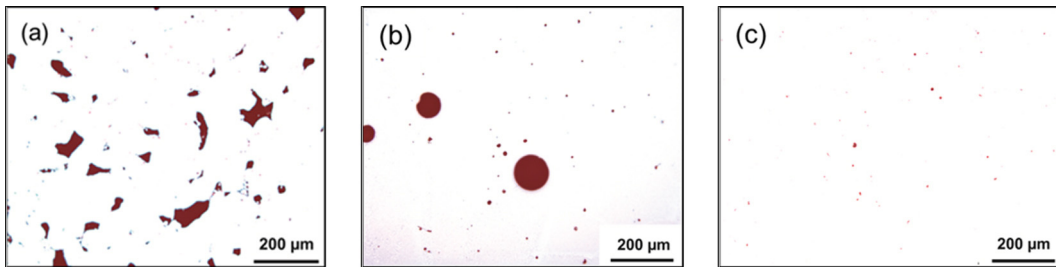


Fig. 3. Polished micro-sections for the selected batches: (a) batch A; (b) batch F; (c) batch G.

measured in the gage length. Exemplary polished micro-section of batch A with low energy density is shown Fig. 3(a), that of batch F with high energy density without base plate heating in Fig. 3(b) and (c) is for the batch H with base plate heating. Average relative density of batches manufactured at low energy density (batches A–D) was found to be 92.20% determined by pore area in polished section. For the batches manufactured at high energy density (E–H), relative density higher than 99% is achieved. Bonding defects are evident in low energy density samples; whereas only gas porosity is visible in batches manufactured with high energy density. A difference in the pore fraction of batches without base plate heating (E and F) and with base plate heating (G and H) was found out: the relative density turns out to be 99.51% and 99.67%, respectively. Though the difference is very small, however, together with elimination of relatively large size gas pores due to the use of base plate heating, it was found critical for fatigue performance. Irregular morphology for low energy density samples (Fig. 3a) is due to bonding deficiency. Pore morphology remains circular for high density samples in both configurations i.e., without and with base plate heating (Fig. 3b and c).

3.2. Microstructure

Fig. 4 shows the detailed microstructural analysis of the samples. Fig. 4(a) portrays an overview of the bead and layer structure in a low energy density sample (batch A) taken with an optical microscope. Bonding defects and gas porosity are evident in this sample. Fig. 4(b–d) are SEM images of a high energy density sample (batch H) in increasing magnification. Parabolic cross-sections correspond to the boundaries of welding beads, and only gas porosity is visible as in Fig. 4(b). It is evident from Fig. 4(c) that the microstructure represents a eutectic transformation. Dark background represents α -Al, and columnar dendrites grow along the scanning direction which is further resolved in Fig. 4(d) where eutectic formation occurs between bright Si dendrites. Similar microstructures for fast cooling processes have been obtained in the studies of Dinda et al. (2013) for Al 4047 processed by direct metal deposition, Nikanorov

et al. (2005) for Al–Si alloy processed by fast cooling of a levitated melt and (Song et al., 2014) for NiCr alloys in selective laser melting.

Investigations were carried out to explore the possible effects of base plate heating and post-process stress-relieving heat treatment on the microstructural features. Fig. 5 portrays the typical microstructure of batches F and H; and the microstructural parameters, averaged over six micrographs, are summarized in Table 3. It was observed that the width of dendrites increased by base plate heating. Formation of small Si particles is also observed by base plate heating. Change in dendritic width can be attributed to the change in cooling rate caused by base plate heating at 200 °C.

3.3. Mechanical properties and fractography

3.3.1. Quasistatic properties

Results of the quasistatic tensile behavior of SLM-generated samples are shown in Fig. 6 as characteristic stress-strain curves, and the complete results along with standard deviation are summarized in Table 4 for the complete test plan. Samples with low energy density (batches A–D) have an ultimate tensile strength (σ_{UTS}) about 45% lower than that of batches with high energy density (batches E–H); whereas the corresponding yield strength is about 20% lower. A slight decrease in ultimate tensile strength and yield strength observed, e.g., for batches F and H as compared to batches E and G, respectively, is due to the stress-relieving heat treatment after the SLM process. Though samples with high energy density (batches E–H) have excellent tensile strength σ_{UTS} and yield strength $\sigma_y, 0.2\%$ —almost four times that of sand-cast and double that of die-cast Al–Si alloy (, 152–177), the quasistatic

Table 3
Microstructural parameters of batches F and H.

Batch	Base plate heating (°C)	Post-process stress relief(°C)	Dendritic width [μm]
F	0	240	0.35
H	200	240	0.56

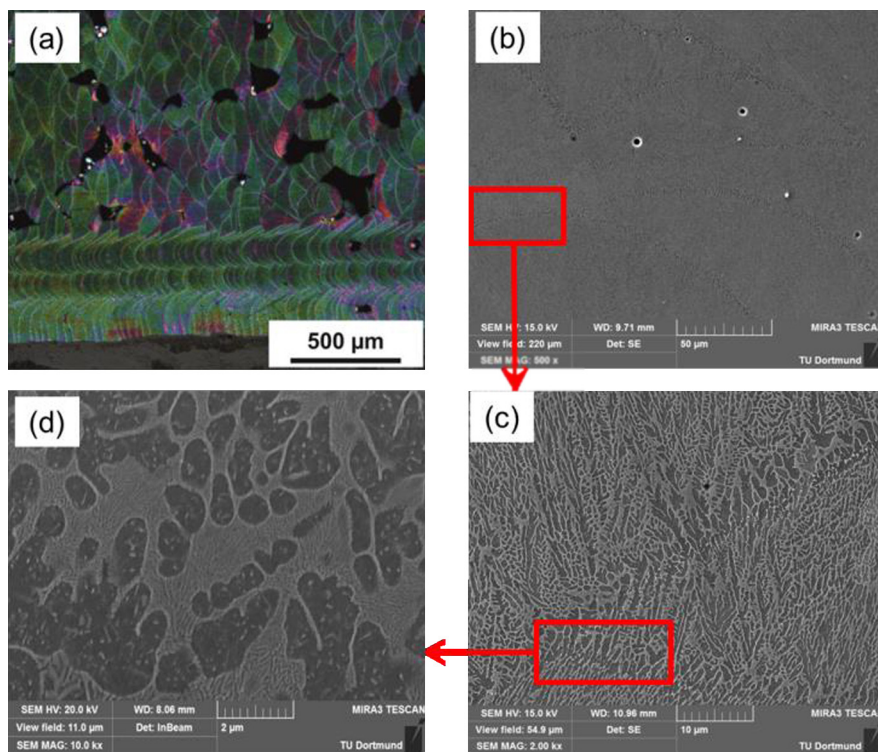


Fig. 4. Microstructural evolution: optical microscopic view of low energy density sample ((a) batch A); SEM micrographs of high energy density (batch H) in increasing magnification (b–d); (build direction transverse to the plane).

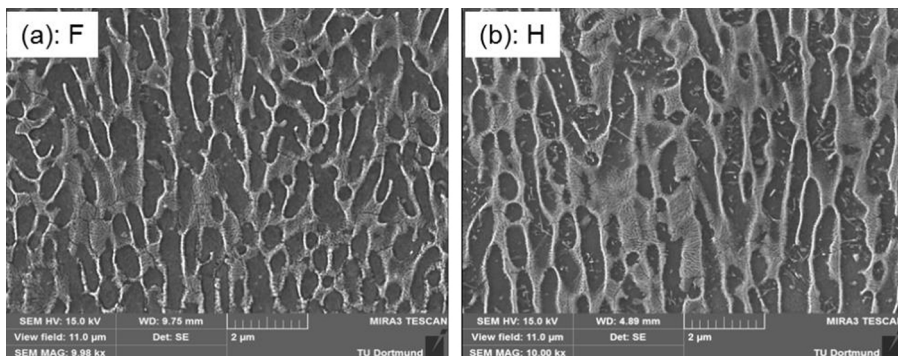


Fig. 5. Dendritic features without base plate heating (a); and with base plate heating (b); (build direction transverse to the plane).

performance of samples with low energy density (batches A–D) is still sufficient as compared to that of die-cast alloy. It shows the possibility to manufacture selective porous structures for lightweight design, possessing desired and sufficient properties, by increasing

process speed and, therefore, lowering production costs. The relatively small difference in yield strength (ca. 20%) is remarkable compared to the difference in energy density which is about 50%.

Table 4
Quasistatic properties of batches A to H.

Batch	Factors	Quasistatic properties				
		Energy density [J/mm ³]	Base plate heating [°C]	Post-build stress relief	σ_{UTS} [MPa]	$\sigma_{y, 0.2\%}$ [MPa]
A	Low (20)	Low (0)	Low (as-built)	231.2 ± 5.2	183.9 ± 9.0	1.18 ± 0.09
B	Low (20)	Low (0)	High (240 °C)	219.5 ± 6.1	180.3 ± 6.5	1.05 ± 0.05
C	Low (20)	High (200)	Low (as-built)	190.1 ± 3.4	153.7 ± 4.7	0.98 ± 0.12
D	Low (20)	High (200)	High (240 °C)	230.4 ± 3.7	186.5 ± 3.4	1.12 ± 0.10
E	High (39.6)	Low (0)	Low (as-built)	418.9 ± 9.6	220.5 ± 9.4	3.91 ± 0.27
F	High (39.6)	Low (0)	High (240 °C)	372.3 ± 7.2	218.0 ± 6.9	3.41 ± 0.29
G	High (39.6)	High (200)	Low (as-built)	369.3 ± 3.4	202.2 ± 4.3	4.38 ± 0.16
H	High (39.6)	High (200)	High (240 °C)	361.1 ± 4.5	201.5 ± 3.7	4.05 ± 0.15
Sand-cast Al 443 (, 152–177)				130	55	8
Die-cast Al 443 (, 152–177)				230	110	9

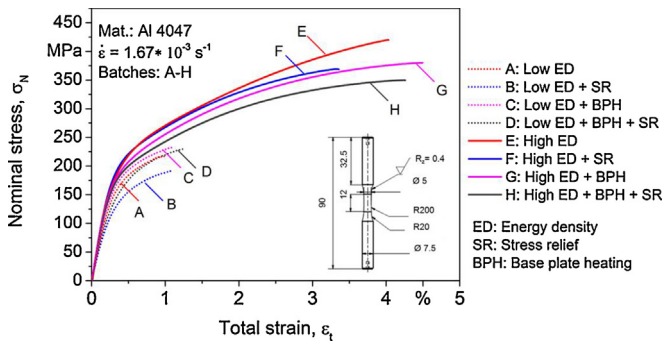


Fig. 6. Representative stress–strain curves for quasistatic tensile tests of batches A to H; specimen geometry in the inset.

The decrease in strength and fracture strain with reduced energy density can be explained by fractographic analysis of the tensile test samples. Representative fractographs for batch A and batch E are shown in Fig. 7. Porous area in terms of un-melted powder particles are visible in (a). The fracture in batch A can be characterized by crack initiation from macro-pores followed by a rapid propagation phase. Although there are some dimples representing a ductile failure, the space between macro-pores was not sufficient enough to allow for a reasonable amount of plastic deformation. So low energy density samples resulted in small fracture strain with an accompanied decrease in strength. Fracture surface of batch E shows spherical dimples from micro-pores which initiated crack formation and propagated with plastic deformation until failure, resulting in an increased fracture strain, and so a high strength.

A relevant observation is the effect of base plate heating (BPH). Batch G and H, with base plate heating, show slightly reduced strength and a proportional increase in fracture strain $\varepsilon_{t,\max}$ as compared to batches E and F. This is due to the Hall–Petch effect manifested due to decrease in cooling rate by base plate heating. Reduced cooling rate favors increased dendritic width (Fig. 5), which is responsible for altered mechanical properties. Fig. 8 shows the main effects of the investigated parameters as marginal means. As expected, energy density has the highest effect on quasistatic properties. But the point of interest is the relatively small difference of effect size on yield strength as compared to a relatively large difference in economic input in terms of energy density. It opens up the possibility of manufacturing graded structures with different levels of input power to a component by differentiating between critical and non-critical features of a component. Different focus diameters of the laser beam can then be employed for different regions of the same component. Manufacturing of graded structures has recently been reported by some researchers. Niendorf et al. (2013) have used different laser power systems to achieve different texture in 316L steel. They have used 1 kW laser for manufacturing coarse-grained material; whereas using 400 W laser

system for fine-grained material. In an extended article (Niendorf et al., 2014), they have reported their findings related to local properties which can fulfill local functionalities. They have found out that local mechanical properties were graduated in different stacks of textures in terms of hardness. However, the comprehensive results of their investigations are yet to be reported. Murr et al. (2012) have also shown the feasibility of graded microstructure in Ti–6Al–4V alloy. To achieve such graduated properties, many modifications in the manufacturing setup, software systems as well as design approach will be required. Improvements in powder delivery system for nozzle-based systems would be required to manufacture parts with multi-materials. Oxman et al. (2014) have reported initial results of their work-in-progress related to robotic control for 3-D swarm printing at architectural scales. The work in this field is at the rudimentary level and needs to be proven in terms of manufacturability as well as economic feasibility. This strategy can be helpful for application of the process for large volumes.

Base plate heating reduces the tensile strength and yield strength with a corresponding increase in fracture strain. The effect is statistically significant (p -value = 0.006) as found out by carrying out multivariate analysis of variance (MANOVA). However, the effect of post-process stress-relieving heat treatment shows no statistical significance on any of the quasistatic mechanical properties. This is due to the fact that the effect of stress-relief has been diminished when carried out on the specimens manufactured with base plate heating.

3.3.2. Cyclic properties

Cyclic properties were determined only for high energy density samples keeping in view the established effect of porous structures on fatigue behavior and life. Load increase tests were carried out for batches E–H to determine the course of material deformation and damage during a fatigue test so that a suitable stress could be selected for the proceeding constant amplitude tests. The results can be seen in Fig. 9 which shows that the material response can be divided into three stages. No considerable change occurs until 80 MPa followed by development of micro-cracks until 110 MPa. These micro-cracks result in a technical macro-crack after 110 MPa and propagate uniformly until fracture. From these results, stress amplitude of 120 MPa was selected for further constant amplitude tests.

Fig. 10 shows the results of four constant amplitude tests for each of the investigated batches in the form of average values (μ) and standard deviation (σ). Though batch E, without base plate heating and without post-process stress-relief, has the best fatigue performance, but it is accompanied by a very high fatigue scatter. Post-process stress-relief (batch F) has decreased the fatigue life and also decreased the scatter. Batches G and H, with base plate heating have a decreased fatigue life, due to coarse microstructure caused by reduced cooling rates. It also results in a sufficiently reduced fatigue scatter. The effect of stress relief on the fatigue

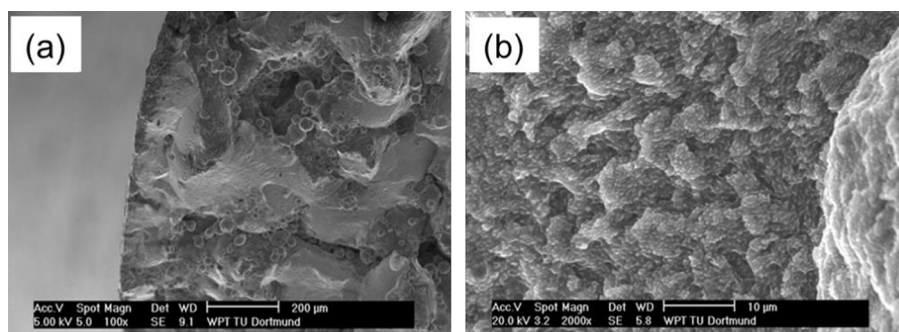


Fig. 7. Fracture surface of batch A built with low energy density (a); and batch E with high energy density (b).

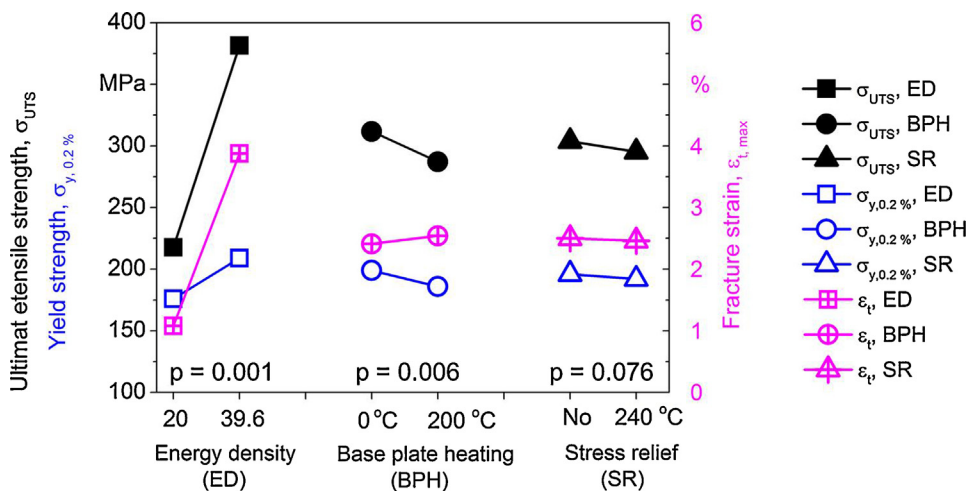


Fig. 8. Marginal means of the quasistatic parameters for SLM process parameters.

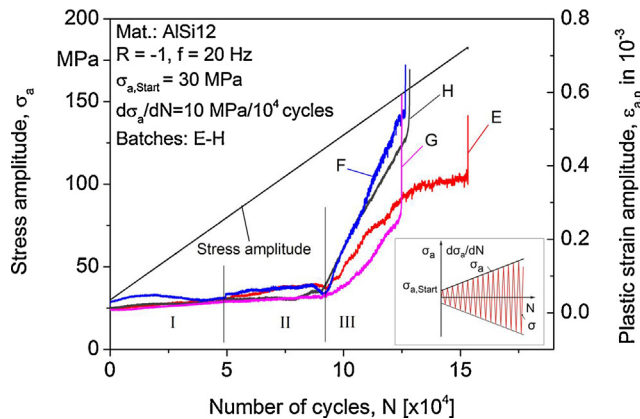


Fig. 9. Continuous load increase tests for batches E–H; schematic of the test strategy in the inset.

performance for the samples without base plate heating (batch F as compared to batch E) is pronounced; whereas the effect of stress relief (batch H as compared to batch G) does not remain significant after base plate heating. The effect can be explained by the presence of some residual stresses. The effect decreases for base plate heating, because after base plate heating, stress relief has negligible effect. The results of constant amplitude tests, in this regard, seem consistent with the results of tensile tests, where the effect of stress

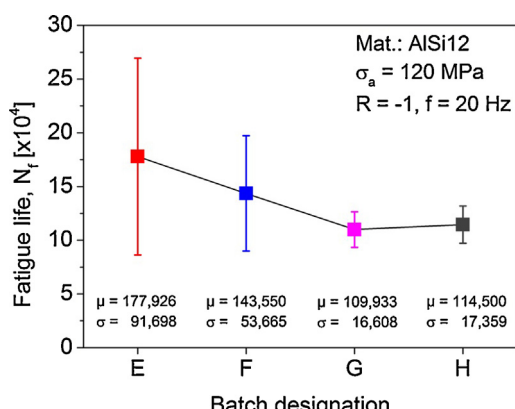


Fig. 10. Fatigue life and scatter determined in constant amplitude tests for batches E–H (statistics from four constant amplitude tests for each batch).

relief was diminished after base plate heating as compared to the effect without base plate heating. Effect of base plate heating has been observed in the results of porosity as well as microstructural observations. Due to high cooling rates in the SLM process, internal stresses are caused within the component due to high thermal gradients. These internal stresses also cause stress-induced cracks. The stress-induced cracks have increased the scatter in fatigue life due to internal crack initiation in the samples without base plate heating. Heating the base plate reduces the cooling rate, and relatively small thermal gradients result in decreased internal stresses and, therefore, the possibility of stress-induced cracking. The fatigue scatter was significantly reduced due to reduction of large size pores and stress-induced cracks in the samples with base plate heating.

To investigate these differences on the basis of process-induced changes, discussed in Section 3.1, fractured specimens with large scatter were studied under scanning electron microscope (SEM). In the batches E and F, difference in the pore size where crack initiation occurred was found to be the cause of scatter. In the specimens where crack initiation occurred from the surface, the specimens endured longer life; whereas the specimens in which crack initiation occurred from some sub-surface defects resulted in smaller lives which resulted in a higher fatigue scatter. The sub-surface crack initiation is exemplified in Fig. 11 for the specimens from batches E and F. There was a large section of material defect due to insufficient melting in one of the specimens from batch E. Similarly, sub-surface as well as multi crack initiation was observed in one of the specimens of batch F due to internal defects which caused an early failure. Such anomalies were not found in batches G and H, samples with base plate heating, resulting in sufficiently reduced fatigue scatter. All the failures in batches G and H were initiated from surface or near-surface, and without any material defects. This behavior is well-explained by the absence of any considerable material defects in the polished micrograph of the corresponding batch (Fig. 3c). Based on the fractographic investigations, the following observations can be made. Even in the high energy density samples, there are still some defects caused by insufficient melting. Sub-surface crack initiation depends on the size of the defect as well as on the location of the defect from the specimen surface. Within about 250 μm from the specimen surface, defects of more than 50 μm have been found critical which caused early crack initiation resulting in reduced fatigue lives. Some defects of size larger than 50 μm in the core of the specimen were observed without causing early crack initiation. The phenomenon can be explained by development of stress concentration on the near-surface pores

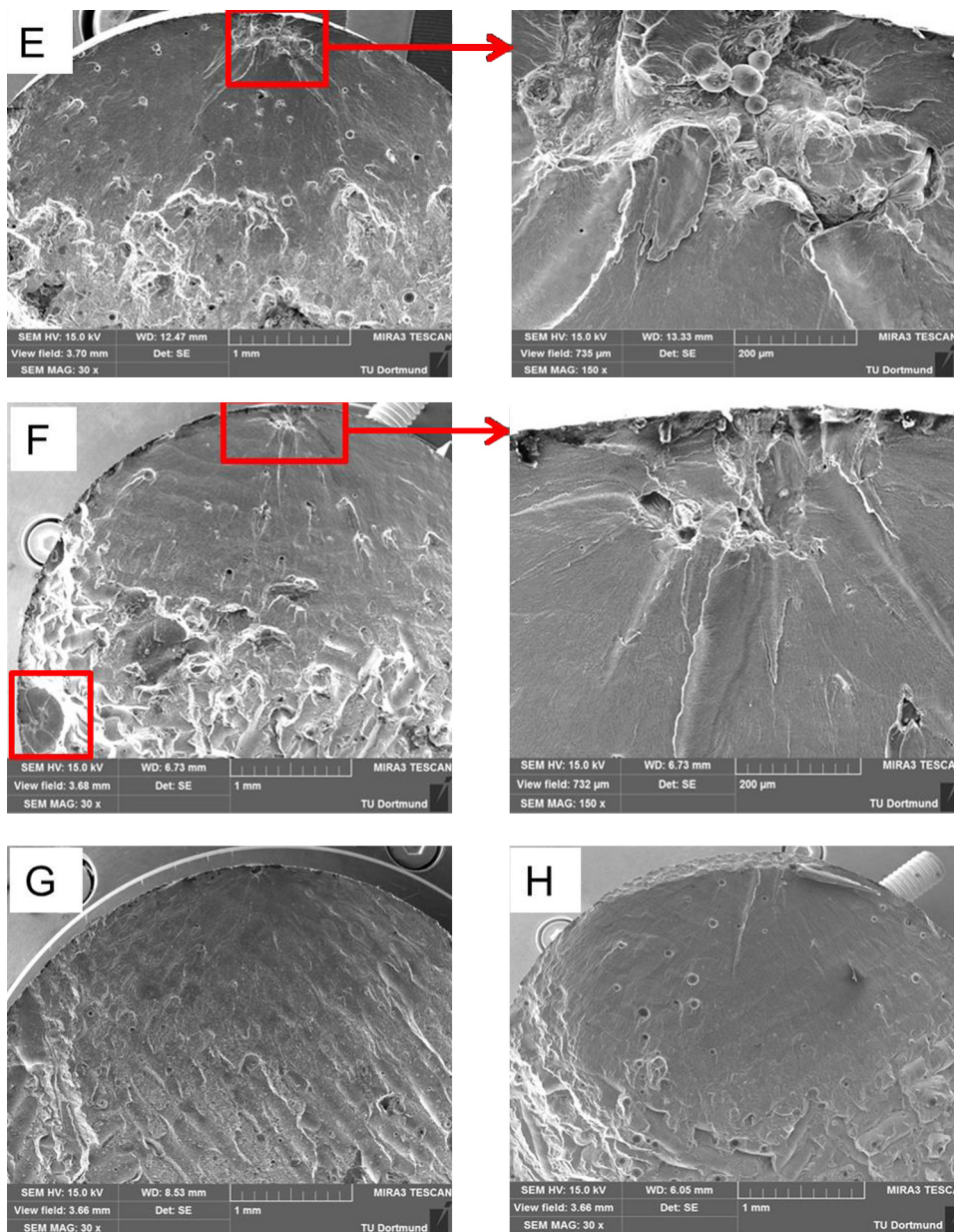


Fig. 11. Crack initiation from defects (batches E and F); and dominantly from surface (batches G and H).

due to surface weakness effect. Therefore, laser re-melting is recommended on the locations which are considered fatigue critical in the components. Combination of base plate heating together with selective re-melting at fatigue critical locations can sufficiently improve the reliability of SLM components under cyclic loading.

From the results of load increase test (Fig. 9), no considerable cyclic damage could be observed until 80 MPa; and that was estimated as the fatigue strength for the batch. It was validated by two constant amplitude tests at 80 MPa which demonstrates the utilization of load increase tests to study the deformation and damage behavior. Further, constant amplitude fatigue tests were carried out to generate a complete Woehler curve for the best among the investigated treatments (batch H) in terms of reliability.

Fig. 12 shows the complete Woehler curve with 50% failure probability together with the model of the Basquin line. Fatigue strength of 80 MPa at 10^7 cycles is a good result for AlSi alloy, for which fatigue strength at 10^7 cycles ranges from 55 to 70 MPa. The calculated standard deviation $s(\sigma_a)$ in fatigue strength is 9.63 MPa

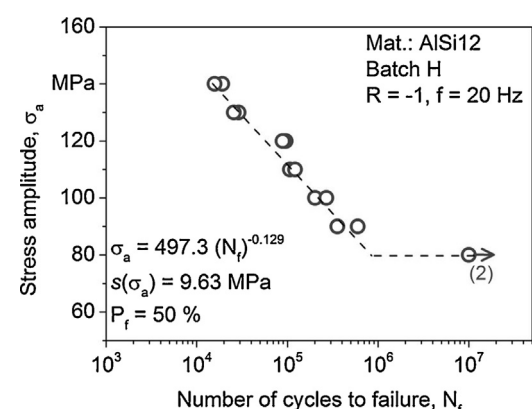


Fig. 12. Woehler curve for batch H.

which is quite good for additive manufactured samples, where fatigue scatter has been considered as a point of concern (Wycisk et al., 2013).

4. Conclusions

Almost fully solid substrate is formed by selective laser melting using high energy density; however, it contains a small number of intermittent large pores (up to 100 μm). These types of defects were eliminated by heating the base plate to 200 °C. Base plate heating helps in controlling the microstructural features in-process by decreasing the cooling rate resulting in a coarse microstructure.

Tensile strength and yield strength values four times that of sand-cast alloy and twice the corresponding properties of die-cast alloy were obtained. The increase in strength is attributed to the fine microstructure achieved by high cooling rate in the process. This increase in strength is, however, accompanied by a corresponding decrease in fracture strain. Yield strength still higher than those of cast alloys was obtained by reducing the energy density to 50%, thus doubling the build rate. It demonstrates the feasibility of manufacturing selective porous structures possessing required and sufficient properties by SLM, thus keeping the process costs in control. Using low energy density at non-critical locations is recommended for cost saving.

Base plate heating slightly decreases the quasistatic strength as well as fatigue strength owing to its effect on microstructural parameters. However, this slight decrease is accompanied by a beneficial effect in terms of sufficient decrease in fatigue scatter. The effect of base plate heating in the removal of residual stresses as well as elimination of large sized pores, and reducing fatigue scatter in turn, is pronounced as compared to post-process stress relief. Pores of size larger than 50 μm located within 250 μm from the outer surface are the preferred sites of crack initiation. Therefore, using high energy density together with re-melting at critical locations is recommended for fatigue reliability. The fatigue strength was successfully estimated employing load increase tests. Fatigue strength of SLM-manufactured AlSi12 alloy outperform the reference data available for cast material.

Acknowledgements

The lead author, Shafaqat Siddique, would like to thank Higher Education Commission (HEC), Pakistan and German Academic Exchange Service (DAAD), Germany for their financial support in terms of a research fellowship.

References

- Bartkowiak, K., Ullrich, S., Frick, T., Schmidt, M., 2011. New developments of laser processing aluminium alloys via additive manufacturing technique. *Physics Procedia* 12, 393–401.
- Buchbinder, D., Meiners, W., Wissenbach, K., Poprawe, R., 2014. Selective Laser Melting of Aluminium Die-Cast Alloy—Correlations between Process Parameters, Solidification Conditions and Resulting Mechanical Properties. *J. Laser Appl.* 27, S29205.
- Buchbinder, D., Schleifenbaum, H., Heidrich, S., Meiners, W., Büttmann, J., 2011. High power selective laser melting (HP SLM) of aluminum parts. *Physics Procedia* 12, 271–278.
- Dinda, G., Dasgupta, A., Bhattacharya, S., Natu, H., Dutta, B., Mazumder, J., 2013. Microstructural characterization of laser-deposited Al 4047 alloy. *Metall. Mater. Trans. A: Phys. Metall. Mater. Sci.* 44, 2233–2242.
- Dinda, G., Dasgupta, A., Mazumder, J., 2012. Evolution of microstructure in laser deposited Al-11.28% Si alloy. *Surf. Coat. Technol.* 206, 2152–2160.
- Emmelmann, C., Sander, P., Kranz, J., Wycisk, E., 2012. Laser additive manufacturing and bionics: redefining lightweight design. *Physics Procedia* 12, 364–368.
- Hirsch, J., 2008. Aluminium alloys. Their physical and mechanical properties. In: *Proceedings of the 11th International Conference on Aluminium Alloys*. Wiley-VCH, Weinheim (22–26 Sept. 2008, Aachen, Germany).
- Kearney, A.L., 1990. Properties of cast aluminum alloys. In: *ASM Handbook. ASM Handbook Materials International*, Materials Park, pp. 152–177.
- Kempen, K., Thijss, L., Yasa, E., Badrossamay, M., Verheecke, W., Kruth, J.P., 2011. Process Optimization and Microstructural Analysis for Selective Laser Melting of AlSi10Mg. In: *Proceedings of Solid Freeform Fabrication Symposium*, pp. 484–495.
- Leuders, S., Thöne, M., Riemer, A., Niendorf, T., Tröster, T., Richard, H.A., Maier, H.J., 2013. On the mechanical behaviour of titanium alloy TiAl6V4 manufactured by selective laser melting: fatigue resistance and crack growth performance. *Int. J. Fatigue* 48, 300–307.
- Manfredi, D., Calignano, F., Krishnan, M., Canali, R., 2013. From powders to dense metal parts: characterization of a commercial AlSiMg alloy processed through direct metal laser sintering. *Materials* 6, 856–869.
- Murr, L.E., Martinez, E., Hernandez, J., Collins, S., Amato, K.N., Gaytan, S.M., Shindo, P.W., 2012. Microstructures and properties of 17–4 PH stainless steel fabricated by selective laser melting. *J. Mater. Res. Technol.* 1, 167–177.
- Murr, L.E., Quinones, S.A., Gaytan, S.M., Lopez, M.I., Rodela, A., Martinez, E.Y., Hernandez, D.H., Martinez, E., Medina, F., Wicker, R.B., 2009. Microstructure and mechanical behavior of Ti-6Al-4V produced by rapid-layer manufacturing, for biomedical applications. *J. Mech. Behav. Biomed. Mater.* 2, 20–32.
- Niendorf, T., Leuders, S., Riemer, A., Brenne, F., Tröster, T., Richard, H.A., Schwarze, D., 2014. Functionally graded alloys obtained by additive manufacturing. *Adv. Eng. Mater.* 16, 857–861.
- Niendorf, T., Leuders, S., Riemer, A., Richard, H.A., Tröster, T., Schwarze, D., 2013. Highly anisotropic steel processed by selective laser melting. *Metall. Mater. Trans. B: Process Metall. Mater. Process. Sci.* 44, 794–796.
- Nikanorov, S., Volkov, M., Gurin, V., Burenkov, Y.A., Derkachchenko, L., Kardashev, B., 2005. Structural and mechanical properties of Al-Si alloys obtained by fast cooling of a levitated melt. *Mater. Sci. Eng. A* 390, 63–69.
- Oxman, N., Duro-Rojo, J., Keating, S., Peters, B., Tsai, E., 2014. Towards robotic swarm printing. *Archit. Des.* 84, 108–115.
- Siddique, S., Wycisk, E., Frieling, G., Emmelmann, C., Walther, F., 2015. Microstructural and Mechanical Properties of Selective Laser Melted Al 4047. *Appl. Mech. Mater.* 752–753, 485–490.
- Song, B., Dong, S., Coddet, P., Liao, H., Coddet, C., 2014. Fabrication of NiCr alloy parts by selective laser melting: columnar microstructure and anisotropic mechanical behavior. *Mater. Des.* 53, 1–7.
- Thijss, L., Varhaeghe, F., Craeghs, T., Van-Humbeeck, J., Kruth, J.P., 2010. A study of the microstructural evolution during selective laser melting of Ti-6Al-4V. *Acta Mater.* 58, 3303–3312.
- Vilaro, T., Colin, C., Bartout, J.D., Nazé, L., Sennour, M., 2012. Microstructural and mechanical approaches of the selective laser melting process applied to a nickel-base superalloy. *Mater. Sci. Eng. A* 534, 446–451.
- Walther, F., 2014. Microstructure-oriented fatigue assessment of construction materials and joints using short-time load increase procedure. *MP Mater. Test.* 56, 519–527.
- Walther, F., Eifler, D., 2007. Cyclic deformation behavior of steels and light-metal alloys. *Mater. Sci. Eng. A* 468, 259–266.
- Wong, M., Tsopanos, S., Sutcliffe, C.J., Owen, I., 2007. Selective laser melting of heat transfer devices. *Rapid Prototyping J.* 13, 291–297.
- Wycisk, E., Emmelmann, C., Siddique, S., Walther, F., 2013. High cycle fatigue (HCF) performance of Ti-6Al-4V alloy processed by selective laser melting. *Adv. Mater. Res.* 816, 134–139.
- Yadroitshev, I., Krakhmalev, P., Yadroitsava, I., 2014. Selective laser melting of Ti6Al4V alloy for biomedical applications: temperature monitoring and microstructural evolution. *J. Alloys Compd.* 583, 404–409.



Selective laser melting of aluminium and aluminium metal matrix composites: review

T. B. Sercombe & X. Li

To cite this article: T. B. Sercombe & X. Li (2016) Selective laser melting of aluminium and aluminium metal matrix composites: review, *Materials Technology*, 31:2, 77-85, DOI: [10.1179/1753555715Y.0000000078](https://doi.org/10.1179/1753555715Y.0000000078)

To link to this article: <http://dx.doi.org/10.1179/1753555715Y.0000000078>



Published online: 24 Mar 2016.



Submit your article to this journal 



Article views: 34



View related articles 



View Crossmark data 

Selective laser melting of aluminium and aluminium metal matrix composites: review

T. B. Sercombe* and X. Li

Selective laser melting (SLM) is gaining importance as companies begin to exploit its advantages to produce parts that will enable them to enter the market sooner, at a lower cost and/or with parts having an increased geometric complexity. Since aluminium is the second most popular engineering material after steel, its use in SLM was inevitable. In this review, we look at the SLM of aluminium and aluminium matrix composites. We explore some of the inherent difficulties in working with aluminium including the presence of a stable oxide layer, high reflectivity and thermal conductivity and poor flowability of the powder. We also review the unique microstructures that are produced during the SLM process and its effect on the mechanical properties. Included in this is the effect of heat treatment on the structure and properties. Finally, we look at the benefits and problems of producing aluminium metal matrix composites using SLM.

Keywords: Selective laser melting, Aluminium, Metal matrix composites

This paper is part of a special issue on 3D Printable Materials

Selective laser melting of aluminium alloys

Selective laser melting (SLM) is one of the important additive manufacturing processes, as it has the ability to produce near full density components, directly from computer models, in a range of important engineering alloys. Titanium and its alloys are ideal target materials for selective laser melting, as the materials are expensive and problematic to process using conventional manufacturing technologies. Titanium is difficult to machine, coupled with the high cost of the removed material, which adds to the component cost. In addition, during the casting of titanium, protection from oxidation is required, increasing manufacturing costs. Therefore, the net shape ability, high material utilisation and minimal machining that characterise SLM make it an attractive alternative. In contrast, SLM of aluminium does not have the same drivers. It has relatively low cost, is easy to machine and can be die cast into complex shapes. Nonetheless, SLM of aluminium is gaining increasing importance and has been driven largely by the geometric flexibility that the process offers, as well as the enhanced properties resulting from the fine grain size formed during the rapid cooling.

Selective laser melting is a complex metallurgical process that requires an understanding of the role of a large amount of interrelated process parameters. Broadly, these parameters can be divided into four key areas that are related to the laser, the scanning strategy, properties of the powder and the temperature of the part bed. These have been well summarised by

Aboulkhair *et al.*,¹ which is shown in Fig. 1. In terms of optimising the performance of SLM manufactured components, a predominant goal is to achieve near 100% density. Hence, many studies have focused on the optimisation of parameters in order to achieve this trait, in particular the effect of scan speed, hatch spacing and laser power. However, aluminium has several power related characteristics that have a big impact on the successful processing.

Powder related characteristics

Selective laser melting of aluminium poses several unique challenges in producing high density components. These are mostly characteristics of the powder and include stability of oxide layer, poor flowability, high reflectivity and high thermal conductivity.

Oxide

The thermodynamic stability and passivating nature of the ubiquitous sesquioxide cover all aluminium. The oxidation of a metal M may be represented by



The free energy of formation ΔG of the oxide is given by

$$\Delta G = -RT\ln K_3 \quad (2)$$

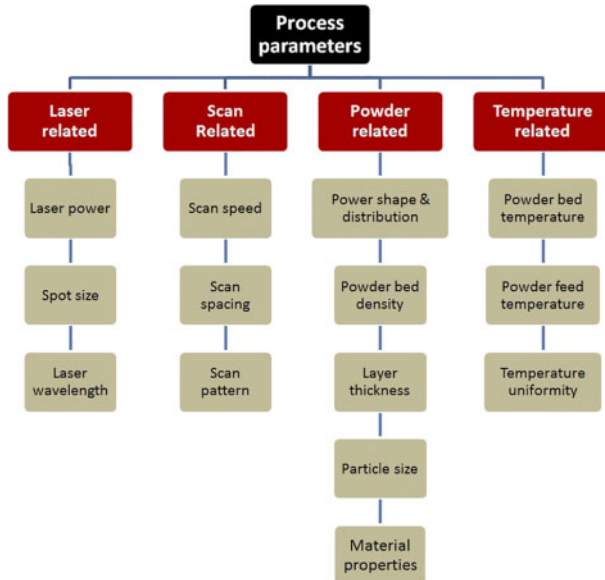
where R is the gas constant, T is the temperature in kelvin and K_3 is the equilibrium constant given by

$$K_3 = (PO_2)^{-1} \quad (3)$$

where PO_2 is the partial pressure of oxygen when reaction (1) is at equilibrium. For aluminium at 600°C, a $PO_2 < 10^{-50}$ atm is required to reduce the oxide.² This is not attainable. Hence, it is neither possible to reduce

The University of Western Australia, School of Mechanical and Chemical Engineering, Perth, WA 6009, Australia

*Corresponding author, email tim.sercombe@uwa.edu.au



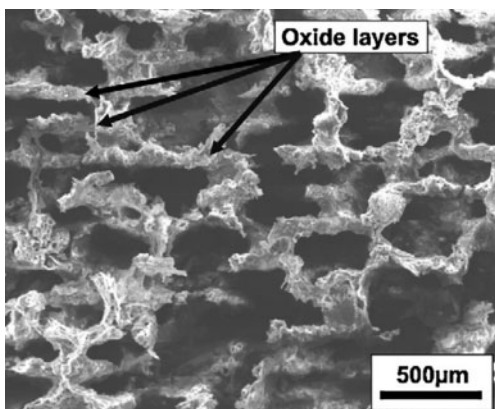
1 Important parameters in selective laser melting (adapted from Ref. 1)

the oxide nor prevent oxide from forming on freshly exposed metal.

It has been shown that significant amounts of oxide are present within the selective laser melted aluminium and tended to form between scan tracks rather than between layers, as shown in Fig. 2.³ It is also expected that the oxide would form on top of the melt pool, which may retard its spreading and alter the wetting characteristics and result in a porous structure with weak mechanical properties.⁴ However, provided that sufficient energy is imparted, this surface oxide will break up and become encapsulated within the melt pool.³ However, it may then act as a microcrack in the system and, therefore, be detrimental to the final mechanical properties of the product.⁴

Flow

Aluminium generally has poor flowability, which can impede the deposition of a thin layer of powder that is critical to the SLM process. The poor flow of aluminium powder is related to two characteristics: non-spherical shape and low density. During the atomisation process, the formation of oxide islands on the powder surface acts as pinning points and constrains the surface tension

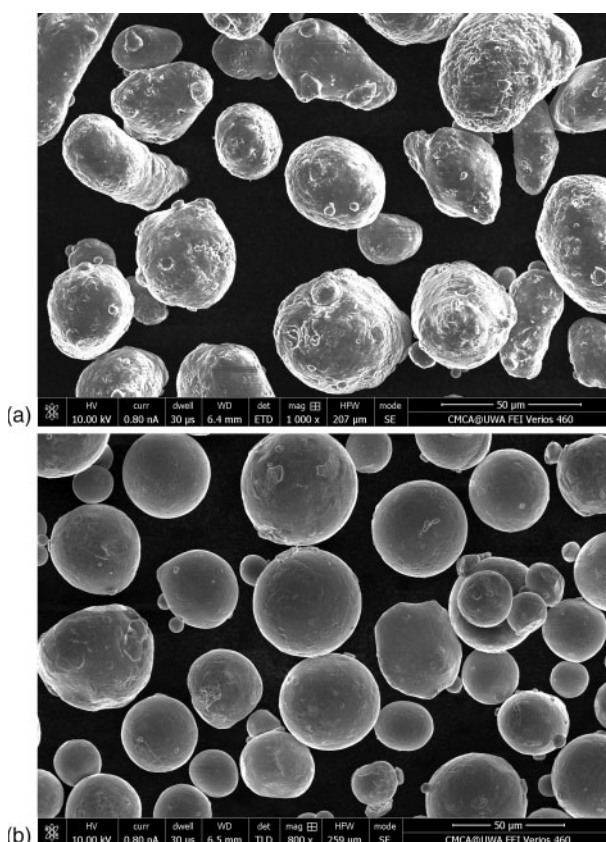


2 Image (SEM) of selective laser melted 6061 after deep etching with NaOH to reveal oxide (from Ref. 3)

forces that are attempting to spheroidise the molten particle.⁵ The result is that Al tends to have a non-spherical morphology, even when atomised under an inert atmosphere. A comparison between the shape of Al–12Si and Ti–6Al–4V powder is given in Fig. 3. This figure clearly shows that the Al powder is less spherical than the Ti–6Al–4V, which impacts on the powder flowability. The low density of the aluminium particles are also a factor in flowability as the very strong inter-particle cohesion, mainly ascribed to van der Waals forces, dominates the particle weight.⁶

Reflectivity and conductivity

Aluminium is highly reflective of the laser energies in the infrared range. At the typical 1 μm wavelength of modern SLM lasers, aluminium will only absorb 7% of the incident laser energy.⁷ Although the actual absorption of a powder bed will be higher due to multiple absorption and reflection events, higher than expected laser energies are required in order to overcome the reflectivity. In addition, there will be a significant difference in absorptivity between previously melted (i.e. solid) aluminium and the neighbouring powder. Hence, the temperature gradients are likely to form during the use of overlapping scan tracks, which may lead to balling as a result of temperature gradient driven convective flow (i.e. the Marangoni effect). Interestingly, Si has a very high absorptivity (~70%),⁷ and this may be a factor in the success of Al–Si based alloys (which are detailed below). Since Si has very low solubility in solid Al,⁸ prealloyed Al–Si powder will contain particles of essentially pure Si. Thus, it is possible that these



3 Images (SEM) of a Al–12Si and b Ti–6Al–4V powder; Al powder is clearly less spherical than Ti–6Al–4V (author's own images)

particles, especially those near the surface of the powder particle, will readily absorb the laser energy and heat rapidly. Heat transfer into the surrounding aluminium (within a given prealloyed particle) will then occur, causing melting. For this approach to be successful, rapid heat transfer needs to occur within a given particle (from the Si to the Al). The time τ required for the diffusion of heat across a particle of diameter D is given by

$$\tau \approx \frac{D^2}{\alpha} \quad (4)$$

where α is the thermal diffusivity ($\sim 1 \text{ cm}^2 \text{ s}^{-1}$ for Al at room temperature and $0.7 \text{ cm}^2 \text{ s}^{-1}$ at 600°C).⁹ Typically, the particle size of the powder used in SLM is $<50 \mu\text{m}$, and therefore, the time required to diffuse across the powder particle is a few tens of microseconds. This is two orders of magnitude less than the interaction time (few milliseconds). In reality, the fine distribution of the Si within the atomised prealloyed powder results in an effective diffusion distance of much less than the particle diameter, and therefore, the heat transfer may be considered to be instantaneous.

In addition to aluminium's high reflectivity, it has very high thermal conductivity κ . Thus, not only does a significant amount of the laser energy gets reflected, but there is also rapid heat conduction away from the melt pool into the already formed solid and/or substrate. The net result of this is threefold. First, more laser energy is required than for materials with lower conductivity. Second, there is a greater difference between the thermal conductivities of the solid and powder possibly causing density differences depending on whether or not the area being built is on solid or powder. Finally, the width of the melt trace will be much larger than for low conductivity metals as heat is conducted outwards, melting the surrounding powder. For example, our own research has shown that, under optimum conditions for Al-12Si ($\kappa, \sim 100 \text{ W m}^{-1} \text{ K}^{-1}$),¹⁰ the melt trace width is $\sim 200 \mu\text{m}$, while for titanium ($\kappa=6.7 \text{ W m}^{-1} \text{ K}^{-1}$)¹¹ and stainless steel ($\kappa = 21.4 \text{ W m}^{-1} \text{ K}^{-1}$),¹⁰ it is 100 and $130 \mu\text{m}$ respectively. Although a large melt trace width can be compensated for via a beam offset, it will affect the size of the smallest feature that can be produced.

Composition

Despite the above difficulties, the SLM of aluminium can be successfully performed. The majority of this work has been carried out on Al-Si based alloys (e.g. Al-12Si and AlSi10Mg),^{1,3,4,6,12-27} with a small amount on 6061,³ as well as Al-Cu and Al-Zn alloys.¹² However, in the latter two systems, only single line scans were performed. The Al-Si system is generally thought to be most suitable for SLM due to its narrow freezing range. Another factor may be the amount of material that undergoes isothermal solidification. During solidification, the nucleated particles will grow until they impinge and join onto their neighbours. It is at this point when the strength of the solidifying structure starts to form, and the application of stress can result in cracking and distortion. The Al-12Si and AlSi10Mg alloys will undergo isothermal solidification during this critical final solidification stage and, therefore, should be less prone to cracking and distortion.

By far, the most widely studied alloys are the Al-10Si-0.5Mg, which is equivalent to the casting alloy A360 and

Al-12Si (casting alloy 413). For these two high Si content alloys, there appears to be very little difference between their processing. The as processed microstructure is extremely fine, consisting of a cellular dendritic α -Al with very fine, dendritic Si particles.^{13,16,19,27} Also typical of the microstructure are areas of coarser grains, which are located at the boundary of the molten pool. In this region, the heat from subsequent laser scan lines and layers raises the temperature of the material causing a heat affected zone to form. The microstructure of these materials is discussed further below.

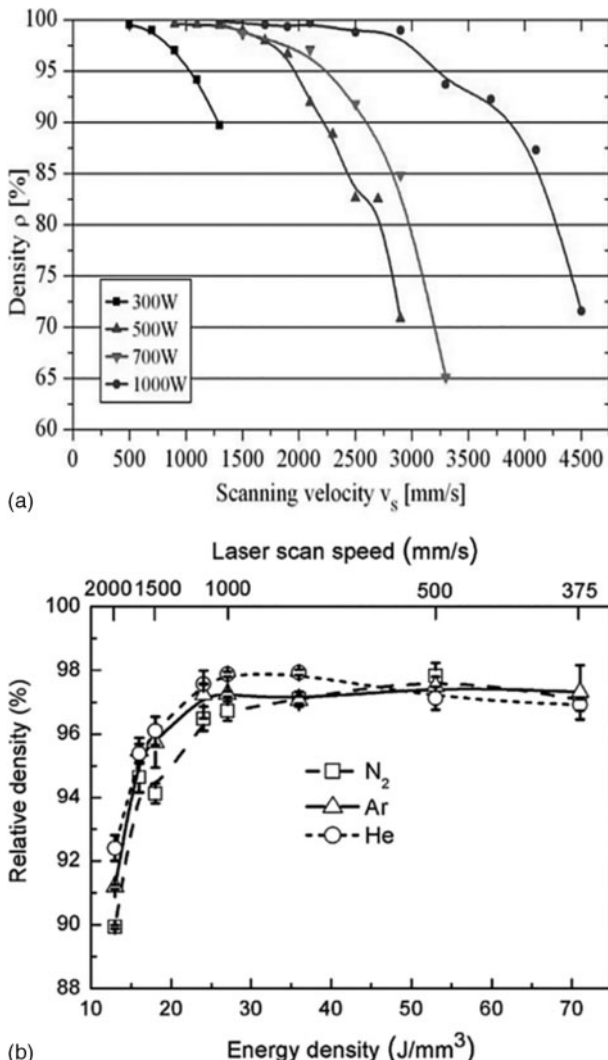
Laser and scan related parameters

By far, the most commonly studied parameters for the SLM of Al is the effect of the laser energy density on the porosity and properties of the parts. The energy density E is given by

$$E = \frac{P}{vst} \quad (5)$$

where P is the laser power (W), v is the scan speed (mm s^{-1}), s is the scan spacing (mm) and t is the layer thickness (mm). Thus, increasing laser power, decreasing scan speed or scan spacing or less commonly layer thickness all cause an increase in energy density. Generally, it is reported that a minimum energy density (or speed below a critical value) is required to produce maximum density,^{1,3,14,23,27} as shown in Fig. 4. At lower energies (higher speeds), there is significant porosity caused by incomplete melting.^{1,23,26} Buchbinder *et al.*¹⁴ used a high power (1000 W) SLM machine to process AlSi10Mg powder. They concluded that a faster build speeds, along with high density, could be attained using such high power lasers, as shown in Fig. 4. Wang *et al.*²⁷ similarly found that high density could be attained provided that the energy density was $>40 \text{ J mm}^{-3}$, and this was true when processing in Ar, N₂ and He (Fig. 4b). In almost all cases, SLM has been performed using a continuous laser at a wavelength of $1.06 \mu\text{m}$. There has been one report¹⁶ where both Al-12Si and AlSi10Mg were processed using pulsed YAG laser. Although parts with a fine microstructure could be produced, the maximum density that could be achieved for Al-12Si and AlSi10Mg was ~ 94 and 95% respectively.

In contrast to the effect of laser energy, little work has been performed on investigating the scanning strategy.^{1,23,26} Read *et al.*²³ used a statistical approach to optimise not only the scan speed and scan spacing but also the size of the islands in a checkerboard style strategy. A more detailed study on the role that the scanning strategy plays in the formation of the porosity was undertaken by Aboulkhair *et al.*¹ They compared six different scanning strategies and reported that by optimising the scanning speed and hatch spacing only, the maximum density that could be reached was 97.7%. However, by employing more sophisticated strategies (such as presintering), densities $>99.5\%$ could be attained. A summary of their results is shown in Fig. 5. Thijs *et al.*²⁶ used the scanning strategy not to improve the density, but rather to affect the texture. They showed that if the scanning of the laser is performed only in one direction, a strong partial $<100>$ fibre along the build direction forms. If, however, the vectors are rotated 90° between layers, a weak $<100>$ cubic texture forms



4 Effect of scan speed on density of a AlSi10Mg12Si at different laser powers (scan spacing of 0.15 mm and layer thickness of 50 μm)¹⁴ and b Al-12Si under different atmospheres;²⁷ both results show that there is decrease in density once critical speed has been exceeded

along the build direction. Thus, isotropic or anisotropic parts can be produced through appropriate choice of scanning strategy.

Microstructure, properties and heat treatment

Microstructure

The SLM process is characterised by rapid heating and cooling. For Al-12Si, the cooling rate has been predicated to be $>10^3 \text{ K s}^{-1}$.¹⁹ Therefore, the microstructure of parts is extremely fine grained. At a macroscale, the structure consists of overlapping half-moon melt pools, as shown in Fig. 6a. Owing to the overlap of scanning vectors, the size of the microstructural features are usually slightly smaller than the size of the molten pool that is formed during processing.²⁶ At a higher magnification (Fig. 6b), the microstructure consists of very fine 0.5–1 μm cellular aluminium surrounded by a network of nanosized Si particles.^{1,16,19,20,22,24,27} Similar microstructures have been reported in melt spun Al-Si ribbons²⁸ and form due to the very high cooling rate.

The as processed microstructure contains at least two distinct regions: one significantly finer than the other,

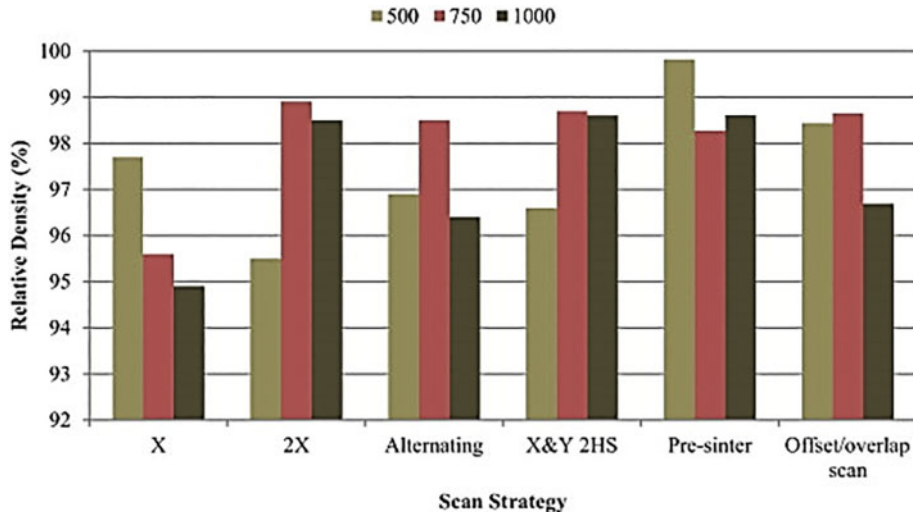
as shown in Fig. 7. Inside the melt pool, fine cellular dendrites tend to grow towards the centre of the melt pool. At the edges of the melt pool, the material is affected by the heat generated by both the overlapping scan lines and creation of subsequent layers, which causes localised coarsening. Even in this coarsen region, the microstructure is extremely fine in comparison to those resulting from castings. As discussed below, this fine microstructure results in enhanced properties.

Properties

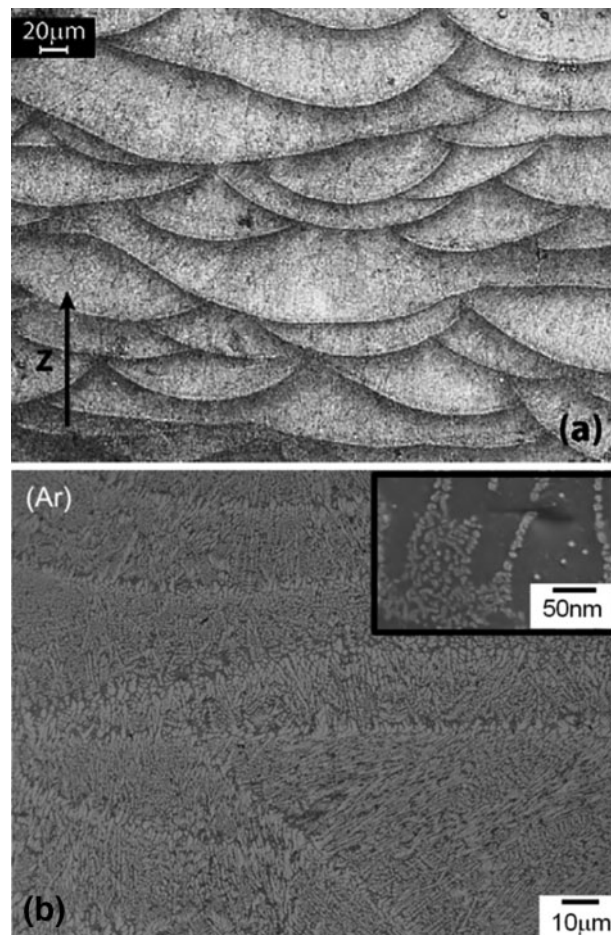
Owing to the rapid solidification, the cellular aluminium is supersaturated in Si.^{19,22} Li *et al.*¹⁹ used TEM energy dispersive X-ray spectroscopy mapping and determined that the Si concentration in the as processed was ~7 wt-%. This far exceeds the maximum equilibrium solubility of ~1.6 wt-%⁸ and is even greater than what has been reported in melt spinning.^{29,30} Since the equilibrium solubility of Si in solid Al is low, during solidification, the advancing solidification front must reject the solute into the liquid. Since solidification occurs very rapidly in SLM, rejection of the Si cannot occur fast enough, and therefore, it becomes trapped in the Al matrix. The Si atom, being smaller than Al (Si atomic radius is 111 pm against Al's 118 pm), induces solid solution hardening when dissolved in the Al.³¹ Hence, the extended solubility, along with the very fine grain structure, will cause an increase in strength over conventionally processed (e.g. cast) material. A summary of reported properties is given in Table 1. In general, the strength of the Al-12Si and AlSi10Mg alloys is approaching 400 MPa, with the ductility around 3–5%. This is greater than that of cast material, which typically has an as processed strength and ductility of 300 MPa and 2–3% respectively.³² As a consequence of these enhanced properties, SLM could well be an attractive alternative to casting.

Owing to the layer by layer manufacturing approach of additive manufacturing, properties are often dependent on the testing direction, with those parallel to the build direction usually lower. For aluminium, the reported data in the literature tend to suggest that the only orientation sensitive property is ductility, which is normally reported to be lowest in the build direction.^{17,20} Although the reasons for this have not been well investigated, Kempen *et al.*¹⁷ suggested that the low ductility was due to the presence of border pores, which form at the start and end of each scan vector. Since when a sample is built along the build direction, there are more layers, it follows that there will be more border pores, which act as critical defects and initiate failure at lower strains.

The fatigue properties have received much less attention than static properties. In the most comprehensive study, Brandl *et al.*¹³ investigated the effect of platform temperature, build direction and heat treatment on the fatigue strength of AlSi01Mg. This work concluded that the peak hardening process (i.e. T6) has the biggest effect on the fatigue strength. Although heating the substrate slightly decreased the fatigue strength, it removed any orientation dependence of the properties. By choosing the best combination of parameters, a fatigue limit of ~200 MPa (no substrate heating, 0° orientation and T6 heat treatment) could be attained. At the other extreme, a material that had been processed with a substrate temperature of 300°C, 90° orientation and in the as built

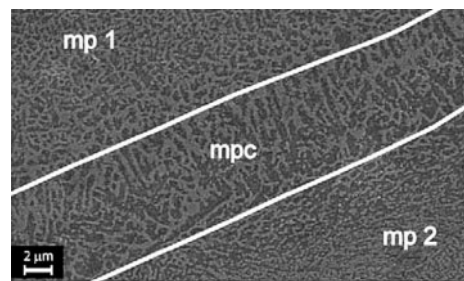


5 Influence of scanning strategy on relative density of AISi10Mg parts (from Ref. 1)



6 Microstructure of a AISi10Mg (Ref. 20) and b Al-12Si (Ref. 27) after selective laser melting: in a, half-moon shaped melt pools are clearly visible, while b shows fine cellular aluminium (light grey phase) surrounded by Si (dark grey); insert in b, SEM image showing very fine scale of Si particles

condition had a fatigue strength of ~ 100 MPa. This work also identified the crack initiation site, which were pores or unmelted particles, and concluded that improved processing was required to increase the density and avoid imperfections in the material. Siddique *et al.*²⁴



7 Image (SEM) image of AISi10Mg alloy after etching with Weck's reagent; between two melt pools (mp1 and mp2) is area of coarser microstructure (mpc) (from Ref. 20)

investigated the effect of the processing condition of both the tensile and fatigue strength of Al-12Si. Using continuously increasing load tests, they also found that heating the base plate decreased the fatigue, while a low temperature (240°C) post-heat treatment had very little effect. They reported a 10^7 run out at ~ 80 MPa. This work also found that the crack initiation sites were pores, especially those $>50\text{ }\mu\text{m}$ and located within $250\text{ }\mu\text{m}$ of the surface.

Heat treatment

The extremely fine microstructure produced in the SLM process also responds well to heat treatment, with a range of different properties able to be generated. During elevated temperature annealing, two main events occur. First, there is a rapid decrease in the amount of Si that is trapped in the cellular Al, which causes an increase in the volume fraction of Si.^{19,22} This will decrease the amount of solid solution hardening and therefore the strength. Second, the nanosized Si particles coarsen into spherical particles that are up to $\sim 2\text{ }\mu\text{m}$ in size.^{13,19,22} The heat treatment process has also created a homogeneous microstructure, with the melt pools and two-scale structure of the as proceeded material no longer evident.

It has been shown that, in the as processed material, there is an orientation relationship between the Al and Si, which can be expressed as $(111)_{\text{Si}}:(200)_{\text{Al}}$, and is different to that in cast material.³³ This enables the Si phase to grow along the most stable plane with the

Table 1 Summary of reported properties for Al-12Si and AlSi10Mg alloys

Alloy	Condition/direction	Yield strength/MPa	Tensile strength/MPa	Strain to failure/%	Reference
Al-12Si	Optimised	202.2±4.3	369.3±3.4	4.38±0.16	24
	Optimised	260	380	3	22
	Heat treated 450°C for 6 h	95	140	15	22
	Ar	223±11	355±8	4.2±0.6	27
	N ₂	224±7	368±11	4.8±0.6	27
	He	221±11	242±43	1.5±0.4	27
	As processed	240	360	4	19
	2 h @ 500°C	110	190	25	19
	X	...	420	...	14
	Z	...	360	...	14
AlSi10Mg	X	~250	~330	1.2	23
	Z	~240	~320	~1	23
	X	...	391±6	5.5±0.4	17
	Z	...	396±8	3.47±0.6	17
	X	243±7	330±3	6.2±0.3	20
	Z	231±3	329±2	4.1±0.2	20

lowest free energy: the most dense packed plane {111}_{Si} and is the reason that the Si phase grows into a spherical morphology. As a consequence of the heat treatment, the ductility of the alloy can be increased substantially, albeit at the cost of strength. For example, Prashanth *et al.*²² reported a tensile ductility in Al-12Si of ~14% in samples heat treated for 6 h at 450°C, while Li *et al.*¹⁹ heat treated the same alloy at 500°C for 4 h and measured 25% ductility.

The author's own unpublished work on the properties of various Al-Si alloys produced using SLM is summarised in Table 2 and compared to the handbook data for Al-Si casting alloys in Fig. 8. There are several key trends that these data reveal. First, it is apparent that the properties of SLM material occupy a different (better) area of property space. Second, the as processed (F) yield strength decreases with Si content. This is not surprising as lower Si contents will likely mean that less excess Si becomes trapped in the solution, which in turn causes a drop in the solid solution hardening. The drop becomes more pronounced once the Si content is <7 wt-%, which agrees well with the amount of Si measured in solution in Al-12Si.¹⁹ Solution treatment (T4) decreases the strength and increases the ductility. However, the biggest change occurs in the Mg free alloys where the ductility is ~25%. In the alloys containing Mg, the ductility is lower (~12–17%), while the strengths tend to be higher. It is likely that, due to the presence of Mg, these alloys are undergoing a natural aging process (formation of Mg₂Si precipitates).³¹ Third, the as processed ductility is generally low (although higher than equivalent casting alloys) except in the cast of Al-5Si,

where it is ~14%. This again ties in well with the measured extended solubility. It is possible that in the Al-5Si alloy, there is only a small amount of excess Si in the solution as well as lower amounts of crack initiating free Si particles. These would combine to enhance the ductility. Finally, in the Al-Si-Mg alloys in the peak aged (T6) condition, the material has a very good balance of strength and ductility. Significant strengthening is occurring, which indicates that the Mg content is still reasonably high, despite loss of Mg being reported during SLM.¹ On balance, the best as processed properties are achieved with the Al-5Si alloy (good strength combined with high ductility), while the Al-12Si alloy produces the best properties in the T4 condition, and the AlSi7Mg has the best peak aged properties. Thus, selection of the alloy should be made based on whether or not heat treatment will occur.

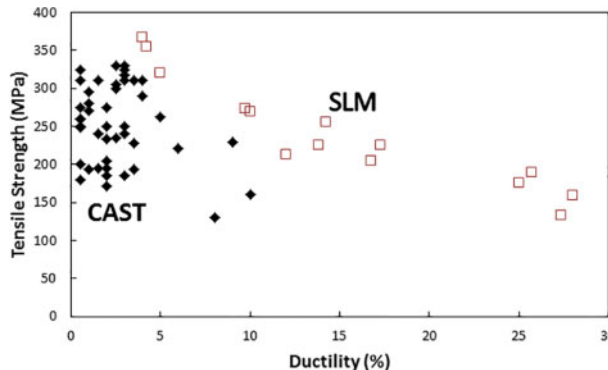
Summary

Despite the obstacles posed by the high reflectivity and conductivity, oxide layer and poor flowability of the powder, aluminium components with high density, excellent mechanical properties can be produced via SLM. Work in this area has almost exclusively focused on Al-Si alloys, which have been based on conventional casting alloys. As a result of the high cooling rate, the microstructure produced is extremely fine and consists of a supersaturated cellular Al matrix surrounded by nanosize Si particles and, therefore, mechanical properties exceeding cast material. In addition, simple heat treatments can be used to create unique microstructures, some of which possess very high ductility.

Table 2 Selection of properties from various selective laser melted aluminium alloys (author's unpublished work)*

Alloy	Heat treatment	Yield strength/MPa	Tensile strength/MPa	Strain to failure/%
Al-12Si	F	223.5	355.1	4.2
	T4	100.6	175.4	25.0
Al-Si10Mg	F	207.8	367.7	4
	T4	119.4	212.3	12
AlSi7Mg	T6	209.6	269.1	10
	F	192.8	320.1	5
	T4	108.7	204.4	16.8
Al-5Si	T6	227.4	273.1	9.7
	F	145.8	255.8	14.2
	T4	66.7	132.9	27.3

* F: as processed; T4: 4 h@500°C; T6: T4 + 18 h@160°C.



8 Strength and ductility plot for Al-12Si produced via casting and SLM: parts produced from SLM clearly have better strength–ductility relationship; data for casting from Ref. 32 and for SLM from author's own unpublished work

Selective laser melting of aluminium matrix composites (AMCs)

Many modern technologies require materials with combinations of properties that cannot be met by conventional metal alloys, ceramics and polymeric materials. By combining two or more physically distinct phases, composites can be produced with aggregate properties that are different, and often far superior, from the constituents individually. Aluminium alloys are often used in applications for their low density and corrosion resistance; however, they are often let down by their low stiffness and relatively poor wear resistance. The automotive, marine and aerospace industries are particularly interested in the production of aluminium metal matrix composites (AMMCs) because introduction of a reinforcement phase gives the potential to produce components with a high stiffness/weight ratio. Future use of aluminium MMCs within these fields is heavily dependent on the ease of fabrication and material properties obtained and hence are underpinned by the chemical compatibility between the matrix and reinforcement.

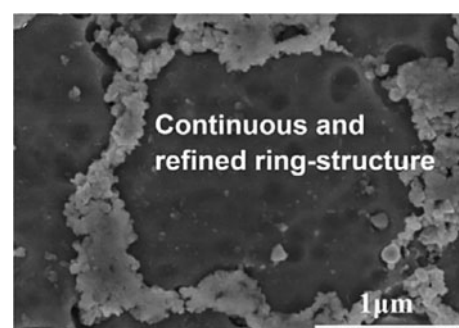
Casting is a commonly used method to produce AMMCs; however, preventing segregation^{34,35} of the heavier composite particles and reactions between them and the melt³⁶ are two of the main issues that this process faces. In addition, subsequent machining of the cast part (e.g. to remove risers and runners) is difficult due to the presence of the hard reinforcing phase and therefore increases costs.³⁷ Powder metallurgy routes, and in particular press and sinter processing, overcome both the segregation issues and the need for significant machining.³⁸ However, the parts usually suffer from low density and lower mechanical properties. Despite these difficulties, AMMCs have successfully been used as components in automotive, aerospace, optomechanical assemblies and thermal management applications.³⁹

Selective laser melting offers the potential to combine the benefits of both casting and powder metallurgy approaches. Since SLM uses powder as the feedstock, the segregation problems are minimised (compared to melt processing). Subsequent melting by the laser facilitates the possibility of high density parts, similar to casting. However, since the goal of the SLM process is to produce net shaped parts, little, if any, machining is

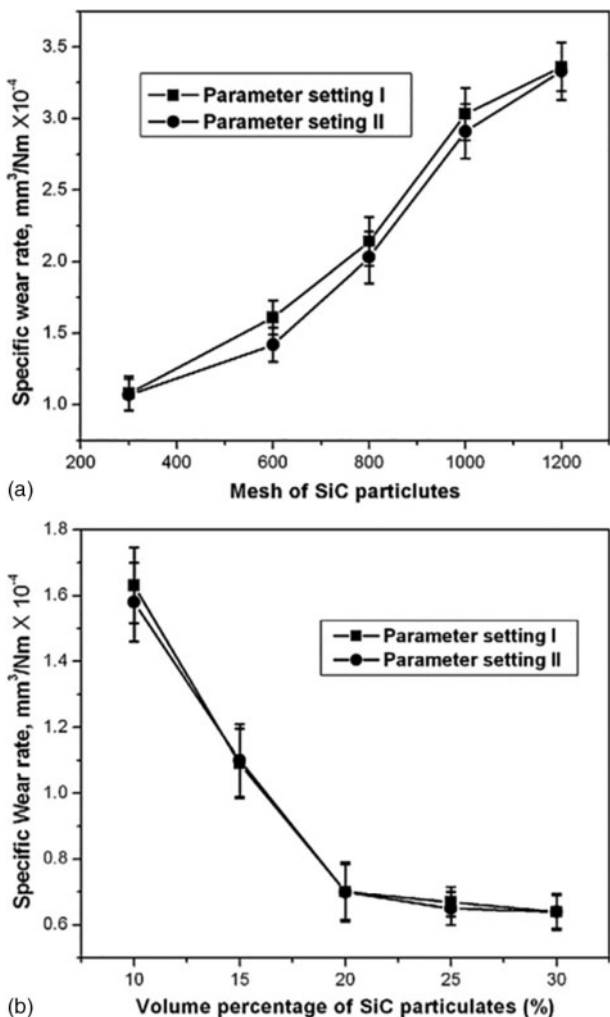
required. Finally, SLM is characterised by rapid heating and cooling, and the material remains in the molten state for only a very short time. This should minimise any reactions between the reinforcing phase and the aluminium.

Introducing a secondary particle into the Al matrix by SLM can result in the enhancement of mechanical properties only if the final AMC microstructure can be optimised by controlling the processing parameters. For example, Gu *et al.* report the fabrication of AlSi10Mg/TiC nanocomposite parts with an improved microhardness of 188.3 HV0.1, a tensile strength of 486 MPa and elongation $\sim 10.9\%$ by SLM.⁴⁰ This improvement in mechanical properties was attributed to the combined effects from two strengthening mechanisms: grain refinement strengthening and grain boundary strengthening. Both of these originated from the novel microstructure that was produced, which consisted of a ring structured nanoscale TiC reinforcement in AlSi10Mg matrix, as shown in Fig. 9.⁴⁰ Further, it was shown that the structure could be tailored through changing the laser energy density. They also found that the TiC reinforcement in the SLM fabricated parts experienced a microstructural change from the standard nanoscale particle morphology (the average size is 77–93 nm) to the relatively coarsened submicron structure (the mean particle size is 154 nm) with increasing laser energy density.⁴¹ The distribution of the TiC particle also becomes homogenised as the laser energy density increased. These together gave rise to a considerably low coefficient of friction of 0.36 and a reduced wear rate of the SLM fabricated AlSi10Mg/TiC AMCs.⁴¹ Ghosh and Saha successfully fabricated Al4.5Cu3Mg/SiC AMCs with improved wear properties via SLM.⁴² They found that the wear resistance decreased with increasing SiC particle size (Fig. 10a), which was attributed to the limited plastic deformation of the surface material when large SiC particles tend to be embedded with the matrix alloy. The wear resistance was also shown to improve with increasing content of the SiC as shown in Fig. 10b, primarily as a result of the increased hardness. However, this trend stopped for additions $\geq 20\%$ SiC due to the effect of abrasive wear and cracking.⁴² In their study, cracks were generated at the interface between the SiC and Al alloy due to the difference in coefficients of thermal expansion and two types of residual stresses formed during SLM, namely, thermal stress and contraction stress.

As such, it can be seen that the interfacial microstructure including phase formation between the Al matrix and the reinforcements hold the key to achieving



9 Continuous ring of nanoscale TiC in AlSi10Mg matrix (from Ref. 40)



10 Effect of a SiC size and b volume per cent of SiC on wear rate of AlSi10Mg/SiC AMC (from Ref. 42)

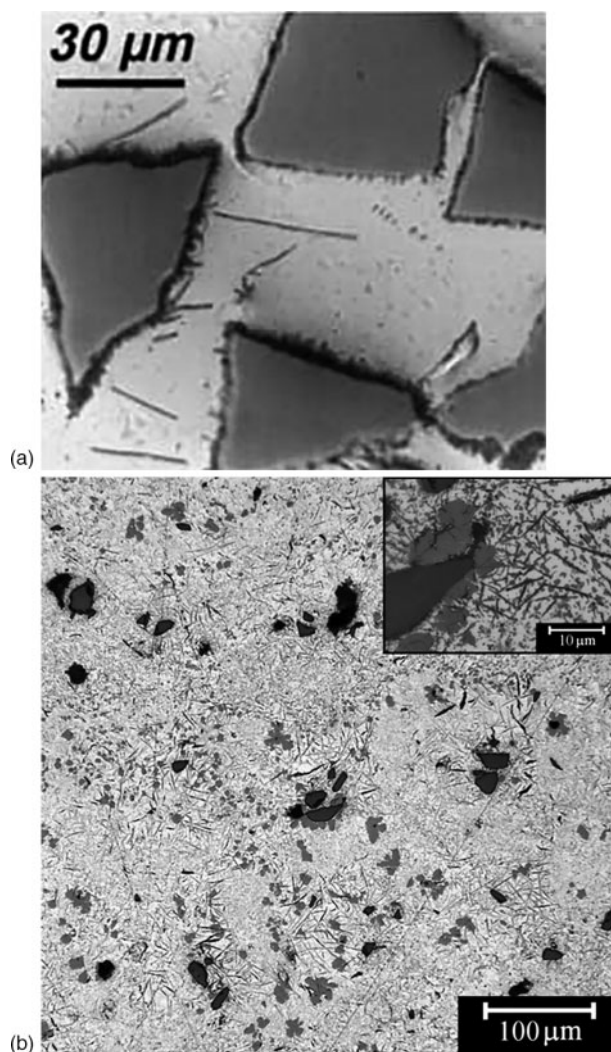
desired properties. Therefore, more work has been focused on investigating and controlling the interfacial microstructure between the Al matrix and the reinforcements. For example, advanced *in situ* AMCs with different additions of Fe_2O_3 into pure Al were successfully fabricated using SLM by Dadbakhsh and Hao.⁴³ The influence of the Fe_2O_3 content and SLM processing parameters on the microstructure and phase formation in the AMCs and the resultant hardness of the components were systematically investigated. Through varying the SLM parameters and the Fe_2O_3 content, the microstructure and the *in situ* formed hard phases in the AMCs could be tailored. At higher Fe_2O_3 content, an enhanced hardness was obtained, originating from a very fine, well bonded, homogeneous distribution of hard particles including Al_2Fe , AlFe , Fe_3Al as well as equilibrium $\text{Al}_{13}\text{Fe}_4$ (Al_3Fe) in the Al matrix.⁴³ It is also interesting to note that the porosity induced by entrapped gas can also be mitigated by increasing the Fe_2O_3 content.⁴³

Ocelik *et al.* investigated the reaction zone at the interface between Al and SiC in the Al/SiC AMCs fabricated using laser melt injection, which is similar to SLM regarding the melting process.⁴⁴ Randomly oriented large Al_4C_3 plates ($\sim 30 \mu\text{m}$ in length) were observed to be embedded in the Al matrix, probably formed from free carbon. In addition, a large amount of coherent

small Al_4C_3 plates were also found, which were formed by reaction between the solid SiC and the molten Al during laser melt injection (see Fig. 11a). These small Al_4C_3 plates on the surface of the SiC caused particle cracking.⁴⁴ In our recent study of SLM of Al12Si with SiC particles, it was found that, although high (97 + %) density could be attained, both needle shape and spherical Al_4C_3 were observed in the microstructure (Fig. 11b). This was accompanied by the loss of SiC. It is also found that the extent of SiC breakdown was closely related to the laser energy density with higher laser density resulting in more breakdown.⁴⁵ Two possible theories were proposed for the breakdown: reaction theory and melt theory, although not one theory could completely explain the results. Hence, it was concluded that both mechanisms were in operation.

Summary

This paper has reviewed the SLM of both aluminium and AMMCs. Aluminium suffers from poor flowability, high reflectivity and thermal conductivity as well as the presence of a dense and stable oxide layers. These are all barriers to their successful processing. Nonetheless, SLM of aluminium can be performed with good results.



11 Dark reaction products visible around SiC particles in a Al-SiC AMC produced using laser melt injection⁴⁴ and b selective laser melted Al-12Si (Ref. 45)

However, the work has largely been limited to the Al–Si base alloys, which are copies of conventional casting alloys. Hence, there may be an opportunity to undertake alloy design to investigate whether or not alloys with improved processing can be designed. As a result of the high cooling rate, the mechanical properties of the material are generally superior to that from casting, and the alloy responds well to simple heat treatments, with high ductility possible.

Both *in situ* and *ex situ* AMCs have been produced using SLM, and it appears to be a promising technique to overcome problems with conventional processing routes. Additions of TiC resulted in a material with high hardness and reduced wear rates. However, despite the high cooling rate and short interaction times, breakdown of SiC appears to be problematic, with the formation of Al₄C₃ needles in the microstructure. *In situ* reaction of Fe₂O₃ with the aluminium matrix resulted in a material with very high hardness.

Acknowledgements

Part of this work was supported by the Australian Research Council (ARC) Discovery Project no. DP0986067. The authors also acknowledge the facilities and the scientific and technical assistance of the Australian Microscopy & Microanalysis Research Facility at the Centre for Microscopy, Characterisation & Analysis, The University of Western Australia, a facility funded by the University, State and Commonwealth Governments.

References

- N. T. Aboulkhair, N. M. Everitt, I. Ashcroft and C. Tuck: *Addit. Manuf.*, 2014, **1–4**, 77–86.
- L. S. Darken and R. W. Gurry: ‘Physical chemistry of metals’, 1953, New York, McGraw-Hill.
- E. Louvis, P. Fox and C. J. Sutcliffe: *J. Mater. Process. Technol.*, 2011, **211**, (2), 275–284.
- S. Dadbakhsh and L. Hao: *J. Alloys Compd.*, 2012, **541**, 328–334.
- A. Ozbil, A. Unal and T. Sheppard: ‘Influence of oxygen on morphology and oxide content of gas atomised aluminum powders’, in ‘Physical chemistry of powder metals- production and processing’, (ed. W. M. Small); 1989, The Minerals, Metals and Materials Society.
- L. J. Jallo, M. Schoenitz, E. L. Dreizin, R. N. Dave and C. E. Johnson: *Powder Technol.*, 2010, **204**, (1), 63–70.
- D. R. Lide and W. M. Haynes: ‘CRC handbook of chemistry and physics: a ready-reference book of chemical and physical data’ **Vol. 1**; 2009, Boca Raton, FL, CRC Press.
- Anon: ‘ASM handbook’ 3, ‘Alloy phase diagrams’; 1992, Materials Park, OH, ASM International.
- F. R. Schwartzberg: ‘Cryogenic materials data handbook’ **Vol. 2**; 1970, Wright-Patterson Air Force Base, OH, Air Force Materials Laboratory.
- M. Bauccio: ‘ASM metals reference book’, 3rd edn; 1993, Materials Park, OH, ASM International.
- M. Boivineau, C. Cagran, D. Doytier, V. Eyraud, M. H. Nadal, B. Wilthan and G. Pottlacher: *Int. J. Thermophys.*, 2006, **27**, (2), 507–529.
- K. Bartkowiak, S. Ullrich, T. Frick and M. Schmidt: *Phys. Procedia A*, 2011, **12A**, 393–401.
- E. Brandl, U. Heckenberger, V. Holzinger and D. Buchbinder: *Mater. Des.*, 2012, **34**, 159–169.
- D. Buchbinder, H. Schleifenbaum, S. Heidrich, W. Meiners and J. Bültmann: *Phys. Procedia A*, 2011, **12A**, 271–278.
- F. Calignano, D. Manfredi, E. P. Ambrosio, L. Iuliano and P. Fino: *Int. J. Adv. Manuf. Technol.*, 2013, **67**, (9–12), 2743–2751.
- R. Chou, J. Milligan, M. Paliwal and M. Brochu: *JOM*, 2015, **67**, (3), 590–596.
- K. Kempen, L. Thijss, J. van Humbeeck and J. P. Kruth: *Phys. Procedia*, 2012, **39**, 439–446.
- K. Kempen, L. Thijss, E. Yasa, M. Badrossamay, W. Verheecke and J. P. Kruth: ‘Process optimization and microstructural analysis for selective laser melting of AlSi10Mg’, ‘Proc. 22nd Annual Int. Solid Freeform Fabrication Symp. – An additive manufacturing conference’, Austin, TX, USA, August 2011’, 484–495.
- X. P. Li, X. J. Wang, M. Saunders, A. Suvorova, L. C. Zhang, Y. J. Liu, M. H. Fang, Z. H. Huang and T. B. Sercombe: *Acta Mater.*, 2015, **95**, 74–82.
- D. Manfredi, F. Calignano, M. Krishnan, R. Canali, E. Ambrosio and E. Atzeni: *Materials*, 2013, **6**, (3), 856–869.
- E. Olaikianni, R. F. Cochrane and K. W. Dalgarno: *J. Mater. Process. Technol.*, 2011, **211**, (1), 113–121.
- K. G. Prashanth, S. Scudino, H. J. Klauss, K. B. Surreddi, L. Löber, Z. Wang, A. K. Chaubey, U. Kühn and J. Eckert: *Mater. Sci. Eng. A*, 2014, **A590**, 153–160.
- N. Read, W. Wang, K. Essa and M. M. Attallah: *Mater. Des.*, 2015, **65**, 417–424.
- S. Siddique, M. Imran, E. Wycisk, C. Emmelmann and F. Walther: *J. Mater. Process. Technol.*, 2015, 205–213.
- M. Simonelli, C. Tuck, N. Aboulkhair, I. Maskery, I. Ashcroft, R. Metall and R. Hague: *Metall. Mater. Trans. A*, 2015, 1–10.
- L. Thijss, K. Kempen, J.-P. Kruth and J. van Humbeeck: *Acta Mater.*, 2013, **61**, (5), 1809–1819.
- X. J. Wang, L. C. Zhang, M. H. Fang and T. B. Sercombe: *Mater. Sci. Eng. A*, 2014, **A597**, 370–375.
- Y. Birol: *J. Alloys Compd.*, 2007, **439**, (1–2), 81–86.
- Z. Chen, Y. Lei and H. Zhang: *J. Alloys Compd.*, 2011, **509**, (27), 7473–7477.
- J. H. Li, M. Z. Zarif, G. Dehm and P. Schumacher: *Philos. Mag.*, 2012, **92**, (31), 3789–3805.
- I. J. Polmear: ‘Light alloys: metallurgy of the light metals’, 1995, London, Arnold.
- Anon: ‘ASM handbook’ **Vol. 2**, ‘Properties and selection nonferrous alloys and special-purpose materials’; 1990, Materials Park, OH, ASM International.
- S. Hegde and K. N. Prabhu: *J. Mater. Sci.*, 2008, **43**, (9), 3009–3027.
- J. Hashim, L. Looney and M. S. J. Hashmi: *J. Mater. Process. Technol.*, 2002, **123**, (2), 251–257.
- K. Kambakas and P. Tsakiroopoulos: *Mater. Sci. Eng. A*, 2006, **A435–A436**, 187–192.
- J. Viala, M. Peronnet, F. Bosselet and J. Bouix: 1999.
- J. P. Davim: ‘Machining of metal matrix composites’, 2012, Springer.
- H. Kuhn: ‘Powder metallurgy processing: the techniques and analyses’, 2012, Burlington, Elsevier Science.
- M. K. Surappa: *Sadhana*, 2003, **28**, (1–2), 319–334.
- D. Gu, H. Wang, D. Dai, P. Yuan, W. Meiners and R. Poprawe: *Scr. Mater.*, 2015, **96**, 25–28.
- D. Gu, H. Wang, F. Chang, D. Dai, P. Yuan, Y. -C. Hagedorn and W. Meiners: *Phys. Procedia*, 2014, **56**, 108–116.
- S. K. Ghosh and P. Saha: *Mater. Des.*, 2011, **32**, (1), 139–145.
- S. Dadbakhsh and L. Hao: *Int. J. Adv. Manuf. Technol.*, 2014, **73**, (9–12), 1453–1463.
- V. Ocelik, J. A. Vreeling and J. T. M. De Hosson: *J. Mater. Sci.*, 2001, **36**, (20), 4845–4849.
- L. C. Astfalck, G. K. Kelly, X. Li, T. B. Sercombe, 2015, unpublished work.

Microstructure and Mechanical Properties of AlSi10Mg Parts Produced by the Laser Beam Additive Manufacturing (AM) Technology

Idan Rosenthal · Adin Stern · Nachum Frage

Received: 8 August 2014 / Revised: 28 September 2014 / Accepted: 8 October 2014 / Published online: 18 October 2014
© Springer Science+Business Media New York and ASM International 2014

Abstract Selective laser melting (SLM) is an additive manufacturing (AM) technique for fabrication of near net-shaped parts directly from computer-aided design data from a series of layers each one melted on top of the previous one by a laser beam. AlSi10Mg specimens were produced by the SLM technique from gas atomized pre-alloyed powders. The study shows the distinctive layered macrostructure, and the extremely fine cellular dendritic microstructure obtained by the SLM AM process, along with the remarkable tensile testing results for AlSi10Mg components. High thermal gradients determine the small grain sizes of the microstructure. Electron microscopy revealed anisotropy of the parts, inherent to the AM-SLM process, dependent on the build orientation. A ductile, dimpled failure mode was observed in these specimens as expected for a relatively ductile microstructure. It is shown that AlSi10Mg parts produced by SLM display room temperature mechanical properties comparable or even exceeding to those of conventionally cast AlSi10Mg.

Keywords Additive manufacturing · Al alloy · Selective laser melting · Mechanical properties

Introduction

Additive manufacturing (AM) is an appropriate approach for low volume production of geometrically complex lightweight structures. A limited number of investigations on AM of Al-based alloys by selective laser melting (SLM) have been reported [1–3]. There are some difficulties in the successful

AM by SLM of Al-based powders. First, the excellent thermal conductivity and high reflectivity (91%) of Al significantly increase the laser power required for melting and secondly, the oxidation of the alloys leads to entrapped oxide inclusions, which create weak spots within the components. The AM technique is a layer-by-layer manufacturing process. A single layer of metal is “deposited” upon a previous layer resulting in complex, time-dependent temperature profiles within the part being fabricated. The exposure period of the laser irradiation is in the range of milliseconds, and the process can be considered as high power density—short interaction time [4]. The microstructure of the as-built aluminum AM-SLM parts is reported to be a very fine cellular-dendrite solidification structure [2]. The formation of this fine dendritic structure upon laser treatment was previously observed in various laser processing techniques, such as laser surface remelting and laser deposition [5]. It was found by Dinda et al. that the high-energy density of the laser along with a directional heat transfer leads to a directional solidification [5]. Moreover, by repeating the deposition of the beads layer after layer, a [100] fiber or cube texture depending on the scanning direction is formed. It has to be pointed out that very high heat inputs during laser deposition process results in a width of a deposited layer of about 1 mm, while a width of a track typically formed in AM-SLM is only 100 μm . In this paper, we describe the unique macro- and microstructural architectures and tensile properties of AM-SLM processed AlSi10Mg alloy.

Experimental

SLM System and the Building Process

The machine for AM is equipped with a 400 W Nd-YAG laser, and a scanning velocity of about 1 m/s was applied.

I. Rosenthal (✉) · A. Stern · N. Frage
Materials Engineering Department, Ben-Gurion University of
the Negev, P.O Box 653, 8410501 Beersheba, Israel
e-mail: idanros@bgu.ac.il

Particle size of the AlSi10Mg alloy powder was in the range of 25–50 μm . The starting AlSi10Mg powder was characterized by x-ray diffraction (XRD). Tensile specimens were built in two different directions (vertically and horizontally) and underwent machining with surface roughness and tolerances in accordance with the ASTM E-8 (round specimen, spec 3) standard. The specimens were manufactured using a technique referred to as strip scanning with a continuous change of the scanning direction between each successive layer. The specimens were divided to 8-mm-wide stripes, which were scanned back and forth. Throughout the scans, there were overlapping areas, resulting in remelting of previously melted and solidified regions. Density of the samples was about 2.63 g/cm^3 . All the built parts underwent a stress-relieving heat treatment at 300 °C for 2 h.

Optical and Electron Microscopy (OM and SEM)

The macro- and microstructure of the specimens were characterized by optical and scanning electron microscopy (SEM), equipped with an energy-dispersive spectrometer. The specimens were prepared by conventional metallographic methods, with a fine 0.5 μm diamond polish and etched using Flick's reagent (90% H_2O_2 , 10% HF).

Mechanical Properties

Tensile tests were conducted using a universal testing machine. A series of six specimens with two differing build directions were tested, and the stress-strain curves were analyzed. Microhardness tests were conducted using a microhardness tester with 100gf load. The fracture surface was observed in order to clarify the failure mode and its correlation with the microstructure.

Results and Discussion

Alloy Microstructure

Solidification and phase transformations of Al-Si alloys occur according to the Al-Si phase diagram (Fig. 1), with a eutectic composition of about 11–12 wt% of Si. The alloy used in this work is close to the eutectic point, and a lamellar microstructure is expected after solidification and cooling. Actually, this kind of the microstructure is commonly observed in Al-Si cast alloys with similar Si contents (Fig. 2).

The SLM process of adding material track after track and layer after layer together with the fast and directional cooling rates creates a unique macrostructure in the components (Fig. 3). The macrostructure is determined by the

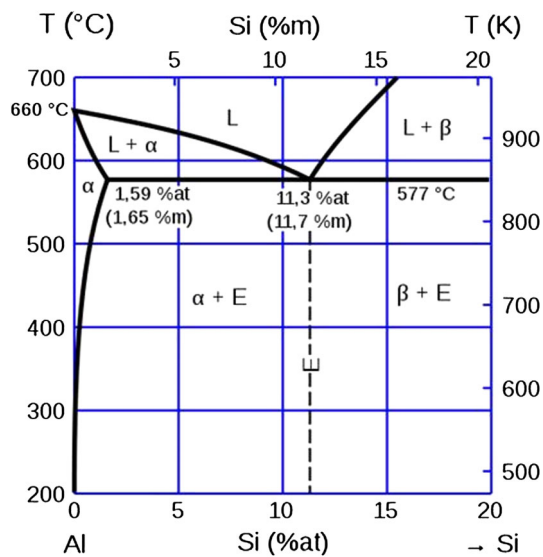


Fig. 1 Eutectic region of an Al-Si phase diagram (Makhoul and Guthy [6])

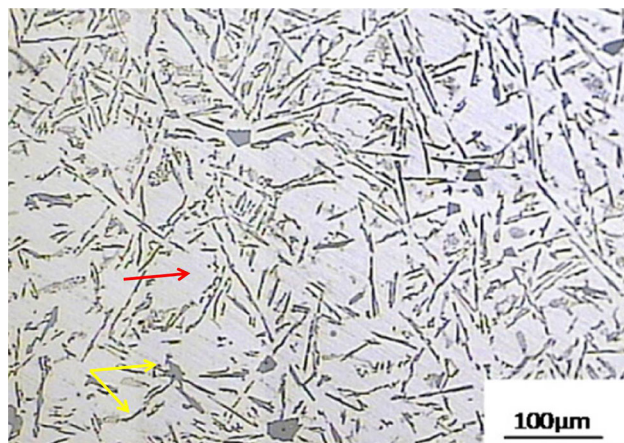


Fig. 2 Typical microstructure of an Al-Si cast alloy. Red arrow marks the Al matrix; Yellow arrows mark the Si particles in the eutectic mixture [7]

way in which the different individual melt pools are combined. In other words, it is defined by the method of scanning the product's cross section and is also known as the building strategy of the component. In Fig. 3(a) and (b), two cross-sectional views are shown: top and front views. It is shown that the solidified melt pools are approximately half-cylindrical in shape, and the approximate size can be determined based on the cross section of the front view. The melt pool height was determined to be about 150 μm and the width to be about 300 μm (Fig. 4). The applied hatch spacing of 200 μm causes an overlap of about 33% of the melt pool width between neighboring scan tracks. Due to the half-cylindrical shape of the melt pool and the

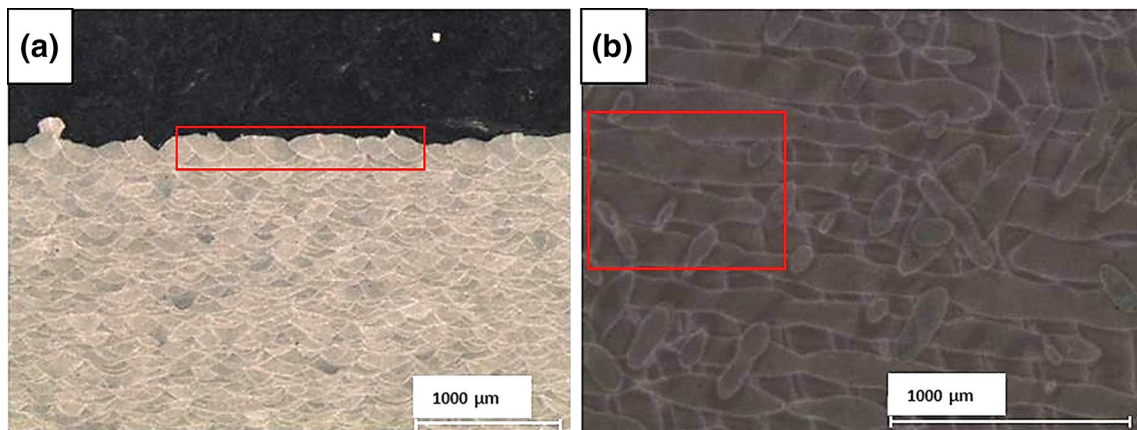


Fig. 3 Macrostructure of the specimens, examples for track segments are marked in red: (a) front view showing the “fish scale” morphology with melt pool overlapping; (b) top view showing variation of shape and discontinuity of the melt pools produced in different layers



Fig. 4 Close up of track segments, showing the dimensions of the half-cylindrical melt pools. Early formation of a defect can be seen marked by the arrow

partial remelting of formerly deposited layers, the cross section of melt pools from different layers can be observed in the top view. Due to the variations in depth and shape of the melt pools, they are not always continuous; melt pools produced in up to four different layers are marked in Fig. 3(b).

The microstructure of the components fabricated by the AM method is the end result of pre-alloyed powder melting/solidification, while the adjacent neighboring tracks cause partial remelting of the solidified tracks. During the build process, each initial seam was remelted locally up to four times, ensuring chemical homogeneity and microstructural regularity of the final structure. The combined effect of directional cooling and rapid solidification induced by repeated thermal cycles has a profound influence on the microstructures of the alloy deposited as explained in the previous paragraph. The microstructure of

the AM samples differs completely from those fabricated by casting (as seen in Fig. 2). This has a direct effect on mechanical properties and is addressed in the mechanical properties section.

For both building directions, the microstructures within each layer share similarities and depend on the level of thermal gradient and its direction at the boundary of the moving fusion zone (FZ). Three main areas of different microstructures are observed in the samples (Fig. 4), namely 1-coarse FZ, 3-fine FZ cellular structure inside the melt pool, and 2-heat-affected zone (HAZ) appearing as broken cells between the FZs. The relatively narrow HAZ is attributed to the limited amount of heat from the concentrated laser beam.

The intercellular network is broken outside the FZ (area 2) by coarsening of the silicon phase into idiomorphic

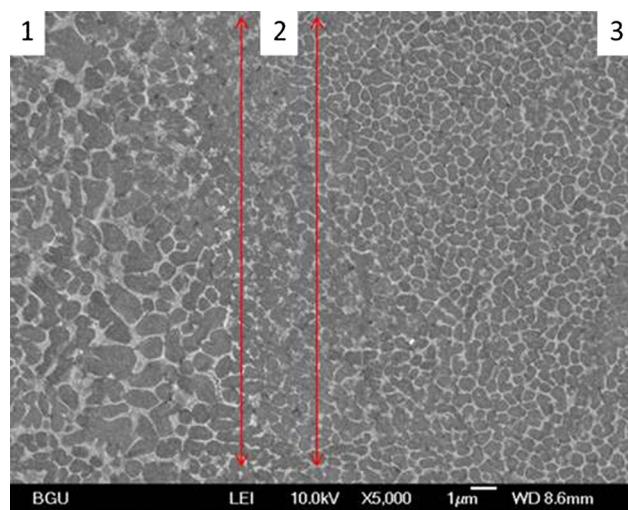


Fig. 5 Microstructures of the fusion zone; 1—coarse fusion zone; 2—heat-affected zone; 3—fine fusion zone

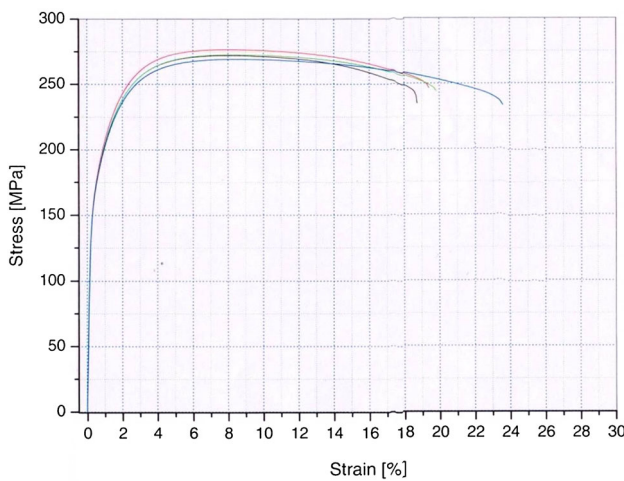


Fig. 6 Engineering stress–strain curves for the vertical build direction specimens

Table 2 Properties of the specimens fabricated in the horizontal build direction

Young's modulus, GPa	Yield stress, MPa	UTS, MPa	Elongation at UTS, %
71.3	168	267	8.6
69.0	170	267	9.5

particles, as a result of the formation of a narrow partially melted zone in the HAZ adjacent to the fusion front. The fast melting process of the stochastic powder bed can induce vigorous melt pool movements which sometimes lead to faults acting as starting points for defects such as channels and/or pores bridging between layers.

Some semi-quantitative correlations between microstructure and SLM parameters may be derived from the experimental observations and data reported in literature [2, 8, 9]. The solidification structure depends on the thermal gradient in the melt pool (G , K/m) and the growth rate (R , m/s) [8]. The growth rate (R) depends on the speed of the moving laser beam or heat source (V) and the angle between the direction of the moving source and the growth direction of the solidifying material. The G/R ratio determines the stability of the solidification front and the resulting solidification mode. For an increasing R and a constant G , the solidification can change from a stable planar solidification front, at low values of R , to cellular and finally dendrite solidification morphologies with increasing values of R . The product of G and R (K/s) gives the cooling rate, and the higher product yields a finer structure [8].

Over the course of AM-SLM, the thermal gradient and growth rate vary over the FZ. The growth rate even reaches zero at the melt pool edge, where the laser movement direction is perpendicular to the heat transfer direction.

According to Fig. 4, the morphology of the solidification structure does not change throughout the sample, while the degree of grain size does vary. This means that the G/R ratio is approximately constant and both G and R change in a similar way; however, the product of G and R varies notably.

In order to roughly estimate the R value for the AM-SLM process, we used the experimental value of cooling rate 10^6 K/s, obtained during rapid solidification of 40-μm-thick ribbons of Al-12 wt% Si [9] and the highest temperature gradient in the FZ (10^6 K/m) suggested by Thijs et al. [2]. Thus, the calculated R value is about 1000 mm/s.

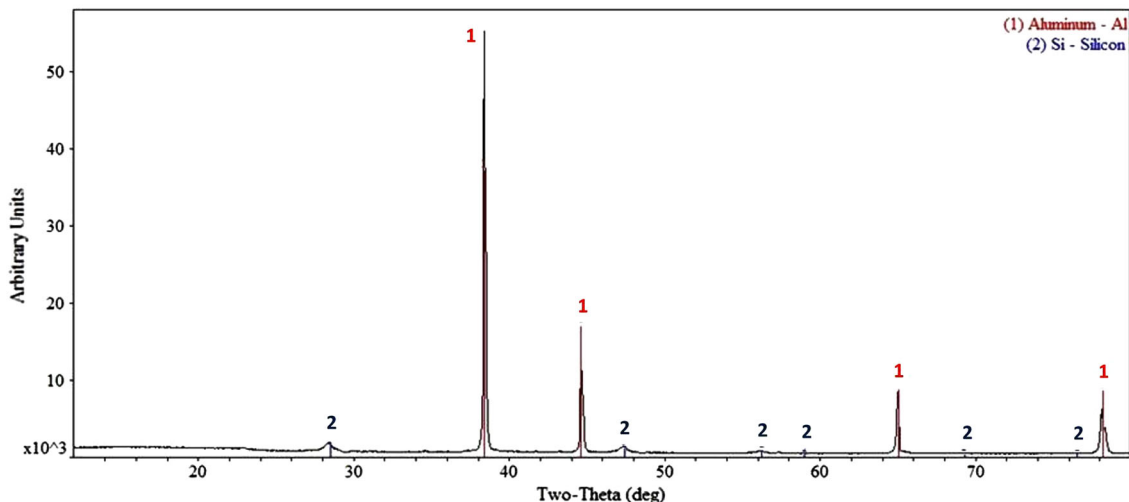


Fig. 7 XRD results for the AlSi10Mg AM-SLM processed part showing peaks in relation to the Al phase (1) and Si phase (2)

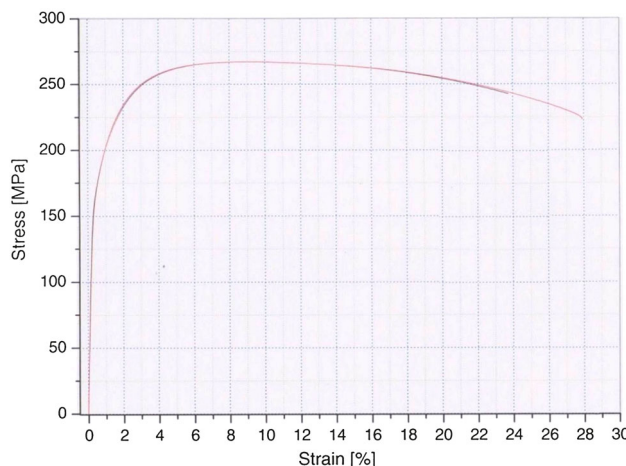


Fig. 8 Engineering stress–strain curves for the horizontal direction specimens

This value is close to the scanning velocity of the laser beam used in this research.

Tensile Properties

Samples Fabricated in the Vertical Build Direction

The results of testing are given in Table 1 and Fig. 5.

There are no remarkable differences between mechanical properties of the heat-treated cast alloys [10, 11] and the AM samples, except for the values of elongation which are significantly higher than those reported in the literature for cast alloys after T6 treatment (3.5% elongation). The improved elongation of the AM-processed parts is attributed to the fine microstructure. Moreover, in regular Al–Si cast alloys, a strengthening mechanism is related to the formation of Mg₂Si precipitates. However, in AM parts,

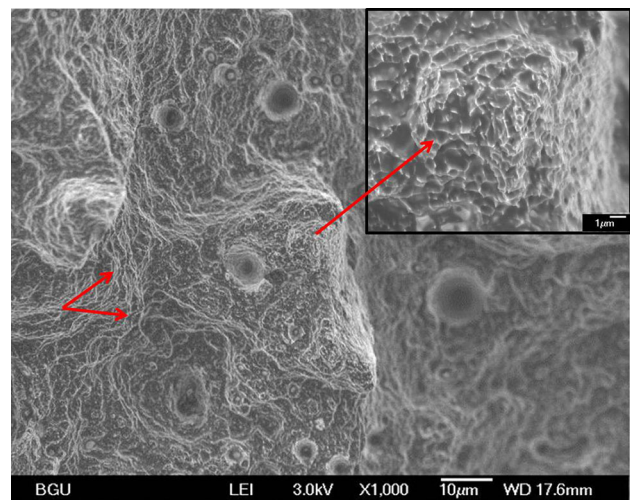


Fig. 10 Fracture surface of the specimen built in the horizontal direction. Arrows mark the “dimpled ridges”; a higher magnification is shown in the *top right corner*

these precipitates were not detected by SEM (Fig. 4) and XRD analysis (Fig. 6). The absence of the precipitates may also lead to the increase in elongation value.

Samples Fabricated in the Horizontal Direction

The results of testing are given in Table 2 and Fig. 7.

The main difference in the properties of the specimens fabricated in horizontal direction compared with vertically built specimens is the higher values of the elongation. This reflects an expected anisotropy of AM specimens, since a directional solidification takes place during the process.

Microhardness of the AM specimens fabricated in both horizontal and vertical build directions was about 94 ± 5 HV (Fig. 8).

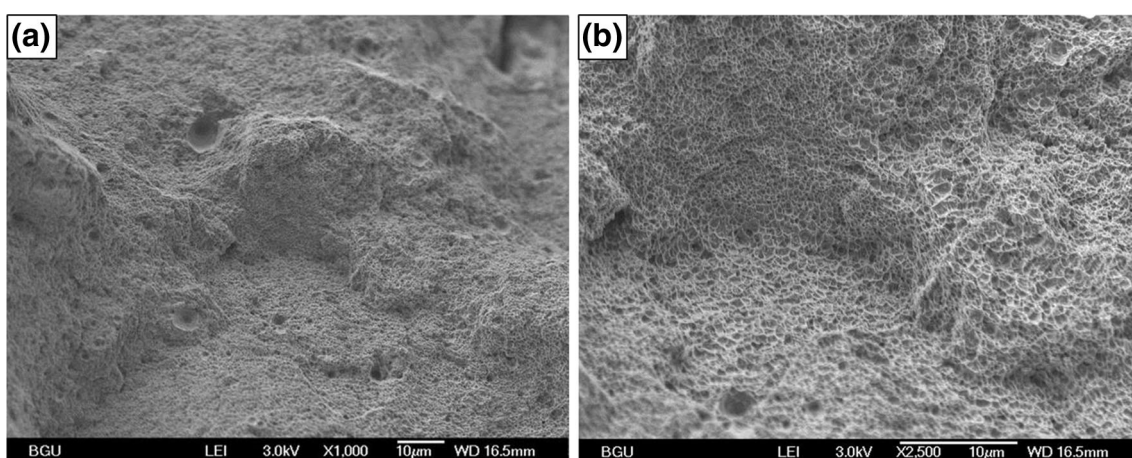


Fig. 9 Fracture surface of the specimen fabricated in the vertical build direction. (a) The dimpled structure between weakly bonded layers is revealed. (b) Higher magnification of the fine dimples

Fractography

The specimen fabricated in the vertical building direction exhibited a predominantly ductile failure (dimpled structure) located in-between weakly bonded layers (Fig. 9a). The extremely fine cellular Al–Si eutectic microstructure is discernible (Fig. 9b), and no un-melted starting powder particles were detected. Only micro-porosity (10–50 μm) was observed which can be attributed to gas entrapment (Fig. 9a).

The fracture surface of the horizontally built specimen (Fig. 10) differs completely from the vertical build direction specimens and further confirms the anisotropy attained during the AM process. This specimen displays fine dimples, without a visible cellular structure, but rather dense lines along ridges. Pores are still present in this specimen, suggesting their relation to the process. As opposed to the failure in-between weakly bonded layers of the samples fabricated in the vertical build direction, the failure of the sample fabricated in the horizontal direction occurs within each layer and provides the slightly higher elongation values (see Tables 1, 2).

Conclusions

Macro- and microstructure along with mechanical properties of the parts fabricated by AM-SLM process were investigated. The macrostructure of the product is a collage of solidified track segments, which were remelted several times by the adjacent neighboring tracks. The microstructure consists of fine cellular dendrites, which reflect high thermal gradients and rapid progression of the scanning laser during the AM process. Microstructural analysis revealed anisotropy of specimens depending on the building direction. AM-SLM processed specimens have significantly improved elongation properties in comparison to specimens fabricated by conventional casting processes. The analysis of the fracture surfaces indicates a ductile

mode of failure and the presence of the residual porosity. Further investigation has to be conducted in order to clarify the effect of processing parameters on the microstructure and the mechanical properties of products.

Acknowledgments We would like to thank Sharon Tuvia (1982) Ltd. for providing the facilities and materials for this research. We would also like to thank Ofer Sabag, Asher Turgeman and Moshe Cohen from the NRCN for their assistance with mechanical testing.

References

- D. Buchbinder, H. Schleifenbaum, S. Heidrich, W. Meiners, J. Bültmann, High Power Selective Laser Melting (HP SLM) of Aluminum Parts. *Phys. Proc.* **12**, 271–278 (2011)
- L. Thijs, K. Kempen, J.P. Kruth, J.V. Humbeeck, Fine-Structured Aluminium Products with Controllable Texture by Selective Laser Melting of Pre-alloyed AlSi10Mg Powder. *Acta Mater.* **61**, 1809–1819 (2013)
- E. Brandl, U. Heckenberger, V. Holzinger, D. Buchbinder, Additive Manufactured AlSi10Mg Samples using Selective Laser Melting (SLM): Microstructure, High Cycle Fatigue and Fracture Behavior. *Mater. Des.* **34**, 159–169 (2012)
- W.M. Steen, *Laser material processing*, 3rd edn. (Springer, Berlin, 2003), pp. 279–284
- G.P. Dinda, A.K. Dasgupta, J. Mazumder, Evolution of microstructure in laser deposited Al–11.28%Si alloy. *Surf. Coat. Technol.* **206**, 2152–2160 (2012)
- M.M. Makhlof, H.V. Gathy, The aluminum–silicon eutectic reaction: mechanisms and crystallography. *J. Light Met.* **1**, 199–218 (2001)
- R. Wang, W. Lu, Direct electrolytic Al–Si alloys (DEASA)—an undercooled alloy self-modified structure and mechanical properties, in *Electrolysis*, ed. by V. Linkov (Intech, Rijeka, 2012), pp. 107–140
- S. Kou, *Welding Metallurgy*, 2nd edn. (Wiley, New Jersey, 2003)
- Y. Birol, Microstructural characterization of a rapidly-solidified Al–12 wt% Si alloy. *J. Mater. Sci.* **31**, 2139–2143 (1996)
- ASTM Standard B26/B26M, *Standard Specification for Aluminum-Alloy Sand Casting* (ASTM International, West Cons-hohocken, 2012)
- K. Kempen, J. Thijs, J.V. Humbeeck, J.-P. Kruth, Mechanical properties of AlSi10Mg produced by selective laser melting. *Phys. Proc.* **39**, 439–446 (2012)

The Effect of Atmosphere on the Structure and Properties of Selective Laser Melted Al-12Si Alloy

X. J. Wang^{a,b}, X.P. Li^a, L. C. Zhang^c, M. H. Fang^b, and T. B. Sercombe^{a,*}

^a*School of Mechanical and Chemical Engineering, The University of Western Australia, 35 Stirling Highway, Crawley, Perth, WA 6009, Australia*

^b*School of Materials Science and Technology, China University of Geosciences (Beijing), No. 29 Xueyuan Road, Haidian District, Beijing 100083, China*

^c*School of Engineering, Edith Cowan University, 270 Joondalup Drive, Joondalup, Perth, WA 6027, Australia*

Abstract

Al-12Si components were manufactured by Selective Laser Melting (SLM) using three different atmospheres: argon, nitrogen and helium. The atmosphere type did not affect the part's density or hardness and all components reached near full relative density (>97%). The mechanical properties of the components produced in Ar and N₂ were superior to those in He, especially the ductility, which has been attributed to the formation of pore clusters in the microstructure. The mechanical properties in SLM-produced components are superior to those produced using conventional method.

Keywords: Aluminium alloys; selective laser melting; mechanical properties; Atmosphere; microstructure; atmosphere

* Corresponding author. Email: tim.sercombe@uwa.edu.au

Introduction

Aluminium and its alloys are widely used in engineering structures and components because of its light weight and high corrosion resistance. Traditional fabrication methods of aluminium components such as casting, forging, and extrusion require tooling or dies to shape the parts. These are relatively expensive and time-consuming to produce, especially for small production runs of complex parts. Indirect rapid manufacturing of aluminium components is possible, but requires a two-stage process of green part production followed by infiltration [1]. It therefore takes 2-3 days to produce a part. There are other indirect methods but they typically require the production of a lost wax model and subsequent investment casting, which is not a true rapid manufacturing technology as it still requires the fabrication of a mould. More recently, the production of aluminium components directly from a computer model has become possible through a process known as Selective Laser Melting (SLM) [2-9]. During the SLM process, a high intensity laser beam selectively scans a thin powder bed, melting the metal particles which solidify to form a solid layer. The build platform then moves down by the thickness of one layer (typically 50-100 μm), a new layer of powder is deposited on top and the process continues until the part is complete. One of the key advantages of SLM is its ability to produce near net for any tooling or machining [1, 10-12]. For the SLM of aluminium, work has concentrated on the processing of an alloy commonly referred to as AlSi10Mg (nominal composition Al – 10 wt% Si - 0.4 wt% Mg) [2, 3, 6-9], which is equivalent to the casting alloy A360.0 [13]. There has been considerably less work published on Al-12Si and 6061[4, 5], both of which reported low densities.

Selective Laser Melting is a complex physical metallurgical process, involving many parameters (typically including scanning speed, laser power, scan spacing, layer thickness, and scanning strategy), and it therefore requires a comprehensive understanding of the effect of these for optimal manufacturing. Considerable effort has been expended on a wide range of materials (including aluminium) to optimize the parameters with the aim of improving density (see, for example, [4, 5, 11, 14, 15]) and surface quality/roughness [8, 11, 16, 17]. In addition, the build orientation has been shown to have an effect on the properties of SLM produced parts, with the vertical (build) direction resulting in the lowest properties [6, 18, 19]. Among all the processing parameters, the effect of laser scan speed, laser power, layer thickness has been the most widely studied. In contrast, there has only been a small amount of work focused on the effect of atmospheric oxygen content on the quality of laser melted parts [20]. For the processing of Al-based alloys, the atmosphere used has been either Ar [2, 4-7] or not stated [3, 8, 9]. Hence it is apparent that role of the atmosphere type has not been studied in detail.

During the conventional press-and-sinter processing of metals, the atmosphere is often reactive and used for such purposes as oxide reduction and binder/lubricant removal [21]. For the sintering of aluminium, it is generally considered that a nitrogen atmosphere is more effective for densification than other atmospheres [22, 23]. This has been attributed to the reaction of the Al with the nitrogen to form aluminium nitride [22-25]. However, little has been reported on the role of the atmosphere during Selective Laser Melting. In this work, we have reported that the atmosphere type has essentially no effect on the densification process during selective laser melting but

does have some effect on the mechanical properties of the resultant parts.

Experimental

The details of the Al-12Si powder used in this work are summarized in Table 1. The composition of the powder was measured using inductively coupled plasma atomic emission spectroscopy (Spectrometer Services Victoria, Australia). Flowability and apparent density was measured according to Metal Powder Industries Federation Standards 03 and 04 [26], respectively. Nitrogen content of laser melted parts was measured using Leco nitrogen analysis (Spectrometer Services Victoria, Australia). Three samples from each atmosphere were analysed. The particle size was measured using a Malvern Mastersizer Plus. A scanning electron image (Tescan Vega3) of the powder, Figure 1, shows that it is almost spherical in shape, and contains significant numbers of satellites. Selective laser melting was performed on a Realizer SLM 100 (ReAlizer GmbH, Germany). Prior to building the chamber was purged with either an argon, nitrogen or helium atmosphere until the oxygen content was <0.1%. In all cases, the gases were of high purity, containing <10ppm O₂. During building, a slight positive pressure of 10 to 30 mbar was maintained inside the chamber. Cubes with dimension of 10 × 10 × 10 mm³ were manufactured using a laser power (at the part bed) of 200 W ($\lambda=1.06\mu\text{m}$), laser beam diameter of 35μm, laser scan speeds between 375 – 2000 mm s⁻¹, and hatch spacing (distance between scan lines) of 0.15 mm. Parts were built by scanning the laser across the surface in 3mm stripes. The direction of scanning was rotated through 90° between successive layers. The layer thickness was kept constant at 50 μm. Density was measured using Archimedes' method, following Metal Powder Industries Federation Standard 42

[26], and is presented as a percentage of the theoretical density ($2.65\text{g}/\text{cm}^3$). For each condition, three specimens were measured and the results averaged. The microstructure of the XZ (vertical) section was examined by mounting the samples in epoxy and polishing using standard metallographic techniques. Optical microscopy was performed on unetched samples using an Olympus PMG3 optical microscope. The microstructure was also investigated at high magnification using a Zeiss 1555 VP-FESEM. Vickers Hardness was measured on the polished cross-sections using a Mitutoya AVK-C2 Hardness Tester with a 20 g load. An average of twelve indents was taken for each condition. Tensile tests were carried out on as fabricated, but machined specimens, using an Instron 5982 machine at a cross head speed of 1mm/min. The samples had a cross-sectional area of 4 x 6mm and the size of the parallel gauge length was 16mm. The reported tensile properties are the average of five individual samples that had been built aligned to the x-direction (i.e. perpendicular to the build direction), as shown in Figure 2.

Results and Discussion

Figure 3 shows the effect of incident volumetric laser energy density and laser scan speed on the density of the SLM-produced samples under high purity argon, nitrogen and helium atmospheres. The volumetric laser energy density, E , is a key factor that affects the quality of parts fabricated by selective laser melting and is a measure of the energy supplied by the laser beam to a volumetric unit of powder and is defined by [15]

$$E = \frac{P}{v \cdot h \cdot t} \quad \text{Equation 1}$$

where P is the laser power (W), v is the scan speed (mm s^{-1}), h is the hatch spacing (mm), and t is the layer thickness (mm). As Equation 1 shows, a lower laser power

and/or higher scan speed, hatch distance or layer thickness decreases the laser energy density, which is needed to heat and melt the powder. From Figure 3, it is apparent that for all atmospheres, the density of the samples increases with increasing E up to $\sim 30 \text{ J/mm}^3$, at which point the samples are $>97\%$ dense. Further increasing the energy did not result in any improvement in the density. Hence, it appears that once the powder has become fully molten, there is little benefit in increasing the energy further. In fact, excess energy can be detrimental for the surface finish as it can result in balling [16]. Below this threshold energy level of $\sim 30 \text{ J/mm}^3$, there is insufficient energy to completely melt the powder, which results in porosity and a decrease in density [5]. In all three atmospheres, the same trend is evident, and it may be concluded that there is no significant difference in density between using argon, nitrogen or helium atmospheres.

The Vickers hardness at different scan speeds (volume energy densities) is shown in Figure 4. By comparing Figure 3 with Figure 4, it is apparent that there is a strong correlation between Vickers hardness and density. Again, the atmosphere has essentially no effect on the Vickers Hardness and the peak hardness measured was $\sim 115 \text{ HV}$, which is significantly higher than reported values of as-cast Al-12Si ($\sim 85 \text{ HV}$) [27] and similar is similar to what has been reported from a Selective Laser Melted AlSi10Mg alloy [6, 9].

Figure 5 shows the microstructure of the vertical section (X-Z) of parts produced under argon, nitrogen and helium at a scan speed of 500 mm s^{-1} ($>97\%$ density). This Figure shows the microstructure over a range of magnifications. Fig 5(a), (c), (e) and (g) are at a low magnification and show the general structure of the material. In Figure

5(b), (d), and (f) the microstructure is shown at higher magnification, including an insert which is a high resolution SEM image. In these micrographs, the laser tracks created during the SLM processing are clearly visible. These tracks are typical microstructural features in samples manufactured by selective laser melting [2, 3, 7, 9]. The microstructures produced in the three different atmospheres are very similar over the range of magnifications shown. The structure consists of a cellular Al matrix, surrounded by a nano-meter sized Si particle (the light particles in the insert of Fig 5(b), (d) and (f)). It is apparent that the powders have completely melted and resolidified very quickly, resulting in a microstructure similar to that of rapidly solidified Al-12Si ribbons [28]. The fine scale of the microstructure it a possible reason for the improved hardness over conventionally cast material. For the samples processed in Ar and N₂ there is a small amount porosity remaining in the structure (dark dots in Fig 5(a) and (c)). In He however, there seems to be two different microstructure formed (in terms of porosity). The majority of the microstructure is similar to that produced in Ar or N₂, and is shown Fig 5(e). However, in isolated areas, a high porosity region occurs, Fig 5(g), which consists of spherical pores up to approximately 50µm in diameter. It is apparent that the size of these areas is quite low, as the overall density is unaffected. Why such porous regions form is not currently understood, however they have a consequence for the mechanical properties, as discussed below.

The as-processed tensile properties at different energy levels/scan speeds are shown in Figure 6. Similar to the density and hardness, there is an overall trend of increasing strength and ductility with increasing laser energy density for all three

atmospheres. At low laser energies, the high level of porosity degrades the tensile properties of the material, irrespective of the atmosphere used. An increase porosity causing an adverse effect on the properties has been well documented for both casting [29-32] and Selective Laser Melting [12, 33, 34]. However, when processed under the same conditions (which produces parts of the same density – see Figure 3), samples produced in He have reduced ductility and also slightly lower ultimate tensile strength, compared to those samples produced in Ar and N₂. This difference is also shown in Table 2. For these samples, which have all been processed at a laser scan speed of 500mm/s, there is no statistical difference in the density. However, it is evident that the properties, especially the ductility, are significantly lower in He than in Ar or N₂ (which have similar properties). The reason for the lower ductility may be explained with reference to Figure 7. This Figure shows that the sample processed in He contains significantly more porosity on the fracture surface than those produced in Ar or N₂. The properties, particular the ductility, of cast Al-Si alloys have a strong correlation with the amount of porosity present on the fracture surface [35, 36]. In particular, it is the projected area of the micro-voids on the fracture surface, rather than the volumetric porosity as measured by the bulk density, that is most important [37, 38]. Since SLM can be considered as repeated micro-scaled casting events, it is not surprising that the same effects appear to be occurring here. Although the overall bulk density is similar in all three atmospheres, there is clustering of pores in the samples produced in He, through which the failure occurs (Figure 7(c)). These clusters, therefore, contribute to the reduced ductility of the samples produced in He.

There is no significant difference in the mechanical properties (Table 3) or nitrogen content (Table 3) of the samples processed in Ar or N₂. During conventional sintering, enhanced densification occurred due to the formation of AlN, which takes some time to form [39]. However, during SLM, the material is only molten for very short time and therefore it is unsurprising that AlN does not form.

Table 2 also compares the mechanical properties of the Al-12Si alloy manufactured by SLM with those of conventionally cast material. The SLM-produced Al-12Si alloy (in an Ar or N₂ atmosphere) has significantly superior properties over the as-cast material. For example, compared with the as-cast properties, the SLM-produced material has approximately 1.5 times the yield strength, 20% greater ultimate tensile strength, and double the elongation to failure. This can be attributed to the morphology of the Si phase, which is present as small, rounded particles in the SLM produced materials compared with the coarse needles typical of castings. Similar improved properties over cast material has been reported in Selective Laser Melted AlSi10Mg [3, 6, 9].

It appears that the role of the atmosphere is only to protect the sample from oxidation and it is not playing an active role in the processes. Due to the fact that there is no difference in processing between Ar and N₂, reduced manufacturing costs may be achieved by using lower cost N₂, rather than the customary Ar.

Conclusion

Samples from an Al-12Si alloy were manufactured by selective laser melting using argon, nitrogen and helium atmospheres. Unlike the conventional sintering of aluminum in which N₂ is the preferred atmosphere, there is no significant difference in density or hardness when using argon, nitrogen or helium. However, results have

shown that a He atmosphere produces lower ductility, probably a result of the formation of pore clusters in the microstructure. Both argon and nitrogen atmospheres result in the SLM produced parts having significantly enhanced properties compared with conventionally produced material: 1.5 times the yield strength, 20% higher ultimate tensile strength and twice the elongation to failure.

Acknowledgements

This research was supported under the Australian Research Council's Discovery Projects funding scheme (DP0986067) and LIEF grant (LE110100094).

References

1. Sercombe, T.B. and G.B. Schaffer, *Rapid Manufacturing of Aluminum Components*. Science, 2003. **301**(5637): p. 1225-1227.
2. Brandl, E., et al., *Additive manufactured AlSi10Mg samples using Selective Laser Melting (SLM): Microstructure, high cycle fatigue, and fracture behavior*. Materials & Design, 2012. **34**(0): p. 159-169.
3. Buchbinder, D., et al., *High Power Selective Laser Melting (HP SLM) of Aluminum Parts*. Physics Procedia, 2011. **12, Part A**(0): p. 271-278.
4. Louvis, E., P. Fox, and C.J. Sutcliffe, *Selective laser melting of aluminium components*. Journal of Materials Processing Technology, 2011. **211**(2): p. 275-284.
5. Olakanmi, E.O., R.F. Cochrane, and K.W. Dalgarno, *Densification mechanism and microstructural evolution in selective laser sintering of Al–12Si powders*. Journal of Materials Processing Technology, 2011. **211**(1): p. 113-121.
6. Kempen, K., et al., *Mechanical Properties of AlSi10Mg Produced by Selective Laser Melting*. Physics Procedia, 2012. **39**(0): p. 439-446.
7. Thijss, L., et al., *Fine-structured aluminium products with controllable texture by selective laser melting of pre-alloyed AlSi10Mg powder*. Acta Materialia, 2013. **61**(5): p. 1809-1819.
8. Calignano, F., et al., *Influence of process parameters on surface roughness of aluminum parts produced by DMLS*. The International Journal of Advanced Manufacturing Technology, 2013. **67**(9-12): p. 2743-2751.
9. Manfredi, D., et al., *From Powders to Dense Metal Parts: Characterization of a Commercial AlSiMg Alloy Processed through Direct Metal Laser Sintering*. Materials, 2013. **6**(3): p. 856-869.
10. Roberts, A.P., et al., *Elastic moduli of sintered powders with application to components fabricated using selective laser melting*. Acta Materialia, 2011. **59**(13): p. 5257-5265.
11. Yasa, E., D. Jan, and K. Jean-Pierre, *The investigation of the influence of laser re-melting on density, surface quality and microstructure of selective laser melting parts*. Rapid Prototyping Journal, 2011. **17**(5): p. 312-327.
12. Zhang, L.C., et al., *Manufacture by selective laser melting and mechanical behavior of a biomedical Ti-24Nb-4Zr-8Sn alloy*. Scripta Materialia, 2011. **65**(1): p. 21-24.
13. *ASM handbook Vol 15 - Casting*. 1990, Materials Park, Ohio: ASM International.
14. Li, R., et al., *Densification behavior of gas and water atomized 316L stainless steel powder during selective laser melting*. Applied Surface Science, 2010. **256**(13): p. 4350-4356.
15. Simchi, A., *Direct laser sintering of metal powders: Mechanism, kinetics and microstructural features*. Materials Science and Engineering: A, 2006. **428**(1-2): p. 148-158.
16. Gu, D. and Y. Shen, *Balling phenomena in direct laser sintering of stainless steel powder: Metallurgical mechanisms and control methods*. Materials & Design, 2009. **30**(8): p. 2903-2910.
17. Spierings, A.B., N. Herres, and G. Levy, *Influence of the particle size distribution on surface quality and mechanical properties in AM steel parts*. Rapid Prototyping Journal, 2011. **17**(3): p. 195-202.
18. Chlebus, E., et al., *Microstructure and mechanical behaviour of Ti—6Al—7Nb alloy produced by selective laser melting*. Materials Characterization, 2011. **62**(5): p. 488-495.
19. Takaichi, A., et al., *Microstructures and mechanical properties of Co—29Cr—6Mo alloy*

- fabricated by selective laser melting process for dental applications.* Journal of the Mechanical Behavior of Biomedical Materials, 2013. **21**(0): p. 67-76.
20. Rombouts, M., et al., *Fundamentals of Selective Laser Melting of alloyed steel powders*. CIRP Annals - Manufacturing Technology, 2006. **55**(1): p. 187-192.
21. German, R.M., *Powder metallurgy and Particualte Materials Processing*. 2005, Princeton, N.J.: Metal Powder Industries Federation.
22. Schaffer, G.B. and B.J. Hall, *The influence of the atmosphere on the sintering of aluminum*. Metallurgical and Materials Transactions A, 2002. **33**(10): p. 3279-3284.
23. Schaffer, G.B., et al., *The effect of the atmosphere and the role of pore filling on the sintering of aluminium*. Acta Materialia, 2006. **54**(1): p. 131-138.
24. Kent, D., et al., *A novel method for the production of aluminium nitride*. Scripta Materialia, 2006. **54**(12): p. 2125-2129.
25. MacAskill, I.A., et al., *Effects of magnesium, tin and nitrogen on the sintering response of aluminum powder*. Journal of Materials Processing Technology, 2010. **210**(15): p. 2252-2260.
26. *Standard Test Methods for Metal Powders and Powder Metallurgy Products*. 2009, Princeton, New Jersey USA: Metal Powder Industries Federation
27. Basavakumar, K.G., P.G. Mukunda, and M. Chakraborty, *Dry sliding wear behaviour of Al-12Si and Al-12Si-3Cu cast alloys*. Materials & Design, 2009. **30**(4): p. 1258-1267.
28. Birol, Y., *Microstructural evolution during annealing of a rapidly solidified Al-12Si alloy*. Journal of Alloys and Compounds, 2007. **439**(1-2): p. 81-86.
29. Rice, R.W., *Comparison of stress concentration versus minimum solid area based mechanical property-porosity relations*. Journal Of Materials Science, 1993. **28**(8): p. 2187-2190.
30. Roy, N., A.M. Samuel, and F.H. Samuel, *Porosity formation in Al-9 Wt Pct Si-3 Wt Pct Cu alloy systems: Metallographic observations*. Metallurgical and Materials Transactions A, 1996. **27**(2): p. 415-429.
31. Samuel, A.M. and F.H. Samuel, *A metallographic study of porosity and fracture behavior in relation to the tensile properties in 319.2 end chill castings*. Metallurgical and Materials Transactions A, 1995. **26**(9): p. 2359-2372.
32. Sun, X., K.S. Choi, and D.S. Li, *Predicting the influence of pore characteristics on ductility of thin-walled high pressure die casting magnesium*. Materials Science and Engineering: A, 2013. **572**(0): p. 45-55.
33. Kruth, J.P., et al., *Selective laser melting of iron-based powder*. Journal of Materials Processing Technology, 2004. **149**(1-3): p. 616-622.
34. Li, R., et al., *316L Stainless Steel with Gradient Porosity Fabricated by Selective Laser Melting*. Journal of Materials Engineering and Performance, 2010. **19**(5): p. 666-671.
35. Gokhale, A.M. and G.R. Patel, *Origins of variability in the fracture-related mechanical properties of a tilt-pour-permanent-mold cast Al-alloy*. Scripta Materialia, 2005. **52**(3): p. 237-241.
36. Surappa, M.K., E. Blank, and J.C. Jaquet, *Effect of macro-porosity on the strength and ductility of cast Al 7Si 0.3Mg alloy*. Scripta Metallurgica, 1986. **20**(9): p. 1281-1286.
37. Lee, C.D., *Effects of microporosity on tensile properties of A356 aluminum alloy*. Materials Science and Engineering: A, 2007. **464**(1-2): p. 249-254.
38. Lee, C.D., *Variability in the tensile properties of squeeze-cast Al-Si-Cu-Mg alloy*. Materials Science and Engineering: A, 2008. **488**(1-2): p. 296-302.
39. Sercombe, T.B. and G.B. Schaffer, *On the role of magnesium and nitrogen in the infiltration of aluminium by aluminium for rapid prototyping applications*. Acta Materialia, 2004. **52**(10): p.

- 3019-3025.
40. Suárez-Peña, B. and J. Asensio-Lozano, *Microstructure and mechanical property developments in Al-12Si gravity die castings after Ti and/or Sr additions*. Materials Characterization, 2006. **57**(4–5): p. 218-226.

Table 1. Summary of the characteristics of the Al-12Si powder

Composition (wt %)				Particle size (μm)			Flowability (s/50g)	Apparent density (%)
Al	Si	Fe	Cu	d_{10}	d_{50}	d_{90}	21.0	55.8
Bal	12.2	0.12	0.003	27	38	51		

Table 2. Comparison of the tensile properties for the Al-12Si alloys produced using selective laser melting under purity argon, nitrogen and helium (laser power: 200 W; laser scan speed: 500 mm/s) and by conventional casting method: yield strength $\sigma_{0.2}$, ultimate tensile strength σ_{UTS} and ductility δ . Error bars show one standard deviation. The load was applied perpendicular to the build direction (see Figure 2).

Processing methods	Density (%)	$\sigma_{0.2}$ (MPa)	σ_{UTS} (MPa)	δ (%)	Reference
SLM under N ₂	97.8±0.4	224±7	368±11	4.8±0.6	This work
SLM under Ar	97.5±0.3	223±11	355±8	4.2±0.6	This work
SLM under He	97.1±0.4	221±11	342±43	1.5±0.4	This work
Die casting	-	145	300	2.5	[40]

Table 3. Nitrogen content of the powder and SLM'ed parts produced at an energy density of 53 J/mm³ (at the laser speed of 500 mm/s). No significant difference in the nitrogen content was measured. Three samples were analysed for each condition and the error in the measurement as ±0.01 wt%.

Processing methods	Nitrogen content (wt%)
Powder	<0.01
SLM under N ₂	0.01
SLM under Ar	<0.01
SLM under He	0.02

Figure Captions

Figure 1. Scanning electron micrograph of the Al-12Si powder used.

Figure 2. Orientation of the tensile bar relative to the building direction.

Figure 3. Relative density of the SLM-produced Al-12Si samples as a function of incident laser energy. There is a general trend of increasing density with laser energy density, up to $\sim 30\text{J/mm}^3$, after which the density plateaus. There is no significant difference between the three atmospheres. Individual points are an average of 3 tests and error bars show one standard deviation.

Figure 4. The effect of laser energy density on the hardness of SLM-produced Al-12Si in Ar, N₂ and He atmospheres. Similar to Fig. 2, the hardness increases with energy density and there is no significant difference between atmospheres. Individual points are an average of 12 tests. Error bars show one standard deviation.

Figure 5. Optical microstructures of the parts manufactured under argon (a) and (b), nitrogen (c) and (d) and helium (f-g) and an energy density of 53 J/mm³ (500mm/s). With the exception of some areas containing high levels of porosity (g), there is no difference between the microstructures.

Figure 6. Tensile properties of the SLM-produced Al-12Si samples under argon, nitrogen and helium. ($\sigma_{0.2}$: yield strength, σ_{UTS} : ultimate tensile strength). There is no difference between the properties of the Ar and N₂ produced samples. For those manufactured in He, the ductility and ultimate tensile strength are significantly reduced.

Figure 7. Fracture surfaces of the Al-12Si samples produced using different

atmosphere (nitrogen, argon and helium). It is apparent that under He, there is significantly more porosity of the fracture surface than in the other two atmospheres.

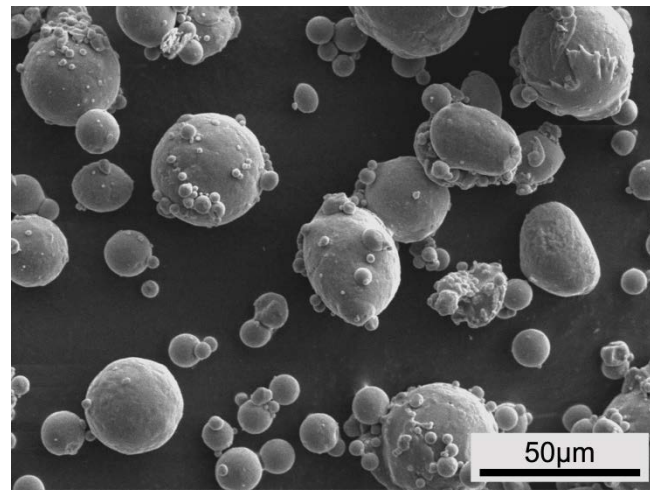


Fig. 1. X.J. Wang et al.

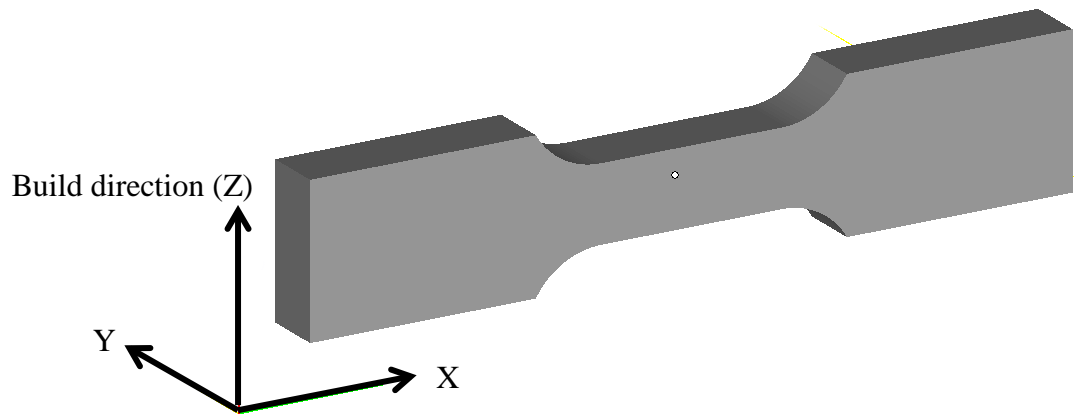


Fig. 2. X.J. Wang et al

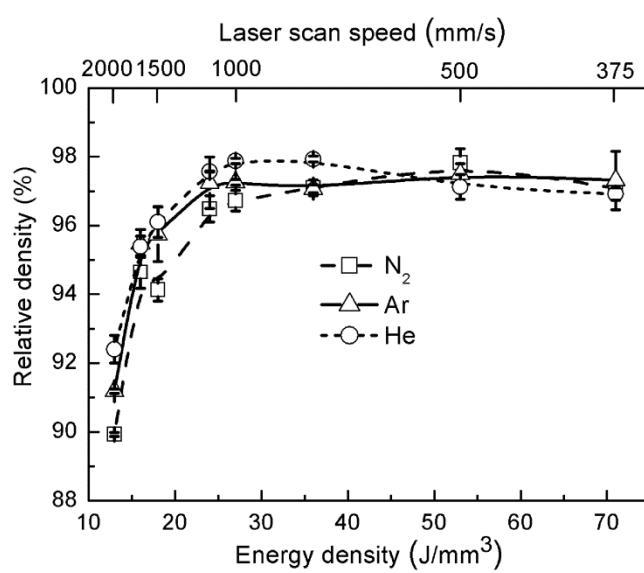


Fig. 3. X.J. Wang *et al.*

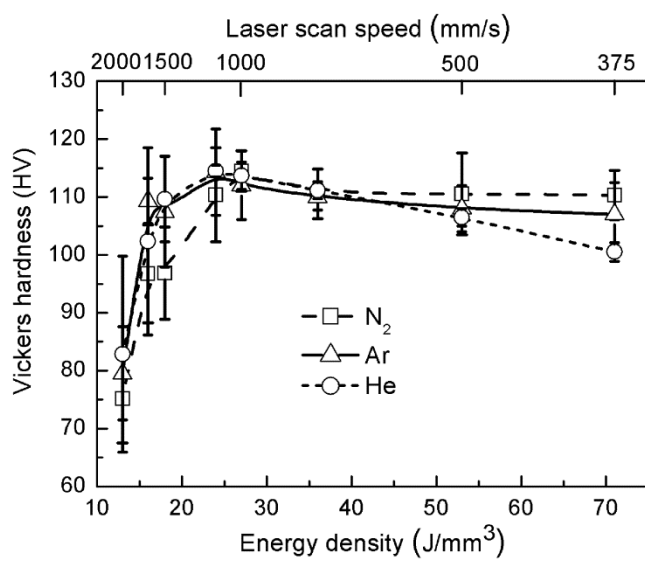
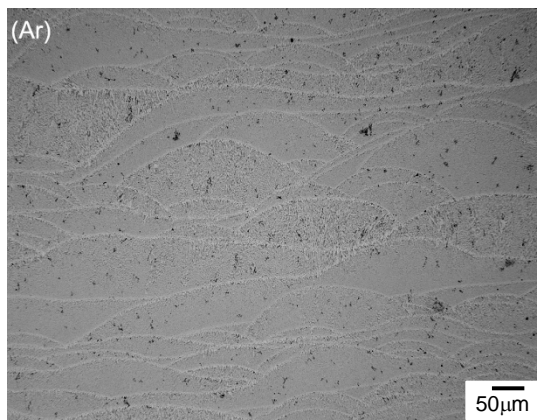
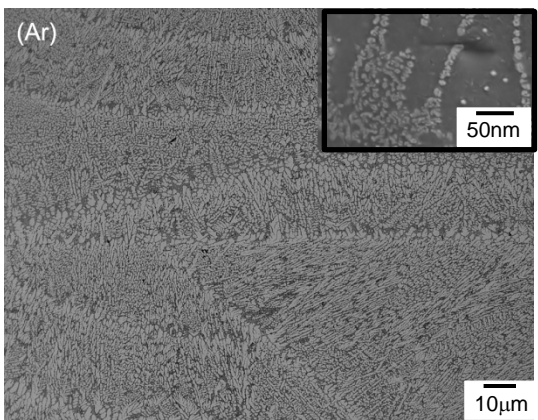


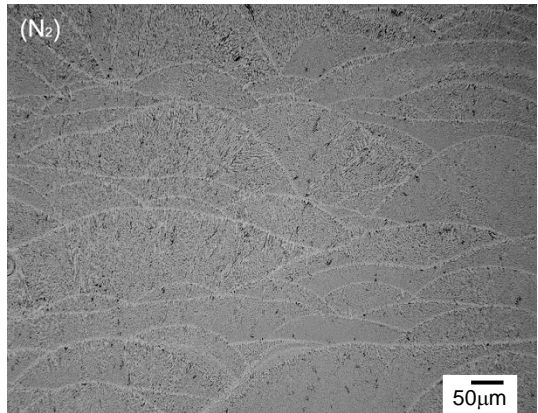
Fig. 4. X.J. Wang *et al.*



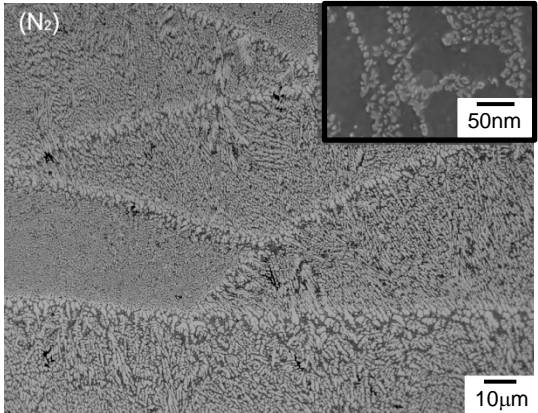
(a)



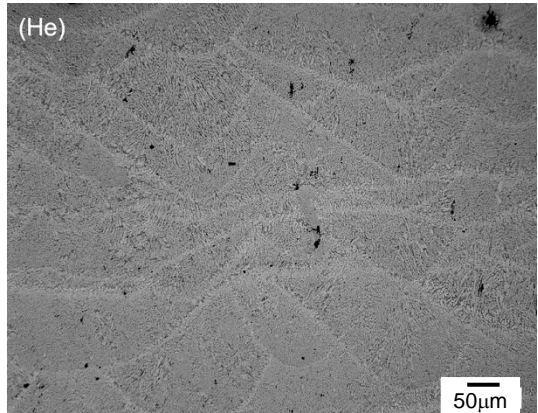
(b)



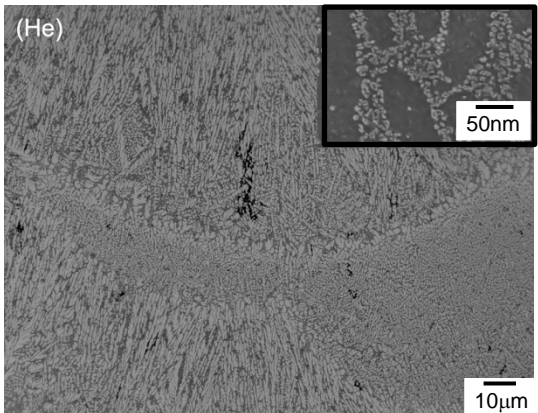
(c)



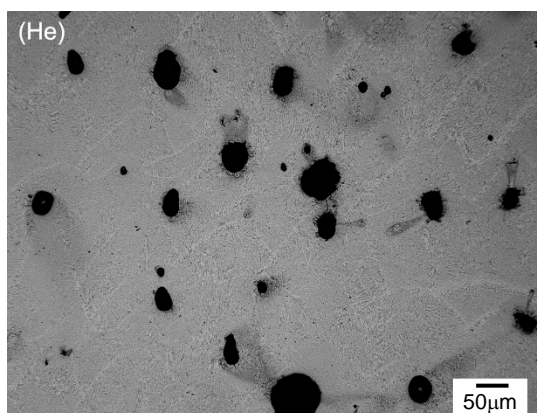
(d)



(e)



(f)



(g)

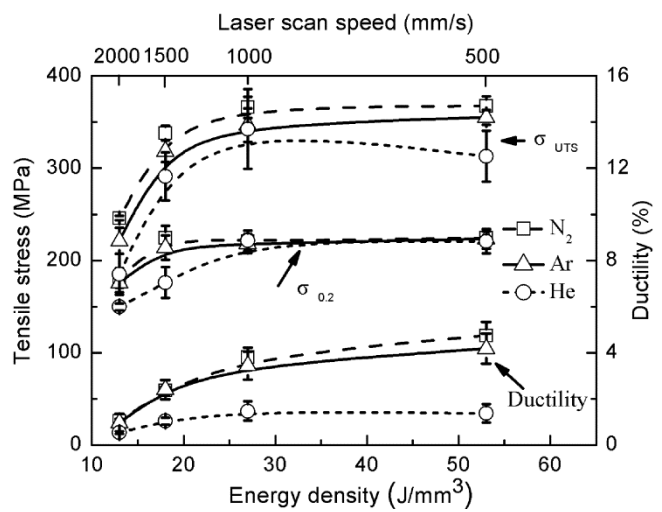


Fig. 6. X.J. Wang *et al.*

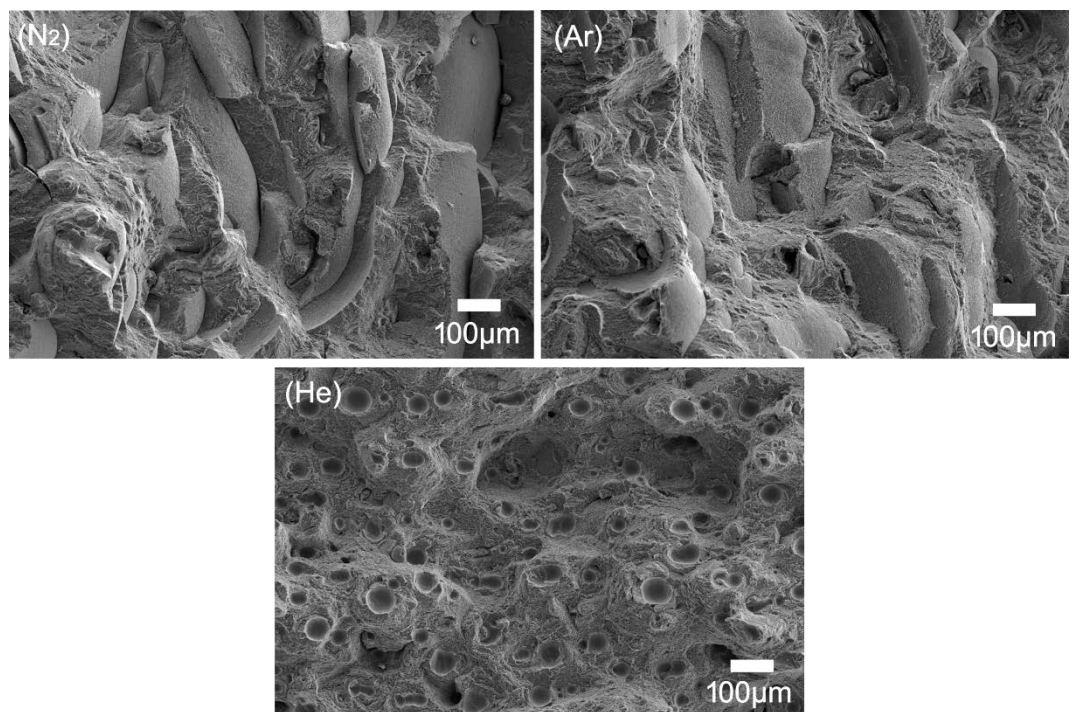


Fig. 7. X.J. Wang *et al.*